



Universität Hamburg
DER FORSCHUNG | DER LEHRE | DER BILDUNG

Development of Crown-ether Based Materials for Selective Harvesting of Lithium from Aqueous Resources

Dissertation



submitted by
Iklima Oral
Hamburg 2022

Faculty of Mathematics, Informatics, and Natural Science
Department of Chemistry

in conformity with requirements for
the degree of *Doctor rerum naturalium* (Dr. rer. nat.)
submitted to the Universität Hamburg

"The roots of education are bitter, but the fruit is sweet"
-Aristotle-

Supervisor: Prof. Dr. Volker Abetz
1st Referee: Prof. Dr. Volker Abetz
2nd Referee: Prof. Dr. Horst Weller

Defense Committee:
Prof. Dr. Volker Abetz
Prof. Dr. Wolfgang Maison
Prof. Dr. Michael Steiger

Date of Oral Defense: 09.12.2022

The submitted dissertation was prepared under the supervision of Prof. Dr. Volker Abetz at the Institute of Physical Chemistry (Chemistry Department, MIN Faculty) of the Universität Hamburg. The work on the PhD was conducted from September 2018 to April 2022. The dissertation was submitted in September 2022.

This dissertation is submitted as a cumulative thesis. It thus contains reprints of the five first-author Publications which include the main results of the work on this thesis (Chapter 5). Except for Publication 2, which was prepared by equal contributions of Sabrina Tamm (Universität Hamburg) and me, all Publications were mainly prepared by me with the assistance of the coauthors as indicated in Chapter 5 and 6. The contributions of coworkers to the presented unpublished results (Chapter 6) are acknowledged at the relevant positions in this dissertation as well.

Publications

This cumulative theses includes reprints of the five first-author publications that have been published prior to this dissertation. These appear in their original form in Chapter 5. An overview is given in the following.

1.) Thermodynamic Study of Crown Ether-Lithium/Magnesium Complexes based on Benz-1,4-Dioxane and its Homologues

Iklima Oral, Fanny Ott, and Volker Abetz

Phys. Chem. Chem. Phys. **2022**, *24*, 11687-11695.

doi.org/10.1039/D2CP01076C

2.) Lithium Selectivity of Crown Ethers: The Effect of Heteroatoms and Cavity Size

Iklima Oral,* Sabrina Tamm,* Carmen Herrmann and Volker Abetz

*: both authors contributed equally to this project

Separation and Purification Technology **2022**, *294*, 121142.

doi.org/10.1016/j.seppur.2022.121142

3.) Synthesis of Poly(methacrylic acid)-*block*-Polystyrene Diblock Copolymers at High Solid Contents via RAFT Emulsion Polymerization

Iklima Oral, Larissa Grossmann, Elena Fedorenko, Jana Struck, and Volker Abetz

Polymers **2021**, *13*, 3675.

doi.org/10.3390/polym13213675

4.) A Highly Selective Polymer Material using Benzo-9-crown-3 for the Extraction of Lithium in Presence of Other Interfering Alkali Metal Ions.

Iklima Oral and Volker Abetz

Macromol. Rapid Commun. **2021**, *42*, 2000746.

doi.org/10.1002/marc.202000746

5.) Improved Alkali Metal Ion Capturing utilizing Crown Ether-based Diblock Copolymers in a Sandwich-type Complexation

Iklima Oral and Volker Abetz

Soft Matter **2022**, *18*, 934.

doi.org/10.1039/d1sm01815a

Abbreviations

12C4	12-crown-4
14C4	14-crown-4
15C5	15-crown-5
18C6	18-crown-6
1A12C4	1-aza-12-crown-4
9C3	9-crown-3
AB15C5	1-aza-benzo-15-crown-5
bc	after complexation
AFM	atomic force microscopy
Al³⁺	aluminium (III)
AO	atomic orbital
AP	acetophenone
ATRP	atom transfer radical polymerization
Ar	argon
B9C3	benzo-9-crown-3
B12C4	benzo-12-crown-4
B14C4	benzo-14-crown-4
B15C5	benzo-15-crown-5
bc	before complexation
Bischoffit	MgCl ₂ ·6H ₂ O
BMED	bipolar membrane ED
C-PCM	conductor-like polarizable continuum model
Ca²⁺	calcium
CaCl₂	calcium chloride
CaCO₃	calcium carbonate
CaO	calcium oxide
Carlanit	KMgCl ₃ ·6H ₂ O
CC	creative commons
CDI	capacitive deionization
CE	crown ether

Cl₂	chlorine gas
Cl	chlorine
CMC	critical micelle concentration
CNT	carbon nanotubes
CO₂	carbon dioxide
Co²⁺	cobalt (II)
CrCl₃	chromium(III) chloride
CRP	controlled radical polymerization
Cs⁺	caesium
CTA	chain transfer agent
Cyanex 923[®]	a mixture of four trialkylphosphine oxides
DA12C4	4,10-diaza-12-crown-4
DB12C4	dibenzo-12-crown-4
DB14C4	dibenzo-14-crown-4
DCC	<i>N,N</i> -dicyclohexylcarbodiimide
DCM	dichloromethane
DCU	<i>N,N</i> -dicyclohexylurea
DFT	density functional theory
DL	Desal
DMAP	4-dimethylaminopyridine
DMF	<i>N,N</i> -dimethylformamide
DMSO	dimethyl sulfoxide
DNA	desoxyribonucleic acid
DOX	1,4-Dioxane
ED	electrodialysis
EDTA	ethylenediaminetetraacetic acid
ET	evaporation time
EV	electric vehicle
Fe³⁺	iron (III)
FeCl₃	iron (III) chloride
GGA	generalized gradient approximation
gypsum	CaSO ₄ ·2H ₂ O
H₂SO₄	sulfuric acid
Halit	NaCl
Halit + gypsum	NaCl·CaSO ₄ ·H ₂ O

HBTA	benzoyl-1,1,1-trifluoroacetone
HCl	hydrochloric acid
HCP	hexagonal close packing
HOMO	highest occupied molecular orbital
IEF-PCM	integral equation formalism polarizable continuum model
IEM	ion-exchange membrane
IUPAC	international union of pure and applied chemistry
ISL	intermediate segregation limit
K⁺	potassium
KCl	potassium chloride
LAM	less activated monomer
LDA	local density approximation
Li⁺	lithium
Li₂CO₃	lithium carbonate
Li₂O	lithium oxide
Li₂SO₄	lithium sulfate
LiAlO₂	lithium aluminate
LIBs	lithium-ion batteries
LiCl	lithium chloride
LiFePO₄	lithium iron phosphate
LiMn₂O₄	lithium manganese oxide
LiOH	lithium hydroxide
LIS	lithium ion-sieve
LIX 54	α -acetyl- <i>m</i> -dodecylacetophenone
LLE	liquid-liquid extraction
LMO	lithium manganese oxide
LTO	lithium titanium oxide
LUMO	lowest unoccupied molecular orbital
MAA	meth(acrylic acid)
MAM	most activated monomer
MCDI	membrane capacitive deionization
MIBK	methyl-iso-butyl ketone
Mg²⁺	magnesium
MgCl₂	magnesium chloride
MgO	magnesium oxide

Mg(OH)₂	magnesium hydroxide
Mn³⁺	manganese (III)
MnO₂	manganese oxide
MO	molecular orbital
MOF	metal–organic framework
Na⁺	sodium
Na₂CO₃	sodium carbonate
Na₂SO₄	sodium sulfate
NaCl	sodium chloride
NaClO₄	sodium perchlorate
NAO	natural atomic orbital
NaOH	sodium hydroxide
NBO	natural bond orbital
NF	nanofiltration
NHO	natural hybrid orbital
Ni²⁺	nickel (II)
NIPS	non-solvent induced phase separation
NLMO	natural (semi-)localized molecular orbital
NMP	N-oxide mediated polymerization
PAA	poly(arylic acid)
PCM	polarizable continuum model
PEI	polyetherimide
PES	potential energy surface
PISA	polymerization-induced self-assembly
PLS	pregnant leach solution
PMAA	poly(metharylic acid)
PMAA-<i>b</i>-PS	poly(methacrylic acid)- <i>block</i> -polystyrene
PS	polystyrene
PSMCDI	permselective exchange MCDI
Pt	platinum
RAFT	reversible addition–fragmentation chain transfer
Rb⁺	rubidium
RO	reverse osmosis
RTILs	room temperature ionic liquids

S-ED	selective ED
SCFT	self-consistent field theory
SDS	sodium dodecyl sulfate
SD	slater determinant
SEM	scanning electron microscopy
SF	separation factor
Shellsol[®]D70	an iso-aliphatic non-polar solvent
SNIPS	self-assembly of block copolymers in combination with non-solvent induced phase separation
SSL	strong segregation limit
Sylvinit	NaCl-KCl
Sylvit	KCl
TA12C4	1,4,7,10-tetraazacyclododecane-12-crown-4
TA14C4	1,4,7,10-tetraazacyclotetradecane-14-crown-4
TBP	tributyl phosphate
THF	tetrahydrofuran
TOPO	trioctyl phosphine oxide
TPPO	triphenyl phosphin oxide
UF	ultrafiltration
USA	Unites States of America
UV-vis	ultraviolet-visible
VSEPR	valence shell electron pair repulsion
VOC	volatile organic compounds
WSL	weak segregation limit
ZnCl₂	zinc chloride



Symbols

α	separation factor
δ_d	disperse solubility parameter
δ_h	hydrogen bonding solubility parameter
δ_H	Hildebrand solubility parameter
δ_p	polar solubility parameter
δ_t	total solubility parameter
ΔH^\ominus	enthalpy of reaction
ΔH_{hydr}^0	hydration enthalpy
ΔH_{mix}	molar enthalpy of mixing
ΔG_{mix}	free molar enthalpy of mixing
ΔS^\ominus	entropy of reaction
ΔS_{mix}	molar entropy of mixing
Δ_T	Lydersen correction for non-ideality
ε	relative permittivity of the medium
ε_0	permittivity of the vacuum [$8.854 \cdot 10^{-12} \text{ C V}^{-1}\text{m}^{-1}$]
ε_m	porosity
ε_{LR}	hardness of the interaction in the Lennard-Jones model
η	viscosity
θ	angle between dipole of the point charge and dipole moment
μ	dipole moment
ρ	density
$\rho^{\text{def}}(r)$	deformation density
$\rho^{\text{free}}(r)$	charge density of the atoms
$\rho^{\text{pro}}(r)$	charge density pro molecule
σ_{LJ}	distance between attraction and repulsion = 0
τ	tortuosity
φ	relative twist angle

φ_i	volume fraction of the polymer chain segment of component i
$\chi_{A,B}$	Flory-Huggins-Stavermann interaction parameter
χN	degree of segregation
Ψ	wave function
\AA	Ångström
\mathbf{a}_c	area of the stabilizing chain
$c_{A/B}$	polarization coefficients for atoms A and B
c	concentration
c_p	concentration of the permeate
c_f	concentration of the feed
C_i	contribution of the first-order functional group of type i
C	Coulomb
C_{tr}	transfer constant
D	domain distance
D_i	contribution of the second-order functional group of type i
dq	heat quantity
dw	performed work
E	energy
E_{coh}	molar cohesion energy
E_d	cohesion energy from disperse forces
E_p	cohesion energy from polar forces
$E_{ne}(\rho)$	energy of the electron–nucleus interaction
$E_{ee}(\rho)$	energy of the electron–electron interaction
$E_{KS}(\rho)$	energy of the Kohn-Sham orbitals
E_h	cohesion energy from hydrogen bonding
$E_{XC}(\rho)$	exchange correlation energy
e_j	cohesive energy of a structural group
E_i	cohesive energy of a solvent or polymer
f	initiator efficiency
F_j	molar constant of attraction
F_t	molar constant of polarity
F_t	molar constant of attraction
G	Gibbs energy

$h_{A/B}$	NHOs for atoms A and B
h	hour
H	enthalpy
<i>i</i>	stoichiometric factor of the metal ion
<i>I</i>	initiator
I_s	ionic strength
J	volumetric flux
<i>j</i>	structural groups according to the group contribution theory
$J(\rho)$	functional of the electrostatic repulsion between two electrons
KC	Kozeny-Carman constant
k_i	decomposition rate coefficient on the initiator
kJ	kilo Joule
k_t	termination rate coefficient
k_p	propagation rate coefficient
k_{tr}	transfer rate coefficient
<i>K</i>	equilibrium constant or complex constant
k_B	Boltzmann constant
<i>l</i>	distance of the particle charges
l_c	length of the core forming block
L_p	permeability coefficient
M	metal ion
M_{CTA}	molar mass of the CTA
m_j	number of functional groups in the structure
min	minutes
$M_{n,theo}$	theoretical number average molar mass
M_M	molar mass of the monomer
<i>Mo</i>	monomer
Mt	million tons
<i>n</i>	stoichiometric factor of the CE
<i>N</i>	number of functional groups
N_i	polymerization degree of component <i>i</i>
n_j	number of structural groups <i>j</i> according to the group contribution theory
<i>p</i>	pressure
P	packing parameter

p_c	monomer conversion
ppm	parts per million
P_n / P_m	propagating radical
q_1, q_2	elementary charges of the ions [$\pm 1.605 \cdot 10^{-19}$ C per positive or negative charge]
Q	stoichiometric factor of the used salts
r	distance
R	radical
R	gas constant
R_a	distance to correlate partial solubility parameters
rpm	rounds per minute
R_t	retention
r_m	membrane pore radius
SA	internal surface
S	entropy
$t\Delta_g U$	molar energy of vaporization
$t\Delta_\infty U$	molar energy of separation
t	tons
T	temperature
T_b	boiling point
T_{cr}	critical temperature
$T_k(\rho)$	kinetic energy of the electrons
$T_{SD}(\rho)$	total wave function composed of N orbitals calculated by the slater determinant
TWh	terawatt-hours
v	charge of the anion
U	internal energy
V	volume
V	Volt
$v(\vec{r})$	external potential function
$v_{eff}(\vec{r})$	effective potential function
V_i	molar volume of i
V_{LJ}	Lennard-Jones potential
$v_{xc}(\vec{r})$	exchange–correlation potential
W	constant according to the group contribution theory

w_i^{Hirsh}	Hirshfeld weighting factor
x_m	membrane thickness
y	stoichiometric factor of the anion
\mathbf{Y}	anion
z	charge of the cation
z_1	nearest neighbor in the lattice model



Contents

Abbreviations	iii
Symbols	ix
1 Zusammenfassung	1
2 Abstract	5
3 Introduction	9
3.1 The high demand for energy - a curse or a blessing?	11
3.2 Lithium – <i>the white gold</i>	18
3.2.1 The worldwide lithium reserves	20
3.2.2 Lithium recovery	23
3.2.2.1 Lithium from ores	23
3.2.2.2 Lithium from brines and seawater	28
3.3 Supramolecular chemistry	50
3.3.1 Nature of supramolecular interactions	52
3.3.1.1 Ion–ion interaction	53
3.3.1.2 Ion–dipole interaction	54
3.3.1.3 Dipole–dipole interaction	56
3.3.1.4 Hydrogen bonding	57
3.3.1.5 Halogen bonding	62
3.3.1.6 Cation– π interactions	64
3.3.1.7 Anion– π interactions	66
3.3.1.8 Aromatic–aromatic interactions	67
3.3.1.9 Dispersion interactions	69
3.3.2 Crown ethers	70
3.4 Electronic structure calculations	82
3.4.1 Density functional theory	83
3.4.1.1 Hohenberg-Kohn and Kohn-Sham theorems	84
3.4.1.2 Exchange–correlation potential	87
3.4.1.3 Molecular structure optimization	88
3.4.1.4 Hirshfeld population analysis	89
3.4.1.5 Natural bond orbital analysis	90

3.4.1.6	Solvent models	91
3.5	Lithium selective polymer materials	93
3.5.1	Polymers	93
3.5.2	Radical polymerization	94
3.5.3	Controlled radical polymerization	96
3.5.4	The RAFT polymerization	97
3.5.5	RAFT emulsion polymerization	105
3.5.6	Post-modification of polymers	110
3.6	Thermodynamics of block copolymers	115
3.7	Solubility parameters	119
3.7.1	Hildebrand solubility parameters	120
3.7.2	Hansen solubility parameters	123
3.7.3	Hoy solubility parameters	125
3.7.4	Flory-Huggins-Staverman interaction parameter according to Hansen	128
3.8	Membranes	131
3.8.1	Definition and properties of membranes	131
3.8.2	Membrane fabrication	136
3.8.2.1	Non-solvent-induced phase separation	136
3.8.2.2	Self-assembly of block copolymers and non-solvent-induced phase separation	139
4	Objective of this Work	143
5	Published Results	147
5.1	Publication 1:	147
5.2	Publication 2:	158
5.3	Publication 3:	171
5.4	Publication 4:	192
5.5	Publication 5:	205
6	Unpublished Results	211
6.1	Aza crown ethers: The effect on lithium complexation using different cavity sizes and donor atoms	211
6.1.1	Experimental section	216
6.1.1.1	Materials	216
6.2	Membrane fabrication	217
6.2.1	Determination of the solubility properties of unknown polymer structures	217
6.2.1.1	Hansen solubility parameters	218
6.2.1.2	Hoy solubility parameters	220
6.2.1.3	Evaluation of partial solubility parameters according to Hansen and Hoy	223

6.2.1.4	Flory–Huggins–Staverman interaction parameters	225
6.2.2	PMAA- <i>b</i> -PS membranes	229
6.2.3	First attempts on the fabrication of lithium adsorber membranes . . .	238
6.2.4	Experimental section	241
6.2.4.1	Materials	241
6.2.4.2	Membrane preparation	241
6.2.4.3	Membrane characterization	242
7	Discussion	243
7.1	Review of the investigated crown ethers	243
7.2	Predicting crown ether–cation complexes using density functional theory . . .	245
7.3	Review on polymer-based lithium adsorber	246
7.4	Outlook	249
8	References	253
9	Appendix	281
9.1	Authors contributions to the publications	281
9.2	Supporting information of publication 1	284
9.3	Supporting information of publication 2	295
9.4	Supporting information of publication 3	313
9.5	Supporting information of publication 4	325
9.6	Supporting information of publication 5	337
9.7	Solubility parameters	344
9.8	Safety	352
10	Acknowledgments	363
11	Eidesstattliche Versicherung	369

Zusammenfassung

Lithium, der Hauptrohstoff der Lithium-Ionen Batterien – dem Herzstück der nachhaltigen Automobilbranche und portable Elektrogeräte – ist ein weltweit begehrtes Metall, dessen Nachfrage und Preis stetig wachsen. Ein Großteil des Lithiums befindet sich in wässrigen Ressourcen wie in Salzseen, in Ozeanen, oder in Geothermalwasser. Lithium ist weltweit verfügbar, jedoch gibt es bis heute keine umweltfreundliche und unbedenkliche Extraktionsmethode von Lithium. Viele momentan gebräuchliche Methoden, besonders in Südamerika, stehen aufgrund dieser nicht nachhaltigen Durchführung zurecht in der Kritik. Damit die Elektromobilbranche weiterhin einen positiven Einfluss auf die Umweltprobleme in dieser Welt nehmen kann, muss die Nachfrage an Lithium weiterhin gesättigt werden. In dieser Arbeit wird ein Lithium-selektives Polymermaterial hergestellt, um die Extraktion von Lithium aus wässrigen Quellen zu vereinfachen und ökonomisch sowie ökologisch sinnvoller zu gestalten. Zielanwendung dieses Materials liegt in der Lithiumextraktion aus den Weltmeeren, da dort über 230 Milliarden Tonnen (und damit ein Vielfaches der an Land als Feststoff vorkommenden Ressourcen) verfügbar sind.¹

Kronenether eignen sich besonders gut als organische Lithiumadsorbermaterialien. Diese können in vielen unterschiedlichen Ringgrößen und Strukturen vorliegen und sind dadurch intrinsisch selektiv gegenüber einer Bandbreite von Metallionen. Im ersten Teil dieser Arbeit werden unterschiedliche Kronenetherstrukturen untersucht und der Einfluss der Ringmodifikation auf die Alkali- und Erdalkimetallextraktion beschrieben. Dabei wurden Kronenethergrößen variiert, verschiedene Donoratome im Kronenetherring untersucht, Stöchiometrien der Komplexe analysiert und thermodynamische Parameter wie die Komplexbildungskonstante, Entropie und Enthalpie bestimmt. Es wurde gezeigt, dass besonders *Sandwich* Komplexe (bestehend aus zwei Kronenether und einem Metallion), starke Komplezierungen mit Metallionen ausbilden. Die Hydrophilie der Kronenether sowie eine passende Käfiggröße (14-gliedrige Kronenether) unterstützen die Selektivität der Lithiumextraktion gegenüber anderen Metallionen.

Da die synthetische Modifikation von Kronenethern oft anspruchsvoll und zeitintensiv sein kann, wurden computerchemische Kalkulationen auf Basis der Dichtefunktionaltheorie (DFT) unterstützend durchgeführt, um weitere Kronenether sowie deren Elektronendichteverteilungen und Komplexbildungskonstanten theoretisch zu berechnen. Zusätzlich wurde die Vergleich-

barkeit der kalkulierten Trends anhand eines praktischen Beispiels verglichen. Dabei zeigte sich, dass die theoretischen Berechnung zwar höhere Komplexbildungskonstanten ergaben, der Trend der Komplexstabilität mit dem zugehörigen Metallion jedoch gut übereinstimmte.

Ein weiterer großer Hauptbestandteil dieser Arbeit war die Synthese von einem Polymethacrylsäure-*block*-Polystyrol (PMAA-*b*-PS) Diblockcopolymer, dessen Herstellung industriell im großen Maßstab realisiert werden kann. Dabei fiel die Wahl auf dieses Polymer, da über die Säuregruppe der Methacrylsäure eine Post-Modifizierung mit einem passenden Kronenether an das Polymer realisiert werden kann. Das PMAA-*b*-PS Polymer wurde mittels Reversibler Additions-Fragmentierungs Kettenübertragungspolymerisation (RAFT) in Emulsion in einer zweistufigen *one-pot* Synthese hergestellt. Die Polymerisation erfolgte in Wasser als kontinuierliche Phase mit einer Gesamtfeststoffkonzentration von 50 wt%; dabei konnten Polymerketten von bis zu 170 kDa mit engen Molmassenverteilungen von $D \approx 1.4$ hergestellt werden. Die Vorteile einer solchen Methode sind offenkundig: Die Monomere sind großtechnisch gut verfügbar und Wasser als Reaktionsmedium ist unbedenklich und lokal verfügbar. Zudem erlaubt der hohe Feststoffgehalt eine wirtschaftliche Herstellung und eine einfachere Isolation des Endproduktes. Im Anschluss an die Synthese des Polymers wurden die Kronenether mittels einer Veresterungsreaktion nach Steglich an das PMAA-*b*-PS Diblockcopolymer verknüpft. Es wurden drei verschiedene polymerbasierte Kronenethermaterialien hergestellt bestehend aus einem neungliedrigen Benzo-9-Krone-3, einem 12-Krone-4 und einem 15-Krone-5 Kronenether. Für diese Polymere wurden die Extraktionseigenschaften für die Ionen Lithium, Natrium und Kalium untersucht. Dabei zeigten sich um mindestens 10000 fach höhere Komplexbildungskonstanten des modifizierten Polymers im Vergleich zu dem zugehörigen freien Kronenether. Die außergewöhnlichen Stabilitäten der Komplexe sind auf den geringen Entropieverlust bei Komplexbildung zurückzuführen, der durch bereits lokal gebundene Kronenether entsteht.

Um die Extraktionseigenschaften der polymerbasierten Kronenether weiter zu erhöhen, wurden diese in eine Membranstruktur überführt. Zuerst wurde dafür das Grundpolymer PMAA-*b*-PS mittels einer *Selbstorganisation von Diblockcopolymeren in Kombination mit Nicht-Lösungsmittel induzierter Phasenseparation* in eine asymmetrische, hexagonal angeordnete Zylinderstrukturmembran gebracht. Hierfür wurde reines 1,4-Dioxan als Lösungsmittel für die Gießlösung und Wasser als Fällungsbad verwendet. Der Vorteil von solchen asymmetrischen Membranen ist die Erhöhung der Gesamtoberfläche durch räumliche Anordnung der nanoskopischen, extraktionsfähigen Einheiten. Polystyrol dient der Gesamtstruktur lediglich für deren mechanische Festigkeit, um eine möglichst lange Stabilität und damit Haltbarkeit der Polymermembran zu gewährleisten. Zur Unterstützung der Herstellung von Polymermembranen dieses unbekanntes Systems wurden zuvor Löslichkeitsparameter nach Hansen und Hoy bestimmt und die Mischbarkeit mit Lösungsmitteln vorhergesagt. Erste Versuche zur Membranherstellung eines mit 12-Krone-4 Kronenether modifizierten Diblockcopolymers ergaben bereits vielversprechende Membranstrukturen.

Abstract

Lithium, the primary raw material of lithium-ion batteries – the most crucial part within the development of a more sustainable electromobility – is a globally coveted and precious metal whose demand and price are constantly growing. Lithium is found in aqueous resources such as salt lakes, oceans, and geothermal water. Lithium is available worldwide but until today there is no environmentally friendly and safe extraction method for lithium at hand. Many methods, especially in the South American regions, are pilloried by local residents because of their uneconomic and ecologically dubious conduct. In order to thrive for the whole electromobility sector and continue to at least push society towards a more sustainable mindset (for which this work is partially dedicated), the demand for lithium needs to be covered (which is for sure not the only way, but a step into the right direction). Hence, a polymer-based material is studied within this dissertation that selectively complexes lithium and thus could be used in the extraction of lithium from aqueous resources. The target application of this material will be lithium extraction from oceans, as over 230 billion tons (and therefore much more than on land) are available in these waters.¹

In this work, crown ethers (CEs) were chosen as an organic lithium-adsorbent material. These can exist in many different structures, allowing selectivity for a wide range of metal ions. In the first part of this work, different CE structures are investigated, and the influence of their modification on the alkali and alkaline earth metal extraction is described. CE sizes were varied, different donor atoms in the CE ring were investigated, stoichiometries of the complexes were analyzed, and thermodynamic parameters such as the complexation constant, entropy and enthalpy were determined. It was shown that especially sandwich complexes (consisting of two CEs and one metal ion) form strong complexations with metal ions. The hydrophilicity of the CEs and a fitting cavity size (14-membered CEs) support the selectivity of lithium in favor of other metal ions.

Since the modification of CEs can often be challenging and time-consuming supporting computational chemistry calculations based on density functional theory (DFT) were performed to determine CE structure geometries, their electron density distributions, and other physical parameters such as the complexation constant K . In addition, the comparability of the calculated trends was compared for a practical example. It was found that the theoretical calculation often yielded to higher complexation constants than the synthetic example, yet,

the trend of complex stability was in good agreement with the experiment.

Another significant portion of this work was focused on the synthesis of a poly(methacrylic acid)-*block*-polystyrene (PMAA-*b*-PS) diblock copolymer, the preparation of which can be realized industrially on a large scale. This polymer was chosen because the meth(acrylic acid) (MAA) group allows post-modification in which the CEs can be linked to the polymer. The PMAA-*b*-PS polymer was prepared by reversible addition-fragmentation chain transfer (RAFT) polymerization in emulsion in a two-step but one-pot approach. The polymerization was carried out using water as a continuous phase at a total solids concentration of 50 wt%, producing polymer chains of up to 170 kDa with narrow molecular weight distributions of $D \approx 1.4$. This approach has several advantages: The monomers are readily available also in large quantities, water is a locally sourced and harmless liquid, and the high solids content allows for an economic production also facilitating facile isolation of the final product. Subsequently, after the synthesis of the base polymer, the CEs were linked to the PMAA-*b*-PS diblock copolymer using a Steglich esterification reaction. Three different polymer-based CE materials were prepared: a 9-membered benzo-9-crown-3 (B9C3), a 12-crown-4 (12C4), and a 15-crown-5 (15C5) polymer CE. For these polymers, the extraction properties of the ions of lithium, sodium, and potassium were investigated. The complex constants were much higher than the corresponding free CE. The uniquely stable properties of the CEs are caused by a low entropy loss during complex formation as the CEs are already bound to the polymer backbone.

To further enhance the extraction strength of the polymer-based CEs, they were fabricated in membranes. First, the base polymer PMAA-*b*-PS was transformed into an integral asymmetric membrane with hexagonally-packed cylinders using a self-assembly of block copolymers in combination with non-solvent induced phase separation (SNIPS). For this purpose, pure 1,4-Dioxane (DOX) was used as a solvent for the casting solution and water was used as a precipitation bath. The advantage of such asymmetric membranes is the ordered spatial arrangement of the nanoscopic extractable unit and thus an increased total surface area. Polystyrene (PS) serves as mechanical support for the membrane to ensure mechanical stability and durability. To further assist the preparation of polymer membranes of this unknown system solubility parameters according to Hansen and Hoy were determined, and the miscibility with solvents was predicted. These initial experiments on membrane preparation of a 12C4 CE functionalized diblock copolymer were already promising and build the basis for future work.

Introduction

This Chapter explains the topics and objectives of the Publications in Chapter 5 and the unpublished results in Chapter 6 and is divided into eight Sections. In the first Section, 3.1, energy and its impact on humanity and the environment are framed. Section 3.2 explains the features of lithium ions (the raw material of a promising energy storage medium) and their current extraction techniques. In Section 3.3 the topic of supramolecular chemistry is introduced, different adsorber materials and their extractability towards metal ions is discussed. This background information explains the selection of adsorbers in Publications 1, 2, 4, and 5. Section 3.4 discusses the simulation of electronic structure calculations, which can be a promising tool for the selection of proper adsorber materials for metal ions (publication 2). In Section 3.5, selective lithium polymer-based materials are discussed. The preparation of such systems is presented in more detail, combining polymerization techniques such as RAFT and emulsion polymerization (publication 4 and 5). In Section 3.6, the thermodynamics of block copolymers is summarized. Section 3.7. frames the solubility behavior of block copolymers and the most relevant theories. In the last Section, 3.8, the theoretical aspects of a membrane, which is the target material in this thesis for lithium extraction, are described (Chapter 6: unpublished results).

To gain your energy from the right sources means you gain more energy from less; reducing the retarding factors means you have less friction that wastes your energy; focusing your motive power towards the direction of the collective human movement means you use others' energy to boost your energy.

Gain more energy, waste less energy, spend the energy so next time you'll need less to achieve more. Increase human mass, reduce retarding force, and increase the force accelerating the human mass. Follow this process with reason.

Gain more, waste less, spend efficiently, learn.

-Nikola Tesla-

3.1 The high demand for energy - a curse or a blessing?

When we think about energy, we usually imagine factories, pollution, or political and military wars. Nowadays, we typically associate energy with something negative, but today's life demands a lot of energy and there are also a lot of advantages. However, before these points are described in detail, the definition of energy will be explained in the following.

Energy is a word with various meanings. Scientists describe it as a quantity that is transferred to an object to perform work on it or induce a temperature change in it. Energy comes in many forms such as heat, light, inertial, electrical, chemical, and gravitational energy, grouped into potential/stored energy or kinetic/working energy. Energy forms can be transformed into each other, however the total amount of energy remains the same in the universe. Thus, when energy is consumed, it is not destroyed but only transformed. This means that energy can neither be produced from nothing nor destroyed to nothing (*first law of thermodynamics*). For instance, when we are using a gasoline-fueled car to drive, the car engine burns gasoline, converting chemical energy (of the gasoline) to mechanical energy (of the pistons in the engine) and heat; the mechanical energy part is eventually transformed into inertial energy – the car moves.^{2,3}

Economically, the term energy production is often used, which is physically impossible according to the *law of conservation of energy*. In an economical way, it refers to the conversion of, e.g., electrical energy into chemical energy. Likewise, energy consumption is not physically correct. Still, it is nevertheless used in the economic sense to describe the transition from usable primary energy to a form of energy that can no longer be used (e.g., waste heat in the environment), which is physically called entropy increase. In the following, the terms energy consumption and energy production are used in the economic sense.

Life without energy can no longer be imagined in today's world. Our society is highly dependent on it, and its demand will not stop, as it is needed anytime and anywhere. In Figure 3.1, the primary energy consumption in the world is presented, highlighting some big economies like China, USA, Europe, and exclusively Germany. Primary energy defines the energy content from natural sources. These include, for example, hard coal and lignite, crude oil, natural gas, solar energy, wind power, hydropower, and geothermal energy. Since 1990, the worldwide energy consumption has increased by up to 58 %. China is one of the leading economies whose consumption has more than tripled since 2000 (Figure 3.1 right) to almost 40.000 terawatt-hours (TWh). The second largest energy consumer are the United States of America (USA), with a consumption of over 25.000 TWh. Europe's energy consumption has remained almost constant over the years. Similar to Germany, where energy consumption has fallen very little since 1990.⁴

The countries huge energy needs show that access to safe, clean, economical, and local energy production is essential since dependence on energy sources from abroad is a significant risk for every country and could endanger national security as it was shown in recent political events such as the Iranian revolution of 1979, the Persian Gulf War of 1991, the Iraq invasion

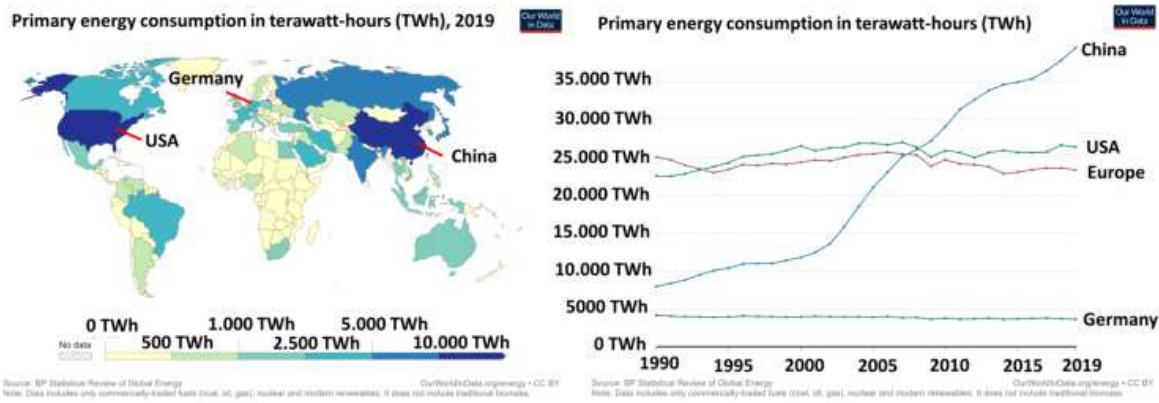


Figure 3.1: Primary energy consumption in TWh in the world in 2019 (left) and in China, USA, Germany, and Europe from 1990-2019 (right). This image is licensed by creative commons (CC) attribution 4.0 international public license. Labels were enlarged and the countries themselves were labeled.⁴

of 2003, or Russia's attack on Ukraine in 2022. Moreover, the high energy consumption over the years brought some disadvantages for the environment, such as global warming, acid rain, and radioactive waste.⁵⁻⁷

But where does the energy that is being used actually come from? The energy content available to humankind is called the energy base. This consists of energy reserves (mostly finite) and energy sources (regenerative/renewable). Energy reserves are divided into fossil and recent reserves. Fossil energy supplies are based on biological or organic compounds derived from dead plant or animal matter – for example, coal, lignite, natural gas, or crude oil – are based on mineral deposits resulting from very early phases of the earth's creation such as energy contents of uranium deposits and nuclear fusion feedstock. Recent reserves cannot be changed by humans and are based on physical-chemical reactions such as the energy content of biomass. In principle, renewable energy is defined as inexhaustible (wind energy, hydropower, or biomass). Energy sources provide energy for a very long period of time compared to energy reserves. The term regenerative is used extensively in the outside world. Still, strictly speaking, the term regenerative applies only to naturally occurring renewable primary energies and not to the resulting secondary or final energies or carriers. For example, electricity generated such as from wind energy is not called renewable because it is only available as long as the corresponding conversion plant is in operation. Nevertheless, it is often referred to as regenerative electricity, which, strictly speaking, would not be correct.²

In Germany, mineral oil is still one of the most consumed primary energy sources, followed by natural gas, renewable energies, hard coal and lignite, and nuclear energy. The share of mineral oil has remained relatively constant over the last 20 years, while the share of natural gas and renewable energies has increased since 1990 from 15 to 27 % and 1.3 to 16 %, respectively (Figure 3.2).⁸

With the recently declared war from Russia (or at least its president) on Ukraine, a major energy supplier for Germany is uncertain. After all, besides the Netherlands and Norway,

Russia is the dominant natural gas supplier for Germany with over 50 %. A possible supply freeze from Russia would jeopardize the energy supply, especially in winter. The best solution is the use of renewable energy. Therefore, the development of these technologies should have the highest priority to secure the country's energy needs. This is especially important for electricity generation. The green power supply has increased to 6 % in 2000 and 46 % in 2020. The goal is to generate 40-45 % of electricity from renewable sources by 2025. A comparison of electricity generation in 2018 is shown in Figure 3.3. Wind and solar energy make up the most significant contribution, but these energies are highly weather-dependent, followed by biomass and hydropower.⁹

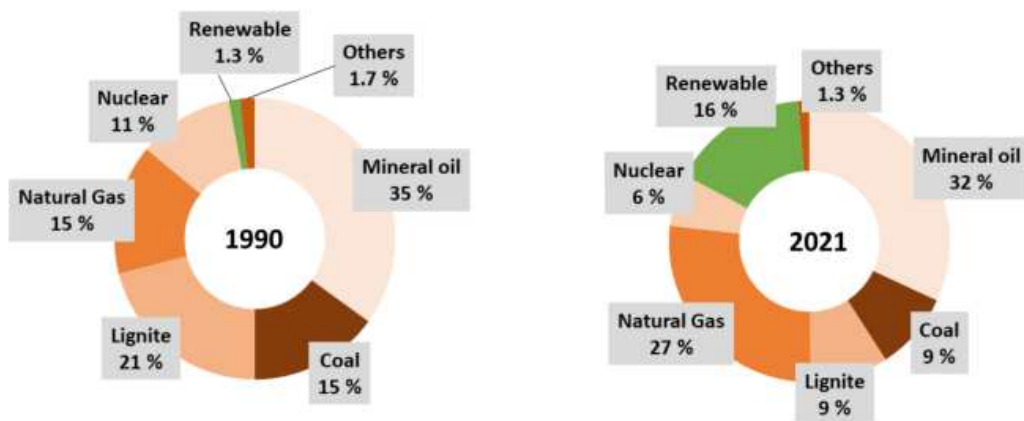


Figure 3.2: Primary energy consumption in Germany 1990 (left) and 2021 (right). The data was taken from AG Energiebilanz and the illustration was reproduced with permission from the *Umweltbundesamt*.^{8,10}

With the recent events, power system flexibility and location independency to adapt to the power supply and demand changes become more essential. The development of better storage technologies is one of the solutions to enable energy security during low productions, high demands, or extraordinary events such as military invasions. In particular, electrochemical energy storage is one of the most promising systems and is, therefore, one of the fastest-growing segments delivering uninterrupted power supply and load-shifting capacity. The battery is one of the most widely used electrical energy storage devices besides the fuel cell. They are used extensively in everyday life since they can store a high amount of energy in a relatively small mass and volume. Electrochemical capacitors also known as super capacitors are another leading candidate, which store higher energy than conventional capacitors and deliver it faster (within seconds) than batteries. Nonetheless, the specific energy needs to be improved to compete with the performance of batteries. In Figure 3.4, the Ragone plot, which presents energy storing devices to compare the energy density, is illustrated with the battery storage

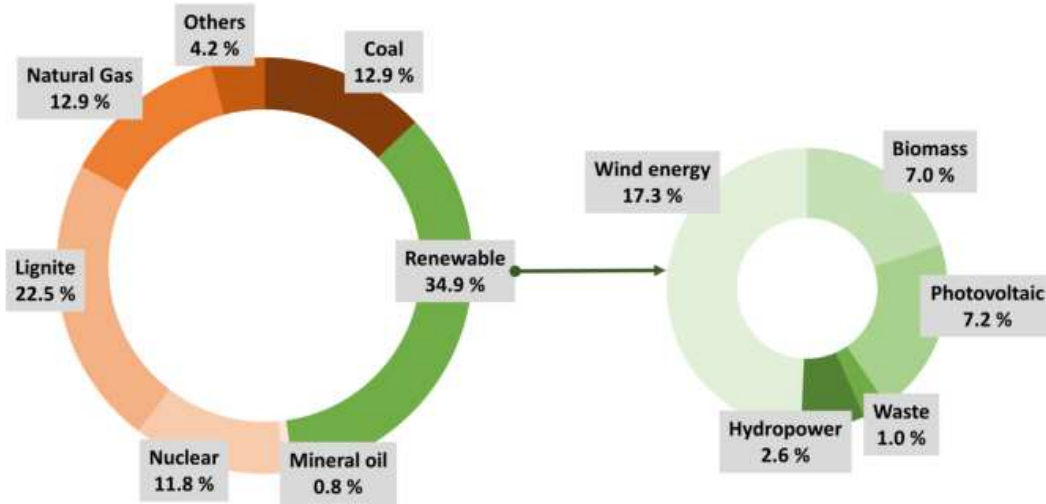


Figure 3.3: Energy balance of electricity generation in Germany (left) and the renewable share used (right) in 2018. Due to the still very low amount of geothermal energy it is combined in the part of photovoltaic. Data taken from *AG Energiebilanz*.^{9,10}

devices in focus.^{11,12} Alessandro Volta introduced the first commercial energy storage device in 1799, the so-called Volta-pile (key in the development of telegraph technology). Followed by the invention of the Daniell cell in 1836, the lead acid battery in 1859 by Gaston Plante, which was one of the first used storage systems for electric vehicles (EVs), the Leclanche cell in 1886, the nickel-cadmium battery invented by Waldemar Junger in 1899 and it was not until 1985 that the first lithium-ion batteries (LIBs) were created. It took another six years until the first of the LIBs was commercialized. The Ragone plot demonstrates why the current LIBs devices are the predominant battery energy storage technologies for EVs. It has higher energy densities (almost double the energy density of the before used nickel-cadmium battery), expanded cycling life and lower self-discharge rates.¹¹⁻¹⁴

To counteract one of the drawbacks of increased energy demand, such as global warming, electric cars have been targeted as a big part of reducing carbon dioxide (CO₂) emissions. After all, a large part of the emissions of the last decades came from vehicles with fossil fuels.^{15,16} With the increase of EVs, a higher demand of lithium (Li⁺) was generated since they have an important role in meeting the global goals on climate change. But *how green are electric vehicles?* It matters how the electricity is made, more precisely, how much coal is being burned to charge the battery of the EV. Only the possession of an EV does not lead independently to a more environmentally conscious mobility. Therefore, electricity production through renewable energy is a severe point on which further investment must be made in the future with the highest priority. In addition to green power generation, the lithium extraction technologies are also of profound importance. Other controversial issues regarding production, storage, and energy use are still present and need further research. However, these cannot

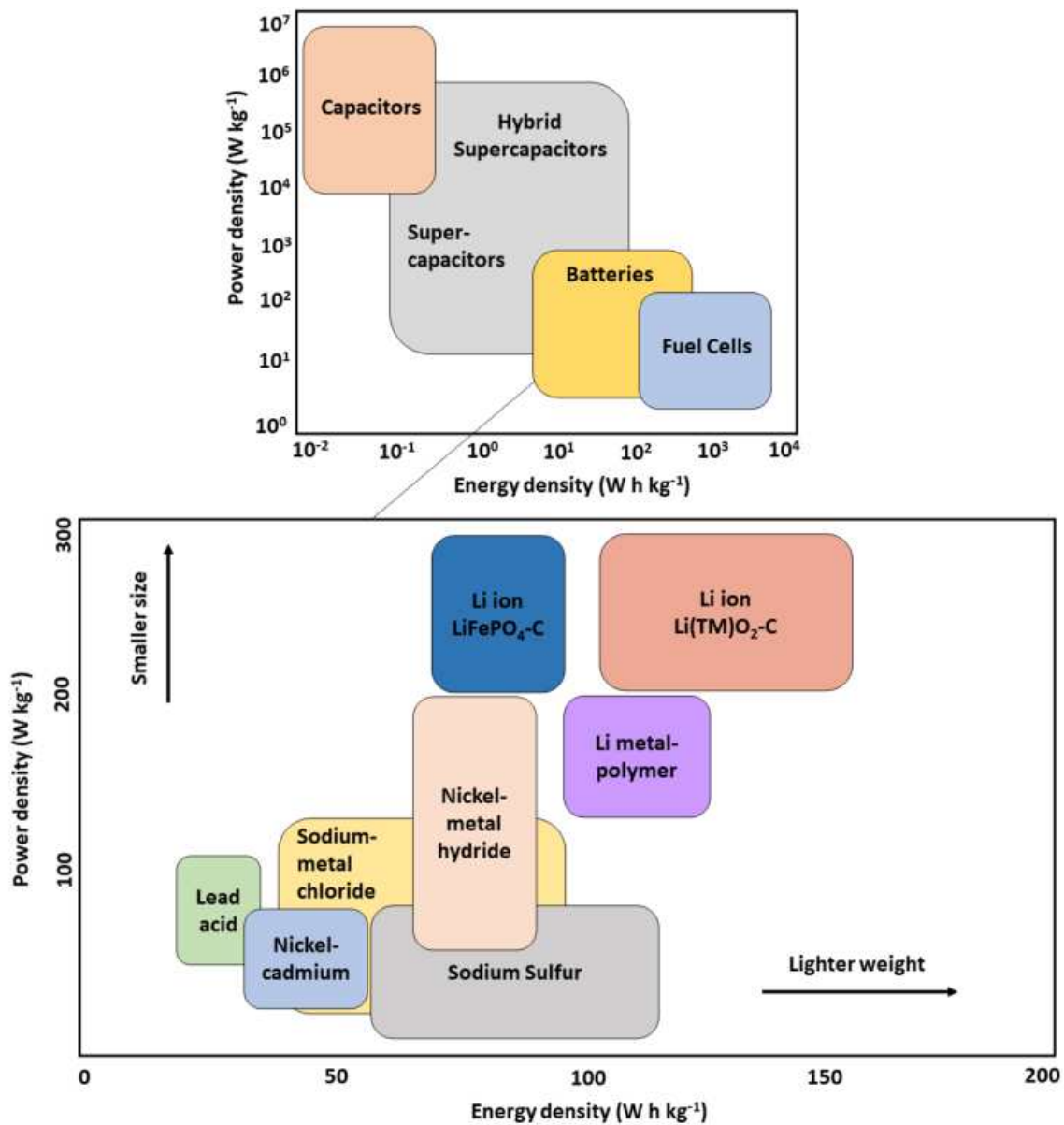


Figure 3.4: Ragone plot of the power-energy density range for various electrochemical energy storage devices. Image was created from the data known from the Publications of Vandeginste et al. and Yang et al.^{17,18}

be covered in one Ph.D. generation. Thus, in this thesis, the issues of lithium production are examined in more detail, and the goal is to offer a possible greener alternative to lithium production to make the world a greener and more environmentally friendly place.

At the end of this Chapter, we will recap our thoughts on energy. The necessity of energy for today's time is no longer restrained, we develop faster and can create many new things through energy. However, how this energy is used is a crucial point to reduce all the negative aspects associated with energy. Therefore, the sentence of Nikola Tesla quoted at the beginning of the Chapter is urgently to be taken to heart.

Gain more, waste less, spend efficiently, learn.

Use energy more responsibly, generate power and heat via renewable resources to keep the world safe and to ensure national security around the globe. There is enough energy in the world for all people on earth.

3.2 Lithium – *the white gold*

As mentioned in the previous Chapter, LIBs are one of the most essential energy storage systems. They bring many benefits and have a positive impact on the environment. However, *how environmentally friendly is the production of lithium compounds in such battery systems?* In this Section, the crucial properties of the main raw material *lithium* is described, where it can be found in the world (subsection 3.2.1), how it can be extracted, which methods are currently being used, and what impact they have on the environment (subsection 3.2.2).

Lithium is the lightest metal with very interesting chemical features. It is electrochemically active, has a high redox potential, the highest specific heat capacity of any solid element, and a low thermal expansion coefficient. The various properties are the reason why lithium is used in essential applications such as ceramic glass, nuclear fusion, pharmaceuticals, adhesives, lubricant grease, cement, electrode welding and very importantly in LIBs.^{19,20} The substantial increase in demand for EVs has led to a rapid expansion in the consumption of lithium compounds since it is a limited resource and only available in a few territories in the world.

The battery industry is the highest consumer of lithium with about 65 %. Consumption has more than doubled over the last decade.²¹ The lithium demand was independently determined to be almost 20 Mt from 2010 to 2100 by Gruber et al.²² and 17.5 Mt by Yaksic and Tilton et al.,²³ respectively (after consideration of recycling).²⁴ The total global lithium reserves in 2021 were estimated to be 22 Mt. The reserves of the main countries are shown in Figure 3.5 (left), with Chile, Australia, and Argentina having the largest reserves. In Figure 3.5 (right), the percentage reserves and demand increase is compared to the year before from 2016 till 2021. Lithium consumption has been increasing over the years, and although in 2020 and 2021 the COVID-19 pandemic severely curtailed life, the lithium consumption increased. In 2021, an increase of approximately 33 % from the previous year was identified, with only a slight rise in reserve growth, which most likely results from the previous year's restricted life and thus less lithium consumption in 2020. When comparing to the time before the pandemic, a lithium consumption growth of 18 % from 2018 to 2019 is observed. If it will be assumed that the lithium reserves remain 22 Mt and the annual growth will be 18 %, we will reach a lithium bottleneck in 2044 at the latest. By 2050, 40 Mt more of lithium than available will be needed (Figure 3.6). However, since the COVID-19 pandemic is not yet over, statistics may vary. Nonetheless, even if more sources are discovered, the scarcity will likely be reflected in the price, which could significantly threaten the EV industry and its en-

3.2. LITHIUM – THE WHITE GOLD

vironmental contribution.^{21,25} Therefore, resource identification, cheap and environmentally friendly extraction, and recycling of such batteries (not discussed in this work) must have the highest priority so that the climate goals can be achieved for our planet.

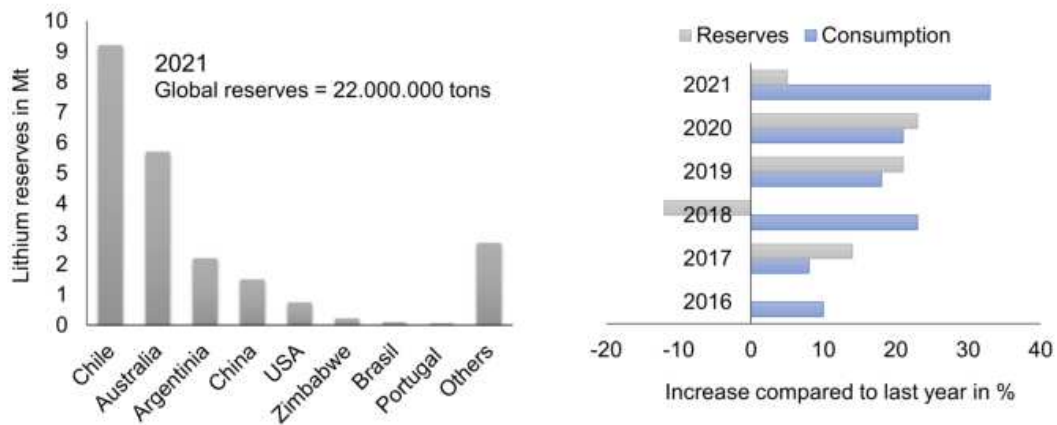


Figure 3.5: Global lithium reserves in 2021 illustrating the countries with the main Li^+ resources in Mt (left) and the Li^+ consumption and reserves compared to the previous year in percentage from 2016 to 2021. Data taken from the United States Geological Survey.^{21,25}

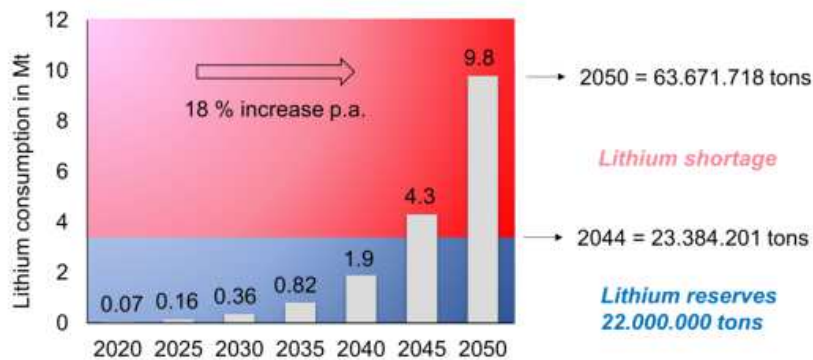


Figure 3.6: Li^+ consumption from 2020 to 2050 if an 18 % increase of each year is assumed and the Li^+ resources from 2021 remain the same. The red background represents the area with Li^+ shortage and the blue background the area where the lithium demand can be compensated. Data was withdrawn from the United States Geological Survey. The idea of the illustration was taken from Bae et al..^{21,25}

3.2.1 The worldwide lithium reserves

Before starting the discussion on lithium reserves, it is first necessary to clarify the terms resources and reserves, which have already been mentioned in the previous Chapter. These terms have not been used correctly in many Publications and cause data to be misunderstood. In this thesis, we want to avoid this issue and define the two terms properly.

Resources are the geologically secured quantity that is theoretically available, while reserves are the quantities that can also be practically extracted under technical and socio-economic conditions. Thus, reserves are the relevant quantities for production, while resources are rather academic quantities.²⁶ Reserves are also highly dependent on technology, development, environmental demand, and political and social issues. For example, technological developments can increase reserves because new types of deposits become accessible or production costs can be reduced. Decreasing concentrations, on the other hand, would increase extraction costs and thus reduce reserves. An overview of the world's resources and reserves in 2021 is shown in Figure 3.7. Chile and Australia are the countries with the most lithium reserves to date.



Figure 3.7: Lithium resources and reserves around the globe in 2021. Data was taken from the US Geological Survey.²⁵

Economic concentrations of lithium can be found mainly in ores or brines, which represent the commercial lithium reserves. Australia is the highest lithium producer with 43.5 % of the global production followed by Chile with 32.8 %.^{6,21,27} Australia, Zimbabwe, and Canada are the leading countries in recovery of lithium from ores. Some of the most promising ores are shown in Table 3.1. Around 56 % of the total lithium resources come from brines and are located in the *lithium triangle* or the also called *ABC* (Argentina, Bolivia, and Chile) region.

Table 3.1: Lithium ores and their corresponding lithium content. The table was reproduced from Bae et al. with permission from the Royal Society of Chemistry.²¹

Ore	Chemical formula	Li content (wt%)
Spodumene	LiAlSi ₂ O ₆	3.73
Petalite	LiAlSi ₄ O ₁₀	2.09
Amblygonite	(Li,Na)AlPO ₄ (F,OH)	3.44
Lepidolite	K(Li,Al) ₃ (Si, Al) ₄ O ₁₀ (F,OH) ₂	3.58
Eucryptite	LiAlSiO ₄	5.51

Table 3.2: Lithium brines and their corresponding Li⁺, Mg²⁺ concentration and the ratio of the two ions. The data vary slightly in some Publications, which are cited in the first column after the deposit name.

Brine	Country	Li ⁺ (wt%)	Mg ²⁺ (wt%)	Mg ²⁺ /Li ⁺ (wt%)
Salar de Atacama ^{21,26,28,29}	Chile	0.157	0.965	6.15
Maricunga ²⁶	Chile	0.092	0.74	8.00
Salar de Uyuni ^{21,28}	Bolivia	0.0321	0.65	20.25
Cauchari ²⁶	Argentina	0.062	0.18	2.84
Olaroz ²⁶	Argentina	0.09	0.18	2.00
Hombre Muerto ^{26,28}	Argentina	0.062	0.089	1.46
Rincon ²⁶	Argentina	0.04	0.034	8.5
Silver Peak ^{21,26,29}	USA	0.03	0.04	1.33
Great Salt Lake ^{26,28,29}	USA	0.006	0.8	133.33
Bonneville ²⁸	USA	0.0057	0.4	70.17
Salton Sea ²⁸	USA	0.022	0.028	1.27
Searles Lake ^{26,28}	USA	0.0083	0.034	4.10
Smackover ²⁶	USA	0.038	0.75	20
Clayton Valley ²⁸	USA	0.0163	0.019	1.17
Zabuye ^{28,29}	China	0.97	0.001	0.001
Da Qaidam ²¹	China	0.02	1.3	65
Dead Sea ^{28,29}	Israel	0.002	3.4	1700
Sua Pan ²⁸	India	0.157	-	-

Seawater contains around 230 Bt of lithium, however it only exists in very low concentrations of 0.1-0.2 mg·L⁻¹.¹ Table 3.2 gives an overview of some of the brine deposits in the world with the corresponding Li⁺ and magnesium (Mg²⁺) concentration. The two ions are listed since they have very similar ionic radii, making the lithium recovery more difficult and thus, the recovery vary greatly depending on the Mg²⁺/Li⁺ ratio. The lower the ratio, the easier the isolation of lithium from brines. Due to the properties of Mg²⁺ (e.g. the much higher weight compared to Li⁺), this metal is not suitable as a raw material for batteries, therefore the isolation of it is obligatory.

3.2.2 Lithium recovery

This subsection briefly reviews the current technologies, which have been used to extract lithium from ores and brines (based on the review article from Liu et al.³⁰). Some methods will be mentioned that only exist on a laboratory scale. However, these developments are also significant to review to give the reader an insight into the promising technologies which might be commercially available in the near future.

3.2.2.1 Lithium from ores

Around 35 % of the lithium is extracted from ores, 85 % of it from Australia in the Greenbushes deposit.^{31,32} The first step to gain lithium from ores is generally done by crushing the mineral. Afterwards, the material is processed through flotation, magnetic separation, optical sorting, or heavy material separation to obtain a 4-6 % lithium compound concentration.³¹⁻³³ The crude lithium compound is dissolved by roasting (heating mineral at high temperatures) and leaching (converts metals into soluble salts in aqueous media). Thermal processing is done by adding metal hydroxides, salts, or acids to obtain leachable compounds such as lithium sulfate (Li_2SO_4), lithium carbonate (Li_2CO_3), or lithium chloride (LiCl). The raw material is then precipitated to remove further impurities such as calcium (Ca^{2+}), Mg^{2+} , aluminium (III) (Al^{3+}), and iron (III) (Fe^{3+}). Depending on the concentrations, ion exchangers or simple evaporations leading to precipitation are used afterwards to remove remain impurities. To obtain the pure marketable product for the battery industry, the materials are crystallized, carbonized, or electrodialyzed to obtain lithium hydroxide (LiOH), Li_2CO_3 , or LiCl . A flow-sheet for the processing of α -spodumene, Petalite, Lepidolite and Amblygonite is exemplary shown in Figure 3.8.³³

Spodumene is the most commonly used mineral for lithium recovery in an industrial scale, therefore, the recovery technique for spodumene is reported here in more detail.³² First, the mineral is crushed and refined by flotation, achieving a purity of the lithium compound of about 6 %. It is then roasted or calcined at about 1040-1100 °C. A conversion from α -spodumene to β -spodumene takes place, which is less inert and thus more reactive to chemical reactions and can be leached more easily.^{32,34} At the roasting procedure, the minerals react with oxygen and form oxides such as lithium oxide (Li_2O) or Li_2SO_4 .³⁵ Calcination is carried out in the absence of oxygen and at high temperatures. Additives such as lime or limestone are added. In the process of calcination, a simple decomposition caused by the high temperature (over 1000 °C) can take place, or a structural change can be induced.³⁶ Acidic, alkaline and sometimes chlorination processes can be used to obtain the lithium-containing market product for the battery industry. These are described in more detail below.

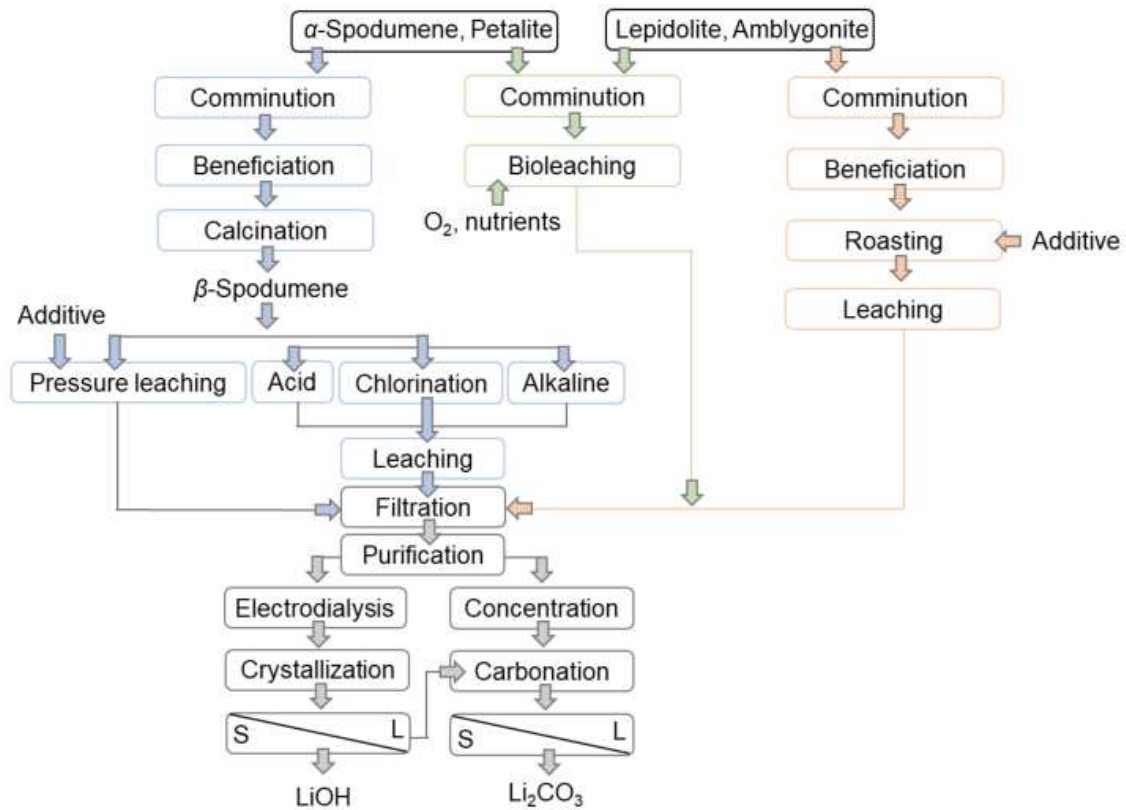


Figure 3.8: Flowsheet of the lithium compound production from ores. L labels the liquid, and S the solids. Reproduced from Meng et al. with permission from Taylor & Francis.^{32,33}

Acid process In the acid process, the β -spodumene is ground again, and sulfuric acid (H_2SO_4) is added at $250\text{ }^\circ\text{C}$ to generate Li_2SO_4 . Afterwards, the whole mixture is immersed with water in a pregnant leach solution (PLS). The excess of H_2SO_4 is neutralized with calcium carbonate (CaCO_3). Afterwards, the obtained calcium-saturated lithium-bearing PLS is separated from the rest of the solid. A pH control process dissolves the other impurities such as Ca^{2+} , Al^{3+} , Mg^{2+} , Fe^{3+} , e.g., Mg^{2+} is converted into solid magnesium oxide (MgO)/magnesium hydroxide ($\text{Mg}(\text{OH})_2$) by adding calcium oxide (CaO) at a pH value of 9.3. The lithium solution is then co-extruded via an ion exchanger or several evaporation processes to increase the lithium concentration from 5 to $14\text{ g}\cdot\text{L}^{-1}$. Afterwards, sodium carbonate (Na_2CO_3) is used at about $100\text{ }^\circ\text{C}$ to carbonize lithium and obtain lithium carbon crystals and sodium sulfate (Na_2SO_4). The lithium carbonate is centrifuged, washed, dried, and sold to the battery market. Briefly, the treatment of H_2SO_4 with β -spodumene is an effective process, but this method has some disadvantages, such as the need for a very high acid concentration, which adversely affects the subsequent cleaning processes. The roasting of β -spodumene with H_2SO_4 at high temperatures also requires special equipment, which leads to increased investment and operating costs.³²

Alkaline process In contrast to the acid process, the β -spodumene is mixed with CaCO_3 or Na_2CO_3 to allow the lithium to react to Li_2CO_3 or lithium aluminate (LiAlO_2). It then reacts with CO_2 to form Li_2CO_3 . A solid-liquid separation unit is used to separate the remaining salts and ores from the Li_2CO_3 solution. The solution is evaporated at 90°C . Li_2CO_3 is obtained if Na_2CO_3 ash, or LiOH if CaCO_3 was used for neutralization. The precipitated lithium product is refined while the rest goes through the same processes again.³²

Chlorination process The chlorination of metal ions is carried out with the addition of hydrochloric acid (HCl), sodium chloride (NaCl), potassium chloride (KCl), or chlorine gas (Cl_2), between $800\text{-}1100^\circ\text{C}$, depending on the mineral source. The main product of this reaction is the recovery of LiCl , which is leached and purified with water (similar to the acid process).³²

In conclusion, the lithium extraction from ores is very efficient since high lithium concentrations are obtained, and low production times are required to obtain the target product. However, a significant disadvantage is the energy-consuming process of conversion from α -spodumene to β -spodumene. This step requires a lot of energy, and therefore, high operating costs are needed. Recently, a faster and more selective conversion via hybrid microwave heating has been observed.³⁷ So far, this method has not been carried out on a larger scale. Therefore, further research is needed on microwave treatment, energy transfer, and induced thermal stress on the irradiated minerals before using it on an industrial scale.³⁴ Moreover, the air-pollution which is caused through the crushing of the minerals is a huge drawback considering the goals of climate change. In addition, for some minerals (with a substantial degree of hardness), the processing is a challenge and must be carried out under harsh conditions. Thus, equipment must be more robust, which would increase investment costs.³²

3.2.2.2 Lithium from brines and seawater

Brines are categorized in geothermal brines, oilfield brines, and continental brines. The latter accounts for almost 60 % of the world's lithium production. The brine *salar de uyuni*, one of the major lithium resources, located in Bolivia can be seen in Figure 3.9. In contrast to ores, the lithium concentration in brines is smaller and ranges from 200 to 700 ppm (a few ranging up to 1000 ppm), depending on the source (compare Tab. 3.1 and Tab 3.2). In addition to Li^+ , several other metals, e.g., Mg^{2+} , sodium (Na^+), potassium (K^+), and Ca^{2+} , are found in salt lakes. In recent years, many technologies have been developed to separate these, such as precipitation, solvent extraction, ion-sieves, or ionic membranes, which will be discussed in detail below.³²

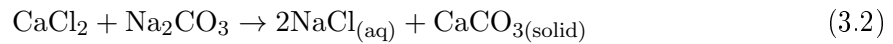
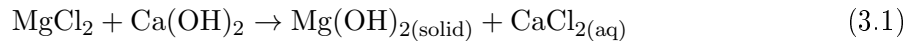


Figure 3.9: Salar de Uyuni in Bolivia. The image is a royalty free image from the website www.pixabay.com.

Precipitation The solar evaporation–precipitation process is one of the major techniques, which is used to isolate lithium from brines. The process and its difficulty strongly depend on the composition of the brine. As soon as the $\text{Mg}^{2+}/\text{Li}^+$ ratio exceeds 6, the standardized method can no longer be used. Unfortunately, many brines have a high Mg^{2+} content, e.g., 80 % of the brines in China have a very high $\text{Mg}^{2+}/\text{Li}^+$ ratio of up to 1837:1.^{30,38} Therefore, some research has been done on the isolation of Li^+ from Mg^{2+} .

First, we will discuss the currently most used technology for lithium recovery, the solar evaporation–precipitation process. It is worth mentioning that this technology should be applied in areas with dry climates since only in this way it is possible to evaporate the brines in an appropriate time window. Brines occur mainly in areas with low precipitation, which supports this technology. The composition of the brines determines the crystalline species obtained as the final product and the procedure of the purification steps.³⁰ However, the applied technologies are often very similar. First, the brine is stored in shallow ponds. The water evaporates for 1-2 years, depending on how dry the region is and whether rainy seasons or similar natural phenomena extend the evaporation time. Once the threshold for precipitation is reached, the brine is transferred to the next pond. The order of precipitation

begins usually with NaCl (Halit), KCl (Sylvit), and NaCl·KCl (Sylvinit). Depending on the salt content of the brine, other magnesium or alkali salts may precipitate. After these steps, a lithium concentration of the brine of approximately 6 % is reached. Mg²⁺, Ca²⁺, and boron are afterwards separated from the solution. The MgCl₂ is converted into Mg(OH)₂ through the addition of lime, as illustrated in Eq. 3.1. The addition of Li₂CO₃ or Na₂CO₃ is used to remove calcium from the brine (Eq. 3.2 and 3.3). The boron in the brine is removed by solvent extraction, while the CaCO₃ produced by Eq. 3.2 and 3.3 is recycled. If any residual of Ca²⁺ or Mg²⁺ is present, ion exchange processes are performed to achieve the desired purity. Finally, Na₂CO₃ is added to the brine to precipitate Li₂CO₃, which is done closely to the boiling point of water, as the solubility of Li₂CO₃ decreases with increasing temperature.³²



In the following, a concrete example of lithium isolation from the brine in Cauchari-Olaroz (Argentina) is shown in Figure 3.10. The Cauchari-Olaroz project is the third largest brine project globally, at an altitude of 4000 m.³⁹ As with the other precipitation methods, lithium recovery begins with the evaporation of the brine until about 1.3 wt% of lithium is reached. The evaporation time is about 180 days, during which the volume of the brine is reduced by 80-90 %. The interfering magnesium and sulfate salts are precipitated with lime to Mg(OH)₂ and CaSO₄·2H₂O (gypsum). The brine is further condensed to remove potassium from the brine. The brine is acidified with HCl to obtain boric acid, which is then extracted with organic solvents. After the brine is boron-free, sodium hydroxide (NaOH) separates the remaining magnesium as Mg(OH)₂. In the last step, the lithium is precipitated after carbonization to Li₂CO₃ (purity: 99.5 %). The mother liquor is reused to neutralize the boron-free acid to recover the remaining lithium.³²

Alternative precipitation routes have been developed to decrease the production time. One of them is the precipitation of LiAlO₂, which is less soluble in water.⁴⁰⁻⁴² The method had been improved by the use of a MgAlCO₃-layer double hydroxide materials (MgAlCO₃-LDHs) to separate magnesium from a concentration that was initially 117 g·L⁻¹ down to 0.02 g·L⁻¹.⁴³ Another work proved that the addition of aluminium powder with NaCl forms LiCl·2Al(OH)₃·xH₂O, which can easily be crystallized.⁴⁴ In a lithium brine with high sulfate content, Li₂SO₄·H₂O crystals can be formed by thermal evaporation or ethanol addition.⁴⁵

In summary, lithium isolation from brines is more economical than extraction via ores. The purity of the lithium compounds obtained via brine is very high, but the process is highly weather-dependent, very time-consuming, and involves a large amount of water consumption.

This poses a significant challenge to the environment. Many people in South America are already protesting against lithium from the brines, as these countries are arid and have hardly any water available.⁴⁶ In addition, high concentrations of impurities are a significant challenge for the lithium recovery from brines and make the precipitation of lithium more difficult.

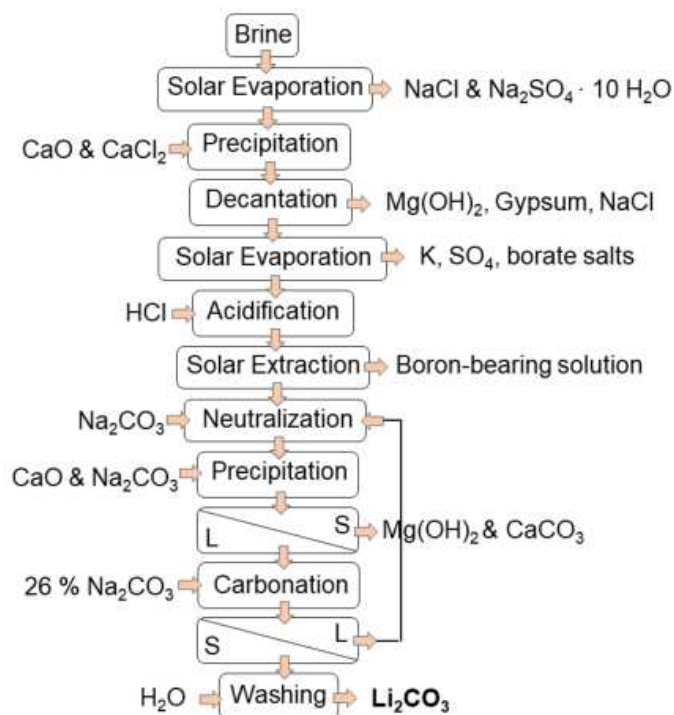
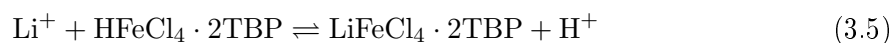


Figure 3.10: Flowsheet of the solar evaporation-precipitation process of the brine from the Cauchari-Olaroz region in Argentina. Reproduced from Tran et al. with permission from Elsevier.³³

Solvent Extraction The solvent extraction process is often used to isolate metals from aqueous resources, as the method is cheap, easy to perform, and environmentally amiable.^{47–49} In the following, three different solvent extraction systems are described, including neutral extraction materials, synergistic solvent extraction systems, and room temperature ionic liquids (RTILs). CEs are a particularly crucial group for solvent extractions, however this group will not be discussed in this Chapter, since it is described in depth in Section 3.3.

Neutral extraction systems One of the most promising systems consists of tributyl phosphate (TBP)/kerosene + iron (III) chloride (FeCl₃), where TBP is the neutral organophosphorus-containing extraction reagent, kerosene the diluent, and FeCl₃ is the coextraction reagent. Lithium extraction with the neutral extraction system is a cation exchange mechanism that reacts with the first formed species, which is only formed at a high chlorine (Cl⁻) concentration (Eq. 3.4 and 3.5). The extraction capacity of TBP decreases in the following trend $H^+ > Li^+ > Na^+$. Thus, the lithium can be extracted by adding HCl to TBP resulting in the first formed species $HFeCl_4 \cdot 2TBP$.³⁸



The coordination of Li^+ takes place at the $\text{P}=\text{O}$ bond from the TBP molecule (Figure 3.11). As mentioned above, the concentration of the Cl^- plays a significant role. It has been shown that magnesium chloride (MgCl_2) as a Cl^- source increases the extractibility of Li^+ due to the higher salting-out effect compared for example to calcium chloride (CaCl_2).⁵⁰ Thus, the combination of TBP, kerosine, and FeCl_3 in brines with a high MgCl_2 concentration is very well applicable. Other co-extraction compounds such as zinc chloride (ZnCl_2) and chromium(III) chloride (CrCl_3) have also been investigated. However, FeCl_3 showed the best co-extractant capacity.⁵¹ Some of the most commonly used neutral extractands can be found in Figure 3.11.

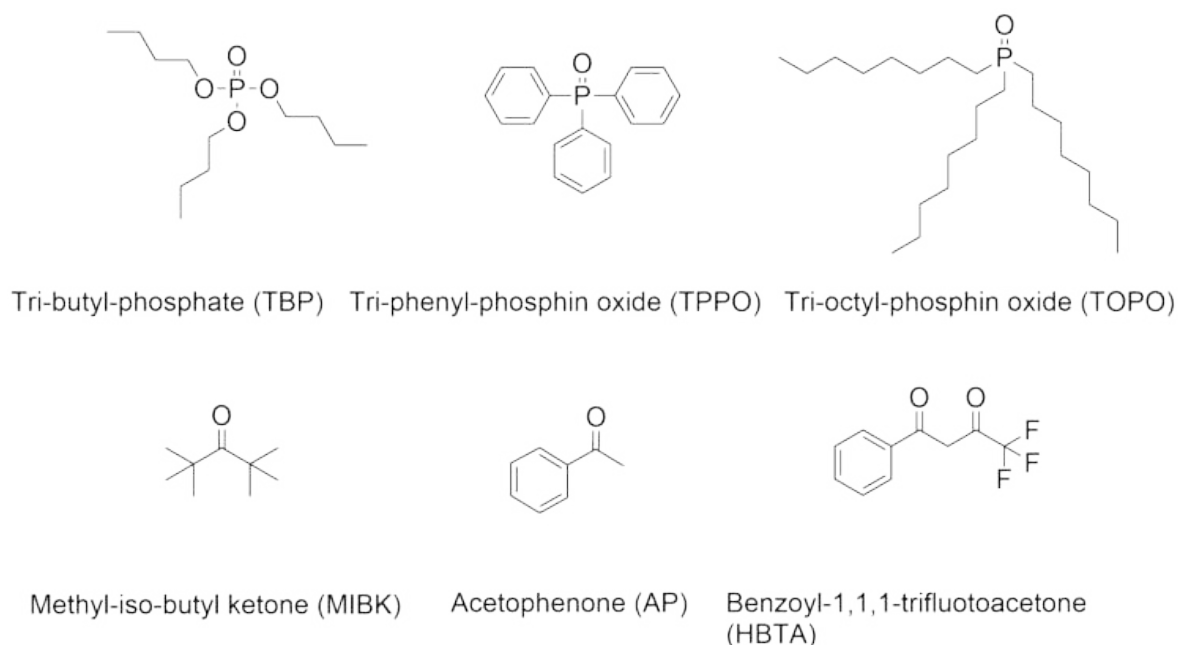


Figure 3.11: Neutral extractants for the solvent extraction of lithium.^{30,49}

In the following, some disadvantages of the solvent extractions with $\text{TBP} + \text{FeCl}_3 +$ kerosene systems are explained as well as first methods that have been found to solve these problems. For example, a disadvantage of the solvent extraction with FeCl_3 is the solubility in the aqueous phase. Therefore, extractions must be strictly guarded. The stability of the ferric ions can be ensured for the washing and stripping process using a $6 \text{ mol}\cdot\text{L}^{-1}$ HCl solution. On the other hand, strong acids have the disadvantage of damaging the instruments by corrosion. In addition, a third phase can occur during solvent extraction if less than 80 % TBP is present in the organic phase. Another typical disadvantage that is often a problem of solvent extraction is the dissolution of the extractants in the solution, leading to environmental

pollution.³⁰

In the work of Zhao et al., ketones were investigated as extractants or diluents for TBP, some of which are shown in Figure 3.11 below, in kerosene with FeCl_3 . These behaved similarly to the TBP molecule in that the lithium complexation occurs at the C=O bond instead of the P=O bond. Still, it was demonstrated that ketones as polar solvents have a more substantial influence on lithium extraction than non-polar solvents.⁵² The combination of TBP (polar solvent) and ketones (neutral extractant) significantly increases the extraction of lithium and prevents the formation of a third phase by promoting the solubility of the extracted complex. A notable example is the use of TBP/methyl-iso-butyl ketone (MIBK) + FeCl_3 .^{47,53} On the other hand, it was also mentioned that non-polar solvents show better complexing properties with lithium than polar solvents since molecular weight most likely plays a role in complexation, such as trioctyl phosphine oxide (TOPO).⁵⁴ Lee et al. showed that solvents with hydrogen bonding affinity decrease the extraction efficiency.⁵⁵

The diversity of organic reagents for solvent extraction has resulted in many new innovative systems. The most promising ones will be discussed further in the following.

Synergistic solvent extraction systems Synergistic solvent extraction systems can keep solvent loss low, improve the separation factor (SF), and thus increase lithium recovery. In the traditional TBP/kerosene+ FeCl_3 system, the addition of a synergist (e.g., β -ketones) can create such a system. In this case, the TBP acts as the extractant and FeCl_3 as the co-extractant. The mechanism proceeds analogously to the mechanism described above. The formation of LiFeCl_4 and TBP occurs, which is connected to the synergist via a hydrogen bond. How strongly the synergist affects the complex depends on the functional group of the synergist, such as C=O, P=O, or R-NCO. In the case of β -ketone, the synergism is created by combining it as a chelate and a neutral solvent ligand. In this process, the protons of the β -ketone are first displaced, forming an ionized β -ketone which coordinates with lithium, resulting in the chelate complex. Afterwards, the adduct is included with the neutral solvent.^{30,54} This system has excellent lithium extraction properties. Pranolo et al. found that a system made of α -acetyl-*m*-dodecylacetophenone (LIX 54), a mixture of four trialkylphosphine oxides (Cyanex 923[®]) in an iso-aliphatic non-polar solvent (Shellsol[®]D70), efficiency recovered 97 % of lithium and reached a SF of 1560 versus sodium (see Figure 3.12).⁵⁶ In addition, the ionic component of brines has an additional influence on the complexing efficiency of lithium with synergists.⁴⁹

In conclusion, the synergistic systems have already shown some advantages over the traditional systems, but the formation of the third phase when TBP is used is still a big issue. In addition, these systems have only been used on a laboratory scale, the price of the extraction reagents and synergists is too high and therefore not suitable for an industrial scale (until an economy scale is reached). Furthermore, the mechanism is not precise, which is also a challenge for large-scale production.

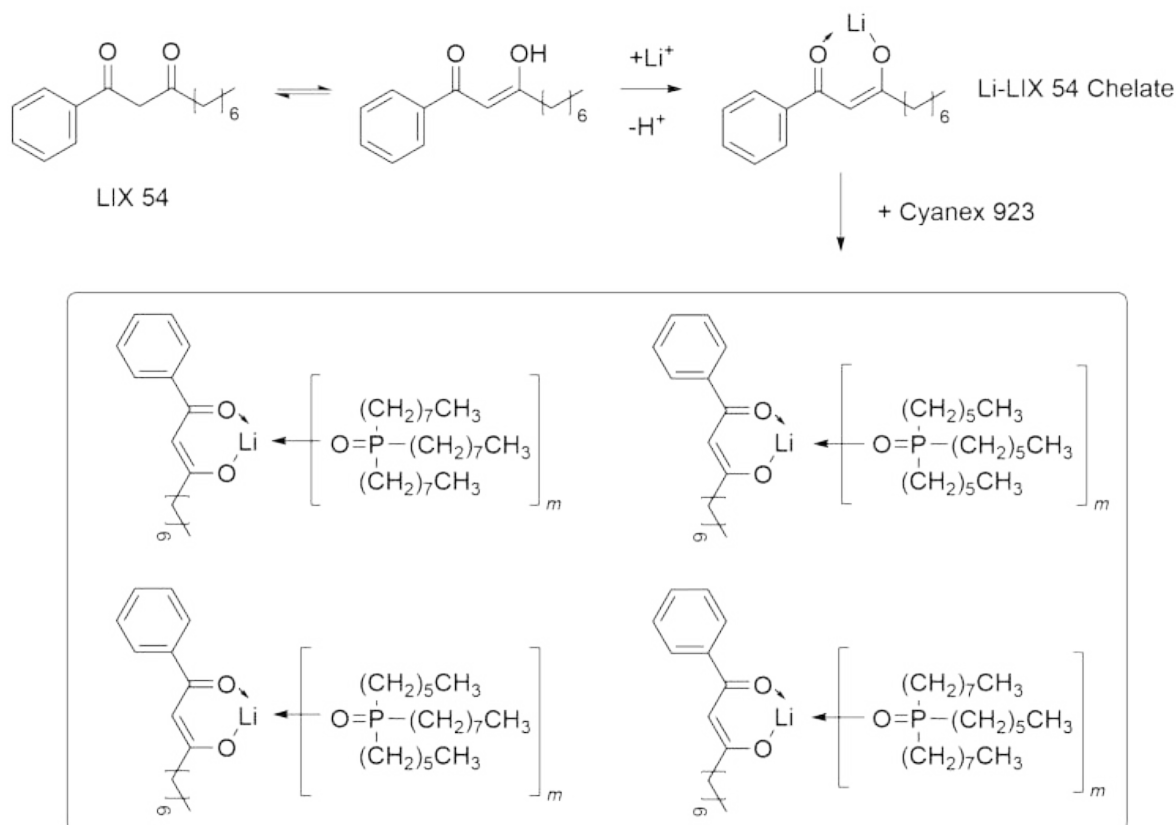


Figure 3.12: Illustration of the reaction mechanism of Li-LIX 54-Cyanex 934. Reproduced with permission from Swain et al. from John Wiley and Sons.⁵⁴

Room temperature ionic liquid systems One other major group for solvent extraction are the RTILs. They have the advantage that they are less volatile, non-flammable, have adjustable viscosity, and have high thermal stability. RTILs are often alternatives for volatile solvents, but they can also be used as extraction agents.⁵⁷ In addition, through an advanced multi-stage counter-current process, lithium extraction efficiencies can reach nearly 100 %.³⁰ In addition, these materials have the advantage that lithium can be selectively isolated from magnesium, which is still a significant problem for many systems.⁵⁸

The group of Shi et al. has studied some research on imidazole RTILs as solvents in conjugation with TBP and some functional RTILs as extractants for lithium from brines.^{48,59,60} Exceptionally high selectivities of lithium over Mg and high lithium extraction efficiencies of about 90 % were obtained by the system $[C_4mim][PF_6]/TBP+FeCl_3$ (or sodium perchlorate ($NaClO_4$)). The extraction is based on a cation exchange mechanism with the formation of $[Li \cdot 2TBP]^+$ in the ionic liquid system. Different chain lengths were also investigated, and it was found that the hydrophobicity of the RTILs deteriorates the extraction efficiency of lithium.⁶¹

Briefly, RTILs are solvent and synergist and their advantages over traditional solvent extraction systems are clear, however during the procedure there is a loss of ionic liquid in the exchange mechanism and contamination of the solution. Moreover, the prediction of the

properties is not yet clearly understood, and the syntheses have only been performed on a laboratory scale. Therefore, further work is needed to commercialize and apply them in an industrial scale.

Primary solvent extraction methods have been presented in this Chapter. The most promising material based on TBP and FeCl_3 could be improved by new innovative extended ways like synergistic systems consisting of β -ketones or RTILs. High lithium extraction efficiencies could be achieved. However, these processes have only been carried out on a laboratory scale. The application of the methods in the industry involves some challenges, such as the fabrication of such systems, which are often very expensive, or harsh reaction conditions, which require better equipment. In addition, the extraction process is not yet apparent, so further research is needed before these materials can be used on an industrial scale. Nevertheless, these materials have the potential to be used in the future as a more environmentally friendly method compared to the previously mentioned solar–evaporation precipitation process.

Ion-sieve adsorption Lithium ion-sieve (LIS) is an adsorbent material that offers a new effective method to selectively recover lithium from brines and seawater even if other interfering ions are present in the aqueous resource. Due to the tremendous selectivity towards lithium, high purity lithium products are easily accessible. The efficiency is much higher than the previously described methods, and benefits from many other advantages like no additional purification steps are necessary, a high theoretical uptake capacity, a low regeneration loss of the raw materials, low energy consumption, and no additional burden on the environment. Despite these many advantages, the question appears: *why are these materials not yet used industrially?*

Many LIS consist of manganese oxide compounds, which have the disadvantage that they partially dissolve in water. In addition, the material is tough to granulate, making it more difficult in the adsorption process in an industrial scale. Nonetheless, electrochemical methods have significantly improved lithium adsorption and desorption performances in recent years and are, therefore, again in the focus of current research.⁶² This paragraph discusses the chemical structure, mechanism, lithium uptake capacity and regeneration in more detail. Processing for industrial column operation is explained, and the advantages and challenges of material formation technologies are compared.

LIS are adsorbents with remarkable features such as low toxicity, low cost, chemical stability, and high lithium capacity uptake, which can be divided into two categories, the lithium manganese oxide (LMO) and lithium titanium oxide (LTO) LISs. LMOs are the most popular LIS as they show higher lithium selectivity, high adsorption capacity, and excellent regeneration performance. On the other hand, the LTO-type LIS offer higher structural stability due to the titanium oxide bond energy, a lower dissolution loss, and longer recyclability. However, adsorption rates are prolonged and what poses a much bigger problem is the limited use of lithium adsorption in case of application of an electrical potential.^{62–64} Both groups will be discussed in detail below. Many other inorganic hydrous oxide ion-sieves have also been in-

vestigated, and the associated lithium adsorption capacity determined. Figure 3.13 overviews some of the most promising LISs.

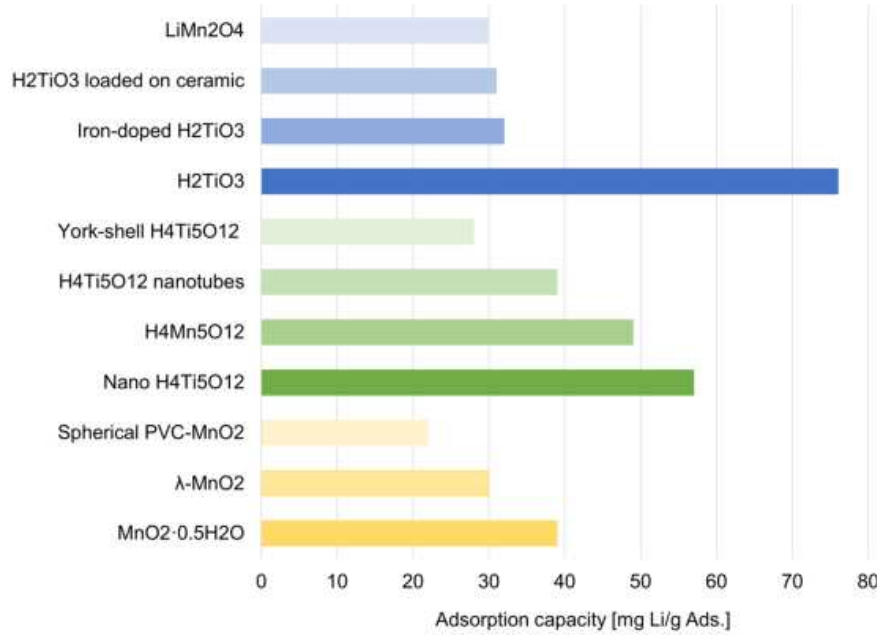
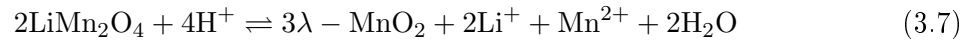


Figure 3.13: Overview of the most promising LISs and their corresponding adsorption capacity. Reproduced with permission from Liu et al from Elsevier.³⁰

Lithium manganese oxide (LMO) Manganese oxide (MnO_2) occurs in many different forms, most notably in the modifications of α -, β -, γ -, and λ - MnO_2 , with λ - MnO_2 showing the highest lithium affinity among them.³⁰ Thus, the latter has been intensively studied as a lithium adsorbent and cathode material.^{64–66} Generally, the LMOs are prepared by acid addition of the LMO compound (Figure 3.14); almost all protons replace the lithium ions. Reaction techniques such as solid-state reaction, hydrothermal processes, or sol-gel method are used to prepare the precursors.^{67–71} The precursor morphology characterizes the structure and performance of the LIS. The particular properties of LIS are based on the spinel lattice structure, framework, and memory effect; for the latter, the ion size and the energy of dehydration play the most crucial role. Ions exceeding the size of Li^+ (0.074 nm) cannot fill the exchange places including Na^+ (0.102 nm), K^+ (0.138 nm), and Ca^{2+} (0.100 nm). The only ion that could serve the site instead of lithium would be the Mg^{2+} (0.072 nm), however this one has a much higher dehydration energy ($(\Delta G_h^\circ)_{\text{Li}} = -475 \text{ kJ}\cdot\text{mol}^{-1}$, $(\Delta G_h^\circ)_{\text{Mg}} = -1980 \text{ kJ}\cdot\text{mol}^{-1}$) and therefore Mg^{2+} is energetically less preferred to fill the sites.^{72,73} The ion exchange mechanism was proposed by Shen and Clearfield⁷⁴ (Eq. 3.6) and the surface disproportionation by Hunter⁶⁷ (Eq. 3.7).





It is assumed that both mechanisms take place.⁷⁵ The preparation of the precursor determines the ratio of the respective group sites.⁷⁶ For the ion-sieve λ - MnO_2 (spinel-type), the Li selectivity is explained, for example, by the ion exchange mechanism between Li^+ and H^+ , so that the H^+ content of λ - MnO_2 correlates with the adsorption capacity.⁷⁷ The mechanism of lithium (de)intercalation is shown in Figure 3.14. A detailed description of the mechanism theories can be found in the review article from Weng et al. and will not be further discussed here.⁶⁴

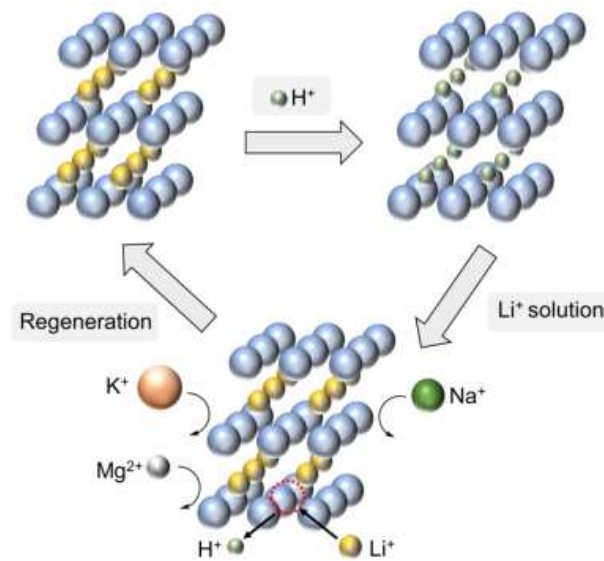
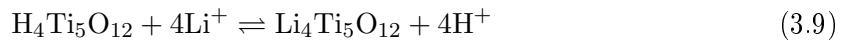


Figure 3.14: Illustration of the LIS effect. Reproduced with permission from Xu et al. from Elsevier.⁶²

One of the main problems of LMOs is the dissolution of MnO_2 in water, which leads to significant water pollution and has prevented their industrial application so far. An explanation of the mechanism of the dissolution was recently made explained by Gao et al. using $\text{Li}_{1.6}\text{Mn}_{1.6}\text{O}_4$ as LMO. They showed that an electron is transferred from Mn^{3+} in the bulk phase to Mn^{4+} in the acidic environment. Above a specific concentration, i.e., when enough electrons were transferred, the Mn^{4+} was converted to Mn^{2+} and dissolved simultaneously. It is worth mentioning that Mn^{3+} can easily be disproportionated and is most likely the reason why the LMOs dissolve in water after some time. Currently, research is being done to suppress this reaction by reducing the lattice constant or other modification approaches.⁷⁸

Lithium titanium oxide (LTO) LIS based on titanium oxide are the other group of ion sieves that do not have the issue of ion sieve dissolution and have therefore attracted significant attention. As mentioned above, the precursor structures define the properties of the ion sieve. While all LMOs show spinel structures, e.g., H_2TiO_3 LTOs show a layered structure. The intercalation/decalation mechanism of layered structure LMOs is less complex compared to spinel structures. Figure 3.15 shows the spinel and layered structure of Li_2MnO_3 and Li_2TiO_3 .⁶² The adsorption mechanism based on a ion exchange mechanism is shown in Eq. 3.8 and 3.9. Lithium complexation is exceptionally high for this particular example of the H_2TiO_3 ion sieve since the exchange sites of the layers are very narrow. The selectivity of lithium towards the other ions shows the following trend $\text{Li}^+ \gg \text{Na}^+ > \text{Mg}^{2+} > \text{Ca}^{2+} > \text{K}^+$. The SF of Li^+ to the other ions is at least over 100.⁷⁹ It was shown that the SF of Li^+ to Mg^{2+} could reach a value of 4783, which is a very high selectivity and can hardly be achieved by other methods.^{30,79}



A theoretical adsorption capacity of $142.9 \text{ mg}\cdot\text{g}^{-1} \text{ Li}^+$ was determined for the LTO of H_2TiO_3 .⁸⁰ However, max 40 % of the theoretical value has been achieved so far, which is most likely due to the low Li^+ content of the precursor ($\beta\text{-Li}_2\text{TiO}_3$) and aggregation of the particles resulting from the preparation of it at high temperatures. It was also shown that the preparation of LTO based on anatase instead of rutile achieved a high adsorption capacity of $39.2 \text{ mg}\cdot\text{g}^{-1}$.⁸¹ He et al. also studied this system and obtained an adsorption capacity of $57.8 \text{ mg}\cdot\text{g}^{-1}$ under optimal reaction conditions.⁷³ The work of Luwagou et al. confirmed for H_2TiO_3 an adsorption capacity up to $94.5 \text{ mg}\cdot\text{g}^{-1}$, which is far superior to all other LIS.⁸² In addition, after more than 100 extraction cycles less than 10 % capacity loss was determined.^{30,83}

The progress of nanotechnology has had a significant influence on LIS. As mentioned above, the structure of the precursor is crucial. Different morphologies such as nanorods, nanowires, nanoparticles, nanoblooms, nanotubes, and nanofibers could be produced through the combination of nanosynthesis techniques.⁸⁴⁻⁸⁸ Performance, as well as reusability, were improved.³⁰

In the paragraph about LMOs, the problems of manganese and its dissolution in water were discussed, which most-likely results from the disproportionation of the manganese (III) (Mn^{3+}). The specific electron configuration ($[\text{argon (Ar)}] 3d^5 4s^2$) distorts the lattice structure resulting from the Jahn-Teller effect.⁸⁹ Therefore, some research has dealt with doping the material structure, replacing Mn^{3+} with Fe^{3+} , cobalt (II) (Co^{2+}), or nickel (II) (Ni^{2+}).^{62,90-92} For example, by incorporating Fe^{3+} , the ion sieve can be magnetically recycled, which is a green alternative recycling option for recovering Li^+ .⁶² In the work of Wang et al., LTO

LIS were replaced with Fe^{3+} , and successful magnetic separation of LIS from suspension was achieved without loss of adsorption.^{43,93} In another publication of Zhao et al., the addition of Fe^{3+} to LMOs decreased the dissolution in water and increased the recyclability by magnetic separation.^{30,94}

Since the LIS are usually used in powder form and thus have disadvantages such as liquidity, permeability, efficiency, and energy consumption, new forms have been developed by granulation, foaming, membranes, fiber formation, and magnetization.^{95–98} However, some of these methods reduce the stability, adsorption efficiency of Li^+ , and capacity. Therefore, using such systems on an industrial scale is still a big challenge, which requires further research.³⁰

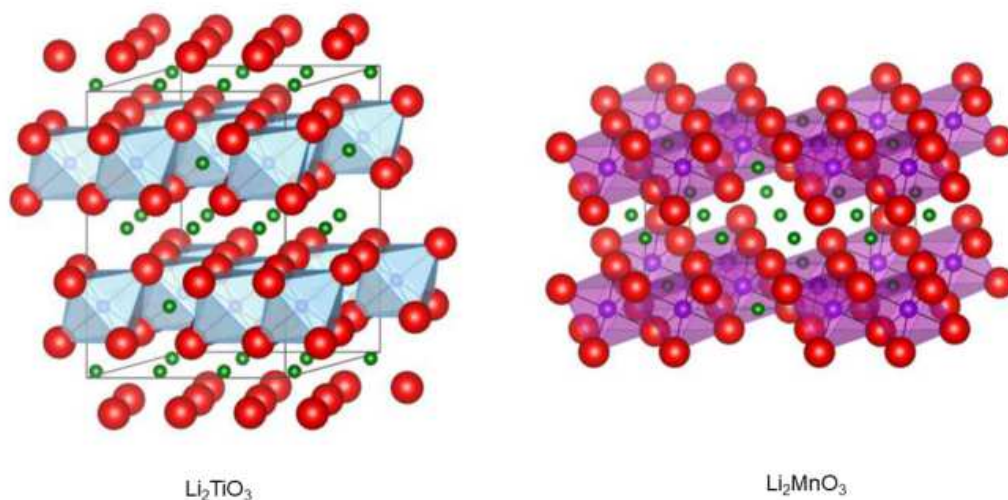


Figure 3.15: Structure models for ideally ordered Li_2TiO_3 (left) and Li_2MnO_3 (right). The green dots represent lithium, red oxygen, blue titanium, and purple manganese, respectively. Reused with permission from Watanabe et al. from Elsevier.⁹⁹

Membrane technology Membrane technology is an already established industrial process used for the separation or recovery of different groups of substances and has also been investigated for the separation of metal ions. The membrane applications relevant for the separation of metal ions can be divided into three groups (based on the driving force of the separation): nanofiltration (pressure-driven), liquid membrane (chemical potential driven), electrodialysis, and membrane electrolysis (electrical potential driven). Some of them will be reviewed in the application of Li^+ recovery. The structure for describing the membrane technology is based on the review articles by Li et al. and Liu et al.^{19,30}

Nanofiltration membrane Nanofiltration (NF) technology is one of the new processes in membrane technology. Its properties are between ultrafiltration (UF) and reverse osmosis (RO) membranes. The separation efficiency is triggered by sieve and Donnan effects. Physical properties such as pore size, membrane thickness, and surface charge density have also an impact on the membrane separation performance. Charged surfaces of the membrane allow the separation of multivalent ions (such as the separation of Mg^{2+} and Li^+).^{19,30} Sun et al. used a Desal (DL) NF membrane (DL-2540 NF) to separate Mg^{2+} from Li^+ from brines that has been successfully applied up to a $\text{Mg}^{2+}/\text{Li}^+$ ratio of 20.¹⁰⁰ In another work, a 3B02S NF membrane was tested in a brine with a high $\text{Mg}^{2+}/\text{Li}^+$ ratio, with successfully separating of Mg^{2+} .¹⁰¹ The NF membrane exhibited similar properties with a positively charged surface and subsequent modification with ethylenediaminetetraacetic acid (EDTA).^{41,102} The stability of NF membranes was investigated by salinity and pH. It was reported that an increasing salt concentration of the solution strongly decreased the flow rate. In addition, it was shown that low pH made the separation of Mg^{2+} to Li^+ more efficient by increasing the dielectric exclusion of multivalent ions. The $\text{Mg}^{2+}/\text{Li}^+$ ratio thereby decreased from 13.25 to 0.17.¹⁰² One other promising result was shown by Zhang et al., where a NF membrane with hydroxyl-containing multi-walled carbon nanotubes (CNT) fabricated from polyetherimide (PEI)/M-CNTs (MPMC) was employed.¹⁰³ This example achieved a separation of divalent ions from monovalent ions of about 97 %. However, a NF membrane based on metal-organic frameworks (MOFs) obtained the best results so far. A $\text{Mg}^{2+}/\text{Li}^+$ selectivity of 1815 was obtained, while the flux could be maintained at a high value of about $6.7 \text{ mol m}^{-2} \text{ h}^{-1}$.¹⁰⁴ The separation of anions present in brines or seawater was also investigated using a NF membrane.^{105,106}

In summary, the NF membranes already show many excellent properties for separating ions from brines and seawater. However, difficulties can occur at high $\text{Mg}^{2+}/\text{Li}^+$ ratios. An even bigger problem are fouling phenomena, which can drastically deteriorate permeability and selectivity.

Electrodialysis Electrodialysis (ED) is an electro-membrane process used, for example, to desalinate brines.¹⁰⁷ In ED, anion and cation exchange membranes are arranged alternately.¹⁹ As soon as an electric field is switched on, the cations and anions migrate through the ion-exchange membrane (IEM) to the respective electrodes.

For the application of membranes, the separation of monovalent from divalent ions is fundamental since the multivalent ions are often present in a higher concentration in brines or seawater. Therefore, the development of IEM that separate mono from divalent ions are of great importance. This is done by replacing the standard IEM by monovalent selective IEMs, called selective ED (S-ED).¹⁰⁸ The monovalent ions Li^+ , Na^+ , K^+ migrate through the membrane, and the multivalent ions such as Ca^{2+} and Mg^{2+} are blocked. Since the concentration of the monovalent ions is thus increased, Li_2CO_3 can be precipitated at 80-90 °C (as it is proceeded in the commercial precipitation process of ores or brines).¹⁰⁹

The S-ED technology was investigated in a synthetic brine with a $\text{Mg}^{2+}/\text{Li}^+$ mass ratio

of 150, achieving a Li^+ extraction efficiency of 95.3 %.¹⁰⁶ Thus, technical superiority over NF filtration was achieved at high $\text{Mg}^{2+}/\text{Li}^+$ ratios. The selectivity of Li^+ over other competing monovalent ions and anions such as SO_4^{2-} and HCO_3^- was also investigated.^{110,111} It was found that K^+ is more competitive to Li^+ than Na^+ , most-likely due to the small hydration radius. Furthermore, anion investigation showed that the migration of Mg^{2+} is affected, but not that of Li^+ , which is due to the strong attraction of Mg^{2+} to SO_4^{2-} and the formation of MgHCO_3 . In this context, it should also be mentioned that an NF membrane has recently been developed by Ge et al., which has achieved a double selectivity of Na^+ over Mg^{2+} compared to the IEM.¹⁹

Besides the traditional ED, there is also the bipolar membrane ED (BMED), which finds application in isolating LiOH from a saline solution. Once an electric field is applied, the water dissociates into H^+ and OH^- , which is used to produce LiOH from the original Li_2CO_3 compound. Purities of 95 % are obtained.^{112–115}

S-ED can selectively separate Li^+ from multivalent ions, but the efficiency is poorer once Li^+ is separated from other monovalent ions.^{116,117} RTILs are a possible alternative since, as discussed in the previous Section, they are highly selective, bring high stability, and are less volatile. ED was combined with the RTIL TMPA-TFSI, which suppresses the transfer of Li^+ from the anode to the cathode due to the low conductivity of Li^+ (Figure 3.16).¹¹⁸ Thus, the concentration at the anode is higher and can be recovered more easily. A separation factor of Li^+ to Na^+ of 2 and Li^+ to K^+ of 3.5 was achieved when a voltage of 2-3 V was applied.¹¹⁹

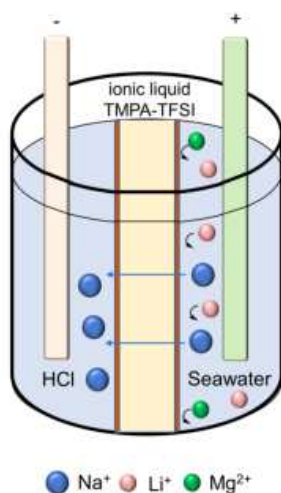


Figure 3.16: Illustration of the RTIL based on TMPA-TFSI ED. Li^+ is blocked by the ionic membrane. Reproduced from Liu et al. with permission from Elsevier.³⁰

Briefly, the S-ED are valuable methods to recover lithium in an environmentally friendly way. However, further research is needed to improve selectivity, especially for the other monovalent ions.¹⁹

Permselective exchange membrane capacitive deionization In capacitive deionization (CDI), anions and cations are adsorbed on the electrodes by an electric field.^{120–122} When the electric potential is charged or discharged, the ions are desorbed in a reverse manner to regenerate the electrodes. The deionization efficiency has been improved by capacitive membrane ionization. In the membrane capacitive deionization (MCDI), the IEMs are inserted between two porous oppositely charged electrodes. The ion selectivity of the IEM allows cations and anions to migrate to oppositely charged electrodes.^{91,123} To separate ions selectively, MCDIs have been extended with a permselective exchange MCDI (PSMCDI), which can be used to separate lithium and keep energy consumption low. A typical PSMCDI setup is shown in Figure 3.17. Li^+ migrates through the monovalent cationic exchange membrane before adsorbing at the cathode. Mg^{2+} is blocked by the membrane and remains in feed solution. The energy consumption was just about $1.8 \text{ Wh}\cdot\text{mol}^{-1} \text{ Li}^+$, which is much lower than the traditional ED technology ($40\text{--}270 \text{ Wh}\cdot\text{mol}^{-1} \text{ Li}^+$).^{124,125}

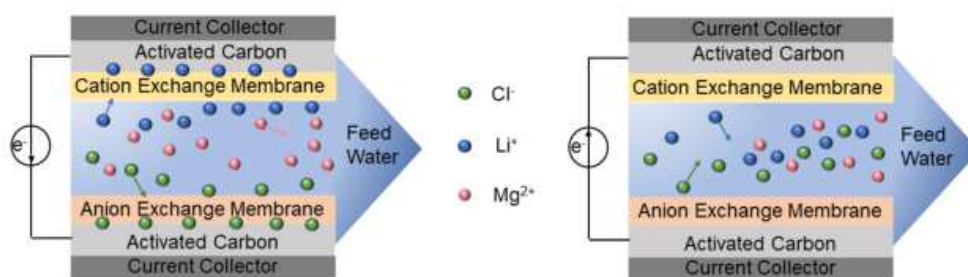


Figure 3.17: Illustration of PSMCDI lithium extraction of the adsorption (left) and desorption process (right). Reproduced with permission from Shi et al. from Elsevier.¹²⁶

Briefly, some of the promising membrane technologies and their advantages and disadvantages are summarized in Table 3.3. NF is an effective method to reduce the ratio of $\text{Mg}^{2+}/\text{Li}^+$. ED with monovalent IEMs, bipolar membrane, and the liquid membrane has established many new methods for Li^+ isolation. However, this method is only relevant for low concentrations. Also, the production is complex and thus limits the application on a technical scale.

Many different methods have been presented in this Chapter. Some of these techniques are already in industrial use, some are about to be commercialized, and some still need further research. In summary, many attempts have been made to improve extraction efficiencies and rates, increase the selectivity of Li^+ over Mg^{2+} and Na^+ , improve cyclic performance, and optimize and simplify operating conditions. Multiple functional groups such as β -ketones have been used as synergists or ionic liquids through various organic syntheses in solvent extraction. The main problem of organic compounds is their production of it, which is associated with a high cost and effort. The LIS technology is currently receiving much attention because of its excellent selectivity, high thermal capacity, and good cycling stability. This method is still limited industrially, as there are some uncertainties about the de/intercalation mechanism and the mold processing still poses some problems. Membrane electro dialysis combining solvent

Table 3.3: Overview of membrane-based technologies.⁹⁵

Method	Mechanism	Scale	Efficiency	Advantage	Limitation
NF	Steric hindrance, Donnan exclusion	Full	SF of Li ⁺ over Mg ²⁺ is 2.6-10.4, with MOFs 1815	low footprint	Membrane fouling, high investment and operation costs
S-ED	Electrical potential difference as a driving force for moving ions	Pilot	Recovery >95 %	High selectivity of monovalent ions and eco-friendly	Membrane fouling, energy cost increases with increasing saltinity
PSMCDI	Electrostatic adsorption	Laboratory	Recovery >83 %	High efficiency and eco-friendly	Low desorption efficiency

extraction and electrochemistry has also made some progress. However, further research is needed to ensure the applicability at high salt concentrations and obtain the material at a low cost.

An influential functional group that has been ignored so far is the compound of the CEs. In this thesis, the main focus is based on this group of organic adsorbers. In the following Chapter about *Supramolecular Chemistry*, the category of adsorbers is described in detail and the reason for choosing it in this work will be explained.

3.3 Supramolecular chemistry

This Chapter describes *supramolecular chemistry*, which has already been considered a very effective method for selectively obtaining metal ions. What makes this chemistry so special and why it is well suited to extract lithium ions from brines or seawater will be explained in detail.

Supramolecular chemistry is also referred to as the *chemistry beyond the molecules*. In 1987, Jean-Marie Lehn, Donald J. Cram, and Charles J. Pedersen received the Nobel Prize for developing molecules that form structure-specific interactions with each other without forming covalent bonds.^{127,128} The linkage of the molecules occurs through ionic bonds, hydrogen bonds (and other dipolar interactions), metal coordination interactions, halogen bonds, and aromatic stacking. A typical example is a CE–metal bond, where the CE is the host and the metal ion the guest ion (Figure 3.18). In host–guest bonding, the guest orients itself in the intrinsic binding cavity of the host. The binding energy between host and guest is a measurable quantity and is often presented as a characteristic feature to determine the energetic state of the new resulting bond. The formed supramolecule has unique properties that go beyond the properties of the individual components.

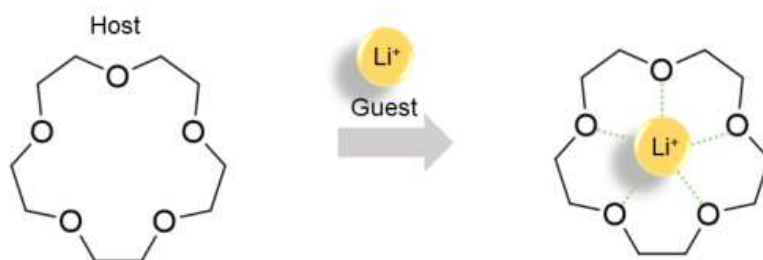


Figure 3.18: CE–cation interaction exemplary shown for the 15-crown-5 and Li^+ .

In the following, the newly formed bond of the supramolecule and its features is described. To keep things simple, it will be defined using a commonly known host–guest interaction. The host is usually a large molecule such as an enzyme or a macrocycle with a cavity containing convergent binding sites like basic Lewis donor atoms or hydrogen bond donors. The guest can be a cation, anion, ion pair, dye, analyte, hormone, pheromone, or neurotransmitter, which have divergent binding sites such as a spherical Lewis acidic, metal cation or hydrogen bond acceptor anion. The binding site is defined as the part that can participate in non-covalent binding.

Besides the host–guest interaction, many other reaction processes lead to the formation of supramolecules. An essential difference between host–guest binding, which often occurs in solution, is the host has extra molecular cavities that are only important in crystalline solids (Figure 3.19). Cavities are the gaps between multiple hosts. In contrast, in cavitands, the

host has permanent intramolecular cavities, which are based on a thermodynamic equilibrium bonding process, while in the crystallization process, host-guest bonding is a thermodynamically and a kinetically driven process (resulting from the transition from solution to solid). Moreover, in crystals, not every host is occupied by a guest, so they can be non-stoichiometric. Systems that can self-assemble, such as gels, liquid crystals, and supramolecular polymers, forming non-covalent bonds, also belong to the supramolecular structures class (in Section 3.6., 3.7, and 3.8, the topic of self-assembly is discussed in further detail).

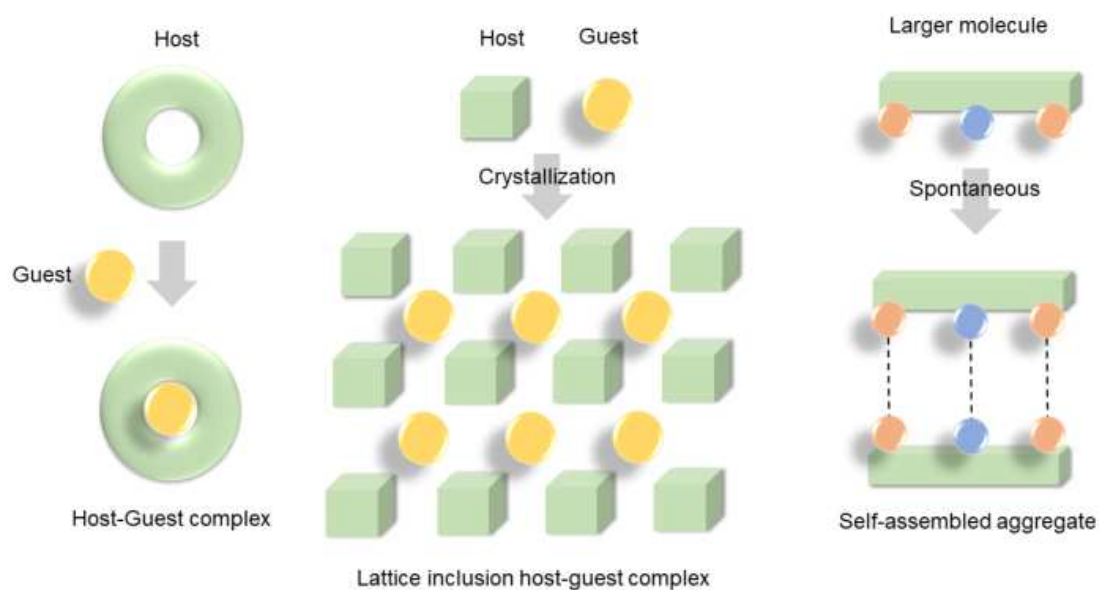


Figure 3.19: Types of supramolecular assembly process by a cavitate and guest, crystal packing of host molecules, in the solid state to obtain a lattice inclusion complex, and spontaneous self-assembly molecule. Reproduced with permission from J-W. Steed and J.L. Atwood from John Wiley and Sons (Figure 1.1 and 1.3 were combined).¹²⁹

In conclusion, modern supramolecular chemistry goes far beyond the original definition of the host-guest interaction. It includes molecular devices and machines, molecular recognition, self-assembly, self-organization, crystal engineering, supramolecular materials, and dynamic covalent chemistry. It also has an overarching significance in biology and nanochemistry. Due to its rapid development, supramolecular chemistry has become a valuable tool to unite molecules and materials, especially crucial for modern technology.¹²⁹

3.3.1 Nature of supramolecular interactions

This Chapter intends to explain the choice of adsorbents, the mechanism of ion complexation, and its dependence on various parameters that are part of Publications 1, 2, 4, and 5.

In supramolecular chemistry, at least two atoms are part of the structure, held together by non-covalent chemical bonds such as hydrogen bonding, ion pairing, interactions between π -acids and π -bases, metal-ligand bonding, Van-der-Waals attractive forces, solvent reorganization, and partially formed and broken covalent bonds (transition states). When considering the supramolecular system, it is advisable to examine the different interactions and the effects that are important in both interaction sides, such as solvation, ion-pairing, crystal lattice, to understand the complex system better. The different interactions and effects will be explained in more detail based on the textbook of J-W. Steed and J.L. Atwood "Supramolecular chemistry" and S. Kubik "Supramolecular chemistry".^{129,130} Attempts were made to present more current research results to illustrate examples of the respective interactions.

3.3.1.1 Ion-ion interaction

The ion-ion interaction is the prototype of an electrostatic interaction between a positively and negatively charged ion and is comparable in strength to the covalent bond ($100\text{-}350\text{ kJ mol}^{-1}$).^{131,132} The energy of this interaction is described according to Coulomb's law (Eq. 3.10).^{126,133} The values q_1 and q_2 are the charges of the particles, ε the dielectric constant of the solvent or medium, and ε_0 the dielectric constant of the vacuum. As soon as q_1 and q_2 have different charges, the attraction energy of the particles is $E < 0$. Based on Eq. 3.10, the attraction becomes weaker when the distance between the ions increases or the medium becomes more polar. It is worth mentioning that Eq. 3.10 assumes only point charges.¹³⁴ However, in reality, ions have finite radii and come together only up to a certain distance since the electron clouds of the respective ions repel each other at some point. In addition, the relative permittivity only partially explains the effects of the medium. Solvation of the binding sites, i.e., the direct interaction of binding sites and solvent molecules and reorganization of the solvent molecules as soon as a supramolecular structure is formed, are crucial for the actual interaction of the molecules.¹²⁹

$$E = \frac{q_1 \cdot q_2}{4 \cdot \pi \cdot \varepsilon \cdot \varepsilon_0 \cdot r} \quad (3.10)$$

Furthermore, ions also exist in different structures. For example, inorganic anions can be linear, trigonal, planar, tetrahedral, or octahedral.¹³⁵ For organic ions, the structures are even more complex; their interaction depends on the approach direction of the binding partner. In addition, charges are distributed throughout the molecule by inductive and mesomeric effects. Therefore, electrostatic interactions in such molecules are weaker and depend on many more factors than shown in Eq. 3.10. Nevertheless, the formula gives information about the efficiency of the exchange, which is directly correlated with the number of charges of the bonding partners.¹²⁹

3.3.1.2 Ion–dipole interaction

Ion–dipole interactions occur between a charged molecule and polar uncharged molecules.¹³⁶ Their strength depends on the magnitude of the ion’s attractive and repulsive forces and the polarized partial charges of a molecule. The bonding of a Li^+ with a polar component such as water is an example of an ion–dipole interaction. The hydration enthalpy (ΔH_{hydr}^0), which is crucial for ions in water, decreases in the following order: $\text{Mg}^{2+} > \text{Ca}^{2+} > \text{Li}^+ > \text{Na}^+ > \text{K}^+$; $-1949 > -1604 > -531 > -416 > -334 \text{ kJ mol}^{-1}$.^{129,137} The energies are crucial and result from the primary and secondary hydration sphere, which is especially effective for the Li^+ and thus results in a low conductivity. Eq. 3.11 determines the dipole bond with θ , the angle between the dipole of the point charge to the dipole moment μ ($\mu_1 = q_2 \cdot l$), and the distance l between the charges forming the dipole.^{129,136}

$$E = \frac{\mu_1 \cdot q_2 \cdot \cos(\theta)}{4 \cdot \pi \cdot \varepsilon \cdot \varepsilon_0 \cdot r^2} \quad (3.11)$$

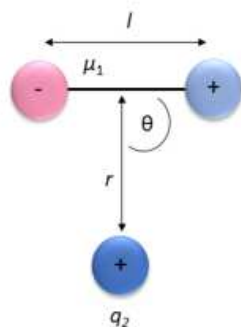


Figure 3.20: Illustration of the ion–dipole interaction with l the distance between the partial charges, r the distance between the cation and the diatomic molecule, and θ the angle. In the presented image $E = 0$, since $\theta = 90^\circ$. The idea of the illustration was inspired by the work of J-W. Steed and J.L. Atwood.¹²⁹

Coordinative bonds (formerly dative bonds) are also part of the ion–dipole interactions that interact with non-polarizable metal cations and hard bases (see Figure 3.18). The hydration energies of anions resulting from ion–dipole interactions are usually very high and must be balanced by the receptor. Thus, anion receptors in water are much more likely to bind if they carry a positive charge.^{129,130}

Table 3.4 shows the ΔH_{hydr}^0 of some cations and anions often found in brines or seawater. Ion–dipole interactions increase linearly with the charge density of the ion, with the smaller ions having stronger ΔH_{hydr}^0 and thus interacting better with water molecules.^{130,137} The charge distribution for small ions to a smaller volume is higher compared to charge density distributed to a larger volume. Therefore, electrostatic potential is less negative, and the electrostatic interaction is weaker. Moreover, the enthalpy of hydration decreases for $\text{I}^- > \text{Br}^- > \text{Cl}^- > \text{F}^-$.^{129,130,137}

Comparing Li^+ and Mg^{2+} , which have a very similar ionic radius in aqueous solution ($\text{Li}^+ = 0.60 \text{ \AA}$ and $\text{Mg}^{2+} = 0.65 \text{ \AA}$), ΔH_{hydr}^0 of Mg^{2+} is almost four times larger than the one from Li^+ , which correlates with Eq. 3.11. ΔH_{hydr}^0 of anions is generally larger than of cations, although, for example, the ionic radius of F^- is larger than Na^+ . This higher ΔH_{hydr}^0 results due to the orientation of the water molecules to the ion's first hydration shell. In the case of the cation, the water molecule approaches with the oxygen atom and in the case of the anion with the positively polarized protons, which are smaller than the oxygen atoms (Figure 3.21). The water molecules approach the anions at a minimal distance so that the ion-dipole interaction is stronger in comparison with the cation-oxygen interaction.^{129,130}

Table 3.4: ΔH_{hydr}^0 and ionic radius of anions and cations. Data was taken from S. Kubik.¹³⁰

Cation	Cation radius [\AA]	ΔH_{hydr}^0 [kJ mol^{-1}]	Anion	Anion radius [\AA]	ΔH_{hydr}^0 [kJ mol^{-1}]
Li^+	0.60	-531			
Na^+	0.95	-416	F^-	1.36	-510
K^+	1.33	-334	Cl^-	1.81	-367
Mg^{2+}	0.65	-1949	Br^-	1.95	-336
Ca^{2+}	0.99	-1604	I^-	2.16	-291

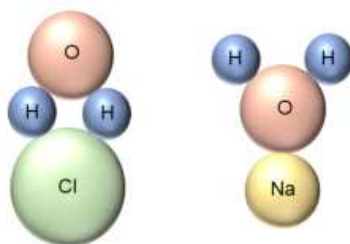


Figure 3.21: Illustration of the interaction between the water molecule and an anion or cation, which is orientated viceversa, respectively. The idea of the illustration was taken from S. Kubik.¹³⁰

3.3.1.3 Dipole-dipole interaction

A dipole-dipole interaction is very weak ($5\text{-}50 \text{ kJ mol}^{-1}$) and results from two or more uncharged polar molecules.¹³⁸ Such an interaction is observed in solvents with a permanent dipole moment. These include, for example, water, chloroform, acetone, or dimethyl sulfoxide (DMSO). The dipoles are aligned so that the positive and negative ends can approach each other. How strong a dipole-dipole bond is depends on the magnitude of the dipole moment and the arrangement of the dipoles. Eq. 3.12 describes this behavior. With the energy dependency by the factor $\frac{1}{r^3}$, it is clear that the energy drops more rapidly as the distance of the dipoles moves away compared to the ion-ion and ion-dipole interactions. The last term represents the arrangement of the dipoles in space by the angles θ_1 , θ_2 and φ (Figure 3.22).^{129,130}

$$E = -\frac{\mu_1 \cdot \mu_2}{4 \cdot \pi \cdot \varepsilon \cdot \varepsilon_0 \cdot r^3} (2 \cdot \cos \theta_1 \cdot \cos \theta_2 - \sin \theta_1 \cdot \sin \theta_2 \cdot \cos \varphi) \quad (3.12)$$

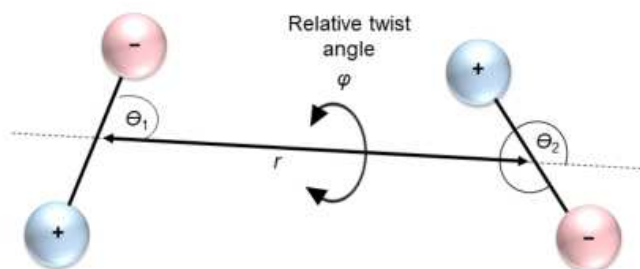


Figure 3.22: Illustration of the dipole interaction at the distance r and the angles θ_1 , θ_2 and φ representing the orientation of the dipoles in space. The illustration was inspired by the work of S. Kubik and J.W. Atwood.^{129,130}

3.3.1.4 Hydrogen bonding

Hydrogen bonds are one of the most essential interactions other than covalent interactions, which are of particular importance in biochemistry, such as the structure of deoxyribonucleic acid (DNA), whose double helix is based on hydrogen bonds.¹³⁹ These bonds behave similarly to ion–dipole or dipole–dipole interactions, depending on the structure of the binding partner created by an electronegative atom and a proton-containing interaction partner. Strictly speaking, hydrogen bonding is a combination of electrostatics, polarization and dispersion.¹²⁹ Figure 3.23 shows the schematic structure of a hydrogen bond. X-H is the hydrogen bond donor with X (usually an electronegative heteroatom). Y is a neutral or charged molecule that is the binding partner of the proton donor and interacts with the positively polarized hydrogen atom. This includes not only electronegative heteroatoms but also π -systems.¹³⁰

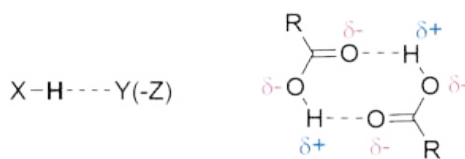


Figure 3.23: Schematic illustration of the hydrogen bond with H being the proton, X typically the electronegative heteroatom, Y the hydrogen acceptor, and Z the corresponding molecule species (left). An exemplary hydrogen bonding between electronegative atoms (red δ_-) and proton-containing partners (blue δ_+) is presented (right).

Depending on the molecule, the electrostatic interactions of H and Y can vary. The strength of the alternating effect can be investigated by IR and NMR spectroscopy.¹⁴⁰ As soon as hydrogen bonding occurs between H and Y, the strength of the X-H bond decreases. This weakening causes the X-H vibrational band to move to lower wavenumbers and become more intensive and broader in the IR spectrum. At the same time, a new H-Y vibrational

band is formed, which can also be observed in the IR spectrum. In the NMR spectrum, hydrogen bonding causes a shielding of the proton; therefore, the signal of the proton participating in hydrogen bonding shifts to lower frequencies.^{130,140}

The strength of the interaction of proton transfer from the donor to the acceptor is determined by the degree of acidity of the donor and the degree of the base of the acceptor. A complete proton transfer is also possible if it is thermodynamically favored. However, it leads to an ion pair that forms a salt bridge, stabilized by hydrogen bonding and ionic interactions.¹³⁰

As shown in Figure 3.23, hydrogen bonding can occur at multiple sites, leading to symmetric bonding of the molecules.^{141,142} Such bonds are strong and comparable to a weak covalent bond (50-150 kJ mol⁻¹ in the gas phase). However, hydrogen bonds are usually weaker than this and range between 15-50 kJ mol⁻¹ and may even be less than 15 kJ mol⁻¹ in exceptional cases, making them similarly weak as dispersion interactions.¹³⁰

Features of the hydrogen bond donor The strength of the hydrogen bond depends on the size of the partial charge.¹⁴³ In the series HI < HBr < HCl < HF, the donor strength increases with increased electronegativity. The trend follows the size of the dipole moments and not their acidity, which would be most prominent for HI and most minor for HF. However, as soon as the proton is bound to structurally similar molecules with the same atomic species, the electron density of the proton can be shifted by the substituents, which leads to a better hydrogen bond donor and stabilizes the negative charge caused by the deprotonation. Thus, a correlation between acidity and donor strength can also be observed in these cases. An example is the acetic acid derivative with electronegative substituents (e.g., Cl) in the α position, which shifts the electron density of the acid. The more chlorine atoms present, the higher the hydrogen bond donor strength (Figure 3.24).¹³⁰

NH groups' hydrogen bond donor strength, e.g., amides or thioamides, behaves similarly. Sulfur has a larger atomic radius than oxygen and can carry a more negative charge. Therefore thiols are more acidic than alcohol compounds. The charge transfer from N to S in thioamides is greater than the charge transfer from N to O in amides, and thus the NH groups in thioamides are also better hydrogen bond donors (Figure 3.24).^{130,144,145}

However, it is worth mentioning that weakly polarized X-H bonds also act as hydrogen bonding donors. Even C-H bonds can work as such, depending enormously on structural parameters, such as electronegative substituents on the carbon atom that increase the partial charge on the proton or the hybridization of the C atom, which is strongest for sp orbitals and weakest for sp³ orbitals. Therefore, aromatic C-H bonds are suitable hydrogen bond donors. Prominent examples are the 1,4-disubstituted and 1,2,3-triazole rings, which combine an intensely polarizing CH group with a significant dipole moment resulting from the three nitrogen atoms.^{130,146,147}

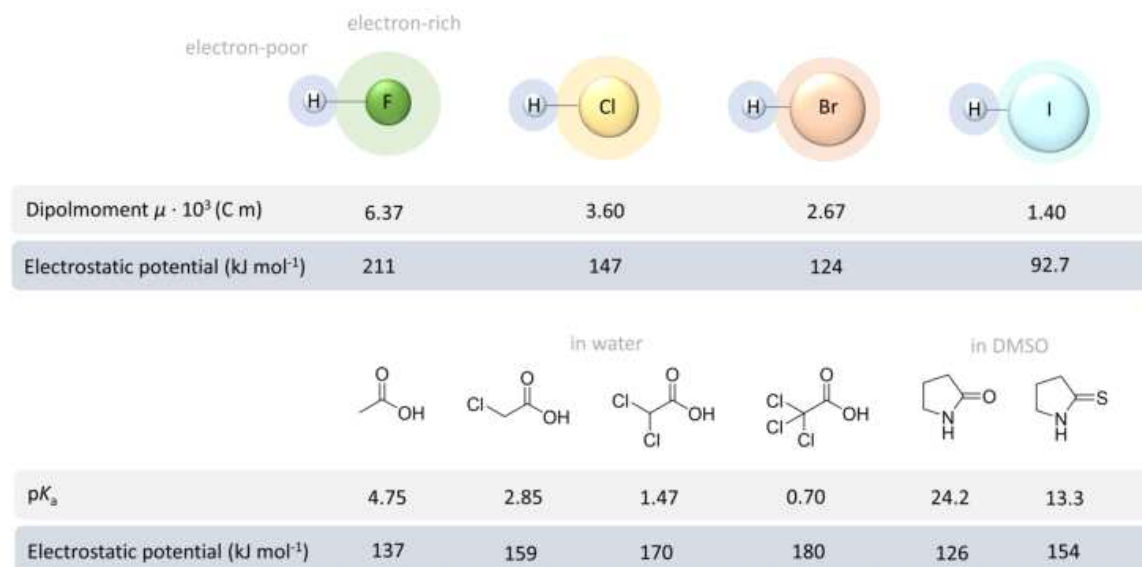


Figure 3.24: Electrostatic potential of X-H bonds and the corresponding dipolmoment (above) and the electrostatic potential as well as pKa value for some α acetic acid derivates and *N*-methyl acetamide and *N*-methyl thioacetamide. The data was taken from S. Kubik and the illustration was inspired by this work as well.¹³⁰

Features of the hydrogen bond acceptor Hydrogen bonding is particularly pronounced for anions with a high charge density. In the case of halogenides, the charge density increases in the following order $I^- < Br^- < Cl^- < F^-$. The same tendency occurs when water molecules hydrate anions; this property can be considered hydrogen bonding. For neutral molecules, the situation is more complex. Oxygen atoms have a higher electronegativity and higher partial charge than nitrogen atoms and are therefore better acceptors; fluorine, on the other hand, is a very poor acceptor (but in the halogen series, the strongest acceptor) since it has a very strong electronegativity and does not like to share electrons. Moreover, elements from the third period like sulfur or phosphorus are very weak acceptors because these atoms are huge and have a small electronegativity and, therefore, a small charge density.^{130,148}

Geometry of the hydrogen bond As soon as interactions are linked to dipoles, the directional dependence plays an important role, as Eq. 3.11 and 3.12. The hydrogen bonds behave analogously, which are most pronounced as soon as the proton approaches the point of highest electron density in the acceptor. The optimal arrangement is where the donor points directly towards the free electron pair of the acceptor. The alignment can be explained by the valence shell electron pair repulsion (VSEPR) theory model. This shows that amines or nitriles as acceptors form linear hydrogen bonds preferentially, and X-H bonds are orientated to acceptors with more than one lone pair at a certain angle.^{130,149,150}

Number of hydrogen bonds Besides structural aspects also the number of hydrogens play an essential role. Generally, the complex stability increases with higher number of hydrogen bondings, however, this is only possible if structural constraints will not occur on the compound. Such bonds do not always necessarily lead to a more stable bond, especially when the geometries deviate significantly from the optimal geometry. However, multiple bonds can also be generated by two or more parallel hydrogen bonds in spatial proximity. In this case, the number of bonds and their orientation is decisive for the stability of the bond. A typical example is double-stranded DNA.^{151,152}

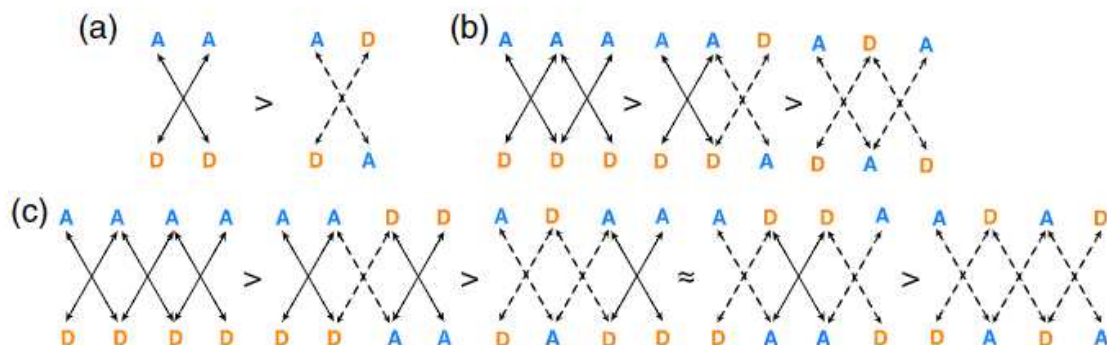


Figure 3.25: Some examples of multi bond hydrogen bond interactions with A representing the acceptors and D, the donors. (a) illustrates the doubly (b) triply, and (c) quadruply hydrogen bonded arrays. The solid line labels attractive interactions, while the dashed line illustrates the repulsive interactions, respectively. Reproduced with permission from L. J. Karas.¹⁵³

The complexes are most stable when one binding partner consists exclusively of donors and the other consists only of acceptors. In addition to the attractive interactions, there are also repulsive interactions between two or more protons, reducing the stability. If only repulsive interactions occur, the complex stability decreases by several orders of magnitude.^{130,154,155}

3.3.1.5 Halogen bonding

The halogen bond is also a non-covalent interaction that behaves similarly to hydrogen bonds. In contrast to the hydrogen bond discussed above, a halogen instead of a proton is shared between donor and acceptor components. The strength of the interaction increases in the following tendency: $\text{Cl} < \text{Br} < \text{I}$. In the hydrogen and halogen bond interactions, both, donor and acceptor are electronegative or contain electron-withdrawing atoms or groups. The acceptor is often a Lewis base (with free electron pairs). In contrast to the halogen bond, in the hydrogen bond, the proton is partially positively charged, and thus the attractive interaction is well understood. In the case of the halogen interaction, however, it is not apparent at first glance that its bond of an electronegative atom, the halogen, interacts with other electronegative compounds. Analysis of the electrostatic potential surface of an organic halide shows that the charge distribution around the halogen is anisotropic, with a negative potential around the axis superimposed on the X-Hal bond and a positive potential observed

in the X-Hal extension of the bond, the so-called σ -hole. In Figure 3.26, some example halogen compounds are shown.^{130,156,157}

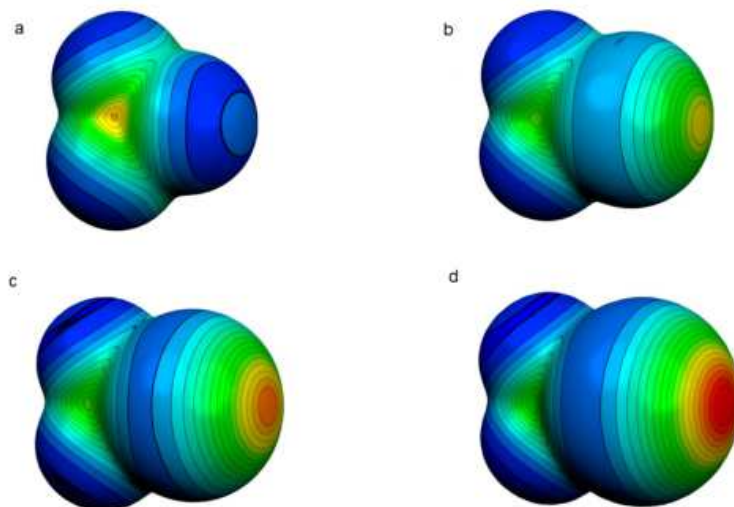


Figure 3.26: Molecular electrostatic potential of the internal surface in Hartrees of a) CF_3F , b) CF_3Cl , c) CF_3Br , d) CF_3I . One fluorine atom is not visible in the structure view since it is located on the other side of this surface illustration. The color code covers the potential range with red and blue being the absolute maximum in the negative and positive potential, respectively. Reprinted with permission from Clark et al. from Springer (Fig. 1-4 were combined).¹⁵⁷

The fluorine hemisphere is negative, as shown in Figure 3.26a, but the positive region is more substantial the more significant the halogen atom (indicated by the yellowish to red transition). The σ -hole is the reason for the halogen bond interactions, but these are not only dependent on the halogen atom but also strongly dependent on the halogen environment. For example, the halogen compound CF_3Cl , CF_3Br , and CF_3I are stronger with the three electronegative fluorine atoms; without them e.g., the CH_3Cl structure shows no σ -hole.^{130,156,157}

The σ -hole is induced by the halogen atom's orbitals and hybridization. The degree of hybridization is low in halogens so that the free electron pairs occupy the s, p_x or p_y orbital. The p_z orbital is thus available for bond formation. The visibility of the σ -hole at the X-Hal bond is due to the orthogonality of the p orbitals and the depletion of the electron density. As shown in Figure 3.26, fluorine atoms do not show the formation of a σ -hole. Fluorine is the element with the highest electronegativity and the most significant amount of sp^3 hybridization; these properties reduce the anisotropy of the charge distribution around the halogen atom. The directionality of the halogen bond also has a considerable effect on the size of the σ -hole, so even slight deviations from the ideal angle of 180 degrees lead to the reduction of the positive potential. Electrostatic models can help to observe this direction dependence. The necessity and importance of these models will be discussed in more detail in Section 3.4. However, it is worth mentioning that those models cannot explain the whole complexity of such interactions, however, they can help to understand the situation in supramolecular systems.^{130,156,157}

At the beginning of the Chapter, the similarity of the halogen bond to the hydrogen bond was pointed out. In the following, the essential differences between these bonds will be explained. In the halogen bond, the positive potential can be changed considerably by simply replacing the halogen atom. In addition, the anisotropy effect causes the halogen bond to have a significant degree of directionality. Furthermore, halogens as for example iodine are much softer than a proton and prefer softer acceptors. Thus, they are less susceptible to solvent effects because the solvation effect is not as pronounced as for protons. Halogen bonds are therefore called the "hydrophobic sister interaction" of hydrogen bonding.^{130,156,157}

3.3.1.6 Cation- π interactions

This Chapter discusses the interactions between a π -system and cations in more detail, since this thesis deals with lithium complexation. Before the π -cation interactions are described in more detail, one of the best-known π -systems, the benzene ring, is described.¹³⁰

Figure 3.27a shows the electrostatic potential surface for benzene. Both ring surfaces show a pronounced negative potential (red area). The six C-H bonds shift the electron density towards the edge forming a positive potential. The six dipoles of the C-H bond combine to form a permanent quadrupole moment, characterized by two dipoles adjacent to each other. These two dipoles compensate each other; the benzene ring is apolar. As soon as a cation approaches the center of one side, an attraction develops between the benzene ring and the cation. This interaction is called the cation- π interaction and is not limited to benzene rings but a wide range of π -compounds. The first observation of such an interaction was between benzene and a potassium ion in the gas phase.^{130,158}

Lariat ethers, CE with additional substituents, are another well-known example for π -cation interactions. The lariat ether in Figure 3.28 shows a stretched conformation in the solid-state, in that the indolyl groups point away from the ring. Without π -cation interactions, the conformation of the compound will not change, but as soon as these interactions take place, a conformational change occurs; both indolyl rings surround the ion.^{130,159}

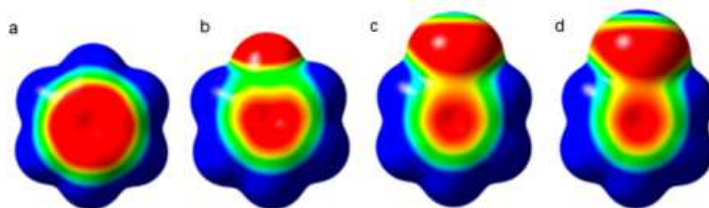


Figure 3.27: Electrostatic surface potential surface of benzene, fluorobenzene, chlorobenzene, and bromobenzene. Reprinted from Mottishaw et al. from ACS (permission was not required).¹⁵⁸

Electrostatic models have shown that the strength of the π -cation interaction is strongest when the cation is above or below the benzene ring, where the most negative potential is located. In the case of benzene, this would be in the middle of the ring. Some other benzene derivatives with their associated electrostatic potentials are shown in Figure 3.29.¹³⁰

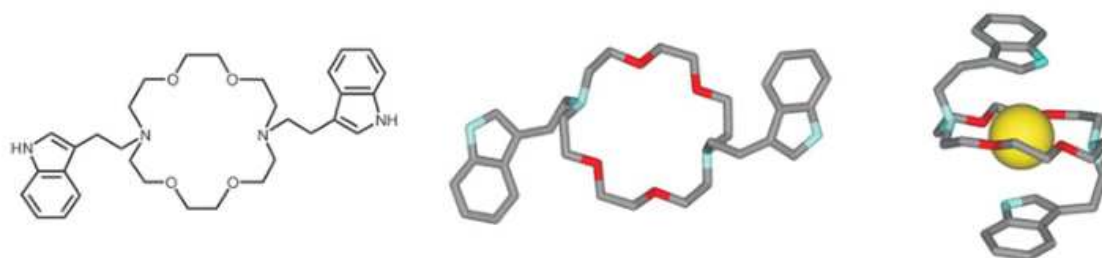


Figure 3.28: Molecular structure of *N,N'*-bis(2-(3-indolyl)ethyl)-4,13-diaza-18-crown-6, the solid-state X-ray structure and its complex with K^+ (from left to right). Reprinted with permission from W. Lu et al. from Elsevier.¹⁵⁹

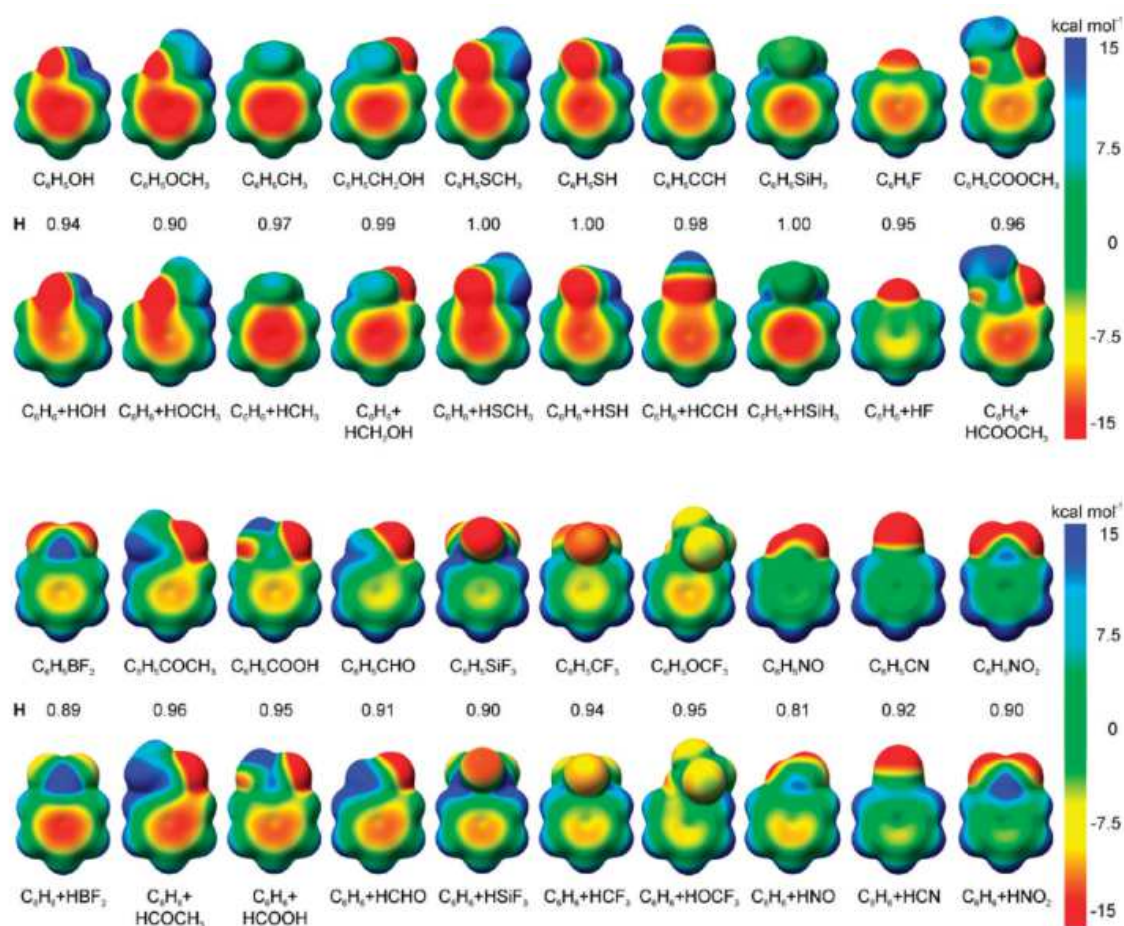


Figure 3.29: Molecular structure of the electrostatic potential surface of various benzene derivatives and the corresponding electron density surfaces ($0.001 e/au^3$). Reused with permission from Wheeler and Houk from ACS.¹⁶⁰

As soon as the arrangement of the cation deviates from this position, the weakening of the bonds is seen as the electrostatic interaction is reduced. Electrostatic models showed that the interaction between a cation and a π -system is strongly dependent on the charge density for the π -cation interaction in the gas phase. For alkali metal ions, the interaction increases in the following trend: rubidium (Rb^+) < K^+ < Na^+ < Li^+ . However, this trend is affected by the

solvent. For example, lithium and sodium ions in water show complexes with benzene weaker than rubidium ions in water since the affinity to form solvation shells is very high. Therefore, the interaction in the solution depends on the cation- π interaction's intrinsic strength and the solvation shell's strength.^{130,161}

3.3.1.7 Anion- π interactions

Anion- π interactions are based on electrostatic interactions between an anion and the positive potential of electron-deficient aromatic systems (see Figure 3.30), which is further enhanced when the anion is close enough to the π -system to exert ion-induced polarization to the π -system.¹⁶² However, these interactions have been difficult to detect experimentally and it is not easy to attribute determined binding energies exclusively to the anion- π interaction. The anion- π exchange has not yet been established, but it is becoming critical.¹³⁰ Since the anions have been less intensively investigated in this work, they will not be discussed in more detail. Nevertheless, it should be mentioned that such an interaction exists. For readers, who may want to have more background on this topic, the works of Schottel et al.,¹⁶² Politzer et al.,¹⁶³ and Erdelyi¹⁶⁴ are recommended.

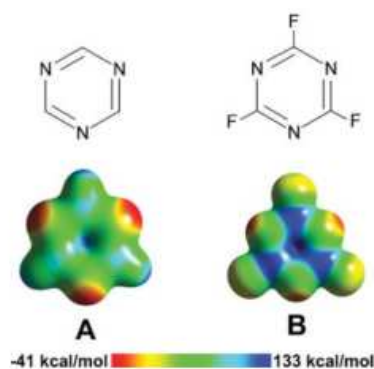


Figure 3.30: Molecular structure of the electrostatic potential surface of 1,3,5 triazine and trifluoro-1,3,5-triazine. Reprinted with permission from Schottel et al. from chemical society reviews.¹⁶²

3.3.1.8 Aromatic-aromatic interactions

As already shown in the cation- π and anion- π interactions, aromatic systems have regions of positive and negative electrostatic potential. Thus, interactions among two aromatic systems can also occur, provided the arrangement of these aromatics is favorable. In the example of benzene, the arrangements T-shaped (or edge-to-face) arrangement of two benzenes are most favorable because the positively polarized hydrogen atoms along the edge approach the face of the other benzene ring where the most negative electrostatic potential is highest (Figure 3.31). Aromatic rings can also be arranged in parallel if substituents of the aromatic compounds prevent a perpendicular arrangement or if solvent effects force such an arrangement. In the parallel configuration, the interaction is attractive only if the aromatic structures are shifted,

i.e., the edge of the aromatic ring lies over the negatively polarized portion of the other aromatic system. If the aromatic rings are stacked, there is no interaction, and therefore the often mentioned π - π stacking in literature, which is often equated with an interaction, should be viewed with caution. Stacking is favored only when the two aromatic rings have opposite electrostatic potential. An example of such interactions are benzene and hexafluorobenzene (see Figure 3.31 right).^{130,165,166}

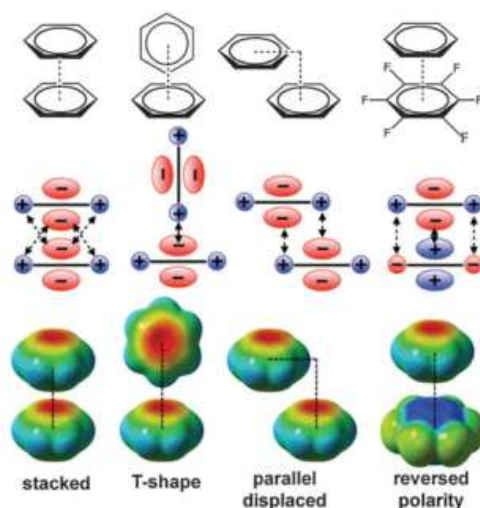


Figure 3.31: The molecular structure of the electrostatic potential surface of two benzene rings arranged in stacked, t-shaped, and parallel displaced formation and the stacked conformation of benzene and fluoro benzene (from left to right). Reprinted with permission from Matthews et al. from royal society of chemistry.¹⁶⁵

The π - π interaction goes beyond electrostatic interactions if the highest occupied molecular orbital (HOMO) of the donor and the lowest unoccupied molecular orbital (LUMO) of the acceptor are correctly aligned so that the energy gap between them is so small that superposition of the orbitals occurs. These mentioned charge-transfer interactions are often visually visible since the electron transfer from the HOMO to the LUMO requires energy in the visible range. Thus, such interactions can be observed in the ultraviolet-visible (UV-vis) spectrum.¹⁶⁷

3.3.1.9 Dispersion interactions

The weakest non-covalent interaction is the dispersion or Van-der-Waals interaction. They are the basis for interactions between apolar atoms or molecules without anisotropic charge distributions like noble gases or alkanes. These interactions are described by the Lennard-Jones potential V_{LJ} , which is divided into an repulsive (positive sign) and an attracting (negative sign) term (Eq. 3.13).^{?,130}

$$V_{\text{LJ}} = 4\varepsilon\left[\left(\frac{\sigma_{\text{LJ}}}{r}\right)^{12} - \left(\frac{\sigma_{\text{LJ}}}{r}\right)^6\right] \quad (3.13)$$

The variable σ describes the distance at which attraction and repulsion cancel each other out so that $V_{\text{LJ}} = 0$ ($\sigma_{\text{LJ}} = r$). ε , which depends on the polarizability of the bonding partners, describes the hardness of the interaction. Figure 3.32 describes the relationship between V_{LJ} and r . It can be observed that repulsion occurs at small distances, i.e., where orbitals of the interacting molecules overlap (Pauli repulsion). At a distance of $r > \sigma_{\text{LJ}}$, a small region is attractive; with a larger r to σ_{LJ} ratio, the attraction becomes weaker with a factor of r^{-6} . Since the strength of the induced dipole-dipole interactions increases with the increasing polarizability of the binding partners, the small range of attraction is often explained by oscillating dipoles. The movement of electrons in the molecule causes a fluctuating dipole moment, forming a complementary dipole moment with the respective binding partner.¹³⁰

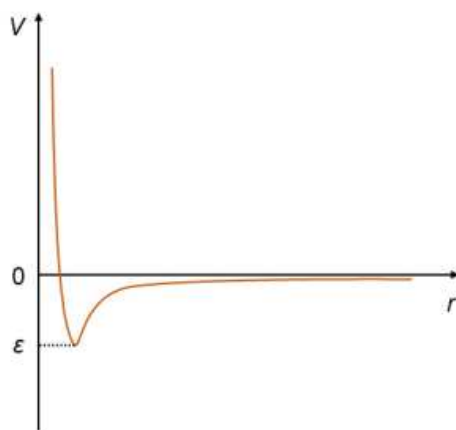


Figure 3.32: Lennard-Jones-potential.

Dispersion interactions increase in strength as the contact areas between two molecules increase. Intramolecular dispersion interactions are the basis for the stabilization of strongly hindered molecules. In Figure 3.33, two steric molecules are shown: 1,1,1,2,2-hexaphenylethane (left) and 1,1,1,2,2-hexakis(3,5-di-*tert*-butyl phenyl)ethane (right). The latter should be more unstable due to the even larger sterical groups; however, this molecule is more stable because of the intramolecular dispersion interaction of the *tert*-butyl groups with the aromatic residues. Since supramolecular complexes are structurally complex and often have many functional groups (polarizable units), intermolecular dispersion interactions lead to similarly strong sta-

bilizations.^{130,168} Such interactions are weak compared to the before mentioned interactions, however the dispersion interaction should not be ignored in a complexation process.

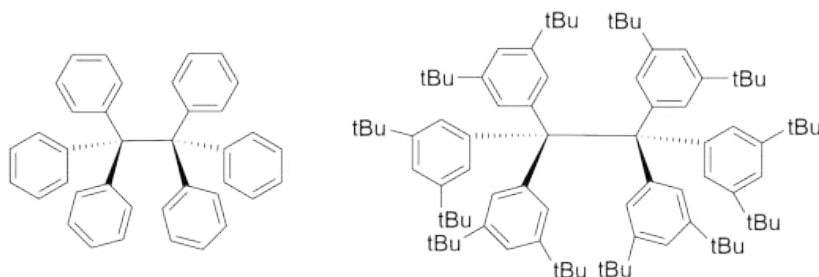


Figure 3.33: Molecular structure of 1,1,1,2,2-hexaphenylethane (left) and 1,1,1,2,2-hexabis(3,5-di-tert-butyl phenyl)ethane (right). To show the functional groups more clearly, bond angles of the structure were neglected.

3.3.2 Crown ethers

In this Chapter, CEs are introduced as a structural adsorber class for cations. These adsorbent materials represent the main part of this thesis. They were investigated in Publications 1, 2, 4, and 5. The following describes the structures, nomenclature, synthesis, and metal ion complexation properties of CEs.

In the selective complexation of metal ions from aqueous solutions, CEs play an essential role as adsorber material and have been studied for several decades. CEs consist of ethyleneoxy units and form macrocyclic polyether rings that can *crown* metal ions. Charles J. Pedersen was the discoverer of this chemical structure class. Since CEs can appear in a wide variety of modifications, the international union of pure and applied chemistry (IUPAC) names can become very complicated, long, and confusing. Therefore, Pedersen proposed the term *crown* for macrocyclic polyether rings. The CEs nomenclature has prevailed until today. The preceding number indicates the total number of atoms in the ring, and the trailing number specifies the heteroatoms in the ring. If substitutes such as benzene rings are connected to the CE, the prefix *benzo* is placed in front. The prefix *aza* and *thia* is used for nitrogen and sulfur, respectively, if nitrogen or sulfur atoms are replaced as donor atoms instead of the general oxygen donor atom within the CE ring. Some examples of the nomenclature are illustrated in Figure 3.34. Some of these structures can be found in Publications 2, 4 and 5.

Synthesis of crown ethers The CE structures are predominantly prepared via Williamson ether synthesis as shown in publication 1. Diols react with ditosylates or dihalogenides (dichlorides, dibromides, or diiodides) in the presence of a base to form CEs. During the synthesis of CEs and the desired [1+1] macrocyclization, [2+2] products or even larger rings can also be produced. Williamson ether synthesis is an irreversible reaction. Therefore, product formation is kinetically controlled. The product with the lowest Gibbs free energy of activation dominates in the reaction mixture. If the product is a ring with a favorable ring tension,

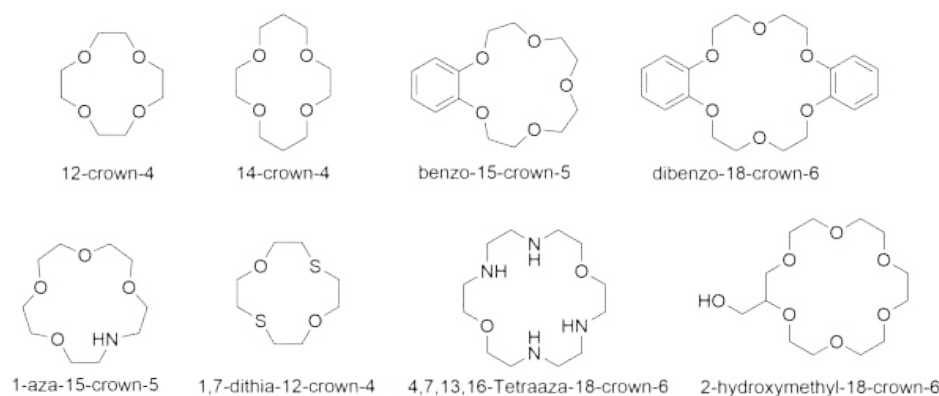


Figure 3.34: Illustration of some CE structures and their corresponding names according to the rules of the CE nomenclature.

there is no enthalpic loss for the system. The process is entropy controlled. Thus, both enthalpy and entropy play essential roles in CE synthesis. Therefore, intramolecular as well as intermolecular reaction pathways must be considered. Intramolecular reactions are usually entropically more favorable because the number of molecules in the solution is not reduced. Therefore, as far as small or medium-sized rings are formed as a product, such reactions are very efficient. However, suppose the distance between the two reacting groups becomes larger, the entropic term of the intramolecular interaction becomes less favorable. The linear precursor loses conformational degrees of freedom in forming a new conformation during ring formation. Therefore, macrocycles usually have low yields.

One method to suppress the formation of larger rings and increase the yield of smaller rings is to add a cation as a template that fits well into the cavity of the formed CE ring, such as the addition of K^+ to synthesize the 18-crown-6 (18C6) CE (see Figure 3.35). In this case, the cation most-likely does not influence the first reaction of the groups, but it does impact the direct building of the product. This results in folding of the linear chain and consequent convergence of the reacting groups. The unfavorable activation entropy is thus reduced, and the disadvantageous term, which is related to the restriction of conformational mobility, is compensated for by complex formation. Incorporating ion templates reduces the Gibbs free energy of activation of the macrocyclization, and the formation of the [1+1] macrocyclization can be better controlled.

Crown ether–metal ion complexes The complexation of metal ions with CEs is based on ion–dipole interactions depending on the cation, stabilizing orbital interactions between charge transfer and polarization, and Pauli repulsive orbital interactions.¹⁶⁹ During complexation, the metal is located in the center of the CE ring. The stabilization of the CE–metal ion complex depends on several factors such as the relative sizes of the ion and the cavity of the CE, the number and type of donor heteroatoms (according to the HSAB principle) in the ring, the coplanarity of the oxygen atoms, the symmetrical arrangement of the heteroatoms, steric hinderance of the CE, ion affinity and behavior towards the solvent, and the electrical

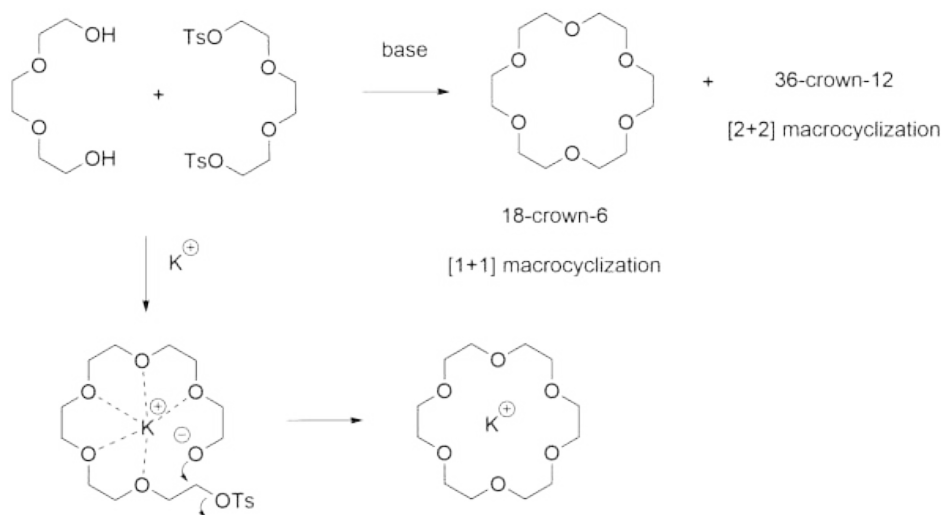


Figure 3.35: Illustration of the Williamson ether synthesis using a non-ionic base or K^+ as a base forming [1+1] and [2+2] macrocyclic polyethers or for the latter only the smaller 18C6 CE.

charge of the ion.¹²⁷ However, it is worth mentioning that even though in some cases the cavity size of the CE and metal ion do not match, higher ordered complexes like the so-called sandwich or club sandwich complexes can be formed (Figure 3.36). These kind of complexes are the reason for reduced selectivity of CE for a specific cation (see publication 4 and 5).¹⁷⁰

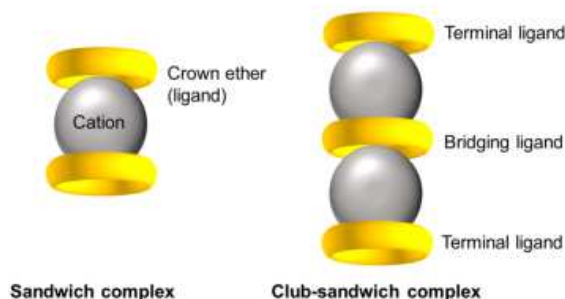


Figure 3.36: Illustration of CE–metal ion complexes forming a sandwich (left) and a club sandwich (right) complex. The yellow rings represent the ligand and the grey circle the metal ion.

To avoid the formation of higher ordered complexes, steric substituents can be incorporated to the CE to prevent the CEs from being orientated parallel to each other, forming sandwich- or club sandwich complexes.^{170,171} Some successfully prepared CEs preventing sandwich complexes' formation are shown in Figure 3.37. However, these CE compounds are costly to produce and economically unfeasible.

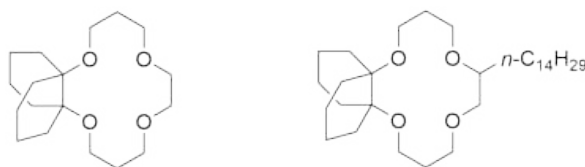


Figure 3.37: Bulky decalino-14-crown-4 (left) and tetradecyldecalino-14-crown-4 (right) CE.¹⁷⁰

Crown ether as lithium ion adsorber Lithium extraction from brines can be performed by choosing the appropriate CE size for the desired cation; an overview of the data of Li^+ , Na^+ , K^+ , Mg^{2+} , Ca^{2+} and the lithium selective CEs 12C4, benzo-12-crown-4 (B12C4), 14-crown-4 (14C4), benzo-14-crown-4 (B14C4), and dibenzo-14-crown-4 (DB14C4) and the corresponding selective order of the alkali metals Li^+ , Na^+ , K^+ , Rb^+ , and caesium (Cs^+) are shown in Tab. 3.5. In aqueous resources, the concentrations of Mg^{2+} and Na^+ are usually very high, therefore, the selectivity of these two ions over Li^+ is the main challenge. Mg^{2+} , in particular, as the properties and ion size are very similar to Li^+ . Also the selectivity toward Na^+ is still a big part of current research since the lithium ion selective CEs (forming single complexes with Li^+), often form sandwich complexes with Na^+ .

As mentioned above, predicting a successful complexation depends on the sizes of ions and cavity of the CEs and the HSAB theory. The latter describes a strong interaction between atoms with high electron density (hard base) in the CE ring and ions with high electron density (hard acids). Accordingly, oxygen in the CE ring has a stronger interaction with Li^+ than, for example, nitrogen atoms or sulfur atoms due to its higher charge density. The significant ions' size, electron density, and hardness are shown in Tab. 3.6.

Table 3.5: Parameters of lithium selective CEs.⁵⁴

CE	Cavity size Å	Selectivity order	Li/Na ratio
B12C4	1.20-1.50	$\text{Li}^+ > \text{Na}^+ > \text{K}^+ > \text{Rb}^+ > \text{Cs}^+$	1.8
B14C4	1.20-1.50	$\text{Li}^+ > \text{Na}^+ > \text{K}^+ > \text{Rb}^+$ (no Cs^+)	4.7
DB14C4	1.20-1.50	$\text{Li}^+ > \text{Na}^+ > \text{K}^+ > \text{Rb}^+ > \text{Cs}^+$	0.6
12C4	1.20-1.50	$\text{Li}^+ > \text{Na}^+ > \text{K}^+ > \text{Rb}^+, \text{Cs}^+$	1.7
13C4	1.20-1.50	$\text{Li}^+ > \text{Na}^+ > \text{K}^+ > \text{Rb}^+ > \text{Cs}^+$	2.3
14C4	1.20-1.50	$\text{Li}^+ > \text{Na}^+$ (no $\text{K}^+, \text{Rb}^+, \text{Cs}^+$)	20
15C4	1.20-1.50	$\text{Li}^+ > \text{Na}^+ > \text{K}^+, \text{Cs}^+ > \text{Rb}^+$	3.5
15C5	1.70-2.20	-	-
18C6	2.60-3.20	-	-

Tab. 3.5 confirms for the 14C4 the strongest Li^+ selectivity. The geometric structures from the top and the side view are presented for the complexes with Li^+ , Mg^{2+} , and Na^+ (Figure 3.38). The Li^+ and Mg^{2+} are located in the plane of the oxygen atoms. While the Na^+ lies above this plane, resulting from the larger ion radius compared to Li^+ . The 14C4 is so far the best fitted cavity to the diameter of Li^+ and causes therefore the least conformational change of the CE. The Na^+ complex, on the other hand, must undergo conformational changes

Table 3.6: Parameters of the most commonly found cations in brines and seawater.^{30,172}

Cation	Cation diameter [Å]	Charge density [$q \cdot \text{Å}^{-1}$]	Hardness η [eV]
Li ⁺	1.48	1.11	35.1
Na ⁺	2.04	0.86	21.1
K ⁺	2.76	0.66	-
Mg ²⁺	1.74	2.32	32.5
Ca ²⁺	2.00	1.75	19.7

and less extensive desolvation of cation and ligand which leads to mutually-compensating enthalpy and entropy changes (Figure 3.39). A detailed explanation of the thermodynamic parameters is given in the next Section. It is worth mentioning that only single complexes were considered.¹⁷³ However, 14C4 CEs can also form sandwich complexes with ion radii that overcome the cavity size of the 14C4 such as Na⁺. Therefore the selectivity of Li⁺ where Na⁺ is present is reduced. One way to overcome the undesired sandwich complexation with Na⁺, is the incorporation of steric groups (see Figure 3.37), which lower the mobility of the CE. However, the syntheses of such CE are very complex and involve many synthetic steps. Therefore, using such systems is not feasible on a large scale from an ecological and financial point of view. In publication 1, an attractive method for the selective complexation of Li⁺ in presence of other interfering alkali metal ions is presented.

It is worth mentioning, that there are other supramolecular ligands that can complex Li⁺, such as spherands or cryptands. However, these groups will not be discussed since they have not been used in this thesis.

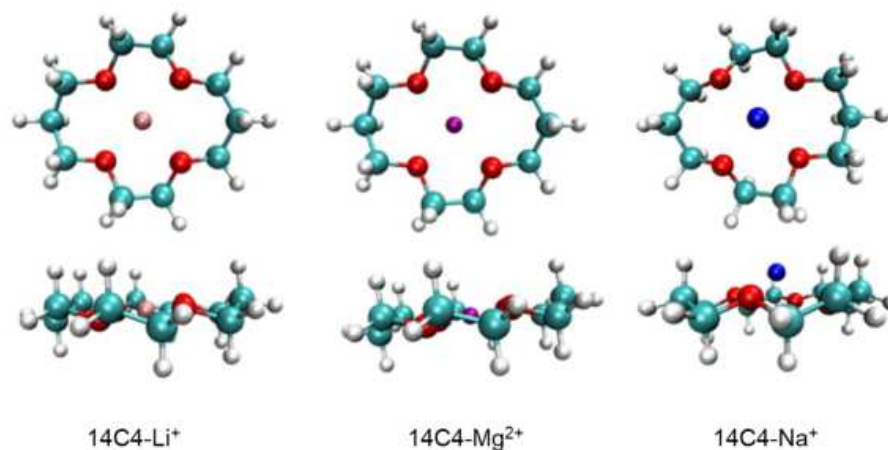


Figure 3.38: Geometrically optimized structures of 14C4 with Li⁺, Mg²⁺, and Na⁺. The red dots represent the oxygen atoms, the turquoise the carbon atoms, the white the hydrogen atoms, pink the Li⁺, violet the Mg²⁺, and blue the Na⁺. Reused with permission from Tian et al. from Springer.^{174,175}

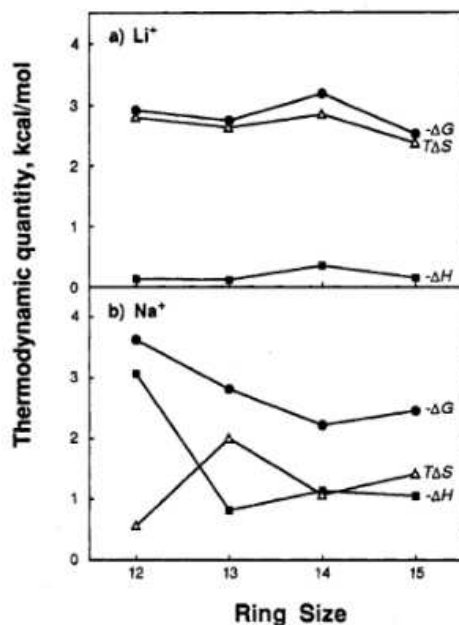
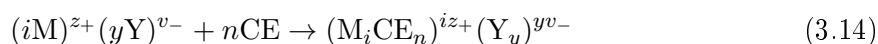


Figure 3.39: Thermodynamic quantity of 12-15 membered CE rings for complexes with Li⁺ (top) and Na⁺ (bottom). Reused with permission from Inoue et al. from ACS.¹⁷³

Determination of the complex stability The stability of a CE–cation complex can be determined by the thermodynamic binding constant K . The binding constant is often named formation constant, association constant, stability constant or complex constant K . The latter was used in the Publications 1, 2, 4, and 5, therefore it will named the same in this thesis. The complex constant K results from the law of mass.^{176,177} A typical CE–metal complexation reaction overview can be described as shown in Eq. 3.14, where M is the metal ion and Y the anion. The variables i and y are the stoichiometric factors of the cations and anions, z and v the charges of the cations and anions, and n the stoichiometric factor of the CEs participating in the complex.



By using the law of mass action and including the activities of each species, the equilibrium constant (complexation constant) K can be established according to Eq. 3.15. The average activity of a system can be determined via the Debye–Hückel equations, but for this, the compositions must already be known. For highly diluted concentrations, it is assumed that the activity coefficient differs only very slightly from 1. The simplified Debye–Hückel theory is valid for ionic strengths up to 0.01 mol/L.¹⁷⁸ The Davies equation can be used for higher concentrations, which, however, already shows deviations of up to 10% for concentrations above 0.5 mol/L.^{179,180} Since highly diluted solutions (ionic strengths below 0.01 mol/L) are used in this work, the activities can be determined via Eq. 3.16.

$$K = \frac{[(M_iCE_n)^{iz_+}(Y_y)^{yv_-}]}{(a_{\pm} \cdot ([M^{z_+}]^i \cdot [Y^{v_-}]^y)) \cdot [CE]^n} \quad (3.15)$$

$$a_{\pm} = Q \cdot \gamma_{\pm} \cdot c \quad (3.16)$$

The stoichiometric ratio of the ions are included via the stoichiometric factor Q , γ_{\pm} represents the mean activity coefficient, and c the concentration of the species. Q is determined according to Eq. 3.17 and the mean activity coefficient γ_{\pm} according to Eq. 3.18. The dimensionless factor A is for water under standard conditions 0.509.¹⁸¹ The ionic strength (I_s) is determined according to Eq. 3.19. In summary, the complexation constant K can be calculated with the known concentration of the solutions according to Eq. 3.20. For $K > 1$, the equilibrium is on the side of the products; for $K < 1$, the equilibrium is on the side of the starting components.

$$Q = (i^i \cdot y^y)^{\frac{1}{i+y}} \quad (3.17)$$

$$\log \gamma_{\pm} = -A|z_+ \cdot v_-| \cdot \sqrt{I_s} \quad (3.18)$$

$$I_s = \frac{1}{2} \sum_i c \cdot z_+ \cdot v_- \quad (3.19)$$

$$K = \frac{[(M_iCE_n)^{iz_+}(Y_y)^{yv_-}]}{(Q \cdot ((\gamma_+ \cdot [M^{z_+}]^i) \cdot (\gamma_- \cdot [Y^{v_-}]^y))) \cdot [CE]^n} \quad (3.20)$$

If the concentrations of the metal salts in water before and after extraction are known, the CE-cation complex can be determined according to Eq. 3.21-3.24. The indices bc and ac refer to the species before and after complexation.

$$[(M_iCE_n)^{iz_+}(Y_y)^{yv_-}] = [complex] = [M_i^{z_+}Y_y^{v_+}]_{bc} - [M_i^{z_+}Y_y^{v_+}]_{ac} \quad (3.21)$$

$$[M^{z_+}]^i = [M_i^{z_+}Y_y^{v_+}]_{bc} - (i \cdot [complex]^i) \quad (3.22)$$

$$[Y^{v_-}]^y = \frac{y}{i} \cdot [M_i^{z_+}Y_y^{v_+}]_{bc} - (y \cdot [complex]^y) \quad (3.23)$$

$$[CE]^n = [CE]_{bc} - (n \cdot [complex]^n) \quad (3.24)$$

In this work, the extraction experiments were studied in a two-phase extraction. The CE and the metal salts are dissolved in different solvents, which are not miscible to each other.

The volume of the two solvents must be identical. Otherwise, the volume ratio of the solvents must be included in Eq. 3.20. This is not the case in this work, so Eq. 3.20 can be used without hesitation to determine the complex constant K .

Thermodynamics of complexation In this Section, further thermodynamic analysis methods are presented that provide information on the voluntariness of complex formation. The total energy of a system (internal energy U) is the sum of all kinetic and potential energies, which depends on temperature and pressure. Thus, the internal energy U is a state variable. According to the 1st law of thermodynamics, the changes of the internal energy U are equal to the sum of the supplied heat quantity dq and the performed work dw in a closed system.¹⁸² As already described in the energy Chapter (Section 3.1), energies cannot be generated or consumed out of nothing. According to the law of conservation of energy, they can only be transformed into each other.

$$dU = \delta w + \delta q \quad (3.25)$$

In a system with constant pressure p and variable volume V , a part of the volume work $p dV$ is exchanged with the environment, which is described by the change of the enthalpy dH (Eq. 3.26). The enthalpy is also a state function. The amount of heat added no longer corresponds to the change in internal energy U .¹⁸³

$$dH = \delta w + \delta q + p \cdot dV = dU + p \cdot dV \quad (3.26)$$

To make statements about the spontaneity of the state functions, the 2nd law of thermodynamics is introduced. This states that the change in entropy dS measures the degree of disorder, which increases in spontaneous reactions.¹⁸³ The entropy change is reciprocal to the temperature and increases proportionally with the amount of heat supplied. Since the complex formation is a reversible process, the change in entropy dS is described for a reversible process (Eq. 3.27).

$$dS = \frac{\delta q}{T} \quad (3.27)$$

The supplied heat quantity dQ can be replaced with dH if the volume work performed occurs in an isobaric system (Eq. 3.28). The change in entropy dS is spontaneous when $dS > 0$. If the entropy contribution does not change during a reaction, this inevitably leads to increased entropy in the environment (Clausius inequality, Eq. 3.29).¹⁸³

$$dS = \frac{dH}{T} \quad (3.28)$$

$$TdS \geq dH \quad (3.29)$$

Based on Eq. 3.29 the Gibbs free energy dG is formed (Eq. 3.30). dG is a state variable

that indicates the direction of a chemical reaction, which relates to the properties of the system and does not relate to the environment. The reaction is exergonic as soon as $dG_{T, p} \leq 0$. When the enthalpy of the reaction decreases ($dH \leq 0$) and the entropy increases ($dS \geq 0$), the reaction proceeds spontaneously at all temperatures. Endergonic reactions are characterized by a $dG_{T, p} \geq 0$.¹⁸³

$$dG = dH - TdS \quad (3.30)$$

Since all state functions depend on temperature and pressure, changes in state variables are often given off under standard conditions. The Gibbs-Helmholtz equation describes this relationship (Eq. 3.31), which can also be described in relation to the equilibrium constant K with R being the gas constant (Eq. 3.32).¹⁸³

$$\Delta G^\ominus = \Delta H^\ominus - T\Delta S^\ominus \quad (3.31)$$

$$\Delta G = \Delta G^\ominus - RT\ln K \quad (3.32)$$

In the equilibrium state, the Gibbs energy dG is 0, therefore, Eq. 3.32 can be transformed into Eq. 3.33. By combining Eq. 3.31 and Eq. 3.33, Eq. 3.34 is obtained, the Van't Hoff equation.^{184,185} With this equation, the enthalpy of reaction ΔH^\ominus and the entropy of reaction ΔS^\ominus can be determined by determining the equilibrium constant (complex constant) K at different temperatures T (only valid for small temperature changes).¹⁸³ Therefore, investigation of varying complexation constants K at different temperatures was also used in publication 1 to calculate entropy and enthalpy contributions during the CE-cation complex.

$$\Delta G^\ominus = -RT\ln K \quad (3.33)$$

$$\ln K = -\frac{\Delta H^\ominus}{R} \cdot \frac{1}{T} + \frac{\Delta S^\ominus}{R} \quad (3.34)$$

In this Chapter, the properties of supramolecular chemistry, especially the different interactions that can take place, were described. The CEs were introduced, and other properties depending on the modification were explained. Thermodynamic data can help to understand the complexation process better. Since there are many possibilities to modify CEs and thus change the thermodynamic properties in a targeted way, a simulation method, which has already been successfully introduced for CE systems, is presented in the following Chapter to restrict the modifications of the CE in a more targeted way to obtain Li^+ selective CEs.

3.4 Electronic structure calculations

Summarized from the previous Chapter, modifications of CE structures can influence the selectivity toward the desired metal ion. However, syntheses of CEs and experimental evaluation of the thermodynamic parameters for CE–cation complexes can be challenging and time-consuming. Multi-step syntheses often have to be carried out, and extraction experiments have to be repeated several times to gain reliable data.

Quantum chemical methods can be applied to predict the binding properties of supramolecular structures.^{186–189} During the last decade, the accuracy and efficiency have been improved by applying molecular dynamics or other statistical methods based on approximations such as empirical force field methods, sometimes combined with Monte Carlo approaches or DFT.^{190–192} The latter is commonly used to simulate CE complexes with metal ions.^{193–195} In Figure 3.40, the publication rate of DFT simulations of the last decades is shown, as well as the Publications of DFT methods for describing CE complexes. The DFT calculation is increasingly adopted by scientists and used for predicting structures and properties. The application of DFT to the prediction of CEs is still scarce in comparison and currently averages 36 Publications in 2021 and 22 Publications in 2022 (Web of Science).¹⁹⁶ In publication 2, a comparison of CE–cation complexes is made using DFT and experimental data. Since theoretical chemistry is usually daunting for many scientists, the following Section is intended to facilitate understanding of the results in publication 2 and to describe the theoretical models based on DFT in more detail.

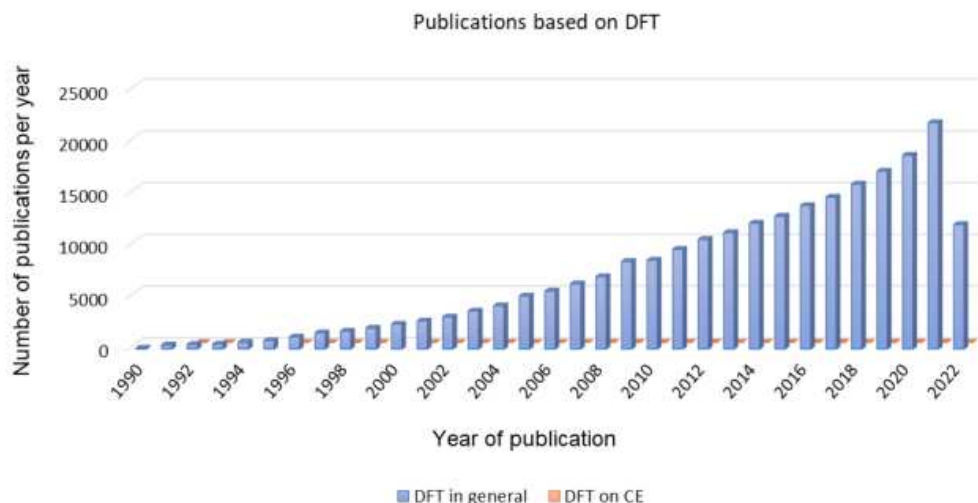


Figure 3.40: DFT Publications per year (blue bars) and DFT Publications on CE per year (orange bars) according to *web of science*;¹⁹⁶ Date: 10/08/2022.

3.4.1 Density functional theory

Numerical solutions of the Schrödinger equation for a particular system are also defined as electronic structure calculations.^{197,198} These deviate from typical theories of modeling. Such analyses do not include external parameters and allow the study of the speculative system. These methods are helpful qualitative support, especially concerning the determination of the binding energies of an atom or molecule - a physical property that is physically inaccessible. Solving the Schrödinger equation, however, is not so easily accomplished. Exact solutions of the equations are only determinable in times that increase exponentially with size. Only very small, simple systems can be calculated precisely. To perform calculations in a polynomial-time window, approximations can be made, but these lead to a loss of accuracy and thus predictability. Treatments of electron–electron interactions are one of the main problems. Physical and chemical properties depend on electron interactions with each other and atoms. These interactions cannot be separated or considered in approximation.^{199,200} Among the most successful and well-known methods for determining electronic structures are DFT and quantum chemistry, which describe approximations for the electron–electron interactions.²⁰¹

In this work, the DFT method is applied to predict CE structures and their interactions with metal ions. DFT calculates the electronic structures of atoms, molecules and solids based on the fundamental laws of quantum mechanics. Unlike other methods, DFT determines single-body density functions as fundamental variables instead of multi-body wave functions. The density function is a function consisting of only three spatial coordinates and is therefore applicable even for large, complicated systems. The foundations of DFT are the Hohenberg-Kohn and Kohn-Sham theorems, which are described in the following.

3.4.1.1 Hohenberg-Kohn and Kohn-Sham theorems

The Hohenberg-Kohn theorem describes the properties of a system of electrons in the ground state by the system’s electron density. The theorem is divided into two parts. The first Hohenberg-Kohn theorem describes the electron density in the ground state via the electric potential on which all electrons interact (except the constant shift of the energy). The Hamilton operator in the Schrödinger equation is thus fixed and all its properties. The second Hohenberg-Kohn theorem describes that by varying the electron density in a given system of N interacting electrons, only states with higher energy than the energy of the ground state can be formed. The energy can be determined by systematic variation of the electron density in the ground state. Thus, the main challenge of DFT is to find the corresponding functional.^{202–205}

The total energy of a system ($E(\rho)$) is described by the sum of the kinetic energy of the electrons ($T_k(\rho)$), the energy of the electron–nucleus interaction ($E_{ne}(\rho)$), and the energy of the electron–electron interaction ($E_{ee}(\rho)$) (see Eq. 3.35). The latter term also consists of the functional of the electrostatic repulsion between two electrons ($J(\rho)$) and non-classical effects like the exchange correlation energy ($E_{XC}(\rho)$) (Eq. 3.36). The kinetic energy has a significant

fraction of the total energy; therefore, inaccurate approximations can significantly impact the calculations.^{204–206}

$$E(\rho) = T_k(\rho) + E_{ne}(\rho) + E_{ee}(\rho) \quad (3.35)$$

$$E_{ee}(\rho) = J(\rho) + E_{XC}(\rho) \quad (3.36)$$

The exact form of the kinetic energy functional can be described using a total wave function composed of N orbitals calculated by the Slater determinant ($T_{SD}(\rho)$) (total wave function composed of N orbitals, Eq. 3.37). The electron density is determined from the sum of the electron densities of the Kohn-Sham function (Eq. 3.38). However, it is to be noted that an interaction-free system (reference system) is described with the Slater determinant (SD). Therefore, the reference system and the real system must have an identical electron density since the system's energy is a functional density.^{204–206}

$$T_{SD}(\rho) = \sum_{i=1}^N \left\langle \phi_i \left| -\frac{1}{2} \nabla^2 \right| \phi_i \right\rangle \quad (3.37)$$

$$\rho(\vec{r}) = \sum_{j=1}^N |\phi_j(\vec{r})|^2 \quad (3.38)$$

The exact functional is determined by the difference between the same kinetic energy and the one calculated with the determinant wavefunction and the difference between the exact electron–electron interaction under the classical Coulomb-interaction and the form of the exchange–correlation functional $E_{XC}(\rho)$ (Eq. 3.39). All not precisely determinable terms are described in the exchange–correlation functional.²⁰⁶

Utilizing the effective potential function ($v_{\text{eff}}(\vec{r})$), the energy of the Kohn-Sham orbitals ($E_{KS}(\rho)$) can be determined with N solutions of the system of equations, which makes the computational effort less than the solution of the Schrödinger equation with N electrons since they are independent solutions of the Schrödinger equation (Eq. 3.40). The one-electron Schrödinger equations are also defined as Kohn-Sham equations (Eq. 3.41). ε_j defines the orbital energy of the corresponding Kohn-Sham orbital ϕ_j .^{205,207}

$$E_{XC}(\rho) = (T_k(\rho) - T_{SD}(\rho) + E_{ee}(\rho) - J(\rho)) \quad (3.39)$$

$$E_{KS}(\rho) = T_{SD}(\rho) + E_{ne}(\rho) + E_{XC}(\rho) + J(\rho) \quad (3.40)$$

$$-\frac{1}{2} \nabla^2 + v_{\text{eff}}(\vec{r}) - \varepsilon_j \phi_j(\vec{r}) = 0 \quad (3.41)$$

In Eq. 3.42, the effective potential function is shown with external potential function ($v(\vec{r})$), which describes the interaction of the electrons through the atomic nucleus. The second more complex term describes the electrostatic interaction of the electrons with each other. The last term, exchange–correlation potential ($v_{xc}(\vec{r})$), describes the exchange–correlation potential with the help of which the functional can be defined according to Eq. 3.43.^{205,206}

$$v_{eff}(\vec{r}) = v(\vec{r}) + \int \frac{p(\vec{r}')}{|\vec{r} - \vec{r}'|} d^3r' + v_{xc}(\vec{r}) \quad (3.42)$$

$$v_{xc} = \frac{\delta E_{xc}}{\delta \rho} \quad (3.43)$$

The effective potential thus occurs in the Kohn-Sham equation and is additionally dependent on the density; the solutions of these equations must be determined interactively. Thus, the Kohn-Sham equation is solved with the newly found potential, from which a new potential is determined until a stable solution is located (see also Self-Consistent-Field-Method).^{205,206}

3.4.1.2 Exchange–correlation potential

By the Kohn-Sham theorem, however, the problem of the exact determination of the functional was shifted towards the $v_{xc}(\vec{r})$. Strictly speaking, $v_{xc}(\vec{r})$ depends on the point r and the electron densities at all locations. In most cases, this value cannot be determined precisely, however, it has been shown that approximations are often sufficient for the solution of $v_{xc}(\vec{r})$.^{205,208} Three exemplary approximation methods are presented in the following.

Local density approximation (LDA): In this approximation, $v_{xc}(\vec{r})$ is assumed to be a function of the electron density at the location $p(\vec{r})$. This approximation is valid when the density is approximately the same everywhere for conduction electrons in the metal. However, LDA calculations lead to an overestimation of bond strengths in the general case of up to 1 eV/bond.^{207,208}

The generalized gradient approximation (GGA) describes the approximation by density and derivatives by location.

In the hybrid method, a part of the exchange–correlation potential is calculated according to the DFT, and another is calculated as the exchange energy of the Kohn-Sham function as in the Hartree-Fock method. B3LYP is one of the most known hybrid methods; since it is much more accurate than the first described, nonetheless, it is also associated with the highest computational effort.^{209,210}

The most significant deviations in real values or constraints are due to the exchange–correlation potential. GGA binding energies deviate up to 20 % from experimental values. In addition, Van-der-Waals bonds are not described since they are based on a long-range correlation of the charge distribution. Furthermore, band gaps of HOMO and LUMO determined from Kohn-Sham functions are too low in the first two methods presented. Therefore,

in publication 2, the hybrid method was chosen as an approximation method to determine $v_{xc}(\vec{r})$.²¹¹

In general, the calculations of the DFT are performed in the Born-Oppenheimer approximation. Thus, only the electrons are treated quantum mechanically.²¹²

3.4.1.3 Molecular structure optimization

The position of the atoms in a molecule indicates the structure, which has specific energy for a given structure and electronic state. The potential energy surface (PES) describes the variation of the molecule's energy in a defined state depending on the molecule's structure.²¹³

Starting from the target molecular structure, the gradient method can be applied to defining the minima. For this purpose, the energy gradient must be defined beforehand, which can be determined via the partial derivative of $E = E(\vec{R})$ according to the nuclear coordinates. Subsequently, the method is continued in the direction of the negative gradient until convergence appears. The knowledge of the second derivative is, e.g. necessary for the fast converging Newtonian method. As an optimization, quasi-Newtonian methods have been developed using low-cost approximations of the second derivative. Both ways are used to optimize the molecular structure.²¹³⁻²¹⁶

Vibrational frequency calculations can also perform the determination of a minimum. However, local and global minima cannot be distinguished by this method. The computational effort increases for more complex structures with molecule size or exciting states.²⁰⁵

3.4.1.4 Hirshfeld population analysis

With determinations of charge distributions within a molecule, the strength of CE-cation complexes can be better understood by estimating the chemical interactions, which can be determined via methods such as Mulliken, Löwdin, and Voronoi deformation density population analysis. In particular, Hirshfeld population analysis is often used for this purpose, as it was done in publication 2.

The Hirshfeld population analysis is based on the partitioning and weighting of the real space derived of the overlapping atomic electron densities. A system of free unbound atoms is designed, which are located at the same distances from each other as the real molecular system. The atoms possess the charge density of the atoms ($\rho^{\text{free}}(r)$), the sum of it is expressed in Eq. 3.44 and represents the charge density pro molecule ($\rho^{\text{pro}}(r)$).²¹⁷⁻²¹⁹

$$\rho^{\text{pro}}(r) = \sum_i \rho_i^{\text{free}}(r - R_i) \quad (3.44)$$

The real molecular system with density $\rho(r)$ is partitioned into atomic fragments whose charge densities are proportional to the densities of the system of free atoms at each locus. The received deformation density ($\rho^{\text{def}}(r)$) expresses the difference between the molecular and the free atomic charge densities (Eq. 3.45). Each atomic position in the system is attributed

a Hirshfeld weighting factor (w_i^{Hirsh}) with regard to the atomic fractions, which is given by Eq. 3.46. Integration over the deformation density, modified by this weighting factor, gives the net charge of the atom i to which the weighting is referred. The deviation from the outcome of the integration to the number of electrons in the neutral state gives the desired Hirshfeld charge as shown in Eq. 3.47. A significant feature of this analysis is the stability and diversity of the basis sets.²¹⁷⁻²¹⁹

$$\rho^{\text{def}}(r) = \rho(r) - \rho^{\text{pro}}(r) \quad (3.45)$$

$$w_i^{\text{Hirsh}}(r) = \frac{\rho_i^{\text{free}}(r - R_i)}{\rho^{\text{pro}}(r)} \quad (3.46)$$

$$q_i = - \int w_i^{\text{Hirsh}}(r) \rho^{\text{def}}(r) dr \quad (3.47)$$

3.4.1.5 Natural bond orbital analysis

Besides the Hirshfeld population analysis, natural bond orbitals (NBOs) analysis is another tool for predicting electron density distributions in atoms and bonds. It is particularly well suited for evaluating intermolecular interactions such as metal–ligand bonds.^{154,166,220} This method is based on quantum mechanical calculations, first introduced by Löwdin.²²¹ These orbitals utilize the N -electron wave function based on classical Lewis bonding theory. NBOs are part of natural localized orbitals, which also belong to the natural atomic orbitals (NAOs), natural hybrid orbitals (NHOs), natural (semi-)localized molecular orbitals (NLMOs). They can be classified between atomic orbitals (AOs) and molecular orbitals (MOs).²²²

Each wave function (Ψ) feature can be reproduced by these sets of orthonormal, naturally localized orbitals. The NBOs investigate hybridization and covalency phenomena within the polyatomic wavefunction. The NBO model should nearly match the natural Lewis structure (with more than 99% agreement), with free electron pairs and localized bonds. An NBO for a conventionally localized σ -bond between the A and B atoms (σ_{AB}) is construed based on the NHOs, which in turn results in a linear combination of NHOs with $c_{\text{A/B}}$ as polarization coefficients for atoms A and B, and $h_{\text{A/B}}$ as NHOs for atoms A and B (Eq. 3.48).²²²⁻²²⁴

$$\sigma_{\text{A,B}} = c_{\text{A}} h_{\text{A}} + c_{\text{B}} h_{\text{B}} \quad (3.48)$$

Taking into account a maximum occupation number in combinations with orthonormality leads to expressions that are compact for describing atomic and bonding properties within a molecular system. The occupied NBO $\sigma_{\text{A,B}}$ can be employed to characterize covalent effects within the A-B bond, going from strictly covalent ($c_{\text{A}} = c_{\text{B}}$) to ionic ($c_{\text{A}} \gg c_{\text{B}}$) to ionic. This effects in the formation of antibonding NBOs ($\sigma_{\text{A,B}}^*$) by analogy, characterizing the non-covalent portions of the bond. The conventional bond can then be defined by the Lewis-like donor NBO (occupation number close to 2) in combinations with the non-Lewis-like acceptor

NBO (occupation number close to 0).²²²⁻²²⁴

The deviation of the occupation values from the optimal values is attributed to the delocalization of electrons, which causes a variation in the system's total energy. The drop in the total energy attained by the mixing of donor and acceptor quantifies the interaction between the NBO and can be expressed by the stabilization energy E^2 .²²²⁻²²⁴

3.4.1.6 Solvent models

Most calculations using DFT are performed in vacuum. Solvent effects are not determined, which makes comparability with experimental values difficult. Therefore, the analyses were extended with solvent models, which are briefly mentioned in this Section. In publication 2, both vacuum and solvent calculations were performed.

Individual calculations of solvent molecules take a long time to compute. Therefore, solution effects are performed with an approximation of structureless, polarizable media. The basic polarizable continuum model (PCM), as well as the further developed conductor-like polarizable continuum model (C-PCM) and the integral equation formalism polarizable continuum model (IEF-PCM), are determined based on dielectric constants of the simulated media. In publication 2, the IEF-PCM method was chosen as the solution simulation. Here, the solute molecule is located in a solvent cavity, which is surrounded by a dielectric medium, a shell of solvent spheres located at the cavity surface. It polarizes the dielectric medium, which induces an electrostatic field on the solute molecule, and therefore influences the electron density of the molecule. Thus, IEF-PCM considers the impact of the surrounding charge, which predicts the reaction potential of the molecules within the solute cavity. One of the main benefits of this model is the various possibilities of solvent environments.²²⁵⁻²²⁹

3.5 Lithium selective polymer materials

Lithium extraction and CE were described in detail in the previous Chapters. The complex properties were supported using DFT to avoid costly synthetic preparation of CE. The following Chapter describes polymer-based CE systems. In addition, the industrial importance of these materials will be highlighted. Since polymers are a particular structural class that we encounter in many different forms in daily life, polymers are first described in general, as well as their syntheses and unique properties. Subsequently, the linkage of polymers with CEs is discussed, which are part of Publications 3, 4, and 5.

3.5.1 Polymers

Polymers consist of repeating smaller chemical units (monomers) which are combined to a larger structure by a series on building blocks forming a polymer chain. Polymers can include hundreds to over million atoms. The longer the chain, the heavier the weight of the polymer chain, the higher the viscosity due to the greater surface area. However, if we think about a chain, we think about something linear. Nonetheless, this is not always the case, they can for example be grafted. Polymers also do not have to be made of the same repeating unit, however, if this is the case, those polymers are called homopolymers. If the polymer is based of more than one monomer species, the polymers are called copolymers. Based on the location of the repeating unit within the polymer chain copolymers can be divided in random (statistical), block, branched, graft, or alternating polymers. An overview of these structures can be found in Figure 3.41.²³⁰ Basically, polymers can be synthesized by radical-, cationic-, anionic-, coordinative- polymerization, polycondensation, or polyaddition.

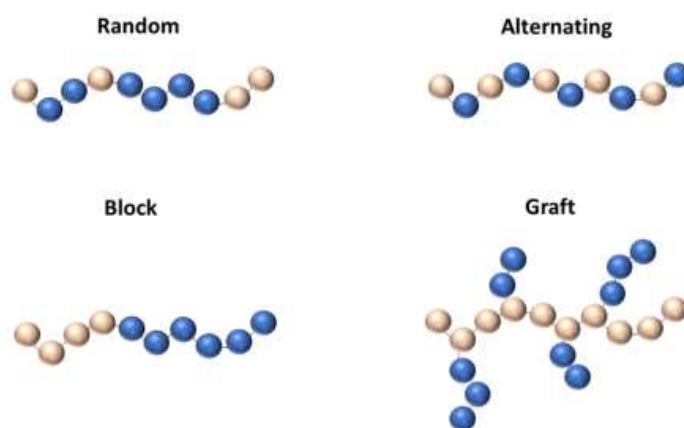


Figure 3.41: Illustration of some possible polymer architectures. The blue and orange dots represent different monomers.

This work uses a particular type of radical polymerization, therefore only radical polymerizations are further explained.

3.5.2 Radical polymerization

In this Section, the fundamental theories of radical polymerization are presented. In addition, the application of free radical polymerization in various technical homogeneous and heterogeneous systems is described.

Radical polymerization is started via radicals, as already indicated by the name. Radicals are rarely formed from monomers without additional additives. Therefore, initiators are often added, decomposing into radicals by electrochemical reactions and thermal or radiation chemical excitations. The formed radical attaches to the monomer and grows further by the additional addition of monomers. A macroradical is created, which can react further with monomers or react with itself or other radicals. The last two reactions lead to termination reactions, which is the reason, why after a small conversion, constant concentrations of radicals occur (this does not include the individual radical species). In this steady-state condition, the rate-determining step is the initiator decay since termination and building of radicals have approximate the same concentration. If the initiator concentration is low, the growing macroradicals are mainly terminated by mutual deactivation. Ideally, the rate of polymerization is proportional to the monomer concentration. Experimentally, the ideal reaction kinetics is only achieved at low conversions and small initiator concentrations.^{231,232}

In general, polymers can be polymerized employing bulk radical polymerization, solution and precipitation reactions, suspension polymerization, and emulsion polymerization. Among these, substance polymerization theoretically represents the most straightforward process. No solvents are necessary for this process. However, serious heat dissipation problems occur primarily in exothermic processes such as opening a C-C double bond, as with monomers for radical polymerization. In addition, viscosity is a common problem, especially when polymer chains with high molecular masses are to be obtained (gel effect). These problems are circumvented by stopping the polymerization of substance at conversions between 40-60%. Dissolution and precipitation reactions follow the same kinetic laws as substance polymerization. Both polymerizations are strongly limited by heat input and viscosity, although the solvent makes this effect less pronounced. Precipitation polymerization is called precipitation polymerization if the polymer is not soluble in the monomer. The kinetics are similar to solvent polymerization, but polymerization rates in the solid and liquid phases may differ. Suspension polymerization is a widespread and industrially relevant process. A poorly water-soluble monomer is dispersed in this medium and forms droplets stabilized by inorganic suspending agents or protective colloids. A soluble monomer initiator is added to start the polymerization. A substance polymerization is carried out by monomer droplets, whereby the surrounding water in which the monomer droplet is located is a suitable coolant. Thus, heat dissipation, a significant disadvantage of substance polymerization, does not occur. Also, viscosity increases are less pronounced due to spatial separation. Emulsion polymerization is similar to suspension polymerization, where the monomer is insoluble in the emulsion medium (often water), and soaps are used as dispersants. In addition, the initiators must be soluble

in the emulsion medium. Section 3.5.5 describes the emulsion polymerization process in more detail since the polymers synthesized in this work were prepared via this process.^{231,232}

In this work, the aim is to synthesize a diblock copolymer due to the unique property of gaining features of both blocks, e.g., thermal, mechanical, and dissolution behavior can be modified, which leads to many new applications of polymers.

Diblock copolymers can be produced via living or controlled radical polymerizations. The latter will be described in more detail below, as this method was used in this work to prepare such polymers. For further interest in living polymerizations (e.g. anionic polymerizations), the reader is referred to the works of Müller et al.,²³³ Hirao et al.,²³⁴ and Hogen-Esch et al.²³⁵

3.5.3 Controlled radical polymerization

The goal of controlled radical polymerizations is to reduce the probabilities of chain termination or transfer reactions by lowering the radical concentrations in the system. The growth reaction should occur preferentially to the termination reaction, and in addition, the initiation rate should be several times greater than the termination reaction. The various techniques of CRP are based on a balance between active and dormant chain ends. The active chain end reacts with a terminator molecule, which is too unreactive to add monomers but can be cleaved off again so that the chain can continue to grow. This mechanism leads to a minimal concentration of active chains. Three main mechanisms are distinguished: the N-oxide mediated polymerization (NMP), the atom transfer radical polymerization (ATRP), and the reversible addition-fragmentation and transfer method (RAFT).^{236,237} The latter approach is explained in more detail below, as it has been intensively studied and used as a method for the polymerization of diblock copolymers in this thesis.

3.5.4 The RAFT polymerization

In 1995, chain transfer agents (CTAs) were first used to synthesize macromolecules, making them the first examples of RAFT polymerization. With the development of reaction conditions and CTAs, properties similar to those of living polymerizations were obtained.

The early developments of RAFT polymerization came from developing automotive coatings under more environmentally friendly conditions. Specifically, RAFT polymerizations were used to produce acrylic coatings with low VOC content (volatile organic compounds, e.g., solvents) with low dispersities and a safely adjusted functionality.²³⁸ In further work, aqueous coatings and pigment dispersants were prepared to utilize emulsion polymerizations (surfactant-free), which are also the main subject of publication 3. The unique properties of such polymerizations will be discussed again below and should be left as they are for the time being. However, the disadvantage of RAFT is the slow polymerization rate and limitation of high polymer chain length, as well as the CTA which has to be removed prior to use, which is why such polymerizations have only been used to a limited extent in the industry to date.

In 1998, RAFT polymerizations with thiocarbonylthio compounds (dithioester, trithiocarbonate, xanthate, and dithiocarbamate) were used as RAFT CTAs for the first time. The publication of this work in ACS, Macromolecules is currently the most cited paper (4000 times quoted) in the journal (Web of Science). First, this work was reported in a CSIRO/DuPont patent and subsequently published at the beginning of 1998. The patent was one of the most cited patents in the field of chemistry until 2005, and more patents related to RAFT are being written. In the meantime, the area of RAFT polymerization is so large that various reviews with different aspects and applications have been published. Especially the photoinitiated RAFT polymerization is more and more in focus. In the last 3 years, at least 30 reviews on RAFT have been written, which shows the wide range of applications of this polymerization technique.²³⁸

In the following, the mechanism, kinetic properties, and combination of RAFT with emulsion polymerizations are summarized, and their applicability on an industrial scale is discussed.

The RAFT mechanism The RAFT mechanism is an increasingly widespread polymerization technique characterized by the fact that this process can be carried out in various solvents, bulk, solution, or dispersion. The mechanism is divided into five stages: initiation, pre-equilibrium, reinitiation, main equilibrium, and termination (see Figure 3.42). As with any conventional radical polymerization, RAFT polymerization starts with initiation. This can be accomplished by a thermal decomposition of a free radical species, such as azo initiators.^{239–241}

After several additions of monomers, a propagating radical (P_n^{\cdot}) is formed, which reacts with the CTA to create the intermediate RAFT radical. This step is the pre-equilibrium of the RAFT mechanism and affects how efficient the CTA will interact in the RAFT polymerization. The intermediate radical can either react back if $k_{\text{-add}} \gg k_{\text{g}}$ and thus has no influence on the polymerization process and control over the molecular weight since the active radical is not transferred between the chains. If $k_{\text{g}} \geq k_{\text{-add}}$, a polymer chain with a thiocarbonylthio end group and the R^{\cdot} radical is formed.^{239–243}

The cleaved radical R^{\cdot} can be reinitiated when it reacts with further monomers to form a new growing chain. However, it can also react back to the macro-CTA. Once all of the starting CTA has been consumed, the macro-CTA is solely present in the reaction mixture and follows the main equilibrium. This equilibrium is based on the dormant polymeric dithiocarbonyl species and the P_n^{\cdot} or P_m^{\cdot} propagating radical chain. To ensure that all polymer chains grow simultaneously, the reaction rate of the main equilibrium must be faster than the propagation.^{239–241}

The quantification of the chain transfer constant can be determined by Eq. 3.97 and 3.98; this depends on the speed of chain transfer k_{tr} and growth rate k_{p} . When $C_{\text{tr}} \geq 10$, narrow molecular mass distributions are achieved. The transfer constant can also be defined the other way around; this value plays an important role, especially for monomers with envious

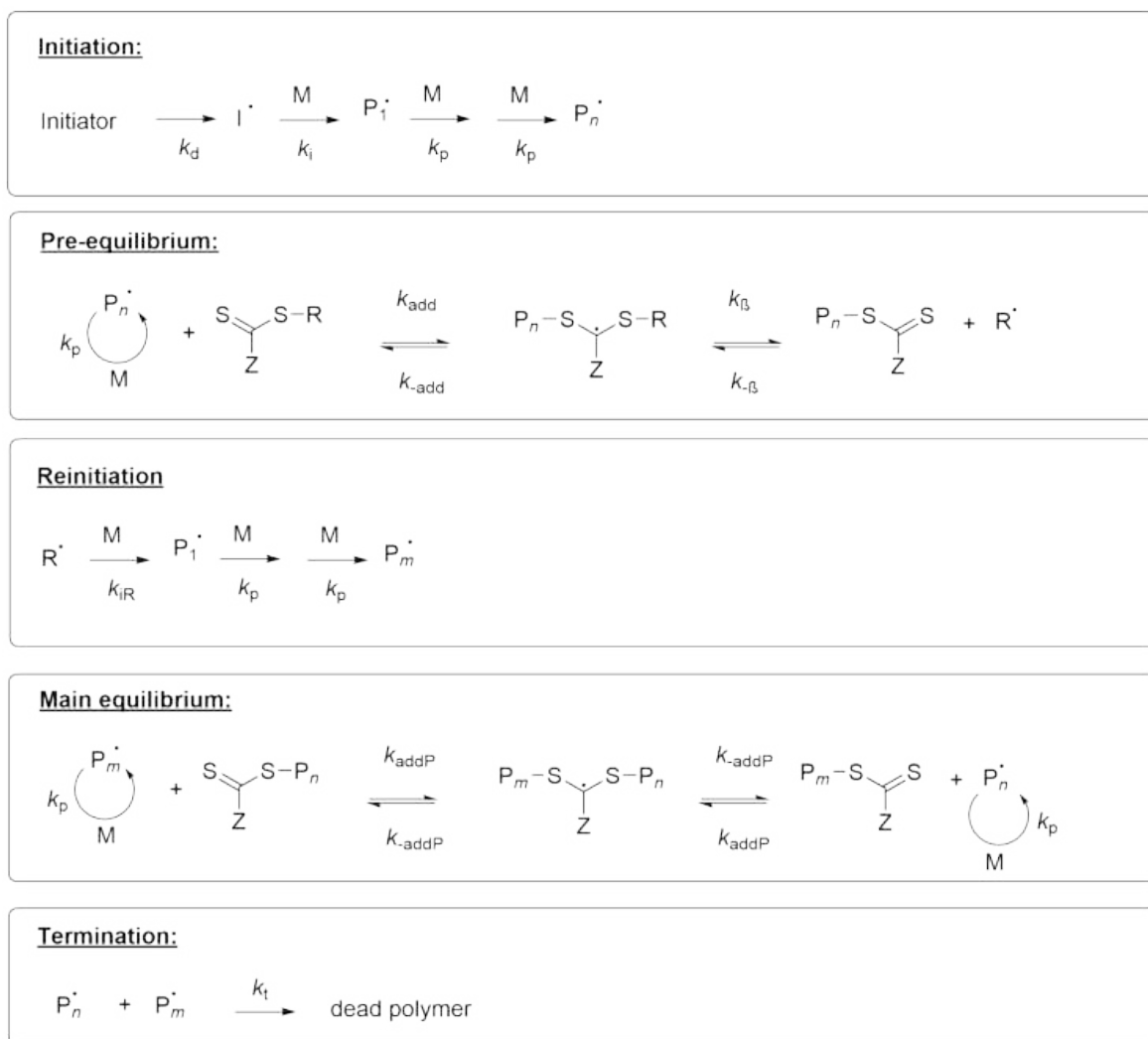


Figure 3.42: Illustration of the RAFT mechanism including the initiation, pre-equilibrium, reinitiation, main equilibrium, and termination.

k_p values. Furthermore, reinitiation, and propagation should be fast enough to suppress termination.^{239–241}

$$k_{tr} = k_{add} \frac{k_\beta}{k_{-add} + k_\beta} \quad (3.49)$$

$$C_{tr} = \frac{k_{tr}}{k_p} \quad (3.50)$$

Chain transfer agents and monomer classes The choice of different monomers is a significant advantage over ATRP and NMP. The option of different CTAs allows a wide range of polymer syntheses. A distinction is made between two classes: the most activated monomers (MAMs) and the less activated monomers (LAMs). MAMs have their vinyl group conjugated to a double bond (butadienes, isoprene), to an aromatic ring (styrene), and a carbonyl group

(methacrylates) or nitriles (acrylonitriles). LAMs are characterized by a double bond next to a functional group such as oxygen, nitrogen, halogens, or sulfide-free electron pairs or saturated carbonates (e.g., vinyl acetates, N-vinylpyrrolidones). Theoretically, all monomers that can also be used in a free radical polymerization are possible monomers for the RAFT polymerization. Only monomers that may react with the thiocarbonylthio group are excluded from this polymerization technique. Primary and secondary amines belong to these groups, as they are strongly nucleophilic but can still be applied if for example the pH of the reaction medium is adjusted. For successful RAFT polymerization, the C=S bond of the CTA must be more reactive to radical addition than the C=C bond of the monomer. This can be controlled with the proper choice of Z and R groups. The Z group controls the reactivity of the C=S bond towards radical addition and maintains the stability of the intermediate radical. For MAMs, trithiocarbonates (Z= s-alkyl) or dithiobenzoates (Z = Ph) are popular CTAs. The former was studied in publication 3, and the kinetic influence of varying the Z group on RAFT polymerization was investigated. Xanthates (Z=O-alkyl) or dithiocarbamates (Z=N-alkyl) are again selected for LAMs, since LAMs are poor homolytic groups due to their high reactivity. These Z groups form less stable interradsicals and provide easier cleavage of the radical to be propagated, since a more stable intermediate product acts as a radical scavenger and limits polymerization. The lone pair of electrons on the oxygen (xanthates) and nitrogen (dithiocarbamates) is delocalized in the thiocarbonyl group and therefore disables the C=S bond for radical addition and destabilizes the radical intermediate. This phenomenon enhances the propagation and fragmentation of the intermediate, providing control over the polymerization of LAMs, but hardly gives control over the polymerization of MAMs.^{240,244}

The proper choice of the R group influences the radical addition to the CTA, the fragmentation of the intermediate formed since the R group should be a good leaving group. The growth from the R group must be quickly reintegrated to allow simultaneous initiation of all chains (step 3 of the RAFT mechanism) to obtain a narrow molecular mass distribution. Therefore, a compromise between the stability of the radical and the steric effects has to be found. On the one hand, it must form a stable radical. On the other hand, it must be reactive enough to add to a monomer. Figure 3.43 summarizes the information on CTAs to date and shows a selection of R and Z groups proposed for specific monomer classes to ensure successful controlled RAFT polymerization.^{240,244}

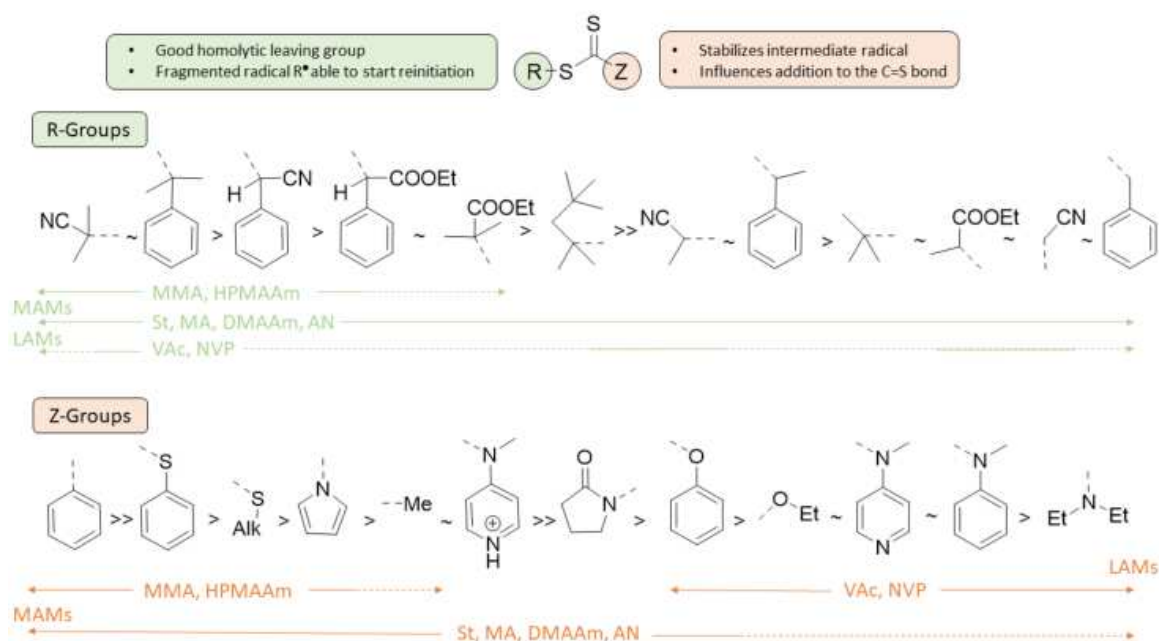


Figure 3.43: Guidelines for selection of R and Z group of CTAs for specific groups of monomers. Dashed lines indicate partial control. MMA= methyl methacrylate, HPMAAM= *N*-(2-hydroxypropyl)methacrylamide, St= styrene, MA= methyl acrylate, DMAAm= dimethyl acrylamide, AN= acrylonitrile, VAc= vinyl acetate, NVP= *N*-vinylpyrrolidone.

Kinetics of the RAFT polymerization Chain livingness plays an essential role in RAFT polymerization, which can be increased by reducing the initiator concentration. However, this has no negative influence on the reaction rate. The reaction rate is similar to that of conventional radical polymerization. It is determined by the factors of propagation rate (k_p), monomer concentration $[Mo]$, initiator efficiency (f), decomposition rate coefficient of the initiator (k_i), initial initiator concentration $[I]_0$, and the termination rate coefficient (k_t), as shown in Eq. 3.51 (neglecting RAFT retardation and chain-length-dependent termination).²⁴⁰

The livingness of the chains can be determined via Eq. 3.52, provided that the initial concentrations of the CTA $[CTA]_0$ and $[I]_0$ are known. The factor 2 in the denominator defines that one molecule of the initiator generates two primary radicals with a specific efficiency f , typically 0.5 for diazo initiators, which are also used in this work (see Publications 3, 4 and 5). The last term in the denominator describes, after chain termination, the number of chains that are generated with f_c as coupling factor, which is 1 for bimolecular termination by combination and 0 for termination by disproportionation.²⁴⁰

$$R_p(t) = k_p \cdot [Mo] \sqrt{\frac{f \cdot k_d \cdot [I]_0 \cdot e^{-k_d \cdot t}}{k_t}} \quad (3.51)$$

$$L = \frac{[CTA]_0}{[CTA]_0 + 2 \cdot f \cdot [I]_0 \cdot (1 - e^{-k_d \cdot t}) \left(1 - \frac{f_c}{2}\right)} \quad (3.52)$$

In contrast to ATRP or NMP, polymerizations up to 100 % monomer conversion can be produced without loss of chain livingness. As explained above, the radical species determines the number of dead chains. Furthermore, polymerization can continue even if complete monomer conversion has already been achieved. However, as soon as a new initiator is used for chain extension, a small amount of homopolymer is formed due to the formation of the newly initiated species, which can also be calculated from the newly introduced amount of initiator and thus kept low. With RAFT polymerization, the construction of up to 20 blocks is possible without extensive interruptions and prior purification by, e.g., precipitation or dialysis, as it would be necessary with ATRP and NMP to produce block copolymers.²⁴⁰

One of the significant limitations of controlled radical polymerizations is the molar mass. This is why until today, anionic polymerization is used for preparing long chains with narrow molar mass distribution. The techniques based on reversible deactivation, such as NMP and ATRP, show a higher rate of termination or other side reactions at higher degrees of polymerization since the time in which the radical is within the growing chain also increases can lead to the possible destruction of the radical chain end. In RAFT polymerization, as the time increases and the degree of polymerization is high, the amount of dead chains at the end of the polymerization decreases, therefore often polymerization degrees below 60-70 % are targeted, to ensure livingness of the polymer chain. Still, at some concentration of the radical source, the number of chains termination is independent of other parameters. In general, the lower the degree of repetition, the higher the proportion of CTA and the higher the livingness of the chains. RAFT polymerization is thus an outstanding technique for preparing polymers with small molar masses. The theoretical number average molar mass ($M_{n,theo}$) can be determined according to Eq. 3.53, where $[Mo]_0$ is the initial concentration of the monomer, p the monomer conversion, and M_M and M_{CTA} are the molar masses of the monomer and CTA. Eq. 3.53 can practically simplified in Eq. 3.54.²⁴⁰

$$M_{n,th} = \frac{[Mo]_0 \cdot p \cdot M_M}{[CTA]_0 + 2 \cdot f \cdot [I]_0 \cdot (1 - e^{-k_d \cdot t}) \left(1 - \frac{f_c}{2}\right)} + M_{CTA} \quad (3.53)$$

$$M_{n,th} = \frac{[Mo]_0 \cdot p \cdot M_M}{[CTA]_0} + M_{CTA} \quad (3.54)$$

The synthesis of polymer chains higher than 100 kDa requires special reaction conditions; all molar masses below are easily accessible via RAFT polymerization, according to Eq. 3.51, the description of the polymerization rate, high molar masses can be obtained by using high monomer concentration, initiators with high efficiency or high decomposition rate, and polar solvents, which are known to lower the transition state of the propagating radicals by reducing the activation energy. Low temperatures, low radical concentrations and high monomer concentrations resulting in high solids concentration, high viscosity, and low termination reactions.²⁴⁰

For hydrophobic monomers, emulsion polymerization has been established to achieve high molecular weights. These hardly cause terminations due to the segregation effect due to low side reactions and high polymerization rate. This polymerization technique is discussed intensively in the following Section, and the advantages are described with the linkage of RAFT polymerization.²⁴⁰

3.5.5 RAFT emulsion polymerization

Emulsion polymerization is a commonly used process both on the laboratory and industrial scale. The advantage of this polymerization technique is the use of green solvents, relatively low viscosity, faster polymerization rates, and good heat transfer. With this technique, it is possible to achieve higher molar masses under short reaction times and reasonable control, which would not be possible with, e.g., solvent polymerizations.²⁴⁵

Conventional emulsion polymerizations consist of a water-insoluble monomer, an aqueous initiator, and a surfactant well above the critical micelle concentration (CMC) that stabilizes the monomer droplets in the continuous phase. The initiation and the chain propagation start in the ongoing phase and lead to a dispersion of colloidal polymer particles (see, Figure 3.44). These particles are also called latex. The advantage of combining RAFT polymerization with the emulsion technique is the replacement of the surfactant with the macro-CTA, which stabilizes the particles. Conventional surfactants such as sodium dodecyl sulfate (SDS) have a direct effect on particle size. If one wants to obtain nano-sized latex particles, a large amount of surfactant is necessary, which limits both the polymerization and the quality of the product. Surfactants can usually only be separated from the product at great expense, e.g., by dialysis, so the alternative possibility of macro-CTA is an attractive and industrially relevant alternative.^{246,247}

The emulsion process is usually divided into three stages: the micelles' formation, the polymerization within the micelles, and the consumption of residual monomer. In the case of RAFT emulsion polymerization, a macro-CTA is chosen as the surfactant stabilizer, while all other components remain the same as in conventional emulsion polymerization. The monomer pots usually have a size of about 10 μm . As soon as the concentration of the stabilizing block is higher than the CMC, micelles with a size of 5-10 nm are formed.^{246,247}

As in any free radical polymerization, the initiator starts the reaction with the monomers. In RAFT emulsion polymerization, this takes place in the continuous phase. Oligomer radicals are produced, which can either diffuse into an already existing micelle or form a new micelle once the CMC is reached. Thus, in the first phase, the number of particles and the polymerization rate increase as the number of polymerization loci increases.²⁴⁶⁻²⁴⁸

After the first stage, all free macro-CTA chains are converted to micelles, and particle nucleation ends. As soon as only polymer particles and monomer droplets are left, stage 2 starts. Polymerization takes place within the micelles. The monomer droplets in the continuous phase diffuse into the micelles. An equilibrium between the monomer diffusion and the polymerization rate is established, resulting in a constant monomer concentration in the mi-

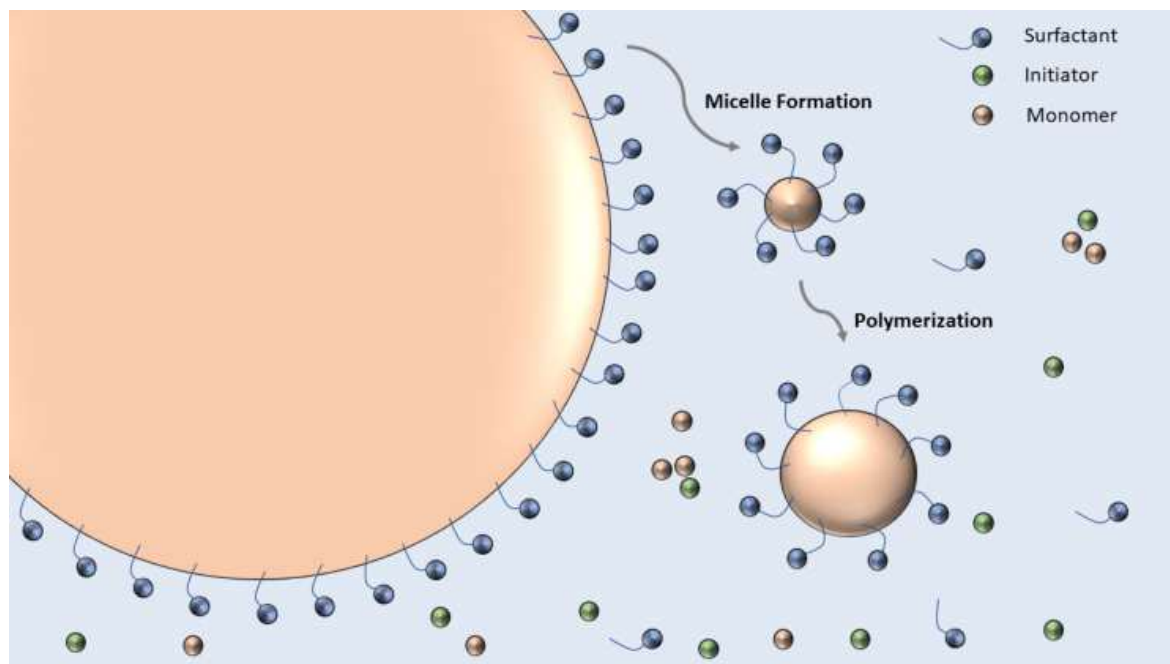


Figure 3.44: Illustration of the conventional emulsion polymerization.

celles. The active radical chain within the micelles grows as long as monomer re-diffuses from the monomer droplets (until it is terminated) or leaves the micelle into the aqueous phase. The latter plays a less important role in stage 2. The particle sizes grow as more monomers are incorporated, and thus the chain length increases.^{246,247,249}

At the end of stage 2, no more monomer droplets are present, and monomers in the micelles have been consumed (stage 3). With increased conversion, the monomer concentration in the particles decreases. Growth rates and termination are diffusion-controlled, which leads to an increase in polymerization rate. In addition, the radical is less likely to leave the particles so that multiple radicals can be present in a particle without immediate termination. Eventually, the growth rate and thus the polymerization rate decreases. The polymerization is finished as soon as the monomer is consumed.^{246–248}

The synthesis of AB diblock copolymers in a selective solvent for one block shows self-assembly properties, which can form specific morphologies. The RAFT emulsion polymerization is a typical example of a polymerization-induced self-assembly (PISA). The targeted morphologies of the latex particles can be defined by the packing parameter P (see Figure 3.45). However, kinetically trapped spherical particles were predominantly obtained in the RAFT emulsion polymerizations, even though other morphologies could be theoretically obtained.^{250,251}

The first results of RAFT emulsion polymerization via PISA were published by Hawket et al. A poly(acrylic acid)-*block*-poly(*n*-butyl acrylate) was prepared, first making the polyacrylic acid macro-CTA as a stabilizer and then polymerizing butyl acrylate as a hydrophobic moiety to the macro-CTA.^{252–254} The molecular weights were in agreement with theoretical

data, and narrow molecular weight distributions were obtained, confirming the controllability of the reaction. After the first emulsion RAFT polymerization via PISA, RAFT mediated PISA was quickly transferred to aqueous and organic dispersion polymerisation.

Compared to emulsion polymerization, in dispersion polymerization, the monomer is soluble in the continuous phase and becomes insoluble during polymerization. In dispersion polymerization, many diblock copolymer polymerizations can be conducted in aqueous and organic media (e.g. low molecular alcohols). In dispersion polymerizations, non-spherical particles were obtained more easily compared to RAFT emulsion polymerisation via PISA. Other morphologies such as worms or vesicles were observed by varying the nature or molar mass of the stabilizing block, core-forming block, or total mass fraction. However, this has not been observed for every dispersion system, so it quickly became apparent that particle production via PISA is complicated and system dependent.^{108,250,251,255}

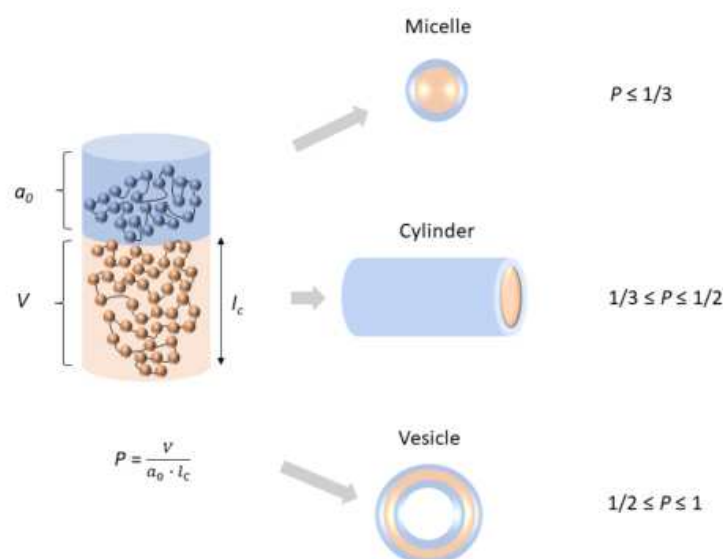


Figure 3.45: Illustration of the determination of the packing parameter. The blue chain represents the selective block for the solvent (stabilizing block), while the orange block represents the non-soluble block for the solvent (core forming block). The packing parameter P is determined by the volumen of the core forming block V , the optimal head group area occupied by the stabilizing red chain (a_0), and the length of the core-forming blue chain, l_c .

Nonetheless, both RAFT emulsion polymerizations and dispersion polymerizations were successfully observed in PISA. Block copolymer particles were generated in a few hours under high solids conditions. There are even some polymer latex syntheses where no preformed stabilization block is necessary. In these examples, the stabilizer and the core-forming block are carried out in the same reactor. A typical example is the RAFT emulsion polymerization with acrylic acid or MAA as stabilizing block in water and the subsequent choice of a monomer that is not soluble in water. This technique is also referred to as a one-pot process and is

particularly attractive because the stabilizing block does not need to be prepared and purified from other side reagents beforehand; the apparatus set-up is simple and not very cumbersome and therefore suitable for industrial scale.²⁵⁶⁻²⁵⁸ This work also exploited this technique for diblock copolymer synthesis (see Publications 3, 4, and 5).

Over the last years, several different CTAs, macro-CTAs, and core-forming blocks have been discovered for RAFT emulsion and dispersion polymerisation. Some examples are shown in Figure 3.46.

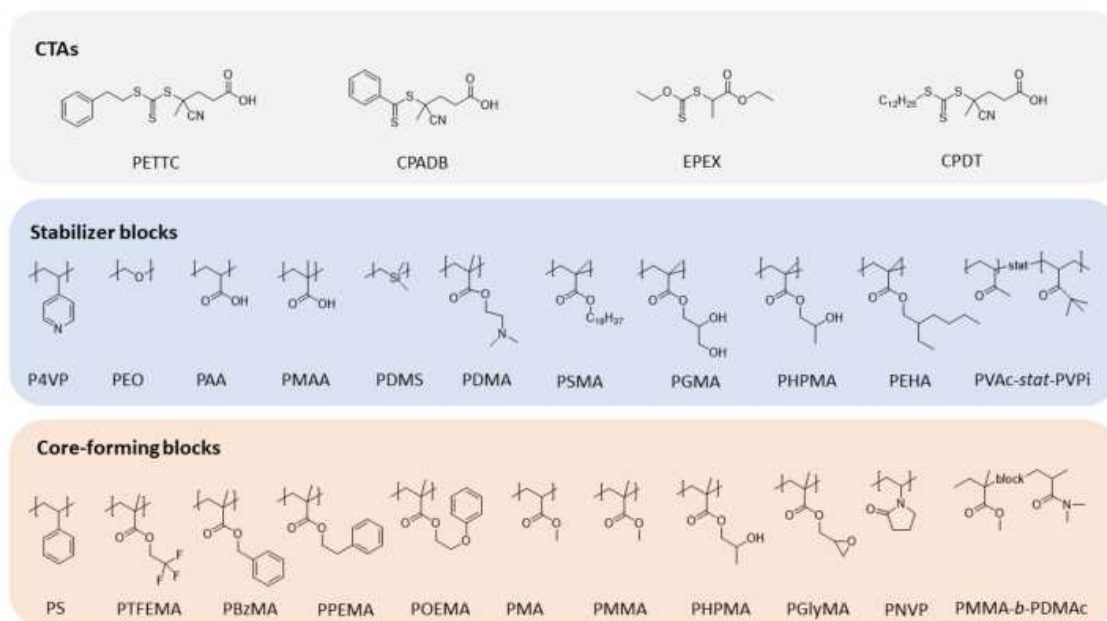


Figure 3.46: Chemical structures of some CTAs, stabilizer blocks and core-forming blocks used in emulsion and aqueous or non-aqueous dispersion polymerization via RAFT. PETTC = 4-cyano-4-(2-phenylethane sulfanylthiocarbonyl) sulfanylpentanoic acid, CPADB = 4-Cyanopentanoic acid dithiobenzoate, EPEX = S-(1-ethyl propionate) O-(ethyl xanthate), CPDT = 4-cyano-4-pentanoate dodecyl trithiocarbonate, P4VP = poly(4-vinylpyridine), PEO = poly(ethylene oxide), PAA = poly(acrylic acid), PMAA = poly(methacrylic acid), PDMS = poly(dimethyl siloxane), PDMA = poly(2-(dimethylamino)ethyl methacrylate), PSMA = poly(stearyl methacrylate), PGMA = poly(glycerol monomethacrylate), PHPMA = poly(2-hydroxypropyl methacrylate), PEHA = poly(ethylhexyl acrylate), PVAc-stat-PVPi = poly(vinyl acetate-stat-vinyl pivalate), PS = polystyrol, PTFEMA = poly(2,2,2-trifluoroethyl methacrylate), PBzMA = poly(benzyl methacrylate), PPEMA = poly(2-phenylethyl methacrylate), POEMA = poly(2-phenoxyethyl methacrylate), PMA = poly(methyl acrylate), PMMA = poly(methyl methacrylate), PGlyMA = poly(glycidyl methacrylate), PNVP = poly(N-vinyl pyrrolidone), PMMA-*b*-PDMAc = poly(methyl methacrylate)-block-poly(dimethyl acrylamide).

This work aimed to develop a polymer material that is both inexpensive and produced in large quantities, as well as to link lithium adsorbers to the polymer. Therefore, it is necessary to use a polymer material that carries functional groups that allow subsequent annealing.

To accomplish these task, poly(methacrylic acid) (PMAA) was chosen as the functionalizing unit because it can be polymerized in water, is inexpensive, and the carboxyl group allows functionalization with CEs as lithium adsorbers. Thus a polymer system can be cre-

ated that benefits from non-toxic solvents and fast reaction times, ensuring the industrial appeal of the material. Polystyrene was chosen as the core-forming component because of its monomer (styrene) low cost, easy accessibility, and mechanical stability. In publication 3, the PMAA-*b*-PS diblock copolymer was investigated at various high solid fractions to make the polymer material more favorable and attractive for industrial applications (see publication 3).

The following Chapter describes and discusses the bonding possibilities of the PMAA-*b*-PS polymer with the CE.

3.5.6 Post-modification of polymers

As already discussed in the previous Chapter, this work aims to produce a lithium extractable based polymer material, which is much more advantageous than common low molecular weight lithium adsorbers due to its easier isolation from water by, e.g., precipitation and further processability in, e.g., membranes (see Chapter 3.6).

There are many different ways to embed new functionalities into a polymer. The aim is to produce a material that would be as inexpensive as possible to manufacture with little effort, on a large scale, and therefore industrially feasible.

The synthesis of functional polymers with defined molecular mass, composition, and architecture is a significant challenge, especially when steric groups such as the CEs used in this work are involved. To obtain the target polymer, two different routes can be used, either the functional group is already in the monomer and polymerized, protected with protecting groups if necessary; however, the use of controlled polymerizations comes with some requirements which can lead to difficulties for monomers with steric or multiple functional groups as side reactions can occur and control can be lost. Probably the most straightforward technique is post-modification after polymerization. The method of post-modification is highly desirable when several properties are targeted to be combined, like the polymer lithium adsorber material prepared in this work. It is essential that the functional group which is incorporated into the polymer material should not start a unwanted polymerization with e.g. solvents or impurities. Some of the most commonly used reactions for post-modification are shown in Figure 3.47. For a more detailed description of the respective responses, the reader is referred to the review articles by Klok et al.^{259,260}

From a mechanical point of view, substitution reactions are the most widespread post-modification reactions. These include, for example, the chlorination of polyethylenes via free radical substitution or the esterification, amidation, and hydrolysis of reactions with PAA or PMAA derivatives. Other industrially relevant post-modifications include the functionalization of cellulose via esterification, the hydrolysis of polyvinyl acetate, and the amidation of styrene. Oxidation and reduction reactions play only a minor role.

As this work will deal with the post-modification of PMAA, esterification was chosen as the technique. Since the development of the Fischer storage method, this has been a very commonly used method for the esterification of carboxylic acids. One of the significant disadvantages of this very easy-to-implement method is the synthesis under acidic conditions.

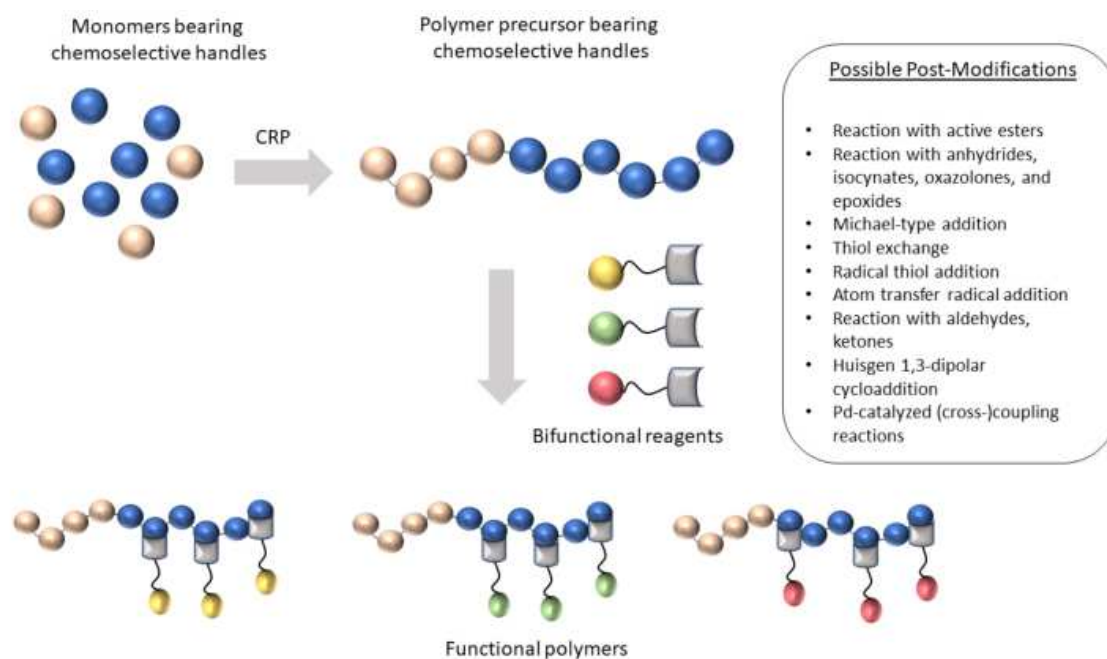


Figure 3.47: Illustration of the post-modification with the most favorite post reactions. The blue dots represent the monomers with the chemoselective handles. The yellow, green, and red dot represent different functional groups which can be incorporated to the polymer system. The orange dot represent a hydrophobic monomer which will not interfere in the post-modification process, e.g. PS. Reprinted with permission from Gauthier et al. from Wiley & Sons.²⁵⁹

An alternative approach, especially for steric groups, is the Steglich esterification. This has already been used to modify polymers. The advantage of this synthesis is the neutral and mild reaction condition at ambient temperatures and neutral pH values. The Steglich esterification was first published by Wolfgang Steglich and Bernhard Neises and requires the addition of a catalyst 4-dimethylaminopyridine (DMAP) and an amide coupling reagent *N,N*-dicyclohexylcarbodiimide (DCC).²⁶¹ Catalytic amounts of DMAP are necessary because they have better nucleophilicity than alcohol. Thus, the reaction rate increases, so the reaction can also be carried out under mild conditions. The DMAP reacts with the *O*-acylisourea intermediate to form the activated electrophilic acrylate pyridinium intermediate, which prevents the 1,3-rearrangement of the *O*-acylisourea medium to an *N*-acyl urea species, which is subsequently incapable of reacting with the alcohol species.²⁶² Figure 3.48 shows the general reaction overview of the Steglich esterification.

The reaction overview shows that the functional group to be attached to the polymer must carry an OH group, so the CEs used must be modified with an OH group. In this work, the self-prepared CE were prepared with a benzene ring based on the catechol and then modified with an aldehyde group via the Duff reaction and subsequently reduced to obtain an OH group on the benzene ring as the target product (the reaction conditions are shown in publication 1). This procedure has the advantage that the CEs are much cheaper than the commercially available OH functionalized ones. The comparison of the adsorber materials in

the polymer and the free CE can be found in Publications 4 and 5, as well as the syntheses of the modified CE and the Steglich esterification.

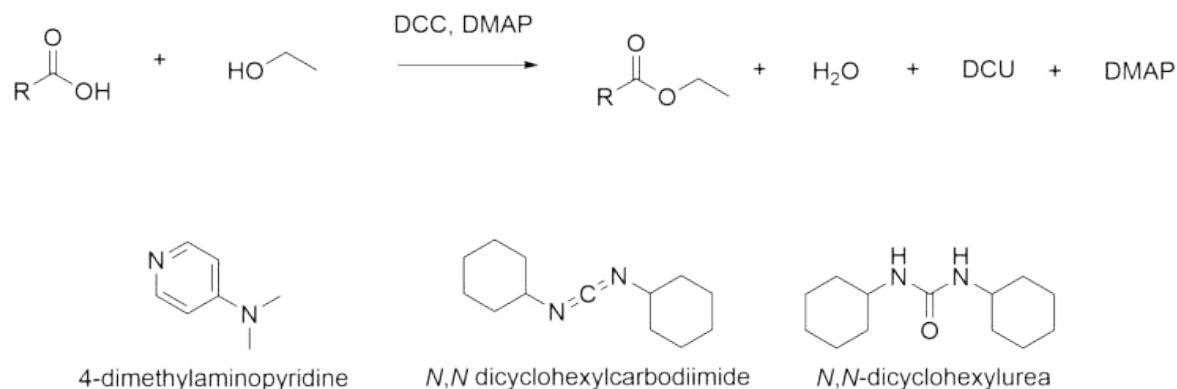


Figure 3.48: Reaction overview of the Steglich esterification and the structure illustrations of DMAP, DCC, and DCU.

In this Chapter, RAFT emulsion polymerization was introduced, and the possible synthesis of the PMAA-*b*-PS polymer material was described in a one-pot synthesis, which avoids complex and costly purification of intermediates and allows the reactions to be carried out in a green solvent such as water. The subsequent post-modification of the acid group of PMAA with a Steglich esterification enables a synthetic, easily isolable lithium extraction polymer material, which can be prepared by low-cost reactants (compared to many other post-modification reactions).

To make the CE-based polymer material even more attractive, producing polymer films/membranes is another step in this direction. Through membranes, the functional groups can be better oriented and thus increase the surface area that comes into contact with the aqueous lithium-containing source. In addition, the isolation of such materials is even more accessible and thus allows many advantages over materials in powder form.

3.6 Thermodynamics of block copolymers

Before introducing the Chapter on membranes, the thermodynamic background of block copolymers is described to make the processes of membrane production more understandable for the reader.

Block copolymers are macromolecules consisting of at least two polymer blocks that are covalently bonded together. Block copolymers might consist of hydrophilic and hydrophobic parts, if this is the case, they are called amphiphilic block copolymers. If the blocks have different properties, they cannot be mixed into each other, and segregation occurs. Due to the covalent bond between the blocks, macroscopic segregation is not possible, but microphase segregation can occur, which is in the order of 5-100 nm. The miscibility of two components, such as homopolymers, can be determined by the change in the free molar enthalpy of mixing (ΔG_{mix}), in which the enthalpy (ΔH_{mix}) and entropy of mixing (ΔS_{mix}) influences are considered (Eq. 3.55). If, for example, ΔG_{mix} is negative, there is miscibility between the components.^{230,263}

$$\Delta G_{\text{mix}} = \Delta H_{\text{mix}} - T \cdot \Delta S_{\text{mix}} \quad (3.55)$$

The Flory-Huggins-Staverman theory can determine the contributions of the entropic (Eq. 3.56) and enthalpic terms (Eq. 3.57). The basis of this theory is an inelastic lattice model and the assumption of random mixing of the polymer chains. R is the gas constant, N_i the polymerization degree of component i , and φ_i the volume fraction of the polymer chain segments. When polymer chains are mixed, there is an increase in disorder in the system ($\Delta S_{\text{mix}} > 0$). If the degree of polymerization N_i increases, the influence of ΔS_{mix} on ΔH_{mix} decreases since fewer mixing configurations are possible.^{230,263,264}

$$\Delta S_{\text{mix}} = -R \cdot \left[\frac{\varphi_A}{N_A} \cdot \ln \varphi_A + \frac{\varphi_B}{N_B} \cdot \ln \varphi_B \right] \quad (3.56)$$

The molar enthalpy of the mixture ΔH_{mix} is described according to Eq. 3.57. The Flory-Huggins-Staverman interaction parameter $\chi_{A,B}$ describes the extent of incompatibility between polymers A and B under the influence of the interaction energies of the segments ε (Eq. 3.58), with k_B as the Boltzmann constant and z defined as the nearest neighbor in the lattice model. If $\chi_{A,B}$ is positive, both blocks are incompatible. The contact of the same segment polymers is favored over that of different polymers. No segregation occurs only if the mixture entropy can balance the enthalpic fraction. If $\chi_{A,B}$ is negative, the interaction of the two segments of different polymers A and B is favored, and the polymers are miscible.^{230,263,264}

$$\Delta H_{\text{mix}} = R \cdot T \cdot \varphi_A \cdot \varphi_B \cdot \chi_{A,B} \quad (3.57)$$

$$\chi_{A,B} = \left(\frac{z}{k_B \cdot T} \right) \left[\varepsilon_{AB} - \frac{1}{2} (\varepsilon_{AA} + \varepsilon_{BB}) \right] \quad (3.58)$$

Substituting the Eq. 3.56 and Eq. 3.57 into Eq. 3.55 gives the following relationship for the free enthalpy of mixing ΔG_{mix} (Eq. 3.59).

$$\Delta G_{\text{mix}} = -RT \cdot \left[\frac{\varphi_A}{N_A} \cdot \ln \varphi_A + \frac{\varphi_B}{N_B} \cdot \ln \varphi_B + \varphi_A \cdot \varphi_B \cdot \chi_{A,B} \right] \quad (3.59)$$

As mentioned before, ΔS_{mix} is small for long macromolecular chains due to the large configurational entropy, thus weak repulsive interactions between segments of different chains can already yield to phase separation. If ΔG_{mix} is positive, macrophase separation occurs in the case of two homopolymers (e.g. in blends). In the case of diblock copolymers with different properties of the blocks, macrophase separation is impossible. Instead, microphase separation occurs to keep the number of contact sites and segment interactions between incompatible segments small ($\chi_{A,B} > 0$). Therefore, the Flory-Huggins-Staverman theory is not valid to describe the entropic contributions to the free energy. Other theories had to be introduced which will be discussed further below.^{230,263–265}

Linear block copolymers with two dissimilar blocks A and B are the easiest and most investigated block copolymers. The thermodynamic equilibrium is defined by a *competition* among interfacial energy and entropic drawback caused by the chain stretching. The morphologies of the structures formed from microphase separation depend on the block volume fraction φ_i , the degree of polymerization N , and the Flory-Huggins-Staverman interaction parameter $\chi_{A,B}$. The first two parameters can be controlled through polymerization stoichiometry and affect the translational and configurational entropy.^{230,263–265}

Figure 3.49 shows a phase diagram obtained from the calculation of Matsen and Bates for a diblock copolymer with equal statistical segment length using the standard Gaussian chain model based on the Self-Consistent Field Theory (SCFT).²⁶⁶ In this illustration, the degree of segregation (χN) as a function of the volume fraction of block A φ_A (in Figure 3.49 is defined as f_A).²⁶⁷ In case χ or χN is sufficiently decreased, the entropic contribution to the free energy outweighs it, and the block copolymer chains are in a disordered phase with undisrupted random coil conformations. When χN is increased to a critical point, transitions of disordered diblock copolymers from order-to-disorder are observed, leading to a microphase separation between two blocks. Above the critical point of an order-disorder transition, an order-order transition between other microphase structures takes place when ϕ is modified.^{230,263,264,268–270}

The ordered region can be divided into three different classes; the weak segregation limit (WSL, $\chi_{A,B} N \approx 10$), intermediate segregation limit (ISL, $10 < \chi_{A,B} N < 100$) and the strong segregation limit (SSL, $\chi_{A,B} N > 100$).²⁷²

A molten symmetric diblock copolymer with adequate segment lengths was described by Leibler based on Landau's theory. He identified a second order phase transition with a volume fraction of φ_A 0.5 and $\chi_{A,B} N = 10.5$. When these values are exceeded, the system is changed to an ordered lamellar state. For unequal volume fractions $\varphi_A \neq 0.5$, a transition from the disordered to the ordered state with a first order phase transition occurs. Spherical

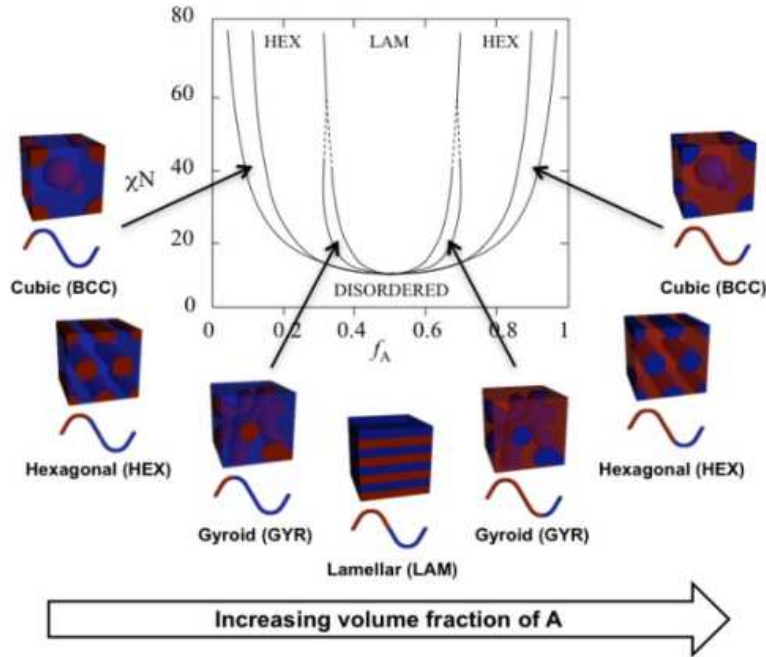


Figure 3.49: Theoretical phase diagram of a linear diblock copolymer with similar statistic segment length and flexibility of the composed components according to SCFT. Reused with permission from Swann et al. from MDPI.²⁷¹

structures (cubic-space centered) are obtained. The domain distance D is an orientation of the phase separation strength of lamellar-forming systems and is proportional to the degree of polymerization N ($D \propto N^{1/2}$).²⁷³

Polymer chain interactions increase in the ISL range. Matsen discovered the gyroid phases, which correlate with the degree of polymerization N according to $D \propto N^{0.8}$.²⁷³

In the SSL, the polymer chains are stretched with the formation of sharp boundaries between the domains depending on the concentration, which consists of only one component. Wasserman and Helfand described the theoretical model of SSL based on SCFT.^{274–276} The microphase separation depends on the contact at the interfaces of the microdomains, the stretching of the polymer chains, and the localization of the linkage points at the interfaces. The free energy according to Semenov was described using an asymptotic approximation of $\chi_{A,B}N \rightarrow \infty$ with the assumption of highly stretched polymer chains.²⁷⁷ The following relationship was established for the domain distance D : $D \propto \alpha N^{2/3} \chi^{1/6}$.²⁷⁸

In summary, the morphology of AB diblock copolymers with similar segment lengths can be predicted with the parameters $\chi_{A,B}N$ and φ_A . This is no longer the case for terpolymers, for which at least three interaction parameters ($\chi_{A,B}$, $\chi_{B,C}$, $\chi_{A,C}$), and two independent composition variables φ_A , φ_B must be used to determine the morphology of ABC triblock terpolymers. Thus a much higher number of morphologies can arise. In addition, also architecture plays a crucial role, e.g., block order, linear or branched topologies. Terpolymers will not be discussed further in this work. In case of further interest, the reader is referred to the

works of Abetz and Simon²⁷⁹ and Hadjichristidis et al..²⁸⁰

3.7 Solubility parameters

Another essential part is the properties of the block copolymer in terms of solubility behavior. Therefore, the different theories are explained and discussed in this Section.

The solubility parameters are essential for the successful and targeted production of polymer membranes via the SNIPS process. The Hildebrand, Hansen, and Hoy solvent parameters are described, and the technique of group contribution method is explained, which is a helpful tool for identifying the solubilities of unknown compounds. Finally, the Hansen solubility parameters are linked to the Flory-Huggins-Staverman interaction parameters to obtain information on the polymer–polymer and polymer–solvent interactions.

In a specific temperature and pressure range, liquid and solid aggregate states are more stable under certain environmental conditions than gaseous aggregate states. In these condensed phases, negative potential energies are generated by the interactions or cohesive forces between the molecules.²⁸¹

The molar cohesion energy ($-U$ or E_{coh}) is defined as the internal molar energy of a material (U) about an ideal gas at a constant temperature, see Eq. 3.60, with ${}_t\Delta_g U$ as the molar energy of vaporization and ${}_t\Delta_\infty U$ as the energy of separation of the molecules. The cohesive forces in condensed phases can thus be expressed quantitatively in terms of cohesive energy density (CED). They can be described as cohesive energy (E_{coh}) per unit volume in Eq. 3.61.^{282,283}

$$-U = {}_t\Delta_g U + {}_t\Delta_\infty U \quad (3.60)$$

$$CED = \frac{E_{\text{coh}}}{V} \quad (3.61)$$

According to these equations, Scott and Hildebrand described the solvent parameters, usually known as the Hildebrand parameter.^{282,284} Hansen extended this basic knowledge and introduced the Hansen solubility parameters.²⁸⁵ These parameters are explained in more depth in the following, and the theoretical calculations based on group contribution method for solvents and polymers are introduced. The connection of the solvent parameters to the Flory-Huggins-Staverman interaction parameter is established.

3.7.1 Hildebrand solubility parameters

The solvent parameters were introduced to describe the enthalpy of mixing ΔH_{mix} of apolar liquids, which have also been extended to polar liquids and polymer solutions. Hildebrand and Scott first described the term solvent parameter.^{282,284} At the same time, also Scatchard, established the theoretical relationship for ΔH_{mix} as a function of the cohesion energy of i

($E_{\text{coh},i}$), volume fraction of i (φ_i), and the molar volume of i (V_i), see Eq. 3.62.²⁸⁶ The Hildebrand solvent parameter δ_{H} was defined from this relationship and is expressed in Eq. 3.63 via E_{coh} , which describes the attractive forces between molecules.^{282,287}

$$\Delta H_{\text{mix}} = V \cdot \left(\left(\frac{E_{\text{coh},1}}{V_1} \right)^{\frac{1}{2}} - \left(\frac{E_{\text{coh},2}}{V_2} \right)^{\frac{1}{2}} \right)^2 \cdot \varphi_1 \varphi_2 \quad (3.62)$$

$$\delta_{\text{H}} = \left(\frac{E_{\text{coh}}}{V} \right)^{\frac{1}{2}} \quad (3.63)$$

For polymer and solvent to be miscible, the contribution of the mixing enthalpy ΔH_{mix} from Eq. 3.62 must be smaller than the contribution of the mixing entropy ΔS_{mix} (Eq. 3.55). If $\delta_1 = \delta_2$, in case of normal solutions, a free entropy of mixing $\Delta G_{\text{mix}} < 0$ is obtained. Therefore, the differences in the solvent parameters should be low so that the components are readily miscible.²⁸⁷ For Eq. 3.62 to be valid, some assumptions must be made as followed:²⁸²

- the mixture of two components occurs without volume change and constant pressure.
- the interaction of the molecules is molecule-centered and is not influenced by other molecules
- the mixture of the components is random, and the distribution is independent of the temperature
- during the mixing, no complexation or other particular associations occur

These assumptions are mostly not valid in the real case, however, they help for further empirical relations.²⁸²

The determination of Hildebrand solubility parameters can be determined experimentally, indirectly, or by relation to other physical parameters. The Hildebrand solubility parameter for solvents can be obtained by measuring the vaporization energy. This is not straightforward in the case of polymers since their intrinsic lack of volatility means that the enthalpy of vaporization cannot be determined. In addition, the Hildebrand solubility parameter is influenced by the number of crosslinks (if any) and the distribution of side chains. Therefore, the solubility parameter for polymers is indirectly determined by solubility tests with solvents with known solubility parameters or by swelling tests on crosslinked polymers.²⁸⁷

To determine the solubility parameters of polymers without time-consuming physical measurements, the method of group contribution theory can be used, which is based on the assumption that the contributions of the different structural groups are additive to the thermodynamic properties;²⁸² according to this method, a cohesive energy of a solvent or polymer (E_i) results from the sum of the cohesive energies e_j of the number n_j of structural groups j in the molecule (Eq. 3.64).²⁸⁷ From this relationship, SMALL has identified an additive relationship of the molar constant of attraction F_j , which is defined according to Eq. 3.65.²⁸⁸

$$E_i = \sum_j n_j \cdot e_j \quad (3.64)$$

$$F_j = (E_{i,j} \cdot V_{i,j})^{\frac{1}{2}} \quad (3.65)$$

According to Eq. 3.63, the solubility parameter for unknown polymers can be determined via the added values of the different structural groups of a compound (Eq. 3.66) with V_i as the molar volume of a repeating unit, ρ the polymer density, and M the molecular weight. Thus, the Hildebrand solubility parameter of a repeat unit in the polymer is theoretically predictable via the group contribution method for the molar volume.^{282,287}

$$\delta_i = \left(\frac{E_i \cdot V_i}{V_i^2} \right)^{\frac{1}{2}} = \frac{\sum_j F_j}{V_i} = \frac{\rho \sum_j F_j}{M} \quad (3.66)$$

The group contribution theory is derived in summary, i.e., from simple systems, and it is therefore not surprising that in most cases, there is no complete agreement with experimental data. Still, even rough estimates are helpful to get an orientation to the solvent choice and more helpful than a total lack of information.²⁸³ The advanced group contribution methods of HOY²⁸⁹ and STEFANIS and PANAYIOTOU²⁹⁰ are more comprehensive methods for calculating solvent parameters and will be discussed further below, since they have been used in this thesis.

3.7.2 Hansen solubility parameters

For the description of the enthalpy change of the mixture of apolar solvents, the HILDEBRAND solubility parameters show good agreement with experimental data. Still, there are no consistent results for polar systems.²⁸² Therefore, Hansen postulated an extension of the HILDEBRAND solubility parameter theory to polar and hydrogen bonding capable systems.²⁹¹ The extension is based on the partitioning of the cohesive energy of a liquid into three interaction contributions: the contribution from dispersive forces (E_d), the contribution from polar forces (E_p), and the contribution from hydrogen bonding (E_h), see Eq. 3.67.^{282,283,285}

$$E_{\text{coh}} = E_d + E_p + E_h \quad (3.67)$$

Suppose the addition of these contributions is divided by the molar volume. In that case, the description of the HANSEN solubility parameters is obtained according to Eq. 3.68 with δ_t as the total solubility parameter, δ_d the disperse, δ_p the polar, and δ_h the hydrogen bonding term of the solubility parameter.^{282,285}

$$\delta_t^2 = \delta_d^2 + \delta_p^2 + \delta_h^2 \quad (3.68)$$

A collection of Hansen solubility parameters for various solvents and polymers was performed and determined by Hansen through physical measurements such as enthalpy of va-

porization, dipole moments, and experimentally conducted solvent tests. By correlating the partial solubility parameters from Eq. 3.68 with two materials, the distance R_a can be determined as shown in Eq. 3.69.²⁸⁵

$$R_a^2 = 4(\delta_{d1} - \delta_{d2})^2 + (\delta_{p1} - \delta_{p2})^2 + (\delta_{h1} - \delta_{h2})^2 \quad (3.69)$$

In this equation, for example, index 1 represents the polymer, and index 2 the solvent. Due to the simple calculation, the method is particularly suitable for solvent selection. Also relevant is the relative energy difference (RED) number defined by the quotient of R_a and the radius of the Hansen solubility parameter sphere R_o , which represents the maximum value for R_a at which solubility is present or other interactions such as swelling in polymers (Eq. 3.70). The R_o value is determined predominantly experimentally by various solubility tests using different solvents with known Hansen solubility parameters. Suitable solvents have a RED number less than 1; unsuitable solvents have a value greater than 1.^{285,290}

$$RED = \frac{R_a}{R_o} \quad (3.70)$$

According to Stefanis and Panayiotou,²⁹⁰ the group contribution method represents an extended modern method for determining solubility parameters. In this method, the molecular structures are divided into two characteristic properties of functional groups: the first-order functional groups, which describe the basic molecular structure, and the second-order functional groups, which capture the overall functions in the system and are based on conjugation theory. Using regression analysis literature of known organic compounds with known partial solubility parameters, the contributions for different first and second-order functional groups were determined. By summing these contributions for the desired structure, the Hansen solubility parameters can be determined according to Eq. 3.71-3.73. Here, C_i is the contribution of the first-order functional groups of type i with the number of groups n_i in the structure. Similarly, D_j is the second-order contribution, and correspondingly, m_j is the number of groups in the system. W is the constant and is 0 if there are no second-order functional groups. Otherwise, the value is 1.²⁹⁰

$$\delta_d = \left(\sum_i n_i C_i + W \sum_j m_j D_j + 17.3231 \right) MPa^{\frac{1}{2}} \quad (3.71)$$

$$\delta_p = \left(\sum_i n_i C_i + W \sum_j m_j D_j + 7.3548 \right) MPa^{\frac{1}{2}} \quad (3.72)$$

$$\delta_h = \left(\sum_i n_i C_i + W \sum_j m_j D_j + 7.9793 \right) MPa^{\frac{1}{2}} \quad (3.73)$$

For the last two equations, these are provided only for solubility parameter values greater

than $3\text{MPa}^{1/2}$. If smaller values are obtained, the Stefanis and Panayiotou Eq. 3.74 and 3.75 have been proposed.²⁹⁰

$$\delta_p = \left(\sum_i n_i C_i + W \sum_j m_j D_j + 2.7467 \right) \text{MPa}^{\frac{1}{2}} \quad (3.74)$$

$$\delta_h = \left(\sum_i n_i C_i + W \sum_j m_j D_j + 1.3720 \right) \text{MPa}^{\frac{1}{2}} \quad (3.75)$$

This group contribution method is beneficial when experimental solubility data are unavailable. Thus, if the structure is known, the Hansen solubility parameters can be predicted using Eq. 3.71-3.75 and the table values of the contributions (see appendix). Due to the variety of first and second-order functional groups, a wide range of structures and functionalities can be represented, and the solubility properties can be theoretically determined.²⁹⁰

3.7.3 Hoy solubility parameters

Similar to the Hansen solubility parameters, the Hoy solubility parameters are also based on the assumption of the splittings of the cohesive energies as described in Eq. 3.68 and 3.69.²⁸⁹ This method consists of four additive molar functions, auxiliary equations, and final expressions for the partial solubility parameters (Eq. 3.76-3.79) with F_t , the molar constant of attraction, F_p , the polar component, and V , the molar volume. In Eq. 3.79, these values are determined additively based on the number N of functional groups i in the structure under consideration. Δ_T represents the Lydersen correction for non-ideality.^{283,290}

$$F_t = \sum N_i F_{t,i} \quad (3.76)$$

$$F_p = \sum N_i F_{p,i} \quad (3.77)$$

$$V = \sum N_i V_i \quad (3.78)$$

$$\Delta_T = \sum N_i \Delta_{T,i} \quad (3.79)$$

In auxiliary Eq. 3.80 and 3.81, α is the molecular aggregation number, T_b is the boiling temperature, and T_{cr} is the critical temperature.²⁸³

$$\log \alpha = 3.39 \left(\frac{T_b}{T_{cr}} \right) - 0.1585 - \log V \quad (3.80)$$

$$\left(\frac{T_b}{T_{cr}} \right) = 0.567 + \Delta_T - (\Delta_T)^2 \quad (3.81)$$

When equating the additive molar functions and the auxiliary equation, the total and partial solubility parameters can be calculated, where B is a basis value of 277 MPA^{1/2} defined by HOY to calculate δ_t .²⁸³

$$\delta_t = \frac{(F_t + B)}{V} \quad (3.82)$$

$$\delta_p = \delta_t \left(\frac{1}{\alpha} \frac{F_B}{F_t + B} \right)^{\frac{1}{2}} \quad (3.83)$$

$$\delta_h = \delta_t \left(\frac{\alpha - 1}{\alpha} \right)^{\frac{1}{2}} \quad (3.84)$$

$$\delta_d = (\delta_t^2 - \delta_p^2 - \delta_h^2)^{\frac{1}{2}} \quad (3.85)$$

It should be noted that the values of Δ_T apply to low molecular weight liquids. Hoy defined distinct contribution values for amorphous polymers, so the solubility parameters for repeat units of polymers can also be used. The auxiliary equations are shown in Eq. 3.86 and 3.87, with n as the number of repeating units per polymer chain segment.²⁸³

$$\alpha(P) = 777 \frac{\Delta_T^{(P)}}{V} \quad (3.86)$$

$$n = \frac{0.5}{\Delta_T^{(P)}} \quad (3.87)$$

After adjusting the auxiliary equations, new total and partial solubility parameter terms (Eq. 3.88, 3.89, and 3.90) are obtained for polymers.²⁸³

$$\delta_t = \frac{(F_t + B/n)}{V} \quad (3.88)$$

$$\delta_p = \delta_t \left(\frac{1}{\alpha^{(P)}} \frac{F_p}{F_t + B/n} \right)^{\frac{1}{2}} \quad (3.89)$$

$$\delta_h = \delta_t \left(\frac{\alpha^{(P)} - 1}{\alpha^{(P)}} \right)^{\frac{1}{2}} \quad (3.90)$$

A listing of the functional groups and their contributions can be found in the appendix. These data were taken from the publication by Durkee,²⁹² in which the author improved the original Hoy contributions concerning the volume contributions.

In summary, the HOY and HANSEN solubility parameters help to predict the solubility properties of unknown polymer systems. Similar to the HANSEN solubility parameters, the RED number can also be determined for the HOY solubility parameters. Again, the same

values apply for $R_a < 0$ = better solubility. The HOY and HANSEN parameters are often similar, but these values should not be interchanged because they were determined differently. As long as both solubility parameter theories show similar trends, applying both approaches increases the informative value of the solubility behavior of the polymer system.²⁹² Therefore both methods are used to determine a suitable solvent system for the SNIPS process (see Chapter 6: unpublished results).

3.7.4 Flory-Huggins-Staverman interaction parameter according to Hansen

The Flory-Huggins-Staverman interaction parameter is divided into an entropic (χ_S) and an enthalpic (χ_H) term.²⁸² By regular solution theory, the enthalpic part can be linked to the total solvent parameter of a solvent (index A) and a polymer (index B) (Eq. 3.91) with V_A as the molar volume of the solvent, R the ideal gas constant, and T the temperature.²⁹³ For non-polar systems, an empirical value of $\chi_S = 0.34$ is often assumed.²⁸²

$$\chi_{AB} = \chi_S + \chi_H = 0.34 + \frac{V_A}{RT}(\delta_A - \delta_B)^2 \quad (3.91)$$

Polymer and solvent are miscible according to Flory if the condition in Eq. 3.92 is fulfilled, from which the critical polymer-solvent interaction parameter χ_c results. In the case of an excess of solvent, the quotient approaches 0, χ_c then assumes a value of 0.5 (Eq. 3.93).²⁸²

$$\chi_{AB} < \frac{1}{2} \left[1 + \left(\frac{V_A}{V_B} \right)^{\frac{1}{2}} \right]^2 \quad (3.92)$$

$$\chi_{AB} = \frac{1}{2} \left[1 + \left(\frac{V_A}{V_B} \right)^{\frac{1}{2}} \right]^2 = 0.5 \quad (3.93)$$

If the polymer-solvent interaction parameter is less than 0.5, this indicates solubility or swellability. This value deviates somewhat for smaller polymers and can also be soluble at values above 0.5, although only sparingly soluble. For polymer blends, a value of 0 should be achieved to obtain theta conditions. Thus, the smaller the value χ_{AB} , the better the miscibility between solvent and polymer.²⁸⁵ The value δ_t should therefore show as slight a difference as possible between the two components.²⁸²

The Hansen solubility parameters can also describe the polymer-solvent interaction parameter (see Eq. 3.94).²⁸⁵ Lindvig et al. extended the Hansen approach with an optimized universal parameter σ with a value of 0.6.²⁹⁴ With this equation, the polymer-solvent interaction parameter of a polymer and solvent can be determined via the partial Hansen solubility parameters and follows the same statements as in Eq. 3.92 and 3.93. The advantage of this method is that the empirical value for the entropy of 0.34 (obtained from data with Hildebrand parameters) does not have to be considered when the Hansen solubility parameters are used.²⁸⁵

The polymer–polymer interaction parameter can be determined by using the total solubility parameters and the enthalpic term from Eq. 3.91 to indicate the polymer–polymer interaction with V_0 as the molar volume of a chain segment (Eq. 3.95). The entropic term should range between 10^{-6} and 10^{-2} , making the enthalpic term the largest.²⁹⁵

$$\chi_{AB} = \sigma \cdot \frac{V_A}{RT} \cdot [(\delta_{dA} - \delta_{dB})^2 + 0.25 \cdot (\delta_{pA} - \delta_{pB})^2 + 0.25 \cdot (\delta_{hA} - \delta_{hB})^2] \quad (3.94)$$

$$\chi_{H,pp} = \frac{V_0}{RT} (\delta_{\text{polyA}} - \delta_{\text{polyB}})^2 \quad (3.95)$$

A much lower critical interaction parameter χ_c for an ideal symmetric polymer consisting of polymers A and B ($N_a = N_b = N$) with a volume fraction of 0.5 is obtained (Eq. 3.96). Especially, blends with long chains (large N) are usually phase-separated since they have a higher value than χ_c . It is worth mentioning, that this approach is related to mainly apolar interactions, such as van-der-Waals interactions. In the case of mixtures with polar interactions, this paragraph loses its explanatory power and has to be considered critically.²⁹³

$$\chi_{c,\text{blend}} = \frac{2}{N} \quad (3.96)$$

The polymer–solvent and polymer–polymer interactions are determined and discussed for the desired polymer membrane systems (see Chapter 6: unpublished results).

3.8 Membranes

This Chapter discusses the definition and fabrication of block copolymer membranes. Various conventional membrane fabrication methods are presented such as the non-solvent induced phase separation (NIPS) and SNIPS, which are based on the fundamentals of Chapter 3.6 and 3.7.

3.8.1 Definition and properties of membranes

Membranes are the perm-selective barriers or interfaces between two phases (e.g. liquids or gas), which allow the selective transport of specific components more readily than others.²⁹⁶ In contrast to many other separation methods such as distillation or crystallization, this technique does not require the addition of additives, or high temperatures and is therefore a relatively low-energy and gentle separation method.²⁹⁷ Large-scale production can be implemented excellently since the apparatus setup is simple and straightforward.^{298,299} Furthermore, the separation of substances by membrane technology can be combined with other separation methods to achieve even better separation efficiency.³⁰⁰

The membrane can be classified in different aspects, e.g., functionality or application, pore size, morphology, and structure.³⁰¹ The driving force of a membrane is generally based on a difference in chemical potential, e.g., a transmembrane pressure, temperature or concentration gradient, or electrical potential.^{302,303} The pressure-driven membrane process can be divided into microfiltration, ultrafiltration, nanofiltration, and reverse osmosis, which have already been mentioned in chapter 3.2 in the summary of lithium-selective membrane technologies.³⁰⁴ Figure 3.50 shows a schematic representation of the different membrane types and driving forces.

Reverse osmosis and nanofiltration membranes operate at very high pressures and separate the minor organic substances such as alkali or alkaline earth metals. In the lower pressure range, ultrafiltration and microfiltration membranes separate larger macromolecules, viruses, colloids, cells, and bacteria.³⁰⁵

A further classification can be made based on the membrane structure, which can be either symmetrical or asymmetrical or porous or non-porous (see Figure 3.51).³⁰⁶ The membrane cross-section of a symmetric membrane is uniform.³⁰⁷ Isotropic porous membranes are similar to conventional filters regarding structure and function, however, the pore size is much smaller in the range of 0.01-10 μm .³⁰⁸ Filtration occurs as a function of the molecular size of components and pore size distribution. Dense membranes, on the other hand, separate components according to their solubility and diffusivity within the membranes with a permeation rate inversely proportional to the thickness of the membranes. Thus, the function of non-porous membranes can be described by the solution-diffusion mechanism and they are mainly used in, e.g., gas separations.³⁰⁹ On the other hand, porous membranes are often used in micro- and ultrafiltration.³¹⁰

Asymmetric membranes, in turn, have a thin separation active layer (<500 nm) supported

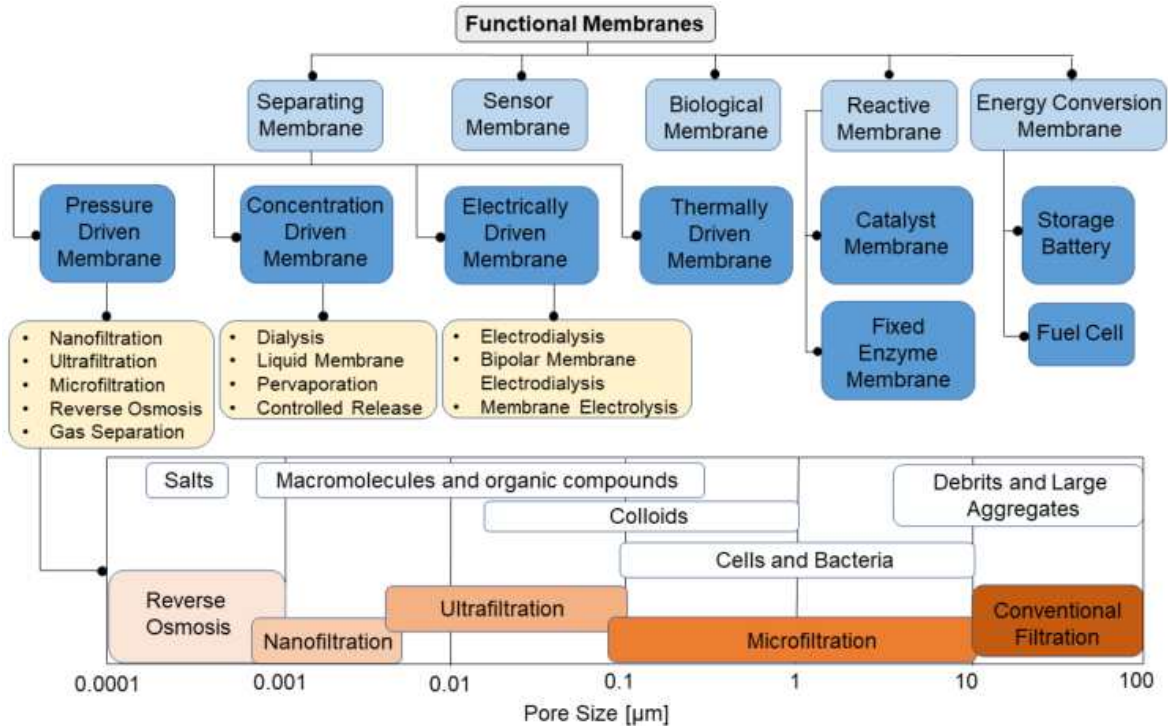


Figure 3.50: Classification of different membrane classes, driving force, and separation performance.³⁰⁴

by a functional sponge structure. The top layer gives usually the membrane the separation properties, while the sponge structure gives the material its mechanical support. The top as well as the sublayer can be created in one step or separately. The layers in composite membranes are formed by different materials in most cases and can therefore optimized independently.³¹¹

The mixture that flows through a membrane is called feed, what is retained is called retentate, and the solution that flows through the membrane is called permeate. A distinction is usually made between two types of filtration, i.e., dead-end and cross-flow filtration.³¹²

In dead-flow filtration, the flow is entirely perpendicular to the membrane with selective retention of individual components, thus resulting in a high yield.³¹³ The filtration resistance is increased over the filtration time as the retentate forms a growing filter cake. To maintain the permeate flow, the pressure must be permanently increased. Therefore, at a certain pressure, the membrane may destabilize and even rupture at the end and be destroyed. To ensure a continuous process, the membranes must be cleaned regularly, e.g., by rinsing or pressure reversal.

Cross-flow filtration is based on a parallel feed that flows along the membrane. Part of the feed is forced through the membrane, while part of the mixture of substances, the retentate, is formed without passing through the membrane. In contrast to the dead-end flow, not all the energy is transferred to the filtration process, but also for maintaining the membrane overflow, so much more power is required than with the dead-end flow.³¹³

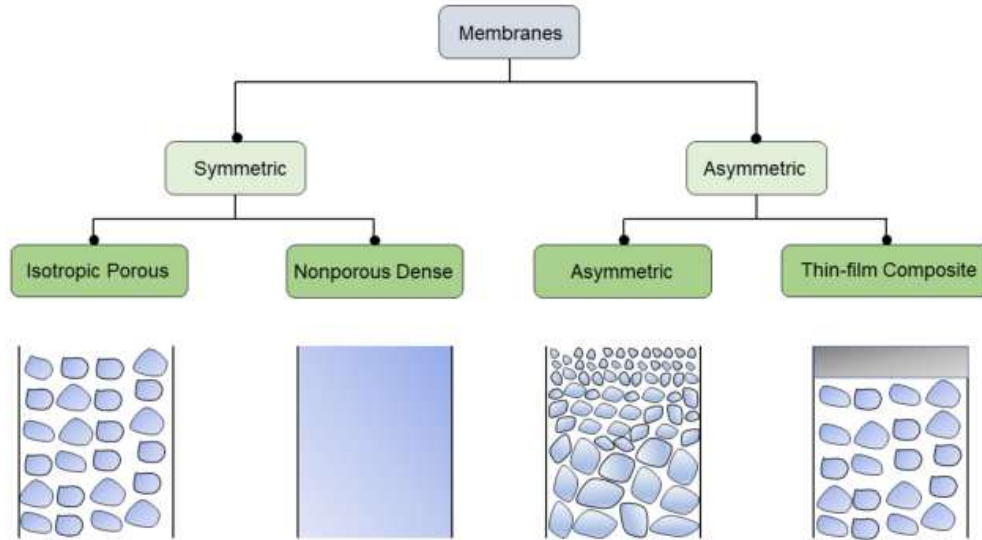


Figure 3.51: Classification of symmetrical and asymmetrical polymer membranes.

The retention (R_t) of a membrane can be described by Eq. 3.97, where c_p and c_f are the dissolved concentrations of a solute in the permeate and feed.^{314,315}

$$R_t = 1 - \frac{c_p}{c_f} \quad (3.97)$$

A semi-permeable membrane is present if the dissolved substance has a retention of 100 %. In the case of multiple substances in solution, the selectivity of a membrane is defined by the separation factor α , where y_a and y_b , and x_a and x_b are the concentrations in the permeate and feed for components A and B, respectively (Eq. 3.98).^{314,315}

$$\alpha_{a,b} = \frac{y_a/y_b}{x_a/x_b} \quad (3.98)$$

Darcy's law defines the volumetric flux J as the function of the pressure difference across the membrane cross-section (Eq. 3.99). Concentration polarization and fouling are not included. The permeability coefficient L_p describes the membrane's structure and the permeate viscosity.^{314,315}

$$J = -L_p \cdot \frac{d_p}{d_x} \quad (3.99)$$

The Hagen-Poiseuille law can obtain a more accurate description of the flux for a cylindrical pore geometry located within the membrane cross-section. In Eq. 3.100, the Hagen-Poiseuille law is described with the porosity ε_m , the membrane pore radius r , the viscosity η , the tortuosity τ , the pressure difference p , and the membrane thickness x_m (equivalent to the length of cylindrical perpendicular pores).³¹⁴⁻³¹⁶

$$J = \frac{\varepsilon_m \cdot r^2}{8 \cdot \eta \cdot \tau} \cdot \frac{\Delta p}{\Delta x_m} \quad (3.100)$$

In the Hagen-Poiseuille equation, it is assumed that all pores have the same size, but this is rarely the case in reality. The Kozeny-Carman equation describes the volume flux J for membranes with irregular structure and tortuosity with SA the internal surface area of the pores, the Kozeny-Carman constant (KC) constant, which is dependent on the structure of the pores, and the tortuosity (Eq. 3.101).^{314,315,317}

$$J = \frac{\varepsilon_m^3}{KC \cdot \eta \cdot SA^2(1 - \varepsilon_m)^2} \cdot \frac{\Delta p}{\Delta x} \quad (3.101)$$

Irreversible deposits of retained substances on the membrane surface lead to increased flow resistance unless the transmembrane pressure rises. Therefore the permeate flux decreases with an increased amount of deposits. This phenomenon is referred to as fouling, which is a common problem in membrane technology for liquid phase applications.^{318,319} Since fouling reduces the permeate flux, it can be counteracted by increasing the transmembrane pressure. However, this leads to increased energy costs and can only be carried out up to physical deformation. Cleaning intervals to release the pores can also be performed, nonetheless, this forces to process interruption and usability of very aggressive chemicals, damaging the membrane material in the long terms. Fouling can be prevented by incorporating hydrophilic triblock copolymers,³²⁰ post-modification at the surface,³²¹ mixing in additives such as microgels,³²² changing the membrane topology,³²³ or increasing shear forces.³²⁴ For more in-depth information, please refer to the review work by Chang et al.³²⁵

3.8.2 Membrane fabrication

In 1861 the first polymer membrane was published; those membranes are much cheaper compared to, e.g., ceramic or glass membranes.³²⁶ The field of block copolymer membranes is relatively young but offers a wide range of possibilities to adjust thermal and mechanical resistance and vary the separation efficiency.³²⁷⁻³²⁹

There are many different ways to produce polymer membranes. For example, porous membranes can be made by sintering, stretch track etching, or by a phase inversion process. Membranes produced by sintering or stretching allow a pore size of 0.1 μm and are therefore only suitable for microfiltration processes. On the other hand, micro- and ultrafiltration membranes can be produced using the track etching or phase inversion process.^{330,331}

Asymmetric membranes, which are produced via the phase inversion process, are of great economic importance because they allow high fluxes, have a thin selective separation layer and contain high-pressure stability due to the porous substructure.³¹¹

In membrane manufacturing, phase separation is achieved by solid-liquid phase separation, starting with a homogeneous polymer solution. In this process, phase separation occurs by transferring a homogeneous polymer solution into a bath of a non-solvent, which is called

NIPS and will be described in the following.^{332–334}

3.8.2.1 Non-solvent-induced phase separation

In the NIPS process, the polymer must be completely soluble in a solvent or solvent mixture; this solvent must be miscible with the non-solvent precipitation bath. In addition, a miscibility gap must be identifiable between polymer, solvent/solvent mixture, and non-solvent. During membrane preparation, the polymer solution is placed on a support, often glass or polyester, and spread with a doctor blade at a defined thickness and speed. Until a specific evaporation time is reached, the liquid polymer film is evaporated until it is placed in a precipitation bath (often water). Due to the interaction of the solvent and the precipitant (non-solvent), phase separation occurs into two coexisting phases to minimize the Gibbs free energy, and a membrane structure is formed.^{315,334,335}

Figure 3.52 describes the phase separation process in more detail by the ternary mixture of polymer, solvent, and non-solvent. The triangular phase diagram is characterized by a homogeneous and thermodynamically stable, metastable, and unstable region. The binodal curve separates the stable area (a, b, c, d) from the metastable region (e). The spinodal curve on the other side separates the metastable region (e) from the unstable one (f). Each point in this diagram shows a mixture of the three compositions located at the respective corners of the triangle (polymer, solvent, non-solvent) and tie lines combining a pair of equilibrium compositions with identical chemical potential, determining the composition of the polymer-rich and polymer-poor phases at each step of the phase separation process.³¹⁵

The phase separation during the NIPS process occurs in the metastable area by nucleation and growth. In the unstable region, spinodal segregation takes place. The thermodynamically stable polymer solution is the starting point of the NIPS process. This is spread onto a support to form a film at time $t=0$ (see Figure 3.52). The time that elapses until the polymer film support is placed in the precipitation bath results in an increase in concentration perpendicular to the film surface due to evaporation of the solvent in which the polymer is dissolved. Hence different concentrations exist at the surface and inside the film. As soon as the polymer film is transferred to the non-solvent bath, the interaction between solvent and non-solvent takes place; at some point during the process, the solution is in the metastable or unstable range. The state with the lowest free enthalpy of mixing ΔG_{mix} is targeted by segregating it into two phases. The sponge-like substructure typical of asymmetric polymer membranes is a specific consequence of spinodal segregation. Starting from the homogeneous region, the more minor phases formed due to segregation in the unstable area, the stronger the incompatibility of the component. The incompatibility is most significant at the surface when the polymer film support is introduced into the precipitation bath. Thus, the segregation is stated at the surface of the polymer solution ($t=1$). The resulting precipitating polymer membrane interferes with the exchange between solvent and non-solvent in the deeper regions of the polymer film. The non-solvent diffuses further into the film, which means that the concentration gradually decreases from the film's surface to the bottom. Thus, the incompatibility between polymer

and solvent/non-solvent also reduces across the cross-section. Segregation is less profound in the membrane, which is in the unstable region and less distant from the homogeneous area, and occurs later ($t=2$).^{315,334,335}

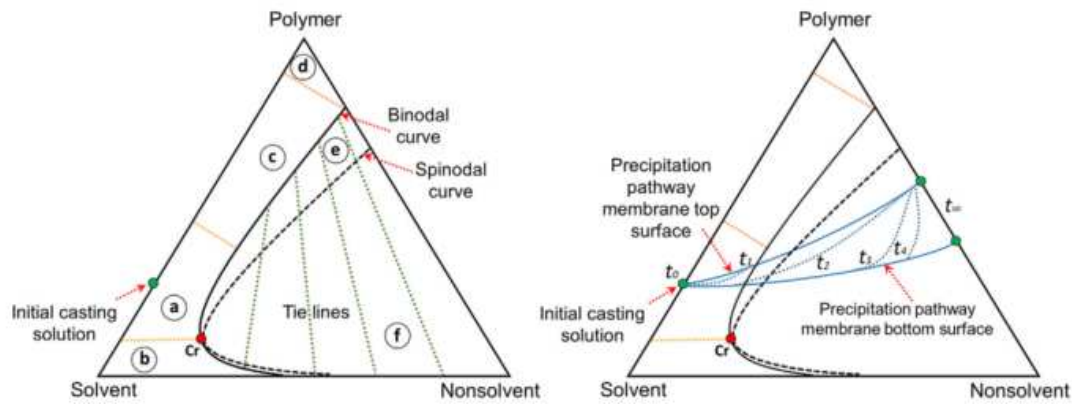


Figure 3.52: Illustration of the ternary phase diagram of a polymer–solvent–nonsolvent system. Various regions inside the diagram are illustrated. a) displays the one-phase stable area with suitable compositions to produce a initial casting solution, b) one-phase stable area with unsuitable compositions to fabricate membranes, c) one-phase gel area, d) glassy area, e) metastable region, and f) unstable area. The critical point (Cr) represents the point where the spinodal and binodal curve touch each other. The right image illustrates the different precipitation pathways of the membrane top surface, in between and the bottom is represented. Reused with permission from Radjabian and Abetz from Elsevier.³¹⁵

3.8.2.2 Self-assembly of block copolymers and non-solvent-induced phase separation

The combination for self-assembly capability with the process of SNIPS is used to prepare isoporous integrally asymmetric block copolymer membranes. This method is based on designing a polymer film by self-assembling the block copolymers and subsequent generation of the porous structure by precipitating a component from the film. The process of the SNIPS method enables the fabrication of pore structures with narrowly distributed mean pore diameter and underlying sponge-like support structure, which can be fabricated in one step. The membrane fabrication is similar to the procedure of the NIPS process. A polymer solution usually consisting of a binary or ternary solvent with different boiling points and solubilities concerning the respective blocks is used. Once the polymer film is spread on support and evaporated for a specific time, the critical step of micro phase separation of the block copolymers occurs at the surface (Figure 3.53). During the evaporation time, the concentration at the surface decreases to a value below the order-disorder solvent concentration. The growth of ordered periodic microdomains appears. The order of the microphase separation is determined by the variation of the polymer chain relaxation rate and the rate of the adequate segregation strength as a function of the solvent concentration. A steep solvent concentration gradient allows for vertically oriented microphase separation that can only grow

a finite distance into the film, with the solvent concentration at the surface below a critical concentration. The bottom layer of the membrane is again closer to the initial concentration of the casting solution. The formed vertically ordered structure is highly swollen since the selective solvents have different boiling points. Therefore, the membrane can transform into a thermodynamically more favorable parallel structure. Thus, the cast film should be added to the precipitation bath after a specific time. During the interaction between solvent and non-solvent, the ordered, vertically aligned structure on the surface is formed.^{315,334,336,337}

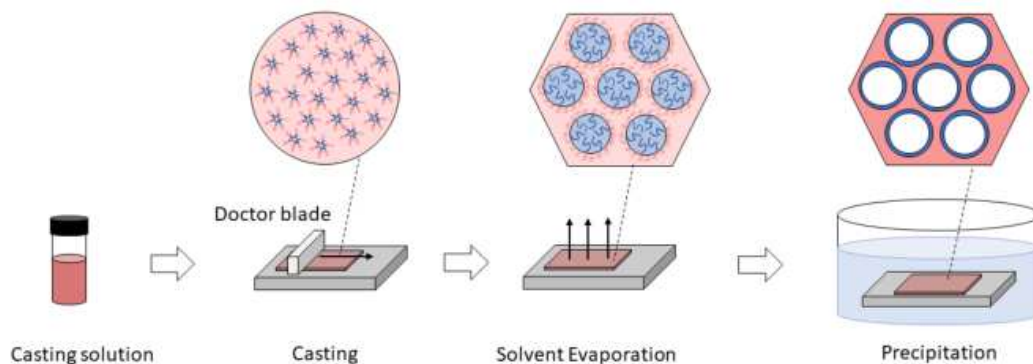


Figure 3.53: Illustration of the SNIPS procedure. Starting from a homogeneous casting solution applied to a support and evaporated for a specific time in the environment, and the subsequent precipitation of the film in a non-solvent.

At the same time, the bottom layer enters an unstable state and forms a sponge-like structure by spinodal decomposition, similar to the NIPS process. With the SNIPS process, integral asymmetric membranes with high pore density and a selective thin layer, as well as vertically aligned cylindrical pores with very narrow pore size distributions, are obtained (Figure 3.54).^{315,334,336,337}

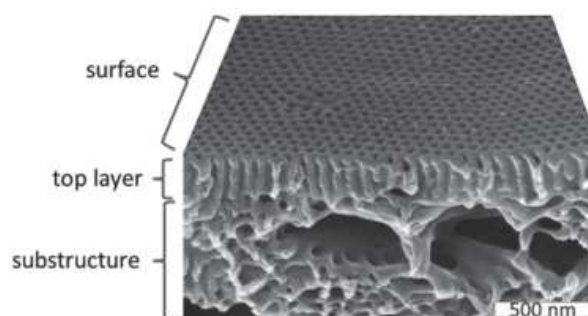


Figure 3.54: Top and cross-section view of an integral asymmetric block copolymer membrane. Reused with permission from V. Abetz from Wiley.³³⁴

The formation of SNIPS membranes requires the right choices of many parameters together, e.g., chain length of the polymer, concentration of the casting solution, solvent composition, evaporation time (ET) and evaporation rate of the solvent. To obtain the optimal processing window, normally it requires a massive trial and error casting. Concerning the selection of the solvent, the solubility parameters can provide a theoretical reference to partially simply the choice of solvents.^{315,334}

According to Hoy and Hansen, theoretical solvent parameters were determined to simplify the manufacturing conditions of block copolymer membranes using the SNIPS method. These methods be described in more detail in Chapter 6.2 (unpublished results). The aim was to find a suitable solvent mixture for the PMAA-*b*-PS polymer, and that of the CE functionalized polymer, which is a unknown polymer structure and therefore no data of the solvent properties exists.

Objective of this Work

The extraction of lithium is a necessary process to sustain future lithium-ion batteries' further development. The production of an adsorbent material with both a good lithium uptake capacity and simple and inexpensive to manufacture so that the material can be scaled up to a larger scale is fundamental to providing enough lithium as a raw material for humanity and thus more environmentally conscious living in the world. In this work, among the many different adsorbent materials for lithium feedstock, the crown ether class was chosen due to its variety of functionalization and therefore adjustable extraction properties.

The topic of the dissertation is mainly divided in four parts: the synthesis and simulation of different crown ether structures and their influence on lithium extraction, the synthesis of an industrially attractive polymer material, the synthesis and lithium extraction properties of crown ether bonded polymer materials, and the preparation of lithium extracting polymer membranes. The parts of the thesis are summarized in Fig. 4.1.

PART I: Synthesis and simulation of different crown ether structures and their influence on lithium extraction

In the first part of this work, different crown ether structures were fabricated to study the lithium extraction capacity in aqueous lithium resources. The influence of the crown ether size, the number and type of heteroatoms in the ring, and the hydrophilicity and hydrophobicity of the crown ether structure on the lithium extraction capacity, was investigated. To obtain a broader range of different crown ether structures and predict more accurate trends of the lithium extraction versus other interfering ions, the DFT simulation method was also used.

PART II: Synthesis of an industrially attractive polymer material

In the second part of the work, a polymer material was chosen that could be produced as green as possible, on a large scale from readily available and inexpensive monomers. In addition, a functional group should be present to bind the crown ethers to the polymer. The PMAA-*b*-PS diblock copolymer was chosen as the target base polymer, as it meets these requirements.

PART III: Synthesis and lithium extraction properties of a crown ether functionalized polymer material.

The third part of the work deals with the linkage of the crown ethers with the PMAA-*b*-PS base polymer and the comparison of the lithium extraction properties of the free crown ethers with that of the polymer-bound crown ethers.

PART IV: Preparation of lithium extracting polymer membranes

In the final part of the work, the powdered polymer-bound crown ether material is to be processed into membranes since these allow easier isolation from the aqueous medium, thus improving the material's handling and providing a larger surface area of the adsorbent material.

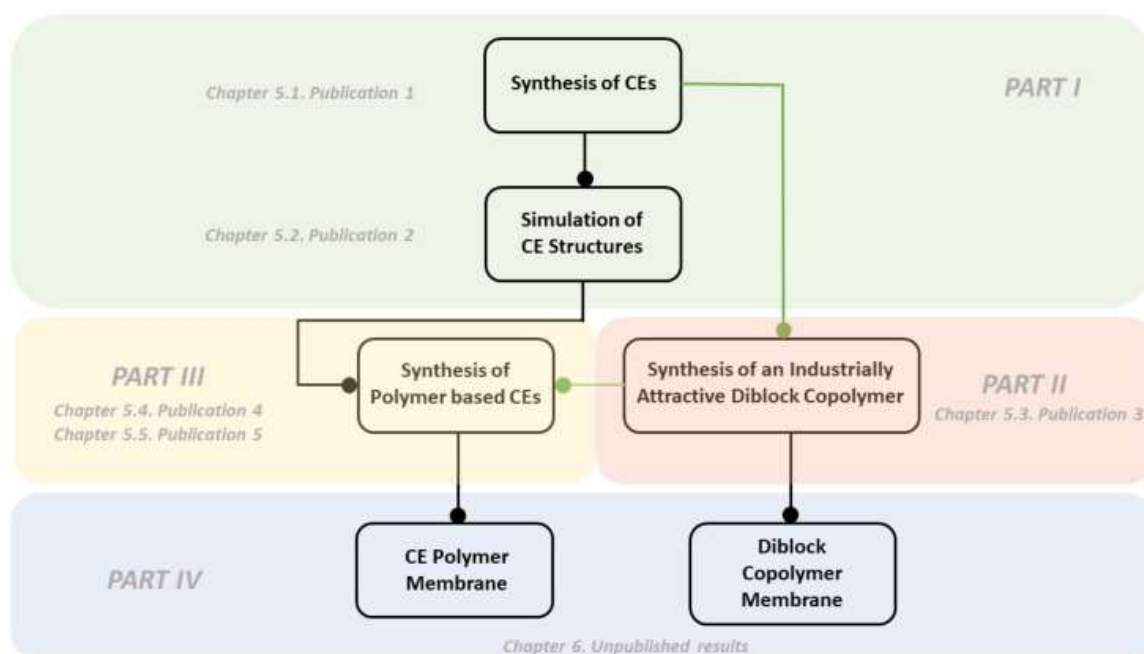


Figure 4.1: Work of the scope: Part I focuses on the synthesis and lithium extractability for different CE structures, part II on the synthesis of an industrially attractive polymer, part III on the connection of part I and II, and part IV on the processing of the polymer into a membrane material.

Published Results

This Chapter contains reprints of the five first-author articles that are the main part of this dissertation. A short synopsis is given for each publication and the support of collaborators, coworkers, and students is acknowledged.

5.1 Publication 1:

Thermodynamic study of crown ether–lithium/magnesium complexes based on benz-1,4-dioxane and its homologues

This work was partially done with the assistance of Fanny Ott (Universität Hamburg) in the context of a bachelor thesis under my supervision and guidance. Her help is gratefully acknowledged.

The first Publication of this thesis focuses on the synthesis of new crown ether structures with different hydrophobicities within the ring to study the effect of lithium complexation in comparison to magnesium, since this ion is due to the alike ionic radius one of the major issues of reduced lithium extraction capability using crown ethers as adsorber from aqueous lithium resources.

In the past, different crown ether sizes, substituents, or donor atoms within the crown ether were studied on different metal ions.^{175,338–340} Still, the influence of hydrophobicity without changing the donor atoms or substituents has never been studied to the best of our knowledge.

Based on the benz-1,4-dioxanes, three different crown ether sizes with only two oxygen donor atoms but an extended alkane chain were investigated for lithium and magnesium complexation. The extraction of the metals by the different crown ethers was studied in a two-phase extraction, with the crown ether initially in the organic phase and the salts in the aqueous phase. UV-responsive anions were used as counterions to the salts so that the aqueous phase could be examined before and after extraction by UV-vis spectroscopy to determine the change in concentration of the metal ions. By calculating thermodynamic quantities such as the complexation constants, free enthalpy, entropy, and enthalpy, conclusions could be drawn

about the stability of the complex.

The increase of the number of C atoms within the crown ether ring (i.e., the growth of the hydrophobicity) showed an increase in the magnesium complexation; decisive for this is the increase of the entropy, while the lithium complexation decreases with higher hydrophobicity. These results thus show stronger complexation towards lithium when more hydrophilic crown ether adsorbers are used.

The Publication is reprinted with permission from I.Oral, F.Ott and V. Abetz, *Phys. Chem. Chem. Phys.*, **2022**, 24, 11687. - published by the Royal Society of Chemistry. The related supporting information is available in Section 9.2.


 Cite this: *Phys. Chem. Chem. Phys.*, 2022, 24, 11687

 Received 4th March 2022,
 Accepted 25th April 2022

DOI: 10.1039/d2cp01076c

rsc.li/pccp

Thermodynamic study of crown ether–lithium/magnesium complexes based on benz-1,4-dioxane and its homologues†

 Iklima Oral,^a Fanny Ott^a and Volker Abetz^{a,b}

The synthesis and characterization of benz-1,4-dioxane crown ethers (CEs) and some of its homologues are described and analyzed. The effect of added C-atom within the CE ring (increasing the hydrophobicity of the CE ring by increasing the number of CH₂-units) on the Li⁺ and Mg²⁺ complexation within a liquid–liquid extraction (LLE) is investigated and thermodynamically analyzed. The complex stability constant *K*, the change of entropy ΔS and enthalpy ΔH , and the Gibbs energy ΔG are determined. The enhanced hydrophobicity of the CE ring results in stronger complexation stability of the Mg²⁺ complex, while the Li⁺ complexes are less favored. This effect mainly occurs due to the increased entropy term with improved hydrophobicity of the CE. These results indicate a stronger extraction of Li⁺ in Mg²⁺-containing aqueous resources if more hydrophilic CEs are used.

1. Introduction

Crown ethers (CE) are well-known for binding metal cations due to their cyclic cavities and electron donor features.¹ CEs are macrocyclic ligands containing ethyleneoxy units, so-called polyethers. Since the name of these compounds is quickly complicated if larger rings are considered, Pedersen suggested the family name *crown ether*. This definition results from the molecular models and the ability to crown metal cations.^{2,3} The general structure of the CE is shown in Fig. 1, where X labels the total number of atoms and Y the total number of heteroatoms within the ring. If the CE arises from an arene catechol compound, the structure is named benzo-X-crown-Y.

The interaction of a CE with a cation is mainly based on the interaction of charge (the metal cation) and dipole (donor atom within the CE ring), which can be influenced by the orientation of the donor atom, cavity size of the CE, type of donor atom (according to the HSAB principle), the substitution of electron-donating and withdrawing compounds and solvent.⁴ The large variability of the CE structures and their properties is why they are used in many different applications such as isotope separations,⁵ ion determination sensors,⁶ phase transfer catalysts,⁷ and ion transport through membranes.^{8,9}

The application of CEs in solvent extraction is particularly noteworthy since it presents several benefits such as high selectivity, fast extraction rates, and easy application due to simple equipment on a laboratory and industrial scale. Especially in applications with polymers, improved adsorption properties and product recovery are more straightforward.^{10–12} The solvent extraction with CEs has been widely used to recover alkali and alkaline-earth metal ions such as Li⁺, Na⁺, K⁺, Mg²⁺, and Ca²⁺.^{10,13–16} Different cavity sizes, heteroatoms within the ring such as nitrogen or sulfur, substituents, and complex stoichiometries have been investigated.^{17–20} To remove the metal ions from the CE–metal complex, a temperature increase in the system releases the ions from this complex, as shown in the work of Warshawsky and Kahana.²¹

In this work, we synthesized different CEs based on benz-1,4-dioxane by increasing the cavity with an increased alkane chain (increasing the hydrophobicity of the CE). The effect of changing the ring size and increasing hydrophobicity surroundings on metal ion complexation is studied without incorporating other factors such as donor atoms or attached

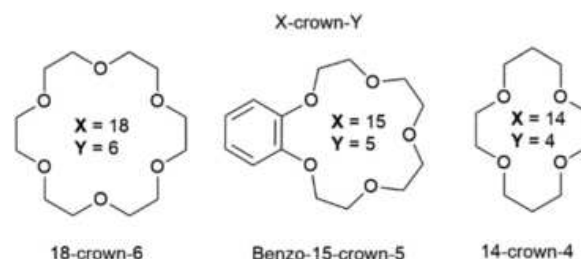


Fig. 1 Illustration of different CE structures.

^a Institute of Physical Chemistry, Universität Hamburg, Grindelallee 117, 20146 Hamburg, Germany

^b Helmholtz-Zentrum Hereon, Institute of Membrane Research, Max-Planck-Straße 1, 21502 Geesthacht, Germany. E-mail: volker.abetz@hereon.de

 † Electronic supplementary information (ESI) available. See DOI: <https://doi.org/10.1039/d2cp01076c>


substituents. In this work, we will focus on the complexation stability of benz-1,4-dioxane-based CE with the alkali metal ion Li^+ and the alkaline-earth metal ion Mg^{2+} . In terms of Li^+ recovery from brines or seawater, the often-higher Mg^{2+} concentration leads to significant issues due to its similar behavior. Lithium and its compounds are widely used in industrial applications due to their physical and chemical properties and are therefore highly required.²² Especially in the electric vehicle industry, the demand has increased tremendously. The annual global lithium use was estimated to be 57 700 tons in 2019 and 2020, an 18% increase from 49 100 tons in 2018.²³ Numerous CE adsorbents have been tested for Li^+ recovery. For example, the complex stability with benzo-15-crown-5, 12-crown-4, and 14-crown-4 CEs adsorbents have shown excellent complexation properties with Li^+ ; however, complexations with Mg^{2+} and Na^+ were also possible.^{18,24–32} To selectively extract Li^+ from aqueous resources, the complexation behavior of Li^+ and the other metal ions is of great importance. Especially the complexation properties of Li^+ and Mg^{2+} are of great interest since they have almost the same ion diameter in aqueous solution.^{33,34}

In this work the introduced benzo-6-crown-2 (B6C2), benzo-7-crown-2 (B7C2), and benzo-8-crown-2 (B8C2) structures (Fig. 2) are investigated regarding metal ion complex stability since, as far as we know, such adsorbents have not yet been studied. Moreover, the influence of the hydrophobic environment within the ring on the respective ions will be tested and discussed. The thermodynamic properties of Li^+ and Mg^{2+} complexes will be further investigated by determining the enthalpy and entropy change during the complexation process.

2. Results and discussion

2.1. Synthesis of benz-1,4-dioxane crown ethers and homologues

One of the most widely used methods for the syntheses of CEs is the Williamson ether synthesis, which was introduced by Alexander William Williamson.³⁵ The Williamson ether synthesis is a variant of the nucleophilic substitution second-order reaction ($\text{S}_{\text{N}}2$), characterized by a transition state. An alcohol, here: catechol **1**, is converted into an dialcoholate **2** with the aid of a non-nucleophilic base K_2CO_3 (Fig. 3).³⁶ It is worth mentioning that the alkoxides exhibit a higher nucleophilicity than alcohols, due to their increased electron density at the partially negatively charged oxygen atom, which accelerates the speed of the reaction. Due to their high base strength, ether synthesis is limited to the use of primary alkyl halides, since otherwise

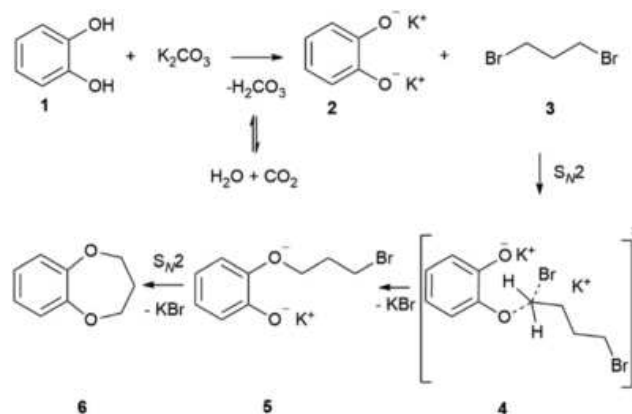


Fig. 3 Illustration of the reaction mechanism of dipotassium catecholate with 1,3-dibromopropane under $\text{S}_{\text{N}}2$ conditions to synthesize B7C2.

side-reactions would occur from the competing bimolecular elimination reaction (E2). It is worth mentioning that the use of phenoxides principally can lead to another side reaction, the C-alkylation. However, this can be prevented by using inert solvents such as benzene, toluene, xylene or polar aprotic solvents such as dimethylformamide (DMF) and dimethylsulfoxide (DMSO) to favor the oxygen alkylation.³⁶ In the next step, the dialcoholate **2** reacts with a primary dihalogenide **3** (here: 1,3-dibromopropane) *via* a concerted, five-membered transition state **4** to form a new ether bond. An alkyl dibromide was chosen as an alkyl dihalide since the leaving capacity of the leaving group correlates with its ability to stabilize the negative charge and increases within the group $\text{F} < \text{Cl} < \text{Br} < \text{I}$ due to increasing polarization capacity. In a further $\text{S}_{\text{N}}2$ reaction, the oxygen nucleophile intramolecularly attacks the electrophilic center of the C–Br bond **5** and forms the seven-membered B7C2 CE ring **6** with two oxygen donor atoms. The synthesis of B8C2 follows the same reaction mechanism. For this, 1,4-dibromobutane was used as an alkyl dihalogenide. The synthetic routes were adapted/modified from the work of Y.-F. Ji *et al.*³⁷ and H.-L. Zhu.³⁸ Since these CEs have not been previously considered as ligands, sufficient analysis of these structures is performed by nuclear magnetic resonance (NMR) spectroscopy (Fig. 4) and infrared (IR) spectroscopy (Fig. S3 and S7, ESI[†]), differential scanning calorimetry (DSC) measurements (Fig. S4 and S8, ESI[†]), and mass spectrometry (MS) (Fig. 5). The ^1H NMR data before purification of the products and the ^{13}C NMR spectra are also documented in the ESI.[†] The data of the ^1H - and ^{13}C spectra are in good agreement with the data from the literature. To the best of our knowledge, the gas chromatography-MS (GC-MS), IR spectroscopy, and DSC data of these compounds have not been reported before.

The molecular ion peak found at 151 000 m/z agrees with the calculated molecular weight for approximately B7C2 ($M = 151.178 \text{ g mol}^{-1}$). The main fragmentation reactions consist of a benzyl cleavage. The delocalized π -electron system of the aromatic compound favors the formation of a stable benzyl ion (80 000 m/z). The possible minor cleavage product is 1,3-cyclobutadiene (52 000 m/z), formed by re-ionization. The peak

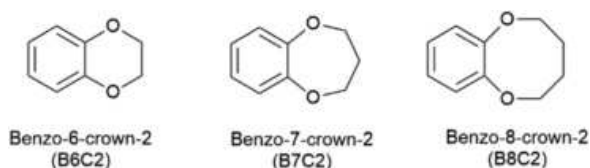


Fig. 2 Benz-1,4-dioxane-based CEs with an increased alkali chain.



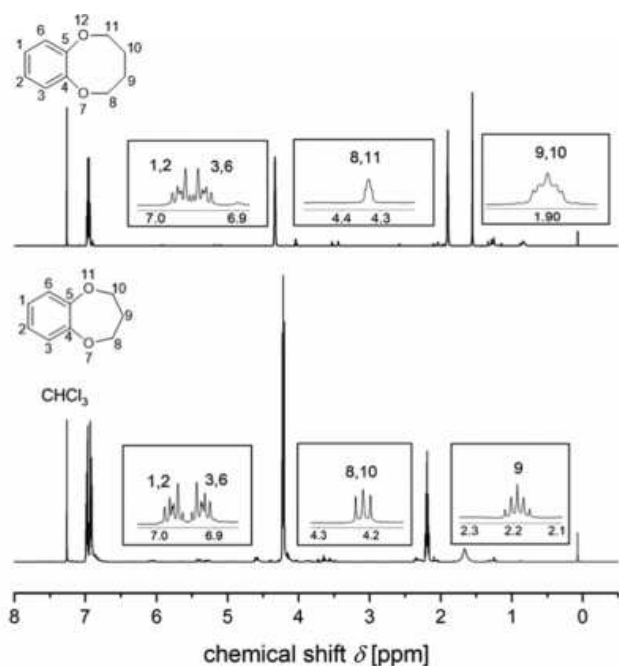


Fig. 4 ^1H NMR spectrum of the B7C2 (bottom) and B8C2 (top). The spectrum was recorded in CDCl_3 and shows the significant signals and their multiplicities on larger scale.

at 121 000 m/z shows a fragmentation based on a benzyl cleavage and hydrogen rearrangement, followed by McLafferty rearrangement and fragmentation. Instead of the McLafferty rearrangement, direct fragmentation of the radical cation is possible, whose quinoid cleavage product leads to the peak at 109 000 m/z . The GC-MS spectrum of the B8C2 shows a molecular ion peak at 164 000 m/z , which is in good agreement with the calculated molecular weight of $M = 164\,080$ m/z . The cleavage product of the McLafferty rearrangement at 121 000 m/z has a lower intensity than B7C2. Thus, it can be assumed that the formation of this molecule ion peak decreases with the

increasing ring size of the CE, which is most likely due to the steric relief caused by the chain breakage.

2.2. Pre-extraction experiments

In the following, the extraction properties of the newly synthesized B8C2 and B7C2 CEs and B6C2 (commercially available) with Li^+ and Mg^{2+} in a liquid-liquid extraction (LLE) are investigated and the effect of ring size and hydrophobicity environment of the ring are discussed. To ensure that the CEs remain in the organic phase during the LLE, blank tests were performed. For this purpose, the CE was dissolved in an organic phase (here: DCM) and LiCl in the aqueous phase. The two-phase mixture was shaken vigorously, and the aqueous phase was subsequently analyzed by UV-vis spectroscopy. Since LiCl shows no absorption in the UV-vis spectrum, any visible signal should refer to the CE. Fig. S13 (ESI †) clearly shows that no absorption maximum is observed in the aqueous phase after extraction for the B7C2 and B8C2 CE structures. The B6C2 shows a small signal (black curve) below 1% and thus one can conclude that the CE-cation complex remains mainly in the organic phase.

2.3. Determination of the thermodynamic complex constant K

The extractability of the metal salts by B6C2, B7C2, and B8C2 was investigated using a reference series of the respective cation. To determine the complexing properties of the CEs, the complex constant K was determined. To ensure UV-vis spectroscopic evaluation of salt complexation, counterions were used that allow π - π^* excitation in the ultraviolet to visible spectral range through conjugated double bond systems and (anti-)auxochromic groups. The chosen metal salt dyes and their corresponding UV-vis spectrum can be found in the ESI † (Fig. S9–S12).

For the LLE of the CE and cation dye, a molar ratio of CE to metal ion ranging from 25:1 to 11:1 was used. The reaction can be described as shown in eqn (1).

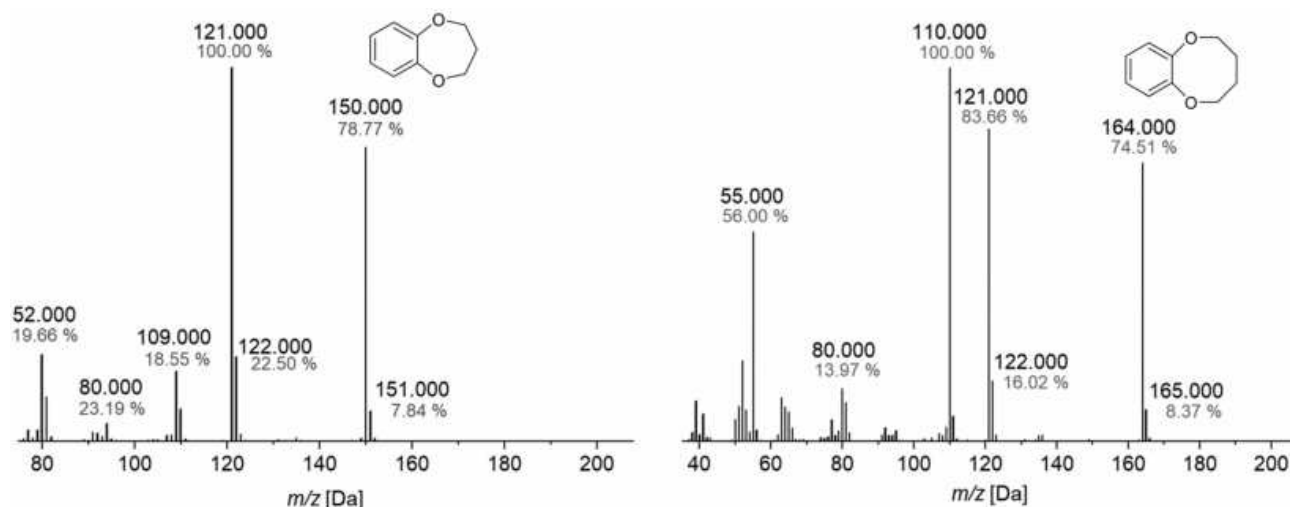
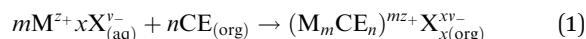


Fig. 5 GCMS spectrometry of B7C2 (left) and B8C2 (right).





where m and x are the stoichiometric factors of the cation M of charge z_+ , and the corresponding counterion X of charge v_- , and n as the equivalents of the CE obligatory for complexation. For all cations $m = 1$ applies, while $x = 1$ applies for Li^+ and $x = 2$ applies for Mg^{2+} . A calibration curve of each salt solution was performed before extraction to determine the concentration in the aqueous phase using the Lambert–Beer law. The calibration was performed shortly before the measurement series and conducted using the same stock solution as the extraction experiments to guarantee the most precise data. The complex constant K of the extraction process was calculated according to the law of mass (eqn (2)):^{10,39}

$$K = \frac{[(M_mCE_n)^{mz+} X_{x(org)}^{xv-}]}{(Q \cdot (\gamma_+[M^{z+}]^m) \cdot (\gamma_-[X^{v-}]^x)) \cdot [CE]^n} \quad (2)$$

with the mean activity coefficients γ_{\pm} and the stoichiometric coefficient Q . Due to the electroneutrality condition, only the activity of the entire system can be determined. Therefore, the mean activity coefficient γ_{\pm} is applied for γ_- and γ_+ , which can be calculated according to the Debye–Hückel-equation (see eqn (3)).

$$\log(\gamma_{\pm}) = -A \cdot |z_+ v_-| \cdot \sqrt{I_a} \quad (3)$$

I_a is the ionic strength and A is a dimensionless factor, which has a value of 0.509 at 25 °C.⁴⁰ The ionic strength I_a can be calculated according to eqn (4):

$$I_a = \frac{1}{2} \sum_i c_i \cdot z_i^2 \quad (4)$$

With c_i , the molar concentration of the ion (mol L⁻¹) and z_i the charge number of the ions. The stoichiometric coefficient Q can be calculated according to eqn (5).

$$Q = (m^m \cdot x^x)^{\frac{1}{m+x}} \quad (5)$$

2.4. Extraction studies of B6C2, B7C2 and B8C2 with Li⁺ and Mg²⁺

In the following, the complex stability of B6C2, B7C2, and B8C2 at different concentrations with Li⁺ and Mg²⁺ at 25 °C is determined. The complexation constant K was calculated for a single and a sandwich-type cation–CE complexation. An illustration of the newly formed structure is exemplarily presented in Fig. 6 for the B7C2 with Li⁺ and Mg²⁺ and the corresponding anions. Since Li⁺ and Mg²⁺ are preferentially complexed in coordination number (CN) 4,^{41,42} a sandwich complex can be assumed (two CE ligands crown one metal ion). Furthermore, the cavity size of the CE might be too small for the metal ions to fit into the CE cavity.³⁴ Therefore, the data presented here are calculated based on the assumption of a sandwich-type complexation.

In the complexation process of metal ions from aqueous solutions, the formation of the hydration shell plays an essential role.

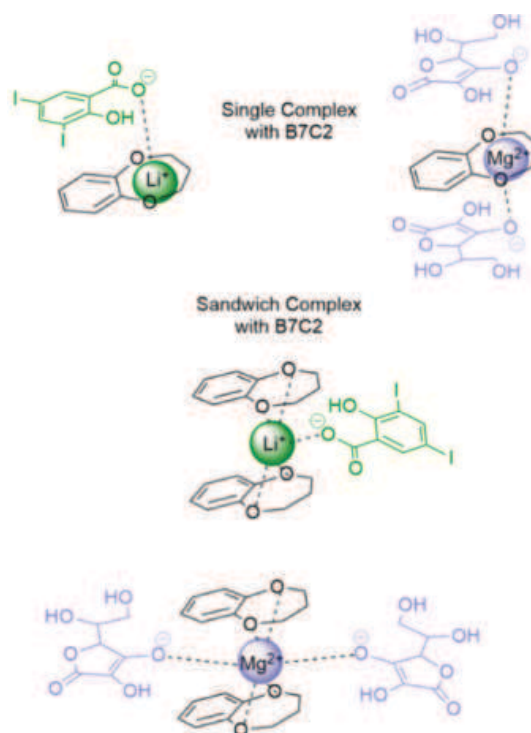


Fig. 6 Schematic illustration of the B7C2–Li and Mg single and sandwich-type complex with corresponding anions.

The hydration shell must first be removed from metal ions to be complexed. The strength of the hydration shell depends on the charge and the size of the metal ion. The energy freed when one mole of ions undergoes hydration is called the hydration enthalpy ΔH_{hyd} , which is the highest for Mg^{2+} (-1922 kJ mol⁻¹), followed by Li^+ (-521 kJ mol⁻¹).⁴³ The evaluated complex stability constants K for the molar ratio of CE to metal ion ranging from 25 : 1 to 11 : 1 for single and sandwich-type complexation can be found in Fig. S14 and Table S1 (ESI[†]). A graphical illustration of the complexation constants K of the respective complexes is shown in Fig. 7 (values refer to the more likely sandwich-type complexation). It is already known that the substitution of the oxygen donor atoms with less electronegative atoms such as nitrogen favors the complexation of Mg^{2+} (as expected according to the HSAB principle). However, the influence of a more hydrophobic environment with a simple alkyl chain has not been studied yet. The introduction of a more hydrophobic ring shows a stronger complex stability constant K for Mg^{2+} which is indicated by the following trend B8C2 = B7C2 > B6C2. For Li^+ , on the other hand, the trend is *vice versa* showing an increased $\log K$ in the following trend: B6C2 \approx B7C2 > B8C2 and thus decreasing with higher hydrophobicity of the ring. According to the HSAB principle Li^+ (hardness $\eta = 35.12$) is a harder base than Mg^{2+} ($\eta = 32.55$),^{44,45} which could explain the obtained trend.

2.5. Temperature-dependent extraction studies of B6C2, B7C2 and B8C2 with Li⁺ and Mg²⁺

In the following, enthalpic and entropic values are determined experimentally by temperature-dependent LLE to clarify the differences of complex stability for the B6C2, B7C2 and B8C2



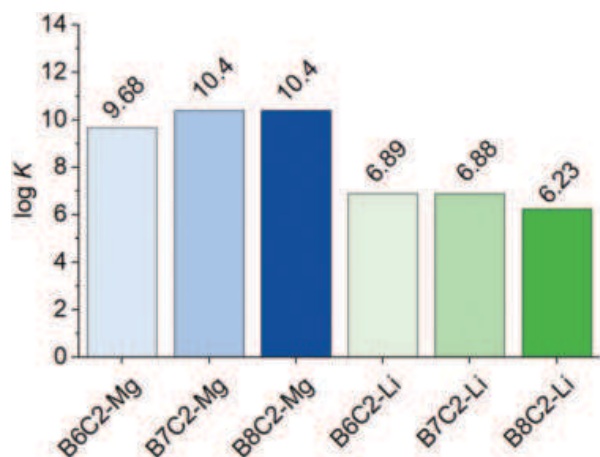


Fig. 7 $\log K$ of the CE:metal ion complexes with B6C2, B7C2, and B8C2 with Mg^{2+} and Li^+ at a constant molar ratio of CE:metal ion of 14:1.

CEs more precisely. The relation between the complex constant K and temperature is described by the Van't Hoff equation (VH, eqn (6)) assuming that ΔH and ΔS are temperature independent.

$$\ln K = -\frac{\Delta H}{R} \cdot \left(\frac{1}{T}\right) + \frac{\Delta S}{R} \quad (6)$$

The VH equation arises from the combination of the Gibbs energy of reaction and the Gibbs energy isotherm equation, which is described in eqn (7) and (8). R labels the molar gas constant ($8.314 \text{ J mol}^{-1} \text{ K}^{-1}$).

$$\Delta G = \Delta H - T\Delta S \quad (7)$$

$$\Delta G = -RT \ln K \quad (8)$$

The so-called VH plot results from eqn (6). The natural logarithm $\ln K$ is a linear function of the reciprocal temperature $1/T$. The plot of the values results in a linear regression, where the slope gives $-\frac{\Delta H}{R}$ and the intercept $\frac{\Delta S}{R}$. The VH plots are shown in Fig. S15 (ESI[†]) and the corresponding values to determine ΔS and ΔH can be found in Table S2 (ESI[†]). The data of the enthalpy and entropy changes ΔH and ΔS after complexation of B6C2, B7C2, and B8C2 with Li^+ and Mg^{2+} are shown in Fig. 8. The green bar labels ΔH and the blue bar labels ΔS .

Generally, an enthalpy gain occurs if new interactions proceed between the metal ion and the donor atoms of the CE. On the other hand, the anion interacts less pronounced in the organic phase compared to the aqueous phase, resulting in an enthalpy loss.³⁹ The enthalpy change ΔH is highest for the B6C2 for Li^+ and decreases rapidly when the ring size as well as the hydrophobicity increases. In fact, negative values are obtained for the B7C2 and B8C2 CEs, which might be due to the weaker ΔH_{hyd} of Li^+ compared to Mg^{2+} , making the desolvation less energy-consuming and, therefore, enthalpic change more favorable. However, this is not the case for B6C2-Li. The energy contributions are significantly higher for the Mg^{2+} complexes, which is most likely due to the stronger bonding of the water molecules to the Mg^{2+} in the aqueous phase. In

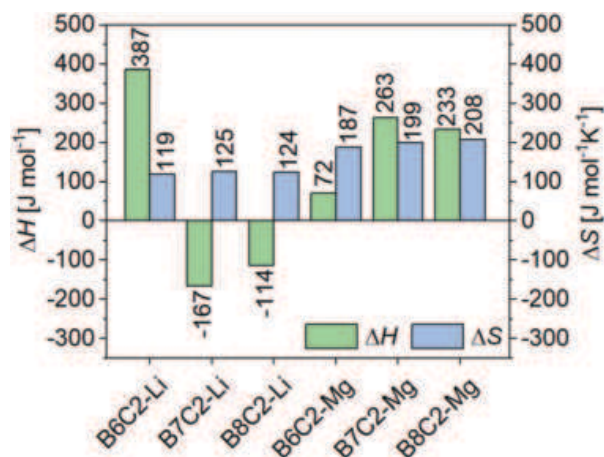


Fig. 8 Enthalpy and entropy changes after complexation of the CE with the metal ions Li^+ and Mg^{2+} at a constant molar ratio of CE:metal ion of 14:1. The green bars represent the change in enthalpy ΔH after extraction and the blue bars the change in entropy ΔS , respectively.

addition, two anions have to be freed from the hydration shell compared to the Li complex to form the CE-Mg complex (compare with Fig. 6). In addition, ΔH increases for the more hydrophobic CE rings such as B7C2 and B8C2 in comparison to B6C2.

The change of Gibbs energy of a system is an interplay between ΔH and ΔS . The change of entropy ΔS is almost identical for Li^+ complexes and increases only slightly with increasing hydrophobicity of the CE. On the other hand, ΔS increases with growing hydrophobicity for the CE-Mg complexes, which is most likely the reason for the higher complex stability K (Fig. 7). The higher ΔS of Mg^{2+} complexes compared to Li^+ ones most-probably result from the released water molecules, which were strongly bound to the Mg^{2+} ion before complexation. As previously mentioned, the hydration enthalpy ΔH_{hyd} is almost four times larger than the enthalpy that would be required to desolvate lithium. Accordingly, the water molecules are much more strongly bound to the Mg^{2+} . In addition, in the case of the Mg^{2+} complexes, two anions are attached to the complex so that twice the amount of water molecules are released. In contrast, the formation of complexes in the organic phase also leads to entropy loss since the CEs lose mobility. The larger the complex, the greater this loss. The entropy loss is thus more significant for a sandwich-type complex compared to a single complex. The change in entropy ΔS is, therefore an interplay between the gain in entropy due to the release of water molecules in the aqueous phase and the loss of entropy due to the binding of the ligands and anions to the metal ion in the organic phase.

To describe the energy of a system and its voluntariness of the complex formation, the Gibbs energy ΔG is used. Fig. 9 shows the calculated ΔG values calculated according to eqn (7) by performing extraction at room temperature (grey bar) and by eqn (8) conducting temperature-dependent extractions using the VH equation (ΔG (VH), orange bar). Both ΔG values agree well with each other. All reactions are exergonic and proceed



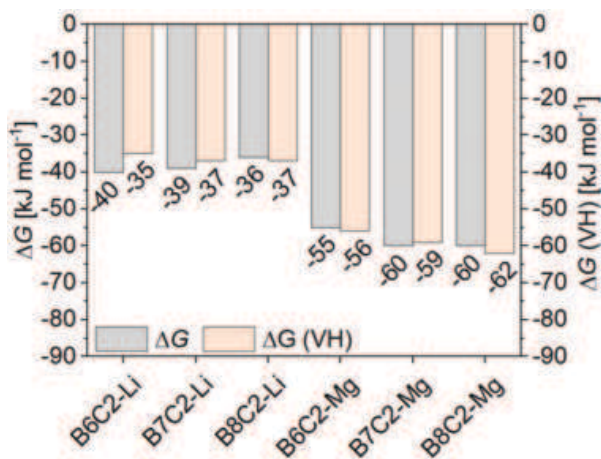


Fig. 9 Gibbs energy calculated by the Gibbs–Helmholtz equation (ΔG), grey bars and from the Gibbs energy isotherm equation based on the Van't Hoff plot (ΔG (VH)), orange bars at a constant molar ratio of CE : metal ion of 14 : 1). The data represent the values for $T = 25^\circ\text{C}$.

voluntarily, with the Mg^{2+} complexes being more favorable. This effect is more pronounced with increasing hydrophobicity of the CE ring.

The CEs prepared in this work are new adsorbents for lithium isolation that have not been previously considered in the group of benz-1,4-dioxane homologues with an increasing alkane chain. In addition, CE B7C2 in particular is less expensive in comparison to the commercially available 12-crown-4 and 15-crown-4 CEs that are commonly used for lithium isolation and since it is less soluble in water, the yield of complexed lithium is larger.

3. Conclusions

B7C2 and B8C2 CEs were synthesized and compared with B6C2 in LLE to investigate the Li^+ and Mg^{2+} extractability from aqueous solution. Thermodynamic parameters such as the complex stability constant K , the Gibbs energy ΔG (calculated from room temperature and temperature-dependent extractions), and the change in entropy ΔS and enthalpy ΔH were determined and discussed. The increase of the number of C atoms within the CE ring (higher hydrophobicity) leads to higher Mg^{2+} complex stability, while the Li^+ complex stability is decreased. The higher stability of Mg^{2+} complexes is most likely based on a greater change in change of entropy ΔS with increasing hydrophobicity. In summary, the data reported here show that the effect of hydrophobicity has brought us much closer to the selective extraction of Li^+ over Mg^{2+} and that these results can further narrow the choice of future adsorbents for lithium extraction to find a suitable material.

4. Experimental

4.1 Materials

1,4-Benzodioxane (98%, Sigma-Aldrich, Schnellendorf, Germany), (+)-Mg-(L)-ascorbate (98%, Sigma-Aldrich, Schnellendorf, Germany),

lithium 3,5-diiodosalicylate (>99%, LIS, Sigma-Aldrich, Schnellendorf, Germany), potassium carbonate (99%, Sigma-Aldrich, Schnellendorf, Germany), catechol (99%, Sigma-Aldrich, Schnellendorf, Germany), dichloromethane (DCM) (>99%, Acros, Schwerte, Germany), petrol ether (technical grade), ethyl acetate (technical grade), 1,3-dibromopropane (>99%, Sigma-Aldrich, Schnellendorf, Germany), 1,4-dibromobutane (>99%, Sigma-Aldrich, Schnellendorf, Germany), 2-propanol (>99%, Sigma-Aldrich, Schnellendorf, Germany) *n*-hexane (95%, VWR Chemicals, Darmstadt, Germany), chloroform- d_1 (>99%, EurisoTop, Saarbrücken, Germany) were used as received without further purification unless noted otherwise. Deionized water was purified with a Milli-Q[®] integral water purification system.

4.2 Methods

Fourier transform infrared spectroscopy (FTIR). The ATR-FTIR spectra were taken on powders of ground dry interpenetrating network gel samples with a Bruker IFS 66V/S FTIR, with a wide-band Mercury Cadmium Telluride (MCT) detector, KBr mid-IR beam splitter, and Pike diamond-ATR module. Each spectrum was averaged over 64 scans at a resolution of 2 cm^{-1} .

Nuclear resonance spectroscopy (NMR). ^1H NMR and ^{13}C NMR spectra were recorded at ambient temperature using a 500 MHz Bruker AVANCE II spectrometer in CDCl_3 . The residual signals at $\delta = 7.26$ for CDCl_3 were used as an internal standard for the chemical shifts.

UV/Vis spectroscopy. The UV-Vis spectra were recorded with a spectrophotometer UV5 from METTLER TOLEDO at room temperature using a scan time of 10 s.

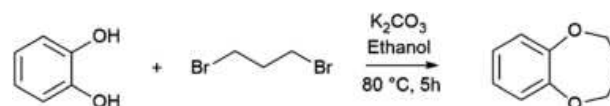
Gas chromatography (GC) with mass spectrometry (MS) coupling. The measurements were carried out in a Thermo ISQ LT EI coupled to a Thermo Trace 1300.

Differential scanning calorimetry. DSC measurements were conducted on a DSC 204 F1 Phoenix from Netzsch. The experiments were run with a scanning rate of 10 K min^{-1} at different temperature ranges and conducted under an inert nitrogen atmosphere. A sample between 5–10 mg was weighed into a 40 μL aluminum crucible which was capped afterward using a pierced lid. The data processing was performed by the Netzsch software Protheus analysis.

4.3 Synthetic procedures

In this work, the preparation of the crown ethers was carried out in a modified form according to a prescription of Huang *et al.*³⁷ The reactions took place under a nitrogen atmosphere.

Synthesis of benzo-7-crown-2

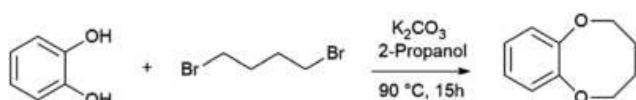


Catechol (5.6 g, 51 mmol, 1.0 eq.), 1,3-dibromopropane (14 g, 7.1 mL, 69 mmol, 1.4 eq.) and potassium carbonate (25 g, 0.18 mol, 3.5 eq.) were dissolved in ethanol (27% (v/v), 150 mL). The green mixture was heated under reflux for 5 h at 80°C and turned into an orange mixture. The reaction was cooled to room



temperature and filtrated under reduced pressure. The crude product was purified two times with column chromatography on silica gel with a mobile phase of petrol ether and ethyl acetate (30 : 1 v/v) and (25 : 1 v/v). The product was obtained as a colorless oil (4.1 g, 54%). $^1\text{H NMR}$ (500 MHz, CDCl_3 , 25 °C): δ [ppm] = 7.00–6.91 (m, Ar-H, 4H), 4.22 (t, 3J (H, H) = 3 Hz, O-CH₂, 4H), 2.19 (quint., 3J (H, H) = 3 Hz, -CH₂, 2H); $^{13}\text{C NMR}$ (500 MHz, CDCl_3 , 25 °C): δ [ppm] = 152 (C₄), 124 (C₄-CH-CH), 122 (C₄-CH-CH), 70.9 (O-CH₂-), 32.2 (-CH₂); GC-MS (EI): m/z (%): [M]⁺ calcd for C₉H₁₀O₂⁺: 151.08, found 151.00 (8) [M⁺], 121.00 (100) [C₇H₇O₂⁺], 109.00 (19) [C₆H₄O₂⁺], 80.00 (23) [C₆H₆⁺], 51.02 (20) [C₄H₃⁺]; IR (KBr): $\tilde{\nu}$ [cm⁻¹] = 3037 (w), 2950 (m), 2866 (w), 1580 (m), 1490 (s), 1246 (s), 1048 (s), 751 (s).

Synthesis of benzo-8-crown-2



Catechol (6.7 g, 61 mmol, 1.0 eq.) was dissolved in 2-propanol (14% (v/v), 170 mL). After adding potassium carbonate (29.5 g, 214 mmol, 3.5 eq.), 1,4-dibromobutane (7.65 mL, 14 g, 64 mmol, 1.0 eq.) was added dropwise to the reaction mixture. The turbid reaction mixture was heated under reflux for 15 h at 90 °C. The red solution was cooled to room temperature and subsequently extracted 5 times with dichloromethane. The eluate was washed with water and brine. Any residue of solvent was removed under reduced pressure. The orange residue was purified two times with column chromatography on silica gel with a mobile phase of *n*-hexane and ethyl acetate (8 : 1 v/v) and (10 : 1 v/v). The product was obtained as a light-yellow-colored oil (0.3 g, 3%). $^1\text{H NMR}$ (500 MHz, CDCl_3 , 25 °C): δ [ppm] = 6.98–6.93 (m, Ar-H, 4H), 4.34–4.32 (m, O-CH₂, 4H), 1.91–1.89 (m, -CH₂, 4H); $^{13}\text{C NMR}$ (500 MHz, CDCl_3 , 25 °C): δ [ppm] = 150 (C₄), 124 (C₄-CH-CH), 123 (C₄-CH-CH), 72.8 (O-CH₂-), 27.1 (-CH₂); GC-MS (EI): m/z (%): [M]⁺ calcd for C₁₀H₁₂O₂⁺: 165.09, found 165.00 (8) [M⁺], 121.00 (84) [C₇H₇O₂⁺], 110.00 (100) [C₆H₄O₂⁺], 80.00 (14) [C₆H₆⁺], 55.00 (56) [C₄H₃⁺]; IR (KBr): $\tilde{\nu}$ [cm⁻¹] = 3069 (w), 2931 (m), 2870 (w), 1578 (m), 1490 (s), 1242 (s), 972 (s), 753 (s).

4.4 Liquid-liquid extraction

The organic phase was prepared by dissolving appropriate amounts of CE ($m \approx 3$ mg) in 3 mL dichloromethane (concentration of the CE c_{CE} ranging from 6.0×10^{-3} to 8.0×10^{-3} mol L⁻¹). The aqueous phase was prepared by diluting salts in water at CE : salt molar ratio between 25 : 1 to 11 : 1 (concentration of the salts c_{Salt} ranging from 2.0×10^{-4} to 8.0×10^{-4} mol L⁻¹). For all extraction experiments, the volume ratio of dichloromethane–water was 1 : 1. The extraction proceeded by vigorously shaking the vial for 45 min at 500 rpm at specific temperatures. Phase separation was guaranteed by waiting 30 min after extraction. The aqueous phase was adequately diluted, and the remaining concentration of the metal ion was measured by a UV-vis spectrometer.

4.5 Temperature-dependent liquid-liquid extraction

Temperature-dependent extractions were performed with a constant molar concentration of CE : salt = 14 : 1. The extraction conditions were carried out analogously to the conditions described above, with only the temperature being changed in a range between 10 and 30 °C. For the temperature setting, a cooling and heating thermomixer MKR13 (DITABIS) was used, which has a temperature accuracy of ± 0.1 °C. The thermomixer was used for the temperature adjustment. To additionally determine the temperature in the solution, a water sample was placed into the thermomixer in which an additional thermometer permanently measured the temperature.

Author contributions

I. O. and V. A.: conceptualization. I. O. and F. O.: methodology, investigation, data curation, formal analysis, and validation; V. A.: supervision and resources; I. O.: writing the original draft; I. O. and V. A.: review and editing of the original draft.

Conflicts of interest

There are no conflicts to declare.

Acknowledgements

The authors acknowledge the NMR spectroscopy and mass spectrometry division of the Department of Chemistry at the Universität Hamburg, and Prof. Dr Weller for providing access to the DSC instrument.

Notes and references

- J. C. Shen, W. L. Jiang, W. Di Guo, Q. Y. Qi, D. L. Ma, X. Lou, M. Shen, B. Hu, H. B. Yang and X. Zhao, A rings-in-pores net: Crown ether-based covalent organic frameworks for phase-transfer catalysis, *Chem. Commun.*, 2020, **56**, 595–598.
- C. J. Pedersen, Cyclic Polyethers and Their Complexes with Metal Salts, *J. Am. Chem. Soc.*, 1967, **89**, 7017–7036.
- G. W. Gokel, W. M. Leevy and M. E. Weber, Crown ethers: Sensors for ions and molecular scaffolds for materials and biological models, *Chem. Rev.*, 2004, **104**, 2723–2750.
- A. Boda, S. Musharaf Ali, H. Rao and S. K. Ghosh, Ab initio and density functional theoretical design and screening of model crown ether based ligand (host) for extraction of lithium metal ion (guest): Effect of donor and electronic induction, *J. Mol. Model.*, 2012, **18**, 3507–3522.
- F. Yan, H. Liu, H. Pei, J. Li, Z. Cui and B. He, Polyvinyl alcohol-graft-benzo-15-crown-5 ether for lithium isotopes separation by liquid–solid extraction, *J. Radioanal. Nucl. Chem.*, 2017, **311**, 2061–2068.
- M. Kamenica, R. R. Kothur, A. Willows, B. A. Patel and P. J. Cragg, Lithium ion sensors, *Sensors*, 2017, **17**, 2430.
- P. E. Stott, J. S. Bradshaw and W. W. Parish, Modified Crown Ether Catalysts. 3. Structural Parameters Affecting Phase



- Transfer Catalysis by Crown Ethers and a Comparison of the Effectiveness of Crown Ethers to That of Other Phase Transfer Catalysts, *J. Am. Chem. Soc.*, 1980, **102**, 4810–4815.
- 8 S. Tas, B. Zoetebier, M. A. Hempenius, G. J. Vancso and K. Nijmeijer, Monovalent cation selective crown ether containing poly(arylene ether ketone)/SPEEK blend membranes, *RSC Adv.*, 2016, **6**, 55635–55642.
- 9 A. Casadellà, A. H. Galama, O. Schaetzle and K. Loos, Effect of Diffusion and Migration on the Selectivity of a Polymer Inclusion Membrane Containing Dicyclohexano-18-crown-6, *Macromol. Chem. Phys.*, 2016, **217**, 1600–1606.
- 10 I. Oral and V. Abetz, A Highly Selective Polymer Material using Benzo-9-Crown-3 for the Extraction of Lithium in Presence of Other Interfering Alkali Metal Ions, *Macromol. Rapid Commun.*, 2021, **42**, 2000746.
- 11 I. Oral, L. Grossmann, E. Fedorenko, J. Struck and V. Abetz, Synthesis of Poly(methacrylic acid)-*block*-Polystyrene Diblock Copolymers at High Solid Contents via RAFT Emulsion Polymerization, *Polymers*, 2021, **13**, 3675.
- 12 I. Oral and V. Abetz, Improved alkali metal ion capturing utilizing crown ether-based diblock copolymers in a sandwich-type complexation, *Soft Matter*, 2022, **18**, 934–937.
- 13 K. Kimura, S. Kanokogi and M. Yokoyama, Extraction Spectrophotometry of Lithium Ions Based on Cation- and Photo-Induced Isomerization of Crowned Spirobenzopyran, *Anal. Sci.*, 1996, **12**, 399–403.
- 14 Y. Tian, W. Chen, Z. Zhao, L. Xu and B. Tong, Interaction and selectivity of 14-crown-4 derivatives with Li⁺, Na⁺, and Mg²⁺ metal ions, *J. Mol. Model.*, 2020, **26**, 67.
- 15 K. Sambe, N. Hoshino, T. Takeda, T. Nakamura and T. Akutagawa, Dynamics and Structural Diversity of Li⁺ (Crown Ether) Supramolecular Cations in Electrically Conducting Salts, *J. Phys. Chem. C*, 2020, **124**, 13560–13571.
- 16 Y. Katayama, K. Nita, M. Ueda, H. Nakamura, M. Takagi and K. Ueno, Synthesis of chromogenic crown ethers and liquid-liquid extraction of alkali metal ions, *Anal. Chim. Acta*, 1985, **173**, 193–209.
- 17 R. E. C. Torrejos, G. M. Nisola, S. H. Min, J. W. Han, S. Koo, K. J. Parohinog, S. Lee, H. Kim and W. J. Chung, Aqueous Synthesis of 14-15-Membered Crown Ethers with Mixed O, N and S Heteroatoms: Experimental and Theoretical Binding Studies with Platinum-Group Metals, *ChemPlusChem*, 2019, **84**, 210–221.
- 18 Y. Inoue, T. Hakushi, Y. Liu and L. H. Tong, Molecular Design of Crown Ethers. 12. Complexation Thermodynamics of 12- to 16-Crown-4: Thermodynamic Origin of High Lithium Selectivity of 14-Crown-4, *J. Org. Chem.*, 1993, **58**, 5411–5413.
- 19 Y. Tobe, Y. Tsuchiya, H. Iketani, K. Naemura, K. Kobi, M. Kaji, S. Tsuzuki and K. Suzuki, Synthesis and lithium ion selectivity of 14-crown-4 derivatives having bulky subunits: cis and trans isomers of 2-phenylcyclohexano-14-crown-4,2,3-diphenylcyclohexano-14-crown-4 and 2,3-di-(1-adamantyl)-14-crown-4, *J. Chem. Soc., Perkin Trans. 1*, 1998, (3), 485–494.
- 20 I. Oral, S. Tamm, C. Herrmann and V. Abetz, Lithium Selectivity of Crown Ethers: The Effect of Heteroatoms and Cavity Size, *Sep. Purif. Technol.*, 2022, 121142.
- 21 A. Warshawsky and N. Kahana, Temperature-Regulated Release of Alkali Metal Salts from Novel Polymeric Crown Ether Complexes, *J. Am. Chem. Soc.*, 1982, **104**, 2663–2664.
- 22 G. Martin, L. Rentsch, M. Höck and M. Bertau, Lithium market research – global supply, future demand and price development, *Energy Storage Mater.*, 2017, **6**, 171–179.
- 23 I. Ore, I. O. Pigments, P. Rock, Q. Crystal, R. Earths and S. Ash, *Mineral Commodity Summaries 2021*, 2021.
- 24 S. V. Demin, N. A. Shokurova, L. I. Demina, L. G. Kuz'mina, V. I. Zhilov and A. Y. Tsivadze, Effects of Side-Chain Substituents in Benzo-15-Crown-5 on Lithium Extraction, *Russ. J. Inorg. Chem.*, 2018, **63**, 121–127.
- 25 K. Wilcox and G. E. Pacey, Chromogenic benzo- and monoaza-12-crown-4, 13-crown-4 and 14-crown-4 lithium-selective, *Talanta*, 1991, **38**, 1315–1324.
- 26 C. Shi, Y. Jia, J. Xiao, X. Wang, Y. Yao and Y. Jing, Lithium isotope separation by liquid-liquid extraction using ionic liquid system containing dibenzo-14-crown-4, *J. Mol. Liq.*, 2016, **224**, 662–667.
- 27 K. Nishizawa, S. I. Ishino, H. Watanabe and M. Shinagawa, Lithium isotope separation by liquid-liquid extraction using benzo-15-crown-5, *J. Nucl. Sci. Technol.*, 1984, **21**, 694–701.
- 28 N. Alizadeh, A comparison of complexation of Li⁺ ion with macrocyclic ligands 15-crown-5 and 12-crown-4 in binary nitromethane-acetonitrile mixtures by using lithium-7 NMR technique and ab initio calculation, *Spectrochim. Acta, Part A*, 2011, **78**, 488–493.
- 29 A. Pálsdóttir, C. A. Alabi and J. W. Tester, Characterization of 14-Crown-4 Ethers for the Extraction of Lithium from Natural Brines: Synthesis, Solubility Measurements in Supercritical Carbon Dioxide, and Thermodynamic Modeling, *Ind. Eng. Chem. Res.*, 2021, **60**, 7926–7934.
- 30 Z. Zhang, Y. Jia, B. Liu, H. Sun, Y. Jing, Q. Zhang, F. Shao, M. Qi and Y. Yao, Study on behavior of lithium ion in solvent extraction and isotope separation, *J. Mol. Liq.*, 2021, **324**, 114709.
- 31 H. Wang, J. He, J. Liu, S. Qi, M. Wu, J. Wen, Y. Chen, Y. Feng and J. Ma, Electrolytes Enriched by Crown Ethers for Lithium Metal Batteries, *Adv. Funct. Mater.*, 2021, **31**, 1–9.
- 32 Y. Oba, M. Okuhata, T. Osakai and T. Mochida, Solvate and protic ionic liquids from aza-crown ethers: Synthesis, thermal properties, and LCST behavior, *Phys. Chem. Chem. Phys.*, 2018, **20**, 3118–3127.
- 33 D. Taziaux, J. P. Soumillion and J. L. Habib Jiwan, Photo-physical and complexing properties of new fluoroionophores based on coumarin 343 linked to rigidified crown-ethers, *J. Photochem. Photobiol., A*, 2004, **162**, 599–607.
- 34 S. Obst and H. Bradacsek, Molecular dynamics study of the structure and dynamics of the hydration shell of alkaline and alkaline-earth metal cations, *J. Phys. Chem.*, 1996, **100**, 15677–15687.
- 35 A. Williamson, XXII. – On Etherification, *J. Chem. Soc.*, 1852, **4**, 229–239.
- 36 T. Laue and A. Plagens, *Namen- und Schlagwort-Reaktionen der Organischen Chemie*, Teubner, 4th edn, 2004.
- 37 W. Bin Huang, Y. Guo, J. A. Jiang, X. D. Pan, D. H. Liao and Y. F. Ji, An efficient strategy for protecting dihydroxyl groups of catechols, *Synlett*, 2013, 741–746.



- 38 J. W. Yuan, H. Y. Qiu, P. F. Wang, J. A. Makawana, Y. A. Yang, F. Zhang, Y. Yin, J. Lin, Z. C. Wang and H. L. Zhu, Synthesis of caffeic acid amides bearing 2,3,4,5-tetrahydrobenzo[b][1,4]dioxocine moieties and their biological evaluation as antitumor agents, *Molecules*, 2014, **19**, 7269–7286.
- 39 A. Bey, O. Dreyer and V. Abetz, Thermodynamic analysis of alkali metal complex formation of polymer-bonded crown ether, *Phys. Chem. Chem. Phys.*, 2017, **19**, 15924–15932.
- 40 P. W. Linder and K. Murray, Correction of formation constants for ionic strength, from only one or two data points: An examination of the use of the extended Debye-Hückel equation, *Talanta*, 1982, **29**, 377–382.
- 41 G. Donnay and J. W. Gryder, The oxygen coordinations of lithium, *J. Chem. Educ.*, 1965, **42**, 223.
- 42 C. W. Bock, A. Kaufman and J. P. Glusker, Coordination of Water to Magnesium Cations, *Inorg. Chem.*, 1994, **33**, 419–427.
- 43 A. F. Holleman and N. E. Wiberg, *Lehrbuch der Anorganischen Chemie*, Gruyter, Walter de, 102nd edn, 2007.
- 44 R. G. Parr and R. G. Pearson, Absolute Hardness: Companion Parameter to Absolute Electronegativity, *J. Am. Chem. Soc.*, 1983, **105**, 7512–7516.
- 45 E. C. Koch, Acid-base interactions in energetic materials: I. The Hard and Soft Acids and Bases (HSAB) principle - Insights to reactivity and sensitivity of energetic materials, Propellants, *Explos. Pyrotech.*, 2005, **30**, 5–16.



5.2 Publication 2:

Lithium selectivity of crown ethers: The effect of heteroatoms and cavity size

This work was partially done with the assistance of Sabrina Tamm (Universität Hamburg) in the context of a master thesis under my supervision and guidance. Her support and passion towards this project is gratefully acknowledged. Carmen Herrmann (Universität Hamburg) and her working group are gratefully acknowledged as well for their full support in incorporating the simulation methodology of the DFT and the intensive discussions that ultimately led to this cooperation and publication.

After the results from Publication 1, where it was confirmed that more hydrophilic crown ether systems bind the lithium ions more strongly in comparison to magnesium, in the second Publication of this work, different crown ether systems varied in their size and donor atoms on the metal ions Li^+ , Na^+ , K^+ , Mg^{2+} and Ca^{2+} are examined since these ions are found in nearly all aqueous lithium resources. To avoid complex synthesis procedures, these crown ether systems were simulated and compared using electrostatic calculations, Hirshfeld population and NBO analysis.

15, 12, and 9 ring membered rings were studied with one oxygen donor atom replaced with nitrogen or sulfur in each case. The replacement of the donor atoms and the ring size influenced the complex stability of the different ions. The best selectivity of lithium over magnesium was obtained for the 15-membered ring, where one oxygen atom was replaced with a sulfur atom.

To compare the applicability of the DFT technique with experimental tests, a 15-membered crown ether with nitrogen as one donor atom was chosen which was simulated by DFT in a two-phase extraction similar to the procedure in Publication 1 and compared with laboratory experiments. Although smaller complexation constants were obtained for laboratory experiments, the trends were in good agreement. Thus the combination of geometrical structure optimization, thermodynamic calculation, Hirshfeld population, and NBO analysis has proven to be a valuable tool for predicting interactions of crown ethers and metal ions.

In Section 6.1 *unpublished results* preliminary results of the investigation of nitrogen crown ethers with different amounts of it and different crown ether sizes is experimentally conducted and influence on complexation of Li^+ and Mg^{2+} is discussed.

The Publication is reprinted with permission from I.Oral, S.Tamm, C. Herrmann and V. Abetz, *Separation and Purification Technology*, **2022**, 294, 121142. - published by Elsevier. The related supporting information is available in Section 9.3.



Contents lists available at ScienceDirect

Separation and Purification Technology

journal homepage: www.elsevier.com/locate/seppur

Lithium selectivity of crown ethers: The effect of heteroatoms and cavity size

Iklima Oral^{a,1}, Sabrina Tamm^{a,1}, Carmen Herrmann^{b,*}, Volker Abetz^{a,c,*}^a Universität Hamburg, Institute of Physical Chemistry, Grindelallee 117, 20146 Hamburg, Germany^b Universität Hamburg, Institute of Inorganic and Applied Chemistry & The Hamburg Centre for Ultrafast Imaging, HARBOR Bldg. 610, Luruper Chaussee 149, 22761 Hamburg, Germany^c Institute of Membrane Research, Helmholtz-Zentrum Hereon, Max-Planck-Straße 1, 21502 Geesthacht, Germany

ARTICLE INFO

Keywords:

Crown ether
Density functional theory
Lithium
Natural Bond Orbital analysis
Hirshfeld analysis

ABSTRACT

Lithium is a metal in increasingly high demand due to its use in lithium-ion batteries. However, the extraction from aqueous resources as brines and seawater, which account for a major percentage of worldwide Li⁺ reserves, is challenging due to the presence of other interfering metal ions. Crown ethers (CEs) are known to complex metal cations very effectively, but a fundamental understanding of their potential in lithium extraction is still lacking. Therefore, the selective complexation of Li⁺ over other alkaline (Na⁺, K⁺) and alkaline earth metal (Mg²⁺, Ca²⁺) ions is investigated by density functional theory (DFT) calculations for 15-, 12-, and 9-membered CEs and their derivatives containing in part nitrogen and sulfur instead of oxygen atoms. Structure optimizations of these CEs are performed in vacuum, and complex stabilities are discussed by evaluating the cavity size, the distances between donor atoms and metal ion, and by performing Hirshfeld charge and Natural Bond Orbital analyses. The qualitative trends obtained from these methods are in good agreement with the complex stabilities, which suggests that they can be used to make simplified predictions of complex stabilities. The selectivity for Li⁺ compared to Mg²⁺ in vacuum can be strongly influenced by the ring size, which was the best for B15C5. The general accuracy of DFT is validated by comparing calculations in a polarizable continuum model with the results of a liquid–liquid extraction in a water/dichloromethane mixture using the exemplary extraction of Li⁺, Na⁺, K⁺, Mg²⁺, and Ca²⁺ by aza-15-crown-5. By doing so, the DFT trends are confirmed (with the stability of the Mg²⁺ complex being overestimated while all others are underestimated), suggesting that DFT is a valuable tool for optimizing CE structures to selectively complex Li⁺ or other metal ions. In the context of increasing global lithium demand, the results of this study can serve the further development of selective and sustainable lithium extraction from the largely unexploited resource of seawater.

1. Introduction

Lithium is in growing demand worldwide since it is suitable for various applications, e.g. for ceramics[1], glass[2], pharmaceuticals[3], catalysis[4], grease[5], and rechargeable batteries[6]. The latter is of particular interest in the field of electromobility. The expected growth in this field is approximately estimated at a value of 20 Mt between 2010 and 2100.[7] In the Battery Electric Vehicles (BEVs) industry, lithium is hard to replace due to the low mass and high energy density, enabling small battery dimensions and high recharging efficiency of lithium ion accumulators.[6–9] The limited availability of lithium – being presently

extracted from brines, pegmatites, or sedimentary rocks mainly in South America and China – as well as the serious ecological and political problems with conventional production require the development of alternative methods for lithium recovery.[7,10–13] One abundant option would be seawater, in which the lithium concentration is around 0.18 ppm, which gives a total global lithium amount of 230 Bt.[11,12,14] This enormous amount makes the extraction of lithium from seawater indispensable. In addition, the global distribution of the resource would be much more uniform, and time-consuming purification steps, accompanied by conventional extraction, could be prevented if a suitable extraction mechanism was available. Motivated by these

* Corresponding authors.

E-mail addresses: iklima.oral@chemie.uni-hamburg.de (I. Oral), sabrina.tamm@chemie.uni-hamburg.de (S. Tamm), carmen.herrmann@chemie.uni-hamburg.de (C. Herrmann), volker.abetz@hereon.de (V. Abetz).¹ These authors contributed equally to this work.<https://doi.org/10.1016/j.seppur.2022.121142>

Received 27 January 2022; Received in revised form 19 April 2022; Accepted 21 April 2022

Available online 25 April 2022

1383-5866/© 2022 Elsevier B.V. All rights reserved.

evident advantages, several research groups are currently investigating the possibility of lithium extraction from seawater. These include, among others, Li^+ -absorbing hydrogen-manganese oxide-modified cellulose films[15] or solar-powered electrolysis with Sodium Super Ionic Conductor (NASICON) solid-state electrolytes.[16].

However, the development of a highly lithium-selective and cost-effective material is still challenging, since the concentration of lithium in seawater is significantly lower than the concentration of competing metal ions like Na^+ , K^+ , Mg^{2+} , and Ca^{2+} . [12,15,17] In addition, Li^+ and Mg^{2+} show similar ionic radii in aqueous media, which makes the selective complexation of Li^+ rather than Mg^{2+} demanding. One approach to selectively bind lithium is the extraction via crown ethers (CEs).[8,13,18–20] CE are cyclic ethers with a basic structure usually consisting of ethylene-oxy units (Fig. 1) which are able to complex cations mainly via ion–dipole interactions [8,21–23] (with, depending on the cation, additional stabilizing orbital interactions that represent the charge transfer and polarization and Pauli repulsive orbital interactions).[24–26] The unique properties of CEs allow their use in the fields of phase transfer catalysis[27], chromatography[28,29], substitutes for ionophore antibiotics[30], ion channels[31], sensors [32], and electrodes.[33] Adjustment of the CE ring size and structure can yield a high selectivity towards a specific cation.[8,21,23,34] However, especially the preferential selectivity for Li^+ over Mg^{2+} has rarely been achieved under economically feasible conditions so far. Besides the very similar ionic radii of Li^+ and Mg^{2+} , the latter exhibits a higher electron density and dehydration energy.[8,35,36] Other effects such as the ring strain, the complex stoichiometry, or the favored coordination number of metal ions also play a crucial role for the complex stability, which makes the design of a highly Li^+ -selective CE very challenging.[37–39] Compared to other alkali metal ions 14–crown–4 shows the strongest lithium complexation so far, due to its optimal ratio of cavity size to ion radius.[8,13,18,40] However, larger metal ions such as Na^+ or K^+ can form ML_2 sandwich complexes with 14-crown-4 (with M labeling the metal ion and L the ligand). Those complexes are especially stable due to the enthalpy gain caused by the double amount of interaction partners with the complexed metal ion. By incorporating sterically demanding groups into the CE, sandwich complexation can be prevented.[41] However, this CE synthesis is time-consuming and expensive due to chemically complex starting materials and demanding synthetic routes. It is therefore not possible to achieve sufficient selectivity towards Li^+ only via the frequently discussed size relation between CE cavity and metal ion.[23].

A potential route towards lithium selectivity is placing a rigid benzene ring adjacent to the CE to form additionally cation– π interactions and to prevent preorganization effects.[18,42] Recently, our group has developed a promising lithium-selective material based on this idea: Benzo–9–crown–3 (B9C3) was synthesized and bound as a side group to

the methacrylic acid units of a poly(methacrylic acid)-*block*-polystyrene (PMAA-*b*-PS) diblock copolymer.[43,44] The detailed synthesis of the block copolymer can be found in Ref. [45]. Due to the small size of the CE ring, lithium ions as well as magnesium ions are complexed as a sandwich, while larger ions, such as sodium or potassium, require more than two CEs and probably cannot be complexed because of the lack of mobility in the polymer. Since we focus on the interactions between the atoms and the influence of the heteroatom substitution in the ring on the complex stability as well as for the evaluation of the correlation between population analysis results and the complexation stability, the focus of this work was consistently set on simple complexes of the form ML. Nevertheless, sandwich complexation is conceivable in some cases, as described below. In fact, CEs incorporated into polymers are very attractive due to their easy separation from solutions and mixtures, especially in the form of membranes, as they have a large surface area, flux, good separation and recovery properties as well as great mechanical stabilities.

In addition to the hard-to-reach Li^+ selectivity compared to Mg^{2+} (achieved by Li et al.[46]), further challenges include the competitive Na^+ complexation in a sandwich type complex as well as the high cost and complexity of existing systems. Nevertheless, the work of Li et al. has given the incentive to consider replacing oxygen with less electronegative heteroatoms (with reduced hardness of the donor atom), such as nitrogen and sulfur, and to study their influence on the complexation of Li^+ and Mg^{2+} in more detail. In order to avoid potentially hazardous and time- and resource-intensive chemical reactions, and for increasing the efficiency and sustainability of CE design, computational chemistry approaches have been considered. Density functional theory (DFT) calculations have provided accurate structures and binding energies for supramolecular structures.[47–49] For example, Sun et al. have investigated the selective complexation of benzo-15-crown-5 (B15C5) towards Li^+ over cobalt, nickel, and manganese at different pH values.[42] In that work, both experimental and theoretical results were consistent with preferential Li^+ complexation at pH = 6 with B15C5. Nevertheless, the ions relevant to seawater-based applications were not considered in that study. Despite the many different publications on CE complexes with metal ions, the search for a suitable CE that favors Li^+ complexation over other alkali as well as alkaline earth metals remains ongoing.

In this work, the complexations of the Li^+ , Na^+ , K^+ , Mg^{2+} , and Ca^{2+} using benzo- 15-, 12-, and 9-membered CEs with different donor atoms are investigated by DFT. The exchange of a single oxygen atom with the less electronegative heteroatoms nitrogen and sulfur with larger radii is chosen to observe a possibly better complexation of Li^+ . [35,47] To ensure comparability of the electronic structures, only systems with sp^3 -hybridized donor atoms were considered. The different heteroatoms are investigated replacing one oxygen atom in B15C5, benzo–12–crown–4 (B12C4), and B9C3. First, to gain insight into the stability of the

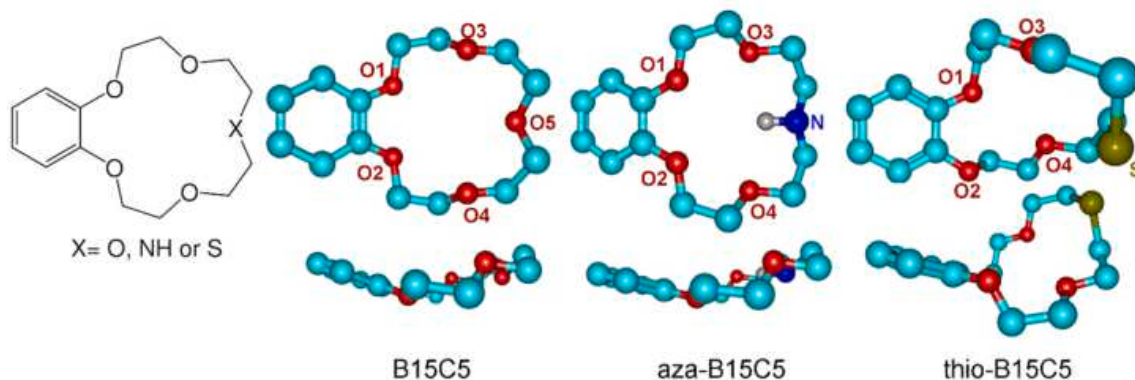


Fig. 1. Lewis structures (left) and energetically optimized ball-and-stick structures of the empty B15C5, aza-B15C5 and thio-B15C5 CEs, the latter shown from two perspectives. The turquoise dots label the carbon atoms, the red dots the oxygen atoms, the blue dots the nitrogen atoms, and the olive-green dots the sulfur atoms. The hydrogen atoms from the C–H bond have been omitted for the sake of clarity.

CE–metal complex and thus to identify factors potentially beneficial to lithium selectivity, DFT is used for calculating the cavity sizes of the CEs, the donor–acceptor distances, the Hirshfeld partial charges, Natural Bond Orbitals (NBO), and the complexes' stability constants K in vacuum. The trends are compared and analyzed with respect to their consistency, in order to assess the suitability of the methods for the design of Li^+ -selective CEs.

Furthermore, to estimate the accuracy of DFT stability constants, decisive for the estimation of the complex formation, are evaluated in a continuum solvent model and compared with the experiment. The stability constants are evaluated experimentally for a liquid–liquid extraction of a water/dichloromethane (DCM) mixture using the extraction of Li^+ , Na^+ , K^+ , Mg^{2+} , and Ca^{2+} by the exemplary selected CE aza-15-crown-5 (aza-15C5).

Although no quantitative matching can be expected between the DFT results and the experiment (among others, due to the approximate description of environmental effects and the approximate nature of the exchange–correlation functional), a qualitative assessment of the complexation behavior of different ions under variation of the CE structures is a realistic goal.

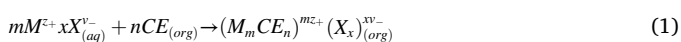
2. Experimental and computational methods

2.1. Materials

Aza-15C5 (98 %, TCI, Eschborn, Germany), DCM (99.9 % extra dry, Acros, Schwerte, Germany), lithium-3,5-diiodosalicylic acid (LIS, 100 %, Sigma-Aldrich, Schnellendorf, Germany), sodium ethyl eosin (NaEE, 100 %, Waldeck, Münster, Germany), potassium ethyl eosin (KEE, 100 %, Carl Roth, Karlsruhe, Germany), 8-anilino-1-naphthalenesulfonic acid hemimagnesium salt (MgA, 100 %, TCI, Eschborn, Germany), fuchsin calcium salt (CaF, 100 %, Carl Roth, Karlsruhe, Germany), 15-crown-5 (15C5, 100 %, Alfa Aesar, Kandel, Germany) were used as received. Ultrapure water (MilliQ® quality, resistivity $> 18.2 \text{ M}\Omega\cdot\text{cm}^{-1}$) was obtained from a Millipore (Darmstadt, Germany) MilliQ® water purification system.

2.2. Procedure of the liquid–liquid extraction

For the liquid–liquid extraction, a molar ratio of CE to metal ions ranging from 25:1 to 10:1 was used in a DCM/water system. After phase extraction at 500 rpm for 45 min and phase separation of 30 min at 25 °C, the aqueous phase was characterized by UV/Vis spectroscopy. The formation of the complex $(M_mCE_n)^{mz+}(X_x)^{xv-}$ occurred corresponding to the reaction in Equation (1)[43]:



where m and x are the stoichiometric factors of the cation M , of charge z_+ , and of the corresponding counterion X (Figure S10), of charge v_- , and n as the equivalents of the CE required for complexation. For all cations, $m = 1$ and $x = 1$, except Mg^{2+} with a value of $x = 2$. A calibration curve of each salt solution was conducted prior to the liquid–liquid extraction to calculate the concentration in the aqueous phase using the Lambert–Beer law. In order to ensure the most accurate values, the calibration was performed shortly before the measurement series and conducted using the same stock solution as for the extraction experiments. The complex constant K of the extraction process was calculated according to Equation (2)[43]:

$$K = \frac{[(M_mCE_n)^{mz+}(X_x)^{xv-}]_{(org)}}{(Q \cdot (\gamma_+ [M^{z+}]^m) \cdot (\gamma_- [X^{v-}]^x)) \cdot [CE]^n} \quad (2)$$

with the mean activity coefficients γ_{\pm} and the stoichiometric coefficient Q . More detailed information regarding the calculation of K can be found in the SI.

2.3. UV/Vis spectroscopy

The UV/Vis spectra were recorded with a spectrophotometer UV5 from METTLER TOLEDO at room temperature. The samples were measured from 190 to 1100 nm. The scan time was 10 s.

2.4. DFT calculations

All calculations were performed with the program package *Gaussian 16* (Rev. C.01).[50] The CEs and the corresponding complexes were simulated in *vacuo* (or, in Section 3.4, with solvent approximated by an Integral Equation Formalism Polarizable Continuum Model (IEF-PCM) model with the dielectric constant of DCM) and without symmetry constraints based on DFT. All calculations were employing the B3LYP exchange–correlation functional[51] in combination with Ahlrichs' def-2-TZVP basis set[52], with Grimme's dispersion correction (DFT-D3)[53]. The DFT with pairwise dispersion correction contributes accurate structures of CE structures.[54] The use of other functionals has shown similar property trends for related compounds.[26] However, best results are obtained by using the B3LYP functional.[54] The presence of local minima was ensured by the absence of imaginary frequencies in the computed vibrational spectra. The molecules were visualized and interatomic distances were evaluated using the program *GaussView 5.0.9*.[55] Hirshfeld partial charges were evaluated as implemented in *Gaussian 16*. The NBO analyses was used as is implemented in *Gaussian 16* (*Gaussian NBO version 3.1*).[56] The evaluation of the interatomic distances, and the visualizations of the calculated structures (including the orbitals of the compound) and of the results of the NBO analysis were performed with the program *Chemcraft 1.8* (build 595b).[57] The change in Gibbs free energy was calculated, as implemented in *Gaussian 16*, in *vacuo* with a temperature of 298.15 K, as well as in a solvent environment according to the reaction: $\text{CE}(\text{CH}_2\text{Cl}_2) + \text{M}^{n+}(\text{H}_2\text{O}) \rightarrow \text{CE}-\text{M}^{n+}(\text{CH}_2\text{Cl}_2)$. [42] An example input file for a molecular structure optimization of aza-15C5 can be found in the SI.

3. Results and discussion

In this work, different alkali and alkaline earth salts are analyzed in combination with different CEs. First, the optimized structures, the cavity size, and the distances of the metal ions to the respective donor atoms are analyzed, followed by Hirshfeld population and NBO analyses. These data are evaluated based on DFT calculations in vacuum, which allows for comparing the trends of these properties for the different cations, heteroatoms, and ring sizes, and for studying how they correlate with the stability constants K of the different CE complexes. In the last part (Section 3.4), theoretical data in solution is compared with experimental work on liquid–liquid extraction with aza-15C5. In this work, we deal with metal ions only and will use the chemical name of the metal and metal ion interchangeably.

3.1. Optimized molecular structures and cavity sizes

The DFT-optimized structures of the 15-membered B15C5, aza-B15C5, and thio-B15C5 are shown in Fig. 1 (since the property trends for the 12- and 9-membered rings are quite similar to the 15-membered ones, their optimized structures can be found in the SI, Figure S2 and S6). In these representations, a structural distortion (relative to a roughly planar ideal CE structure) is observed, which increases with heteroatom size from oxygen over nitrogen and sulfur. Similar observations were made in previous studies.[35,58-60]

The optimized structures of the CEs are investigated for the complexation with Li^+ , Na^+ , K^+ , Mg^{2+} , and Ca^{2+} to verify an influence of the heteroatom substitution on the interaction between donor atom and metal ion (Fig. 2). In the case of K^+ (and to a certain extent also for Ca^{2+}), the cation is pushed out of the ring plane (Fig. 2 (a3), (b3), and (c3), and (a5), (b5) and (c5), respectively), since it exceeds the size of

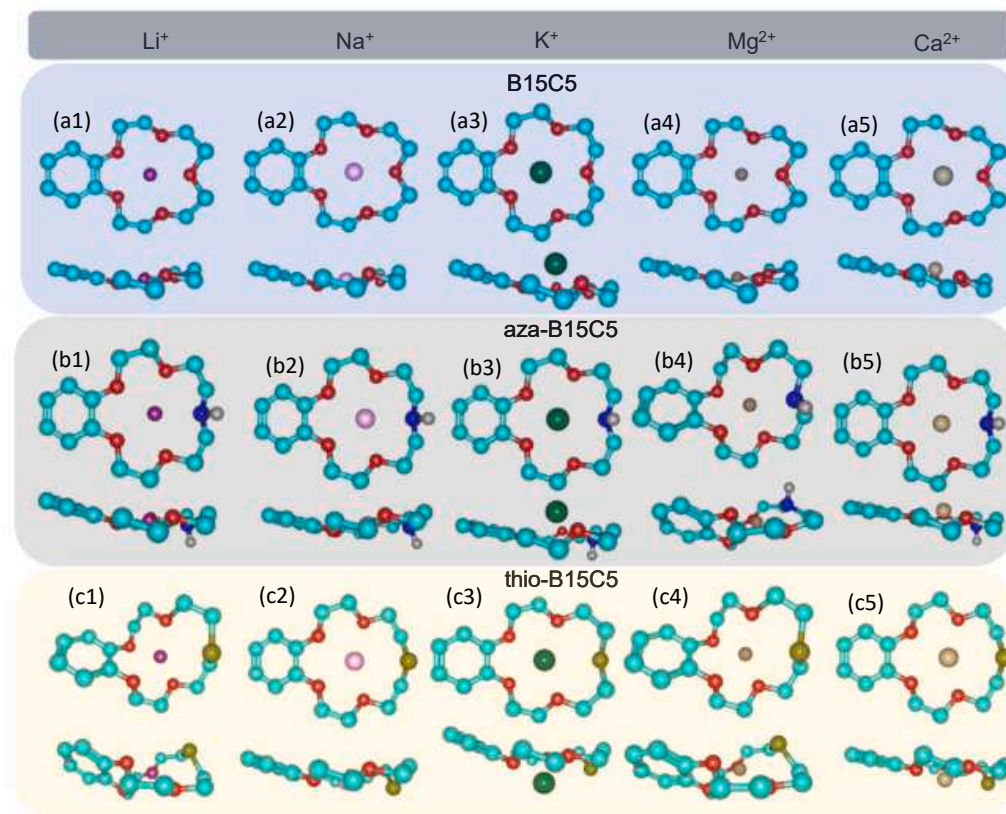


Fig. 2. Optimized structures of the B15C5 (first row), aza-B15C5 (second row), and thio-B15C5 (third row) complexes with Li⁺ (violet; a1, b1, and c1), Na⁺ (pink; a2, b2, and c2), K⁺ (green; a3, b3, and c3), Mg²⁺ (brown; a4, b4, and c4), and Ca²⁺ (beige; a5, b5, and c5), from two perspectives each.

the CE cavity.[43,61,62] As a result, sandwich complexation can be assumed.[63] It is well known that a good size match between CE and cation leads to high complex stabilities[8,23,34,64]. B15C5 with five oxygen atoms shows almost no distortion for all metal-CE complexes (Fig. 2 (a1)–(a5)). In case of the aza-B15C5 and thio-B15C5 CE, however, a significant distortion of the CE framework becomes apparent when small cations such as Li⁺ and Mg²⁺ are complexed (Fig. 2 (b4), (c1), and (c4)).

The calculated distances between each donor atoms and metal, as

well as the cavity size, are listed in **Tab. S1**. In the case of small cations, the distortion is likely caused by the favorable complexation of Li⁺ and Mg²⁺ in a tetrahedral or octahedral coordination.[35,37–39] For aza-B15C5-Mg²⁺, thio-B15C5-Li⁺, and thio-B15C5-Mg²⁺, the distortion is particularly pronounced, presumably resulting from the larger donor atoms (distortion is already observed with empty aza- and thio-B15C5, compare with Fig. 1). The oxygen atoms O1–O4 are located closer to the Li⁺ or Mg²⁺ cation (complexation in the tetrahedral coordination) than in the pure-oxygen derivative B15C5 (Fig. 2 (c1), (b4), (c4) and

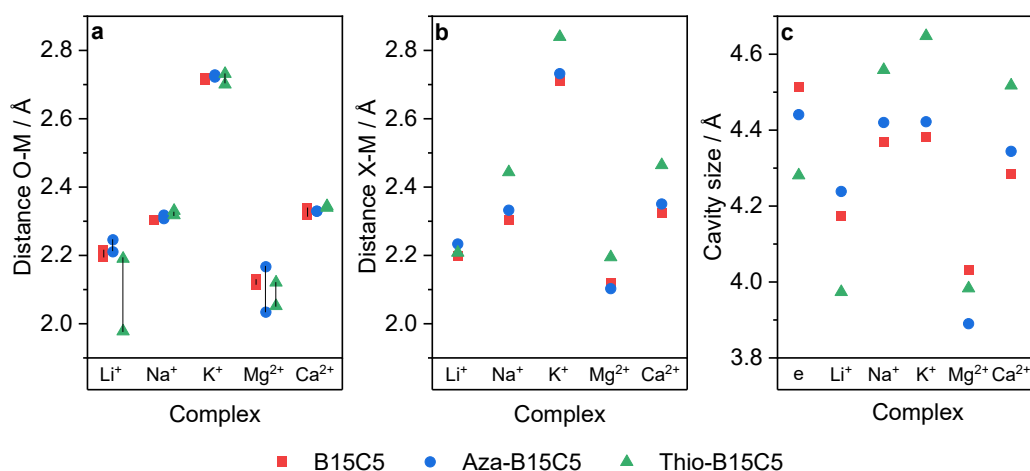


Fig. 3. Distance between the heteroatom X and the metal ion (d_{X-M}^R ; a) of the CE (B15C5, aza-B15C5, and thio-B15C5) and their complexes with Li⁺, Na⁺, K⁺, Mg²⁺, and Ca²⁺, as well as the smallest and largest distance between the oxygen atoms O1–O4 and the metal ion (d_{O-M}^O ; b), and the cavity size of the empty CE (e) and the complexes (d_{CE} ; c).

Fig. 3a), thus increasing the interaction between the donor atoms O1-O4 and the metal ion.[8,35,62] The smallest and largest O-M distances are shown in Fig. 3a. For X = O, N, the smallest and the largest distance increase in the following order: $\text{Mg}^{2+} < \text{Li}^+ < \text{Na}^+ \approx \text{Ca}^{2+} < \text{K}^+$. The same trend is shown for X = S when focusing on the largest O-M distance, while the smallest O-M distance increases in the order $\text{Li}^+ \approx \text{Mg}^{2+} < \text{Na}^+ \approx \text{Ca}^{2+} < \text{K}^+$. For thio-B15C5-Li⁺, the donor atoms O1-O4 show the shortest distances to the Li⁺ cation compared to B15C5 and aza-B15C5. By comparing the optimized structures of aza-B15C5-Li⁺/Mg²⁺ (Fig. 2, (b1) and (b4)), a stronger distortion, evidenced by shorter distances between the cation and heteroatoms and a larger variation of O-M distances (see Table S2 and Fig. 3), is observed when Mg²⁺ is complexed with the aza-B15C5, possibly due to the higher charge density and lower hardness of the Mg²⁺ cation.

The distance $d_{X-M^{n+}}$ between the heteroatom X and the metal ion increases with larger donor atoms in the following order O < N < S and $\text{Mg}^{2+} < \text{Li}^+ < \text{Na}^+ \approx \text{Ca}^{2+} < \text{K}^+$ (Fig. 3b, Table S2). In conclusion, the O-M and X-M distances show similar trends for the cations.

The cavity size d_{CE} of the CE can be evaluated as the mean value of the interatomic distances between the donor atoms from the DFT-optimized structures[18,64,65],

$$d_{CE} = \frac{d_{O1-O4} + d_{O1-X} + d_{O2-O3} + d_{O2-X} + d_{O3-O4}}{n} \quad (3)$$

with d labeling the interatomic distance between two donor atoms, n the amount of donor atoms (here: $n = 5$), and X the hetero-donor atom (here: X = O, N, S). An overview of the cavity sizes d_{CE} of the empty CE as well as of the complexes can be found in Fig. 3c (for more detailed information, see Table S1). The cavity sizes d_{CE} of the empty CE follow the trend B15C5 > aza-B15C5 > thio-B15C5 (with values of 4.51 Å > 4.44 Å > 4.28 Å). The smaller d_{CE} of the aza or thio-CE can be attributed to the more distorted ring structure. The calculated cavity size d_{CE} for B15C5 corresponds to the theoretically determined values known from the literature (4.118 Å).[42] To the best of our knowledge, no theoretical or experimental data of aza-B15C5 and thio-B15C5 have been reported elsewhere so far.

After complexation, the cavity size for X = O, N is smaller than for the empty CEs, resulting in the order $\text{Mg}^{2+} < \text{Li}^+ < \text{Ca}^{2+} < \text{Na}^+ \approx \text{K}^+ < \text{empty}$. For X = S, the cavity size can increase or decrease compared to the empty CE, resulting in the order $\text{Li}^+ \approx \text{Mg}^{2+} < \text{empty} < \text{Ca}^{2+} < \text{Na}^+ < \text{K}^+$. It may be assumed that the smaller cavity size of the Mg²⁺ or Li⁺ complex, in comparison to the Na⁺, K⁺ and Ca²⁺ complexes, is mainly due to the distortion of the ring and the closer positioning of the four donor atoms due to the favored tetrahedral coordination (O1-O4). The increase in cavity size for X = S with Ca²⁺, Na⁺, K⁺ could indicate an unfavorable complexation of CE and cation in a single-ligand complex. Some of these cations have already shown sandwich-type complexes with 15-membered rings.[66-68].

To focus on the comparison between Mg²⁺ and Li⁺ complexation, the cavity sizes d_{CE} of the Li⁺ complexes follow the trend aza-B15C5-Li⁺ > B15C5-Li⁺ > thio-B15C5-Li⁺ with values of 4.24 Å > 4.17 Å > 3.97 Å, while the cavity sizes d_{CE} of the Mg²⁺ complexes follow the trend B15C5-Mg²⁺ > thio-B15C5-Mg²⁺ > aza-B15C5-Mg²⁺, with values of 4.03 Å > 3.98 Å > 3.89 Å. Thus, it seems that the substitution of oxygen by sulfur leads to a smaller cavity size for Li⁺, while the exchange with nitrogen leads to a smaller cavity size for Mg²⁺.

3.2. Hirshfeld- and NBO analysis

To examine the host-guest interactions in more detail, the Hirshfeld population analysis is used, which provides a quantitative description of the local charge distribution.[69,70] In case of complexation, charges are relocated between the entering cation and the negative electrostatic potential region of the CE ring. The latter is based on the presence of the donor atoms X, thus the strongest interaction with the cation occurs here. Complexation-related Hirshfeld charge transfer q_t for an atom X is

given as the difference of the Hirshfeld partial charge of X before ($q_{X(CE)}$) and after complexation ($q_{X(CE-M^{n+})}$) by Equation (4)[42]:

$$q_{t,X} = q_{X(CE-M^{n+})} - q_{X(CE)} \quad (4)$$

and is summarized graphically in Fig. 4 (numerical values can be found in Table S3).

The Mg²⁺ complex exhibits the largest charge transfer in any case, followed by Ca²⁺, which is likely due to their high charge density. For all complexes, the charge density was mainly transferred from the heteroatoms to the metal ion ($q_{t,O5}$, $q_{t,N5}$, $q_{t,S5}$ (Fig. 4)).

This observation is particularly pronounced for the multivalent metal ions in the aza-B15C5 and thio-B15C5 complexes, while the charge transfer for the monovalent cations is smaller, decreasing in the order $\text{Li}^+ > \text{Na}^+ > \text{K}^+$. The two oxygen donor atoms attached to the benzene ring (i.e. O1 and O2), show the weakest local charge distribution in almost all cases due to the adjacent electron-withdrawing benzene group.[42] Assuming that a larger charge redistribution (i.e. a higher q_t) correlates with a stronger bond, this would indicate that binding energies follow similar trends. These results are in good agreement with the calculated distances, except for the preferential charge transfer of Ca²⁺ relative to Li⁺ (see Table S2).

NBO analysis was performed to gain further information on the host-guest interactions within the complexes by transformation of the orbitals into a localized, Lewis-like form. The interaction between the Lewis-like donor NBO (with an occupation of 2) and the unoccupied non-Lewis-like acceptor NBO can be determined via second order perturbation theory, in the form of a stabilization energy $E^{(2)}$ (Equation (5)):

$$E^{(2)} = b_x \frac{F(X, M^{n+})^2}{\epsilon_X - \epsilon_{M^{n+}}} \quad (5)$$

with the occupancy of the donor orbital b_x , the diagonal elements ϵ and the off diagonal NBO Fock matrix element $F(X, M^{n+})$.[42,71,72] The larger $E^{(2)}$, the stronger the interaction between the NBOs.[42] The values for $E^{(2)}$ of the donor NBOs, which are the lone pairs of O, N, and S (LP1 and LP2) and the LP* acceptor NBO of the complexed metal ion, are summarized in Fig. 5. The NBO analysis yielded a positive stabilization energy $E^{(2)}$ for each complex (for more detailed data of the NBO analysis, see Table S4) and increases for X = O, S in the following order $\text{K}^+ < \text{Na}^+ < \text{Ca}^{2+} < \text{Li}^+ < \text{Mg}^{2+}$.

These results are in good agreement with the calculated distances (see Table S2). However, for X = N, $E^{(2)}$ increases according to the following trend: $\text{K}^+ < \text{Na}^+ < \text{Li}^+ \approx \text{Ca}^{2+} < \text{Mg}^{2+}$, which is in a good agreement with the results from the Hirshfeld analysis.

For the B15C5 complex, the stabilization energies $E^{(2)}$ are similarly high for each donor atom since the ring is hardly distorted and therefore all donor atoms interact similarly strongly with the metal ion, as shown in Fig. 2. Nevertheless, the donor atoms O1 and O2 show slightly lower stabilization energies of 19.71 kJ mol⁻¹ compared to the O3 and O4 donor atoms with 22.51 kJ mol⁻¹ and O5 with 23.10 kJ mol⁻¹ due to the electron density-withdrawing benzene ring, correlating with the results from the Hirshfeld analysis. Similar results were obtained for the aza-B15C5 CE, except for the aza-B15C5-Mg²⁺ complex. In this case, $E_{O1}^{(2)}$ is significantly smaller than the other stabilization energies, while $E_{O3}^{(2)}$, $E_{O4}^{(2)}$ and $E_{N5}^{(2)}$ increase compared to B15C5, which is also due to the observed ring distortion when Mg²⁺ is complexed. A similar trend can be found for the strongly distorted thio-B15C5-Li⁺/Mg²⁺ complexes, where the values for $E_{O3}^{(2)}$ and $E_{O4}^{(2)}$ differ slightly from one another, while $E_{O1}^{(2)}$ is significantly reduced compared to $E_{O2}^{(2)}$. The decrease of the stabilization energy $E_{O1}^{(2)}$ is particularly striking, considering its direct linkage to the rigid benzene ring and the larger distance between the cation and O1, compared to the other oxygen atoms present in the ring.

As shown with the optimized structures, the cavity sizes as well as the distances between metal ion and donor atoms, the NBO analysis also suggests that Li⁺ complexation increases by putting a sulfide function

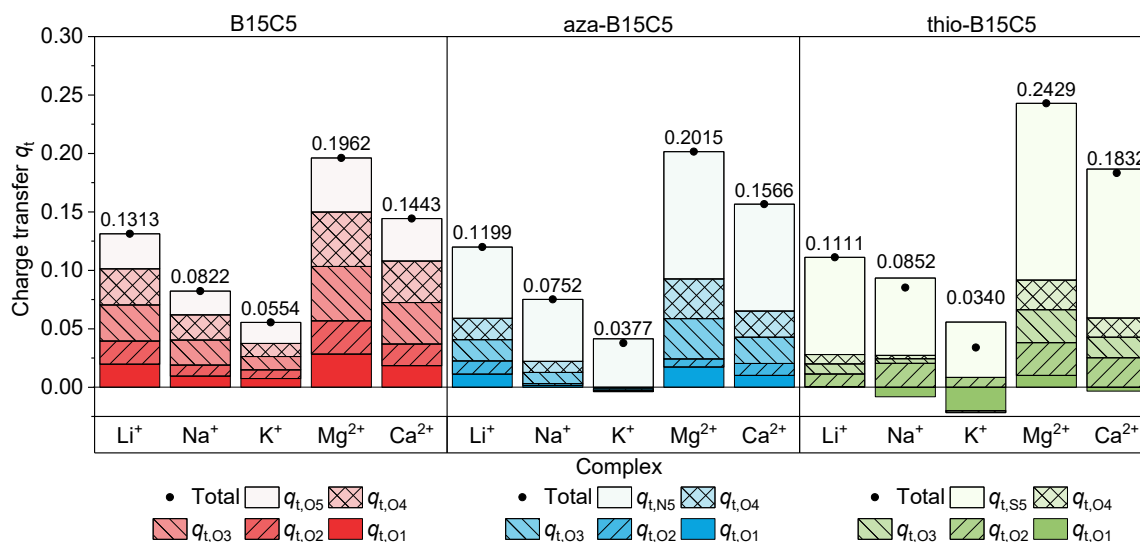


Fig. 4. Hirshfeld charge transfer q_t between the donor atoms (O, N, and S) and Li⁺, Na⁺, K⁺, Mg²⁺, resp. Ca²⁺ within the complexes with the B15C5, aza-B15C5, and thio-B15C5. The sums of the charge transfers are given above the bars.

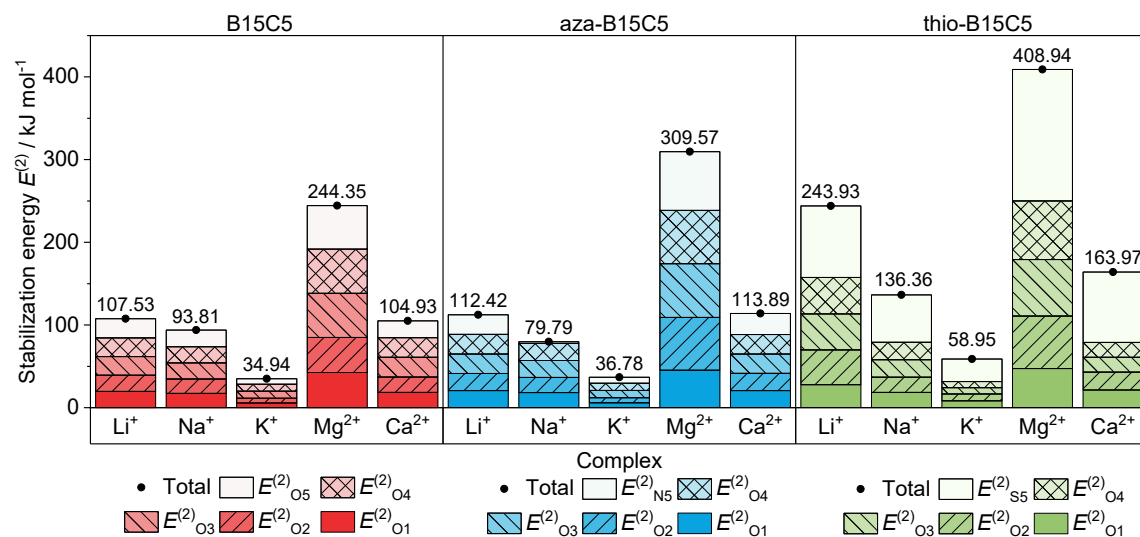


Fig. 5. Stabilization energies $E^{(2)}$ in kJ mol⁻¹ within the complexes of the B15C5, aza-B15C5, and thio-B15C5 with Li⁺, Na⁺, K⁺, Mg²⁺, and Ca²⁺. The contributions of the lone pair donor NBOs (LP1 and LP2 combined) to the interaction with the acceptor NBOs and the sum of these (above the bars) are given.

into the CE. It is worth mentioning that all systems favor the Mg²⁺ complexation. However, the total stabilization energy of the thio-B15C5-Li⁺ complex increases by a factor of 2.27 compared to the B15C5-Li⁺ complex, whereas the analogous Mg²⁺ complexes only show an increase by a factor of 1.67, which suggests an enhanced Li⁺ selectivity compared to its main competitor Mg²⁺. The NBOs for thio-B15C5-Li⁺ are visualized in Fig. 6. The donor NBOs of the sulfur atom show greater overlap with the LP* of the lithium cation than the donor NBOs of each oxygen as it was determined by the Hirshfeld- and NBO analysis. The previously described strong complexation of the Li⁺ and Mg²⁺ cations with aza-B15C5 and thio-B15C5, associated with reduced distances between the metal ion and the four oxygen donor atoms O1-O4 (see Fig. 3), is confirmed by the NBO analysis.

In summary, Mg²⁺ complexation is favored for all systems. However, $E^{(2)}$ increases for nearly all metal ion complexes when an oxygen atom is replaced by nitrogen or sulfur. In case of sulfur, a significant increase in $E^{(2)}$ occurs when Li⁺ is coordinated, originating from the better donor abilities compared to oxygen. Moreover, greater selectivities are also observed with respect to the other metal ions.

3.3. Thermodynamic data

In order to consider the effect of the size relation of the CE and the complexed ion in more detail, the following discussion of the 15-membered CEs will be supplemented by analogous discussions of smaller ring sizes (9- and 12-membered CEs). Complex stability can be quantified via the complex constant K . This specifies the thermodynamic direction of a reaction and results from the Gibbs free energy difference ΔG under standard conditions (298.15 K), the temperature T , and the universal gas constant R according to Equations (6) and (7)[42]:

$$\log(K) = -\frac{\Delta G}{2.303RT} \quad (6)$$

$$\Delta G = G_{CE-M^{n+}} - G_{CE} + G_{M^{n+}} \quad (7)$$

with $G_{CE-M^{n+}}$, G_{CE} , $G_{M^{n+}}$ being the Gibbs free energy for the complex, CE, and salt, respectively. The entropy contribution to the Gibbs free energy is very small in relation to the enthalpy (more details can be found in Table S10).

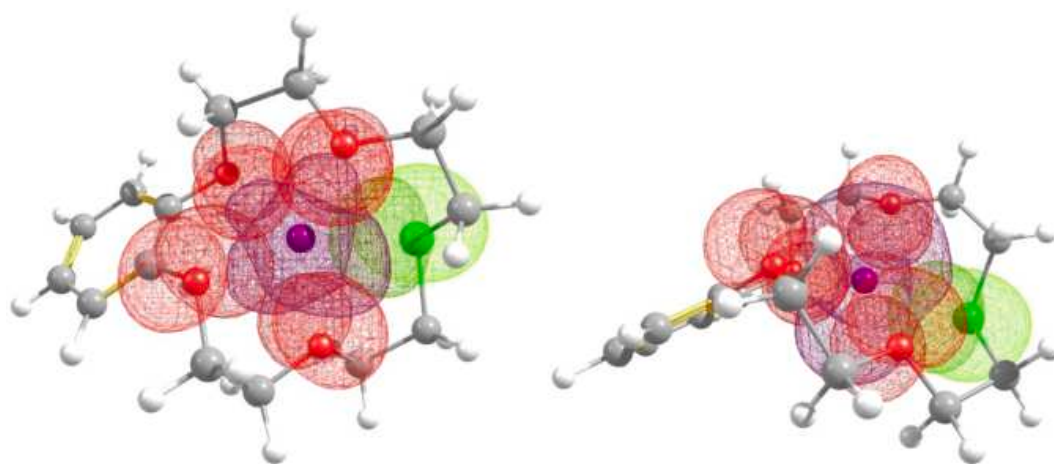


Fig. 6. Representation of the relevant NBOs of the thio-B15C5-Li⁺ complex from different perspectives: Donor-NBOs LP1 and LP2 of oxygen (red) and sulfur (green) with an occupancy near 2, as well as acceptor NBO LP* (purple; occupancy = 0.1316) of lithium. Contour value = 0.05.

The complexation constants for the 15-, 12- and 9-membered CE are compared in Fig. 7 and are summarized, in addition to the Gibbs free energy, in Table S11 – S14. It should be kept in mind that these constants are evaluated in vacuum, and therefore complex stabilities will be strongly overestimated due to charged species in vacuum lacking the stabilization by the solvent as present in the experiment. This effect is especially pronounced for divalent ions. Still, they allow for evaluating the correlation of the chemical concepts discussed above with measurable quantities, and one may expect a reasonable correlation with stability trends in solution (at least if the solvent is not too polar). Complexation constants including the polarizable continuum model (PCM) are given for comparison in the SI (Figure S9). To exclude the additional uncertainty in modeling resulting from the PCM, the thermodynamic calculations in vacuum are the main focus of this manuscript, and will be discussed in the following. This type of calculation is well known also for experimental gas-phase studies of cation complexation by CEs and is suitable for describing host-guest interactions. [73–79] For each complex, the complex constant K increases in the following order: $K^+ < Na^+ < Li^+ < Ca^{2+} < Mg^{2+}$, which is in good agreement with the trends from Hirshfeld and NBO analyses for $X = N$. The positive values confirm the thermodynamic stability of the complexes (in vacuum). Independent of the ring size, there is a preferential complexation of the divalent alkaline earth metals. For these, as for the alkali metal ions, the complex stability increases with decreasing ionic radius. The heteroatom substitution shows a slight positive effect on the complex

stability. For example, the thio-B15C5-Li⁺ complex shows a $7 \cdot 10^4$ times higher stability than B15C5-Li⁺ (Table S11). The complex stability of the complexes with the 12- and 9-membered CE benefits more from the introduction of a nitrogen atom into the ring skeleton. Aza-B9C3-Li⁺ shows an approximately 10^3 times higher, and aza-B12C4-Li⁺ a 10^4 times higher stability than the lithium complexes of the corresponding oxygen-CEs, whereas the thio-CEs only cause a stability increase by a factor of 5 and 20, respectively (see Table S11). In addition, the Mg/Li selectivity decreases for different ring sizes in the following order: B15C5 > B12C4 > B9C3.

Fig. 8 shows a summary of the different methods to evaluate or estimate complex formation for the different CE with Li⁺, Na⁺, K⁺, Mg²⁺, and Ca²⁺, comparing distances, Hirshfeld and NBO analyses, as well as thermodynamic calculations. The values for each method are reported relative to lithium as a reference (with a value of 1). It is evident that all methods yield similar trends, with only slight variations as discussed before, which mostly affect the Ca²⁺ complexes. This suggests that evaluating charge transfer and natural bond orbitals may serve as helpful guides for designing CEs with desired selectivity in future work.

3.4. DFT data in solution in comparison with experimental results

To confirm the comparability of the theoretical results to realistic conditions in the laboratory, thermodynamic values are calculated from the just described theoretical models, now including an approximate

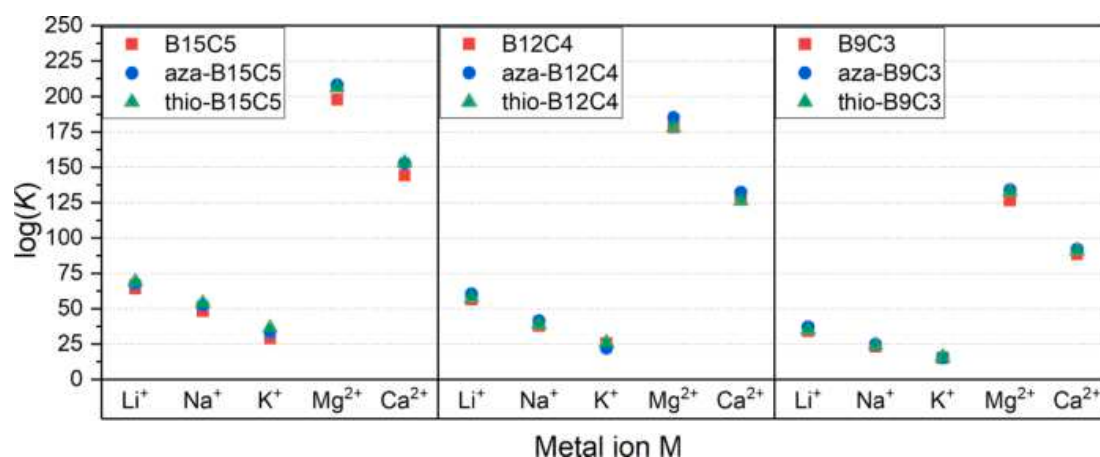


Fig. 7. Logarithm of the equilibrium constant of complex formation of 15-, 12- and 9-membered CE with different metal ions in vacuum. Values were determined via DFT according to Equations (6) and (7).

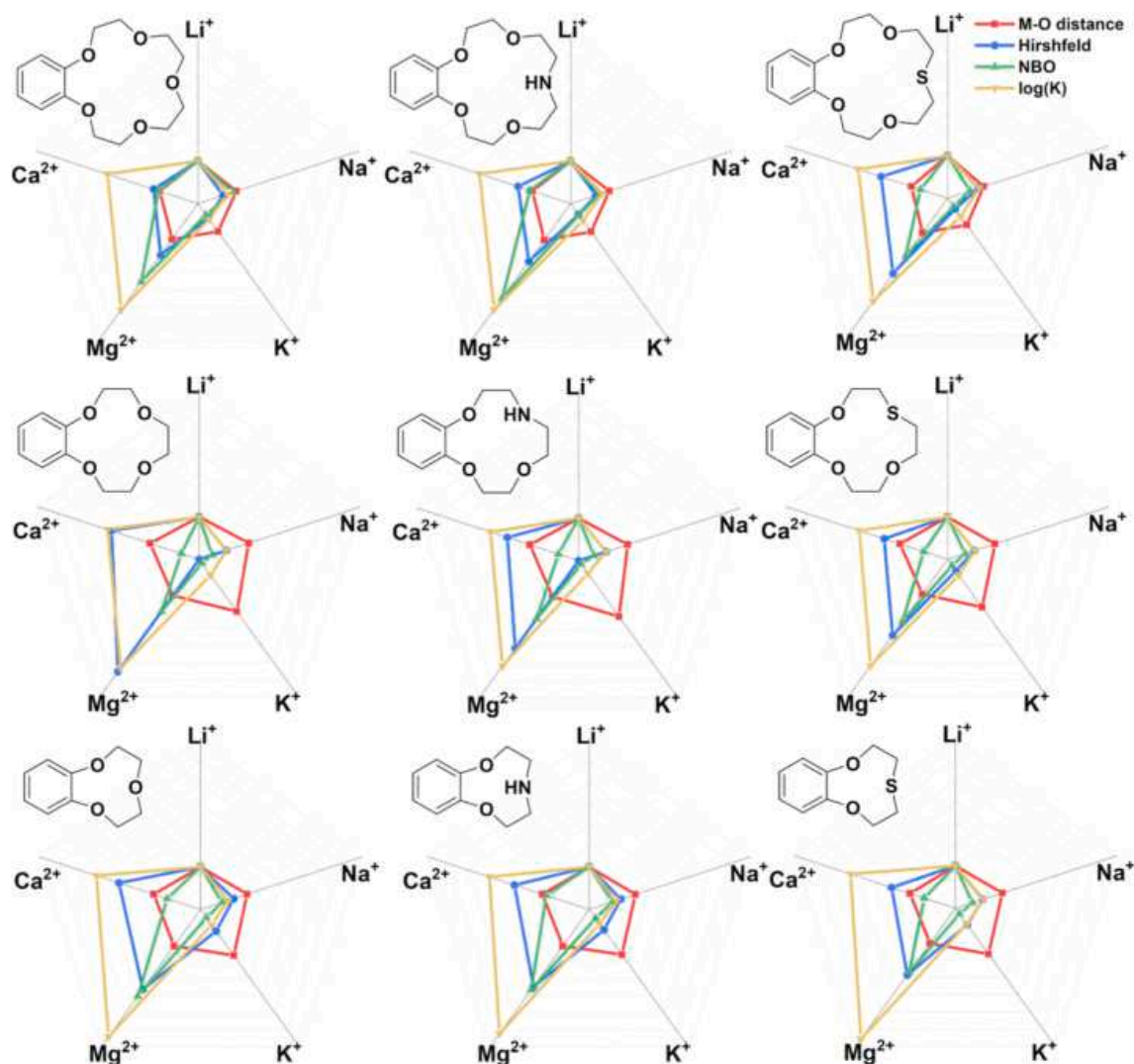


Fig. 8. Comparison of different methods for estimating complex stability within different CE complexes. Lithium is set as a reference point.

model of the solvent via a polarizable continuum model, and compared with experimental data of a liquid–liquid extraction in water/DCM. In this case, however, aza-15C5 (i.e. lacking the attached benzene moiety) is chosen as CE because of its commercial availability.

The structures of the aza-15C5 complexes with the different metal ions were optimized via DFT as shown in Fig. 9. The cavity size and the distances from metal to donor atom were determined, Hirshfeld population and NBO analyses were performed. The results are summarized in Table S9. A comparison of the experimental values for $\log(K)$, shown in Fig. 10, with the geometric and NBO data (showing the consistent trend

$Mg^{2+} > Li^+ > Ca^{2+} > Na^+ > K^+$) and the data of the Hirshfeld population analysis ($Mg^{2+} > Ca^{2+} > Li^+ > Na^+ > K^+$) indicates a good agreement concerning the predominant Mg^{2+} complexation and rather moderate K^+ complexation. However, the former is overestimated in relation to the other ions, analogous to the thermodynamic calculations. Although the values are very close to each other, the Na^+ complexation is computationally estimated to be less favored than Li^+ , contrary to the experimental trend.

The theoretical values discussed up to this point describe the situation of metal ions in *vacuo*, though this is not the most appropriate

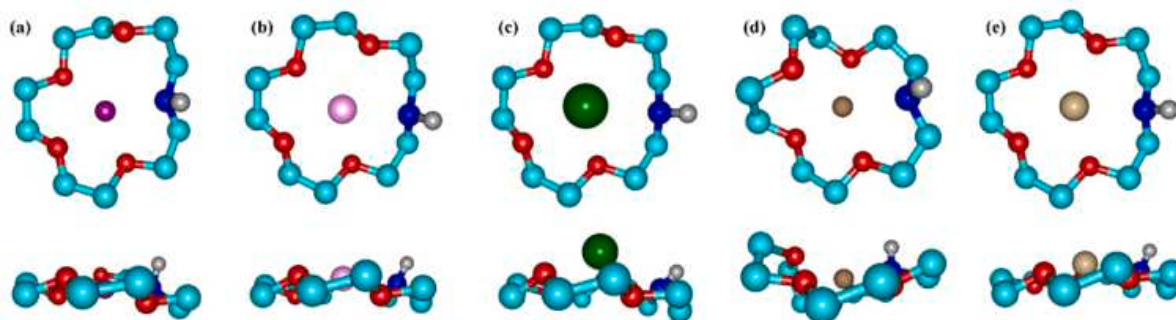


Fig. 9. DFT(PCM)-optimized structures of aza-15C5 complexes with Li^+ (a), Na^+ (b), K^+ (c), Mg^{2+} (d), and Ca^{2+} (e) from two perspectives.

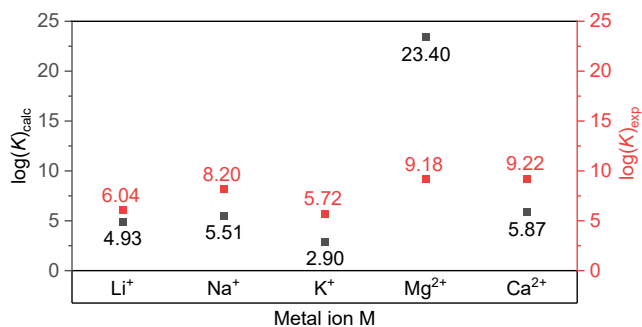


Fig. 10. Comparison of the logarithms of the complex constant K of complex formation of aza-15C5 with Li⁺, Na⁺, K⁺, Mg²⁺, and Ca²⁺, determined via experimental liquid-liquid extraction (LLE; red) and DFT-based calculations (black). Single-ligand complexes were assumed for all calculations. The corresponding anions of the salts can be found in the SI (Figure S10).

description of laboratory conditions for liquid-liquid extraction schemes, as a solvent environment could have significant effects on, e.g., the strength of the host-guest interactions within a complex, on electronic properties of the complex, as well as on the general structure of the CE. [35,64] Metal ions in water create a surroundings hydration shell that must be stripped off before the metal ions can be complexed. [42,76,80] That hydration shell is particularly strong for ions with a high charge density. [81].

To confirm the applicability of the theoretical data to more realistic conditions, the stability of complexation is calculated theoretically and experimentally from liquid-liquid extraction in a DCM/water mixture (considering hydration shells of the metal ions in the aqueous phase and the permittivity of the organic solvent). In such a mixture, the CE is mainly located in the DCM phase and the salt is initially dissolved in the aqueous phase. As a consequence of the immiscibility of both phases, the extraction process takes place at the interface. After successful complexation, the CE-salt complex remains in the DCM phase. The complexation constants K , obtained by LLE, in comparison with the theoretical data, are shown in Fig. 10, indicating a thermodynamically favored complexation in all cases. The deviation between the experimental and the calculated values is due to factors that were not considered in the theoretical calculations, such as the effect of the anion and its hydration shell [42,76,80], the solubility of CE in DCM or other organic solvents [21,35,82], and the type and stoichiometry of the counterions [83-85], along with unavoidable approximations in the exchange-correlation functional. For cations with radii significantly exceeding the order of magnitude of the CE cavity size, ML₂ complexes are also conceivable. However, to keep things simple these have not been calculated here explicitly. Nevertheless, we obtain a qualitatively consistent picture of the experimental trends.

The experimental and DFT based trends are similar, which confirms the applicability of DFT to qualitatively predict CE complexation for the selected cations. More precisely, the trend of complex stability determined via both methods is Ca²⁺ > Mg²⁺ > Na⁺ > Li⁺ > K⁺. In particular, the superiority of the magnesium complexation as well as of the calcium complexation is reproduced by the calculations, which originates from the lower hardness and thus improved interactions in the host-guest system. [86] The absence of the benzene ring and the associated larger structural flexibility of the CE allow a slight distortion of the sodium and calcium complex. [18,87] In absolute terms, however, the complexation of Mg²⁺ is strongly overestimated by DFT, while it is slightly underestimated for the other cations, leading to an overestimation of how much Mg²⁺ complexation is favored. This suggests that a more detailed investigation into appropriate simulation protocols is required if more quantitative predictions shall be made.

4. Conclusion

In this work, the lithium selectivity of three classes of CEs, B15C5, B12C4 and B9C3 (with decreasing ring sizes in that order) was compared with respect to other interfering metal ions as occurring in seawater, such as Na⁺, K⁺, Mg²⁺, and Ca²⁺, using DFT calculations in vacuum. The effects of different donor atoms (O, N, and S) within the CE were analyzed. Based on the theoretically optimized structures, a structural distortion of the CE frameworks was found when O was replaced by N or S, especially when the size relation of the cation and the CE cavity was rather unfavorable. Slightly increased stabilities were achieved when replacing oxygen by nitrogen or sulfur. Hirshfeld- and NBO analysis revealed an improved metal-donor interaction when substituting O by N or S. With only few exceptions, Hirshfeld charge transfer and NBO analyses follow similar trends as the complex stabilities. The best selectivity of Li⁺ over Mg²⁺ was achieved by thio-B15C5. It was shown that the relation of the size of CE and the ion is crucial for selectivity as well as the participation of donor atoms. While these calculations in vacuum are not comparable to liquid-liquid extraction experiments in absolute terms, their qualitative trends agree quite well with those obtained exemplarily in solution. These DFT calculations, including DCM or water environments (as used for liquid-liquid extraction) modeled by a polarizable continuum model, showed in almost all cases lower stability constants than in the experiment (except for Mg²⁺, where they were considerably larger than in the experiment). CE solubility in organic solvents, anion effects, as well as stoichiometry ratios between ion and counter ion were not considered in the calculations. The similar trends observed for the theoretical and experimental data suggest that the combination of geometrical structural optimization, thermodynamic calculation, Hirshfeld population, and NBO analysis could be highly useful for predicting strong interactions between donor atoms and metal ions, with the strong binding of Mg²⁺ presenting a challenge. The systematic study conducted in this work should contribute to the design of host ligands for a stronger complexation of lithium.

Authors contributions

All authors conceived the experiments and calculations. I.O. and S.T. designed and performed all experiments and calculations and wrote the paper, with support by V.A. and C.H. in writing the paper. This work is supported by the Cluster of Excellence 'CUI: Advanced Imaging of Matter' of the Deutsche Forschungsgemeinschaft (DFG) - EXC 2056 - project ID 390715994. All authors analyzed the data.

Declaration of Competing Interest

The authors declare that they have no known competing financial interests or personal relationships that could have appeared to influence the work reported in this paper.

Acknowledgements

The authors thank the High-Performance Computing Center at University of Hamburg for computational resources and Haitao Zhang and Michael Deffner for helpful discussions regarding the DFT calculations.

Appendix A. Supplementary material

Supplementary data to this article can be found online at <https://doi.org/10.1016/j.seppur.2022.121142>.

References

- [1] L.M. Palacios-Romero, H. Pfeiffer, Lithium cuprate (Li₂CuO₂): a new possible ceramic material for CO₂ chemisorption, Chem. Lett. 37 (2008) 862-863, <https://doi.org/10.1246/cl.2008.862>.

- [2] A.R. Kulkarni, H.S. Maiti, A. Paul, Fast ion conducting lithium glasses-Review, *Bull. Mater. Sci.* 6 (1984) 201–221, <https://doi.org/10.1007/BF02743897>.
- [3] N.C. Patel, M.P. DelBello, H.S. Bryan, C.M. Adler, R.A. Kowatch, K. Stanford, S. M. Strakowski, Open-label lithium for the treatment of adolescents with bipolar depression, *J. Am. Acad. Child Adolesc. Psychiatry* 45 (2006) 289–297, <https://doi.org/10.1097/01.chi.0000194569.70912.a7>.
- [4] J.W. Makepeace, T.J. Wood, H.M.A. Hunter, M.O. Jones, W.I.F. David, Ammonia decomposition catalysis using non-stoichiometric lithium imide, *Chem. Sci.* 6 (2015) 3805–3815, <https://doi.org/10.1039/c5sc00205b>.
- [5] B. Lin, I. Rustamov, L. Zhang, J. Luo, X. Wan, Graphene-reinforced lithium grease for antifriction and antiwear, *ACS Appl. Nano Mater.* 3 (2020) 10508–10521, <https://doi.org/10.1021/acsnm.0c02461>.
- [6] B. Scrosati, J. Garche, Lithium batteries: status, prospects and future, *J. Power Sources* 195 (2010) 2419–2430, <https://doi.org/10.1016/j.jpowsour.2009.11.048>.
- [7] P.W. Gruber, P.A. Medina, G.A. Keoleian, S.E. Kesler, M.P. Everson, T. J. Wallington, Global lithium availability: a constraint for electric vehicles? *J. Ind. Ecol.* 15 (2011) 760–775, <https://doi.org/10.1111/j.1530-9290.2011.00359.x>.
- [8] B. Swain, Separation and purification of lithium by solvent extraction and supported liquid membrane, analysis of their mechanism: a review, *J. Chem. Technol. Biotechnol.* 91 (2016) 2549–2562, <https://doi.org/10.1002/jctb.4976>.
- [9] E.C. Everts, Lithium batteries: to the limits of lithium, *Nature* 526 (2015) 93–95, <https://doi.org/10.1038/526S93a>.
- [10] A. Yaksic, J.E. Tilton, Using the cumulative availability curve to assess the threat of mineral depletion: the case of lithium, *Resour. Policy* 34 (2009) 185–194, <https://doi.org/10.1016/j.resourpol.2009.05.002>.
- [11] X. He, S. Kaur, R. Kostecki, Mining lithium from seawater, *Joule* 4 (2020) 1357–1358, <https://doi.org/10.1016/j.joule.2020.06.015>.
- [12] P.K. Choubey, K.-S. Chung, M.-S. Kim, J.-C. Lee, R.R. Srivastava, *Advance review on the exploitation of the prominent energy-storage element lithium. part II: from sea water and spent lithium ion batteries (LIBs)*, *Miner. Eng.* 110 (2017) 104–121.
- [13] A. Pálsdóttir, C.A. Alabi, J.W. Tester, Characterization of 14-Crown-4 ethers for the extraction of lithium from natural brines: synthesis, solubility measurements in supercritical carbon dioxide, and thermodynamic modeling, *Ind. Eng. Chem. Res.* 60 (2021) 7926–7934, <https://doi.org/10.1021/acs.iecr.1c00346>.
- [14] C. Liu, Y. Li, D. Lin, P.C. Hsu, B. Liu, G. Yan, T. Wu, Y. Cui, S. Chu, Lithium extraction from seawater through pulsed electrochemical intercalation, *Joule* 4 (2020) 1459–1469, <https://doi.org/10.1016/j.joule.2020.05.017>.
- [15] L. Tang, S. Huang, Y. Wang, D. Liang, Y. Li, J. Li, Y. Wang, Y. Xie, W. Wang, Highly efficient, stable, and recyclable hydrogen manganese oxide/cellulose film for the extraction of lithium from seawater, *ACS Appl. Mater. Interfaces* 12 (2020) 9775–9781, <https://doi.org/10.1021/acsami.9b21612>.
- [16] S. Yang, F. Zhang, H. Ding, P. He, H. Zhou, Lithium metal extraction from seawater, *Joule* 2 (2018) 1648–1651, <https://doi.org/10.1016/j.joule.2018.07.006>.
- [17] L.S. Balistrieri, J.W. Murray, The influence of the major ions of seawater on the adsorption of simple organic acids by goethite, *Geochim. Cosmochim. Acta* 51 (1987) 1151–1160, [https://doi.org/10.1016/0016-7037\(87\)90208-0](https://doi.org/10.1016/0016-7037(87)90208-0).
- [18] R.E.C. Torrejos, G.M. Nisola, H.S. Song, L.A. Limjuco, C.P. Lawagon, K. J. Parohinog, S. Koo, J.W. Han, W.J. Chung, Design of lithium selective crown ethers: synthesis, extraction and theoretical binding studies, *Chem. Eng. J.* 326 (2017) 921–933, <https://doi.org/10.1016/j.cej.2017.06.005>.
- [19] K. Nishizawa, S.I. Ishino, H. Watanabe, M. Shinagawa, Lithium isotope separation by liquid-liquid extraction using benzo-15-crown-5, *J. Nucl. Sci. Technol.* 21 (1984) 694–701, <https://doi.org/10.1080/18811248.1984.9731102>.
- [20] X. Bai, J. Dai, Y. Ma, W. Bian, J. Pan, 2-(Allyloxy) methylol-12-crown-4 ether functionalized polymer brushes from porous PolyHIPE using UV-initiated surface polymerization for recognition and recovery of lithium, *Chem. Eng. J.* 380 (2020) 122386.
- [21] R.M. Izatt, J.S. Bradshaw, S.A. Nielsen, J.D. Lamb, J.J. Christensen, D. Sen, Thermodynamic and kinetic data for cation-macrocyclic interaction, *Chem. Rev.* 85 (1985) 271–339, <https://doi.org/10.1021/cr00068a003>.
- [22] C.J. Pedersen, Cyclic polyethers and their complexes with metal salts, *J. Am. Chem. Soc.* 89 (1967) 7017–7036, <https://doi.org/10.1021/ja01002a035>.
- [23] J.W. Steed, First- and second-sphere coordination chemistry of alkali metal crown ether complexes, *Coord. Chem. Rev.* 215 (2001) 171–221, [https://doi.org/10.1016/S0010-8545\(01\)00317-4](https://doi.org/10.1016/S0010-8545(01)00317-4).
- [24] A. van der Ham, T. Hansen, G. Lodder, J.D.C. Codé, T.A. Hamlin, D.V. Filippov, Computational and NMR studies on the complexation of lithium ion to 8-Crown-4, *ChemPhysChem* 20 (2019) 2103–2109, <https://doi.org/10.1002/cphc.201900496>.
- [25] M. Sarma, T. Chatterjee, S.K. Das, Ammonium-crown ether based host-guest systems: N-H...O hydrogen bond directed guest inclusion featuring N-H donor functionalities in angular geometry, *RSC Adv.* 2 (2012) 3920–3926, <https://doi.org/10.1039/c2ra20109g>.
- [26] S. Roy, K. Thirumoorthy, U.K. Padidela, P. Vairaprakash, A. Anoop, V. S. Thimmakonda, Organomagnesium crown ethers and their binding affinities with Li⁺, Na⁺, K⁺, Be²⁺, Mg²⁺, and Ca²⁺ ions – a theoretical study, *ChemistrySelect* 6 (2021) 8782–8790, <https://doi.org/10.1002/slct.202102317>.
- [27] L.J. Mathias, Crown ethers and phase transfer catalysis in polymer chemistry, *J. Macromol. Sci.* 15 (1981) 853–876, <https://doi.org/10.1080/0022338108056772>.
- [28] S. Chen, H. Yuan, N. Grinberg, A. Dovletoglu, G. Bicker, Enantiomeric separation of trans-2-aminocyclohexanol on a crown ether stationary phase using evaporative light scattering detection S. J. Liq. Chromatogr. Relat. Technol. 26 (2003) 425–442, <https://doi.org/10.1081/JLC-120017180>.
- [29] Y. Kuwahara, H. Nagata, H. Nishi, Y. Tanaka, K. Takehi, Detection and separation of free amino acid enantiomers by capillary electrophoresis with a chiral crown ether and indirect photometric detection, *Chromatographia* 62 (2005) 505–510, <https://doi.org/10.1365/s10337-005-0658-9>.
- [30] M. Naumowicz, A.D. Petelska, Z.A. Figaszewski, The effect of the presence of crown ether on ion transport across the lipid bilayer, *Cell. Mol. Biol. Lett.* 8 (2003) 383–389.
- [31] A. Cazacu, C. Tong, A. Van Der Lee, T.M. Fyles, M. Barboiu, Columnar self-assembled ureido crown ethers: an example of ion-channel organization in lipid bilayers, *J. Am. Chem. Soc.* 128 (2006) 9541–9548, <https://doi.org/10.1021/ja061861w>.
- [32] F. Sannicolò, E. Brenna, T. Benincori, G. Zotti, S. Zecchin, G. Schiavon, T. Pilati, Highly ordered poly(cyclopentabithiophenes) functionalized with crown-ether moieties for lithium-and sodium-sensing electrodes, *Chem. Mater.* 10 (1998) 2167–2176, <https://doi.org/10.1021/cm980067+>.
- [33] M. Takagi, H. Nakamura, Analytical application of functionalized crown ether-metal complexes, 1986, <https://doi.org/10.1080/00958978608075855>.
- [34] S. De, A. Boda, S.M. Ali, Preferential interaction of charged alkali metal ions (guest) within a narrow cavity of cyclic crown ethers (neutral host): a quantum chemical investigation, *J. Mol. Struct. Theochem.* 941 (2010) 90–101, <https://doi.org/10.1016/j.theochem.2009.11.009>.
- [35] A. Boda, S. Musharaf Ali, H. Rao, S.K. Ghosh, Ab initio and density functional theoretical design and screening of model crown ether based ligand (host) for extraction of lithium metal ion (guest): effect of donor and electronic induction, *J. Mol. Model.* 18 (2012) 3507–3522, <https://doi.org/10.1007/s00894-011-1348-1>.
- [36] J. Korchowiec, B. Korchowiec, W. Priebe, E. Rogalska, DFT study on the selectivity of complexation of metal cations with a dioxadithia crown ether ligand, *J. Phys. Chem. A* 112 (2008) 13633–13640, <https://doi.org/10.1021/jp8066052>.
- [37] G. Donnay, J.W. Gryder, The oxygen coordinations of lithium, *J. Chem. Educ.* 42 (1965) 223, <https://doi.org/10.1021/ed042p223>.
- [38] M.E. Volipin, Y.N. Novikov, Coordination chemistry of graphite, *Pure Appl. Chem.* 60 (1988) 1133–1140, <https://doi.org/10.1351/pac198860081133>.
- [39] C.W. Bock, A. Kaufman, J.P. Glusker, Coordination of water to magnesium cations, *Inorg. Chem.* 33 (1994) 419–427, <https://doi.org/10.1021/ic00081a007>.
- [40] R.A. Bartsch, M.J. Goo, G.D. Christian, X. Wen, B.P. Czech, E. Chapoteau, A. Kumar, Influence of ring substituents and matrix on lithium / sodium selectivity of 14-crown-4 and benzo-13-crown-4-compounds, *Anal. Chim. Acta* 272 (1993) 285–292, [https://doi.org/10.1016/0003-2670\(93\)80581-5](https://doi.org/10.1016/0003-2670(93)80581-5).
- [41] K. Kobiro, New class of lithium ion selective crown ethers with bulky decalin substituents, *Coord. Chem. Rev.* 148 (1996) 135–149, [https://doi.org/10.1016/0010-8545\(96\)01209-X](https://doi.org/10.1016/0010-8545(96)01209-X).
- [42] Y. Sun, M. Zhu, Y. Yao, H. Wang, B. Tong, Z. Zhao, A novel approach for the selective extraction of Li⁺ from the leaching solution of spent lithium-ion batteries using benzo-15-crown-5 ether as extractant, *Sep. Purif. Technol.* 237 (2020), 116325, <https://doi.org/10.1016/j.seppur.2019.116325>.
- [43] I. Oral, V. Abetz, A highly selective polymer material using benzo-9-crown-3 for the extraction of lithium in presence of other interfering alkali metal ions, *Macromol. Rapid Commun.* 42 (2021) 2000746, <https://doi.org/10.1002/marc.202000746>.
- [44] I. Oral, V. Abetz, Improved alkaline metal ion capturing utilizing crown ether-based diblock copolymers in a sandwich-type complexation, *Soft Matter* (2022), <https://doi.org/10.1002/9783527617050>.
- [45] I. Oral, L. Grossmann, E. Fedorenko, J. Struck, V. Abetz, Synthesis of poly (methacrylic acid)-block-polystyrene diblock copolymers at high solid contents via RAFT emulsion polymerization, *Polymers (Basel)* 13 (2021) 3675, <https://doi.org/10.3390/polym13213675>.
- [46] E. Li, J. Kang, P. Ye, W. Zhang, F. Cheng, C. Yin, A prospective material for the highly selective extraction of lithium ions based on a photochromic crowned spirobenzopyran, *J. Mater. Chem. B* 7 (2019) 903–907, <https://doi.org/10.1039/c8tb02906g>.
- [47] K.S. Diao, H.J. Wang, Z.M. Qiu, A DFT study on the metal binding selectivity of 12-crown-4 and its heterocyclic analogs, *J. Mol. Struct. Theochem.* 901 (2009) 157–162, <https://doi.org/10.1016/j.theochem.2009.01.026>.
- [48] E.R. Dobbs, Transport properties, in: R. Dobbs (Ed.), *Helium Three*, Oxford University Press, 2001, pp. 275–311.
- [49] A.A. Bagatur'yants, A.Y. Freidzon, M.V. Alfimov, E.J. Baerends, J.A.K. Howard, L. G. Kuz'mina, DFT calculations on the electronic and geometrical structure of 18-crown-6 complexes with Ag⁺, Hg²⁺, Ag⁰, Hg⁺, Hg⁰, AgNO₃, and HgX₂ (X = Cl, Br, and I), *J. Mol. Struct. Theochem.* 588 (1-3) (2002) 55–69.
- [50] M.J. Frisch, G.W. Trucks, H.B. Schlegel, G.E. Scuseria, M.A. Robb, J.R. Cheeseman, G. Scalmani, V. Barone, G.A. Petersson, H. Nakatsuji, X. Li, M. Caricato, A. V. Marenich, J. Bloino, B.G. Janesko, R. Gomperts, B. Mennucci, H.P. Hratchian, J. V. Ortiz, A.F. Izmaylov, J.L. Sonnenberg, D. Williams-Young, F. Ding, F. Lipparini, F. Egidi, J. Goings, B. Peng, A. Petrone, T. Henderson, D. Ranasinghe, V.G. Zakrzewski, J. Gao, N. Rega, G. Zheng, W. Liang, M. Hada, M. Ehara, K. Toyota, R. Fukuda, J. Hasegawa, M. Ishida, T. Nakajima, Y. Honda, O. Kitao, H. Nakai, T. Vreven, K. Throssell, J. J. A. Montgomery, J.E. Peralta, F. Ogliaro, M.J. Bearpark, J. J. Heyd, E.N. Brothers, K.N. Kudin, V.N. Staroverov, T.A. Keith, R. Kobayashi, J. Normand, K. Raghavachari, A.P. Rendell, J.C. Burant, S.S. Iyengar, J. Tomasi, M. Cossi, J.M. Millam, M. Klene, C. Adamo, R. Cammi, J.W. Ochterski, R.L. Martin, K. Morokuma, O. Farkas, J.B. Foresman, D.J. Fox, Gaussian 16, Revision C.01, (2019).
- [51] A.D. Becke, Density-functional thermochemistry. III. the role of exact exchange, *J. Chem. Phys.* 98 (7) (1993) 5648–5652.
- [52] F. Weigend, R. Ahlrichs, Balanced basis sets of split valence, triple zeta valence and quadruple zeta valence quality for H to Rn: design and assessment of accuracy,

- Phys. Chem. Chem. Phys. 7 (2005) 3297–3305, <https://doi.org/10.1039/b508541a>.
- [53] S. Grimme, J. Antony, S. Ehrlich, H. Krieg, A consistent and accurate ab initio parametrization of density functional dispersion correction (DFT-D) for the 94 elements H-Pu, *J. Chem. Phys.* 132 (15) (2010) 154104.
- [54] K.J. Hintze, A. Lützen, T. Bredow, Structure and stability of supramolecular crown ether complexes, *J. Comput. Chem.* 36 (2015) 1467–1472, <https://doi.org/10.1002/jcc.23950>.
- [55] R.D. Dennington, T.A. Keith, J.M. Millam, GaussView 5.0.9, (2008).
- [56] E.D. Glendening, A.E. Reed, J.E. Carpenter, F. Weinhold, NBO Version 3.1., (n.d.).
- [57] G.A. Andrienko, Chemcraft 1.8 (build 595b), (2020).
- [58] S.X. Hu, J.J. Liu, J.K. Gibson, J. Li, Periodic trends in actinyl thio-crown ether complexes, *Inorg. Chem.* 57 (2018) 2899–2997, <https://doi.org/10.1021/acs.inorgchem.7b03277>.
- [59] R. Das, P.K. Chattaraj, Guest-host interaction in an aza crown analog, *Int. J. Quantum Chem.* 114 (2014) 708–719, <https://doi.org/10.1002/qua.24648>.
- [60] Z. Zhao, H. Tian, M. Zhang, Y. Yang, H. Zhang, Molecular design of macrocyclic compounds for complete removal of thallium(I) from wastewater, *Environ. Sci. Pollut. Res.* 25 (2018) 34550–34558, <https://doi.org/10.1007/s11356-018-3393-0>.
- [61] N. Alizadeh, A comparison of complexation of Li⁺ ion with macrocyclic ligands 15-crown-5 and 12-crown-4 in binary nitromethane-acetonitrile mixtures by using lithium-7 NMR technique and ab initio calculation, *Spectrochim. Acta - Part A Mol. Biomol. Spectrosc.* 78 (2011) 488–493, <https://doi.org/10.1016/j.saa.2010.11.014>.
- [62] C.C. Liou, J.S. Brodbelt, Determination of orders of relative alkali metal ion affinities of crown ethers and acyclic analogs by the kinetic method, *J. Am. Soc. Mass Spectrom.* 3 (1992) 543–548, [https://doi.org/10.1016/1044-0305\(92\)85031-E](https://doi.org/10.1016/1044-0305(92)85031-E).
- [63] S.Y. Lin, S.W. Liu, C.M. Lin, C.H. Chen, Recognition of potassium ion in water by 15-crown-5 functionalized gold nanoparticles, *Anal. Chem.* 74 (2002) 330–335, <https://doi.org/10.1021/ac0156316>.
- [64] A. Boda, S.M. Ali, M.R.K. Shenoi, H. Rao, S.K. Ghosh, DFT modeling on the suitable crown ether architecture for complexation with Cs⁺ and Sr²⁺ metal ions, *J. Mol. Model.* 17 (2011) 1091–1108, <https://doi.org/10.1007/s00894-010-0812-7>.
- [65] R.E.C. Torrejos, G.M. Nisola, S.H. Min, J.W. Han, S. Koo, K.J. Parohinog, S. Lee, H. Kim, W.J. Chung, Aqueous synthesis of 14–15-membered crown ethers with mixed O, N and S heteroatoms: experimental and theoretical binding studies with platinum-group metals, *Chempluschem.* 84 (2019) 210–221, <https://doi.org/10.1002/cplu.201800541>.
- [66] C.Y. Chen, C.T. Cheng, C.W. Lai, P.W. Wu, K.C. Wu, P.T. Chou, Y.H. Chou, H. T. Chiu, Potassium ion recognition by 15-crown-5 functionalized CdSe/ZnS quantum dots in H₂O, *Chem. Commun.* (2006) 263–265, <https://doi.org/10.1039/b512677k>.
- [67] H.R. Yu, J.Q. Hu, X.H. Lu, X.J. Ju, Z. Liu, R. Xie, W. Wang, L.Y. Chu, Insights into the effects of 2:1 “sandwich-type” crown-ether/metal-ion complexes in responsive host-guest systems, *J. Phys. Chem. B.* 119 (2015) 1696–1705, <https://doi.org/10.1021/jp5079423>.
- [68] P.D. Beer, S.W. Dent, Potassium cation induced switch in anion selectivity exhibited by heteroditopic ruthenium(II) and rhenium(I) bipyridyl bis(benzo-15-crown-5) ion pair receptors, *Chem. Commun.* (1998) 825–826, <https://doi.org/10.1039/a800356d>.
- [69] F.L. Hirshfeld, Bonded-atom fragments for describing molecular charge densities, *Theor. Claim. Acta.* 44 (1977) 129–138, <https://doi.org/10.1002/BF00549096>.
- [70] T. Lu, F. Chen, Multiwfn: a multifunctional wavefunction analyzer, *J. Comput. Chem.* 33 (2012) 580–592, <https://doi.org/10.1002/jcc.22885>.
- [71] F. Weinhold, C.R. Landis, Natural bond orbitals and extensions of localized bonding concepts, *Chem. Educ. Res. Pr.* 2 (2001) 91–104, <https://doi.org/10.1039/b1rp90011k>.
- [72] A.E. Reed, L.A. Curtiss, F. Weinhold, Intermolecular interactions from a natural bond orbital, donor-acceptor viewpoint, *Chem. Rev.* 88 (1988) 899–926, <https://doi.org/10.1021/cr00088a005>.
- [73] S. Maleknia, J. Brodbelt, Gas-phase selectivities of crown ethers for alkali metal ion complexation, *J. Am. Chem. Soc.* 114 (1992) 4295–4298, <https://doi.org/10.1021/ja00037a038>.
- [74] T. Wulf, T. Heine, Small crown-ether complexes as molecular models for dihydrogen adsorption in undercoordinated extraframework cations in zeolites, *J. Phys. Chem. C* 124 (2020) 9409–9415, <https://doi.org/10.1021/acs.jpcc.0c02815>.
- [75] J.C. López, C. Pérez, S. Blanco, V.A. Shubert, B. Temelso, G.C. Shields, M. Schnell, Water induces the same crown shapes as Li⁺ or Na⁺ in 15-crown-5 ether: a broadband rotational study, *Phys. Chem. Chem. Phys.* 21 (2019) 2875–2881, <https://doi.org/10.1039/c8cp05552a>.
- [76] Y. Inokuchi, T. Ebata, T.R. Rizzo, UV and IR spectroscopy of transition metal-crown ether complexes in the gas phase: Mn²⁺(benzo-15-crown-5)(H₂O)_{0–2}, *J. Phys. Chem. A.* 123 (2019) 6781–6786, <https://doi.org/10.1021/acs.jpca.9b05706>.
- [77] F. Gámez, B. Martínez-Haya, S. Blanco, J.C. López, J.L. Alonso, Microwave spectroscopy and quantum chemical investigation of nine low energy conformers of the 15-crown-5 ether, *Phys. Chem. Chem. Phys.* 14 (2012) 12912–12918, <https://doi.org/10.1039/c2cp41635b>.
- [78] E. Cristina Stanca-Kaposta, D.P. Gamblin, J. Screen, B. Liu, L.C. Snoek, B.G. Davis, J.P. Simons, Carbohydrate molecular recognition: A spectroscopic investigation of carbohydrate-aromatic interactions, *Phys. Chem. Chem. Phys.* 9 (2007) 4452–4459, <https://doi.org/10.1039/b704792d>.
- [79] V.A. Shubert, W.H. James, T.S. Zwier, Jet-cooled electronic and vibrational spectroscopy of crown ethers: benzo-15-crown-5 ether and 4'-amino-benzo-15-crown-5 ether, *J. Phys. Chem. A* 113 (28) (2009) 8055–8066.
- [80] Y. Tachibana, T. Suzuki, M. Nogami, M. Nomura, T. Kaneshiki, Selective lithium recovery from seawater using crown ether resins, *J. Ion Exch.* 29 (2018) 90–96, <https://doi.org/10.5182/jaie.29.90>.
- [81] N. Wiberg, *Lehrbuch der Anorganischen Chemie*, 102nd ed., De Gruyter, Berlin, 2007.
- [82] Y. Li, P. Huszthy, I. Móczár, B. Szemenyei, S. Kunsági-Máté, Solvent effect on the complex formation of a crown ether derivative with sodium and potassium ions. thermodynamic background of selectivity, *Chem. Phys. Lett.* 556 (2013) 94–97, <https://doi.org/10.1016/j.cplett.2012.11.056>.
- [83] U. Olsher, M.G. Hankins, Y.D. Kim, R.A. Bartsch, Anion effect on selectivity in crown ether extraction of alkali metal cations, *J. Am. Chem. Soc.* 115 (1993) 3370–3371, <https://doi.org/10.1021/ja00061a062>.
- [84] A.F. Danil De Namor, J.C.Y. Ng, M.A. Llosa Tanco, M. Salomon, Thermodynamics of lithium-crown ether (12-crown-4 and 1-benzyl-1-aza-12-crown-4) interactions in acetonitrile and propylene carbonate. the anion effect on the coordination process, *J. Phys. Chem.* 100 (1996) 14485–14491, <https://doi.org/10.1021/jp960519a>.
- [85] J.D. Lamb, J.J. Christensen, S.R. Izatt, K. Bedke, M.S. Astin, R.M. Izatt, Effects of salt concentration and anion on the rate of carrier-facilitated transport of metal cations through bulk liquid membranes containing crown ethers, *J. Am. Chem. Soc.* 102 (1980) 3399–3403, <https://doi.org/10.1021/ja00530a016>.
- [86] R.G. Parr, R.G. Pearson, Absolute hardness: companion parameter to absolute electronegativity, *J. Am. Chem. Soc.* 105 (1983) 7512–7516, <https://doi.org/10.1021/ja00364a005>.
- [87] Z. Talebpour, N. Alizadeh, H.R. Bijanzadeh, M. Shamsipur, Cadmium-113 NMR and theoretical studies of complexation of cadmium ion with 15-crown-5 and benzo-15-crown-5 in acetonitrile and its binary mixtures with water and nitromethane, *J. Incl. Phenom. Macrocycl. Chem.* 49 (2004) 101–106, <https://doi.org/10.1023/B:JIPH.0000031121.36121.52>.

5.3 Publication 3:

Synthesis of poly(methacrylic acid)-*block*-polystyrene diblock copolymers at high solid contents via RAFT emulsion polymerization

This work was partially done with the assistance of Larissa Grossmann (Universität Hamburg), Elena Fedorenko (Universität Hamburg), and Jana Struck (Universität Hamburg) in the context of student laboratory courses under my supervision and guidance. Their help is gratefully acknowledged.

In the first two Publications, different crown ether structures were synthesized or simulated, and the properties of metal ion complexation were described. Since the target material of this work is a crown ether containing membrane, a polymer system is needed that can be linked to crown ethers.

This Publication presents a diblock copolymer consisting of poly(methacrylic acid) and polystyrene. The methacrylic acid group is the linking unit for crown ether functionalization, and the styrene is mechanical support for subsequent membrane production. The synthesis of the PMAA-*b*-PS diblock copolymer is carried out in a one-pot synthesis using RAFT emulsion polymerization. Emulsion polymerization was chosen due to the better heat transfer and less viscosity issues if higher molar masses are targeted, making this technique suitable for preparation in higher scale.

Since the polymerization was carried out using the RAFT polymerization technique and the CTAs act as a stabilizer, different trithiocarbonate CTAs with different hydrophobic Z groups (increasing in their hydrophobicity) were investigated to obtain the best conditions for emulsion polymerization for high weight percentages. In order to keep the synthesis of the polymer material as good as possible, different weight percentages of the emulsion solution in water were also investigated so that less solvent is present and thus less energy is required to produce this polymer. Furthermore, kinetical studies were performed to analyze the speed of the reaction.

The synthesis of PMAA-*b*-PS diblock copolymer by RAFT polymerization was successfully carried out with a CTA bearing a dodecyl group as Z group at 50wt% within 2 hours. The control of the reaction was additionally successfully demonstrated by DLS, TEM, and GPC measurements.

The Publication is reprinted with permission from I. Oral, L. Grossmann, E. Fedorenko, J. Struck and V. Abetz, *Polymers*, **2021**, 13, 3675. - published by MDPI. The related supporting information is available in Section 9.4.

Article

Synthesis of Poly(methacrylic acid)-*block*-Polystyrene Diblock Copolymers at High Solid Contents via RAFT Emulsion Polymerization

Iklima Oral ¹, Larissa Grossmann ¹, Elena Fedorenko ¹, Jana Struck ¹ and Volker Abetz ^{1,2,*}

¹ Institute of Physical Chemistry, Universität Hamburg, Grindelallee 117, 20146 Hamburg, Germany; iklima.oral@chemie.uni-hamburg.de (I.O.); larissa.grossmann@studium.uni-hamburg.de (L.G.); elena.fedorenko@chemie.uni-hamburg.de (E.F.); jana.struck@chemie.uni-hamburg.de (J.S.)

² Helmholtz-Zentrum Hereon, Institute of Membrane Research, Max-Planck-Straße 1, 21502 Geesthacht, Germany

* Correspondence: volker.abetz@hereon.de; Tel.: +49-40-42838-3460

Abstract: The combination of polymerization-induced self-assembly (PISA) and reversible-addition fragmentation chain transfer (RAFT) emulsion polymerization offers a powerful technique to synthesize diblock copolymers and polymeric nanoparticles in a controlled manner. The RAFT emulsion diblock copolymerization of styrene and methacrylic acid (MAA) by using a trithiocarbonate as surfactant and RAFT agent was investigated. The Z-group of the RAFT agent was modified with a propyl-, butyl- and dodecyl- sidechain, increasing the hydrophobicity of the RAFT agent to offer well-controlled polymerization of poly(methacrylic acid)-*block*-polystyrene (PMAA-*b*-PS) diblock copolymers at high solid contents between 30–50 wt% in water. The kinetic data of the PMAA homopolymerization with the three different RAFT agents for various solvents was investigated as well as the RAFT emulsion polymerization of the diblock copolymers in pure water. While the polymerization of PMAA-*b*-PS with a propyl terminus as a Z-group suffered from slow polymerization rates at solid contents above 30 wt%, the polymerization with a dodecyl sidechain as a Z-group led to full conversion within 2 h, narrow molar mass distributions and all that at a remarkable solid content of up to 50 wt%.

Keywords: reversible-addition-fragmentation chain transfer; high solid content; polymerization-induced self-assembly; emulsion polymerization; polystyrene; poly(methacrylic acid); *block* copolymers



Citation: Oral, I.; Grossmann, L.; Fedorenko, E.; Struck, J.; Abetz, V. Synthesis of Poly(methacrylic acid)-*block*-Polystyrene Diblock Copolymers at High Solid Contents via RAFT Emulsion Polymerization. *Polymers* **2021**, *13*, 3675. <https://doi.org/10.3390/polym13213675>

Academic Editor: Leonard Ionut Atanase

Received: 3 October 2021

Accepted: 15 October 2021

Published: 25 October 2021

Publisher's Note: MDPI stays neutral with regard to jurisdictional claims in published maps and institutional affiliations.



Copyright: © 2021 by the authors. Licensee MDPI, Basel, Switzerland. This article is an open access article distributed under the terms and conditions of the Creative Commons Attribution (CC BY) license (<https://creativecommons.org/licenses/by/4.0/>).

1. Introduction

The advent of controlled radical polymerization (CRP) gave rise to a wide variety of well-defined homopolymers and copolymers [1–4]. RAFT is based on degenerative chain transfer, thus, exhibiting quasi-living characteristics while benefiting from the advantages of a radical process. Those advantages include high tolerance towards various functionalities and straightforward feasibility, allowing for the polymerization of a plethora of monomers [5]. The formulation is similar to a free-radical polymerization with the difference that it utilizes a dithioester or any of its derivatives as chain transfer agent (CTA) to control the active radical concentration and hence enabling uncomplicated tailoring of the average molecular weight and dispersity (M_w/M_n) of the polymer. Conventional radical polymerization does not facilitate control, i.e., customized molecular weight distributions, polymer compositions (when it comes to block-like or gradient structures) and polymer architectures. RAFT polymerization can be conducted in a range of solvents [6], including protic solvents such as water [7,8] and lower alcohols such as methanol [9] and ethanol [10], non-polar solvents, e.g., *n*-alkanes [6] and more exotic media such as ionic liquids [9,11]. It can be performed in bulk, solution or dispersion (with emulsion being a subclass of it) [12–14]. The combination of RAFT polymerization and aqueous emulsion

polymerization can be employed with a wide range of hydrophobic monomers, additionally enabling polymerizations up to a high solid content while allowing high molecular weights and still maintaining low viscosities and an excellent heat transfer [15–17]. Furthermore, this combination offers a potential surfactant-free route for the efficient synthesis of nanosized latexes in water. Hawkett et al. [18,19] established the first successful *ab initio* RAFT emulsion polymerization using a poly(acrylic acid) (PAA) macro-CTA, which was chain extended in a emulsion polymerization with *n*-butyl acrylate to form stable latex particles. Charleux et al. established RAFT emulsion polymerization protocols in a series of innovative studies [20,21]. Different hydrophilic stabilizer blocks (prepared from acrylic acid, MAA and acrylamide), hydrophobic core forming blocks (containing *n*-butyl acrylate, styrene, methyl methacrylate, and benzyl methacrylate) and RAFT agents (both trithiocarbonates and dithiobenzoates) were developed [14,20–26]. Other parameters such as pH were studied in detail, the reaction conditions were optimized to provide high monomer conversion within short reaction times, narrow size distributions and good control over the molecular weight [20,27]. In this work, PMAA-*b*-PS diblock copolymers were synthesized via RAFT aqueous emulsion polymerization using MAA as water soluble monomer and styrene as the water-immiscible monomer to produce an amphiphilic diblock copolymer in situ. This approach leads to a PISA and can produce diblock copolymer nanoparticles in the form of either spheres, worms, or vesicles. The general procedure of PISA via RAFT polymerization is the chain extension of a soluble homopolymer by a second monomer in a suitable solvent (as it is in this case a non-solvent for the extended polymer block). During the polymerization, the growing second block becomes more and more insoluble. Eventually, in situ self-assembly occurs and forms diblock copolymer nanoparticles.

The first PMAA block is synthesized via RAFT solution polymerization and forms the stabilizer block, while the second block is the core forming block and is synthesized via RAFT emulsion polymerization afterwards. The PMAA block as stabilizer in the formation of PMAA-*b*-PS block copolymers was deeply investigated by the group of Choe et al. [28]. PMAA-*b*-PS is an attractive block copolymer since the monomers are available on large scale, cheap and with the carboxylic acid within the polymer, it offers a variety of post-modification possibilities [29]. The latter is of particular interest as it allows different properties to be incorporated into the polymer system without the need for complex polymerization techniques.

In here, we will present a detailed study of the synthesis of PMAA-*b*-PS diblock copolymers at high solid concentrations by choosing three different CTAs, making this polymer even more attractive for industrial applications (Figure 1).

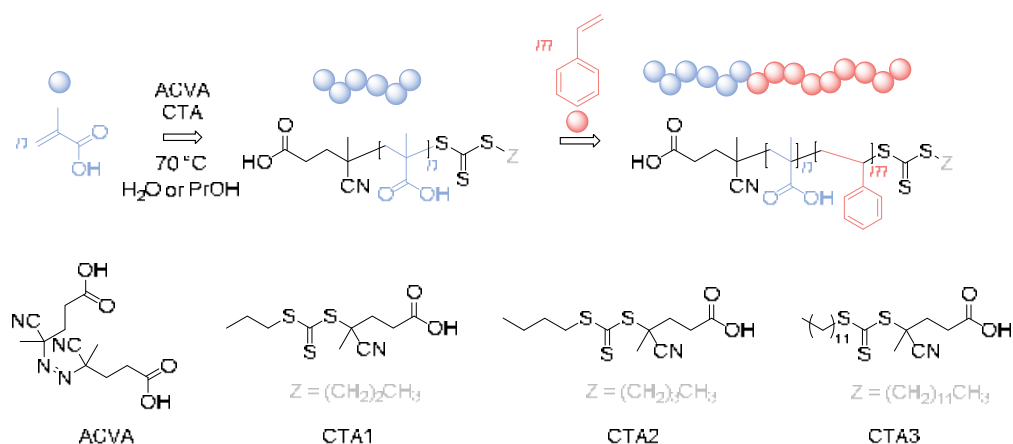


Figure 1. Reaction overview of the RAFT polymerization of PMAA-*b*-PS diblock copolymers using three different CTAs. CTA1: 4-Cyano-4-thiobutylsulfanyl pentanoic acid (CPP), CTA2: 4-Cyano-4-thiobutylsulfanyl pentanoic acid (CBP), CTA3: 4-Cyano-4-thiobutylsulfanyl pentanoic acid (CDTPA).

2. Materials and Methods

2.1. Materials

The 1-propanethiol (99%, Sigma-Aldrich, Schnelldorf, Germany), 1-butanethiol (>99%, Sigma-Aldrich, Schnelldorf, Germany), 4-cyano-4-thioylthiododecylsulfanyl pentanoic acid (CDTPA) (97%, abcr, Karlsruhe, Germany), MAA (>99%, Merck, Darmstadt, Germany), potassium hydroxide (KOH) (85%, Merck, Darmstadt, Germany), carbon disulfide (CS₂) (99%, Merck, Darmstadt, Germany), *p*-tosyl chloride (98%, Merck, Darmstadt, Germany), 4,4'-azobis(4-cyanovaleric acid) (ACVA) (>98%, Sigma-Aldrich, Schnelldorf, Germany), 1,4-dioxane (99%, Grüssing, Germany), ethanol (99%, VWR Chemicals, Darmstadt, Germany), 1-propanol (PrOH) (99%, Grüssing, Filsum, Germany), *N,N*-dimethylformamide (DMF) (99%, VWR Chemicals, Darmstadt, Germany), tetrahydrofuran (THF) (>99%, VWR Chemicals, Darmstadt, Germany), styrene (99%, Grüssing, Filsum, Germany), dichloromethane (DCM) (>99%, Acros, Schwerte, Germany), acetone (>99%, Merck, Darmstadt, Germany), *n*-hexane (95%, VWR Chemicals, Darmstadt, Germany), chloroform-*d*₁ (>99%, Euriso-Top, Saarbrücken, Germany), THF-*d*₈ (>99%, Euriso-Top), dimethylsulfoxide-*d*₆ (>99%, Germany), deuterium oxide (D₂O) (>99%, Euriso-Top, Saarbrücken, Germany), trifluoroacetic acid (TFA) (99%, TCI Chemicals, Eschborn, Germany), NaHCO₃ (>99%, Grüssing, Filsum, Germany), Mg₂SO₄ (>99%, Grüssing, Filsum, Germany), and activated basic aluminum oxide (>99%, grain size between 0.063–0.200 mm, Merck, Darmstadt, Germany) were used as received without further purification unless noted otherwise. Styrene was purified by filtration through basic activated aluminum oxide to remove the inhibitor. Further, 4-Cyano-4-(propylsulfanylthiocarbonyl)sulfanyl pentanoic acid (CPP) and 4-Cyano-4-(butylsulfanylthiocarbonyl)sulfanyl pentanoic acid (CBP) were synthesized according to the literature (see Sections 2.3 and 2.4). Deionized water was purified with a Milli-Q[®] integral water purification system. The subscripts in the designation of the polymers represent the fraction of the respective block in wt% and the superscript represents the overall molecular weight in kDa.

2.2. General Methods

¹H NMR and ¹³C NMR spectra were recorded at ambient temperature using a 300 or 400 MHz Bruker AVANCE II spectrometer in either CDCl₃-*d*₁, D₂O or THF-*d*₈. The residual signals at $\delta = 7.26$ for CDCl₃-*d*₁, $\delta = 4.80$ ppm for D₂O and $\delta = 3.58$ ppm for THF-*d*₈ were used as an internal standard for the chemical shifts.

Molecular weight distributions of the PMAA homopolymers were measured on a PSS[®] Agilent Technologies 1260 Infinity systems utilizing a SURPREMA[®] column system consisting of a precolumn (8 mm × 50 mm, particle size: 5 μm) and three analytical columns (Column 1: 8 mm × 300 mm, particle size: 5 μm, mesh size: 1000 Å; Column 2: 8 mm × 300 mm, particle size: 5 μm, mesh size: 1000 Å; Column 3: 8 mm × 300 mm, particle size: 5 μm, mesh size: 30 Å). The system was operating with a flow rate of 1.0 mL·min⁻¹ at 50 °C and the injection volume of the polymer solution ($c = 1$ g·L⁻¹) was 100 μL. As water was used as an eluent, calibration was achieved using a series of near-monodisperse poly(ethylene oxide) (PEO) or PAA standards. Molecular weight distributions of the PMAA-*b*-PS diblock copolymer were obtained using THF SEC. Polymer solutions were prepared in THF containing toluene as internal reference. The SEC-set-up comprised an Agilent 1260 Infinity series degasser and pump, a combination of three PSS SDV[®] columns (100 Å, 1000 Å, 10,000 Å) connected in series to both, a refractive index and a UV detector. The system was operating at a flow rate of 1.0 mL·min⁻¹ at 30 °C and the injection volume of the polymer solution ($c = 1$ g·L⁻¹) was 100 μL. Calibration was achieved using a series of near-monodisperse polystyrene standards for diblock copolymers. All diblock copolymers were modified via Steglich esterification [30] using methanol as methylation agent to avoid COOH group interactions with SEC columns [31]. To avoid post modification of the polymer, polymer solutions were also prepared in THF with 5 wt% TFA. This ensures that the acid groups do not interact with the PSS SDV[®] columns of the THF SEC.

Dynamic light scattering (DLS) studies were performed using an ALV/CGS-3 Compact Goniometer system at 25 °C at a scattering angle of 90° with an equilibration time of 120 s. Diblock copolymer solutions were diluted in 0.01 wt% prior to light scattering studies. The intensity-average diameter, derived count rate (CR) and polydispersity (PDI) of the diblock copolymer particles were calculated by the cumulants method. Data were averaged over 3 runs. It should be noted that DLS reports intensity-average diameters and implicitly assumes a spherical morphology.

TEM images were taken with an Eagle™ 4k HS 200 kV camera on a FEI™ Tecnai™ G2 Spirit TWIN instrument in bright field mode, operating at an accelerating voltage of 120 kV. Images were processed with TEM imaging and Analysis Offline 4.7 SO3 (FEI™) software and ImageJ 1.53. Samples were prepared on carbon coated copper grids. Polymer dispersions ($c = 1 \text{ mg mL}^{-1}$) were drop cast onto the TEM grid before excess of solution was blotted with filter paper.

The high-performance liquid chromatography mass spectrometry (HPLC MS) experiments were performed using an Agilent 1200 HPLC instrument and an Agilent 6224 time of flight (ToF) sensor. The sample solution was delivered to the electron spray ionization (ESI) source by a syringe pump at a flow rate of 0.4 mL min^{-1} and an injection volume of $1.0 \mu\text{L}$.

2.3. Synthesis of 4-Cyano-4-Thioylthiopropylsulfanyl Pentanoic Acid (CPP)

CPP RAFT agent was synthesized via a modified procedure adapted from Xu et al. [32]. The 1-Propanethiol (5.0 mL, 0.055 mmol) was added dropwise to a solution of KOH (3.9 g, 0.069 mmol) in 20 mL of water under nitrogen atmosphere. CS_2 (3.3 mL, 0.055 mmol) was added in one portion to the resulting reaction mixture and vigorously stirred for 30 min at room temperature. Afterwards, the reaction mixture was cooled to $-5 \text{ }^\circ\text{C}$ and a solution of *p*-tosyl chloride (5.3 g, 0.028 mmol) in distilled acetone (28 mL) was added in portions over 20 min. After stirring an additional 2 h at $-5 \text{ }^\circ\text{C}$, any acetone residue was removed under reduced pressure. The crude product was extracted with DCM (100 mL) and the organic layer was washed three times with deionized water (50 mL). The resulting solution was dried over anhydrous magnesium sulfate, filtrated, and evaporated to dryness to yield bis(propylsulfanylthiocarbonyl) disulfide as a red oil (7.24 g, 87%). In a second step, ACVA (8.89 g, 31.7 mmol) and bis(propylsulfanylthiocarbonyl) disulfide (4.80 g, 15.7 mmol) were dissolved in ethyl acetate (120 mL) and heated under reflux at $85 \text{ }^\circ\text{C}$ for 24 h. After removal of the volatiles in vacuo, the crude product was purified by column chromatography on silica gel with a mobile phase of *n*-hexane/ethyl acetate (3:1 *v/v*). The product was obtained as an orange powder (4.84 g, 55%). $^1\text{H NMR}$ (400 MHz, CDCl_3, δ): 3.31 (t, $^3J(\text{H,H}) = 6 \text{ Hz}$, 2H, $-\text{S}-\text{CH}_2-\text{CH}_2-\text{CH}_3$), 2.72–2.40 (m, 4H, $\text{COOH}-\text{CH}_2-\text{CH}_2-\text{C}-$), 1.87 (s, 3H, $-\text{C}-\text{CH}_3$), 1.73 (m, 2H, $-\text{S}-\text{CH}_2-\text{CH}_2-$), 0.96 (t, $^3J(\text{H,H}) = 6 \text{ Hz}$, 3H, $-\text{CH}_2-\text{CH}_3$); $^{13}\text{C NMR}$ (400 MHz, CDCl_3, δ): 220 (C=S), 178 ($-\text{COOH}$), 119 ($-\text{CN}$), 46.0 (C^4-CN), 39.2 ($-\text{S}-\text{CH}_2-$), 29.2 ($\text{CN}-\text{C}^4-\text{CH}_2-$), 24.8 ($\text{COOH}-\text{CH}_2-$), 22.5 ($\text{S}-\text{CH}_2-\text{CH}_2-$), 21.3 ($\text{CN}-\text{C}-\text{CH}_3$), 13.5 ($-\text{S}-\text{CH}_2-\text{CH}_2-\text{CH}_3$); HRMS (ESI) m/z : $[\text{M}+\text{H}]^+$ calcd. for $\text{C}_{10}\text{H}_{15}\text{N}_3\text{O}_2\text{S}_3$, 278.0338; found, 278.0342.

2.4. Synthesis of 4-Cyano-4-Thioylthiobutylsulfanyl Pentanoic Acid (CBP)

CBP RAFT agent was synthesized via a modified procedure adapted from Xu et al. [32] 1-Butanethiol (5.26 g, 58.3 mmol) was added dropwise to a solution of KOH (3.86 g, 68.8 mmol) in 25 mL of water under nitrogen atmosphere. CS_2 (4.29 g, 28.5 mmol) was added in one portion to the resulting reaction mixture and vigorously stirred for 30 min at room temperature. Afterwards, the reaction mixture was cooled to $-5 \text{ }^\circ\text{C}$ and a solution of *p*-tosyl chloride (5.24 g, 27.5 mmol) in distilled acetone (35 mL) was added in portions over 20 min. After stirring an additional 2 h at $-5 \text{ }^\circ\text{C}$, any acetone residue was removed under reduced pressure. The crude product was extracted with DCM (100 mL) and the organic layer was washed three times with deionized water (50 mL). The resulting solution was dried over anhydrous magnesium sulfate, filtrated, and evaporated to dryness to yield

bis(butylsulfanylthiocarbonyl) disulfide as a red oil (7.96 g, 82%). In a second step, ACVA (2.34 g, 8.35 mmol) and bis(butylsulfanylthiocarbonyl) disulfide (1.41 g, 4.26 mmol) were dissolved in ethyl acetate (30 mL) and heated under reflux at 85 °C for 24 h. After removal of the volatiles in vacuo, the crude product was purified by column chromatography on silica gel with a mobile phase of petrol ether/ethyl acetate (3:2 *v/v*). The product was obtained as an orange powder (2.14 g, 86%). ¹H NMR (300 MHz, CDCl₃, δ): 3.39–3.28 (m, 2H, –S–CH₂–), 2.74–2.63 (m, 2H, C⁴–CH₂–), 2.62–2.31 (m, 2H, –CH₂–COOH), 1.88 (s, 3H, –C⁴–CH₃), 1.68 (m, 2H, –CH₂–CH₂–CH₃), 1.42 (m, 2H, –CH₂–CH₃), 0.94 (t, ³J(H,H) = 7.3 Hz, 3H, –CH₃). ¹³C NMR (400 MHz, CDCl₃, δ): 217 (C=S), 177 (–COOH), 119 (–CN), 46.6 (–C⁴–CN), 37.2 (–C⁴–CH₂–), 33.9 (–S–CH₂–), 31.3 (–S–CH₂–CH₂–), 29.9 (COOH–CH₂–), 25.3 (–C⁴–CH₃), 22.5 (–S–CH₂–CH₂–CH₂–), 14.0 (–CH₂–CH₃).

2.5. Synthesis of PMAA with CPP or CBP

A typical polymerization of PMAA with CPP as CTA adapted from Chaduc et al. was as follows [21]. MAA (3.6 g, 0.042 mol), CPP (0.097 g, 3.5 × 10^{−4} mol), ACVA (0.0098 g, 3.5 × 10^{−5} mol), water (15 mL) and DMF (0.54 mL, 7.0 × 10^{−3} mol) were added to the reaction flask and purged with nitrogen in an ice bath for 30 min. The sealed reaction flask was immersed into a preheated oil bath for 6 h at 80 °C. The reaction was quenched by exposure to air. Water was removed under reduced pressure, the residual oil re-dissolved in ethanol and precipitated into excess of diethyl ether. Any residual diethyl ether, water, or ethanol was removed by drying the precipitate in vacuo at room temperature for 24 h. The conversion was determined by ¹H NMR spectroscopy in D₂O.

2.6. Synthesis of PMAA with CDTPA

A typical polymerization of PMAA with CDTPA as CTA modified from Chaduc et al. was as follows [21]. MAA (2.4 g, 0.028 mol), CDTPA (0.093 g, 2.3 × 10^{−4} mol), ACVA (0.012 g, 4.6 × 10^{−5} mol), ethanol (15 mL) and DMF (0.35 mL, 4.6 × 10^{−3} mol) were added to the reaction flask and purged with nitrogen in an ice bath for 30 min. The sealed reaction flask was immersed into a preheated oil bath for 6 h at 80 °C. The reaction was quenched by exposure to air. The polymer solution was precipitated into excess of diethyl ether. Any residual diethyl ether or ethanol was removed by drying the precipitate in vacuo at room temperature for 24 h. The conversion was determined by ¹H NMR spectroscopy in DMSO-*d*₆.

2.7. One-Pot Synthesis of PMAA-*b*-PS with CPP or CBP

A typical polymerization of PMAA-*b*-PS with PMAA-CPP as macro-CTA was adapted from Chaduc et al. as follows [21]. MAA (3.4 g, 0.040 mol), CPP (0.055 g, 2.0 × 10^{−4} mol), ACVA (0.0056 g, 2.0 × 10^{−5} mol), 14 mL water and DMF (0.48 g, 6.7 × 10^{−3} mol) were added to the reactions flask and were purged with nitrogen in an ice bath for 30 min. The sealed reaction flask was immersed into a preheated oil bath for 6 h at 80 °C to reach full conversion. The reaction was quenched by exposure to air. A sample was taken for ¹H NMR spectroscopy in D₂O and SEC measurements in THF. A solution of styrene (8.3 g, 0.080 mol), ACVA (0.011 g, 4.0 × 10^{−5} mol), and NaHCO₃ (0.012 g, 1.4 × 10^{−5} mol) in water (32 mL) was added to the reaction mixture, degassed with nitrogen for 30 min and immersed into a preheated oil bath for 2 h at 80 °C. After cooling to room temperature, water was removed under reduced pressure, the crude product re-dissolved in THF and precipitated into excess *n*-hexane. Any residual solvent was removed by drying the precipitate in vacuo at room temperature for 24 h. The conversion was determined by ¹H NMR spectroscopy in THF-*d*₈.

2.8. Synthesis of PMAA-*b*-PS with CDTPA

A typical polymerization of PMAA-*b*-PS with PMAA-CDTPA as macro-CTA was adapted from Chaduc et al. as follows [21]. A solution of styrene (1.35 g, 0.013 mol), ACVA (0.0036 g, 1.3 × 10^{−5} mol), and NaHCO₃ (0.0038 g, 4.6 × 10^{−5} mol) and PMAA₁₂₀-CDTPA (0.32 g, 6.5 × 10^{−5} mol) in water (2.5 mL) was added to the reaction flask, degassed with

nitrogen for 30 min and immersed into a preheated oil bath for 2 h at 80 °C. After cooling to room temperature, water was removed under reduced pressure, the crude product re-dissolved in THF and precipitated into excess *n*-hexane. Any residual solvent was removed by drying the precipitate in vacuo at room temperature for 24 h. The conversion was determined by ¹H NMR spectroscopy in THF-*d*₈.

2.9. Determination of the Molecular Weight

The theoretical molecular weights of all polymers are calculated from the following Equation (1):

$$M_{n,th} = \frac{[M]_0 \cdot p \cdot M_M}{[CTA]_0} + M_{CTA} \quad (1)$$

where $[M]_0$ and $[CTA]_0$ are the initial concentrations of monomer and chain transfer agent, p the monomer conversion and M_M and M_{CTA} are the molar masses of monomer and chain transfer agent. It follows that the molar mass increases linearly with conversion, assuming that all CTAs have reacted. The degree of polymerization (DP) is defined by the ratio of monomer to RAFT agent since most polymer chains are created from initiation by the R group of the RAFT agent [5,33].

3. Results and Discussion

3.1. Kinetics of the Homopolymerization of PMAA

The synthesis of PMAA-*b*-PS diblock polymers was performed according to the previous work of Chaduc et al. where the CTA1 was used and different pH-values, solvents, concentrations and reaction times were studied [34]. CTAs with a trithiocarbonate group were proven to be less prone to hydrolysis [35]. A carboxylic acid group was chosen as the R group of the RAFT agent, since it is similar to the structure of MAA, which will be polymerized as the hydrophilic block (see Figure 1). The R group was chosen to be a tertiary radical leaving group which is stable enough to allow both monomer addition and the cleavage process of the pre-equilibrium step of the RAFT mechanism. In here, we used three different CTAs with a trithiocarbonate group containing a *n*-propyl-, *n*-butyl- and *n*-dodecyl- terminus as a Z group to adjust the hydrophilicity of the CTA so that a good balance between the solution and emulsion RAFT polymerization in terms of solubility, reaction time, and latex stability is achieved.

The first series of MAA RAFT solution polymerizations was conducted with CTA1 in water, 1,4-dioxane and ethanol. The CTA1 showed a high effectivity in RAFT polymerizations of methacrylate monomers leading to properly controlled living chains [32]. The polymerization was conducted at 70 °C. The other reaction conditions such as the initial concentration of MAA, initiator and RAFT agent were kept constant. The polymerization of MAA with CTA1 in ethanol led to an inhibition period of 1 h, while the polymerization in 1,4-dioxane and water led to measurable monomer consumption already after 1 h. Almost full conversion in water was observed in less than 4 h, while the polymerization in 1,4-dioxane led to 75% (4 h) and in ethanol to only 48% conversion after 5 h (Figure 2). Similar observations were found in the publication of Chaduc et al. In this publication, methanol was used instead of ethanol, however, comparable results were obtained with a conversion of 59% after 7 h [34].

Although higher experimental $M_{n,exp}$ were verified compared to the theoretical values, a linear trend of M_n with conversion was achieved (Figure 3). The higher $M_{n,exp}$ values are not surprising since the values were measured via SEC against PEO standards. Relatively low dispersities were confirmed in all solvents, although using water led to the lowest dispersity for the PMAA polymerization with CTA1 ($M_w/M_n = 1.07$).

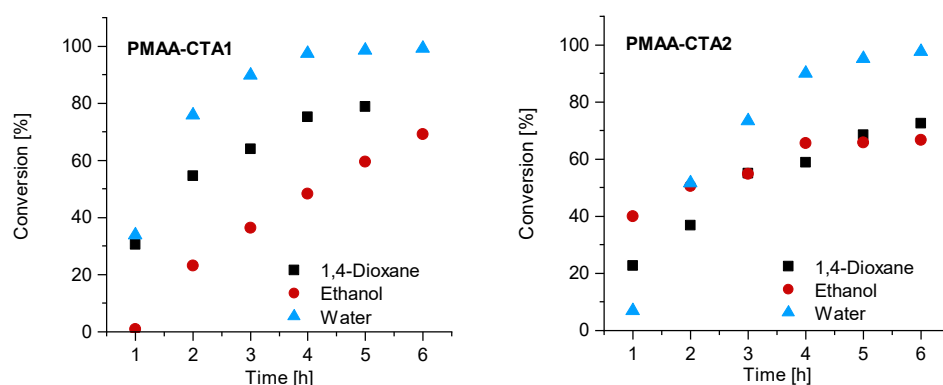


Figure 2. Reaction time versus conversion of the RAFT polymerization of PMAA with CTA1 (left) and CTA2 (right) with a molar ratio of $[MAA]/[CTA] = 120$ and $[CTA]/[ACVA] = 10$.

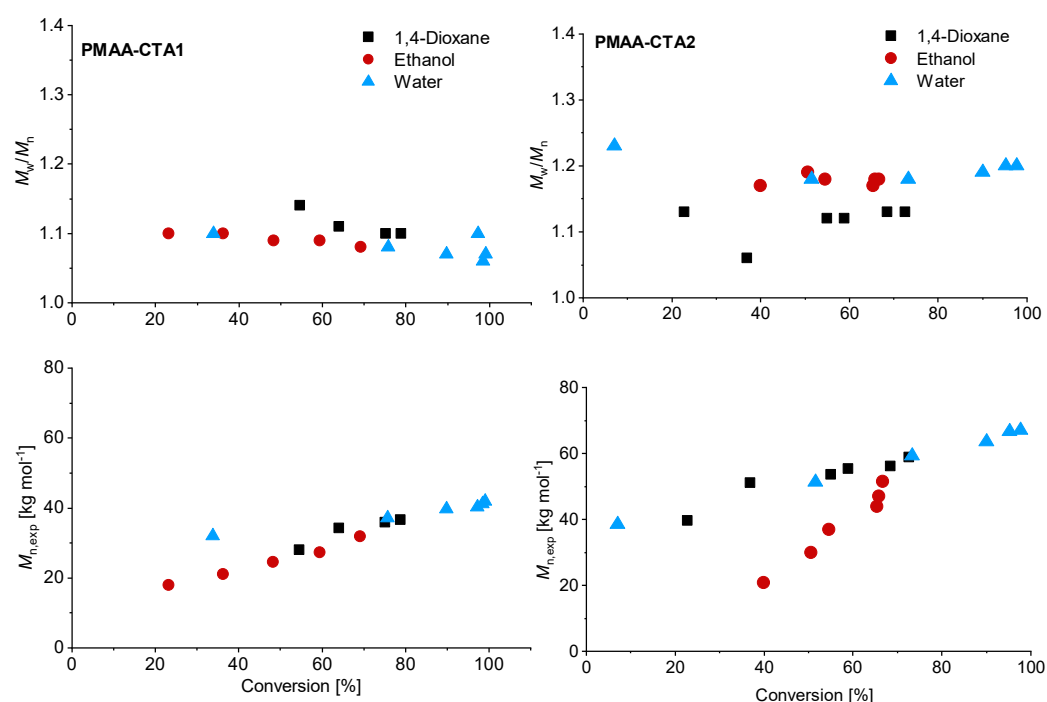


Figure 3. Reaction time versus conversion of the RAFT polymerization of PMAA with CTA1 (left) and CTA2 (right) with a $[MAA]/[CTA] = 120$ and $[CTA]/[ACVA] = 10$. The SEC results were measured in an aqueous set up with PEO standards.

Similar observations were made for the polymerization with CTA2. The inhibition period changed for water to 1 h while the polymerization in ethanol confirmed measurable monomer consumption at this time. These observations are not surprising, since the CTA2 is more hydrophobic and therefore less soluble in water. This results in a lower reaction rate and longer inhibition phase, since fragmentations proceed more slowly. However, after 6 h almost full conversion in water was confirmed. The polymerization in ethanol led to just 67% conversion and in 1,4-dioxane to 73% conversion. SEC measurements showed narrow molar mass distributions in all cases and can be found in Figure 3. An overview about the PMAA polymerization of CTA1 and CTA2 can be found in the Supplementary Information (Table S1). Since all polymerizations showed narrow dispersities, it can be concluded that the solvent has a strong impact on the kinetics, however, the dispersity is less affected.

So far, the PMAA polymerization in water showed the fastest reaction rates and the narrowest molar mass distribution. Kuchta et al. investigated the effect of the propagation rate coefficient k_p in dependency of the solvent [36,37]. MAA tends to self-associate in

bulk forming cyclic dimers. In organic media, however, this self-association step has to compete with the monomer-solvent complexes. This is caused by the hydrogen bonds between the carboxylic groups of monomers and the polar solvent. This self-association in organic media is more pronounced than in water, leading to a higher activation energy and therefore to reduced reaction rates in organic media compared to water [36,37].

In case of the CTA3, water is a non-solvent. Therefore, polymerization with CTA3 was conducted in ethanol, 1-propanol and 1,4-dioxane at 70 °C and 80 °C. For the experiments at 80 °C a [CTA]/[ACVA] ratio of 5 and 10 was investigated. A targeted DP of 120 was adjusted for all experiments (Figure 4). The polymerizations at 70 °C led to low conversions and only in the case of 1,4-dioxane to a conversion of 75% after 19.5 h. To increase the reaction rate and thus the conversion, the reaction temperature was increased to 80 °C. The reaction rates of the polymerizations in ethanol and 1-propanol indeed increased and resulted in the inhibition phase being shortened and conversion being generated after only one hour. However, the conversion was below 50% in all cases. Increasing the initiator concentration to double the initial amount leads to fast reaction rates and high conversions after 4 h. The polymerizations in 1-propanol and 1,4-dioxane show the best reaction conditions, most probably due to better solubilization of the CTA. It should be noted that in case of the polymerization in 1,4-dioxane there were considerable viscosity problems, and it was therefore no longer possible to take samples after 4 h. The polymerization of PMAA with CTA3 in 1-propanol was the most promising reaction with conversions of approximately 80% within 4 h.

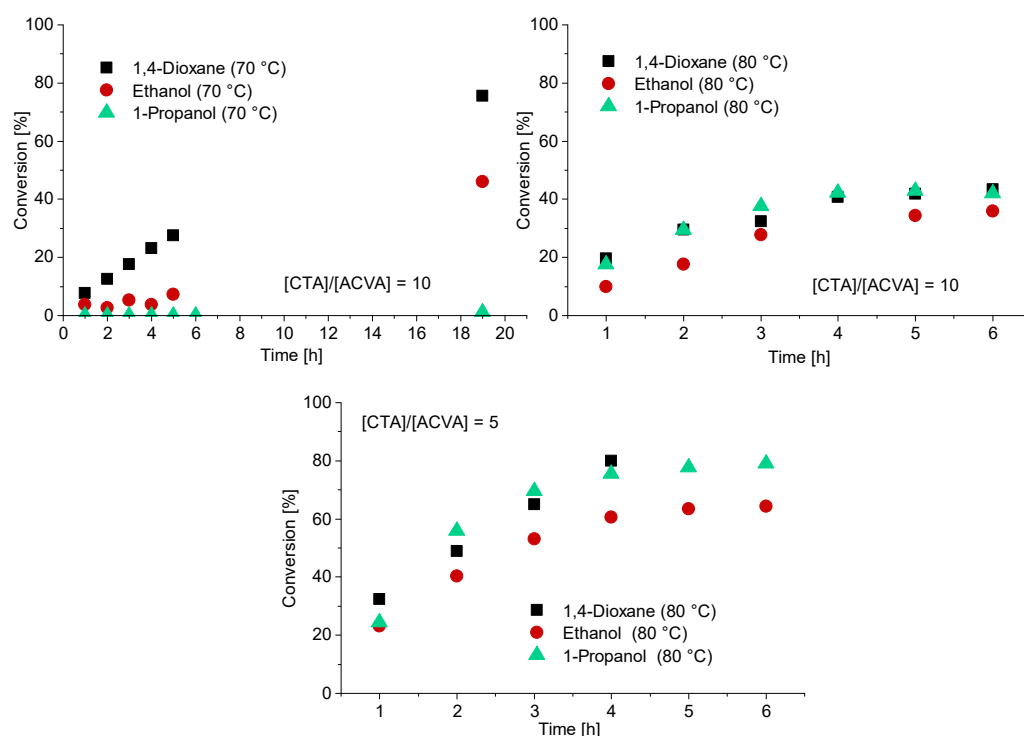


Figure 4. Reaction time versus conversion of the RAFT polymerization of PMAA with CTA3 and a targeted DP of $[MAA]/[CTA3] = 120$ and a molar ratio of $[CTA3]/[ACVA] = 10$. For the polymerizations at 80 °C a kinetical study with a molar ratio of $[CTA3]/[ACVA] = 10$ and 5 is displayed.

SEC measurements showed a linear relationship between conversion and molecular weight in all cases (Figure 5). The polymerization of PMAA with CTA3 in 1-propanol with a $[CTA]/[ACVA]$ molar ratio = 5 at 80 °C showed so far the best reaction conditions and control (molar mass distribution ($M_w/M_n = 1.09$)). A detailed overview can be found in Table S2.

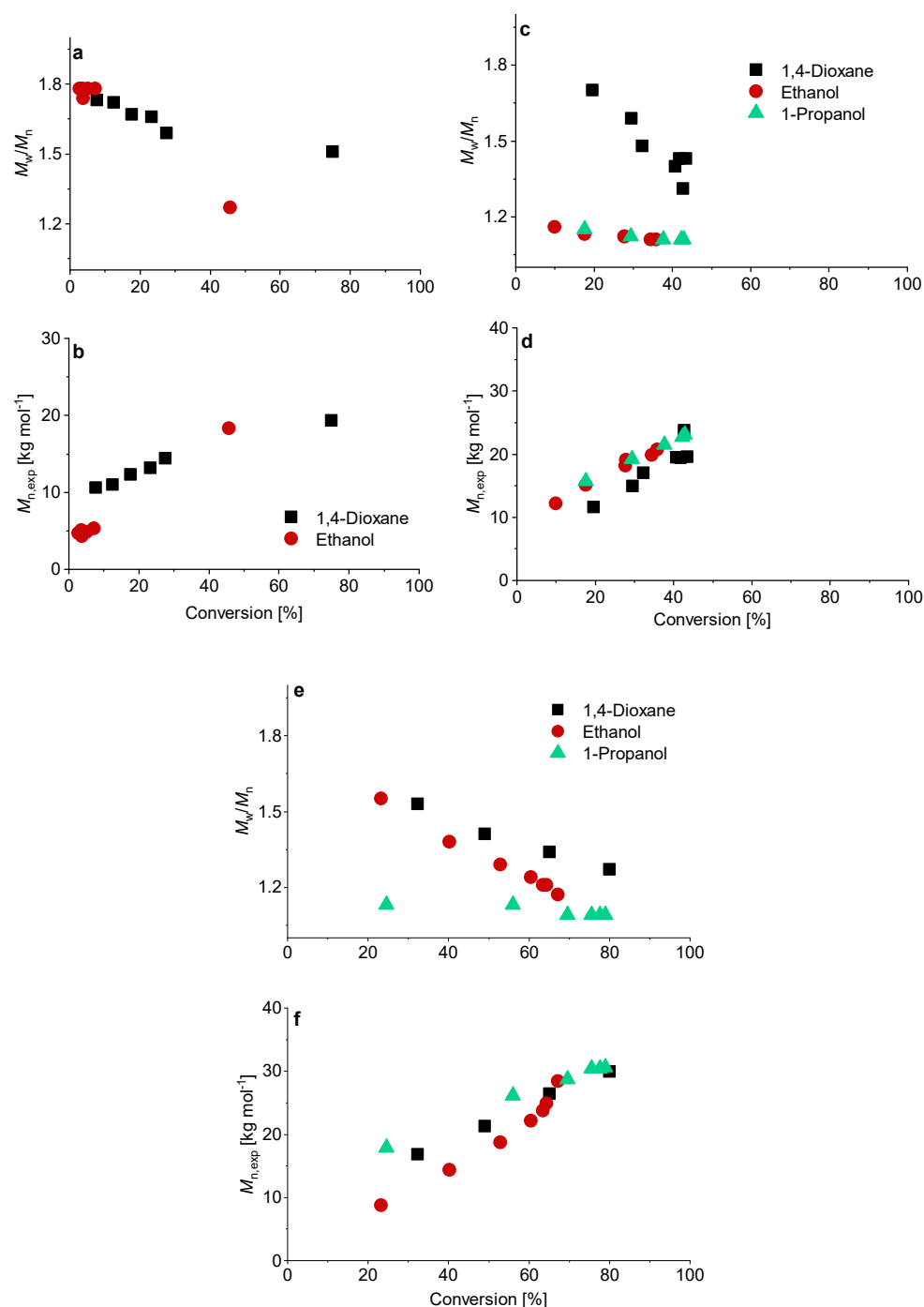


Figure 5. Conversion versus experimental number-average molar mass $M_{n,exp}$ and M_w/M_n of the RAFT polymerization of PMAA with CTA3 and a targeted DP of $[MAA]/[CTA] = 120$ and a molar ratio of $[CTA]/[ACVA] = 10$ at 70 °C (a,b). For the polymerizations at 80 °C a kinetical study with a molar ratio of $[CTA]/[ACVA] = 10$ (c,d) and 5 (e,f) is presented.

Briefly, the polymerizations of MAA with CTA1 and CTA2 show the best reaction conditions in water. Both polymerizations have the advantage that they can be carried out in a green solvent. However, as a stabilizer block for the styrene polymerization, these blocks can reach their limit above a certain concentration of styrene, since these stabilizer blocks are not hydrophobic enough to stabilize the latex above a certain concentration. Therefore, the synthesis of the PMAA stabilizing block with CTA3 is a good alternative for the styrene polymerization. In the following, the influence of the three different stabilizer blocks in the emulsion polymerization of styrene will be investigated in detail.

3.2. Kinetics of the Synthesis of PMAA-*b*-PS with CTA1 via RAFT Emulsion Polymerization

The synthesis of the second block of PMAA-*b*-PS was conducted via RAFT emulsion polymerization in water. The PMAA homopolymer was used as both controlling and stabilizing agent. It is worth mentioning that the polymerization of the second block with CTA1 and CTA2 can be conducted in a one-pot synthesis, since the RAFT solution and emulsion polymerization can both be performed in water and since polymerization in the first step reaches full conversion. Several investigations on the one-pot synthesis with CTA1 have already been published [21–23,38]. Within a few hours, a diblock copolymer in water can be synthesized without intermediate precipitation steps of the homopolymer.

One of the advantages of the emulsion polymerization is the good heat transfer and low viscosity even at higher molecular weights, therefore, this technique was chosen to produce polymers with high molecular weights with the lowest possible by-products and low energy consumption.

The main work focused on the results of Chaduc et al. [21] conducting the reactions at a pH value of 2.5 and a [CTA]/[ACVA] molar ratio of 5. In a typical emulsion experiment, the macro-RAFT agent, ACVA and NaHCO₃ (increases the water solubility of ACVA) were dissolved in water. Afterwards, styrene was added to the reaction, which was proceeded at a pH of 2.5 and a [CTA]/[ACVA] molar ratio of 5. The first experiments were conducted with CTA1 and a solid concentration of 20 wt%. The molar weight fraction of styrene was targeted to be 95% (PMAA₅-*b*-PS₉₅⁵⁴). Samples were taken after 30, 35, 40, 45, 50, 55, 60, and 120 min. An inhibition period of around 30 min can clearly be seen (see Figure 6).

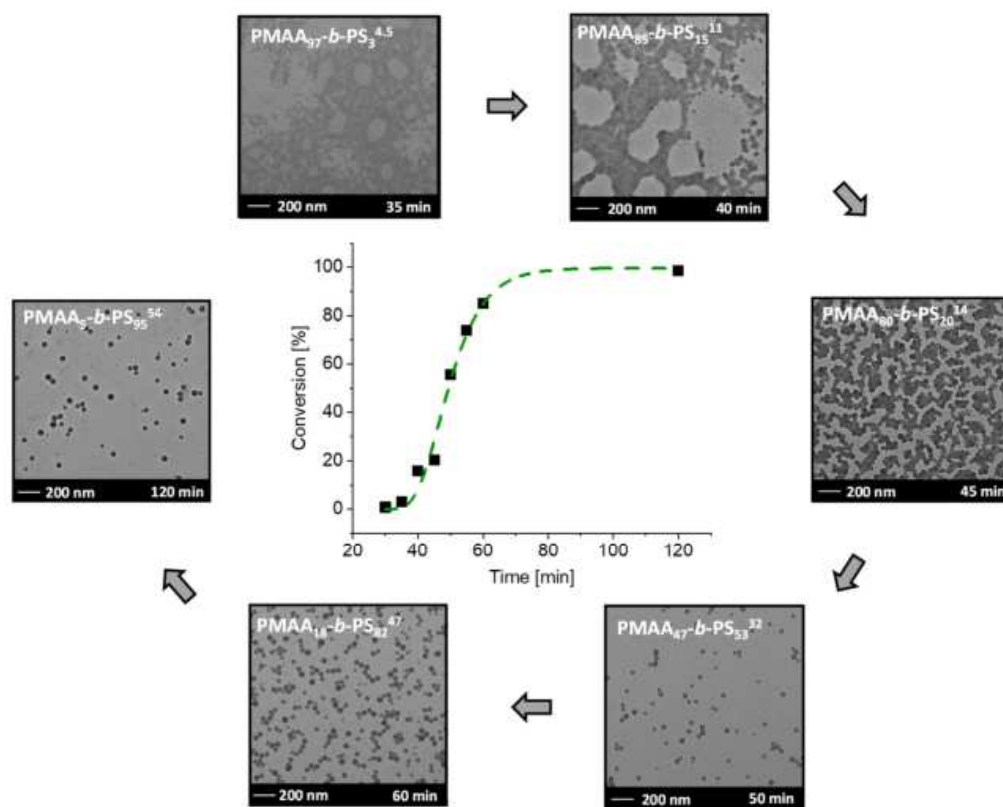


Figure 6. Conversion versus reaction time of the RAFT emulsion polymerization of PMAA₅-*b*-PS₉₅⁵⁴ with CTA1 and a targeted DP of [MAA]/[CTA] = 30 and [Sty]/[CTA] = 502 and a molar ratio of [CTA]/[ACVA] = 5 at 80 °C and the corresponding TEM images after a specific time. The subscripts in the designation of the polymers represent the molar fraction of the respective block in wt% and the superscript represents the overall molecular weight in kDa.

The inhibition period is described as the time, where no monomer conversion is obtained. More precisely, it is the time of the radical transfer to the MAA groups of the RAFT

agent or the exit of the (macromolecular) R groups from the RAFT agent [39,40]. Before micellar nucleation the chain growth is slow as it can be seen during the time between 30–45 min. After micellar nucleation the polymerization rate increases drastically as demonstrated from the samples withdrawn after 45 and 50 min. The conversion increased by 36% in just 5 min. Therefore, it can be concluded that the micellar nucleation is finished after 40–45 min approximately. The fast conversion is due to the mechanistic transition from macro-CTA polymerization in the aqueous phase to macro-CTA polymerization in the micelles after reaching a critical PS block length. Full conversion is achieved within 2 h reaction time.

With time, conversion, molecular weight M_n and the radius of the micelles increased (Table S3). After full conversion a molecular weight of $M_{n,theo} = 54.4$ kDa (calculated according to the determined conversion from NMR spectroscopy, see Equation (1) in the experimental section), a micelle radius of 29 ± 3 nm and a dispersity M_w/M_n of 1.33 was achieved, proving a good control of the emulsion polymerization. Even at a very low molar weight ratio of just 5 wt% of the PMAA stabilizer block, stable micelles were clearly obtainable. They, furthermore, did not coalesce as is visible in the TEM images (Figure 6). Similar morphologies were observed for PMAA₃-*b*-PS₉₇¹⁰⁷ with the same macro-CTA with a targeted DP of $[MAA]/[CTA] = 30$ and $[Sty]/[CTA] = 1002$. The resulting $M_{n,theo}$ was obtained with 102 kDa, a M_w/M_n of 1.42 and a micelle radius of 41 ± 3 nm for diblock copolymer. Clearly, the size of the micelles increases with higher molecular weight. Even though other morphologies are thermodynamically more favorable according to the packing parameter [41], kinetically-trapped spheres result almost in all cases using polystyrene as a major block even though highly asymmetric diblock compositions are targeted [20,22,24,42,43]. The only exception was the synthesis of PMAA₄₀-*b*-PS₆₀⁴⁶ at 20 wt% prepared in a one-pot reaction using CTA1. Besides spherical particles, also worm-like micelles were observed. The corresponding TEM image can be found in the Supplementary Information (Figure S9). In previous publications, other morphologies such as fibers and vesicles were observed using a PMAA-*co*-PEO macro RAFT agent [44,45]. The ionization degree of PMAA as well as the molar mass played a crucial role in the transition of these morphologies. E.g., fiber morphologies were observed at a weight ratio from hydrophilic to hydrophobic of 70/30 to 80/20 at a pH of 5 [44,45]. In our case, a PMAA₄₀-*b*-PS₆₀⁴⁶ diblock copolymer was synthesized with a weight fraction of the hydrophilic block of 60% at a pH of 2.5. In here, we can assume that only a low number of PMAA units were ionized, therefore the block is less hydrophilic than in the case of pH = 5. However, the weight fraction of the hydrophilic block was higher than in the cases of the literature where other morphologies than spheres were observed. Obviously, the ratio of the hydrophilic block as well as the degree of ionization play an important role to obtain other morphologies [44–46]. The previous experiments showed that polymerizations at a solid concentration of 20 wt% were well controlled even at high DPs of styrene. In the next step, the solid content of the emulsion polymerization (and hence also of the resulting dispersion) is investigated. The question is thus: how much water can actually be saved within the emulsion while still ensuring a well-controlled polymerization? Consequently, the PMAA chain extension at high solid concentrations is analyzed for each CTA system.

The PMAA₁₀-*b*-PS₉₀⁴⁵ polymerization with PMAA-CTA1 (DP = 50, $M_w/M_n = 1.25$) was conducted at 20, 25 and 30 wt% in water at 80 °C. An overview of all emulsion polymerizations can be found in the Supplementary Information, Table S11. For all experiments a targeted styrene DP of 400 and a targeted $M_{n,theo}$ of 45 kDa was set. A kinetic study of the synthesis showed that the polymerization in 20 and 25 wt% reached full conversion within 2 h, however the polymerization at 30 wt% reached less than 30% conversion after 5 h (Figure 7). Spherical morphologies were observed in all experiments. SEC data as well as information about the morphology and the size of the particles can be found in Tables S4–S6 and the TEM images in Figures S1–S3.

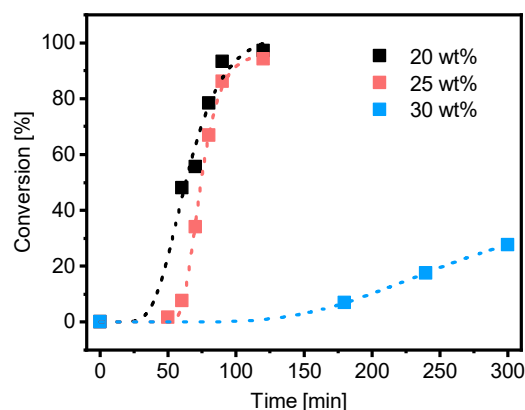


Figure 7. Conversion versus time of the RAFT emulsion polymerization of PMAA₁₀-*b*-PS₉₀⁴⁵ with CTA1 and a targeted DP of [Sty]/[CTA] = 400 and a molar ratio of [CTA]/[ACVA] = 5 at 80 °C and a solid concentration of 20, 25 and 30 wt%.

Polymerization of PMAA-*b*-PS with PMAA-CTA1 as a stabilizer at a solid concentration of 30 wt% shows a very slow polymerization rate. The RAFT stabilizing agent with a propyl group is probably still too hydrophilic to polymerize such a large concentration of styrene. An illustration of the RAFT emulsion polymerization with a hydrophobic and a hydrophilic RAFT agent can be seen in Figure 8. Generally, the emulsion polymerization is divided into three stages: the formation of micellar particles, the polymerization within the micelles and the consumption of the residual monomer in the micelles when the bigger droplets have vanished (Stage III is not shown in Figure 8). In a typical RAFT emulsion polymerization, the emulsion consists of a water-immiscible monomer, a water-soluble initiator, a macro-CTA as a stabilizer (replacing the surfactant in a conventional emulsion polymerization) and water. The monomer droplets have a size of approximately 10 μm and a number density of around 10¹²–10¹⁴ dm^{−3} in the aqueous medium. In case the concentration of the stabilizer block is higher than the critical micelle concentration (CMC), which is mostly the case for micellar nucleation, also micelles are present in the system with a size of approximately 5–10 nm and a number density of around 10¹⁹–10²¹ dm^{−3}.

In case for a hydrophobic RAFT agent, the water-soluble initiator (in here ACVA) starts the polymerization and reacts with monomers (here styrene) in the continuous phase to form oligomer radicals which can either enter preexisting micelles or form new ones. The polymerization was conducted under acidic conditions, in order to form hyper-coiled structures of PMAA that intrinsically contain hydrophobic domains and thus enhance the local styrene concentration in the vicinity of the PMAA macro-RAFT [21,47]. The particle number increases in the first stage as the micelles convert into particles and the rate of polymerization increases due to an increase in the number of polymerization loci. By the end of Stage I all free macro-CTA chains are located in micelles and particle nucleation stops. Stage II sets in when only monomer droplets and polymer particles are present in the system. The polymerization continues inside the particles with monomer migration from the monomer droplets through the aqueous phase into polymeric particles to refill the polymerized monomer. As a result, a steady state between the monomer migration rate and the polymerization rate is accomplished, making the monomer concentration in the polymer micelles constant. The active radical within the particle keeps growing until it terminates upon entry of another radical or until it exits the particle into the aqueous phase. As this process is especially unlikely in the later periods of Stage II, the particles increase in size due to further absorption of monomer and an increase of chain length. At the end of Stage II, all monomer droplets disappear and the leftover monomer in the loci of polymerization is consumed (Stage III). The concentration of the remaining monomer in the polymer particles hence decreases with an increase in conversion, viscosity, and polymer volume fraction. At high conversions, propagation and termination become diffusion controlled, resulting in a speed up of the polymerization rate. Moreover, exit

of the small radical becomes less likely, thereby allowing the particles to have more than one active radical without terminating instantly. Eventually, the propagation rate slows down (due to monomer depletion) resulting in a decrease of the rate of polymerization. The polymerization ends as almost all of the monomer is depleted [40,48–52].

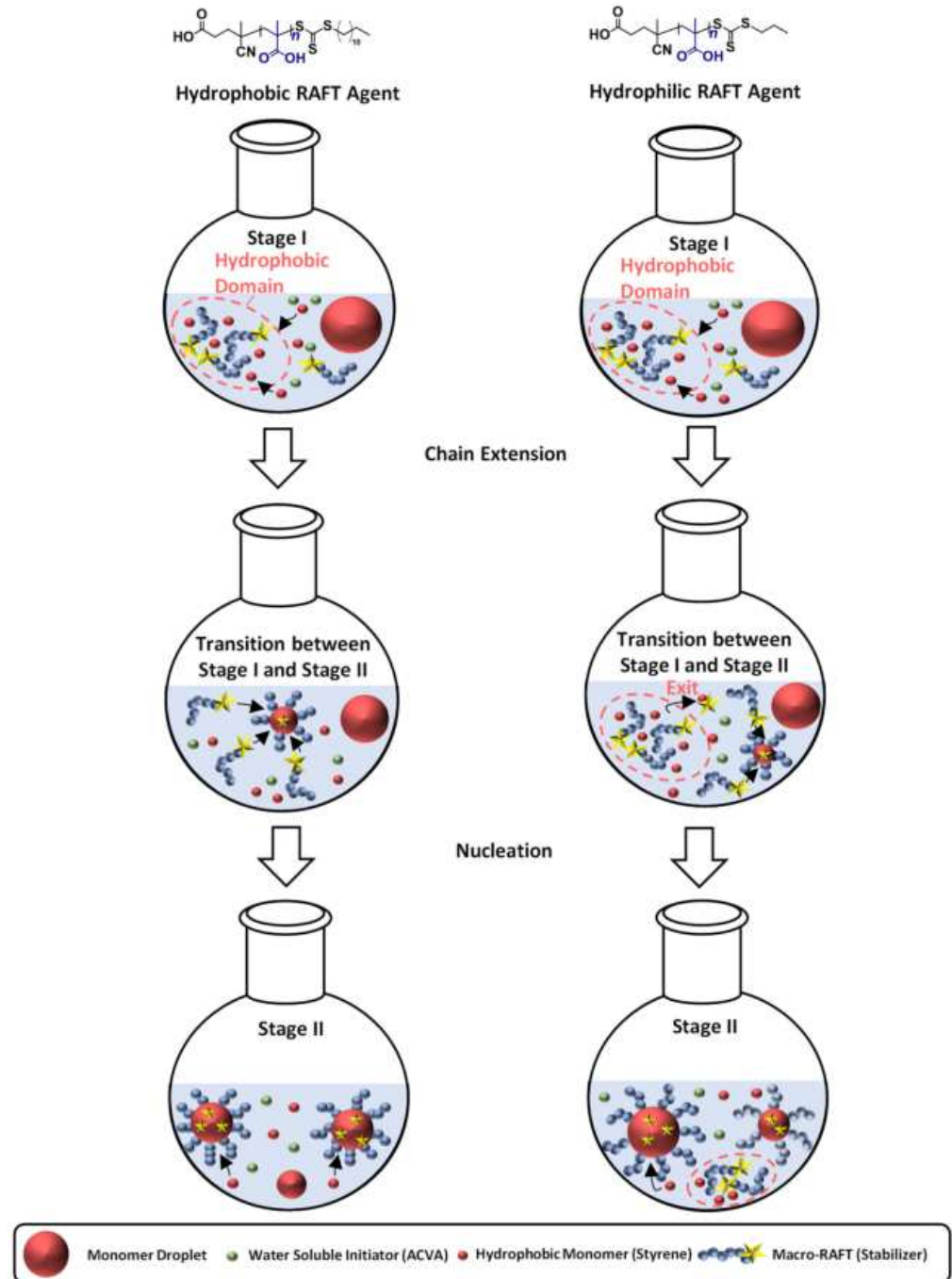


Figure 8. Illustration of the particle formation during an emulsion polymerization for a hydrophilic and hydrophobic RAFT agent as stabilizer with the three characteristics steps. Stage I shows the formation of micellar particles, Stage II the polymerization within the micelles and the transition state between both stages. The blue chains represent the stabilizing chain, the red chain the hydrophobic chain, the green circles label the initiator, the yellow star represents the active RAFT group, and the big red circles represent monomer swollen particles.

In case of a hydrophilic RAFT agent, for example the CTA1 at very high solid concentrations of styrene (above 30 wt%), slow nucleation and polymerization occurs. The group

of Zetterlund et al. described that this phenomenon is caused by the Z-group induced RAFT exit [53]. The Z-group RAFT species is produced by the addition of a radical, entering a precursor particle and fragmentation afterwards to create a PMAA radical (pre-equilibrium of the RAFT mechanism, see Figure 9). The hydrophilic RAFT species, in case only a few units of styrene were added, might exit the hydrophobic domains (shown in Figure 8) due to their different polarities. The loss of RAFT agent from the polymerization loci reduces the chain extension rate, thus, less amphiphilic chains will be created, which impact the colloidal stability negatively, leading to larger and fewer particles [53].

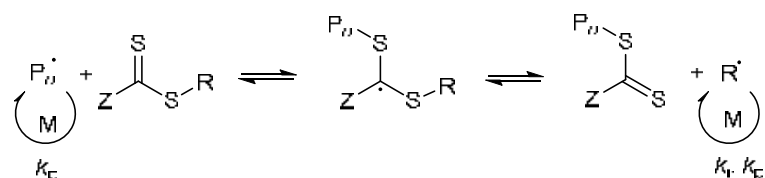


Figure 9. Illustration of the pre-equilibrium of the RAFT mechanism.

In previous publications, some authors have described the long inhibition period as well as no polymerization in a RAFT emulsion polymerization due to the exit of the radical R^{\bullet} from the particle (R group cleavage of the RAFT agent in the pre-equilibrium step of the RAFT mechanism), where it can terminate in the aqueous phase with another initiator-derived radical or after reentry with a growing chain in a particle [40,54–57]. If this is the case, some particles will lose the propagating radical and need to be reinitiated again. This effect results in a lower number of particles [57]. The main difference between the R- and Z-group exit is that the R-group exit does not contain the RAFT functionality. The functionality remains in the particles.

The successfully controlled emulsion polymerization with more hydrophobic RAFT agents for the system of PAA-*b*-PS/PMAA-*b*-PS or similar polymer systems from previous publications (mentioned above) gave us incentive to use more hydrophobic RAFT agents as well and thus achieve polymerizations at higher weight percentages of the hydrophobic second monomer. To the best of our knowledge, no PMAA-*b*-PS polymers have yet been carried out at high solid concentrations above 30 wt%. In the following, the propyl group as the Z-group is exchanged with a butyl and dodecyl terminus.

3.3. The Synthesis of PMAA-*b*-PS with CTA2 via RAFT Emulsion Polymerization

The polymerization of PMAA₂₀-*b*-PS₈₀⁴⁶ with PMAA macro-CTA2 was conducted at 35 and 40 wt% in water. Since the PMAA-CTA2 as well as the PMAA-*b*-PS polymer can be synthesized in water, a one-pot polymerization can be conducted. A DP of [Sty]/[CTA] = 360 was targeted. Compared to the PMAA₁₀-*b*-PS₉₀⁴⁵ diblock copolymer with CTA1, the polymerization reached full conversion even at higher solid concentrations than 30 wt%. After 4 h, full conversion was achieved in all experiments. However, the polymerization at 40 wt% with CTA2 was very viscous after full conversion (see Figure S11). The SEC, DLS and TEM data can be found in Table 1. Very large particle radii of 85 nm and 96 nm were synthesized for 35 wt% and 40 wt% as measured by DLS, when replacing the propyl Z-group with a butyl Z-group. These results fit to the proposed mechanism from Zetterlund et al., which was also shown in Figure 8 for hydrophilic RAFT agents [53]. However, the very large deviation of $M_{n,exp}$ from $M_{n,theo}$ infers a not well-controlled polymerization. Therefore, the Z-group was further modified with a dodecyl terminus.

Table 1. Polymerization of PMAA₂₀-*b*-PS₈₀⁴⁶ with CTA2 at 80 °C in water and a targeted styrene DP of 360 with a [CTA2]/[ACVA] molar ratio of 5. All reactions were polymerized for 4 h. r_{TEM} represents the number-average radius obtained by TEM and r_{DLS} by DLS. $M_{\text{n,theo}}$ represents the theoretical number-average molecular weight of PMAA-*b*-PS. The dispersity $M_{\text{w}}/M_{\text{n}}$ was determined by SEC THF + 50 mmol TFA using universal PS calibration. The PMAA-CTA2 macro-CTA was determined with NMR and aqueous SEC using PEO calibration with $M_{\text{n,theo}} = 8.7$ kDa and a $M_{\text{w}}/M_{\text{n}} = 1.17$.

(<i>w/w</i>) Solids [%]	Conversion [%]	r_{TEM} [nm]	r_{DLS} [nm]	PDI	$M_{\text{n,theo}}$ [kDa]	$M_{\text{n,exp}}$ [kDa]	$M_{\text{w}}/M_{\text{n}}$
35	99	61 ± 4	85.3 ± 0.5	0.09 ± 0.03	46	166	1.57
40	99	70 ± 5	96 ± 2	0.3 ± 0.2	46	158	1.61

3.4. The Synthesis of PMAA-*b*-PS with CTA3 via RAFT Emulsion Polymerization

The polymerization of PMAA-*b*-PS with a CTA using a dodecyl terminus as a Z-group was tested. This CTA is more hydrophobic than CTA1 and CTA2. The R-group was not modified in any experiment. At first a diblock copolymer with a lower molecular weight was targeted. The synthesis of PMAA₂₀-*b*-PS₈₀¹⁸ with CTA3 (DP = 43, $M_{\text{w}}/M_{\text{n}} = 1.11$, $M_{\text{n,theo}} = 3.8$ kDa) at 80 °C in water and a targeted styrene DP of 200 with a CTA3/ACVA molar ratio of 5 was carried out at 40 and 50 wt% solid concentration. Almost full conversion was achieved for both reactions already within 80 min (Figure 10). The hydrodynamic radius r_{DLS} increases linearly with conversion. The final dispersity $M_{\text{w}}/M_{\text{n}} = 1.23$ for both polymerizations indicate a good control over the polymerization. More detailed information can be found in the Supplementary Information, Table S7 and Figures S4 and S5.

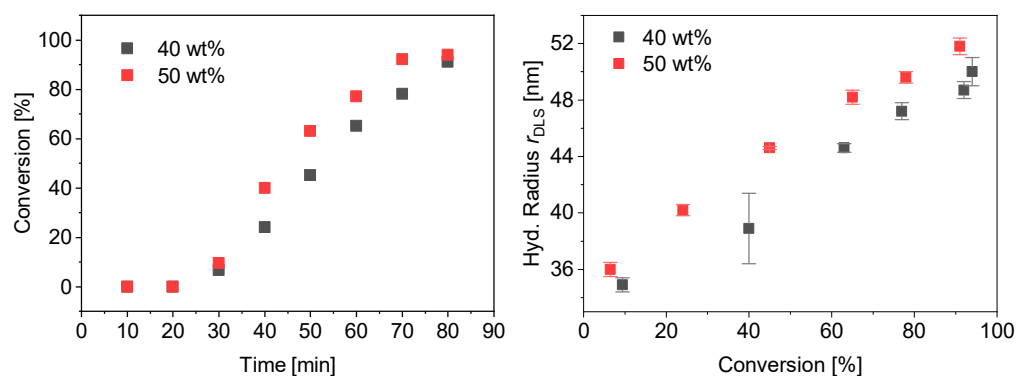


Figure 10. Conversion vs. time data for PMAA₂₀-*b*-PS₈₀¹⁸ with CTA3 at 40 wt% and 50 wt% (left) and average hydrodynamic radius measured by DLS against the conversion (right).

Since the polymerizations at 40 wt% as well as at 50 wt% worked in a controlled and fast manner, polymerizations were carried out at 50 wt% increasing the weight fraction of styrene as well as the total molecular weight. Three different block copolymer compositions were targeted with a weight fraction of 80%, 90% and 95% of styrene using the same macro-CTA3 in all experiments (DP = 95, $M_{\text{w}}/M_{\text{n}} = 1.09$, $M_{\text{n,theo}} = 8.5$ kDa). The kinetic data of the polymerization rate and DLS measurements can be found in Figure 11. More detailed information about the morphology, SEM and TEM results can be found in Tables S8–S10 and Figures S6–S8. A well-controlled polymerization for the reaction with 50 wt% solid content and 80 wt% fraction of styrene was observed. Complete conversion was obtained after 2 h and a dispersity of $M_{\text{w}}/M_{\text{n}} = 1.22$ was achieved. RI und UV detection of the SEC measurement overlapped proving that majority of the chains containing the RAFT group indicating successful chain extension (see Figure S10). The radius of the spherical particles increases linearly with conversion (Figure 10). As described for the mechanism before, the effect of the Z-group plays a significant role in the rate of emulsion polymerization. Both our results and those of Zetterlund et al. confirm the mechanism assumed above. Polymerizations with 90 and 95 wt% styrene resulted in conversions of 60% and 13% after 3 h, respectively. The polymerization of emulsions at 50 wt% requires a good stability of the

colloids which, even with commercial surfactants, must ensure an extremely good control of the reaction and reach their limit. In this work it was shown that polymerization by RAFT with hydrophobic RAFT agents allows such a polymerization in a controlled manner.

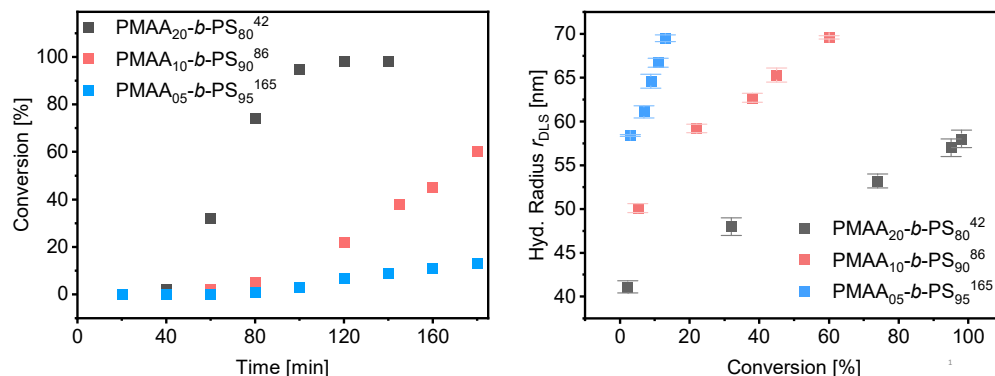


Figure 11. Conversion vs. time data for PMAA-*b*-PS with CTA3 at 50% (left) and average hydrodynamic radius measured by DLS against the conversion (right).

4. Conclusions

The synthesis of PMAA-*b*-PS diblock copolymers at high solid concentrations was investigated by varying the Z-group of the RAFT agent from a *n*-propyl-, to *n*-butyl- and *n*-dodecyl- terminus, making the RAFT agent more hydrophobic. RAFT polymerization of MAA was carried out in water with a trithiocarbonate RAFT agent. A carboxyl group was chosen as the R-group for all experiments. Promising conditions for PMAA polymerizations were found for the propyl and butyl moieties in water (or 1-propanol in case of CTA3). For successive chain extension with PS, the polymerizations performed with a propyl or butyl Z-group could be carried out in a one-pot synthesis. However, these polymerizations resulted in very long polymerization times or uncontrolled conditions when styrene weight concentrations above 30 wt% were chosen. The replacement of the Z group with a dodecyl radical made it possible to carry out the polymerization of PMAA-*b*-PS under very well controlled conditions up to remarkably high solid contents of 50 wt% provided that the PMAA block is long enough. We could also confirm that the influence of the Z-group has a significant effect on the polymerization rate in the RAFT emulsion polymerization. With this synthesis method, we have found a reaction pathway that allows the use of green solvents and due to the high solid concentrations, this system is associated with less by-product and energy consumption. The chosen hydrophilic PMAA block not only offers the possibility of further post-modifications resulting in a variety of functionalized nanoparticles, but these block copolymers are also potential candidates for membrane technology.

Supplementary Materials: The following are available online at <https://www.mdpi.com/article/10.3390/polym13213675/s1>, Table S1: kinetic data of the PMAA polymerization with CTA1 and CTA2; Table S2: kinetic data of the PMAA polymerization with CTA3; Table S3: kinetic data of PMAA₅-*b*-PS₉₅⁵⁴ with CTA1 at 20 wt%, Table S4: kinetic data of PMAA₁₀-*b*-PS₉₀⁴⁵ with CTA1 at 20 wt%; Table S5: kinetic data of PMAA₁₀-*b*-PS₉₀⁴⁵ with CTA1 at 25 wt%, Table S6: kinetic data of PMAA₁₀-*b*-PS₉₀⁴⁵ with CTA1 at 30 wt%, Table S7: kinetic data of PMAA₂₀-*b*-PS₈₀¹⁸ with CTA3 at 40 and 50 wt%; Table S8: kinetic data of PMAA₂₀-*b*-PS₈₀⁴² with CTA3 at 50 wt%; Table S9: kinetic data of PMAA₁₀-*b*-PS₉₀⁸⁶ with CTA3 at 50 wt%, Table S10: kinetic data of PMAA₅-*b*-PS₉₅¹⁶⁵ with CTA3 at 50 wt%; Table S11: overview of all PMAA-*b*-PS diblock copolymers and the corresponding macro-CTAs; Figure S1: TEM image of PMAA₁₀-*b*-PS₉₀⁴⁵ with CTA1 at 20 wt%; Figure S2: TEM image of PMAA₁₀-*b*-PS₉₀⁴⁵ with CTA1 at 25 wt%; Figure S3: TEM image of PMAA₁₀-*b*-PS₉₀⁴⁵ with CTA1 at 30 wt%; Figure S4: TEM image of PMAA₂₀-*b*-PS₈₀²⁶ with CTA3 at 40 wt%; Figure S5: TEM image of the PMAA₂₀-*b*-PS₈₀²⁶ with CTA3 at 50 wt%; Figure S6: TEM image of PMAA₂₀-*b*-PS₈₀⁴² with CTA3; Figure S7: TEM image of PMAA₁₀-*b*-PS₉₀⁸⁶ with CTA3; Figure S8: TEM image of PMAA₅-*b*-PS₉₅¹⁶⁵ with CTA3; Figure S9: TEM image of PMAA₄₀-*b*-PS₆₀⁴⁶ showing worm-like morphologies; Figure S10:

SEC results of PMAA₂₀-*b*-PS₈₀⁴² with CTA3 at 50 wt%; Figure S11: pictures of the polymerization of PMAA-*b*-PS with CTA2 and CTA3 at 40 wt%.

Author Contributions: I.O. conceived and designed all experiments. L.G. performed the PMAA polymerizations with CTA1 and CTA2. Elena Fedorenko performed the PMAA₅-*b*-PS₉₅⁵⁴ polymerizations with CTA 1. J.S. performed the polymerizations of PMAA₁₀-*b*-PS₉₀⁴⁵ at 20, 25 and 30 wt% with CTA1. All other experiments were performed by I.O. I.O. and V.A. analyzed the data and wrote the paper. All authors have read and agreed to the published version of the manuscript.

Funding: This research received no external funding.

Institutional Review Board Statement: Not applicable.

Informed Consent Statement: Not applicable.

Data Availability Statement: The data presented in this study are available on request from the corresponding author.

Acknowledgments: The authors acknowledge the NMR spectroscopic and mass spectrometry division of the Department of Chemistry at the University of Hamburg and Martin Kehden for the SEC measurements.

Conflicts of Interest: The authors declare no conflict of interest.

References

1. Matyjaszewski, K.; Spanswick, J. Controlled/living radical polymerization. *Mater. Today* **2005**, *8*, 26–33. [[CrossRef](#)]
2. Matyjaszewski, K. Atom Transfer Radical Polymerization (ATRP): Current status and future perspectives. *Macromolecules* **2012**, *45*, 4015–4039. [[CrossRef](#)]
3. Acar, M.H.; Matyjaszewski, K. Block copolymers by transformation of living anionic polymerization into controlled/"living" atom transfer radical polymerization. *Macromol. Chem. Phys.* **1999**, *200*, 1094–1100. [[CrossRef](#)]
4. Matyjaszewski, K.; Müller, A.H.E. 50 Years of Living Polymerization. *Prog. Polym. Sci.* **2006**, *31*, 1039–1040. [[CrossRef](#)]
5. Perrier, S. 50th Anniversary Perspective: RAFT Polymerization—A User Guide. *Macromolecules* **2017**, *50*, 7433–7447. [[CrossRef](#)]
6. Fielding, L.A.; Derry, M.J.; Ladmiral, V.; Rosselgong, J.; Rodrigues, A.M.; Ratcliffe, L.P.D.; Sugihara, S.; Armes, S.P. RAFT dispersion polymerization in non-polar solvents: Facile production of block copolymer spheres, worms and vesicles in n-alkanes. *Chem. Sci.* **2013**, *4*, 2081–2087. [[CrossRef](#)]
7. Eggers, S.; Abetz, V. Surfactant-Free RAFT emulsion polymerization of styrene using thermoresponsive macroRAFT agents: Towards smartwell-defined block copolymers with high molecular weights. *Polymers* **2017**, *9*, 668. [[CrossRef](#)]
8. Lauterbach, F.; Abetz, V. An eco-friendly pathway to thermosensitive micellar nanoobjects: Via photoRAFT PISA: The full guide to poly(N-acryloylpyrrolidin)-block-polystyrene diblock copolymers. *Soft Matter* **2020**, *16*, 2321–2331. [[CrossRef](#)]
9. Yang, Y.; Zheng, J.; Man, S.; Sun, X.; An, Z. Synthesis of poly(ionic liquid)-based nano-objects with morphological transitions: Via RAFT polymerization-induced self-assembly in ethanol. *Polym. Chem.* **2018**, *9*, 824–827. [[CrossRef](#)]
10. Ni, H.; Liu, J.; Shi, K.; Wu, M.; Yang, Y.; Zhang, L. PMAA-based RAFT dispersion polymerization of MMA in ethanol: Conductivity, block length and self-assembly. *RSC Adv.* **2016**, *6*, 58218–58225. [[CrossRef](#)]
11. Zhang, Q.; Zhu, S. Ionic Liquids: Versatile Media for Preparation of Vesicles from Polymerization-Induced Self-Assembly. *ACS Macro Lett.* **2015**, *4*, 755–758. [[CrossRef](#)]
12. Perrier, S.; Takolpuckdee, P. Macromolecular design via reversible addition-fragmentation chain transfer (RAFT)/xanthates (MADIX) polymerization. *J. Polym. Sci. Part A Polym. Chem.* **2005**, *43*, 5347–5393. [[CrossRef](#)]
13. Zamfir, M.; Patrickios, C.S.; Montagne, F.; Abetz, C.; Abetz, V.; Oss-Ronen, L.; Talmon, Y. Styrene-vinyl pyridine diblock copolymers: Synthesis by RAFT polymerization and self-assembly in solution and in the bulk. *J. Polym. Sci. Part A Polym. Chem.* **2012**, *50*, 1636–1644. [[CrossRef](#)]
14. Grazon, C.; Rieger, J.; Sanson, N.; Charleux, B. Study of Poly(N,N-diethylacrylamide) Nanogel Formation by Aqueous Dispersion Polymerization of N,N-Diethylacrylamide in the Presence of Poly(ethylene oxide)-*b*-Poly(N,N-dimethylacrylamide) Amphiphilic Macromolecular RAFT Agents. *Soft Matter* **2011**, *7*, 3482–3490. [[CrossRef](#)]
15. Wu, J.; Tian, C.; Zhang, L.; Cheng, Z.; Zhu, X. Synthesis of soap-free emulsion with high solid content by differential dripping RAFT polymerization-induced self-assembly. *RSC Adv.* **2017**, *7*, 6559–6564. [[CrossRef](#)]
16. Siirilä, J.; Häkkinen, S.; Tenhu, H. The emulsion polymerization induced self-assembly of a thermoresponsive polymer poly(N-vinylcaprolactam). *Polym. Chem.* **2019**, *10*, 766–775. [[CrossRef](#)]
17. Liu, J.; Li, J.; Wang, C.Y.; Ren, Q. RAFT surfactant-free cationic emulsion polymerization of styrene: Effect of hydrophobicity of block macro-RAFT agent. *J. Macromol. Sci. Part A Pure Appl. Chem.* **2020**, *58*, 232–242. [[CrossRef](#)]
18. Sprong, E.; Leswin, J.S.K.; Lamb, D.J.; Ferguson, C.J.; Hawke, B.S.; Pham, B.T.T.; Nguyen, D.; Such, C.H.; Serelis, A.K.; Gilbert, R.G. Molecular watchmaking: Ab initio emulsion polymerization by RAFT-controlled self-assembly. *Macromol. Symp.* **2006**, *231*, 84–93. [[CrossRef](#)]

19. Ferguson, C.J.; Hughes, R.J.; Pham, B.T.T.; Hawckett, B.S.; Gilbert, R.G.; Serelis, A.K.; Such, C.H. Effective ab initio emulsion polymerization under RAFT control. *Macromolecules* **2002**, *35*, 9243–9245. [[CrossRef](#)]
20. Chaduc, I.; Crepet, A.; Boyron, O.; Charleux, B.; D'Agosto, F.; Lansalot, M. Effect of the pH on the RAFT polymerization of acrylic acid in water. Application to the synthesis of poly(acrylic acid)-stabilized polystyrene particles by RAFT emulsion polymerization. *Macromolecules* **2013**, *46*, 6013–6023. [[CrossRef](#)]
21. Chaduc, I.; Girod, M.; Antoine, R.; Charleux, B.; D'Agosto, F.; Lansalot, M. Batch emulsion polymerization mediated by poly(methacrylic acid) macroRAFT agents: One-pot synthesis of self-stabilized particles. *Macromolecules* **2012**, *45*, 5881–5893. [[CrossRef](#)]
22. Zhang, W.; D'Agosto, F.; Boyron, O.; Rieger, J.; Charleux, B. One-pot synthesis of poly(methacrylic acid-co-poly(ethylene oxide) methyl ether methacrylate)-b-polystyrene amphiphilic block copolymers and their self-assemblies in water via RAFT-mediated radical emulsion polymerization. A kinetic study. *Macromolecules* **2011**, *44*, 7584–7593. [[CrossRef](#)]
23. Chaduc, I.; Zhang, W.; Rieger, J.; Lansalot, M.; D'Agosto, F.; Charleux, B. Amphiphilic block copolymers from a direct and one-pot RAFT synthesis in water. *Macromol. Rapid Commun.* **2011**, *32*, 1270–1276. [[CrossRef](#)] [[PubMed](#)]
24. Rieger, J.; Zhang, W.; Stoffelbach, F.; Charleux, B. Surfactant-free RAFT emulsion polymerization using poly(N,N-dimethylacrylamide) trithiocarbonate macromolecular chain transfer agents. *Macromolecules* **2010**, *43*, 6302–6310. [[CrossRef](#)]
25. Zhang, X.; Rieger, J.; Charleux, B. Effect of the solvent composition on the morphology of nano-objects synthesized via RAFT polymerization of benzyl methacrylate in dispersed systems. *Polym. Chem.* **2012**, *3*, 1502–1509. [[CrossRef](#)]
26. Manguian, M.; Save, M.; Charleux, B. Batch emulsion polymerization of styrene stabilized by a hydrophilic macro-RAFT agent. *Macromol. Rapid Commun.* **2006**, *27*, 399–404. [[CrossRef](#)]
27. Charleux, B.; Delaittre, G.; Rieger, J.; D'Agosto, F. Polymerization-induced self-assembly: From soluble macromolecules to block copolymer nano-objects in one step. *Macromolecules* **2012**, *45*, 6753–6765. [[CrossRef](#)]
28. Wi, Y.; Lee, K.; Lee, B.H.; Choe, S. Soap-free emulsion polymerization of styrene using poly(methacrylic acid) macro-RAFT agent. *Polymer* **2008**, *49*, 5626–5635. [[CrossRef](#)]
29. Oral, I.; Abetz, V. A Highly Selective Polymer Material using Benzo-9-Crown-3 for the Extraction of Lithium in Presence of Other Interfering Alkali Metal Ions. *Macromol. Rapid Commun.* **2021**, *42*, 2000746. [[CrossRef](#)] [[PubMed](#)]
30. Sabbagh, F.; Muhamad, I.I. Physical and Chemical Characterisation of Acrylamide-Based Hydrogels, Aam, Aam/NaCMC and Aam/NaCMC/MgO. *J. Inorg. Organomet. Polym. Mater.* **2017**, *27*, 1439–1449. [[CrossRef](#)]
31. Lacík, I.; Stach, M.; Kasák, P.; Semak, V.; Uhelská, L.; Chovancová, A.; Reinhold, G.; Kilz, P.; Delaittre, G.; Charleux, B.; et al. SEC Analysis of Poly (Acrylic Acid) and Poly (Methacrylic Acid). *Macromol. Chem. Phys.* **2015**, *216*, 23–37. [[CrossRef](#)]
32. Xu, E.; Smith, A.E.; Kirkland, S.E.; McCormick, C.L. Aqueous RAFT synthesis of pH-responsive triblock copolymer mPEO-PAPMA-PDPAEMA and formation of shell cross-linked micelles. *Macromolecules* **2008**, *41*, 8429–8435. [[CrossRef](#)]
33. Lowe, A.B.; McCormick, C.L. Reversible addition-fragmentation chain transfer (RAFT) radical polymerization and the synthesis of water-soluble (co)polymers under homogeneous conditions in organic and aqueous media. *Prog. Polym. Sci.* **2007**, *32*, 283–351. [[CrossRef](#)]
34. Chaduc, I.; Lansalot, M.; D'Agosto, F.; Charleux, B. RAFT polymerization of methacrylic acid in water. *Macromolecules* **2012**, *45*, 1241–1247. [[CrossRef](#)]
35. Fuchs, A.V.; Thurecht, K.J. Stability of trithiocarbonate RAFT agents containing both a cyano and a carboxylic acid functional group. *ACS Macro Lett.* **2017**, *6*, 287–291. [[CrossRef](#)]
36. Vshivkov, S.A.; Soliman, T.S.; Kluzhin, E.S.; Kapitanov, A.A. Structure of poly(acrylic acid), poly(methacrylic acid) and gelatin solutions. *J. Mol. Liq.* **2019**, *294*, 111551. [[CrossRef](#)]
37. Kuchta, F.D.; Van Herk, A.M.; German, A.L. Propagation kinetics of acrylic and methacrylic acid in water and organic solvents studied by pulsed-laser polymerization. *Macromolecules* **2000**, *33*, 3641–3649. [[CrossRef](#)]
38. Wan, W.-M.; Pan, C.-Y. One-pot synthesis of polymeric nanomaterials via RAFT dispersion polymerization induced self-assembly and re-organization. *Polym. Chem.* **2010**, *1*, 1475. [[CrossRef](#)]
39. Huang, J.; Zhao, S.; Gao, X.; Luo, Y.; Li, B. RAFT Ab Initio Emulsion Polymerization of Styrene Using Poly(acrylic acid)-b-polystyrene Trithiocarbonate of Various Structures as Mediator and Surfactant. *Macromol. React. Eng.* **2014**, *8*, 696–705. [[CrossRef](#)]
40. Thickett, S.C.; Gilbert, R.G. Emulsion polymerization: State of the art in kinetics and mechanisms. *Polymer* **2007**, *48*, 6965–6991. [[CrossRef](#)]
41. Canning, S.L.; Smith, G.N.; Armes, S.P. A Critical Appraisal of RAFT-Mediated Polymerization-Induced Self-Assembly. *Macromolecules* **2016**, *49*, 1985–2001. [[CrossRef](#)] [[PubMed](#)]
42. Cunningham, V.J.; Alswieleh, A.M.; Thompson, K.L.; Williams, M.; Leggett, G.J.; Armes, S.P.; Musa, O.M. Poly(glycerol monomethacrylate)-poly(benzyl methacrylate) diblock copolymer nanoparticles via RAFT emulsion polymerization: Synthesis, characterization, and interfacial activity. *Macromolecules* **2014**, *47*, 5613–5623. [[CrossRef](#)]
43. Truong, N.P.; Dussert, M.V.; Whittaker, M.R.; Quinn, J.F.; Davis, T.P. Rapid synthesis of ultrahigh molecular weight and low polydispersity polystyrene diblock copolymers by RAFT-mediated emulsion polymerization. *Polym. Chem.* **2015**, *6*, 3865–3874. [[CrossRef](#)]

44. Zhang, W.; D'Agosto, F.; Boyron, O.; Rieger, J.; Charleux, B. Toward a better understanding of the parameters that lead to the formation of nonspherical polystyrene particles via RAFT-mediated one-pot aqueous emulsion polymerization. *Macromolecules* **2012**, *45*, 4075–4084. [[CrossRef](#)]
45. Zhang, X.; Boissé, S.; Zhang, W.; Beaunier, P.; D'Agosto, F.; Rieger, J.; Charleux, B. Well-defined amphiphilic block copolymers and nano-objects formed in situ via RAFT-mediated aqueous emulsion polymerization. *Macromolecules* **2011**, *44*, 4149–4158. [[CrossRef](#)]
46. Blanazs, A.; Armes, S.P.; Ryan, A.J. Self-assembled block copolymer aggregates: From micelles to vesicles and their biological applications. *Macromol. Rapid Commun.* **2009**, *30*, 267–277. [[CrossRef](#)]
47. Thompson, S.W.; Guimarães, T.R.; Zetterlund, P.B. RAFT Emulsion Polymerization: MacroRAFT Agent Self-Assembly Investigated Using a Solvachromatic Dye. *Biomacromolecules* **2020**, *21*, 4577–4590. [[CrossRef](#)]
48. Asua, J.M. Emulsion Polymerization: From Fundamental Mechanisms to Process Developments. *J. Polym. Sci. Part A Polym. Chem.* **2004**, *42*, 1025–1041. [[CrossRef](#)]
49. Gilbert, R.G.; Prescott, S.W.; Smulders, W.; Monteiro, M.J.; Ballard, M.J.; Rizzardo, E. RAFT in emulsion polymerization: What makes it different. *Am. Chem. Soc. Polym. Prepr. Div. Polym. Chem.* **2002**, *43*, 130–131. [[CrossRef](#)]
50. Semsarilar, M.; Abetz, V. Polymerizations by RAFT: Developments of the Technique and Its Application in the Synthesis of Tailored (Co)polymers. *Macromol. Chem. Phys.* **2020**, *222*, 2000311. [[CrossRef](#)]
51. Butté, A.; Storti, G.; Morbidelli, M. Miniemulsion living free radical polymerization by RAFT. *Macromolecules* **2001**, *34*, 5885–5896. [[CrossRef](#)]
52. Sanders, C.A.; George, S.R.; Deeter, G.A.; Campbell, J.D.; Reck, B.; Cunningham, M.F. Amphiphilic Block-Random Copolymers: Self-Folding Behavior and Stabilizers in Emulsion Polymerization. *Macromolecules* **2019**, *52*, 4510–4519. [[CrossRef](#)]
53. Guimarães, T.R.; Bong, Y.L.; Thompson, S.W.; Moad, G.; Perrier, S.; Zetterlund, P.B. Polymerization-induced self-assembly via RAFT in emulsion: Effect of Z-group on the nucleation step. *Polym. Chem.* **2020**, *12*, 122–133. [[CrossRef](#)]
54. Luo, Y.; Wang, X.; Li, B.G.; Zhu, S. Toward well-controlled ab initio RAFT emulsion polymerization of styrene mediated by 2-(((Dodecylsulfanyl)carbonothioyl)sulfanyl)propanoic acid. *Macromolecules* **2011**, *44*, 221–229. [[CrossRef](#)]
55. Monteiro, M.J.; Hodgson, M.; De Brouwer, H. Influence of RAFT on the rates and molecular weight distributions of styrene in seeded emulsion polymerizations. *J. Polym. Sci. Part A Polym. Chem.* **2000**, *38*, 3864–3874. [[CrossRef](#)]
56. Huang, J.; Zhao, S.; Gao, X.; Luo, Y.; Li, B. Ab initio RAFT emulsion copolymerization of styrene and acrylonitrile. *Ind. Eng. Chem. Res.* **2014**, *53*, 7688–7695. [[CrossRef](#)]
57. Lansalot, M.; Davis, T.P.; Heuts, J.P.A. RAFT miniemulsion polymerization: Influence of the structure of the RAFT agent. *Macromolecules* **2002**, *35*, 7582–7591. [[CrossRef](#)]

5.4 Publication 4:

A highly selective polymer material using benzo-9-crown-3 for the extraction of lithium in presence of other interfering alkali metal ions

In Publication 4, the polymer material prepared in Publication 3 is linked with a 9-membered crown ether (benzo-9-crown-3), and complexed with the alkali metals Li^+ , Na^+ , and K^+ . The crown ether-based material was prepared by modifying the crown ether with an alcohol group, followed by Steglich esterification of the PMAA-*b*-PS polymer, which was confirmed via ^1H NMR spectroscopy. In addition, the complexation properties of the polymer-based crown ether material are compared with the free crown ethers, and the advantages of a polymer-based crown ether material are clarified.

The extractions with free crown ethers (B15C5, B12C4, and B9C3) and the polymer-bound crown ether (B9C3) were carried out in a two-phase extraction analogous to Publications 1 and 2. The complex formation constants were determined and compared for the different systems. For the 9-membered free crown ether (forming sandwich complexes with Li^+ , Na^+ , and K^+), strong complexation was found for Na, K, and Li, whereas only the lithium-ion was complexed in the polymer-bound crown ether.

To demonstrate the practicality of the polymer system, the Na^+ , K^+ , and Li^+ concentrations were adjusted in a two-phase extraction analogous to the concentrations in the Dead Sea. After extraction of the polymer-bound benzo-9-crown crown ether material, a complexation of lithium of about 60% was obtained. However, lithium is present in deficient concentrations in the Dead Sea ($\text{Li}^+ = 0.014$ g/L, $\text{Na}^+ = 37$ g/L, and $\text{K}^+ = 6.9$ g/L).

With the results of this Publication, it was shown that a polymer-based crown ether material is an attractive adsorbent that can isolate lithium well even in low concentrations of aqueous resources.

The Publication is reprinted with permission from I. Oral and V. Abetz, *Macromol. Rapid Commun.*, **2021**, 42, 2000746 - published by Wiley-VCH GmbH. The related supporting information is available in Section 9.5.



A Highly Selective Polymer Material using Benzo-9-Crown-3 for the Extraction of Lithium in Presence of Other Interfering Alkali Metal Ions

Iklima Oral and Volker Abetz*

The recovery of lithium from global water resources continues to be challenging due to interfering metal ions with similar solution properties. Hence, a lithium-selective diblock copolymer system containing crown ethers (CEs) is developed. A polystyrene-*block*-poly(methacrylic acid) diblock copolymer is synthesized first via a one-pot solution-emulsion reversible addition-fragmentation chain transfer polymerization. A subsequent Steglich esterification yields the CE functionalized polymer. The complexation properties with different alkali metals are first investigated by liquid-liquid extraction (LLE) in dichloromethane (DCM) – water systems using free benzo-9-crown (B9C3), benzo-12-crown-4 (B12C4), and benzo-15-crown-5 (B15C5) CEs as reference components, followed by the correspondingly CE-functionalized polymers. Extraction complexation constants in the aqueous phase are determined and the impact of the complexation constants on the extractability is estimated. The B9C3 CE is especially appealing since it has the smallest cavity size among all CEs. It is too small to complex sodium or potassium ions; however, it forms sandwich complexes with a lithium-ion resulting in extraordinary complexation constants in polymer systems avoiding other interfering alkali metal ions. On this basis, a new material for the efficient extraction of lithium ion traces in global water resources is established.

1. Introduction

Lithium has been drawing considerable interest due to its widespread applications in controlled nuclear fusion fuels,^[1] alloy industries,^[2] pharmaceuticals,^[3] ceramics,^[4] catalysis,^[5] and particularly in rechargeable lithium-ion batteries—a key towards the global electric vehicle industry.^[6–10] The demand for lithium has grown significantly over the last years and the price has expanded immensely since then.^[11,12] Lithium can be gathered from seawater, lithium-containing ores, and lithium-rich salt-lake brines. The latter contributes to around 60% of the total recoverable lithium deposits.^[9] It should be mentioned, however, that most salt-lakes with high concentrations of lithium also suffer from excessive sodium, potassium, calcium, and magnesium contents.^[8] Therefore, further purification steps are mandatory due to similar solution properties shared among these metal ions in an aqueous solution.^[13–17]

In the seawater, there are an estimated 231 trillion tons of lithium. Nevertheless, low concentrations of around 0.178 mg L⁻¹ and the numerous amounts of other interfering metal ions (Na⁺, Mg²⁺, Ca²⁺, or K⁺) with significantly higher concentrations make its recovery more challenging and not economically feasible until now.^[17] Consequently, the design of a high selective lithium extractant suppressing other metal ions becomes the key issue of lithium recovery from seawater or other natural lithium sources. Multivalent ions such as magnesium or calcium are not considered in this work since they can be isolated by electrodialysis or nanofiltration using often cationic surfaces.^[18–22] Besides these metal ions, also high concentrations of chloride, as well as traces of bromide and sulfate anions are present in the seawater.^[23] These anions have an effect on the selectivity in CE extraction of alkali metal ions as spherical anions lead to lower selectivity while non-spherical anions increase the extraction ability due to specific binding sites.^[24] So far, LLE seems to be one of the most promising techniques to extract metal ions from natural sources due to its simplicity, high selectivity, fast reaction rates, convenient handling, and straightforward automation.^[16,25]

I. Oral, Prof. V. Abetz
Institute of Physical Chemistry
Universität
Hamburg
Martin-Luther-King-Platz 6, Hamburg 20146, Germany
E-mail: volker.abetz@hzg.de
Prof. V. Abetz
Helmholtz-Zentrum Geesthacht
Centre for Material and Coastal Research
Institute of Membrane Research
Max-Planck-Straße 1, Geesthacht 21502, Germany

 The ORCID identification number(s) for the author(s) of this article can be found under <https://doi.org/10.1002/marc.202000746>.

© 2021 The Authors. Macromolecular Rapid Communications published by Wiley-VCH GmbH. This is an open access article under the terms of the Creative Commons Attribution License, which permits use, distribution and reproduction in any medium, provided the original work is properly cited.

DOI: 10.1002/marc.202000746

CEs, that is, macrocyclic ligands containing several ether groups, are commonly used for LLE of metal ions.^[26–28] They form well-known host-guest complexes with specific metal ions depending on the size of the CE cavity and metal ion.^[29–31] Complexation can appear in various ways: either ML, ML₂ (sandwich), or M₂L₃ (club sandwich) complexes, or even more complex structures with M being the metal ion and L the ligand can be formed.^[32,33] CEs have been also employed in size-selective ion sensors,^[34] phase-transfer catalysts,^[35] membrane transport,^[36,37] and disposal of nuclear waste.^[38]

Herein, the CEs will be applied for the complexation of selective metal ions in order to recover lithium from a natural source by using a CE with a cavity size only suitable for lithium, suppressing other interfering alkali metal ions. Polymeric systems containing those CEs are especially appealing due to their typically easy separation from solutions or mixtures. We demonstrate a CE-functionalized polystyrene-*block*-poly(methacrylic acid) (PS-*b*-PMAA) diblock copolymer system with a high selectivity towards lithium synthesized in water

via a one-pot solution–emulsion reversible addition–fragmentation chain transfer (RAFT) polymerization and subsequent post-functionalization (Figure 1). The complexation properties with lithium, sodium, and potassium are investigated by LLE in DCM–water systems using three different CEs first, followed by corresponding CE-functionalized polymers. Extraction complexation constants in the water phase are calculated and the contributions of the complexation constants to the extractability are evaluated.

Studying the effect of CE cavities and the number of aromatic groups within the CEs is of importance for designing lithium-selective extractants. There are several factors that play a crucial role in the extraction process of metal ions from the solution. First, there is the enthalpy of solvation, which is essential especially for the studied metal ions in this work. Furthermore, the metal ion should fit properly in the cavity size of the CE. If the metal ion is too small, there is an inevitable energy loss due to weaker ion–dipole interactions. On the other hand, if the metal ion is too large to enter the cavity of the ligand, there will

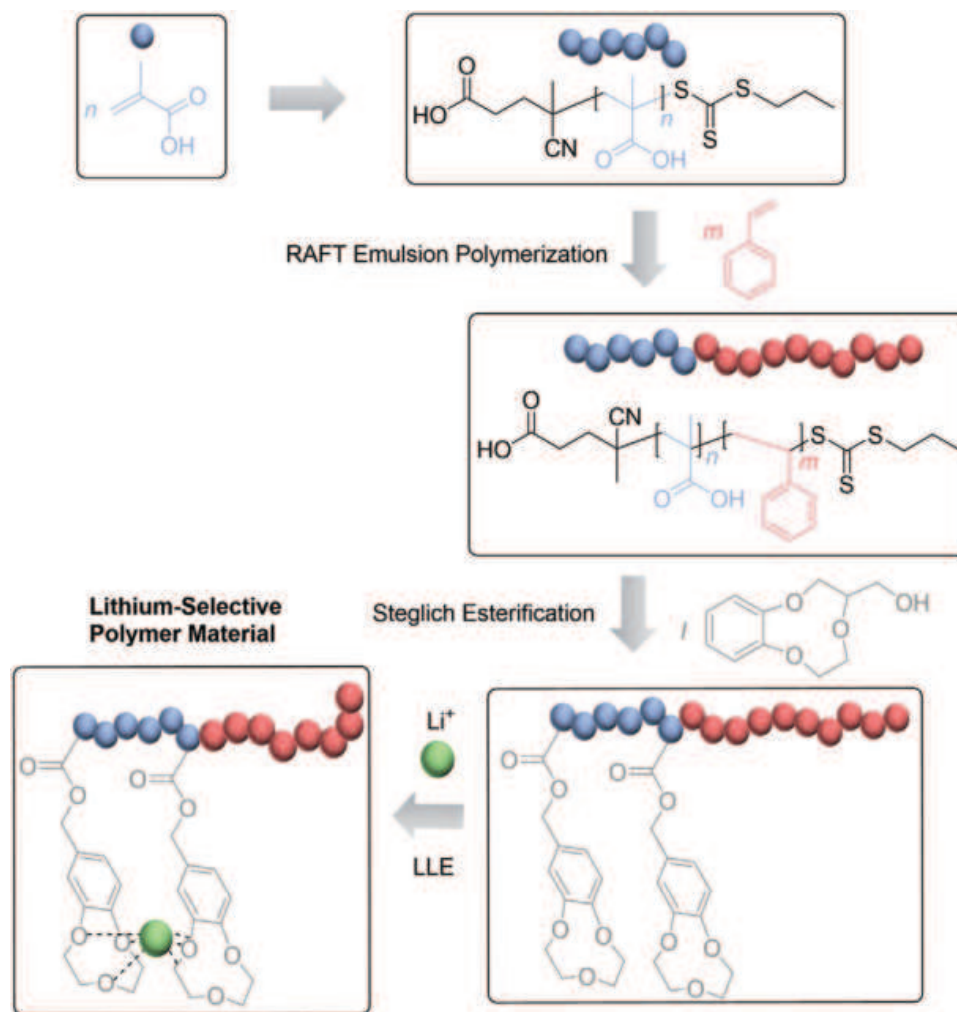


Figure 1. Schematic illustration of the sandwich complexation with lithium in a CE-functionalized polymer, synthesized via a one-pot solution–emulsion RAFT polymerization of MAA and styrene, and subsequent post-modification of the MAA moiety with hydroxyl functionalized benzo-9-crown-3 (B9C3-OH) CEs via Steglich esterification.

be a loss in entropy (yet an increase in ion–dipole interaction) as a higher-order complex (i.e., sandwich or club-sandwich) is potentially formed.^[32,39–41] Since these effects are always competitive, studying the effect of CE cavities for specific metal ions in terms of thermodynamic quantities is mandatory and provided in the following.

2. Results and Discussion

Three different benzo-CEs were analyzed, which can either form single or sandwich complexes with potassium, sodium, or lithium (**Figure 2**). 15-crown-5 CEs (cavity radius: 0.85–1.1 Å) have been successfully used to recover sodium (ionic radius: 0.95 Å) in a single complex or potassium (ionic radius: 1.33 Å) in a sandwich complex. However, Nishizawa et al. discovered also its selectivity with lithium isotopes (ionic radius: 0.60 Å).^[32,42–46] 12-crown-4 CEs (cavity size: 0.50–0.65 Å) form single complexes with lithium, and sandwich complexes with sodium.^[29,31,47] Nevertheless, both CE systems are capable to complex more than one type of metal ion and are therefore not suitable for selective complexation of lithium. Another possibility is the incorporation of sterically hindered groups within the CE, which prohibit the complexation of bigger metal ions. In current literature, several CEs with those sterically hindered side chains were reported and showed high complexation towards lithium.^[48,49] However, synthesis of those CEs was conducted under harsh conditions, several reaction steps, and expensive reagents. Here, we show a more facile and economically effective synthesis to connect this CE to a polymer system and to make this material industrially attractive.

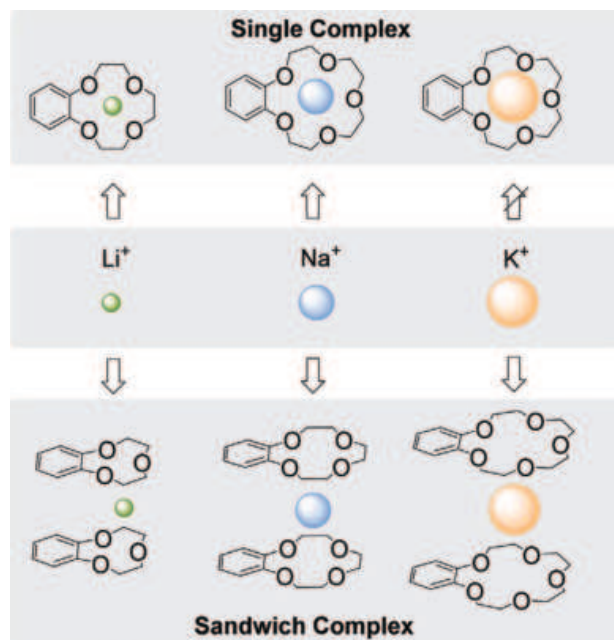


Figure 2. Illustration of an alkali metal complexation of lithium, sodium, and potassium with benzo-9-crown-3 (B9C3), benzo-12-crown-4 (B12C4), and benzo-15-crown-5 (B15C5) CEs, forming either single or sandwich complex.

Previous studies reported higher complexation stability in sandwich formation due to the double amount of ion–dipole interactions.^[32,40] By forming a sandwich complex with lithium, higher complexation stability is expectable. Therefore, a CE with only three oxygen atoms was designed in this work in order to force the lithium to form a sandwich complex with the CE, since it cannot fit in its cavity. In order to prove the superior complexation of B9C3 CEs with lithium, B12C4 and B15C5 CEs were used additionally to extract lithium from an aqueous solution for comparison. The respective stability of each complex was evaluated and compared with each other. The metal ion complexation was conducted in a two-phase water–DCM system and has been described in recent literature with similar extraction systems.^[49–51] A general metal ion extraction is shown in Equation (1):



where M is the metal cation and X the counter anion, m and x are the stoichiometric factors of the metal cation and counter anion, $z+$ and $v-$ are the charges of the corresponding metal- and counter ions, and n is the CE equivalent needed to complex the metal ion. The salts are soluble in the aqueous phase while the CE and the final complex are only soluble in the organic phase. The complex stability was evaluated by calculating the complex constant K via UV absorption of the remaining salt in the aqueous phase. The different UV-responsive salts and their spectra including the calibration curves are shown in **Figure 3** and are used to calculate the final salt concentration in the aqueous phase after extraction (Lambert–Beers law). The complex constant K is evaluated according to the law of mass with incorporation of the formed complex (Equation (2)). In this equation, γ_{+} refer to the mean activity coefficients, and Q to the stoichiometric coefficient. These coefficients are unity in this study, as only monovalent ions are involved. More detailed information can be found in the SI.

$$K = \frac{[(M_m CE_n)^{mz+} X_{x(org)}^{xv-}]}{(Q \cdot (\gamma_{+} [M^{z+}]^m) \cdot (\gamma_{-} [X^{v-}]^x)) \cdot [CE]^n} \quad (2)$$

In order to prove the accuracy of the LLE in DCM–water systems, a B15C5 CE, which has the highest hydrophilicity of the studied CEs, has been dissolved in DCM and extracted with an aqueous sodium chloride solution. The aqueous phase was analyzed after extraction, and only 2.6 % B15C5 CE was detected. Similar results were reported before.^[51] The B12C4 CE showed even less solubility in the aqueous phase of 0.3 % and the B9C3 CE showed no solubility in water, which is not surprising since these CEs are more hydrophobic. The UV–vis calibration curves of the CEs and their absorption maxima are shown in Figures S11 and S12, Supporting Information. In short, after the metal–ion complexation with the CEs, the complexes remain mainly in the organic phase. The extraction process takes place at the interface between the organic and the aqueous phase.

The results of the B9C3, B12C4, and B15C5 CEs extraction with lithium 3,5-diiodosalicylate (LIS), a UV responsive lithium

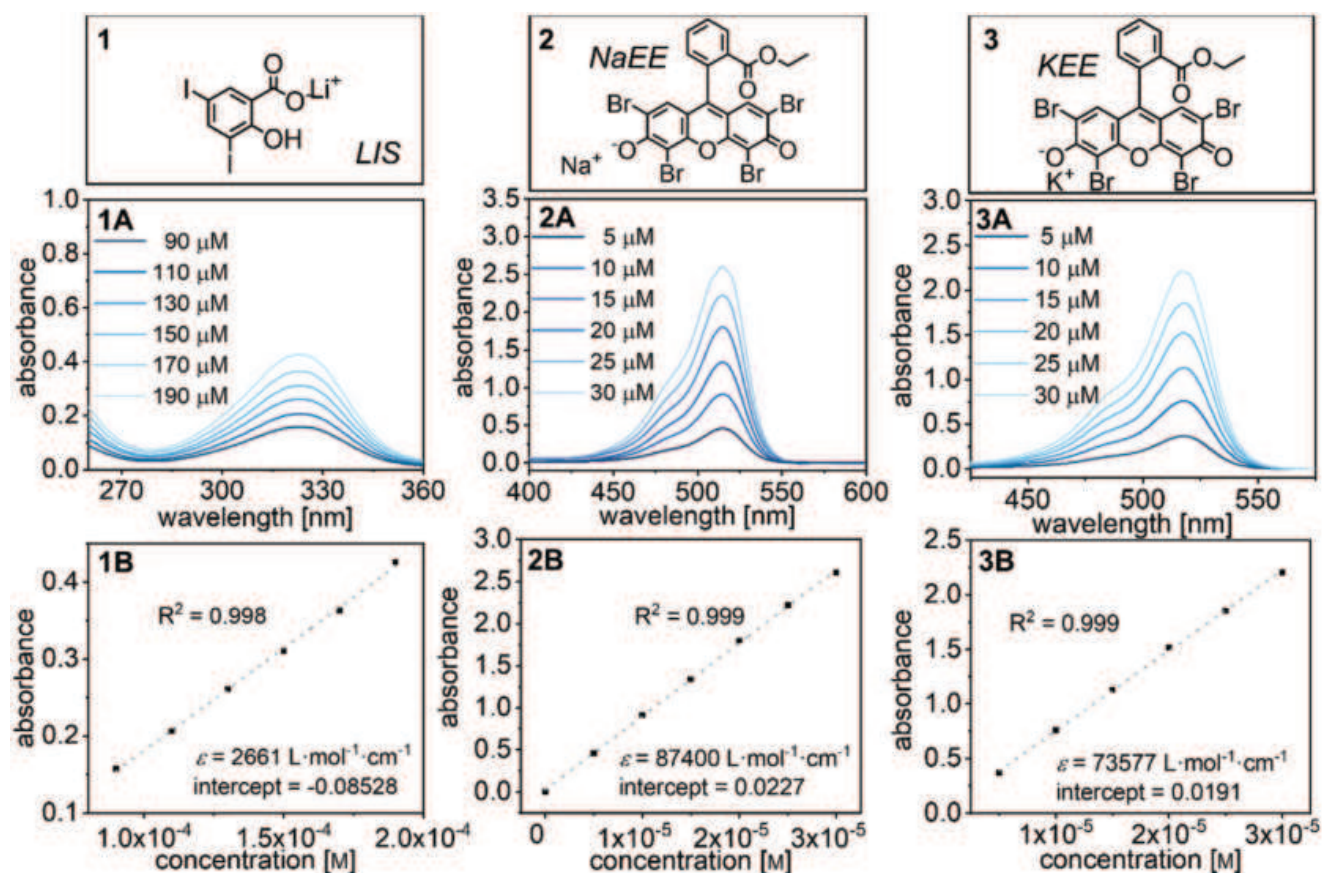


Figure 3. Absorption spectra at different concentrations of 1A) lithium 3,5-diiodosalicylate (LIS), 2A) 2',4',5',7'-tetrabromo eosin ethyl ester sodium salt (NaEE), 3A) 2',4',5',7'-tetrabromo eosin ethyl ester sodium salt (KEE) and absorption maxima versus concentration of 1B) LIS at 323 nm, 2B) NaEE at 515 nm, and 2C) KEE at 517 nm.

salt with an absorption maximum (λ_{max}) at 323 nm, at various CE:salt molar ratios are presented in **Figure 4**. Surprisingly, the B15C5 CE shows higher extractability with lithium compared

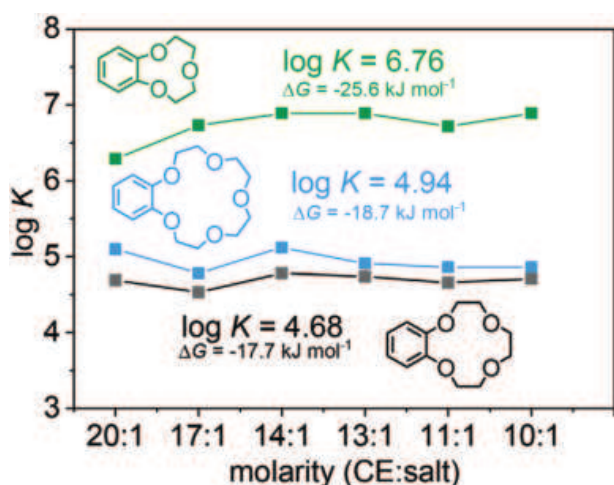


Figure 4. Logarithmic complexation stability K of B9C3 (green curve), B12C4 (black curve), and B15C5 (blue curve) with LIS at different CE:Salt molar ratios and the average of log K and Gibbs free energy ΔG were determined.

to B12C4 CEs according to the average complex constant of log $K = 4.94$. In theory, the lithium complexation with B15C5 CEs should be less pronounced than the complexation with B12C4 CEs (log $K = 4.68$), since the lithium is very small compared to the cavity size of the B15C5 CE, leading to weaker ion–dipole interaction as a result of the greater distance between the metal ion and the oxygen atoms. On the other hand, more oxygen atoms favor the host–guest interaction with the metal ion. In a nutshell, B12C4 CEs show good complexation with lithium, since the cavity size of 0.5–0.65 Å fits well for the lithium-ion with a radius of 0.60 Å; yet, the B15C5 CE shows also good complexation, due to a reasonable interplay between cavity size of the CE and dipole partners for the metal ion. Besides the already satisfying results, the complexation of the B9C3 CE with lithium shows even higher complexation stability with an average complex constant of log $K = 6.76$. This means a roughly 100-fold increased stability of the formed complex. Within the favorable sandwich complex, featuring dipole–ion interactions between six oxygen atoms and the lithium-ion, the resulting enthalpy gain leads to such high complex stability.^[52–54] Similar proportions were previously reported in the literature by Zakurdaeva et al. where the B9C3 CE showed a log K of 3.12, the B12C4 CE a log K of 2.90, and the B15C5 CE a log K of 2.68 with lithium.^[55] The complex constants of B12C4 and B15C5 CEs showed related extraction abilities, while the B9C3 CE

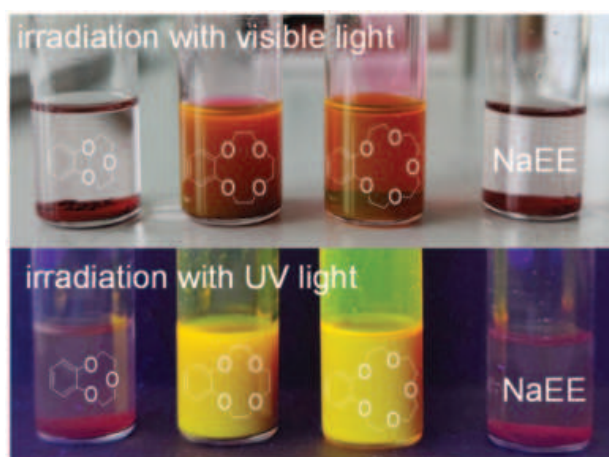


Figure 5. Optical experiment with NaEE in DCM (right) and additionally added CEs.

showed the strongest extractability among the studied CEs. In their study, they extracted lithium chloride from the aqueous phase in a chloroform/water LLE. By calculating the complex constant K , the Gibbs free energy ΔG can be calculated as well ($\Delta G = -RT \ln K$). The negative values of ΔG and the resulting complex stability constants K confirm spontaneous (exergonic) complexation for all systems. As a result, the sandwich formation of B9C3 CE with lithium shows indeed a far larger stability resulting in the highest complexation constant and the most negative ΔG value.

In order to prove a selective lithium complexation with B9C3 CEs, extractions with sodium and potassium were conducted using the 2',4',5',7'-tetrabromoeosin ethyl ester sodium salt (NaEE) and the 2',4',5',7'-tetrabromoeosin ethyl ester potassium salt (KEE). In theory, both cations should not be able to fit in the cavity size of the B9C3 CE. However, it may be possible that sandwich or higher-order complex structures are formed with these metal ions.

First, an optical experiment was conducted (Figure 5). NaEE was used as a sodium dye and placed in each of the four vials with DCM. The NaEE salt is not soluble in DCM but should be dissolved if the CEs are able to complex sodium. B15C5, B12C4, or B9C3 CE were placed in the vials beside the salt. Only the B9C3 CE did not show a color change with the sodium dye. All other CEs had the capability of complexing sodium and turned red (yellow under UV light). The same observations were made for KEE (see Figure S10, Supporting Information). This optical experiment shows once again why B15C5 and B12C4 CEs are not the key CEs for extracting lithium selectively, even though they have the capability of extracting lithium ions. It should be mentioned that, in DCM, the ions cannot form a hydration shell and are therefore not surrounded by water molecules. Thus, the complexation of the metal ions from organic media is more favorable in energy terms since the CEs do not have to surpass a large number of water molecules. Nevertheless, in the herein used LLE in water–DCM, the ions are indeed capable of forming a hydration layer in water. This effect is even more pronounced for smaller ions; hence, lithium exhibits the strongest hydration shell among the studied salts and consequently

consumes the most energy upon dehydration. Hence, a truly selective complexation of lithium in the LLE is essential.

An interesting implementation is the application of these materials for instance in the Dead Sea. The Dead Sea contains approximately 4 % potassium and approximately 30 % sodium ions. Moreover, potassium ions possess significantly larger radii compared to lithium ions and can thus easily be neglected by choosing a suitable CE size, for example by utilizing B9C3 CEs. On the other hand, the ionic radius of sodium ions is just 0.3 Å taller compared to lithium ions and therefore are the bigger issue. In the following sections, the extraction is hence focused on sodium and lithium salts.

In an LLE of water–DCM with sodium salt, the B15C5, B12C4, and B9C3 CEs were used as extraction materials for sodium complexation using NaEE as sodium salt. The complex constant K and the Gibbs free energy ΔG were determined for different CE:salt molar ratios and are illustrated in Figure 6. It is not surprising that the B15C5 and B12C4 show strong complexation with sodium with a $\log K$ of 5.68 and 8.23, respectively. The CE size of B15C5 with a cavity size of 0.85–1.1 Å fits perfectly well for the sodium ion with an ionic radius of 0.95 Å and forms therefore a single complex. On the other hand, the B12C4 CE with a cavity size of 0.50–0.65 Å forms sandwich complexes with sodium. This complexation process leads to an entropy loss, yet, new electrostatic interactions are created which lead to a negative enthalpy gain explaining the high complex stability of $\log K = 8.23$. Surprisingly, the B9C3 CE shows similar complex stabilities as found for the B12C4 CE. For the calculation of this CE, a sandwich formation was assumed. Compared to the visual test, where clearly no complexation occurred with the B9C3 CE in DCM, the radius of the sodium ion increases in water due to the aforementioned hydration shell. It is assumed that the B9C3 CE might be too small to form a sandwich complex with sodium as it was the case for B12C4 (see Figure 5). In that case, an increased possibility to form higher-order

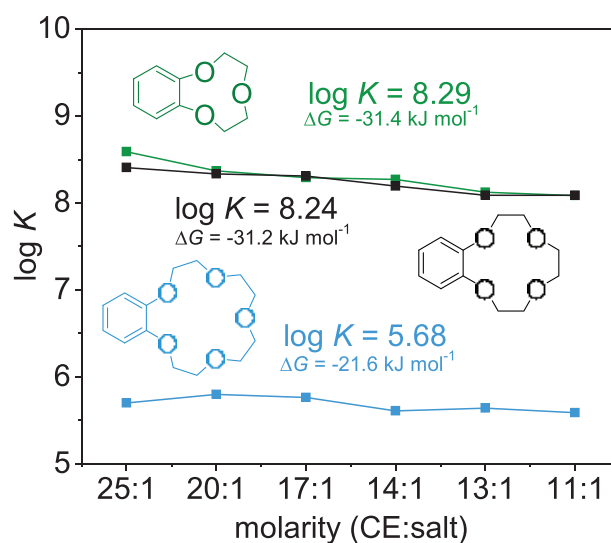


Figure 6. Logarithmic complexation stability K of B9C3 (green curve), B12C4 (black curve), and B15C5 (blue curve) with Na-EE at different CE:Salt molar ratios and the average of $\log K$ and Gibbs free energy ΔG were determined.

complex structures may also increase the overall enthalpy gain.^[43] Besides the possibility of higher-order complex clusters, the sodium needs lower energies to surpass the hydration shell compared to lithium and has therefore a high complex stability constant of $\log K = 8.29$. A similar observation was made by calculating the Gibbs free energy ΔG . Since free CEs have a high mobility in solution, the process of multiple coordination seems not unfeasible. However, this multiple coordination should be highly hindered in polymer systems, where the CE is covalently bound to the backbone and is, therefore, less agile. Hence, the complexation process of lithium and sodium with B9C3 CEs bound polymer systems was investigated and is presented in the following.

Polymer materials are especially attractive in LLE since they are easy to isolate from solution or mixtures. CE-based polymers are well known to extract various metals from aqueous solution via LLE and became a key issue towards the treatment of wastewater. Moreover, these materials can also be used in ion exchange resin or membranes. M. Kazemabad et al.^[56] reported on a polyelectrolyte multilayer membrane (PEMM) with incorporated B15C5 CEs in the poly(ethylene imine) (PEI) main chain structure to achieve stable complexes with lithium rather than potassium. Furthermore, the PEMMs offer superb potential in monovalent/bivalent ion selectivity.^[57] The use of 18-crown-6 in the main chain of poly(arylene ether ketone)s and blending with sulfonated poly(ether ether ketone) (PEEK) led to monovalent cation selective-membranes with good selectivity towards potassium over lithium.^[58] Recently, polybenzoxazines were prepared for metal ion adsorption. The polymer material did not only show complexation with lithium, but also effective catalytic behavior and promote ring-opening polymerization when lithium is bonded to the CE.^[59] Here, a diblock copolymer of PS-*b*-PMAA is considered, since this polymer can be easily functionalized with CEs due to the carboxylic acid groups in the PMAA block. Furthermore, the major polystyrene block gives the polymer its hydrophobicity, which makes it insoluble in water. The synthesis of a PS-*b*-PMAA diblock copolymer with molecular weights up to 100 kDa within a few hours was conducted via a solution-emulsion RAFT polymerization by polymerization-induced self-assembly (PISA). This technique has become a powerful tool for the efficient synthesis of diblock copolymer nanoparticles, it is robust and a highly versatile technique.^[60–62] PMAA diblock copolymers using this technique in dispersion have been intensively studied by the group of S. Armes.^[63,64] The polymerization of styrene via RAFT emulsion polymerization has been intensively studied by our group and has many advantages such as fast reaction rates, economically feasible reaction conditions, and high molar masses with narrow dispersity.^[65,66] The synthesis of PS-*b*-PMAA has one additional advantage, that is, the diblock copolymer can be synthesized in a single batch as initially reported by the group of Charleux et al. for a similar polymer.^[67–69] In our case, methacrylic acid (MAA) was polymerized in water up to high conversions; afterwards, styrene was added to the same vessel and polymerized to obtain the PS-*b*-PMAA diblock copolymer. The benefits of such a polymer system are obvious: it is straightforwardly prepared, the monomers are cheap and available on a large scale, it relies on non-toxic solvents solely, and it can be facilely scaled up.

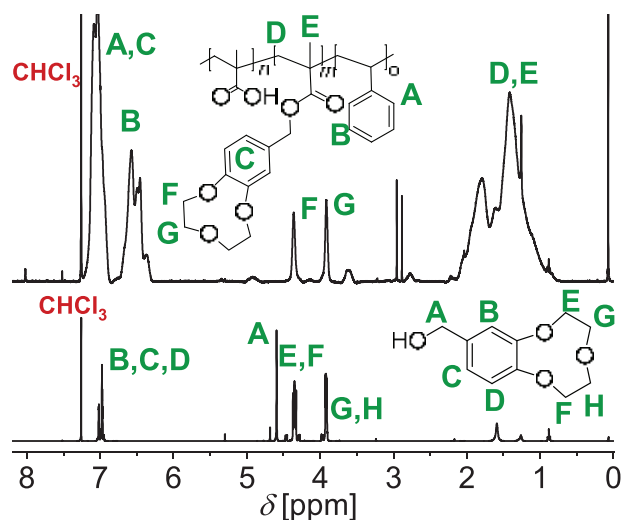


Figure 7. ^1H NMR spectrum of Benzo-9-crown-3 CE (bottom) and PS₆₀-*b*-P(MAA₂₀-*r*-CE3MA₂₀)⁴⁹ diblock copolymer containing randomly distributed CE units (top) in CDCl₃.

The incorporation of a new functional group within the polymer can be easily achieved by post-modification. Some of the efficient reactions are thiol-ene, Michael-addition, nucleophilic activated ester/amine exchange, thiol-disulfide exchange, or Diels-Alder cycloaddition.^[70] In here, the PS₇₀-*b*-PMAA₃₀⁴¹ diblock copolymer was post-modified with hydroxyl-functionalized B9C3 CE via Steglich esterification. A schematic illustration of the monomer preparation can be found in Figure S1, Supporting Information. The successful incorporation of the CE moiety was confirmed by NMR spectroscopy (Figure 7) and IR spectroscopy Figures S17–S19, Supporting Information). The protons of the CE (E, F, and G, H in the B9C3 spectrum) are shown as broad signals indicating that the CEs are covalently bound to the polymer (Peak F and G in the polymer spectrum). The degree of functionalization was calculated by comparing the peak B, which refers to the protons of polystyrene in the *meta* position to the peaks of F or G, which represent the protons of the CE. IR spectroscopy of B9C3 CE (Figure S17, Supporting Information) revealed the characteristic C-O stretch absorption bands at 1230 cm⁻¹ for alkyl aryl ethers and 1053 cm⁻¹ for aliphatic ethers. The PS₇₀-*b*-PMAA₃₀⁴¹ diblock copolymer after post-modification with B9C3 CE revealed the characteristic C-O stretch absorption bands at 1143 cm⁻¹ and 1013 cm⁻¹ (Figure S19, Supporting Information). The C=O stretch of the remained (deprotonated) carboxylic acid groups of the PMAA moiety can be found at 1500 cm⁻¹ and for the C=O stretch of the newly formed ester bond after the Steglich esterification at 1667 cm⁻¹.^[71]

Generally, CEs in polymer materials show high complex stability since the CEs are linked to the polymer and therefore exhibit a decreased entropy loss (compared to free CEs) upon the formation of the metal complex. In addition, the side chains of a polymer including electron donor atoms or ionizable functionalities can further stabilize the complex. Regarding the PS-*b*-PMAA diblock copolymer, MAA is easily ionizable and assists therefore a good complexation with lithium and the CE-based

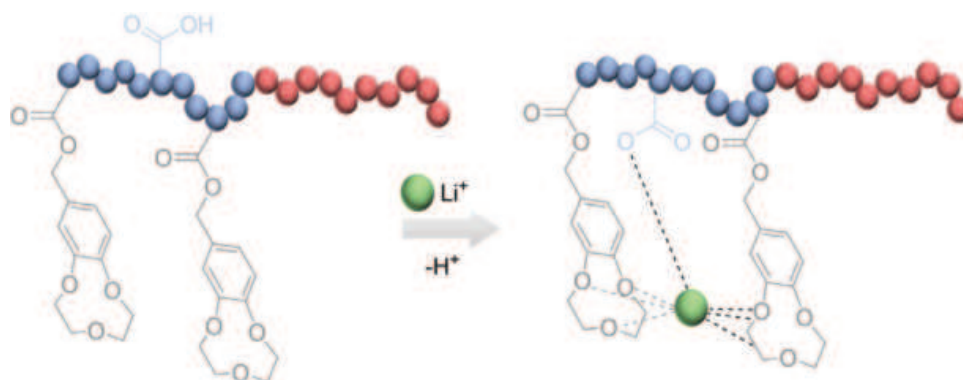


Figure 8. Possible lithium extraction mechanism with MAA side chains. The lithium substitutes the proton in the ionizable side chain and subsequently forms a complex with the CEs.

polymer. A potential complexation mechanism is illustrated in **Figure 8**. Upon incorporation of the lithium cation, the deprotonated carboxylic acid and the CEs both stabilize the ion, which is highly attractive due to manifold interaction sites. Concurrent observations have been reported for a similar system with phosphoric acid side chains.^[72]

Initial qualitative evidence that the PS-*b*-PMAA diblock copolymer containing CEs is well suited for the complexation was shown again by a visual test. A polystyrene-*block*-poly(MAA-*random*-15-crown-5 methyl methacrylate) (PS-*b*-P(MAA-*r*-CE5MA)) polymer was dissolved in DCM (bottom layer) and extracted NaEE salt from water (top layer), which has been proven suitable for this CE size (**Figure 9**). The NaEE salt gives a yellow color under UV-light. The visual test confirms that it is located in the top layer before extraction. After the LLE, the yellowish color moves to the bottom layer, proving

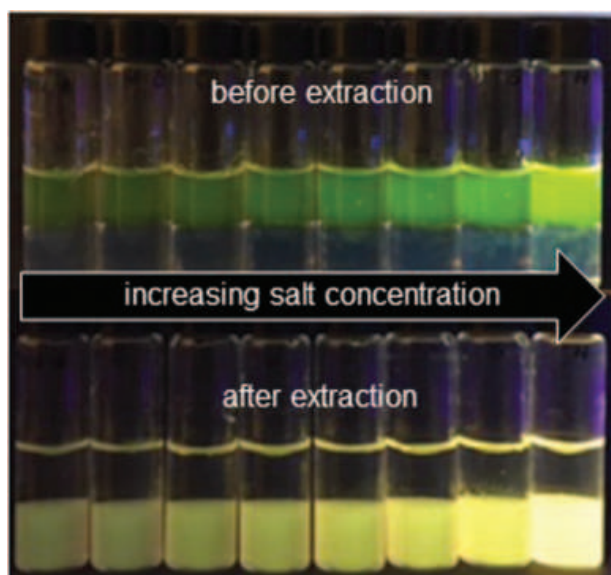


Figure 9. Photograph of the PS₅₀-*b*-P(MAA₂₅-*r*-CE5MA₂₅)⁵⁶ polymer extraction with EE-Na under UV-light. Before extraction, the EE-Na salt is in the aqueous phase (top layer) and after extraction in the organic phase (bottom layer). The concentration of the salt increases from left to right, as it can be seen by the color intensity of the yellow phase.

that the salt is indeed transferred into the organic phase by a successful and seemingly quantitative complexation with the polymer. Since almost complete discoloration is observed in the aqueous phase, it can be assumed that the polymer showed excellent complexation with sodium ions. In order to prove this observation with the desired polymer system containing B9C3 CEs, similar experiments to those of the free CE were conducted by extracting sodium and lithium. The complex stability was investigated by calculating *K* and ΔG .

Similar to the other extractions, the PS₆₀-*b*-P(MAA₂₀-*r*-CE3MA₂₀)⁴⁹ polymer was dissolved in DCM. The subscripts indicate the weight percentage of the block and the superscript gives the target *M_n* of the polymer in kDa. The extraction for this polymer was conducted with NaEE and same extractions times, stirring speed, and phase separation times as for the free CEs were used. A CE:salt molar ratio of 10:1 was targeted for all the extractions with sodium salt. Most notably, the extraction of sodium salt with a polymer system delivered the expected and thus very satisfying results (**Figure 10**). Compared to the free CE, log *K* of the copolymer bound B9C3 CE increased significantly from 7.5 to 11. At first, the value seems reasonably high;

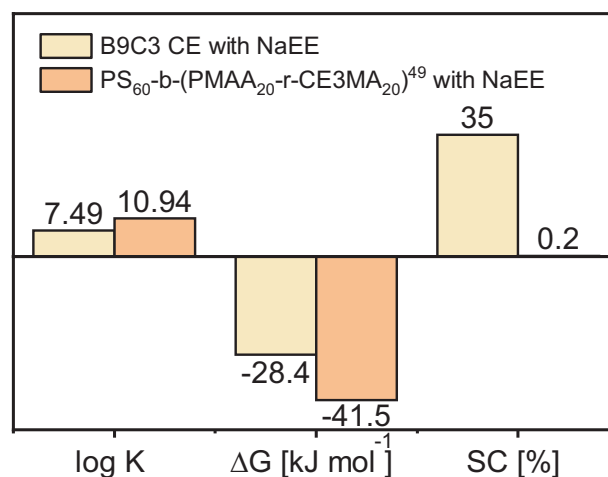


Figure 10. Comparison of the logarithmic complex stability, Gibbs free energy, and SC of free B9C3 and PS₆₀-*b*-(PMAA₂₀-*r*-CE3MA₂₀)⁴⁹ with NaEE.

however, it should be considered that the sodium ion has a quite thin and loose hydration shell, and the complexation of the ion is therefore favorable in energy terms. The Gibbs free energy decreased from -28 to -42 kJ mol^{-1} resulting in a more spontaneous complexation and the salt complexation in percent (SC) was decreased from 35 % to just about 0.2 %. The SC is defined as the ratio of the complex concentration (c_{complex}) and the initial salt concentration in percent. As predicted, the complexation of sodium in the polymer system shrank due to the mobility loss of the CEs. This result indicates the assumed mechanism of the complexation of bigger metal ions such as sodium and potassium to form higher-ordered complexes. The mobility is less pronounced in the polymer system due to the lack of mobility within the polymer material and leads, therefore, to much smaller complex stabilities compared to free CEs in solution. In previous publications, 14-membered CEs showed so far the best complexation with lithium. However, only the incorporation of tetramethyl (metal distribution coefficient $\log D_{\text{Li}} = 3.35$ for lithium and $\log D_{\text{Na}} = -0.02$ for sodium), bicyclopentyl ($\log D_{\text{Li}} = 3.53$, $\log D_{\text{Na}} = 0.13$) and bihexyl ($\log D_{\text{Li}} = 3.23$, $\log D_{\text{Na}} = 0.85$) side chains confirmed complexation without sodium.^[49] Compared to the previously reported CEs, the incorporation of the B9C3 CE within the polymer avoids the synthesis of sterically demanding CEs.

Before investigating the lithium extraction in the polymer system, it should be mentioned that the hydration shell is easier to strip off for sodium than it is for lithium. Therefore, the lithium ions will always need more energy to be complexed.

To prove the lithium extraction capabilities of our new polymer material, LIS was extracted with $\text{PS}_{52}\text{-}b\text{-P}(\text{MAA}_{12}\text{-}r\text{-CE3MA}_{36})^{76}$, using the same extraction conditions as before and using a CE:salt ratio of 13:1 for all extractions. After the extraction, a signal at around 280 nm occurred in the UV-vis spectrum, which is attributed to the polystyrene within the block copolymer (Figure S15, Supporting Information). Since 1.7 % DCM can be dissolved in water and the polymer dissolves in DCM, the signal around 280 nm is not surprising.^[73] However, given that the same volumes were used for all extractions, the error of the extractions remained the same. The final absorption was calculated by constructing a calibration curve at 342 nm, where PS does not show a significant extinction (Figure S15, Supporting Information). The complex stability constant K , the Gibbs free energy ΔG , and the SC were calculated and compared to corresponding values obtained for the free B9C3 CEs (Figure 11). The complex constant for the free B9C3 CE with lithium showed a value of $\log K = 6.9$ and increased in the polymer system to 10. This is indeed remarkable as the polymer complex stability is almost 10^4 times higher than for the free B9C3 CE. The gain of negative enthalpy is possibly due to additional electrostatic interactions between the lithium ion and not only the oxygen atoms of the CE but also the deprotonated carboxylic acid groups in the polymer (Figure 8). Although, the sandwich formation leads to an entropy loss, this loss is less significant compared to a free B9C3 CE and consequently yields a much higher complex stability. The ΔG value decreased from -26 to -39 kJ mol^{-1} which also supports the more favorable extraction by the polymer. Moreover, the SC of lithium in the polymer was around 39 %, while the fraction for sodium in the polymer was just 0.2 % and thus negligibly small.

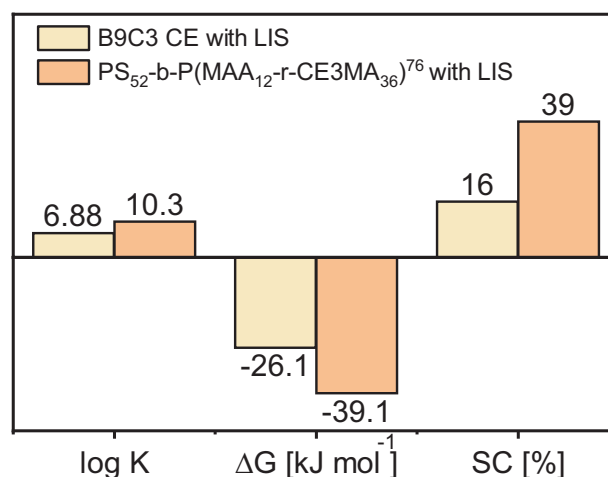


Figure 11. Comparison of the logarithmic complex stability, Gibbs free energy, and SC of free B9C3 and $\text{PS}_{52}\text{-}b\text{-P}(\text{MAA}_{12}\text{-}r\text{-CE3MA}_{36})^{76}$ with LIS.

The $\text{PS}_{70}\text{-}b\text{-P}(\text{MAA}_{7}\text{-}r\text{-CE3MA}_{23})^{120}$ was furthermore used to extract lithium ions from a mixture of salts including sodium, potassium, and lithium ions, with their concentrations being as high as in the Dead Sea, to have a realistic comparison with a global lithium resource.^[23,74] The lithium concentration was set to 0.014 g L^{-1} , the potassium concentration to 6.9 g L^{-1} and the sodium concentration was 37 g L^{-1} . Since the NaEE and KEE salts were not soluble in water at these concentrations, the sodium and potassium salts were replaced with sodium- and potassium chloride. Furthermore, these salts do not show UV-vis signals, therefore, only the signal of the lithium salt is visible in UV-vis spectroscopy. After the extraction process, a $\log K$ of 8.57, $\Delta G = -32.5$ kJ mol^{-1} , and an SC of 60 % was determined. A similar experiment was conducted by replacing the lithium dye with the sodium dye (NaEE) using a concentration of 0.045 g L^{-1} and keeping the same sodium- and potassium chloride concentration to prove that the UV-vis signal in the lithium dye experiment refers really to the lithium-ion complexation, since an anion exchange could occur. However, after this LLE, ≈ 0 % complexation was determined for the NaEE dye. The same experiments were conducted with $\text{PS}_{52}\text{-}b\text{-P}(\text{MAA}_{12}\text{-}r\text{-CE3MA}_{36})^{76}$ and resulted in 53% complexation for the lithium dye experiment and just 4% complexation for the sodium dye experiment. Thus, the absorption signal after the extraction can be referred to the lithium complexation with the CE. These results are very satisfying since at least a 14-fold higher selectivity for lithium was determined compared to sodium and this even at very low concentration of lithium in the presence of 2640 times higher concentration of sodium. As mentioned before, these results support our assumption, that the B9C3 CE is too small for a sandwich complexation with sodium. Higher ordered complex structures would be needed in order to complex the sodium ion with the B9C3 CE, however, this may be hindered by the polymer conformations. It can clearly be stated, that the sandwich formation of B9C3 CE with lithium is more favored compared to the complexation with sodium. Compared to the lithium selectivity by adsorption, more specifically, for lithium ion-sieves consisting of manganese oxide, lower lithium selectivity is obtained. Just recently, a lithium



ion-sieve consisting of nanostructured manganese oxide made of $(\text{NH}_4)_2\text{S}_2\text{O}_8$ revealed a separation factor of 2095 for sodium and lithium, and with the use of $\text{Na}_2\text{S}_2\text{O}_8$, a separation factor of 5521 was reached.^[75] These materials show low toxicity, are cheap, show high lithium capacities, and superb regeneration behavior. However, so far, the upscale of such materials is still challenging as is the lack of adsorbents for industrial applications.^[76] Furthermore, the solvent extraction method utilizing polymer-bound CEs has higher purities and the process is more straightforward. Altogether, our results evidence the successful preparation of a highly lithium selective polymer which prefers the recovery of lithium rather than sodium or potassium and it presents a considerable alternative to other lithium extraction/adsorption processes.

3. Conclusion

In this work, we reported a highly lithium selective CE functionalized diblock copolymer favoring lithium over other interfering alkali metal ions. Three different CEs with different cavity sizes were analyzed and used for LLE of UV-responsive lithium, sodium, and potassium salts. The complex stability and the Gibbs free energy were calculated from UV-vis spectroscopy data. The effect of single or sandwich complexes was investigated with these salts, highlighting the thermodynamic effects of different complex formations on the extractability of these salts. The new B9C3CE showed significantly increased extraction capabilities for lithium due to the enthalpically favorable sandwich formation of this ion between two of the CEs. Coupling this CE to a polymer even multiplies its potential to make complexes (besides being straightforwardly removable from the extraction medium), leading to a 10^4 times higher complex stability. Uptake of other ions like sodium and potassium was additionally proven to be comparatively insignificant, making this polymer highly selective for the extraction of only lithium. In a nutshell, this study illustrates that our CE functionalized diblock copolymer is not only facilely producible, but also a suitable candidate for a selective membrane material, which would overcome viscosity issues and solubility errors in both phases if higher amounts of the polymer are needed. Concerning reversibility, the metal ions can be released by temperature increase, since the salt-coordination mechanism is a temperature-sensitive process as it was reported in a previous publication.^[77] Therefore, this polymer material is very attractive in regards to lithium recovery from the ocean, seawater or salt-lake brines.

4. Experimental Section

Materials: All the reagents were obtained from commercial suppliers and were used as received without further purification unless otherwise noted. Styrene was purified by filtration through basic activated aluminum oxide to remove the inhibitor. 4-Cyano-4-thiolythiopropylsulfanyl pentanoic acid (CPP) was synthesized according to the literature.^[78] B9C3 CE was attained based on a reaction with Catechol.^[79] Deionized water was purified with a Milli-Q integral water purification system. The subscripts in the designation of the polymers represent the fraction of the respective block in wt% and

the superscript represents the overall molecular weight in kDa. The theoretical molecular weights of all polymers are calculated from the following equation:

$$M_{n,th} = \frac{[M]_0 \cdot p \cdot M_M}{[CTA]_0} + M_{CTA} \quad (3)$$

where $[M]_0$ and $[CTA]_0$ are the initial concentrations of monomer and chain transfer agent, p the monomer conversion, and M_M and M_{CTA} are the molar masses of monomer and chain transfer agent.

Liquid-Liquid Extraction of Metal Ions: The organic phase was prepared by dissolving appropriate amounts of CE in 3 mL DCM. The aqueous phase was prepared by diluting salts in water at different concentrations. For all extraction experiments, the volume ratio of DCM-water was 1:1. The extraction proceeded by vigorously shaking the vial for 45 min at 500 rpm at certain temperatures. Phase separation was guaranteed by waiting 30 min after extraction. The aqueous phase was properly diluted, and the remaining concentration of the metal ion was measured by UV-vis spectrometry.

General Methods: ^1H NMR and ^{13}C NMR spectra were recorded at ambient temperature using a 300 or 400 MHz Bruker AVANCE II spectrometer in either CDCl_3 , D_2O , or THF- d_6 . The residual signals at $\delta = 7.26$ for CDCl_3 , $\delta = 4.80$ ppm for D_2O , and $\delta = 3.58$ ppm for THF- d_6 were used as an internal standard for the chemical shifts. Molecular weight distributions were obtained using THF GPC with 5 wt% TFA. Polymer solutions were prepared in THF containing toluene as an internal reference. The GPC-set-up comprised an Agilent 1260 Infinity series degasser and pump, a combination of three PSS SDV columns (100, 1000, and 10 000 Å) connected in series to both, a refractive index and a UV detector. The system was operating with a flow rate of 1.0 mL min^{-1} at 30 °C and the injection volume of the polymer solution ($c = 1 \text{ g L}^{-1}$) was 100 μL . Calibration was achieved using a series of near-monodisperse poly(methyl methacrylate) (PMMA) standards (for macro-CTA synthesis) or polystyrene standards (for diblock synthesis). UV-vis spectroscopy was performed on a Cary 50 (Varian) spectrometer with a range of 250–600 nm with a resolution of 480 nm min^{-1} . FT-IR spectra were recorded for solid samples at room temperature using a Thermo Scientific Nicolet iS10 FT-IR spectrometer fitted with a Golden Gate Diamond ATR accessory. Each spectrum was averaged over 64 scans at a resolution of 2 cm^{-1} .

Synthesis of CPP: CPP RAFT agent was synthesized via a modified procedure adapted from Xu et al.^[78] 1-Propanethiol (5.0 mL, 0.055 mmol) was added dropwise to a solution of potassium hydroxide (3.9 g, 0.069 mmol) in 20 mL of water under nitrogen atmosphere. Carbon disulfide (3.3 mL, 0.055 mmol) was added in one portion to the resulting reaction mixture and vigorously stirred for 30 min at room temperature. Afterwards, the reaction mixture was cooled to -5 °C and a solution of *p*-tosyl chloride (5.3 g, 0.028 mmol) in distilled acetone (28 mL) was added in portions over 20 min. After stirring an additional 2 h at -5 °C, any acetone residue was removed under reduced pressure. The crude product was extracted with DCM (100 mL) and the organic layer was washed three times with deionized water (50 mL). The resulting solution was dried over anhydrous magnesium sulfate, filtered, and evaporated to dryness to yield bis(propylsulfanylthiocarbonyl) disulfide as a red oil (7.24 g, 87 %). In a second step, 4,4'-azobis(4-cyanovaleic acid) (ACVA) (8.89 g, 31.7 mmol) and bis(propylsulfanylthiocarbonyl) disulfide (4.80 g, 15.7 mmol) were dissolved in ethyl acetate (120 mL) and heated under reflux at 85 °C for 24 h. After removal of the volatiles in vacuo, the crude product was purified by column chromatography on silica gel with a mobile phase of *n*-hexane/ethyl acetate (3:1 v/v). The product was obtained as an orange powder (4.84 g, 55 %). ^1H NMR (400 MHz, CDCl_3 , δ): 3.31 (t, $^3J = 6$ Hz, 2H, -S-CH₂-CH₂-CH₃), 2.72–2.40 (m, 4H, COOH-CH₂-CH₂-C-), 1.87 (s, 3H, -C-CH₃), 1.73 (m, 2H, -S-CH₂-CH₂-CH₃), and 0.96 (t, $^3J = 6$ Hz, 3H, -S-CH₂-CH₂-CH₃); ^{13}C NMR (400 MHz, CDCl_3 , δ): 220 (C=S), 178 (-COOH), 119 (-CN), 46.0 (C-CN), 39.2 (-S-CH₂-), 29.2 (CN-C-CH₂-), 24.8 (COOH-CH₂-), 22.5 (S-CH₂-CH₂-), 21.3 (CN-C-CH₃), and 13.5 (-S-CH₂-CH₂-CH₃); HRMS (ESI) m/z : $[M + \text{H}]^+$ calcd. for

$C_{10}H_{15}N_3O_2S_3$, 278.0338; found, 278.0342. Anal. calcd. for $C_{10}H_{15}N_3O_2S_3$: C 43.3; H 5.45; S 34.7; N 5.05 found: C 44.5; H 5.60; S 32.9; N 5.45.

Synthesis of PMAA: A typical polymerization of PMAA was as follows.^[80] MAA (3.6 g, 0.042 mol), CPP (0.097 g, 3.5×10^{-4} mol), ACVA (0.0098 g, 3.5×10^{-5} mol), water (15 mL), and DMF (0.54 mL, 7.0×10^{-3} mol) were added to the reaction flask and purged with nitrogen in an ice bath for 30 min. The sealed reaction flask was immersed into a preheated oil bath for 6 h at 80 °C. The reaction was quenched by exposure to air. Water was removed under reduced pressure, the residual oil re-dissolved in ethanol and precipitated into an excess of diethyl ether. Any residual diethyl ether, water, or ethanol was removed by drying the precipitate in vacuo at room temperature for 24 h. The conversion was determined by ¹H NMR spectroscopy in D₂O.

One-Pot Synthesis of PS-*b*-PMAA: A typical polymerization of PS-*b*-PMAA was as follows:^[80] MAA (3.4 g, 0.040 mol), CPP (0.055 g, 2.0×10^{-4} mol), ACVA (0.0056 g, 2.0×10^{-5} mol), 14 mL water, and DMF (0.48 g, 6.7×10^{-3} mol) were added to the reactions flask and were purged with nitrogen in an ice bath for 30 min. The sealed reaction flask was immersed into a preheated oil bath for 6 h at 80 °C to reach full conversion. The reaction was quenched by exposure to air. A sample was taken for ¹H NMR spectroscopy in D₂O and for GPC measurements in THF after methylation. A solution of styrene (8.3 g, 0.080 mol), ACVA (0.0112 g, 4.0×10^{-5} mol), and NaHCO₃ (0.012 g, 1.4×10^{-5} mol) in water (32 mL) was added to the reaction mixture, degassed with nitrogen for 30 min, and immersed into a preheated oil bath for 2 h at 80 °C. After cooling to room temperature, water was removed under reduced pressure, the crude product re-dissolved in THF and precipitated into excess *n*-hexane. Any residual solvent was removed by drying the precipitate in vacuo at room temperature for 24 h. A 99 % conversion was determined by ¹H NMR spectroscopy in THF-*d*₆ and its distribution analyzed by GPC in THF with 5 wt% Trifluoroacetic acid with a dispersity *D* of 1.30 and a targeted *M_n* of 42 kDa. IR (KBr): $\nu = 2913$ (w), 2853 (w), 1586 (m), 1506 (s), 1452 (m), 733 (s).

Synthesis of Benzo-9-Crown-3: Benzo-9-crown-3 CE was synthesized according to a literature procedure.^[79] Catechol (15.6 g, 0.141 mol) and lithium hydroxide (6.77 g, 0.283 mol) were dissolved in 825 mL water and degassed for 1 h. Bis-2-chloroethylether (16.6 g, 0.141 mol) was added dropwise to the solution under nitrogen flow and was stirred for 30 min at room temperature. The resulting reaction mixture was refluxed for 86 h at 100 °C. The crude product was purified by steam distillation to obtain white crystals (3.91 g, 15 %). ¹H NMR (300 MHz, CDCl₃, δ): 7.15–6.81 (m, 4H, -Ph-H), 4.41–4.29 (m, 4H, Ph-O-CH₂-CH₂-), and 3.98–3.87 (m, 4H, Ph-O-CH₂-CH₂-); GC-MS (EI) *m/z* (%): [M]⁺ calcd. for C₁₀H₁₂O₃, 180.0781 found, 180.0000 (60.91 %); IR (KBr): $\nu = 2950$ (w), 2905 (w), 2857 (w), 1577 (m), 1493 (s), 1230 (s), 1053 (s), 764 (s).

Synthesis of 9-Formyl-Benzo-9-Crown-3: 9-Formyl-benzo-9-crown-3 (B9C3-CHO) was synthesized via a revised procedure to that previously reported by Luo et al.^[81] B9C3 (3.38 g, 1.87×10^{-2} mol) and hexamethylenetetramine (2.63 g, 1.87×10^{-2} mol) were dissolved in trifluoroacetic acid (16 mL) and the mixture was heated at 90 °C for 4 h under nitrogen atmosphere. Afterwards, water (32 mL) was added to the reaction mixture and stirred for another 90 min at 90 °C. The reaction was cooled to room temperature and the pH was adjusted to 7 by adding saturated aqueous NaHCO₃ solution to the mixture. The crude product was extracted with DCM (3 × 10 mL) and the combined organic layers were washed three times with deionized water (3 × 10 mL) and dried over anhydrous magnesium sulfate. The resulting solution was filtrated, and DCM was evaporated under reduced pressure. After removal of the volatiles in vacuo, the crude product was purified by column chromatography on silica gel with a mobile phase of ethyl acetate/*n*-hexane (85/15 v/v). The product was obtained as a yellow-colored oil (3.90 g, 36.6 %). ¹H NMR (300 MHz, CDCl₃, δ): 9.85 (s, 1H, -CHO), 7.56–7.54 (d, ⁴*J* = 2.0 Hz, 1H, CHO-C-CH-C-), 7.54–7.48 (dd, ³*J* = 8.2 Hz, ⁴*J* = 2.0 Hz, 1H, CHO-C-CH-CH-), 7.10–7.03 (d, ³*J* = 8.2 Hz, 1H, CHO-C-CH-CH-), 4.69–4.56 (m, 2H, -C-O-CH₂-), 4.35–4.23 (m, 2H, -C-O-CH₂-), and 4.05–3.85 (m, 4H, -CH₂-O-CH₂-); GC-MS (EI) *m/z* (%): [M]⁺ calcd. for C₁₁H₁₂O₄, 208.073 found, 208.000 (37.98 %).

Synthesis of 4-Methanol-Benzo-9-Crown-3: Benzo-9-crown-3-9-methanol (B9C3-OH) was synthesized according to a literature procedure.^[82]

B9C3-CHO (1.43 g, 6.86×10^{-3} mol) was dissolved in methanol (20 mL) and cooled to 0 °C. Sodium borohydride (0.52 g, 1.37×10^{-2} mol) was added dropwise to the reaction mixture and was then stirred for 2 h at room temperature. The resulting solution was poured into a slight excess of water (40 mL) and subsequently extracted with DCM (3 × 100 mL). The combined organic layers were dried with anhydrous magnesium sulfate, filtrated, and concentrated in vacuo to obtain a white solid (1.44 g, 98 %). ¹H NMR (300 MHz, CDCl₃, δ): 7.06–6.90 (m, 3H, -Ph-H), 4.57 (s, 2H, -CH₂-OH), 4.46–4.19 (m, 4H, Ph-O-CH₂-), and 4.00–3.81 (m, 2H, - Ph-O-CH₂-CH₂-). GC-MS (EI) *m/z* (%): [M]⁺ calcd. for C₁₁H₁₄O₄, 210.0887 found, 210.000 (100 %).

Synthesis of PS-*b*-P(MAA-*r*-CEMA): The typical protocol for the synthesis of PS-*b*-P(MAA-*r*-CEMA) was as follows. PS-*b*-PMAA (1.0 g, 3.5×10^{-3} mol, based on the MAAs group, *M_{n, theo}* = 60 kDa), B9C3-OH (0.19 mL, 1.0×10^{-3} mol), and DMAP (0.043 g, 3.5×10^{-4} mol) were dissolved in dry DMF (50 mL) and refluxed under nitrogen atmosphere. DCC (0.93 g, 4.5×10^{-3} mol) was dissolved in dry DMF (4 mL), and the solution was added dropwise to the reaction mixture and stirred for 24 h at 100 °C. The functionalized polymer was precipitated into excess methanol. Any residual solvent was removed by drying the precipitate in vacuo at 40 °C for 24 h. The product was analyzed by ¹H NMR spectroscopy in CDCl₃. IR (KBr): $\nu = 2928$ (w), 2846 (w), 1667 (w), 1500 (w), 1143 (w), 1013 (w), 757 (m), 700 (s).

Supporting Information

Supporting Information is available from the Wiley Online Library or from the author.

Acknowledgements

The authors acknowledge the NMR spectroscopic and mass spectrometry division of the Department of Chemistry at the University of Hamburg, Horst Weller for granting access to the UV-vis spectrometer, Dr. Felix Lauterbach for his inputs in the calculation formula and constructive advice, and Fanny Ott for the IR measurements.

Open access funding enabled and organized by Projekt DEAL.

Conflict of Interest

The authors declare no conflict of interest.

Data Availability Statement

Research data are not shared.

Keywords

crown ether functionalized polymers, ion extraction, lithium recovery, polymerization-induced self-assembly, water filtration

Received: December 19, 2020

Revised: January 11, 2021

Published online: March 1, 2021

[1] D. Eckhardt, *J. Fusion Energy* **1995**, *14*, 329.

[2] A. Abd El-Aty, Y. Xu, X. Guo, S. H. Zhang, Y. Ma, D. Chen, *J. Adv. Res.* **2018**, *10*, 49.



- [3] O. A. Avramchik, E. I. Korotkova, E. V. Plotnikov, A. N. Lukina, Y. A. Karbainov, *J. Pharm. Biomed. Anal.* **2005**, *37*, 1149.
- [4] L. M. Palacios-Romero, H. Pfeiffer, *Chem. Lett.* **2008**, *37*, 862.
- [5] A. K. Sutar, T. Maharana, S. Dutta, C. T. Chen, C. C. Lin, *Chem. Soc. Rev.* **2010**, *39*, 1724.
- [6] D. Lin, Y. Liu, Y. Cui, *Nat. Nanotechnol.* **2017**, *12*, 194.
- [7] D. Kushnir, B. A. Sandén, *Resour. Policy* **2012**, *37*, 93.
- [8] H. Vikström, S. Davidsson, M. Höök, *Appl. Energy* **2013**, *110*, 252.
- [9] C. Grosjean, P. H. Miranda, M. Perrin, P. Poggi, *Renewable Sustainable Energy Rev.* **2012**, *16*, 1735.
- [10] T. P. Narins, *Extr. Ind. Soc.* **2017**, *4*, 321.
- [11] P. W. Gruber, P. A. Medina, G. A. Keoleian, S. E. Kesler, M. P. Everson, T. J. Wallington, *J. Ind. Ecol.* **2011**, *15*, 760.
- [12] G. Martin, L. Rentsch, M. Höck, M. Bertau, *Energy Storage Mater.* **2017**, *6*, 171.
- [13] J. Song, T. Huang, H. Qiu, X. M. Li, T. He, *Hydrometallurgy* **2017**, *173*, 63.
- [14] J. Yu, M. Zheng, Q. Wu, Z. Nie, L. Bu, *Sol. Energy* **2015**, *115*, 133.
- [15] Z. Xu, H. Zhang, R. Wang, W. Gui, G. Liu, Y. Yang, *Ind. Eng. Chem. Res.* **2014**, *53*, 16502.
- [16] B. Swain, *Sep. Purif. Technol.* **2017**, *172*, 388.
- [17] J. F. Song, L. D. Nghiem, X. M. Li, T. He, *Environ. Sci. Water Res. Technol.* **2017**, *3*, 593.
- [18] M. Irfan, Y. Wang, T. Xu, *Chem. Eng. J.* **2020**, *383*, 123171.
- [19] L. Ge, B. Wu, D. Yu, A. N. Mondal, L. Hou, N. U. Afsar, Q. Li, T. Xu, J. Miao, T. Xu, *Chinese J. Chem. Eng.* **2017**, *25*, 1606.
- [20] J. Lambert, M. Avila-Rodriguez, G. Durand, M. Rakib, *J. Memb. Sci.* **2006**, *280*, 219.
- [21] T. Sata, R. Izuo, Y. Mizutani, R. Yamane, *J. Colloid Interface Sci.* **1972**, *40*, 317.
- [22] B. Van Der Bruggen, A. Koninckx, C. Vandecasteele, *Water Res.* **2004**, *38*, 1347.
- [23] B. S. Krumgalz, F. J. Millero, *Mar. Chem.* **1982**, *11*, 477.
- [24] U. Olsher, M. G. Hankins, Y. D. Kim, R. A. Bartsch, *J. Am. Chem. Soc.* **1993**, *115*, 3370.
- [25] J. Xiao, Y. Jia, C. Shi, X. Wang, S. Wang, Y. Yao, Y. Jing, *J. Mol. Liq.* **2017**, *241*, 946.
- [26] V. V. Yakshin, N. A. Tsarenko, A. M. Koshcheev, I. G. Tananaev, B. F. Myasoedov, *Radiochemistry* **2012**, *54*, 54.
- [27] Y. Katayama, K. Nita, M. Ueda, H. Nakamura, M. Takagi, K. Ueno, *Anal. Chim. Acta* **1985**, *173*, 193.
- [28] R. E. C. Torrejos, G. M. Nisola, H. S. Song, J. W. Han, C. P. Lawagon, J. G. Seo, S. Koo, H. Kim, W. J. Chung, *Hydrometallurgy* **2016**, *164*, 362.
- [29] Y. Yahmin, H. D. Pranowo, R. Armunanto, *Indones. J. Chem.* **2010**, *10*, 106.
- [30] R. M. Izatt, K. Pawlak, J. S. Bradshaw, R. L. Bruening, *Chem. Rev.* **1991**, *91*, 1721.
- [31] A. Ahmed, M. A. Hashimi, K. Ayub, *J. Mol. Liq.* **2020**, *302*, 112577.
- [32] C. J. Pedersen, *J. Am. Chem. Soc.* **1970**, *92*, 386.
- [33] J. W. Steed, *Coord. Chem. Rev.* **2001**, *215*, 171.
- [34] G. W. Gokel, W. M. Leevy, M. E. Weber, *Chem. Rev.* **2004**, *104*, 2723.
- [35] P. E. Stott, J. S. Bradshaw, W. W. Parish, *J. Am. Chem. Soc.* **1980**, *102*, 4810.
- [36] T. B. Stolwijk, E. J. R. Sudholter, D. N. Reinhoudt, *J. Am. Chem. Soc.* **1987**, *109*, 7042.
- [37] A. Casadellà, A. H. Galama, O. Schaetzle, K. Loos, *Macromol. Chem. Phys.* **2016**, *217*, 1600.
- [38] A. Casnati, S. Barbosa, H. Rouquette, M. J. Schwing-Weill, F. Arnaud-Neu, J. F. Dozol, R. Ungaro, *J. Am. Chem. Soc.* **2001**, *123*, 12182.
- [39] J. D. Lamb, R. M. Izatt, C. S. Swain, J. J. Christensen, *J. Am. Chem. Soc.* **1980**, *102*, 475.
- [40] C. J. Pedersen, *J. Am. Chem. Soc.* **1967**, *89*, 2495.
- [41] Y. Liu, L. Tong, T. Hakushi, *J. Chem. Soc., Perkin Trans. 2* **1990**, *5*, 1247.
- [42] K. Nishizawa, S. I. Ishino, H. Watanabe, M. Shinagawa, *J. Nucl. Sci. Technol.* **1984**, *21*, 694.
- [43] C. J. Pedersen, H. K. Frensdorff, *Angew. Chem., Int. Ed. Engl.* **1972**, *11*, 16.
- [44] P. D. Beer, P. K. Hopkins, J. D. McKinney, *Chem. Commun.* **1999**, 1253.
- [45] D. L. Ward, A. I. Popov, N. S. Poonia, *Acta Cryst.* **1984**, *40*, 238.
- [46] Y. Sun, M. Zhu, Y. Yao, H. Wang, B. Tong, Z. Zhao, *Sep. Purif. Technol.* **2020**, *237*, 116325.
- [47] T. Maeda, M. Ouchi, K. Kimura, T. Shono, *Chem. Lett.* **1981**, *10*, 1573.
- [48] K. Kobiro, *Coord. Chem. Rev.* **1996**, *148*, 135.
- [49] R. E. C. Torrejos, G. M. Nisola, H. S. Song, L. A. Limjuco, C. P. Lawagon, K. J. Parohinog, S. Koo, J. W. Han, W. J. Chung, *Chem. Eng. J.* **2017**, *326*, 921.
- [50] W. Zhu, Y. Jia, Q. Zhang, J. Sun, Y. Jing, J. Li, *J. Mol. Liq.* **2019**, *285*, 75.
- [51] A. Bey, O. Dreyer, V. Abetz, *Phys. Chem. Chem. Phys.* **2017**, *19*, 15924.
- [52] N. V. Tkachenko, Z. M. Sun, A. I. Boldyrev, *ChemPhysChem* **2019**, *20*, 2060.
- [53] R. Rencsok, T. A. Kaplan, J. F. Harrison, *J. Chem. Phys.* **1993**, *98*, 9758.
- [54] R. Rencsok, K. A. Jackson, T. A. Kaplan, J. F. Harrison, M. R. Pederson, *Chem. Phys. Lett.* **1996**, *262*, 207.
- [55] O. A. Zakurdaeva, A. F. Asachenko, M. A. Topchiiy, S. V. Nesterov, *J. Radioanal. Nucl. Chem.* **2018**, *316*, 535.
- [56] M. Kazemabad, A. Verliefe, E. R. Cornelissen, A. D'Haese, *J. Memb. Sci.* **2020**, *595*, 117432.
- [57] O. Sanyal, I. Lee, *J. Nanosci. Nanotechnol.* **2014**, *14*, 2178.
- [58] S. Tas, B. Zoetebier, M. A. Hempenius, G. J. Vancso, K. Nijmeijer, *RSC Adv.* **2016**, *6*, 55635.
- [59] M. G. Mohamed, S. W. Kuo, *Macromolecules* **2020**, *53*, 2420.
- [60] Y. Ning, S. P. Armes, *Acc. Chem. Res.* **2020**, *53*, 1176.
- [61] F. D'Agosto, J. Rieger, M. Lansalot, *Angew. Chem., Int. Ed.* **2020**, *59*, 8368.
- [62] M. Semsarilar, V. Abetz, *Macromol. Chem. Phys.* **2020**, *222*, 2000311.
- [63] M. Semsarilar, E. R. Jones, A. Blanazs, S. P. Armes, *Adv. Mater.* **2012**, *24*, 3378.
- [64] M. Semsarilar, V. Ladmiral, A. Blanazs, S. P. Armes, *Polym. Chem.* **2014**, *5*, 3466.
- [65] F. Lauterbach, V. Abetz, *Soft Matter* **2020**, *16*, 2321.
- [66] S. Eggers, V. Abetz, *Polymers* **2017**, *9*, 668.
- [67] I. Chaduc, A. Crepet, O. Boyron, B. Charleux, F. D'Agosto, M. Lansalot, *Macromolecules* **2013**, *46*, 6013.
- [68] W. Zhang, F. D'Agosto, O. Boyron, J. Rieger, B. Charleux, *Macromolecules* **2011**, *44*, 7584.
- [69] W. Zhang, F. D'Agosto, P. Y. Dugas, J. Rieger, B. Charleux, *Polymer (Guildf)* **2013**, *54*, 2011.
- [70] K. A. Günay, P. Theato, H. A. Klok, *J. Polym. Sci., Part A: Polym. Chem.* **2013**, *51*, 1.
- [71] R. Konradi, J. Rühle, *Macromolecules* **2004**, *37*, 6954.
- [72] B. Swain, *J. Chem. Technol. Biotechnol.* **2016**, *91*, 2549.
- [73] R. M. Stephenson, *J. Chem. Eng. Data* **1992**, *37*, 80.
- [74] L. Li, V. G. Deshmane, M. P. Paranthaman, R. Bhave, B. A. Moyer, S. Harrison, *Johnson Matthey Technol. Rev.* **2018**, *62*, 161.
- [75] S. Zandevakili, M. R. Hamghavandi, *Inorg. Nano-Metal Chem.* **2020**, *50*, 382.
- [76] D. Weng, H. Duan, Y. Hou, J. Huo, L. Chen, F. Zhang, J. Wang, *Prog. Nat. Sci.: Mater. Int.* **2020**, *30*, 139.
- [77] A. Warshawsky, N. Kahana, *J. Am. Chem. Soc.* **1982**, *104*, 2663.
- [78] E. Xu, A. E. Smith, S. E. Kirkland, C. L. McCormick, *Macromolecules* **2008**, *41*, 8429.
- [79] A. Khazaei, S. Saednia, M. K. Borazjani, J. Saien, M. Kiani, A. Afkhami, *Supramol. Chem.* **2014**, *26*, 88.
- [80] I. Chaduc, M. Girod, R. Antoine, B. Charleux, F. D'Agosto, M. Lansalot, *Macromolecules* **2012**, *45*, 5881.
- [81] Y. Luo, N. Marets, T. Kato, *Chem. Sci.* **2018**, *9*, 608.
- [82] J. Q. Liu, J. J. Yang, J. F. Li, K. Li, X. D. Xiao, Y. L. Bai, J. W. Wang, *Mol. Catal.* **2017**, *443*, 125.

5.5 Publication 5:

Improved alkali metal ion capturing utilizing crown ether-based diblock copolymers in a sandwich-type complexation

The fifth and final Publication of this work builds on the work of Publication 4. In this communication, three free crown ethers (analogous to the crown ethers in Publication 4, B15C5, B12C4, and B9C3), were compared with the PMAA-*b*-PS bound crown ethers, and the complex stability of a single and sandwich complexation was compared.

As already shown in Publication 4, all three polymer-bound crown ethers showed a much higher complex stability than the free crown ethers, with a complexation constant at least 10.000 times stronger.

In addition, the effect of single and sandwich complexation was investigated using the polymer-bound B12C4 and B9C3 systems. The former forms a single complex with lithium, while the latter forms a sandwich complex. The effect of sandwich complexation ($\log K = 11$) was found to have a slightly more decisive influence on complex stability than single complexation ($\log K = 7.6$). This communication confirms the results from Publication 4. The polymer-bound crown ethers are thus strong metal ion adsorbers, with the sandwich complexation further enhancing this stability.

The Publication is reprinted with permission from I. Oral and V. Abetz, *Soft Matter*, **2022**, 18, 934 - published by The Royal Society of Chemistry. The related supporting information is available in Section 9.6.



Cite this: *Soft Matter*, 2022, 18, 934

Received 25th December 2021,
Accepted 13th January 2022

DOI: 10.1039/d1sm01815a

rsc.li/soft-matter-journal

Improved alkali metal ion capturing utilizing crown ether-based diblock copolymers in a sandwich-type complexation†

Iklima Oral^a and Volker Abetz^{*ab}

The complexation behavior of metals with free crown ethers (CE) and diblock copolymer-based CE is investigated. The latter shows at least 10 000 times stronger complexation than free CEs. On this basis, a highly stable CE complex within the polymer for efficient extraction of metal ions from low concentrations, e.g. lithium in seawater, is presented.

Lithium has drawn great interest due to its utilization in the electrical vehicle industry, glass, ceramics, lubricants, catalysis, alloy industries, and pharmaceuticals.^{1–6} The applications of lithium in the electric vehicle industry have created immense demand, huge price increases, and the consequent shortage of this raw material.⁷ Currently, lithium is gathered mainly from brines by solar evaporation processes, however, the availability of lithium resources on land is limited.^{8,9} Around 230 Bt. of lithium can be found in the seawater, therefore, several recovery techniques have been designed, such as adsorption, solvent extraction, and co-precipitation.^{6,8,10,11} Since many other interfering metal ions, such as Na⁺, K⁺, Mg²⁺, and Ca²⁺, are present in seawater at much higher concentrations than Li⁺, a highly selective recovery of the desired Li⁺ is mandatory.¹²

A high selectivity towards metal ions is provided by crown ethers (CEs), which form well-known host–guest complexes.^{13,14} The complexation of metal ions with CEs arises from ion–dipole interactions depending on the cation, stabilizing orbital interactions between charge transfer and polarization, and Pauli repulsive orbital interactions.¹⁵ The strength of the interaction, and thus the stability of the complex, can be adjusted by the orientation of the donor atoms in the CE, the cavity size, the choice of donor atom (soft or hard, according to the HSAB principle, e.g. N, S, or O), and substitutions of electron withdrawing or donating groups.^{16,17} In addition to the strength of the interaction, the stoichiometry of the

ligand to metal ion plays a significant role (Fig. 1). Single complexes, sandwich-type complexes as well as club sandwich-type structures can be formed (further higher-ordered complex structures are also possible).^{14,18–20} This variability of the complexes makes the CEs ligands irreplaceable in the selective complexation of metal ions.

In previous work, stronger complexations within the polymer as well as in a sandwich-type formation have been reported.^{21,22} The aim of this work is to present stronger complexation by sandwich-type structures of the metal ions of the series Li⁺, Na⁺ and K⁺ and CEs of different sizes with 3, 4 and 5 oxygen atoms within the ring. The complex stability in single, as well as sandwich structures is compared and evaluated. A comparison between free CEs and polymer-based CEs is demonstrated. The latter is of particular interest since the polymer can be easily recovered after complexation by simple precipitation.

15-Crown-5 (15C5), 12-crown-4 (12C4), and benzo-9-crown-3 (B9C3) were chosen as CEs to investigate the single and sandwich complexes with Li⁺, Na⁺, and K⁺ within the polymer. Multivalent ions were not considered in this work, since they can easily be separated by electrodialysis using for example monovalent cationic selective membranes.²³

A poly(methacrylic acid)-*block*-polystyrene (PMAA-*b*-PS) diblock copolymer was chosen (synthesis was reported elsewhere)²⁴ and an overview is shown in Fig. S2 (ESI[†]). The carboxyl groups make the incorporation of CEs straightforward *via* Steglich esterification, if the latter are modified with a hydroxyl group (Fig. 2). The Steglich esterification is a simple reaction to esterify long polymer chains and to obtain high yields by adding dicyclohexylcarbodiimide (DCC) and 4-dimethylaminopyridine (DMAP).^{25,26} The successful incorporation of the CE within the polymer can be analyzed with ¹H NMR spectroscopy. The signals of the CE appear broad in the polymer spectrum proving the newly introduced CE group to the PMAA-*b*-PS diblock copolymer. The average number of CE-esterified repeating units per chain will be called *n*_{CE} – not “degree of polymerization” which would, by definition, be incorrect in a statistical copolymer and is analyzed by ¹H NMR spectroscopy. An example NMR for the 15C5-bonded polymer can be seen in Fig. 3.

^a Institute of Physical Chemistry, Universität Hamburg, Grindelallee 117, 20146 Hamburg, Germany. E-mail: volker.abetz@hereon.de

^b Helmholtz-Zentrum Hereon, Institute of Membrane Research, Max-Planck-Straße 1, 21502 Geesthacht, Germany

† Electronic supplementary information (ESI) available. See DOI: 10.1039/d1sm01815a



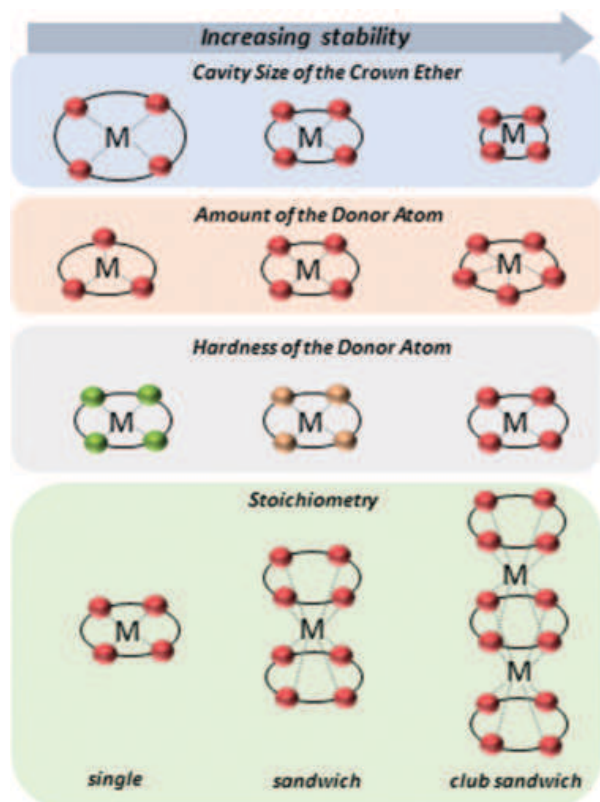


Fig. 1 Illustration of the CEs–metal ion complexes. Different factors are illustrated such as the cavity size of the CE, the amount and hardness of the donor atoms as well as the stoichiometry, which affects the interaction between donor and acceptor (metal ion). The red, green, and orange dot represent oxygen, nitrogen, and sulfur atom, respectively. The dashed line represents the interaction between donor atom and metal ion.

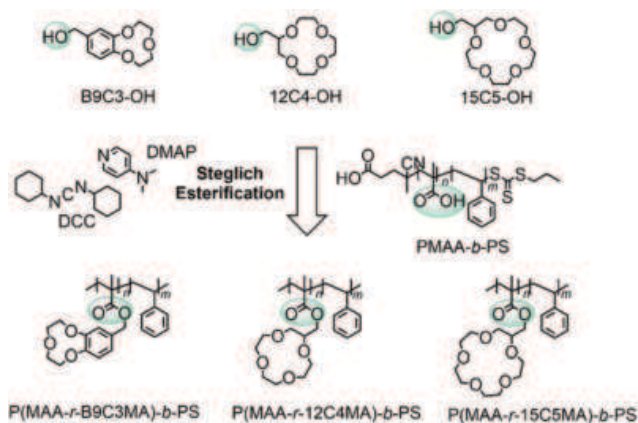


Fig. 2 Reaction overview of the Steglich esterification of PMAA-*b*-PS with hydroxyl functionalized CEs.

A detailed determination of the n CE and the degree of functionalization (DF) can be found in the ESI.†

In the complexation process of metal ions, the dissolved metal ions in water must first be freed from the hydrate shell surrounding them. Among the compared cations, this hydrate shell is most stable for Li^+ and least stable for K^+ .

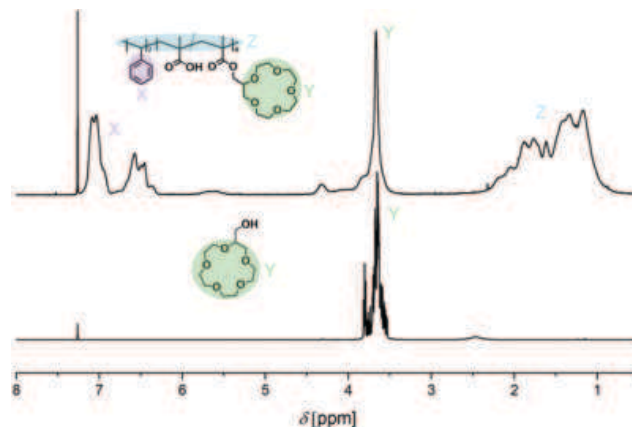
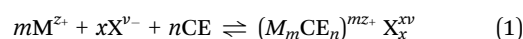


Fig. 3 ^1H NMR spectrum of 15C5-OH (bottom) and P(MAA₂₅-*r*-15C5MA₂₅)-*b*-PS₅₀⁵⁶ diblock copolymer containing randomly distributed CE units (top) in CDCl_3 .

In a single complex, interactions are established between the donor atoms and the metal ions leading to an enthalpy gain.

In a sandwich complexation, the entropy loss is greater because two CEs participate in the complexation process. However, the enthalpy gain is twice as large, since twice as many interactions take place between donor atoms and metal ions (Fig. 1). In conclusion, the complexation of metals by CEs is a thermodynamic process with an interlude between entropy loss and enthalpy gain. In the thermodynamic process, the complexation constant K play an essential role and provide information about the stability of the complex. The general procedure of the metal ion extraction with CEs follows eqn (1):



with M being the metal cation and X, the corresponding anion, m and x represent the stoichiometric factors and z_+ and v_- the charges of the metal cation and counter anion, and n labels the number of CEs necessary for the metal–CE complex. The complex constant K can be evaluated by the law of mass (eqn (2)) and shows by a value above 1 an equilibrium on the side of the products (in here the CE–metal complex, $(\text{M}_m, \text{CE}_n)^{mz+}$).

$$K = \frac{[(\text{M}_m\text{CE}_n)^{mz+} \text{X}_{x(\text{org})}^{xv-}]}{(\text{Q}(\gamma_+[\text{M}^{z+}]^m)(\gamma_-[\text{X}^{v-}]^x))[\text{CE}]^n} \quad (2)$$

Experimentally, the complex constant K of a CE–metal complex is determined by using a two-phase extraction (Fig. 4). The CE is dissolved in the organic phase and the salt of a dye in the aqueous phase. After mixing the two phases, the cation of the salt dye interacts with the CE at the interface. After successful complexation, the CE–metal complex is in the organic phase (dichloromethane was chosen as the organic phase in these experiments). The aqueous phase (salt dye phase) was investigated by absorption spectroscopy due to spectroscopic limitations of the organic phase. The salt concentrations in the aqueous phase before and after extraction



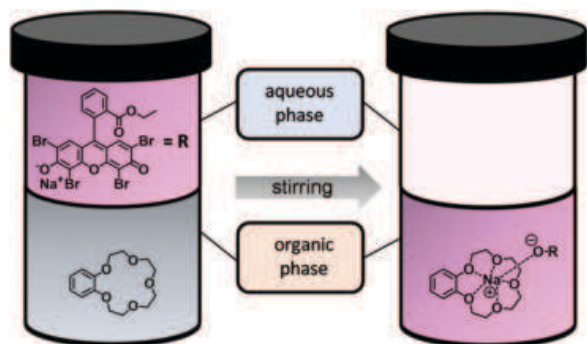


Fig. 4 Two-phase extraction of a dichloromethane/water mixture with B15C5 and 2',4',5',7'-tetrabromoeosin ethyl ester sodium salt (NaEE) as sodium dye. The left side shows the phases before the extraction and the right side afterwards.

were analyzed and the complex constant K was calculated according to eqn (2). A more detailed description of the two-phase extraction and a detailed calculation of the complex constant K can be found in previous publications.^{21,22}

The free CEs benzo-15-crown-5 (B15C5), benzo-12-crown-4 (B12C4) and B9C3 were extracted as shown in Fig. 3. The 15C5 with a cavity size of 1.70–2.20 Å fits perfectly for Na^+ with an ionic diameter (ID) of 2.02 Å and forms well-known “sandwich complexes” with K^+ (ID = 2.76 Å).^{20,27} The values of the complex constant K (pink bar with crosses) can be found in Fig. 5A and B. The B15C5- Na^+ and the (B15C5)₂- K^+ complexes show both stable complexes with values of $\log K$ of 5.71 and 7.93, respectively. It is clear that the sandwich complex with K^+ is more stable than the single complex with Na^+ . This may be due to the smaller hydrate shell of K^+ compared to Na^+ , as well as to the increased content of the enthalpy term due to the interaction of twice as many donor atoms with the metal ion. Similar

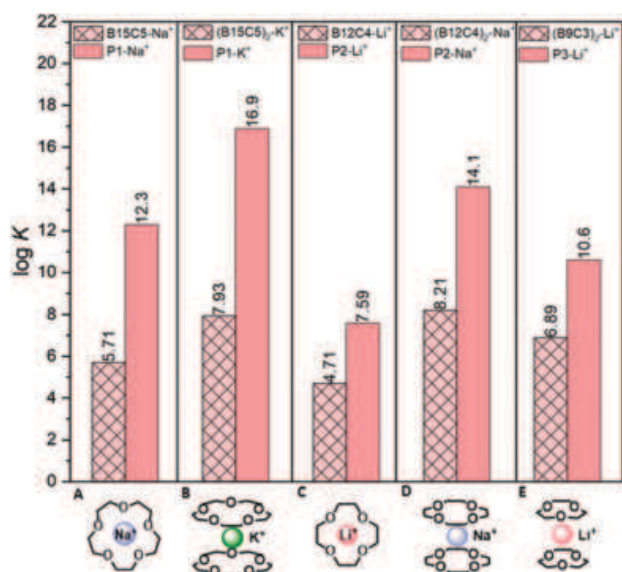


Fig. 5 $\log K$ of the CE complexes of the free CEs and the polymer-based CEs. The pink bar with crosses represents the $\log K$ of the free CE- and the pink bar of the polymer-based CE complexes.

trends are observed for the 12C4 (cavity size of 1.20–1.50 Å), which forms single complexes with Li^+ (ID = 1.48 Å) and sandwich complexes with Na^+ .^{28,29} Both complexes show high complex stabilities with a $\log K$ of 4.71 for the B12C4- Li^+ complex and 8.21 for the (B12C4)₂- Na^+ complex (pink bar with crosses) (Fig. 5C and D). In conclusion, the experiments show a stronger complexation of the sandwich complex compared to the single complex. The B9C3 shows the smallest cavity size among all investigated CEs in this work with a value of approximately 0.25 Å and forms sandwich complexes with Li^+ .^{17,21,30} The only ion that could form a single complex with the B9C3 would be beryllium.³¹ Since this ion is very toxic and only available at extremely low concentrations in aqueous resources (e.g. Be^{2+} concentration in the Arctic Ocean: 9–15 pmol kg^{-1} i.e. $c_{\text{Be}} \approx 80\text{--}140 \text{ pg L}^{-1}$), and there is no evidence that Be^{2+} is found in Li^+ -relevant aqueous resources such as the Dead Sea ($c_{\text{Li}} = 18 \text{ mg L}^{-1}$), experiments with beryllium were not further considered and performed.^{12,32,33} The $\log K$ (6.89) of the (B9C3)₂- Li^+ complex can be seen in Fig. 5E.

In the following, the complex stabilities of the free CEs B15C5, B12C4, and B9C3 are compared with those in the polymer. For this purpose, the degrees of functionalization of the CEs in the polymer were synthesized to be as similar as possible.

It is worth mentioning that the polymers P2 and P3 were functionalized with 12C4 and 15C5 (without a benzene group), since these two CEs were commercially available with a hydroxyl functionality.

The B9C3 CE was synthesized and modified with a hydroxyl group *via* Duff reaction and subsequent reduction with sodium borohydride (NaBH_4). An overview of the synthetic procedure can be found in the SI (Fig. S1, ESI[†]). A detailed report of the post modification of PMAA-*b*-PS with B9C3 and its extraction with Li^+ , Na^+ , and K^+ has already been published elsewhere.²¹ The exact weight fractions of each functionality of the polymers can be taken from Table 1.

To ensure good comparability of the two-phase extraction of the free CE and polymer-based CEs, the same concentration of CE to metal ion was chosen to be 10:1. The P1- Na^+ complex ($\log K = 12.3$) in comparison to the B15C5- Na^+ complex ($\log K = 5.71$; both forming single complexes with Na^+) shows a $\log K$ 10^{6.0} times higher than for the free CE (Fig. 5A). The complexation of K^+ with polymer P1, shows a particularly high complexation constant of $\log K = 16.9$ and thus has the highest complexation constant of all studied systems and ions

Table 1 Sample codes of the CE-based diblock copolymers and the corresponding weight fraction of each block. The subscripts in the designation of the polymers represent the fraction of the respective block in wt% and the superscript represents the overall molecular weight in kDa

Sample code	Polymer	Metal ion extraction
P1	P(MAA ₂₅ - <i>r</i> -15C5MA ₂₅)- <i>b</i> -PS ₅₀ ^{56.3}	Na^+ , K^+
P2	P(MAA ₂₁ - <i>r</i> -12C4MA ₁₉)- <i>b</i> -PS ₆₀ ^{48.6}	Na^+ , Li^+
P3	P(MAA ₂₀ - <i>r</i> -B9C3MA ₂₀)- <i>b</i> -PS ₆₀ ^{49.1}	Li^+



(10^9 times higher than for the free CE). A similar observation can be made for polymer P2. Here, a $\log K$ for Li^+ (formation of a single complex) of 7.59 is achieved, whereas for the free CE a value of 4.71 was obtained. Thus, the value increases by a factor of $10^{2.9}$ in the polymer material, although lithium usually must overcome a very strong bounded hydration shell before it can be complexed.

The complexation of polymer P2 with Na^+ forms a sandwich complex and reaches a $\log K$ of 14.1. It is thus clearly visible that the complexation of the metal ions in the polymer by means of a sandwich complex leads to very stable complexation. The reason for this is most-likely the lower entropy loss within a polymer system, since the CEs are covalently bonded to the polymer and thus have fewer degrees of freedom compared to CEs free in solution.^{21,22} Sandwich complexation makes this effect even more pronounced.

With respect to the stabilization of lithium complexation, it is clear, that the sandwich complexation of polymer P3 with B9C3 units shows a higher complexation constant of $\log K$ 10.6 than polymer P2 with the 12C4 with a $\log K$ of 7.59 (formation of a single complex with Li). From the analyzed data, it can be concluded that sandwich complexation of lithium within a polymer system can achieve more stable complexations and thus may be crucial for complexation of lithium from seawater, where it occurs at very low concentrations. First attempts of successful Li^+ extraction using the P3 polymer in the presence of much higher Na^+ and K^+ concentrations were shown in another publication.²¹ Selective and very stable complexation of lithium within a polymer can thus be a way to isolate the highly desirable raw material.

Author contributions

Iklima Oral and Volker Abetz conceived the experiments, analyzed the data and wrote the manuscript. Iklima Oral designed and performed all experiments.

Conflicts of interest

There are no conflicts to declare.

Notes and references

- A. R. Kulkarni, H. S. Maiti and A. Paul, *Bull. Mater. Sci.*, 1984, **6**, 201–221.
- X. Wu, G. Zhao, X. Wang and W. Liu, *Tribol. Lett.*, 2017, **65**, 1–10.
- L. Gupta, A. C. Hoepker, K. J. Singh and D. B. Collum, *J. Org. Chem.*, 2009, **74**, 2231–2233.
- H. Haferkamp, M. Niemeyer, R. Boehm, U. Holzkamp, C. Jaschik and V. Kaese, *Mater. Sci. Forum*, 2000, **350**, 31–42.
- C. Grosjean, P. Herrera Miranda, M. Perrin and P. Poggi, *Renewable Sustainable Energy Rev.*, 2012, **16**, 1735–1744.
- O. A. Avramchik, E. I. Korotkova, E. V. Plotnikov, A. N. Lukina and Y. A. Karbainov, *J. Pharm. Biomed. Anal.*, 2005, **37**, 1149–1154.
- H. Vikström, S. Davidsson and M. Höök, *Appl. Energy*, 2013, **110**, 252–266.
- J. F. Song, L. D. Nghiem, X. M. Li and T. He, *Environ. Sci.: Water Res. Technol.*, 2017, **3**, 593–597.
- A. Kumar, H. Fukuda, T. A. Hatton and J. H. Lienhard, *ACS Energy Lett.*, 2019, **4**, 1471–1474.
- B. Swain, *Sep. Purif. Technol.*, 2017, **172**, 388–403.
- S. Yang, F. Zhang, H. Ding, P. He and H. Zhou, *Joule*, 2018, **2**, 1648–1651.
- A. Alsabbagh, S. Aljarrah and M. Almahasneh, *Miner. Eng.*, 2021, **170**, 107038.
- C. J. Pedersen, *J. Am. Chem. Soc.*, 1967, **89**, 7017–7036.
- C. J. Pedersen, *J. Am. Chem. Soc.*, 1970, **92**, 386–391.
- A. van der Ham, T. Hansen, G. Lodder, J. D. C. Codée, T. A. Hamlin and D. V. Filippov, *ChemPhysChem*, 2019, **20**, 2103–2109.
- A. Boda, S. M. Ali, M. R. K. Sheno, H. Rao and S. K. Ghosh, *J. Mol. Model.*, 2011, **17**, 1091–1108.
- S. De, A. Boda and S. M. Ali, *J. Mol. Struct. THEOCHEM*, 2010, **941**, 90–101.
- J. W. Steed, *Coord. Chem. Rev.*, 2001, **215**, 171–221.
- S. P. Gromov, A. I. Vedernikov, N. A. Lobova, L. G. Kuz'Mina, S. S. Basok, Y. A. Strelenko, M. V. Alfimov and J. A. K. Howard, *New J. Chem.*, 2011, **35**, 724–737.
- H. R. Yu, J. Q. Hu, X. H. Lu, X. J. Ju, Z. Liu, R. Xie, W. Wang and L. Y. Chu, *J. Phys. Chem. B*, 2015, **119**, 1696–1705.
- I. Oral and V. Abetz, *Macromol. Rapid Commun.*, 2021, **42**, 2000746.
- A. Bey, O. Dreyer and V. Abetz, *Phys. Chem. Chem. Phys.*, 2017, **19**, 15924–15932.
- J. Lambert, M. Avila-Rodriguez, G. Durand and M. Rakib, *J. Membr. Sci.*, 2006, **280**, 219–225.
- I. Oral, L. Grossmann, E. Fedorenko, J. Struck and V. Abetz, *Polymers*, 2021, **13**, 3675.
- D. Barker, M. D. McLeod, M. A. Brimble and G. P. Savage, *Tetrahedron Lett.*, 2001, **42**, 1785–1788.
- N. Bernhard and S. Wolfgang, *Angew. Chem., Int. Ed. Engl.*, 1978, **17**, 522–524.
- J. D. Lamb, R. M. Izatt, C. S. Swain and J. J. Christensen, *J. Am. Chem. Soc.*, 1980, **102**, 475–479.
- M. Gjikaj and A. Adam, *Z. Anorg. Allg. Chem.*, 2006, **632**, 2475–2480.
- Y. Shibutani, S. Mino, S. S. Long, T. Moriuchi-Kawakami, K. Yakabe and T. Shono, *Chem. Lett.*, 1997, 49–50.
- R. Renesok, K. A. Jackson, T. A. Kaplan, J. F. Harrison and M. R. Pederson, *Chem. Phys. Lett.*, 1996, **262**, 207–212.
- M. R. Ganjali, A. Moghimi and M. Shamsipur, *Anal. Chem.*, 1998, **70**, 5259–5263.
- A. N. Shah, M. Tanveer, S. Hussain and G. Yang, *Rev. Environ. Sci. Biotechnol.*, 2016, **15**, 549–561.
- M. Frank, D. Porcelli, P. Andersson, M. Baskaran, G. Björk, P. W. Kubik, B. Hattendorf and D. Guenther, *Geochim. Cosmochim. Acta*, 2009, **73**, 6114–6133.



Unpublished Results

This Chapter includes the results of some preliminary studies and further investigations of Chapter 5. In Section 6.1, further modifications of the CEs are investigated, studying nitrogen-containing CEs with different amount of donor nitrogen atoms and ring sizes on the extraction of Li^+ and Mg^{2+} . In Chapter 6.2, the prepared polymers from Chapter 5 are fabricated into membranes via SNIPS with the prior calculation of the solubility features of the polymers from Chapter 5.

6.1 Aza crown ethers: The effect on lithium complexation using different cavity sizes and donor atoms

In this Section, aza-CEs are studied, which carry at least one nitrogen atom as a donor atom instead of oxygen. Three different 12-membered CE are examined, with one (1-aza-12-crown-4 (1A12C4)), two (4,10-diaza-12-crown-4 (DA12C4)), and four (1,4,7,10-tetraazacyclododecane-12-crown-4 (TA12C4)) nitrogen atoms as donor atoms. In addition, a 14-membered fully substituted aza-CE (1,4,7,10-tetraazacyclotetradecane-14-crown-4 (TA14C4)) is analyzed and compared with analogues of the 12-membered CE. The analyzed CE structures are summarized in Figure 6.1.

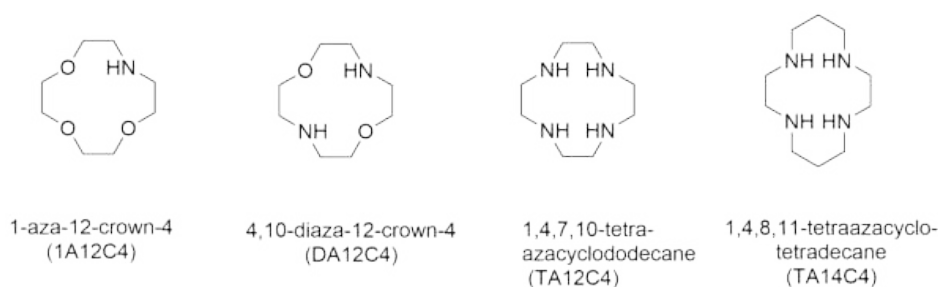


Figure 6.1: Illustration of the different aza-CEs using 1A12C4, DA12C4, TA12C4, and TA14C4.

Aza-CEs have the advantage of being intermediate in their complexation properties between oxygen CEs, which are good at isolating alkali/alkaline earth metals, and cyclams (TA14C4), which have strong complexation properties towards heavy metals. Thus these CEs are capable of complexing a wide range of metal ions.³⁴¹

Aza-CE have an additional advantage that other CE do not offer. They can participate directly in reactions with the amine group without prior attachment of functional groups to the CE structure. By simply adding an acid such as HCl to the aza-CE, the nitrogen atom can be positively polarized, causing the positive nitrogen-atom to repulsively interact with the trapped metal ion and thus freeing the ion from the cavity (Figure 6.2). This method would offer an ecologically and energetically favorable alternative to free the ions from the CEs after complexation, instead of breaking the coordinative bonds by employing high temperature or immense mechanical stress such as rinsing with high water pressure.³⁴²

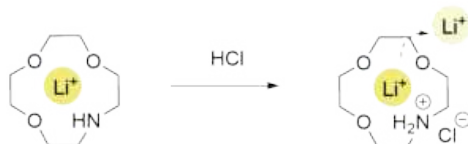


Figure 6.2: Illustration of the release of the lithium ion by simply adding HCl to the aza-CE to create a repulsive interaction between the nitrogen-ion and the cation.

The four different aza-CE are compared for their complexation properties with Li^+ and Mg^{2+} , in a two-phase extraction. Analogous to the extraction experiments in Chapter 5, the CEs are dissolved in the organic phase dichloromethane (DCM) and the salts in water. The concentrations of the aqueous phase before and after extraction are compared, and the complexation constant K is determined assuming for all complexes single conformations between CE and cation. All values above 1 indicate voluntary complexation of the aza-CE with the metal ion.

The logarithmic complexation constant $\log K$ for different concentrations between the CE and metal ion are shown in Fig. 6.3. Table 6.1 shows the averaged $\log K$ values for the different CEs for Li^+ and Mg^{2+} and the $\log K$ ratio of Mg/Li . For the 12-membered CEs, no significant difference is seen in the selectivity of Mg^{2+} over Li^+ . The complexation stability constant for the CE does not decrease for both ions. This is most likely due to the less hard base property of N versus O. Since O atoms are available for the other CEs and exert stronger interactions with the Li^+ and Mg^{2+} (both are very hard acids) according to the HSAB principle (compare Table 3.6), higher $\log K$ are predicted and confirmed.

Table 6.1: Comparison of the $\log K$ values for 1A12C4, DA12C4, TA12C4, and TA14C4 for the extraction with Li^+ and Mg^{2+} .

CE	$\log \bar{K} (\text{Li}^+)$	$\log \bar{K} (\text{Mg}^{2+})$	$\text{Mg}^{2+}/\text{Li}^+$
1A12C4	5.69	9.22	1.62
DA12C4	5.91	9.89	1.67
TA12C4	5.33	8.63	1.62
TA14C4	6.95	12.1	1.74

As already indicated in Publications 2 and 5, not only the hardness of the donors but also the orientation of the CE ring before and after complexation plays an essential role since

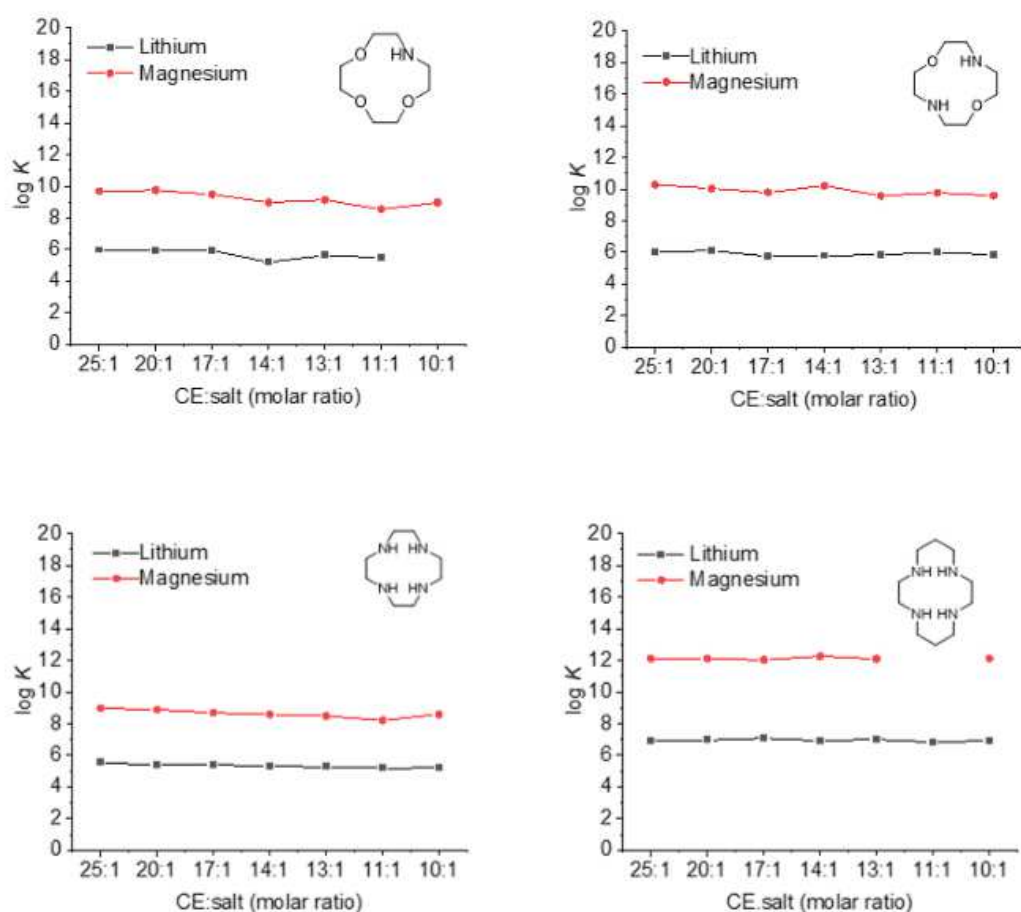


Figure 6.3: Complexation constant K of the two-phase extraction of the aza-CEs with Li^+ , Na^+ , K^+ , Mg^{2+} , and Ca^{2+} at various CE:salt molar ratios.

this can cause the distance between ligand and cation to decrease or increase. Figure 6.4 shows the optimized geometrical structure before and after complexation with the lithium-ion with 1A12C4 and the oxygen analog 12C4 calculated by Boda et. al.¹⁹⁴ Clearly, the structures of the CEs are different before complexation, but they adopt a similar conformation after complexation. The distance of the coordinative bond $\text{Li}^+\text{-N}$ and $\text{Li}^+\text{-O}$ is 1.869 Å and 1.991 Å confirming the alike structure after complexation.¹⁹⁴

Based on the optimized geometry structures of 1A12C4 and DA12C4 from Behjatmanesh-Ardakani³⁴³ (Figure 6.5) the Li^+ fits perfectly in the cavity size of the 1A12C4 and DA12C4 CE. By examining the geometric structure of DA12C4, it is clear that the N-Li^+ bond is longer than the O-Li^+ bond and also confirms that the O-Li bond most likely leads to a stronger coordinative bond due to the stronger attraction according to the HSAB theory. It is not surprising that the TA12C4 CE with four N atoms as donor atoms has the lowest log K of the 12-membered CEs.

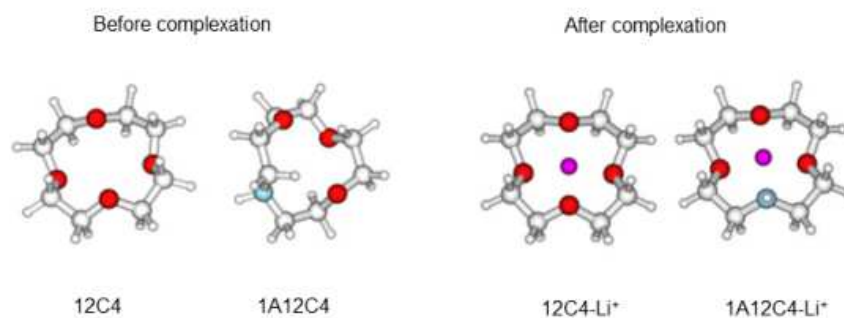


Figure 6.4: Optimized geometries of the 12C4 and 1A12C4 CE at MP2 level of theory using 6-311+G (d,p) basis set. The large white dots represent the carbon-atom, the smaller one the hydrogen atom respectively, while the red dots label the oxygen-atoms and cyan the nitrogen-atom. This image was reused and adapted with permission from Boda et al. from Springer.¹⁹⁴

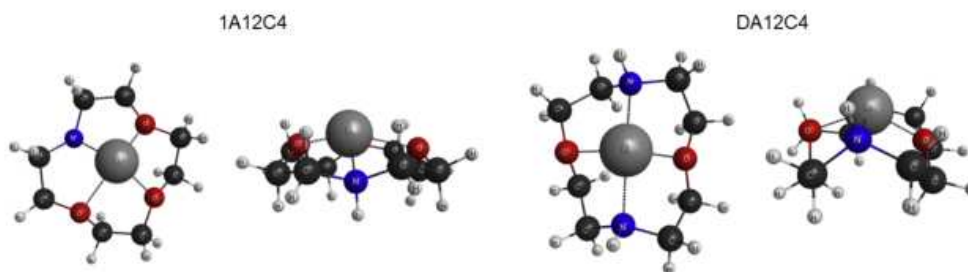


Figure 6.5: Optimized geometries of the 1A12C4 and DA12C4 CE using 6-311+G (d,p) basis set. The white dots represent the hydrogen-atom, the black dots the carbon atom, while the red dots label the oxygen-atoms and cyan the nitrogen-atom. This image was reused and adapted with permission from Behjatmanesh-Ardakani from Elsevier.³⁴³

Like the 14C4 CE, the 14-membered aza-CE shows excellent complex stability towards Li^+ and Mg^{2+} . This CE cavity seems to have the perfect size for the ionic radii of Li^+ and Mg^{2+} and thus strong coordinative interaction between the donor atoms and metal ion can be expected. The advantage over the oxygen analogous 14C4 CE (compare Figure 3.38) is the possibility of releasing the Li^+ from the cavity of the CE, and thus possible positive forcing on four different positions, which increases the chances that the trapped Li^+ in the CE will leave the CE through repulsive interaction effects by adding an acid.

In summary, various 12-membered aza-CEs were studied with different numbers of donor oxygen atoms replaced with nitrogen. It was found that the substitution of one or two nitrogen atoms does not have a significant effect on the complexation constant. However, when all oxygen atoms are replaced with nitrogens, the complexation constant decreases significantly, which is due to the weaker interaction between N and Li^+ since N is a less hard base than oxygen (according to the HSAB principle). Geometrical change after substitution of oxygen atoms is not as pronounced in the 12-membered CE as it was in the 15-membered CE in Publication 2, which is most likely due to the more symmetrical structure of 12-membered

rings compared to 15-membered rings. The 14-membered CE showed the best complexation property with Li^+ and Mg^{2+} due to the ideal cavity size. In addition, no apparent influence was observable from substituting the CE with nitrogen versus the selectivity of Mg^{2+} to Li^+ .

For further work, it is suggested to observe how well the ions leave the CE after addition of acid to the aza-CE. Furthermore, extractions under different pH values should be analyzed to study the influence of the pH condition in regards to the Li^+ extraction.

6.1.1 Experimental section

Only the materials used in this paragraph are described since the extraction experiments, the complexation constant, and characterization calculation were used analogously to Publications 1, 2, 4, and 5.

6.1.1.1 Materials

1A12C4 (98 %, TCI Chemicals), DA12C4 (96 %, TCI Chemicals), TA12C4 (98 %, TCI Chemicals), and TA14C4 (98 %, TCI Chemicals) were used as received. DCM (99 %, Acros) was used as received. Deionized water was purified with a Milli-Q[®] integral water purification system.

6.2 Membrane fabrication

This Section describes the preparation of membranes from the block copolymers investigated in Chapter 5. In Section 6.2.1, the solvent parameters from the different theories according to Hansen and Hoy are presented and discussed. For the unknown structures, group contribution methods according to Stefanis and Panayiotou and Hoy (as described in Section 3.6.4) are calculated, and the solubility properties of the polymers are described. In Section 6.2.2, the preparation of integral-asymmetric block copolymer membranes is presented and discussed.

The work in Section 6.2.1 was partially done with the assistance of Andres Castro Villavicencio in the context of student laboratory courses under my supervision and guidance. His support and dedication of this theoretical project during the Corona pandemic is gratefully acknowledged. The work in Section 6.2.2 was partially done with the assistance of Cristina Maria Plunkett in the context of a student laboratory course under my supervision and guidance. Her support, constant good mood, and dedication during the project and the recording of the AFM images is gratefully acknowledged. Dr. Andreas Meyer is gratefully acknowledged for the set-up and questions regarding the AFM measurements. Dr. Martin Held and Dr. Erik Sebastian Schneider are gratefully acknowledged for their great advices on the preparation of the samples for membrane analysis and the recording and analysis of SEM images. Dr. Zhenzhen Zhang is gratefully acknowledged for the evening discussions about membranes and support on interpreting the membrane images.

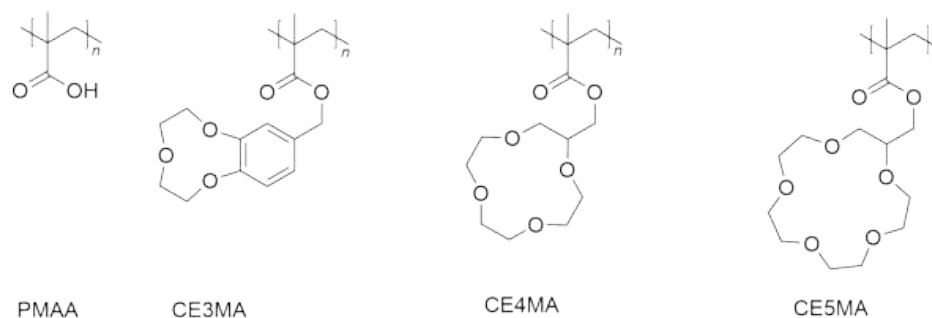


Figure 6.6: Illustration of the repeating units of the random copolymers forming the hydrophilic blocks of the diblock copolymers with polystyrene.

6.2.1 Determination of the solubility properties of unknown polymer structures

In this Section, the solubility parameters of the block copolymers from Chapter 5 are discussed. Since PS and PMAA are known polymers, the solubility properties can be found in the literature.^{285,344,345} Therefore, only the solubility properties of the CE functionalized block copolymers are determined here, according to Hansen and Hoy theory. A summary of the structures can be found in Fig. 6.6 (PS is not shown since its solubility properties are known).

In addition, polymer–solvent and polymer–polymer interaction parameters are determined, summarized and discussed.

6.2.1.1 Hansen solubility parameters

The Hansen solubility parameters are determined for the polymer-based CE polymers via group contribution method of Stefanis and Panayiotou. First, the structures of the repeating unit of the polymer must be divided into first and second-order functional groups. Tab. 6.2 shows an example of this division of first- and second-order structure for the CE functionalized repeating unit CE3MA. In the appendix, Tab. 9.1 and Tab. 9.2, some frequently occurring structural units are summarized with the corresponding values. With these the partial solubility parameters can be determined using Eq. 3.71-3.73. The calculation of the δ_d parameter for CE3MA is exemplary shown in Eq. 6.1 using the values from Tab. 6.2.

$$\begin{aligned}\delta_d &= \left(\sum_i n_i C_i + W \sum_j m_j D_j + 17.3231 \right) MPa^{\frac{1}{2}} \\ &= (3.8972 + 1 \cdot 0.5136 + 17.3231) MPa^{\frac{1}{2}} = 21.82 MPa^{\frac{1}{2}}\end{aligned}\quad (6.1)$$

W is a constant and is close to 0 if no second-order structures are present and 1 if such groups are present.²⁹⁰ Due to the partially present polar structure of the CEs, it is doubtful that small values of δ_p and δ_h are obtained, therefore Eq. 3.74 and 3.75 are not necessary to include.^{290,346}

Table 6.2: First- and second-order calculation of solvent parameters according to Stefanis and Panayiotou.²⁹⁰ n represents the frequency of the first-order structural element, and m from the second-order. The contribution of the unit of the first-order group is defined by C_i and the second-order by D_i .

First-order	Description	n	C_i	$n_i C_i$
-CH ₃	methyl	1	-0.9714	-0.9714
-CH ₂ -	methylene	2	-0.0269	-0.0538
>C<	quaternary carbon	1	1.2686	1.2686
COO	carboxyl	1	0.2039	0.2039
ACCH ₂ -	arom. carbon + methylen	1	0.2753	0.6933
ACH	arom. carbon	3	0.1105	0.3315
AC	substi. arom carbon	2	0.8446	1.6892
CH ₂ O	cyclic ether	3	0.2753	0.8259
			$\sum n_i C_i$	3.8972
Second-order	Description	m	D_i	$m_i D_i$
AC-O-C	arom. carbon + ether	2	0.2568	0.5136
			$\sum m_i D_i$	0.5136

The solubility parameters for CE4MA and CE5MA were determined analogously to CE3MA. Tab. 6.3 shows the first-order and second-order groups and their abundance.

The total solubility parameter δ_t was determined according to Eq. 3.68. Table 6.4 summarizes the three CE polymers with their corresponding partial and total solubility parameters.

Table 6.3: First-order calculation of solvent parameters according to Stefanis and Panayiotou. n defines the frequency of the first-order structural element. Second-order structures are not present and are therefore not included in this table.

First Order	Description	CE4MA	CE5MA
		n	n
-CH ₃	methyl	1	1
-CH ₂	methylene	5	6
-CH<	methine	1	1
>C<	quaternary. carbon	1	1
COOH	carboxyl	1	1
CH ₂ (cycl.)	cycl. ether	4	5

Table 6.4: Summary of the Hansen solubility parameters for CE3MA, CE4MA, and CE5MA calculated with the group contribution method according to Stefanis and Panayiotou.²⁹⁰

Polymer	δ_d	δ_p	δ_h	δ_t
CE3MA	21.8	13.2	6.9	26.4
CE4MA	19.4	11.2	5.5	23.1
CE5MA	19.7	11.1	5.0	23.1

6.2.1.2 Hoy solubility parameters

Compared with the Hansen solubility parameters, the Hoy group contribution method is purely calculative. Thus, no experimental values for polymers or solvents are available. The group fragments differ from those of Stefanis and Panayiotou. Table 6.5 shows an example of the group distribution for PS (a summarized table of different structural groups can be found in the appendix in Table 9.3) and the auxiliary values which are needed to calculate the partial solubility parameters according to the Hoy theory.

The described auxiliary functions (see Eq. 3.86 and 3.87) with the values from Table 6.5 result in the defined values in Eq. 6.2 and 6.3. The total and partial solubility parameters were determined according to Eqs. 6.4-6.7. The solubility parameters of the solvents were calculated using Eq. 3.80 and 3.81. A summary of the Hoy solubility parameters for the most used solvents in membrane preparation via SNIPS and the respective polymers, including PMAA and PS, are shown in Tab. 6.6.

$$\alpha(P) = 777 \cdot \frac{\Delta_T^{(P)}}{V} = 777 \cdot \frac{0.137}{98.77} = 1.078 \quad (6.2)$$

Table 6.5: Auxiliary values for calculating Hoy parameters for PS with F_t the molar constant of attraction, F_p the polar component, V the molar volume, Δ_T the Lyders correction for non-ideality, and N the number of functional groups i .

Group	N_i	$N_i F_{t,i}$	$N_i F_{p,i}$	$N_i V_i$	$N_i \Delta_T^{(P)}$
-CH ₂ -	1	268.98	0	17.51	0.02
>CH-	1	175.89	0	6.46	0.0131
CH _{arom}	5	1199.69	310.92	23.1	0.089
C _{arom}	1	200.70	64.84	23.1	0.0149
	Σ	1845.27	375.76	98.77	0.137

$$n = \frac{0.5}{\Delta_T^{(P)}} = \frac{0.5}{0.137} = 3.650 \quad (6.3)$$

$$\delta_t = \frac{(F_t + B/n)}{V} = \frac{(1845.27 + 227/3.650)}{98.77} = 19.45 \text{ MPa}^{\frac{1}{2}} \quad (6.4)$$

$$\delta_p = \delta_t \left(\frac{1}{\alpha^{(P)}} \frac{F_p}{F_t + B/n} \right)^{\frac{1}{2}} = 19.45 \left(\frac{1}{1.078} \frac{375.76}{1845.27 + 277/3.650} \right)^{\frac{1}{2}} = 8.29 \text{ MPa}^{\frac{1}{2}} \quad (6.5)$$

$$\delta_h = \delta_t \left(\frac{\alpha^{(P)} - 1}{\alpha^{(P)}} \right)^{\frac{1}{2}} = 19.45 \cdot \left(\frac{(1.078 - 1)}{1.078} \right)^{\frac{1}{2}} = 5.22 \text{ MPa}^{\frac{1}{2}} \quad (6.6)$$

$$\delta_d = (\delta_t^2 - \delta_p^2 - \delta_h^2)^{\frac{1}{2}} = (19.45^2 - 8.29^2 - 5.22^2)^{\frac{1}{2}} = 16.80 \text{ MPa}^{\frac{1}{2}} \quad (6.7)$$

The calculated solubility parameters are in a good agreement with the Hoy solubility parameter data of Biresaw et al. where they reported for PS a δ_d value of $16.723 \text{ MPa}^{\frac{1}{2}}$, for $\delta_p = 8.253 \text{ MPa}^{\frac{1}{2}}$, and for $\delta_h = 5.149 \text{ MPa}^{\frac{1}{2}}$.³⁴⁷

Table 6.6: Summary of the Hoy solubility parameters for the polymers and most used solvents in membrane preparation. All data are given in $\text{MPa}^{\frac{1}{2}}$

Polymer	δ_d	δ_p	δ_h	δ_t
PS	16.80	8.29	5.22	19.45
PMAA	22.27	15.21	11.95	29.50
CE3MA	17.20	11.28	11.18	23.41
CE4MA	16.35	10.49	7.70	20.90
CE5MA	16.34	10.40	7.53	20.78
Solvent	δ_d	δ_p	δ_h	δ_t
Acetone	12.60	9.65	11.47	19.58
Acetonitrile	11.40	12.73	18.07	24.88
Chloroform	13.61	14.68	6.36	21.01
Dichlormethane	13.61	11.88	10.13	20.51
Diethylether	14.06	5.44	7.49	16.83
<i>N,N'</i> -Dimethylacetamide	10.52	12.74	15.93	22.95
<i>N,N'</i> -Dimethylformamide	17.19	13.49	11.45	24.67
<i>N,N'</i> -Dimethyl lactamide	10.50	14.11	19.96	26.60
Dimethylsulfoxide	12.83	15.86	13.93	24.70
1,4-Dioxane	16.71	10.36	8.27	21.33
Ethanol	13.65	12.16	19.68	26.86
Ethylacetate	13.21	8.40	11.13	19.21
Ethyl formate	14.15	10.28	15.14	23.13
<i>N</i> -Methyl-2-pyrrolidon	13.07	14.99	15.94	25.48
Pyrrolidon-2-on	17.66	15.43	20.88	31.40
Pyridine	18.47	10.76	5.39	22.04
Sulfolan	10.98	25.26	0.00	27.54
Tetrahydrofuran	16.81	7.99	7.16	19.94
Toluene	16.79	8.12	3.84	19.04

6.2.1.3 Evaluation of partial solubility parameters according to Hansen and Hoy

In Tab. 6.7, a comparison of the solubility parameters of the Hansen and Hoy methods is summarized. According to Hansen and Hoy, the solvent parameters show significantly different values.³⁴⁸ However, the values of the polymers show a similar trend despite the theoretical model behind. The solubility parameters for CE4MA and CE5MA are very much alike due to the similar structure since these polymers differ only in one cyclic ether group. The values for CE3MA are higher since an additional aromatic benzene ring is linked here. The highest solubility parameters are found for PMAA since this polymer has a very high polarity due to the carboxylic acid group and thus provides significantly higher values for δ_p and δ_h .

To estimate the potential miscibility of two components, the following rule of thumb can be followed. The smaller the R_a value (Eq. 3.69, Section 3.6.4.2), the better the miscibility. Table 6.8 and 6.9 show the R_a values according to Hansen and Hoy with the most common solvents in NIPS/SNIPS procedures.

Table 6.7: Summary of the solubility parameters according to Hoy and Hansen for the used polymers. All data are given in $\text{MPa}^{\frac{1}{2}}$

Polymer	Method	δ_d	δ_p	δ_h	δ_t
PS	Hansen	18.5	4.5	2.9	19.3
PS	Hoy	16.8	8.3	5.2	19.5
PMAA	Hansen	17.4	12.5	16.0	26.7
PMAA	Hoy	22.3	15.2	12.0	29.5
CE3MA	Hansen	19.8	13.5	8.2	25.4
CE3MA	Hoy	17.2	11.3	11.2	23.4
CE4MA	Hansen	19.4	11.2	5.5	23.1
CE4MA	Hoy	16.4	10.5	7.7	20.9
CE5MA	Hansen	19.7	11.1	5.0	23.1
CE5MA	Hoy	16.3	10.4	7.5	20.8

Table 6.8: Determination of the R_a values based on the Hansen solubility parameters.

Solvent	$R_{a,PS}$	$R_{a,PMAA}$	$R_{a,CE3MA}$	$R_{a,CE4MA}$	$R_{a,CE5MA}$
Acetone	9.4	9.9	12.9	8.0	8.6
Acetonitrile	15.3	12.0	13.9	10.7	11.2
Chloroform	3.4	13.9	13.0	8.7	8.9
Dichloromethane	3.7	11.7	10.0	5.5	5.7
Diethylether	8.4	15.6	18.0	12.9	13.2
<i>N,N'</i> -Dimethylacetamide	10.7	6.0	10.7	7.1	7.8
<i>N,N'</i> -Dimethylformamide	12.7	4.8	9.9	7.5	8.3
Dimethylsulfoxide	14.0	7.3	8.2	7.3	7.9
1,4-Dioxane	5.3	14.1	12.7	9.6	9.7
Ethanol	17.9	6.0	17.9	15.9	16.6
Ethylacetate	6.9	11.8	14.4	9.5	9.9
Ethyl formate	9.0	9.4	13.6	8.8	9.4
<i>N</i> -Methyl-2-pyrrolidon	9.0	8.8	7.7	3.5	4.2
Pyrrolidon-2-on	15.5	7.9	7.8	8.5	9.0
Pyridine	5.3	11.2	7.2	2.6	2.8
Sulfolan	16.3	9.6	7.1	9.0	9.4
Tetrahydrofuran	6.2	10.5	12.6	8.0	8.5
Toluene	3.4	17.9	14.9	10.8	10.7

The R_a value is beneficial in finding a suitable solvent for the complete block copolymer, which is obligatory to successfully prepare a membrane via NIPS/SNIPS. Unfortunately, when looking at the R_a values calculated from Hansen solubility parameters, no optimal solvent can be found for the blocks PS, PMAA, and CE3MA or CE4MA, and CE5MA. Only the solvents pyridine, dichloromethane, and *N*-methyl-2-pyrrolidon show low values for all polymers except for PMAA. On the other hand, as water is mainly used as precipitating bath, *N,N*-dimethylformamide (DMF), pyridine, tetrahydrofuran (THF), and DOX seem to be the best choice of solvents due to their miscibility with water. The R_a value of PMAA with

these solvents is also the lowest. However, in case of a very low or very high functionalization of the MAA units with CE, the R_a values of the CE polymers and PMAA, respectively, can be neglected.

Similar trends are seen when comparing R_a values based on Hoy solvent parameters. However, the values for the CEs are much smaller than the R_a values based on the Hansen solubility parameters. Also here, solvents such as pyridine, THF, toluene, and DMF appear suitable as solvents to fully dissolve the block copolymer.

Table 6.9: Determination of the R_a values based on the Hoy solubility parameters.

Solvent	$R_{a,PS}$	$R_{a,PMAA}$	$R_{a,CE3MA}$	$R_{a,CE4MA}$	$R_{a,CE5MA}$
Acetone	10.6	20.1	9.3	8.4	8.5
Acetonitrile	17.4	22.7	13.6	14.5	14.6
Chloroform	9.1	18.2	9.3	7.0	7.0
Dichloromethane	9.3	18.3	7.9	6.7	6.8
Diethylether	6.6	19.6	9.3	6.8	6.7
<i>N,N'</i> -Dimethylacetamide	17.1	24.0	14.3	14.5	14.6
<i>N,N'</i> -Dimethylformamide	8.2	10.3	2.2	5.1	5.3
Dimethylsulfoxide	14.0	19.0	10.2	10.8	11.0
1,4-Dioxane	3.7	12.7	3.2	0.9	1.1
Ethanol	16.2	19.1	11.1	13.2	13.4
Ethylacetate	9.3	19.4	8.5	7.5	7.5
Ethyl formate	11.4	17.3	7.3	8.6	8.8
<i>N</i> -Methyl-2-pyrrolidon	14.7	18.8	10.2	11.5	11.6
Pyrrolidon-2-on	17.3	12.8	10.6	14.3	14.5
Pyridine	4.1	11.0	6.3	4.8	4.8
Sulfolan	21.2	27.5	21.8	19.8	19.8
Tetrahydrofuran	2.0	14.0	5.3	2.7	2.6
Toluene	1.4	15.4	8.0	4.6	4.4

In summary, Hoy and Hansen solubility methods can be applied to gain information about the solubility properties of a polymer. Still, it is usually preferable to determine the Hansen solubility parameters since there is an extensive database of experimental determinations for these values and thus closer to reality.

6.2.1.4 Flory–Huggins–Staverman interaction parameters

In addition to the calculation of the R_a values, the Flory–Huggins–Staverman interaction parameter will also serve as a measure to estimate the solubility of a polymer with a solvent. For values below 0.5, miscibility between polymer and solvent applies according to the Flory–Huggins–Staverman solution theory– the smaller this value, the better the miscibility between them.³⁴⁹ These calculations are presented below for the polymers under study in combination with the same solvents as used in the previous Sections.

The interaction between polymer and solvent was estimated according to Hansen’s equation (Eq. 3.94) using the optimized universal parameter for $\sigma = 0.6$. For this purpose, the

Hansen solubility parameters from Table 6.10 were used. The calculation of the interaction between the PS and DOX as solvent is exemplary shown (Eq. 6.8). With a value of 0.15, DOX is a suitable and selective solvent for PS. The other polymers and solvent interactions were calculated analogously and are summarized in Tab. 6.11. All values below 0.5 are marked green in this table and thus indicate good solubility of the polymer with the solvent. It is worth mentioning that the solubility parameters for CE3MA, CE4MA, and CE5MA were determined purely by calculation, and therefore a margin of error must also be considered since no experimental data is available.²⁸⁵

The Hansen solubility parameters for PS and PMAA were adapted from the literature.²⁸⁵ Since PS is the main component of the polymer, its compatibility is essential. The solvents chloroform, dichloromethane, and toluene show the lowest values. However, these solvents are not well suited for the phase inversion process when water is chosen as a precipitant due to their immiscibility with it. Therefore, THF, DMF, pyridine, and DOX are the best alternatives. *N*-Methyl-2-pyrrolidone seems to be the only solvent that shows good solubility with all polymer blocks. However, it should be noted that the values are very close to the solubility limit of 0.5 and are, therefore, just soluble with each other.

Another alternative would be to choose a solvent mixture, which is common in the NIPS/SNIPS process. A combination of DMSO and THF would be suitable according to the calculated values since DMSO shows a good solubility for PMAA, CE3MA, CE4MA, and CE5MA with values below 0.3 and THF is an excellent solvent for PS with a value of 0.19.

In summary, both the R_a values may give guidelines when choosing solvent mixtures for novel block copolymers.

$$\begin{aligned}\chi_{\text{PS-DOX}} &= \sigma \cdot \frac{V_A}{RT} \cdot [(\delta_{\text{dA}} - \delta_{\text{dB}})^2 + 0.25 \cdot (\delta_{\text{pA}} - \delta_{\text{pB}})^2 + 0.25 \cdot (\delta_{\text{hA}} - \delta_{\text{hB}})^2] \\ &= 0.6 \cdot \frac{85.7}{RT} \cdot [(19.0 - 18.5)^2 + 0.25 \cdot (1.8 - 4.5)^2 + 0.25 \cdot (7.4 - 2.9)^2] = 0.15\end{aligned}\quad (6.8)$$

In addition to polymer–solvent interactions, polymer–polymer interactions were also calculated according to Eq. 6.9. Here, $\chi_{\text{A,B}}$ should be close to 0, to achieve θ conditions. An exemplary calculation is shown using the PS–PMAA interaction. The molar volume of the PS repeating unit is used ($99.2 \frac{\text{cm}^3}{\text{mol}}$) since PS constitutes the major component of the polymer.

A summary of the interactions between PS and PMAA, CE3MA, CE4MA or CE5MA is given in Tab. 6.12

$$\chi_{\text{PS-PMAA}} = \frac{V_{\text{m,PS}}}{RT} \cdot (\delta_{\text{t,PS}} - \delta_{\text{t,PMAA}})^2 = \frac{99.2}{RT} \cdot (19.3 - 26.7)^2 = 2.22 \quad (6.9)$$

Table 6.10: Summary of Hansen solubility parameters for the polymers and the most commonly used solvents in a membrane preparation. The data are given in $\text{MPa}^{\frac{1}{2}}$. The molar volume V_m is given in $\frac{\text{mL}}{\text{mol}}$ as well as the reference of the data. If no references are given, the values were calculated using the group contribution method, according to Stefanis and Panayiotou.

Polymer	δ_d	δ_p	δ_h	δ_t	V_m	Ref.
PS	18.5	4.5	2.9	19.3	99.2	282
PMAA	17.4	12.5	16.0	26.7	67.0	282
CE3MA	21.8	13.2	6.9	26.4		
CE4MA	19.4	11.2	5.5	23.1		
CE5MA	19.7	11.2	5.0	23.1		
Solvent	δ_d	δ_p	δ_h	δ_t	V_m	Ref.
Acetone	15.5	10.4	7.0	19.9	74.0	285
Acetonitrile	15.3	18.0	6.1	24.4	52.6	285
Chloroform	17.8	3.1	5.7	18.9	80.7	285
Dichlormethane	18.2	6.3	6.1	20.2	63.9	285
Diethylether	14.5	2.9	5.1	15.6	104.8	285
<i>N,N'</i> -Dimethylacetamide	16.8	11.5	10.2	22.8	92.5	285
<i>N,N'</i> -Dimethylformamide	17.4	13.7	11.3	24.9	77.0	285
Dimethylsulfoxide	18.4	16.4	10.2	26.7	71.3	285
1,4-Dioxane	19.0	1.8	7.4	20.5	85.7	285
Ethanol	15.8	8.8	19.4	26.5	58.5	285
Ethylacetate	15.8	5.3	7.2	18.2	98.5	285
Ethyl formate	15.5	8.4	8.4	19.5	80.2	285
<i>N</i> -Methyl-2-pyrrolidon	18.0	12.3	7.2	23.0	96.5	285
Pyrrolidon-2-on	19.4	17.4	11.3	28.4	76.4	285
Pyridine	19.0	8.8	5.9	21.8	80.9	285
Sulfolan	20.3	18.2	10.9	29.4	95.7	285
Tetrahydrofuran	16.8	5.7	8.0	19.5	81.7	285
Toluene	18.0	1.4	2.0	18.2	106.8	285

According to the values in Tab. 6.12, it can be seen that PS and PMAA are incompatible with a very high value of 2.22. This value decreases after functionalization as the polymer becomes more hydrophobic. However, none of the values is close to 0, which indicates incompatibility for all polymer systems. Thus, these calculations support the assumption that the amphiphilicity of the block copolymers is retained after the functionalization of the PMAA block.

In conclusion, various solubility parameters were calculated using the Hansen and Hoy methods. The solubility behavior of the polymers with other solvents was determined, thus rationalizing the choice of solvents for the NIPS/SNIPS procedure. Therefore, it does make sense to deal with such calculations before approaching blindly to solubility experiments, and hence save resources. From the results calculated in this Chapter, solvents such as THF, DMF, pyridine, or DOX are suitable solvents for the PMAA-*b*-PS copolymer and the CE-functionalized polymers. However, it is also possible to combine the solvents and use a binary solvent mixture such as DMSO and THF.^{350–352}

Table 6.11: Summary of the Flory-Huggins-Staverman interaction parameters for the different polymers and solvents.

Solvent	χ_{PS}	χ_{PMAA}	χ_{CE3MA}	χ_{CE4MA}	χ_{CE5MA}
Acetone	0.39	0.44	0.75	0.29	0.33
Acetonitrile	0.74	0.46	0.62	0.37	0.40
Chloroform	0.06	0.95	0.82	0.37	0.38
Dichlormethane	0.05	0.53	0.39	0.12	0.13
Diethylether	0.45	1.54	2.05	1.05	1.11
<i>N,N'</i> -Dimethylacetamide	0.64	0.20	0.64	0.28	0.34
<i>N,N'</i> -Dimethylformamide	0.75	0.11	0.46	0.26	0.32
Dimethylsulfoxide	0.84	0.23	0.29	0.23	0.27
1,4-Dioxane	0.15	1.03	0.84	0.48	0.49
Ethanol	1.13	0.13	1.13	0.89	0.97
Ethylacetate	0.29	0.82	1.24	0.54	0.59
Ethyl formate	0.40	0.43	0.90	0.38	0.43
<i>N</i> -Methyl-2-pyrrolidon	0.47	0.46	0.35	0.07	0.10
Pyrrolidon-2-on	1.11	0.29	0.28	0.33	0.37
Pyridine	0.14	0.61	0.26	0.03	0.04
Sulfolan	1.53	0.53	0.29	0.47	0.51
Tetrahydrofuran	0.19	0.55	0.78	0.32	0.35
Toluene	0.07	2.06	1.43	0.75	0.73

Table 6.12: Summary of the Flory-Huggins-Staverman interaction parameter for the relevant polymer pairs (i.e. block copolymers).

$\chi_{PS-PMAA}$	$\chi_{PS-CE3MA}$	$\chi_{PS-CE4MA}$	$\chi_{PS-CE5MA}$
2.22	2.05	0.59	0.60

6.2.2 PMAA-*b*-PS membranes

After determining the solubility properties of the polymers in different solvents, the base polymer PMAA-*b*-PS, the preparation of which is intensively discussed in Publication 3, is formed into membranes in this Section. The aim is to establish a membrane fabrication process that has the potential to be adopted on a larger scale without high energy consumption, offer a higher surface, and therefore, better functionality of the adsorber properties, and costs so that the lithium adsorber material can be attractive for industrial use. Thus, for example, water is chosen for the precipitation bath since it is in most areas highly accessible, cheap, and non-toxic.

Membrane preparation of PMAA-*b*-PS by SNIPS method with water as a precipitation bath is a big challenge since PMAA is very hydrophilic and has good solubility in water, which makes the precipitation of the block copolymer challenging. Therefore, two different approaches are investigated in this work. In the first approach, the precipitation bath water is cooled down to reduce solubility of the PMAA and to reduce mobilities to maintain the

morphologies. In contrast, in the second approach, the carboxylic acid groups of the PMAA are complexed by adding salts to the casting solution to enhance microphase separation of PMAA into salt-rich domains before immersion of the cast film into water.

Since there has been no published reports on the preparation of membranes using SNIPS of PMAA-*b*-PS, different parameters, such as the polymer concentration in the casting solution and the ET during membrane preparation, were investigated.

The membrane casting experiments were carried out for PMAA-*b*-PS polymers with PS as the main component (80-90 wt%). DOX was chosen as the solvent due to its low vapor pressure of 4.95 kPa at 25 °C.³⁵³ The entire membrane preparation was carried out in a fume hood to achieve even faster occurring concentration gradients during evaporation. In addition, DOX is water soluble, therefore, it is possible to use water as a precipitation bath, which is advantageous from a toxicological and economic point of view.

From the theoretical evaluation in Chapter 6.2.1 it is evident that DOX is selective for the PS block of the PMAA-*b*-PS. Therefore, micellization with a PMAA core should be facilitated. In addition, it should be noted that the water precipitation bath was kept at temperatures below 5 ° to maintain the uniformity, orientation and regularity of the micelle assembly in the final stage of membrane preparation since mobility of the PMAA block is limited at such low temperatures. The freezing point of DOX is 11.8 °C, thus DOX is frozen below 5 °C, however this is not the case if the polymer is dissolved in DOX.³⁵³

Membrane preparation was performed for block copolymers with number average molar mass of $M_n = 75, 130$ and 170 kDa. The block copolymer with 75 kDa lead to membranes with no clear asymmetric hexagonal close packing (HCP) cylinders including connected sublayer, which is likely due to the fact that the PMAA fraction was too small in the investigated block copolymers favoring spherical microphase-separated structures instead of the required cylindrical ones (compare Fig. 3.49). Therefore, PMAA-*b*-PS polymers with a higher weight fraction of PMAA (i.e. of 20 wt%) were used to prepare the desired membranes with HCP cylinders. The atomic force microscopy (AFM) images of the PMAA-*b*-PS polymer with a M_n of 75 kDa is illustrated in the appendix in Fig. 9.1.

In a second step, PMAA-*b*-PS polymers with a weight fraction of PS of 80 wt% and PMAA of 20 wt% were as well as a $M_n = 130$ kDa ($D=1.35$) and 170 kDa ($D=1.62$) were prepared to obtain membranes with HCP cylinders. It is expected that membranes with distinct pore size will be obtained from these two block copolymers due to their distinct molecular weights and compositions.^{354,355}

In the following, the PMAA-*b*-PS block copolymer with 130 kDa is used for membrane preparation at a total polymer concentration of 15 and 16 wt% and ET of 20, 30, 40, and 50 s. Like in the previous experiments, DOX was chosen as the selective solvent, and solvent evaporation was performed in a fume hood to foster faster evaporation. AFM images of the polymer membranes at 15 wt% and 16 wt% are shown in Figs. 6.7 and 6.8. In fact, an ET between 20-30 s seems suitable to achieve ordered HCP cylinders.

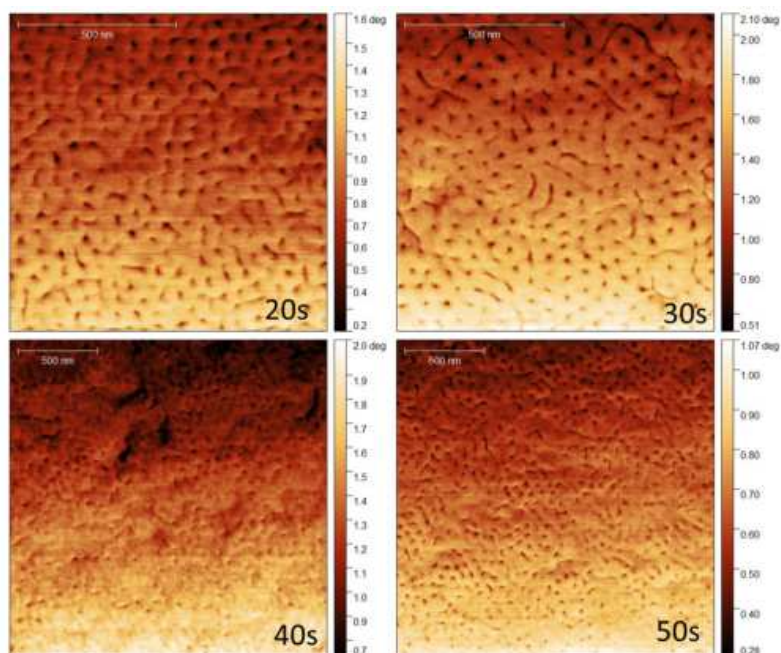


Figure 6.7: AFM images of the phase contrast for the PMAA-*b*-PS polymer with a $M_n = 130$ kDa and PS:PMAA weight percent ratio of 80:20 at a total polymer concentrations of 15 wt% and ET between 20-50 sec.

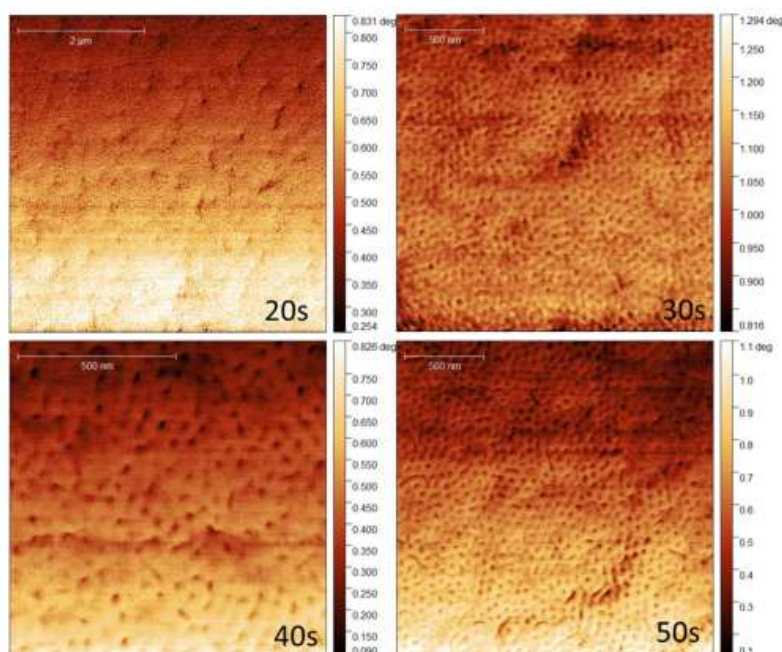


Figure 6.8: AFM images of the phase correction for the PMAA-*b*-PS polymer with a $M_n = 130$ kDa and PS:PMAA weight percent ratio of 80:20 at a total polymer concentrations of 16 wt% and ET between 20-50 sec.

In addition, scanning electron microscopy (SEM) images were taken of the samples with total polymer concentration of 15 and 16 wt% and an ET of 20 s (6.9, 6.10). The top and bottom surface, and the selective-layer cross-section at different areas were measured, which are marked in different colors. The SEM images clearly show HCP cylinders on the surface. The image of the cross-section shows a sponge-like structure with great channel connection, which is advantageous in regard to the permeability. As already suspected from the AFM images, there are hardly any differences between the membrane prepared at 15 and 16 wt%, so both polymer concentrations can be targeted in the casting solution to obtain ordered HCP cylinders.

Further SEM images were taken for the polymer concentration of 16 wt% at an ET of 50 s, where the sponge-structure does look more dense compared to the images at ET = 20 s, due to the too long time period of ET (Figure 6.11).

Furthermore, the influence of polymer molecular weight on membrane production was investigated. Therefore, a polymer with a M_n of 170 kDa was prepared. This order of magnitude plays a significant role in changing the pore size and the mechanical support of the membrane. The PMAA-*b*-PS polymer membrane at 130 kDa and 170 kDa were compared. All those polymer membranes were prepared analogously at the same total polymer concentration of 15 wt% and 30 sec ET. A pore size of 26 nm was measured for the polymer at 130 kDa and 32 nm for the polymer at 170 kDa (Figure 6.12). This means that also for the block copolymer with $M_n = 170$ kDa the ordered structures are preserved, and the pore size can be controlled by the M_n of the polymer.

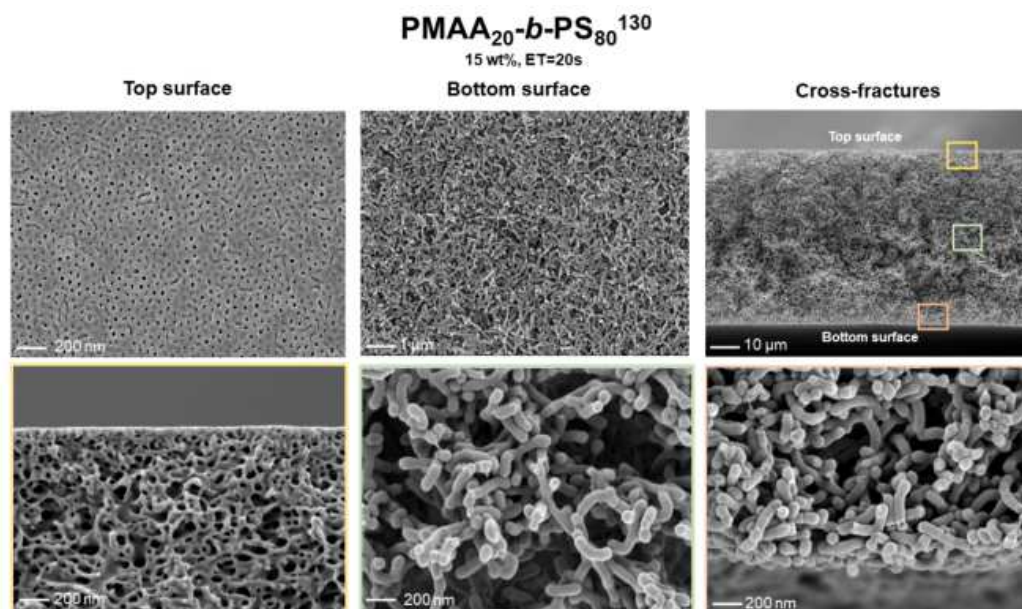


Figure 6.9: SEM images of the PMAA-*b*-PS SNIPS membrane with an $M_n = 130$ kDa at an ET of 20 s and a total polymer weight percentage of 15 wt%. The top surface (top left), bottom (top center), and cross-section (top right) is presented and further zoomed in at three different positions: yellow box = top layer, green box = cross-section layer, and in between orange box = bottom layer.

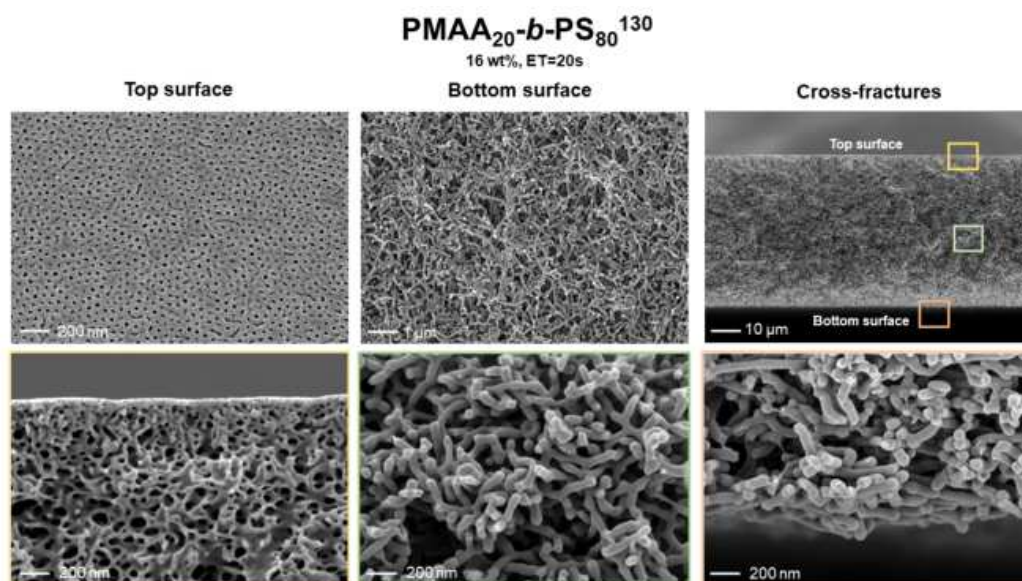


Figure 6.10: SEM images of the PMAA-*b*-PS diblock copolymer with an $M_n = 130$ kDa at an ET of 20 s, and a total polymer weight percentage of 16 wt%. The top surface (top left), bottom (top center), and cross-section (top right) is presented and further zoomed in at three different positions: yellow box = top layer, green box = cross-section layer, and in between orange box = bottom layer.

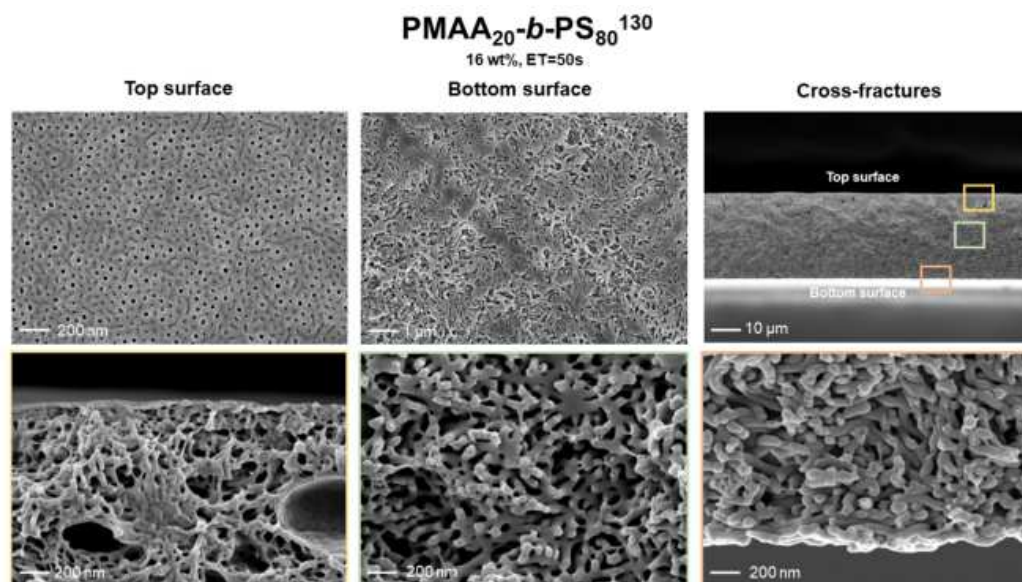


Figure 6.11: SEM images of the PMAA-*b*-PS diblock polymer with an $M_n = 130$ kDa at an ET of 50 s, and a total polymer weight percentage of 16 wt%. The top surface (top left), bottom (top center), and cross-section (top right) is presented and further zoomed in at three different positions: yellow box = top layer, green box = cross-section layer, and in between orange box = bottom layer.

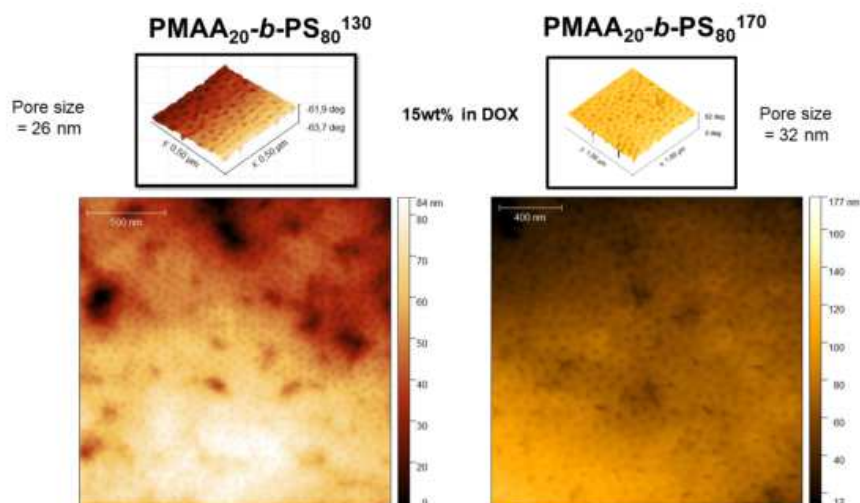


Figure 6.12: AFM images of the height profile for the PMAA-*b*-PS diblock copolymer with a M_n of 130 kDa and 170 kDa and PS:PMAA weight percent ratio of 80:20 at different total polymer concentrations of 15 wt% and an ET of 30 s.

In summary, of the first part, it was shown that asymmetric HCP cylinder morphologies could be obtained in DOX as a solvent with a total polymer weight concentration of 15-16 wt% with an ET of 20-30 s and the use of water as a precipitation bath. Increasing the molar mass made it even possible to specifically increase the pore diameter. However, it should not be hidden that under these conditions, a considerable amount of energy is required to keep the temperature of the water precipitation bath permanently below 5 °C. Therefore, a more feasible and efficient membrane production process was developed which allows the precipitation of the PMAA-*b*-PS in the water precipitation bath at room temperature.

Similar to the work of Cheng et al., in which the preparation of PAA-*b*-PS membranes is described, zinc acetate was added as a salt to the casting solution to complex the carboxylic acid groups.³⁵⁶ Zinc acetate was chosen as a salt since it is soluble in organic solvents. Cheng et al. additionally pointed out the enhanced stability of the self-assembled micelles during membrane formation when carboxylic acid groups are complexed with the zinc metal ion, which act as physical crosslinking points to limit the mobility of the PMAA chain stabilizing the micellar structure. It is worth mentioning that the M_n values of the polymers in their work are much lower ($M_n \approx 84$ kDa) than the polymers used in this work (130-170 kDa).

Following this approach, the PMAA-*b*-PS membrane ($M_n=130$ kDa) was casted with a concentration of 15 wt% of the total polymer concentration and 1 wt% zinc acetate relative to the polymer concentration. As a reminder, salts can act as structure-directing agents to regulate the order and density of the pores.³⁵⁶ Three different ETs of 10, 30, and 40 s. were tested. As mentioned above, water at room temperature was chosen as the precipitation bath. The corresponding AFM images are shown in Figure 6.13, where the membrane sample at ET of 30 s showed highly ordered HCP cylinders. In addition, SEM measurements were

performed for this particular polymer, and images were taken from the surface, bottom, and cross-section (Figure 6.14). Similar to the polymer membranes at 15-16 wt% with an ET of 20 s and just the addition of DOX, equally ordered structures were obtained indicating that the membrane formation process can also be successful at room temperature when structure fostering salts are added to the casting solution.

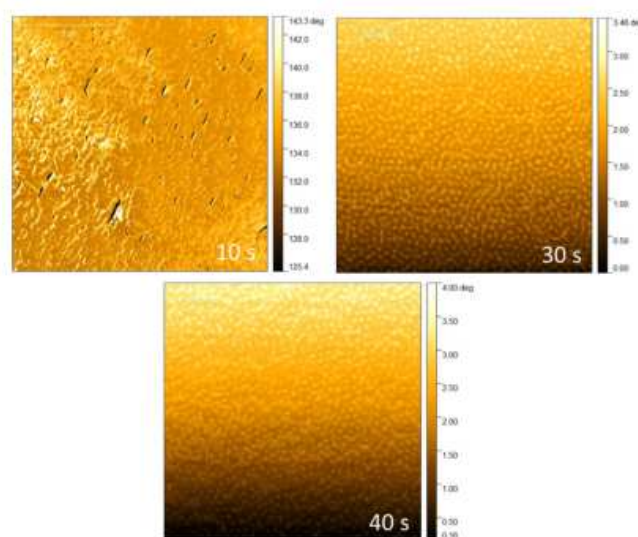


Figure 6.13: AFM images of the phase correction for the PMAA-*b*-PS polymer with a $M_n = 130$ kDa and PS:PMAA weight percent ratio of 80:20 at a total polymer concentrations of 15 wt% with 1 wt% of zinc acetate, and ET between 10-40 s.

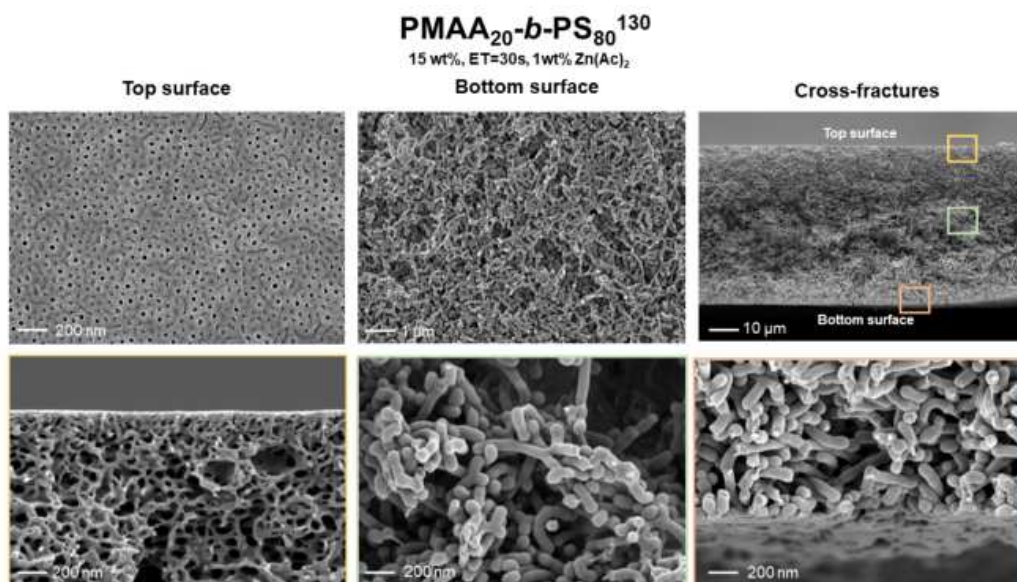


Figure 6.14: SEM images of the PMAA-*b*-PS diblock copolymer with an $M_n = 130$ kDa at an ET of 30 s, and a total polymer weight percentage of 15 wt% with 1 wt% of zinc acetate. The top surface, bottom, and cross-section is presented and further zoomed in at three different positions: yellow box = top layer, green box = cross-section layer, and in between orange box = bottom layer.

In conclusion, PMAA-*b*-PS polymer membranes from block copolymers with two different molecular weights were successfully prepared. This was either achieved by cooling down the aqueous precipitation bath to 5 °C or alternatively add zinc acetate to the casting solution allowing to keep the bath at room temperature. Both conditions are alternatives to provide the primary material for lithium adsorber membranes.

6.2.3 First attempts on the fabrication of lithium adsorber membranes

In this Section, the preparation of first membranes of the lithium-selective CE4MA CE polymers is reported. The membrane morphology is monitored using SEM images. In addition, ideas for further future works are proposed.

The first experiments were performed with a P(MAA-*r*-CE4MA)-*b*-PS polymer with a weight fraction of PS of 78.7 wt%, PMAA of 18.7 wt%, 2.5 wt% of CE4MA, and with a total molar mass of $M_n = 132$ kDa. As a reminder, CE4MA forms single complexes with Li^+ and sandwich complexes with Na^+ and is thus selective towards both ions (see Publication 5).

Membrane preparation conditions were adjusted analogously to those attempted in the previous Section. DOX was chosen as a solvent for the casting solution without adding further additives and a total polymer concentration of 18 wt% was adjusted in this case. Also total solid concentrations at 15 wt% were performed, however, the membrane preparation was not successful since no aligned morphology was visible at the surface. The most successful membrane structure was determined at an evaporation time of 40 s. Due to the fact that no additives were used, a cold water bath was chosen for precipitation to ensure higher purity of the product and to increase the amount of accessible carboxylic acid groups which helps stabilizing cation-ion complexation (Publication 4).

SEM images were taken for this polymer membrane and are shown in Fig. 6.15. The SEM images taken on the membrane surface, however, show spherical (probably closed) structures and the resolution of the pores is not as evident as in the CE-free polymers. Furthermore, the sublayer structure shows a finger-like structure instead of spongy-like structure.

Before lithium extraction experiments can be performed on the membrane, it should be ensured that a structure at least as ordered as that of the PMAA-*b*-PS membranes is obtained to provide the best possible membrane stability and functionality. Therefore, further ideas for the membrane preparation with CEs are suggested below:

Higher total solid concentrations than 18 wt% are proposed since the casting solution was still rather low viscous. For the structures in this work, HCP cylinders were targeted with an approximate total concentration fraction of PS $\approx 80\%$ and P(MAA-*r*-CE4MA) $\approx 20\%$. In fact, the morphology arrangement of gyroid structures would be even more advantageous, though, since, in this case, a larger surface area of the functionalizing units of the CE is given compared to HCP cylinders. These structures are expected at a PS weight fraction of 60-70 wt% (see Figure 3.49). However, the range of gyroid in a block copolymer phase diagram is minimal compared to HCP spheres and thus more challenging to achieve.

Another support for the successful synthesis of polymer membranes would be the addition

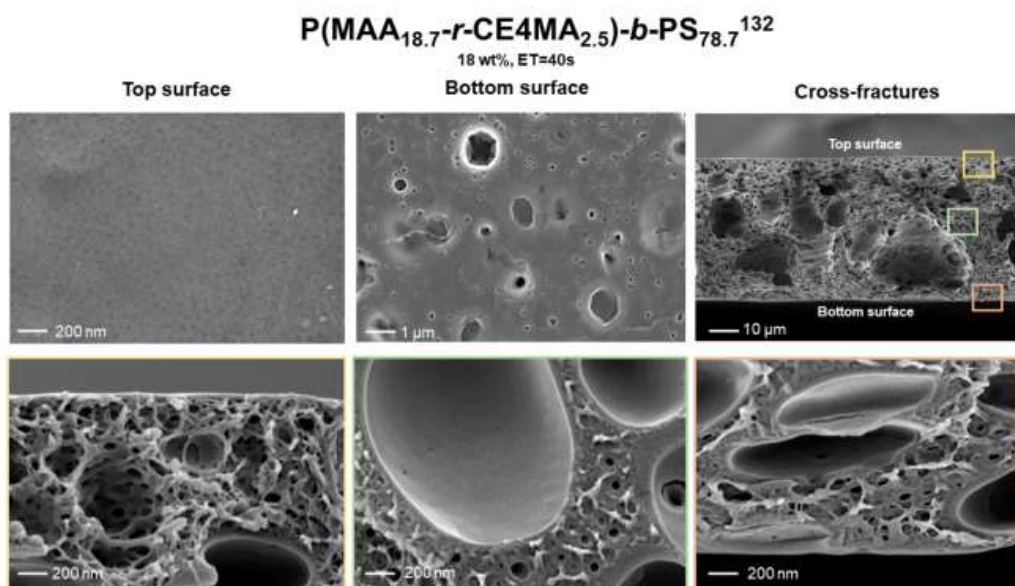


Figure 6.15: SEM images of the P(MAA-*r*-CE4MA)-*b*-PS polymer with an $M_n = 132$ kDa at an ET of 40 s, and a total polymer weight percentage of 18 wt%. The top surface (top left), bottom (top center), and cross-section (top right) is presented and further zoomed in at three different positions: yellow box = top layer, green box = cross-section layer, and in between orange box = bottom layer.

of lithium salts to partially complex the CEs so ordered structures are simpler to obtain. This technique has already been described in literature.³⁵⁷ It should be noted, though, that not all of the CE should be complexed with the pre-added lithium salt, in order to remain high capacity of the lithium-selective polymer membranes.

Furthermore, it would be worth trying another solvent for the casting solution instead of DOX or even switch to binary solvent mixtures. According to Table 6.11, combinations of THF/pyridine or toluene/pyridine could be used for the CE4MA CE since THF as well as toluene is a selective solvent for PS with a Flory–Huggins–Staverman interaction parameter of 0.19 for THF and 0.07 for toluene. However, toluene is not water soluble, thus another precipitation bath such as diethyl ether has to be chosen, which is in face not economically friendly. Pyridine is, on the other hand, a suitable solvent for the CE4MA CE with a Flory–Huggins–Staverman interaction parameter of 0.03. The same solvent tests are proposed for the CE5MA CE. For the CE3MA CE, mixtures between THF/DMSO or toluene/DMSO are suggested, although the former would be the better alternative since toluene and DMSO have a very high boiling point, which is disadvantageous in case of reaching fast concentration gradients during evaporation of the solvent.

Since isoporous asymmetric membranes with ordered HCP cylinders of PMAA-*b*-PS membranes have already been shown, the membranes of the base block copolymer could be post-modified with the CE subsequently after membrane preparation, as it was already conducted by Jiang et al. and Zhang et al. using e.g. post reaction of the hydroxy groups with ethylcyanates in presence of perfluoro(methyl cyclohexane), or solid-gas post modification reac-

tions.^{43,351} For solid–liquid post-modifications, the polymer membrane must be post-modified in a non-solvent for the membrane matrix (i.e. PS). Water would be the easiest and greenest non-solvent for the membrane, unfortunately, many CEs are not water-soluble, so an organic solvent such as diethyl ether or may have to be used to ensure successful post-modification. The advantage of this method is that no new membrane preparation conditions have to be found for the different CE polymers in order to obtain isoporous asymmetric membranes.

6.2.4 Experimental section

The experimental setup of the polymer synthesis is not presented here, since it was produced similar to the reaction conditions of the polymers in Publication 3 and 5. In the following, materials and reaction conditions for the membrane preparations are reported.

6.2.4.1 Materials

The solvents DOX (99 %, Grüssing), DMF (99 %, VWR Chemicals), DCM (>99 %, Acros), and *n*-hexane (95 %, VWR Chemicals) were used as received. Zinc acetate (>99 %, Sigma-Aldrich) was used as received. Deionized water was purified with a Milli-Q[®] integral water purification system.

6.2.4.2 Membrane preparation

Casting solutions were prepared by dissolving PMAA-*b*-PS or P(MAA-*r*-CE4MA)-*b*-PS in DOX. The casting solutions were stirred at 300 rpm at room temperature for at least 24 h and led stay for another 2 h to remove bubbles from the solution before casting. The polymer solution was casted on a glass plate support using a casting knife with a gap height of 200 μm and using water as precipitation bath at temperatures below 5 ° for 4 h or at room temperature for 1 h, if zinc acetate (1 wt% of the total polymer concentration) is added to the casting solution. The cast films were left for a specific ET (10-50 s) under air in a fume hood before immersing it into the precipitation bath. The membranes were dried at 25 ° under reduced pressure for 24 h.

6.2.4.3 Membrane characterization

Scanning electron microscopy SEM was performed using either a LEO Gemini 1550 VP or a Merlin (both from ZEISS, Oberkochen, Germany) at voltage of 3 kV or 5 kV. Cross-sections of the membranes were prepared under cryogenic conditions. The samples were coated with ≈ 2 nm platinum (Pt).

Atomic force microscopy AFM was performed on a JPK Nanowizard microscope in an intermittent contact mode using a Si-tip ($I = 280$ kHz, $r = 10$ nm). Data were visualized and analyzed with the software Gwyddion.

Discussion

This Chapter summarizes the last two Chapters of this thesis. The different CE adsorbers employed in this thesis are outlined, and the most promising CE adsorbers towards lithium are reviewed. The utilization of DFT for predicting CE selectivity towards lithium is overviewed (Section 7.2). Subsequently in Section 7.3, the synthesis conditions of the PMAA-*b*-PS and lithium selective polymers-based CE are reviewed, together with their complexation properties and the preparation of membranes.

7.1 Review of the investigated crown ethers

At the beginning of this thesis, the challenge of environmentally friendly lithium extraction was overviewed, various extraction techniques and materials were presented that are currently used or are in prospect in the near future. Since the topic of lithium extraction should lead a step further into a world with less CO₂ emissions, the lithium extraction processes should be as green as possible to address the issue of environmental pollution.

This work investigated the organic lithium adsorbers of CEs, as these materials are excellent extraction agents for isolating metal ions from aqueous resources. Different modifications and extraction properties towards alkali and alkaline-earth metal ions of CEs adsorbers were investigated in Publications 1, 2, 4, and 5 and are resumed in Figure 7.1. The increasing hydrophobicity within the CE ring was investigated in Publication 1, where the Li⁺ complexation compared to Mg²⁺ was examined; in Publication 4 and 5, the influence of ring size and stoichiometry (e.g. single or sandwich formation) of CE complexes was analyzed; in Publication 2, both ring size and reduced hardness of the donor atom was investigated towards a better complexation of Li⁺ over Na⁺, K⁺, Mg²⁺, and Ca²⁺. In Section 6.1, the effect of nitrogen donor atoms within the CE ring was additionally explored, and the influence of the extractions towards Li⁺ over Mg²⁺ was examined.

How well a CE complexes with metal ions depends on various factors. First and foremost, the HSAB principle is decisive. Hard acids (such as Li⁺ and Mg²⁺) interact with hard bases (such as oxygen). But also the ionic radius and the cavity of the CE play an essential role. If the cation is much smaller than the cavity size of the CE, only fragile coordinative bonds occur since donor atoms and metal ions are positioned too far apart. On the other hand, if the cation

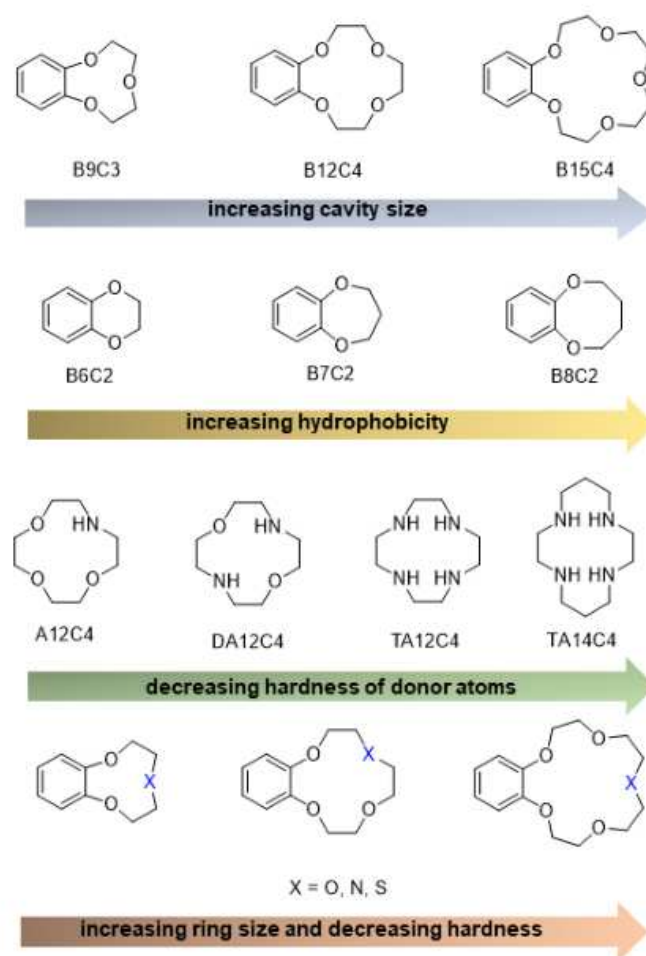


Figure 7.1: Studied CEs in this thesis.

radius is too large, it will not fit into the cavity size of the CE. Then other stoichiometric complexes can be formed, such as sandwich complexes, which are already widely used in metallocene chemistry. However, such complexes can also be prevented by steric substituents, which can matter in case of specific metal ion selectivity. As evident in Publication 2, ring distortions also play a significant role, especially when larger donor atoms, such as sulfur, are present in the CE ring.

In summary, a wide range of modification reactions can be carried out on the CEs; thus, the selectivity towards the target metal ion can be adjusted. From the results of the different projects in this thesis, it was shown that hydrophilic CEs increase the lithium selectivity towards interfering alkali and alkaline earth metal ions (Publication 1). Especially the use of the B9C3 CE forms strong complexes with Li^+ due to its small size forming sandwich complexes instead of simple single complexes (Publication 4). Furthermore, the cavity size of the CE is very crucial, it was shown that 14-membered CE show so far the best complexability towards Li^+ if single complex stoichiometry structures are compared (Chapter 6.1).

7.2 Predicting crown ether–cation complexes using density functional theory

Modifying CEs can take a lot of time and can be even more time consuming if the CE properties are unknown and are unsuccessful in selectively extracting the desired metal ion. Especially if the CE structures have not been prepared yet, the synthesis path to successful preparation can be very tedious. Molecular modeling by computer chemistry is a powerful tool for interpreting complex systems since information on physico-chemical properties such as complex stabilities, cavity sizes, geometric structures of the CEs, and electronic distributions during complexation can be obtained relatively quick. Thus, in a much smaller period of time, one gains an abundance of data that cannot be achieved experimentally by pure diligence. Computational chemistry methods, therefore, allow a narrower selection of potential CE structures for successful complexation of the desired metal ion. However, many of these calculations are still performed in *vacuo* and are mostly far away from real laboratory conditions, but the estimates are increasingly adapted to the real state. In Publication 2, the 1-aza-benzo-15-crown-5 (AB15C5) CE was investigated in a two-phase extraction using molecular modeling based on DFT and compared with the data of experimental extraction experiments. Although much higher complexation constants were determined than in the laboratory experiments, similar trends of the AB15C5 CE complexation properties with the metals Li^+ , Na^+ , K^+ , Mg^{2+} , Ca^{2+} were obtained so that predictions towards CEs complexation properties can still be made and prove therefore DFT as a valuable tool for investigating CE properties before challenging synthetic procedures are performed.

7.3 Review on polymer-based lithium adsorber

A significant part of this thesis and aim was the development of a polymer-based lithium adsorber that shows strong selectivities towards lithium and which is also produced under the most ecological and economical conditions possible and thus can be easily produced on a larger scale so that this material can compete with other materials presented in Chapter 3 and help to saturate the high demand of lithium in the world.

In Publication 3, a PMAA-*b*-PS diblock copolymer was presented using a one-pot RAFT emulsion polymerization. This polymer has amphiphilic properties, PMAA is a very hydrophilic, pH-responsive polymer, which can additionally enter into chemical reactions at the acid group, while PS, as the main component of the polymer, is very hydrophobic, and thus the polymer can undergo microphase separation due to the incompatibility of the two blocks. The advantage of synthesizing the PMAA-*b*-PS block by RAFT emulsion polymerization is that the polymer can be produced in water without the addition of stabilizers, as this property is taken over by the RAFT CTA. Therefore no challenging purification procedures of this polymer, such as dialysis, are necessary. Furthermore, by modifying the CTA, solid concentrations in the emulsion of up to 50 wt% can be achieved without having to deal with

viscosity issues and poor heat transfer. The advantage of high solids concentrations is that less solvent must be added to the product, so less energy is required to proceed the reaction. In addition, the polymer can be produced in one step in just a few hours without intermediate purification methods such as polymer precipitation. Polymers of up to $M_n \approx 170$ kDa with narrow molar mass distributions ($D = 1.4$) could be produced.

In Publications 4 and 5, post-modification reactions were successfully carried out using a Steglich esterification of the PMAA-*b*-PS diblock copolymer. With this esterification method, the B9C3, 12C4, and 15C5 (which carried OH groups) were linked to the PMAA unit of the polymer. The selectivities of these polymers with Li^+ , Na^+ , and K^+ were investigated, and their stability was compared with single and sandwich complexes and their analogous free CEs (publication 5).

The benefit of polymer-based CEs is that the lithium adsorbers are much easier to isolate from the aqueous lithium sources due to their high incompatibility with water. Furthermore, the polymers can be easily recycled by simple precipitation, which is also crucial in regard of our environment. In addition, the complex formation within the polymer material is associated with less energy loss than free CEs. In the polymer, the CE are already bound to the polymer and thus have fewer degrees of freedom than the free CEs. Therefore, once a complex is formed, the entropy loss is much lower than for free CEs, which is the main reason why the complexation constants in the polymer are at least 10000-fold higher than for free CEs. This phenomenon is even more pronounced for sandwich complexes, where two CEs lose their degrees of freedom. This observation was reported in Publication 4 and confirmed with further samples in Publication 5.

The B9C3 in the polymer forming a sandwich complex with Li^+ shows the strongest complexation constant of all studied systems. In addition, it was observed that the B9C3 in the polymer did not extract Na^+ very-well. Extraction experiments were performed simulating salt concentrations similar to the Dead Sea with 0.014 g/L Li^+ , 6.9 g/L K^+ , and 36 g/L Na^+ , in which 60 % of the lithium was complexed, even though the concentration of Li^+ was much lower compared to Na^+ and K^+ .

Another advantage of polymeric materials is that, compared to organic or inorganic materials, they have a bigger surface area of the extractable unit when formed e.g. into membranes. Inorganic and organic materials would first have to be further processed by granulating them, forming foams, or attaching them to nanoparticles to increase handling and Li^+ capacity, however, those processes could also destroy the material or weaken the structure.

The PMAA-*b*-PS polymer from Publication 3 was prepared via SNIPS into asymmetric membranes with an ordered HCP cylinder morphology at the surface and great connecting channels, which are important in regards of permeability. The polymer membrane formation reaction was carried out under two different reaction conditions, one with pure DOX as a solvent for the casting solution with the use of water as a precipitation bath at temperatures below 5 °C, and the other with the addition of zinc acetate into the polymer solution to partially complex the PMAA groups to use water as precipitation bath at room temperature.

As a reminder: PMAA is well soluble in water.

Polymer-based CE membrane preparation was attempted to be prepared analogously to the PMAA-*b*-PS membrane using the 12C4 CE polymer; so far, with pure DOX as the solvent for the casting solution and water as a precipitations bath below 5 °C, no ordered asymmetric membrane could be prepared; therefore; further experiments are required. Once the asymmetric membrane production is successful, lithium extractions should be performed to prove the greater accessibility of the lithium adsorber material, which will bring us a big step closer to the selective extraction of lithium from aqueous resources.

7.4 Outlook

In this thesis, the best selectivity towards lithium was found for the CE3MA functionalized block copolymer building sandwich complexes with Li⁺. However, it was also observed that 14-membered CEs have perfect cavities for the lithium-ion, therefore linking 14-membered CE rings to the PMAA-*b*-PS polymer is worth trying to increase the stability of the lithium complex without sterically challenging sandwich complexes taking place. However, sandwich complexes with Na⁺ would have to be prevented, as they tend to form easily.^{175,358} This is usually controlled by incorporating steric groups into the CE. However, this type of reaction is often challenging to perform and costly since a steric structure must be linked to an already steric CE. A much simpler method would be to connect steric groups carrying an OH group to the PMAA unit of the polymer using Steglich esterification. This way would be much cheaper and easier in proceeding. Ideally, the CE and the steric group are connected alternately in the PMAA moiety to prevent the CE from forming sandwich complexes. For example, hexagonal rings that form an armchair conformation could be applied as steric groups.

The PMAA-*b*-PS diblock copolymer is already produced under very attractive conditions. Therefore, the only thing missing for the perfect production of a polymer-based lithium adsorber is the optimization of the post-modification of the CE with the polymer. So far, the PMAA-*b*-PS polymer has been prepared in a one-pot reaction in water performing a RAFT emulsion polymerization. Since this polymer forms in the emulsion particles such as micelles, the PMAA units are located at the corona, and the PS moiety is the core; thus, the functional groups are easy accessible. The easiest way to proceed would be the addition of a water soluble CE to the emulsion reaction medium. The Steglich esterification can still be performed, since there are water soluble Steglich agents available such as 1-ethyl-3-(3-dimethylaminopropyl)carbodiimide and DMAP. The product would result in a micelle-based CE polymer. The advantage of this reaction is that the complete lithium adsorbable polymer is feasible in a one-pot procedure without intermediate purification steps, which would make this polymer system even cheaper, greener, and easier to produce.

In the last Chapter, the fabrication of ordered asymmetric polymer membranes for the PMAA-*b*-PS system was successfully reported. However, the polymer-based CE membranes still need to be optimized in their reaction conditions. For this purpose, the polymer concen-

tration of the casting solution, the ET of the solvent, and solvent mixtures would have to be further investigated. Since only the CE4MA-functionalized block copolymer has been tested so far, further optimizations can only be proposed. First, the block copolymer concentration of the casting solution could be increased to over 18 wt% since the casting solution was still very liquid below that concentration. Following the calculation of the solubility parameters in Section 6.2, mixtures of solvents of THF/pyridine or toluene/pyridine can also be carried out as a casting solution for the CE4MA-functionalized block copolymer. For the membrane preparation of the CE3MA and CE5MA, solvents of THF/DMSO and toluene/DMSO are proposed; the first would be the better choice due to the lower evaporation point of THF compared to toluene.

Another way for the successful preparation of CE membranes is the modification of the PMAA-*b*-PS membrane, which has already been successfully fabricated by e.g., gas–solid or liquid–solid reactions.³⁵¹ Most important, the membrane must not dissolve in the reaction solvent. Otherwise, the ordered structures would be damaged. This proposed idea has the advantage that different CE materials can be linked to an already ideal membrane so that no new membrane production parameters have to be found for the various systems to gain ordered asymmetric polymer membranes.

Furthermore, the release of ions should be considered in future experiments. As indicated, e.g., in Chapter 6.1, by the possible use of aza-CE, it is possible by the addition of acid to disturb the trapped ions from the ring of the CE by repulsive interactions due to the ionization of the nitrogen donor atom. Another method would be incorporating ionic structures such as betaines or UV-responsive materials, that adopt ionic structures under the incidence of UV light, such as the merocyanine class, into the polymer system. The release of the ion by switching on UV light, is a very fast and environmental friendly method, which is worth working on.

Altogether, we hope to motivate further research on this topic with the results of this work. The successful production of a lithium-selective CE-based polymer membrane could be indeed a truly environmentally conscious alternative to recover lithium from aqueous resources despite the low concentration of it.

References

- [1] T. Lestariningsih, Q. Sabrina, I. Nuroniah, B. Prihandoko, E. Marti Wigayati, C. Rina Ratri, *Journal of Physics: Conference Series* **2019**, *1282*, 1–7.
- [2] M. Kaltschmitt, W. Streicher, A. Wiese, *Erneuerbare Energien*, 6. Aufl., Springer Vieweg, **2020**, S. 1–8.
- [3] U. S. Energy Information Administration, *What is energy?* **2021**, <https://www.eia.gov/energyexplained/what-is-energy/> (accessed: 21.09.2022).
- [4] H. Ritchie, M. Roser, *Our World in Data* **2020**, <https://ourworldindata.org/energy> (accessed: 28.03.2022).
- [5] Hinrichs, Roger A, M. Kleinbach, *Its Use and the Environment*, 5. Aufl., Brooks/Cole, **2013**, S. 1–4.
- [6] D. Liu, X. Guo, B. Xiao, *Science of the Total Environment* **2019**, *661*, 750–766.
- [7] G. A. Marrero, *Energy Economics* **2010**, *32*, 1356–1363.
- [8] Umweltbundesamt, *Primärenergieverbrauch* **2022**, <https://www.umweltbundesamt.de> (accessed: 28.03.2022).
- [9] . Bundesministerium-für-Wirtschaft-und Klimaschutz, *Erneuerbare Energien* **2021**, <https://www.bmwi.de/Redaktion/DE/Dossier/erneuerbare-energien.html> (accessed: 28.03.2022).
- [10] A. G. Energiebilanzen, *Energy - Primärenergieverbrauch* **2022**, <https://ag-energiebilanzen.de/daten-und-fakten/primaerenergieverbrauch/> (accessed: 28.03.2022).
- [11] M. Wayu, *Solids* **2021**, *2*, 232–248.
- [12] S. Kulandaivalu, Y. Sulaiman, *Energies* **2019**, *12*, 2107.
- [13] B. Scrosati, *Journal of Solid State Electrochemistry* **2011**, *15*, 1623–1630.

- [14] V. S. Bagotsky, *Journal of Solid State Electrochemistry* **2011**, *15*, 1559–1562.
- [15] O. Kaarstad, *Energy Conversion and Management* **1995**, *36*, 869–872.
- [16] C. McGlade, P. Ekins, *Nature* **2015**, *517*, 187–190.
- [17] V. Vandeginste, *Applied Sciences* **2022**, *12*, 862.
- [18] M. Yang, J. Hou, *Membranes* **2012**, *2*, 367–383.
- [19] X. Li, Y. Mo, W. Qing, S. Shao, C. Y. Tang, J. Li, *Journal of Membrane Science* **2019**, *591*, 1–13.
- [20] B. Swain, *Separation and Purification Technology* **2017**, *172*, 388–403.
- [21] H. Bae, Y. Kim, *Materials Advances* **2021**, *2*, 3234–3250.
- [22] P. W. Gruber, P. A. Medina, G. A. Keoleian, S. E. Kesler, M. P. Everson, T. J. Wallington, *Journal of Industrial Ecology* **2011**, *15*, 760–775.
- [23] A. Yaksic, J. E. Tilton, *Resources Policy* **2009**, *34*, 185–194.
- [24] S. E. Kesler, P. W. Gruber, P. A. Medina, G. A. Keoleian, M. P. Everson, T. J. Wallington, *Ore Geology Reviews* **2012**, *48*, 55–69.
- [25] U. S. Geological Survey, *Mineral Commodity Summaries 2021* **2021**, 200.
- [26] H. Vikström, S. Davidsson, M. Höök, *Applied Energy* **2013**, *110*, 252–266.
- [27] P. Meshram, B. D. Pandey, T. R. Mankhand, *Hydrometallurgy* **2014**, *150*, 192–208.
- [28] L. Li, V. G. Deshmane, M. P. Paranthaman, R. Bhave, B. A. Moyer, S. Harrison, *Johnson Matthey Technology Review* **2018**, *62*, 161–176.
- [29] C. Grosjean, P. Herrera Miranda, M. Perrin, P. Poggi, *Renewable and Sustainable Energy Reviews* **2012**, *16*, 1735–1744.
- [30] G. Liu, Z. Zhao, A. Ghahreman, *Hydrometallurgy* **2019**, *187*, 81–100.
- [31] L. Talens Peiró, G. Villalba Méndez, R. U. Ayres, *Jom* **2013**, *65*, 986–996.
- [32] F. Meng, J. McNeice, S. S. Zadeh, A. Ghahreman, *Mineral Processing and Extractive Metallurgy Review* **2021**, *42*, 123–141.
- [33] T. Tran, V. T. Luong, *Lithium Production Processes*, Elsevier Inc., **2015**, S. 81–124.
- [34] A. Karrech, M. R. Azadi, M. Elchalakani, M. A. Shahin, A. C. Seibi, *Minerals Engineering* **2020**, *145*, 106085.

-
- [35] F. Margarido, N. Vieceli, F. Durão, C. Guimarães, C. A. Nogueira, *Comunicações Geológicas* **2014**, *101*, 795–798.
- [36] E.-N. M. A. A. Medina, Luiz Fernando, *metallurgical transactions B* **1984**, *15*, 725–726.
- [37] C. Dessemond, G. Soucy, J.-P. Harvey, P. Ouzilleau, *minerals* **2020**, *10*, 519.
- [38] J. F. Song, L. D. Nghiem, X. M. Li, T. He, *Environmental Science: Water Research and Technology* **2017**, *3*, 593–597.
- [39] J. Sterba, A. Krzemień, P. Riesgo Fernández, C. Escanciano García-Miranda, G. Fidalgo Valverde, *Resources Policy* **2019**, *62*, 416–426.
- [40] N. P. Kotsupalo, A. D. Ryabtsev, I. A. Poroshina, A. A. Kurakov, E. V. Mamylova, L. T. Menzheres, M. A. Korchagin, *Russian Journal of Applied Chemistry* **2013**, *86*, 482–487.
- [41] Y. H. Li, Z. W. Zhao, X. H. Liu, X. Y. Chen, M. L. Zhong, *Transactions of Nonferrous Metals Society of China (English Edition)* **2015**, *25*, 3484–3489.
- [42] M. P. Paranthaman, L. Li, J. Luo, T. Hoke, H. Ucar, B. A. Moyer, S. Harrison, *Environmental Science and Technology* **2017**, *51*, 13481–13486.
- [43] H. Wang, Y. Zhong, B. Du, Y. Zhao, M. Wang, *Hydrometallurgy* **2018**, *175*, 102–108.
- [44] X. Liu, M. Zhong, X. Chen, Z. Zhao, *Hydrometallurgy* **2018**, *176*, 73–77.
- [45] K. Ooi, A. Sonoda, Y. Makita, R. Chitrakar, Y. Tasaki-Handa, T. Nakazato, *Hydrometallurgy* **2017**, *174*, 123–130.
- [46] A. M. Vara, *Current Sociology* **2015**, *63*, 100–104.
- [47] W. Xiang, S. Liang, Z. Zhou, W. Qin, W. Fei, *Hydrometallurgy* **2017**, *171*, 27–32.
- [48] C. Shi, Y. Jing, J. Xiao, X. Wang, Y. Yao, Y. Jia, *Separation and Purification Technology* **2017**, *172*, 473–479.
- [49] L. Zhang, L. Li, D. Shi, X. Peng, F. Song, F. Nie, W. Han, *Hydrometallurgy* **2018**, *175*, 35–42.
- [50] Z. Zhou, W. Qin, Y. Liu, W. Fei, *Journal of Chemical and Engineering Data* **2012**, *57*, 82–86.
- [51] Z. Zhou, W. Qin, W. Fei, *Journal of Chemical and Engineering Data* **2011**, *56*, 3518–3522.
- [52] Z. Zhou, S. Liang, W. Qin, W. Fei, *Industrial and Engineering Chemistry Research* **2013**, *52*, 7912–7917.

- [53] W. Xiang, S. Liang, Z. Zhou, W. Qin, W. Fei, *Hydrometallurgy* **2016**, *166*, 9–15.
- [54] B. Swain, *Journal of Chemical Technology and Biotechnology* **2016**, *91*, 2549–2562.
- [55] D. A. Lee, W. L. Taylor, W. J. McDowell, J. S. Drury, *Journal of Inorganic and Nuclear Chemistry* **1968**, *30*, 2807–2821.
- [56] Y. Pranolo, Z. Zhu, C. Y. Cheng, *Hydrometallurgy* **2015**, *154*, 33–39.
- [57] K. N. Marsh, J. A. Boxall, R. Lichtenthaler, *Fluid Phase Equilibria* **2004**, *219*, 93–98.
- [58] R. Bai, J. Wang, D. Wang, Y. Zhang, J. Cui, *Separation and Purification Technology* **2021**, *274*, 119051.
- [59] C. Shi, Y. Jing, Y. Jia, *Russian Journal of Physical Chemistry A* **2017**, *91*, 692–696.
- [60] C. Shi, Y. Jing, Y. Jia, *Journal of Molecular Liquids* **2016**, *215*, 640–646.
- [61] C. Shi, Y. Jia, C. Zhang, H. Liu, Y. Jing, *Fusion Engineering and Design* **2015**, *90*, 1–6.
- [62] X. Xu, Y. Chen, P. Wan, K. Gasem, K. Wang, T. He, H. Adidharma, M. Fan, *Progress in Materials Science* **2016**, *84*, 276–313.
- [63] R. Chitrakar, Y. Makita, K. Ooi, A. Sonoda, *Dalton Transactions* **2014**, *43*, 8933–8939.
- [64] D. Weng, H. Duan, Y. Hou, J. Huo, L. Chen, F. Zhang, J. Wang, *Progress in Natural Science: Materials International* **2020**, *30*, 139–152.
- [65] N. Liu, M. K., J. Pan, Y. Hu, Y. Sun, X. Liu, *Journal of The Electrochemical Society* **2020**, *167*, 040517.
- [66] W. Chen, X. Zhan, B. Luo, Z. Ou, P. C. Shih, L. Yao, S. Pidaparthi, A. Patra, H. An, P. V. Braun, R. M. Stephens, H. Yang, J. M. Zuo, Q. Chen, *Nano Letters* **2019**, *19*, 4712–4720.
- [67] J. C. Hunter, *Journal of Solid State Chemistry* **1981**, *39*, 142–147.
- [68] T. Takada, H. Hayakawa, E. Akiba, *Journal of Solid State Chemistry* **1995**, *115*, 420–426.
- [69] R. Chitrakar, H. Kanoh, Y. Miyai, K. Ooi, *Ind. Eng. Chem. Res.* **2001**, *40*, 2054–2058.
- [70] S. Y. Sun, J. L. Xiao, J. Wang, X. Song, J. G. Yu, *Industrial and Engineering Chemistry Research* **2014**, *53*, 15517–15521.
- [71] M. Seyedahmadian, S. Houshyarazar, A. Amirshaghghi, *Bulletin of the Korean Chemical Society* **2013**, *34*, 622–628.

-
- [72] Y. Marcus, *J. Chem. Soc., Faraday Trans.* **1993**, *89*, 713–718.
- [73] G. He, L. Zhang, D. Zhou, Y. Zou, F. Wang, *Ionics* **2015**, *21*, 2219–2226.
- [74] X. M. Shen, A. Clearfield, *Journal of Solid State Chemistry* **1986**, *64*, 270–282.
- [75] Q. Feng, H. Kanoh, Y. Miyai, K. Ooi, *Chemistry of Materials* **1995**, *7*, 148–153.
- [76] K. Ooi, Y. Miyai, J. Sakakihara, *Langmuir* **1991**, *7*, 1167–1171.
- [77] H. Koyanaka, O. Matsubaya, Y. Koyanaka, N. Hatta, *Journal of Electroanalytical Chemistry* **2003**, *559*, 77–81.
- [78] S. Yang, F. Zhang, H. Ding, P. He, H. Zhou, *Joule* **2018**, *2*, 1648–1651.
- [79] Q. H. Zhang, S. P. Li, S. Y. Sun, X. S. Yin, J. G. Yu, *Chemical Engineering Science* **2010**, *65*, 165–168.
- [80] S. Wang, P. Li, W. Cui, H. Zhang, H. Wang, S. Zheng, Y. Zhang, *RSC Advances* **2016**, *6*, 102608–102616.
- [81] L. Zhang, D. Zhou, G. He, F. Wang, J. Zhou, *Materials Letters* **2014**, *135*, 206–209.
- [82] C. P. Lawagon, G. M. Nisola, J. Mun, A. Tron, R. E. C. Torrejos, J. G. Seo, H. Kim, W. J. Chung, *Journal of Industrial and Engineering Chemistry* **2016**, *35*, 347–356.
- [83] D. Wang, D. Choi, Z. Yang, V. V. Viswanathan, Z. Nie, C. Wang, Y. Song, J. G. Zhang, J. Liu, *Chemistry of Materials* **2008**, *20*, 3435–3442.
- [84] Y. Orooji, Z. Nezafat, M. Nasrollahzadeh, N. Shafiei, M. Afsari, K. Pakzad, A. Razmjou, *Desalination* **2022**, *529*, 115624.
- [85] W. N. Li, J. Yuan, S. Gomez-Mower, S. Sithambaram, S. L. Suib, *Journal of Physical Chemistry B* **2006**, *110*, 3066–3070.
- [86] X. Wang, Y. Li, *Journal of the American Chemical Society* **2002**, *124*, 2880–2881.
- [87] L. Liu, H. Zhang, Y. Zhang, D. Cao, X. Zhao, *Colloids and Surfaces A: Physicochemical and Engineering Aspects* **2015**, *468*, 280–284.
- [88] B. Zhao, M. Guo, F. Qian, Z. Qian, N. Xu, Z. Wu, Z. Liu, *RSC Advances* **2020**, *10*, 35153–35163.
- [89] K. Sato, D. M. Poojary, A. Clearfield, M. Kohno, Y. Inoue, *Journal of Solid State Chemistry* **1997**, *131*, 84–93.
- [90] M. H. Sorour, A. M. El-Rafei, H. A. Hani, *Ceramics International* **2016**, *42*, 4911–4917.
- [91] S. Y. Lee, S. J. Park, *RSC Advances* **2014**, *4*, 21899–21903.

- [92] H. Saravaia, H. Gupta, V. Kulshrestha, *RSC Advances* **2016**, *6*, 106980–106989.
- [93] S. Wang, X. Chen, Y. Zhang, Y. Zhang, S. Zheng, *Particuology* **2018**, *41*, 40–47.
- [94] Q. Zhao, J. M. Gao, Y. Guo, F. Cheng, *Chemistry Letters* **2018**, *47*, 1308–1310.
- [95] F. Xue, B. Wang, M. Chen, C. Yi, S. Ju, W. Xing, *Separation and Purification Technology* **2019**, *228*, 115750.
- [96] G. Zhu, P. Wang, P. Qi, C. Gao, *Chemical Engineering Journal* **2014**, *235*, 340–348.
- [97] Y. Han, H. Kim, J. Park, *Chemical Engineering Journal* **2012**, *210*, 482–489.
- [98] J. L. Xiao, S. Y. Sun, X. Song, P. Li, J. G. Yu, *Chemical Engineering Journal* **2015**, *279*, 659–666.
- [99] A. Watanabe, T. Matsunaga, A. Abulikemu, K. Shimoda, K. Yamamoto, T. Uchiyama, Y. Uchimoto, *Journal of Alloys and Compounds* **2020**, *819*, 153037.
- [100] S. Y. Sun, L. J. Cai, X. Y. Nie, X. Song, J. G. Yu, *Journal of Water Process Engineering* **2015**, *7*, 210–217.
- [101] Q. Bi, Z. Zhang, C. Zhao, Z. Tao, *Water Science and Technology* **2014**, *70*, 1690–1694.
- [102] W. Li, C. Shi, A. Zhou, X. He, Y. Sun, J. Zhang, *Separation and Purification Technology* **2017**, *186*, 233–242.
- [103] H. Z. Zhang, Z. L. Xu, H. Ding, Y. J. Tang, *Desalination* **2017**, *420*, 158–166.
- [104] Y. Guo, Y. Ying, Y. Mao, X. Peng, B. Chen, *Angewandte Chemie - International Edition* **2016**, *55*, 15120–15124.
- [105] X. Wen, P. Ma, C. Zhu, Q. He, X. Deng, *Separation and Purification Technology* **2006**, *49*, 230–236.
- [106] X. Y. Nie, S. Y. Sun, X. Song, J. G. Yu, *Journal of Membrane Science* **2017**, *530*, 185–191.
- [107] T. Xu, Y. Zhang, W. Y. Zhao, M. Zhou, B. Yan, X. Sun, Y. Liu, Y. Wang, *Industrial and Engineering Chemistry Research* **2018**, *57*, 6025–6039.
- [108] Y. Zhang, S. Paepen, L. Pinoy, B. Meesschaert, B. Van Der Bruggen, *Separation and Purification Technology* **2012**, *88*, 191–201.
- [109] J. W. An, D. J. Kang, K. T. Tran, M. J. Kim, T. Lim, T. Tran, *Hydrometallurgy* **2012**, *117-118*, 64–70.
- [110] P. Y. Ji, Z. Y. Ji, Q. B. Chen, J. Liu, Y. Y. Zhao, S. Z. Wang, F. Li, J. S. Yuan, *Separation and Purification Technology* **2018**, *207*, 1–11.

-
- [111] Q. B. Chen, Z. Y. Ji, J. Liu, Y. Y. Zhao, S. Z. Wang, J. S. Yuan, *Journal of Membrane Science* **2018**, *548*, 408–420.
- [112] C. Jiang, Y. Wang, Q. Wang, H. Feng, T. Xu, *Industrial and Engineering Chemistry Research* **2014**, *53*, 6103–6112.
- [113] N. Parsa, A. Moheb, A. Mehrabani-Zeinabad, M. A. Masigol, *Chemical Engineering Research and Design* **2015**, *98*, 81–88.
- [114] S. Bunani, N. Kabay, S. Bunani, M. Arda, K. Yoshizuka, S. Nishihama, S. Bunani, *Desalination* **2017**, *416*, 10–15.
- [115] C. W. Hwang, M. H. Jeong, Y. J. Kim, W. K. Son, K. S. Kang, C. S. Lee, T. S. Hwang, *Separation and Purification Technology* **2016**, *166*, 34–40.
- [116] Z. yong Ji, Q. bai Chen, J. sheng Yuan, J. Liu, Y. ying Zhao, W. xian Feng, *Separation and Purification Technology* **2017**, *172*, 168–177.
- [117] X. Du, X. Ma, P. Zhang, J. Zheng, Z. Wang, F. Gao, X. Hao, S. Liu, G. Guan, *Electrochimica Acta* **2017**, *258*, 718–726.
- [118] T. Hoshino, *Desalination* **2013**, *317*, 11–16.
- [119] T. Hoshino, *Fusion Engineering and Design* **2013**, *88*, 2956–2959.
- [120] M. E. Suss, S. Porada, X. Sun, P. M. Biesheuvel, J. Yoon, V. Presser, *Energy and Environmental Science* **2015**, *8*, 2296–2319.
- [121] Y. Oren, *Desalination* **2008**, *228*, 10–29.
- [122] A. Subramani, J. G. Jacangelo, *Water Research* **2015**, *75*, 164–187.
- [123] A. Siekierka, B. Tomaszewska, M. Bryjak, *Desalination* **2018**, *436*, 8–14.
- [124] J. Choi, H. Lee, S. Hong, *Desalination* **2016**, *400*, 38–46.
- [125] J. Pan, Y. Zheng, J. Ding, C. Gao, B. Van Der Bruggen, J. Shen, *Industrial and Engineering Chemistry Research* **2018**, *57*, 7048–7053.
- [126] W. Shi, X. Liu, C. Ye, X. Cao, C. Gao, J. Shen, *Separation and Purification Technology* **2019**, *210*, 885–890.
- [127] C. J. Pedersen, *Journal of the American Chemical Society* **1967**, *89*, 7017–7036.
- [128] D. J. Cram, *Angewandte Chemie International Edition in English* **1988**, *27*, 1009–1020.
- [129] J. W. Steed, J. L. Atwood, *Supramolecular Chemistry*, 3. Aufl., John Wiley & Sons, Ltd, **2022**.

- [130] S. Kubik, *Supramolecular Chemistry: From Concepts to Applications*, 1. Aufl., De Gruyter, **2020**.
- [131] A. V. Kurkov, I. V. Pastukhova, *Journal of Mining Science* **2010**, *46*, 438–445.
- [132] J. Cui, J. E. Kwon, D. R. Whang, S. Y. Park, *Dyes and Pigments* **2021**, *188*, 109223.
- [133] P. H. Hünenberger, J. A. McCammon, *Journal of Chemical Physics* **1999**, *110*, 1856–1872.
- [134] S. T. Ma, *Mathematical Proceedings of the Cambridge Philosophical Society* **1940**, *36*, 441–445.
- [135] X. H. Ding, S. Wang, Y. H. Li, W. Huang, *Inorganic Chemistry Frontiers* **2015**, *2*, 263–272.
- [136] C. H. Yoder, *Journal of Chemical Education* **1977**, *54*, 402–408.
- [137] C. E. Housecroft, H. D. Brooke Jenkins, *RSC Advances* **2017**, *7*, 27881–27894.
- [138] Z. Mu, Q. Shao, J. Ye, Z. Zeng, Y. Zhao, H. H. Hng, F. Y. C. Boey, J. Wu, X. Chen, *Langmuir* **2011**, *27*, 1314–1318.
- [139] C. Fonseca Guerra, F. M. Bickelhaupt, J. G. Snijders, E. J. Baerends, *Journal of the American Chemical Society* **2000**, *122*, 4117–4128.
- [140] R. J. Abraham, M. Mobli, *Magnetic Resonance in Chemistry* **2007**, *45*, 865–877.
- [141] Z. Feng, H. Zuo, W. Gao, N. Ning, M. Tian, L. Zhang, *Macromolecular Rapid Communications* **2018**, *39*, 1–7.
- [142] X. Ji, B. Shi, H. Wang, D. Xia, K. Jie, Z. L. Wu, F. Huang, *Advanced Materials* **2015**, *27*, 8062–8066.
- [143] S. Scheiner, *Structural Chemistry* **2019**, *30*, 1119–1128.
- [144] Y. Hua, A. H. Flood, *Chemical Society Reviews* **2010**, *39*, 1262–1271.
- [145] A. Allerhand, P. R. von Schleyer, *Journal of the American Chemical Society* **1963**, *85*, 1715–1723.
- [146] A. Johansson, P. Kollman, S. Rothenberg, J. McKelvey, *Journal of the American Chemical Society* **1974**, *96*, 3794–3800.
- [147] P. E. Hansen, *Molecules* **2021**, *26*, 2409.
- [148] A. Kovács, Z. Varga, *Coordination Chemistry Reviews* **2006**, *250*, 710–727.
- [149] R. Taylor, O. Kennard, W. Versichel, *J. Am. Chem. Soc.* **1983**, *105*, 5761–5766.

-
- [150] I. Olovsson, *Zeitschrift fur Physikalische Chemie* **2006**, *220*, 963–978.
- [151] J. Šponer, J. Leszczynski, P. Hobza, *Journal of Molecular Structure: THEOCHEM* **2001**, *573*, 43–53.
- [152] B. A. Schweitzer, E. T. Kool, *J. Am. Chem Soc.* **1995**, *117*, 1863–1872.
- [153] L. J. Karas, C. H. Wu, R. Das, J. I. Wu, *Wiley Interdisciplinary Reviews: Computational Molecular Science* **2020**, *10*, 1–15.
- [154] S. C. van der Lubbe, C. Fonseca Guerra, *Chemistry - An Asian Journal* **2019**, *14*, 2760–2769.
- [155] C. Alvares-Rua, S. García-Granda, S. Goswami, R. Mukherjee, S. Dey, R. M. Claramunt, M. D. Santa María, I. Rozas, N. Jagerovic, I. Alkorta, J. Elguero, *New Journal of Chemistry* **2004**, *28*, 700–707.
- [156] P. Politzer, P. Lane, M. C. Concha, Y. Ma, J. S. Murray, *Journal of Molecular Modeling* **2007**, *13*, 305–311.
- [157] T. Clark, M. Hennemann, J. S. Murray, P. Politzer, *Journal of Molecular Modeling* **2007**, *13*, 291–296.
- [158] J. D. Mottishaw, A. R. Erck, J. H. Kramer, H. Sun, M. Koppang, *Journal of Chemical Education* **2015**, *92*, 1846–1852.
- [159] W. Lu, W. Qiu, J. Kim, O. Okobiah, J. Hu, G. W. Gokel, D. Zhong, *Chemical Physics Letters* **2004**, *394*, 415–422.
- [160] S. E. Wheeler, K. N. Houk, *Journal of Chemical Theory and Computation* **2009**, *5*, 2301–2312.
- [161] C. A. Hunter, C. M. Low, C. Rotger, J. G. Vinter, C. Zonta, *Proceedings of the National Academy of Sciences of the United States of America* **2002**, *99*, 4873–4876.
- [162] B. L. Schottel, H. T. Chifotides, K. R. Dunbar, *Chemical Society Reviews* **2008**, *37*, 68–83.
- [163] P. Politzer, J. S. Murray, T. Clark, *Physical Chemistry Chemical Physics* **2013**, *15*, 11178–11189.
- [164] M. Erdélyi, *Chemical Society Reviews* **2012**, *41*, 3547–3557.
- [165] *Phys. Chem. Chem. Phys.* **2014**, *16*, 3238–3253.
- [166] D. P. Malenov, S. D. Zarić, *Coordination Chemistry Reviews* **2020**, *419*, 213338.

- [167] Y. Liu, K. Liu, Z. Wang, X. Zhang, *Chemistry - A European Journal* **2011**, *17*, 9930–9935.
- [168] S. Rösel, C. Balestrieri, P. R. Schreiner, *Chemical Science* **2016**, *8*, 405–410.
- [169] A. van der Ham, T. Hansen, G. Lodder, J. D. Codée, T. A. Hamlin, D. V. Filippov, *ChemPhysChem* **2019**, *20*, 2103–2109.
- [170] K. Kobiro, *Coordination Chemistry Reviews* **1996**, *148*, 135–149.
- [171] R. E. C. Torrejos, G. M. Nisola, H. S. Song, L. A. Limjuco, C. P. Lawagon, K. J. Parohinog, S. Koo, J. W. Han, W. J. Chung, *Chemical Engineering Journal* **2017**, *326*, 921–933.
- [172] R. G. Parr, R. G. Pearson, *Journal of the American Chemical Society* **1983**, *105*, 7512–7516.
- [173] Y. Inoue, T. Hakushi, Y. Liu, L. H. Tong, *Journal of Organic Chemistry* **1993**, *58*, 5411–5413.
- [174] I. Oral, V. Abetz, *Soft Matter* **2022**, *18*, 934–937.
- [175] Y. Tian, W. Chen, Z. Zhao, L. Xu, B. Tong, *Journal of Molecular Modeling* **2020**, *26*, 1–12.
- [176] T. Maeda, *Talanta* **1979**, *26*, 945–949.
- [177] C. Jiang, D. W. Armstrong, *Electrophoresis* **2010**, *31*, 17–27.
- [178] H. P. Meissner, C. L. Kusik, J. W. Tester, *AIChE Journal* **1972**, *18*, 661–662.
- [179] C. Davies, *Journal of the Chemical Society (Resumed)* **1938**, *122*, 2093–2098.
- [180] J. M. Young, A. Z. Panagiotopoulos, *Journal of Physical Chemistry B* **2018**, *122*, 3330–3338.
- [181] T. Solomon, *Journal of Chemical Education* **2001**, *78*, 1691.
- [182] S. Alipour, A. T. Rezakhani, A. Chenu, A. del Campo, T. Ala-Nissila **2019**, *040201*, 1–6.
- [183] P. Atkins, J. de Paula, *Kurzlehrbuch Physikalische Chemie*, 5. Aufl., John Wiley and Sons Ltd, Weinheim, **2019**.
- [184] Y. Li, P. Huszthy, I. Móczár, B. Szemenyei, S. Kunsági-Máté, *Chemical Physics Letters* **2013**, *556*, 94–97.
- [185] S. Chen, H. Yuan, N. Grinberg, A. Dovletoglou, G. Bicker, *Journal of Liquid Chromatography and Related Technologies* **2003**, *26*, 425–442.

-
- [186] J. G. Brandenburg, M. Hochheim, T. Bredow, S. Grimme, *Journal of Physical Chemistry Letters* **2014**, *5*, 4275–4284.
- [187] A. Ambrosetti, D. Alfè, R. A. Distasio, A. Tkatchenko, *Journal of Physical Chemistry Letters* **2014**, *5*, 849–855.
- [188] S. Grimme, *Chemistry - A European Journal* **2012**, *18*, 9955–9964.
- [189] E. I. Izgorodina, Z. L. Seeger, D. L. Scarborough, S. Y. Tan, *Chemical Reviews* **2017**, *117*, 6696–6754.
- [190] D. Van Der Spoel, M. M. Ghahremanpour, J. A. Lemkul, *Journal of Physical Chemistry A* **2018**, *122*, 8982–8988.
- [191] T. M. Simeon, M. A. Ratner, G. C. Schatz, *Journal of Physical Chemistry A* **2013**, *117*, 7918–7927.
- [192] G. Odriozola, M. Lozada-Cassou, *Physical Review Letters* **2013**, *110*, 1–5.
- [193] K. S. Diao, H. J. Wang, Z. M. Qiu, *Journal of Molecular Structure: THEOCHEM* **2009**, *901*, 157–162.
- [194] A. Boda, S. Musharaf Ali, H. Rao, S. K. Ghosh, *Journal of Molecular Modeling* **2012**, *18*, 3507–3522.
- [195] S. Roy, K. Thirumoorthy, U. K. Padidela, P. Vairaprakash, A. Anoop, V. S. Thimmakondur, *ChemistrySelect* **2021**, *6*, 8782–8790.
- [196] . Web of Science, *Web of Science* **2022**, www.webofscience.com (accessed: 10.08.2022).
- [197] M. P. Teter, M. C. Payne, D. C. Allan, *Physical Review B* **1989**, *40*, 12255–12263.
- [198] Y. Saad, J. R. Chelikowsky, S. M. Shontz, *SIAM Review* **2010**, *52*, 3–54.
- [199] T. E. Simos, P. S. Williams, *Journal of Computational and Applied Mathematics* **1997**, *79*, 189–205.
- [200] A. Soriano, E. A. Navarro, J. A. Portí, V. Such, *Journal of Applied Physics* **2004**, *95*, 8011–8018.
- [201] P. R. C. Kent, *Dissertation* **1999**, *Techniques and Applications of Quantum Monte Carlo*, University of Cambridge.
- [202] N. Argaman, G. Makov, *American Journal of Physics* **2000**, *68*, 69–79.
- [203] A. Görling, *Physical Review A - Atomic, Molecular, and Optical Physics* **1999**, *59*, 3359–3374.
- [204] L. J. Sham, *Physics Today* **1982**, *35*, 36–43.

- [205] M. C. H. W. Koch, *A Chemist's Guide to Density Functional Theory*, 2. Aufl., Wiley-VCH, Weinheim, **2001**.
- [206] A. D. Becke, *Journal of Chemical Physics* **2014**, *140*, 18A301.
- [207] W. Kohn, L. J. Sham, *Phys. Rev.* **1965**, *140*, A1133–A1138.
- [208] K. Burke, *Journal of Chemical Physics* **2012**, *136*, 150901.
- [209] D. Avci, S. Bahçeli, O. Tamer, Y. Atalay, *Canadian Journal of Chemistry* **2015**, *93*, 1147–1156.
- [210] A. D. Becke, *Phys. Rev. A* **1988**, *38*, 3098–3100.
- [211] S. Grimme, *Journal of Chemical Physics* **2006**, *124*, 034108.
- [212] S. Goedecker, W. Hellmann, T. Lenosky, *Physical Review Letters* **2005**, *95*, 1–4.
- [213] H. B. Schlegel, *Wiley Interdisciplinary Reviews: Computational Molecular Science* **2011**, *1*, 790–809.
- [214] J. U. Reveles, A. M. Köster, *Journal of Computational Chemistry* **2004**, *25*, 1109–1116.
- [215] R. Kunz, *Molecular Modelling für Anwender*, 2. Aufl., Teubner Studienbücher, Stuttgart, **1997**.
- [216] J. Reinhold, *Quantentheorie der Moleküle*, 5. Aufl., Springer Spektrum, Wiesbaden, **2013**.
- [217] F. L. Hirshfeld, *Theoret. Claim. Acta* **1977**, *44*, 129–138.
- [218] T. Lu, F. Chen, *Journal of Computational Chemistry* **2012**, *33*, 580–592.
- [219] E. R. Raupach, *Dissertation 2015, Quantenchemische Untersuchungen zur chemischen Bindung an Oberflächen - Entwicklung und Anwendung einer Energie-Dekompositions Methode*, Philipps-Universität Marburg.
- [220] S. X. Hu, J. J. Liu, J. K. Gibson, J. Li, *Inorganic Chemistry* **2018**, *57*, 2899–2997.
- [221] P. O. Löwdin, *Physical Review* **1955**, *97*, 1474–1489.
- [222] F. Weinhold, C. R. Landis, *Chem. Educ. Res. Pract.* **2001**, *2*, 91–104.
- [223] R. Behjatmanesh-Ardakani, F. Pourroustaei-Ardakani, M. Taghdiri, Z. M. Kotena, *Journal of Molecular Modeling* **2016**, *22*, 1–11.
- [224] A. E. Reed, L. A. Curtiss, F. Weinhold, *Chem. Rev.* **1988**, *88*, 899–926.
- [225] E. Cancès, B. Mennucci, J. Tomasi, *Journal of Chemical Physics* **1997**, *107*, 3032–3041.

-
- [226] B. Mennucci, E. Cancès, J. Tomasi, *Journal of Physical Chemistry B* **1997**, *101*, 10506–10517.
- [227] B. Mennucci, *Wiley Interdisciplinary Reviews: Computational Molecular Science* **2012**, *2*, 386–404.
- [228] J. Tomasi, B. Mennucci, R. Cammi, *Chemical Reviews* **2005**, *105*, 2999–3093.
- [229] B. Mennucci, J. Tomasi, R. Cammi, J. R. Cheeseman, M. J. Frisch, F. J. Devlin, S. Gabriel, P. J. Stephens, *Journal of Physical Chemistry A* **2002**, *106*, 6102–6113.
- [230] T. P. Lodge, P. C. Hiemenz, *Polymer Chemistry*, 3. Aufl., Taylor & Francis Group, Boca Raton, **2020**.
- [231] M. Lechner, K. Gehrke, E. Nordmeier, *Makromolekulare Chemie*, 6. Aufl., Springer Spektrum, Berlin, Heidelberg, **2020**.
- [232] S. Koltzenburg, M. Maskos, O. Nuyken, *Polymere - Synthese, Eigenschaften und Anwendungen*, 2. Aufl., Springer Spektrum, Berlin, Heidelberg, **2014**.
- [233] D. Baskaran, A. H. Müller, *Progress in Polymer Science* **2007**, *32*, 173–219.
- [234] A. Hirao, S. Loykulnant, T. Ishizone, *Progress in Polymer Science* **2002**, *27*, 1399–1471.
- [235] J. Smid, M. Van Beylen, T. E. Hogen-Esch, *Progress in Polymer Science* **2006**, *31*, 1041–1067.
- [236] W. A. Braunecker, K. Matyjaszewski, *Progress in Polymer Science* **2007**, *32*, 93–146.
- [237] K. Parkatzidis, H. S. Wang, N. P. Truong, A. Anastasaki, *Chem* **2020**, *6*, 1575–1588.
- [238] C. L. Moad, G. Moad **2021**, *3*, 3–17.
- [239] G. Moad, E. Rizzardo, S. H. Thang, *Australian Journal of Chemistry* **2009**, *62*, 1402–1472.
- [240] S. Perrier, *Macromolecules* **2017**, *50*, 7433–7447.
- [241] A. B. Lowe, C. L. McCormick, *Progress in Polymer Science (Oxford)* **2007**, *32*, 283–351.
- [242] G. Moad, E. Rizzardo, S. H. Thang, *Chemistry - An Asian Journal* **2013**, *8*, 1634–1644.
- [243] S. Matsumura, A. R. Hlil, C. Lepiller, J. Gaudet, D. Guay, Z. Shi, S. Holdcroft, A. S. Hay, *Journal of Polymer Science: Part A: Polymer Chemistry* **2008**, *46*, 7207–7224.
- [244] D. J. Keddie, G. Moad, E. Rizzardo, S. H. Thang, *Macromolecules* **2012**, *45*, 5321–5342.

- [245] J. M. Asua, *Journal of Polymer Science, Part A: Polymer Chemistry* **2004**, *42*, 1025–1041.
- [246] S. C. Thickett, R. G. Gilbert, *Polymer* **2007**, *48*, 6965–6991.
- [247] J. T. O’toole, *Journal of Applied Polymer Science* **1965**, *9*, 1291–1297.
- [248] R. G. Gilbert, S. W. Prescott, W. Smulders, M. J. Monteiro, M. J. Ballard, E. Rizzardo, *American Chemical Society, Polymer Preprints, Division of Polymer Chemistry* **2002**, *43*, 130–131.
- [249] J. Zhou, H. Yao, J. Ma, *Polymer Chemistry* **2018**, *9*, 2532–2561.
- [250] J. Rieger, *Macromolecular Rapid Communications* **2015**, *36*, 1458–1471.
- [251] M. J. Derry, L. A. Fielding, S. P. Armes, *Progress in Polymer Science* **2016**, *52*, 1–18.
- [252] E. Sprong, J. S. Leswin, D. J. Lamb, C. J. Ferguson, B. S. Hawkett, B. T. Pham, D. Nguyen, C. H. Such, A. K. Serelis, R. G. Gilbert, *Macromolecular Symposia* **2005**, *231*, 84–93.
- [253] S. A. Biller, C. Forster, E. M. Gordon, T. Harrity, W. A. Scott, C. P. Ciosek, *Journal of Medicinal Chemistry* **1988**, *31*, 1869–1871.
- [254] N. M. Ahmad, B. Charleux, C. Farcet, C. J. Ferguson, S. G. Gaynor, B. S. Hawkett, F. Heatley, B. Klumperman, D. Konkolewicz, P. A. Lovell, K. Matyjaszewski, R. Venkatesh, *Macromolecular Rapid Communications* **2009**, *30*, 2002–2021.
- [255] N. J. Warren, S. P. Armes, *Journal of the American Chemical Society* **2014**, *136*, 10174–10185.
- [256] I. Chaduc, M. Girod, R. Antoine, B. Charleux, F. D’Agosto, M. Lansalot, *Macromolecules* **2012**, *45*, 5881–5893.
- [257] W. Zhang, F. D’Agosto, O. Boyron, J. Rieger, B. Charleux, *Macromolecules* **2011**, *44*, 7584–7593.
- [258] W. Zhang, F. D’Agosto, P. Y. Dugas, J. Rieger, B. Charleux, *Polymer* **2013**, *54*, 2011–2019.
- [259] M. A. Gauthier, M. I. Gibson, H. A. Klok, *Angewandte Chemie - International Edition* **2009**, *48*, 48–58.
- [260] K. A. Günay, P. Theato, H. A. Klok, *Journal of Polymer Science, Part A: Polymer Chemistry* **2013**, *51*, 1–28.
- [261] B. Neises, W. Steglich, *Angewandte Chemie International Edition in English* **1978**, *17*, 522–524.

-
- [262] A. Jordan, K. D. Whymark, J. Sydenham, H. F. Sneddon, *Green Chemistry* **2021**, *23*, 6405–6413.
- [263] M. Tambasco, J. E. Lipson, J. S. Higgins, *Macromolecules* **2006**, *39*, 4860–4868.
- [264] P. Blend, F.-h.-s. Analysist, *Macromolecules* **1993**, *26*, 1603–1608.
- [265] Z. Zhang, *Dissertation* **2020**, *Isoporous Block Copolymer Membranes with Charged Nanochannels*, Universität Hamburg.
- [266] M. D. Whitmore, J. D. Vavasour, *Acta Polymerica* **1995**, *46*, 341–360.
- [267] A. J. Meuler, M. A. Hillmyer, F. S. Bates, *Macromolecules* **2009**, *42*, 7221–7250.
- [268] N. Hadjichristidis, S. Pispas, G. Floudas, *Block Copolymers: Synthetic Strategies, Physical Properties, and Applications*, John Wiley and Sons Ltd, New Jersey, **2003**.
- [269] P. Medapuram, J. Glaser, D. C. Morse, *Macromolecules* **2015**, *48*, 819–839.
- [270] C. Sinturel, F. S. Bates, M. A. Hillmyer, *ACS Macro Letters* **2015**, *4*, 1044–1050.
- [271] J. M. Swann, P. D. Topham, *Polymers* **2010**, *2*, 454–469.
- [272] M. W. Matsen, *European Physical Journal E* **2010**, *33*, 297–306.
- [273] M. W. Matsen, F. S. Bates, *Macromolecules* **1996**, *29*, 1091–1098.
- [274] S.-m. Mai, J. P. A. Fairclough, I. W. Hamley, M. W. Matsen, R. C. Denny, B.-x. Liao, C. Booth, A. J. Ryan, *Macromolecules* **1996**, *9297*, 6212–6221.
- [275] T. Hosoda, S. P. Gido, J. W. Mays, T. Huang, C. R. Park, T. Yamada, *Journal of Polymer Engineering* **2013**, *33*, 49–59.
- [276] I. Rychkov, *Macromolecular Theory and Simulations* **2005**, *14*, 207–242.
- [277] M. W. Matsen, *European Physical Journal E* **2009**, *30*, 361–369.
- [278] A. N. Semenov, *Zh. Eksp. Teor. Fiz* **1985**, *88*, 1242–1256.
- [279] V. Abetz, P. F. W. Simon, *Phase Behaviour and Morphologies of Block Copolymers*, S. 125–212, Springer Berlin Heidelberg, Berlin, Heidelberg, **2005**.
- [280] N. Hadjichristidis, H. Iatrou, M. Pitsikalis, S. Pispas, A. Avgeropoulos, *Progress in Polymer Science* **2005**, *30*, 725–782.
- [281] A. Barton, *Handbook of Solubility Parameters and other Cohesion Parameters*, 2. Aufl., CRC Press, Boca Raton, **1991**.
- [282] W. Zeng, Y. Du, Y. Xue, H. Frisch, *Physical Properties of Polymers Handbook*, 2. Aufl., Springer New York, New York, **2007**.

- [283] D. Van Kreverlen, K. Te Nijenhuis, *Properties of Polymers*, 4. Aufl., Elsevier, Amsterdam/Oxford, **2009**.
- [284] R. Cartwright, *Perspectives in Public Health* **2010**, *130*, 239–239.
- [285] C. Hansen, *Hansen solubility parameters - A User's Handbook*, 2. Aufl., CRC Press, Boca Raton, **2007**.
- [286] G. Scatchard, *Chemical Reviews* **1948**, *44*, 7–35.
- [287] J. Bandrup, E. H. Immergut, E. A. Grulke, *Polymer Handbook*, 4. Aufl., John Wiley and Sons Ltd, New York, Chichester, Weinheim, Singapore, Toronto, **1999**.
- [288] *Journal of applied chemistry* **2019**, *3*, 71–80.
- [289] K. L. Hoy, *Journal of Coated Fabrics* **1989**, *19*, 53–67.
- [290] E. Stefanis, C. Panayiotou, *International Journal of Thermophysics* **2008**, *29*, 568–585.
- [291] C.M. Hansen, *The Three Dimensional Solubility Parameter and Solvent Diffusion Coefficient. Their Importance in Surface Coating Formulation*, Danish Technical Press, **1967**.
- [292] J. Durkee, *Cleaning with Solvents: Science and Technology*, 1. Aufl., Elsevier, **2013**.
- [293] M. Rubenstein, R. H. Colby, *Polymer Physics*, Oxford University Press, Oxford, **2003**.
- [294] T. Lindvig, M. L. Michelsen, G. M. Kontogeorgis, *Fluid Phase Equilibria* **2002**, *203*, 247–260.
- [295] J. A. Emerson, D. T. Toolan, J. R. Howse, E. M. Furst, T. H. Epps, *Macromolecules* **2013**, *46*, 6533–6540.
- [296] W. Yave, A. Car, J. Wind, K. V. Peinemann, *Nanotechnology* **2010**, *21*, 395301.
- [297] R. S. Murali, T. Sankarshana, S. Sridhar, *Separation and Purification Reviews* **2013**, *42*, 130–186.
- [298] H. Yang, P. Jiang, *Langmuir* **2010**, *26*, 13173–13182.
- [299] R. Fu, Y. Yang, C. Lu, Y. Ming, X. Zhao, Y. Hu, L. Zhao, J. Hao, W. Chen, *ACS Omega* **2018**, *3*, 9146–9154.
- [300] M. C. Sparenberg, S. Chergaoui, V. Sang Sefidi, P. Luis, *Desalination* **2022**, *519*, 115315.
- [301] A. J. Jose, J. Kappen, M. Alagar, *Polymeric membranes: Classification, preparation, structure physiochemical, and transport mechanisms*, Woodhead Publishing, **2018**.

-
- [302] A. Peterlin, *Colloid & Polymer Science* **1985**, *263*, 35–41.
- [303] C. H. Lee, *Journal of Applied Polymer Science* **1975**, *19*, 83–95.
- [304] M. R. Kiani, M. Meshksar, M. A. Makarem, E. Rahimpour, *Topics in Catalysis* **2021**.
- [305] C. K. Chiam, R. Sarbatly, *Separation and Purification Reviews* **2011**, *40*, 126–160.
- [306] M. Issaoui, L. Limousy, *Comptes Rendus Chimie* **2019**, *22*, 175–187.
- [307] B. Stefan, B. Marius, B. Lidia, *Tehnomus*, 227–232.
- [308] P. K. S. Mural, G. Madras, S. Bose, *Nano-Structures and Nano-Objects* **2018**, *14*, 149–165.
- [309] S. S. Ozdemir, M. G. Buonomenna, E. Drioli, *Applied Catalysis A: General* **2006**, *307*, 167–183.
- [310] N. Hampu, J. R. Werber, W. Y. Chan, E. C. Feinberg, M. A. Hillmyer, *ACS Nano* **2020**, *14*, 16446–16471.
- [311] H. Strathmann, K. Kock, P. Amar, R. Baker, *Desalination* **1975**, *16*, 179–203.
- [312] A. Mixa, C. Staudt, *International Journal of Chemical Engineering* **2008**, *2008*, 1–12.
- [313] E. T. Igunnu, G. Z. Chen, *International Journal of Low-Carbon Technologies* **2014**, *9*, 157–177.
- [314] M. Mulder, *Preparation of Synthetic Membranes*, Springer Netherlands, Dordrecht, **1996**.
- [315] M. Radjabian, V. Abetz, *Progress in Polymer Science* **2020**, *102*, 101219.
- [316] J. Huang, X. Wang, X. Chen, X. Yu, *Journal of Applied Polymer Science* **2003**, *89*, 3180–3187.
- [317] Z. Qiao, Z. Wang, C. Zhang, S. Yuan, Y. Zhu, J. Wang, *AIChE Journal* **2012**, *59*, 215–228.
- [318] A. W. Mohammad, C. Y. Ng, Y. P. Lim, G. H. Ng, *Food and Bioprocess Technology* **2012**, *5*, 1143–1156.
- [319] H. Choi, K. Zhang, D. D. Dionysiou, D. B. Oerther, G. A. Sorial, *Separation and Purification Technology* **2005**, *45*, 68–78.
- [320] W. Sun, J. Liu, H. Chu, B. Dong, *Membranes* **2013**, *3*, 226–241.
- [321] H. Ma, C. N. Bowman, R. H. Davis, *Journal of Membrane Science* **2000**, *173*, 191–200.

- [322] S. Maity, B. Mishra, K. Nayak, N. Dubey, B. Tripathi, *Materials Today Chemistry* **2022**, *24*, 100779.
- [323] N. Wisniewski, M. Reichert, *Colloids and Surfaces B: Biointerfaces* **2000**, *18*, 197–219.
- [324] C. Williams, R. Wakeman, *Membrane Technology* **2000**, *2000*, 4–10.
- [325] Y.-R. Chang, Y.-J. Lee, D.-J. Lee, *Journal of the Taiwan Institute of Chemical Engineers* **2019**, *94*, 88–96.
- [326] A. S. Michaelis, *Macromolecular Chemistry–11: Synthetic Polymer Membranes: Practical Applications—Past, Present and Future*, Pergamon Press, **1977**.
- [327] H. A. Mannan, H. Mukhtar, T. Murugesan, R. Nasir, D. F. Mohshim, A. Mushtaq, *Chemical Engineering and Technology* **2013**, *36*, 1838–1846.
- [328] N. N. Krishnan, D. Henkensmeier, J. H. Jang, H. J. Kim, *Macromolecular Materials and Engineering* **2014**, *299*, 1031–1041.
- [329] K. Bicy, D. Rouxel, M. Poncot, I. Royaud, P. Bourson, D. Chapron, N. Kalarikkal, S. Thomas, *Journal of Applied Polymer Science* **2021**, *138*, 1–16.
- [330] N. Hilal, A. F. Ismail, C. J. Wright, *Membrane Fabrication*, Taylor & Francis Group, **2015**.
- [331] B. G. Thiam, A. El Magri, H. R. Vanaei, S. Vaudreuil, *Polymers* **2022**, *14*, 1–16.
- [332] H. Strathmann, K. Kock, *Desalination* **1977**, *21*, 241–255.
- [333] H. H. Wang, J. T. Jung, J. F. Kim, S. Kim, E. Drioli, Y. M. Lee, *Journal of Membrane Science* **2019**, *574*, 44–54.
- [334] V. Abetz, *Macromolecular Rapid Communications* **2015**, *36*, 10–22.
- [335] X. Dong, D. Lu, T. A. Harris, I. C. Escobar, *Membranes* **2021**, *11*, 309.
- [336] S. P. Nunes, *Macromolecules* **2016**, *49*, 2905–2916.
- [337] C. ying Yang, G. dong Zhu, Z. Yi, Y. Zhou, C. jie Gao, *Chemical Engineering Journal* **2021**, *424*, 128912.
- [338] Y. Katayama, K. Nita, M. Ueda, H. Nakamura, M. Takagi, K. Ueno, *Analytica Chimica Acta* **1985**, *173*, 193–209.
- [339] K. Sambe, N. Hoshino, T. Takeda, T. Nakamura, T. Akutagawa, *Journal of Physical Chemistry C* **2020**, *124*, 13560–13571.
- [340] K. Kimura, S. Kanokogi, M. Yokoyama, *Analytical Sciences* **1996**, *12*, 399–403.

-
- [341] K. E. Krakowiak, J. S. Bradshaw, D. J. Z. A.-k. A. Iak, C. A. Diols, *Chem. Rev.* **1989**, *89*, 929–972.
- [342] A. Warshawsky, N. Kahana, *Journal of the American Chemical Society* **1982**, *104*, 2663–2664.
- [343] R. Behjatmanesh-Ardakani, *Computational and Theoretical Chemistry* **2015**, *1051*, 62–71.
- [344] M. M. Coleman, C. J. Serman, D. E. Bhagwagar, P. C. Painter, *Polymer* **1990**, *31*, 1187–1203.
- [345] P. Peng, B. Shi, L. Jia, B. Li, *Journal of Macromolecular Science, Part B: Physics* **2010**, *49*, 864–869.
- [346] D. Mathieu, *ACS Omega* **2018**, *3*, 17049–17056.
- [347] G. Biresaw, C. J. Carriere, *Journal of Polymer Science, Part B: Polymer Physics* **2002**, *40*, 2248–2258.
- [348] C. Özdemir, A. Güner, *European Polymer Journal* **2007**, *43*, 3068–3093.
- [349] G. Ovejero, P. Pérez, M. D. Romero, I. Guzmán, E. Díez, *European Polymer Journal* **2007**, *43*, 1444–1449.
- [350] R. M. Dorin, D. S. Marques, H. Sai, U. Vainio, W. A. Phillip, K. V. Peinemann, S. P. Nunes, U. Wiesner, *ACS Macro Letters* **2012**, *1*, 614–617.
- [351] Z. Zhang, M. M. Rahman, C. Abetz, V. Abetz, *Journal of Materials Chemistry A* **2020**, *8*, 9554–9566.
- [352] M. Radjabian, C. Abetz, B. Fischer, A. Meyer, V. Abetz, *ACS Applied Materials and Interfaces* **2017**, *9*, 31224–31234.
- [353] K. Foroutani, S. M. Ghasemi, B. Pourabbas, *Journal of Membrane Science* **2021**, *623*, 119099.
- [354] J. I. Clodt, B. Bajer, K. Buhr, J. Hahn, V. Filiz, V. Abetz, *Journal of Membrane Science* **2015**, *495*, 334–340.
- [355] S. Rangou, K. Buhr, V. Filiz, J. I. Clodt, B. Lademann, J. Hahn, A. Jung, V. Abetz, *Journal of Membrane Science* **2014**, *451*, 266–275.
- [356] J. Cheng, M. Xu, P. Cheng, W. Zhang, N. Li, Y. Wang, J. Yang, K. Liang, P. Li, H. Yu, X. Qiu, *Journal of Membrane Science* **2019**, *587*, 117086.
- [357] T. Ahmad, C. Guria, S. Shekhar, *Materials Chemistry and Physics* **2022**, *280*, 125805.

- [358] B. P. Czech, D. A. Babb, B. Son, R. A. Bartsch, *Journal of Organic Chemistry* **1984**, *49*, 4805–4810.

9.1 Authors contributions to the publications

1.) Thermodynamic Study of Crown Ether-Lithium/Magnesium Complexes based on Benz-1,4-Dioxane and its Homologues

Iklima Oral, Fanny Ott, and Volker Abetz

Phys. Chem. Chem. Phys. **2022**, *24*, 11687-11695.

doi.org/10.1039/D2CP01076C

I.O. and V.A. designed the project, I.O. and Fanny Ott (F.O.) performed, examined, and evaluated the analytical data. V.A. supervised the project and provided the resources. I. O wrote the original draft. I.O. and V. A. reviewed and edited the original draft. All authors have read and agreed to the published version of the manuscript.

2.) Lithium Selectivity of Crown Ethers: The Effect of Heteroatoms and Cavity Size

Iklima Oral,* Sabrina Tamm,* Carmen Herrmann and Volker Abetz

*: both authors contributed equally to this project

Separation and Purification Technology **2022**, *294*, 121142.

doi.org/10.1016/j.seppur.2022.121142

All authors conceived the experiments and calculations. I.O. and Sabrina Tamm (S.T.) designed and performed all experiments and calculations and wrote the paper, with support by V.A. and Carmen Herrmann (C.H.) in writing the paper. This work was supported by the Cluster of Excellence *CUI: Advanced Imaging of Matter* of the Deutsche Forschungsgemeinschaft (DFG) - EXC 2056 - project ID 390715994. All authors analyzed the data.

3.) Synthesis of Poly(methacrylic acid)-*block*-Polystyrene Diblock Copolymers at High Solid Contents via RAFT Emulsion Polymerization

Iklima Oral, Larissa Grossmann, Elena Fedorenko, Jana Struck, and Volker Abetz

Polymers **2021**, *13*, 3675.

doi.org/10.3390/polym13213675

I.O. conceived and designed all experiments. Larissa Grossmann (L.G.) performed the PMAA polymerizations with CTA 1 and CTA 2. Elena Fedorenko (E.F.) performed the PMAA₅-b-PS₉₅⁵⁴ polymerizations with CTA 1. Jana Struck (J.S.) performed the polymerizations of PMAA₁₀-b-PS₉₀⁴⁵ at 20, 25 and 30 wt% with CTA 1. All other experiments were performed by I.O. I.O. and V.A. analyzed the data and wrote the paper. All authors have read and agreed to the published version of the manuscript.

4.) A Highly Selective Polymer Material using Benzo-9-crown-3 for the Extraction of Lithium in Presence of Other Interfering Alkali Metal Ions.

Iklima Oral and Volker Abetz

Macromol. Rapid Commun. **2021**, *42*, 2000746.

doi.org/10.1002/marc.202000746

Iklima Oral (I.O.) and Volker Abetz (V.A.) conceived the experiments, analyzed the data and wrote the manuscript. I.O. designed and performed all experiments.

5.) Improved Alkali Metal Ion Capturing utilizing Crown Ether-based Diblock Copolymers in a Sandwich-type Complexation

Iklima Oral and Volker Abetz

Soft Matter **2022**, *18*, 934.

doi.org/10.1039/d1sm01815a

I.O. and V. A. conceived the experiments, analyzed the data and wrote the manuscript. I. O. designed and performed all experiments.

9.2 Supporting information of publication 1

The supporting information is reprinted with permission from I. Oral, F. Ott and V. Abetz, *Phys. Chem. Chem. Phys.*, **2022**, *24*, 11687 – published by the Royal Society of Chemistry.

Supporting Information

Thermodynamic Study of Crown Ether–Lithium/Magnesium Complexes based on Benz-1,4-Dioxane and its Homologues

Iklima Oral,^a Fanny Ott,^a and Volker Abetz^{a,b,*}

^a*Institute of Physical Chemistry, Universität Hamburg, Grindelallee 117, 20146 Hamburg,
Germany.*

^b*Helmholtz-Zentrum Hereon, Institute of Membrane Research, Max-Planck-Straße 1, 21502
Geesthacht, Germany. E-mail: volker.abetz@hereon.de*

Benzo-7-crown-2

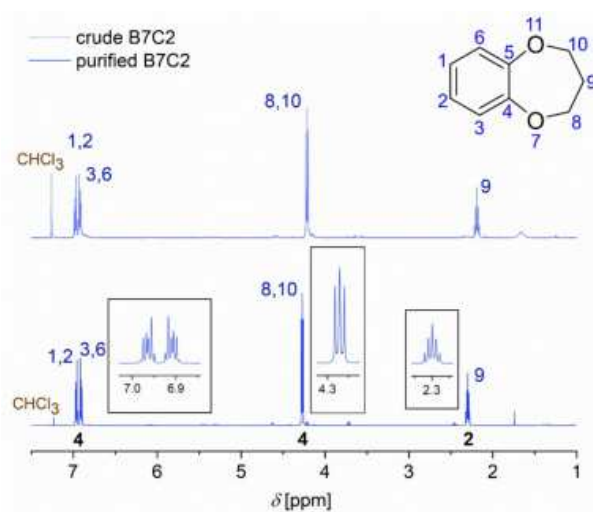


Fig. S1: ¹H NMR spectrum of the crude B7C2 and purified B7C2 after column chromatography treatment.

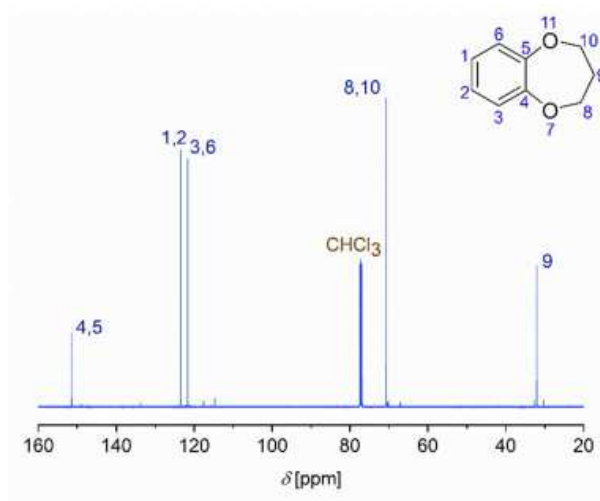


Fig. S2: ¹³C NMR spectrum of the purified B7C2.

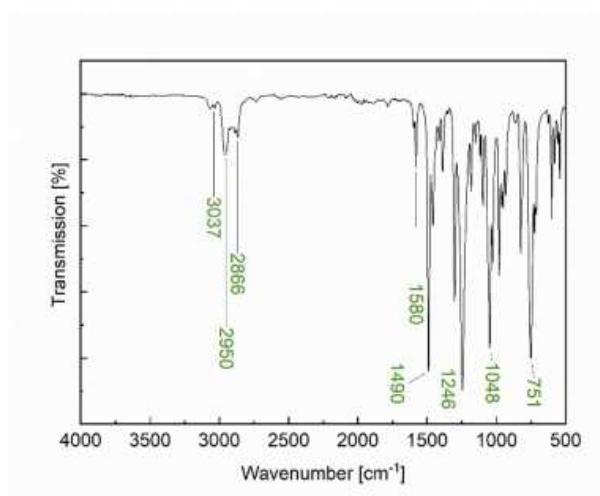


Fig. S3: IR spectrum of the purified B7C2.

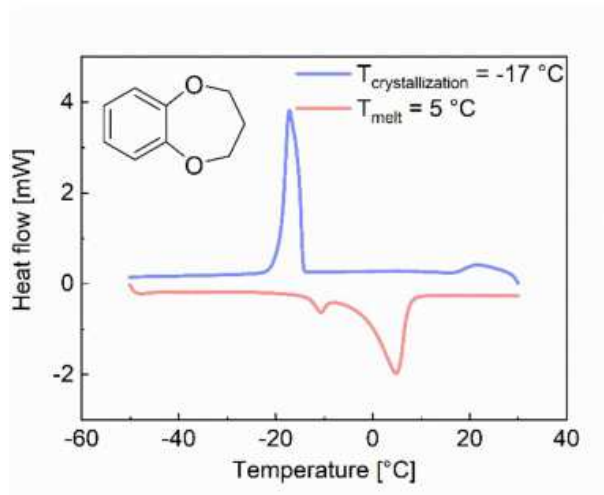


Fig. S4: DSC measurement of the purified B7C2.

Benzo-8-crown-2

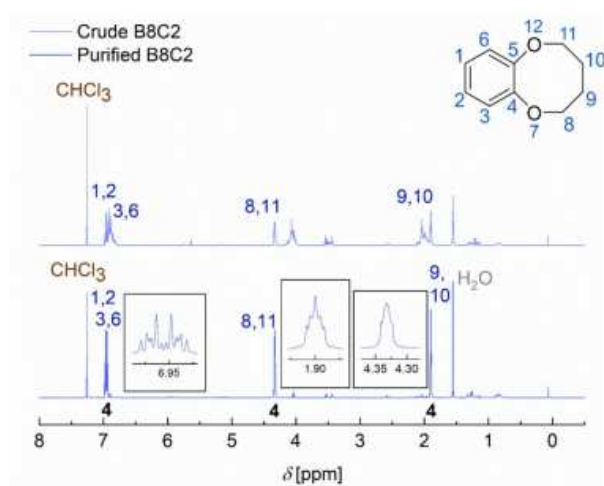


Fig. S5: ^1H NMR spectrum of the crude B8C2 and purified B7C2 after column chromatography treatment.

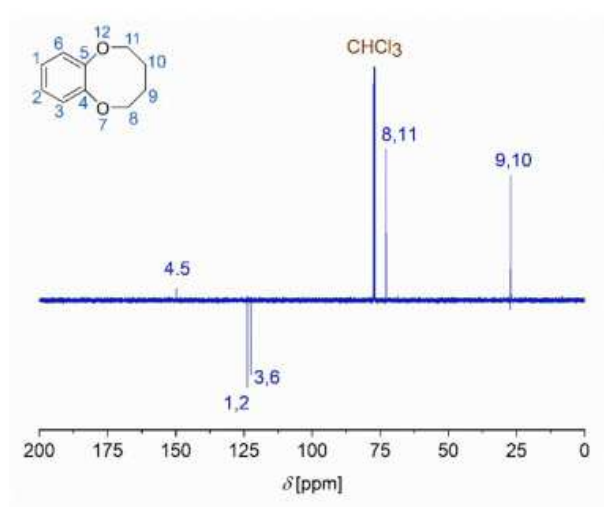


Fig. S6: ^{13}C NMR spectrum of the purified B8C2.

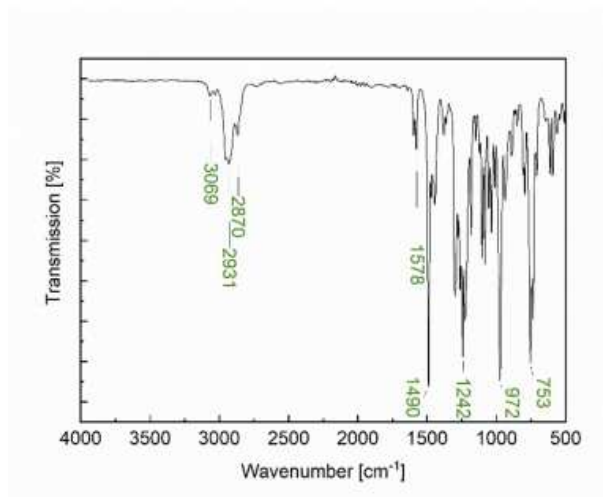


Fig. S7: IR spectrum of the purified B8C2.

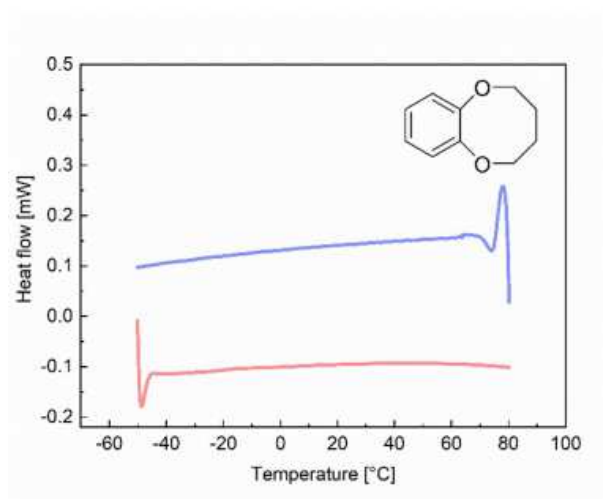


Fig. S8: DSC measurement of the purified B8C2.

UV-vis Data

Lithium

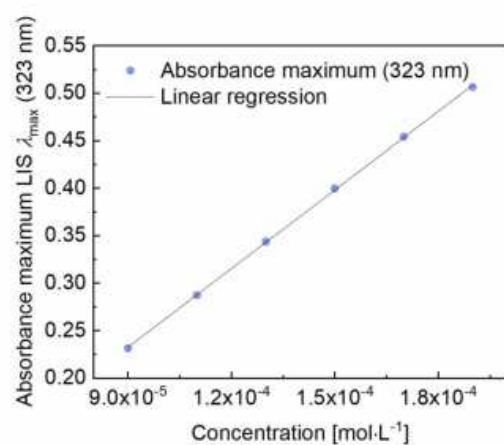


Fig. S9: Absorbance maxima of LIS $\lambda_{\text{max}} = 323$ nm as linear regression against concentration [mol·L⁻¹].

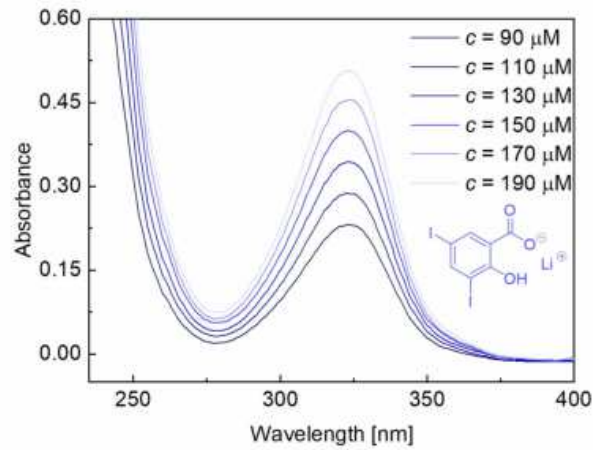


Fig. S10: UV-vis spectrum of LIS at different concentrations [$\mu\text{mol}\cdot\text{L}^{-1}$].

Magnesium

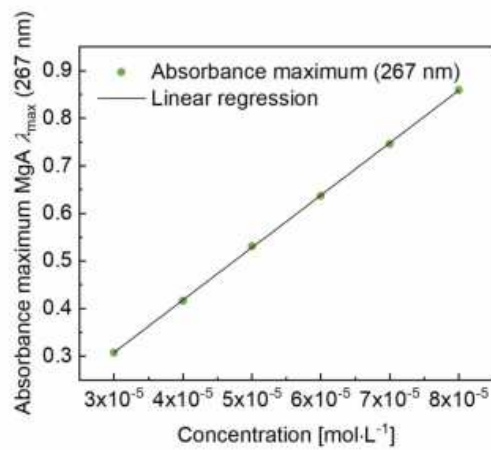


Fig. S11: Absorbance maxima of MgA $\lambda_{\text{max}} = 267 \text{ nm}$ as linear regression against concentration [$\text{mol}\cdot\text{L}^{-1}$].

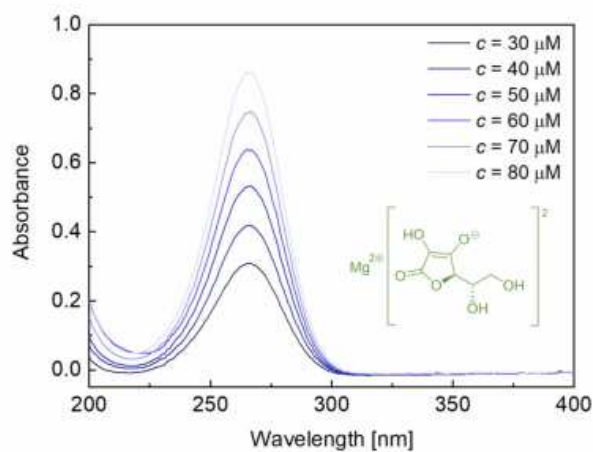


Fig. S12: UV-vis spectrum of MgA at different concentrations [$\mu\text{mol}\cdot\text{L}^{-1}$].

CE solubility measurements in the aqueous phase

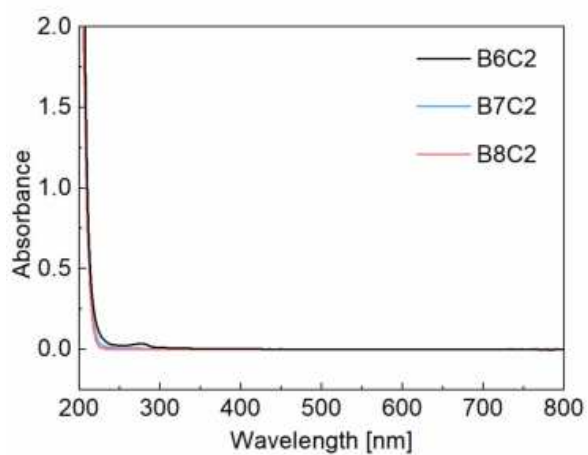


Fig. S13: UV-vis spectroscopy of the aqueous LiCl phase after extraction and formation of the CE-cation complex.

Thermodynamic Evaluation

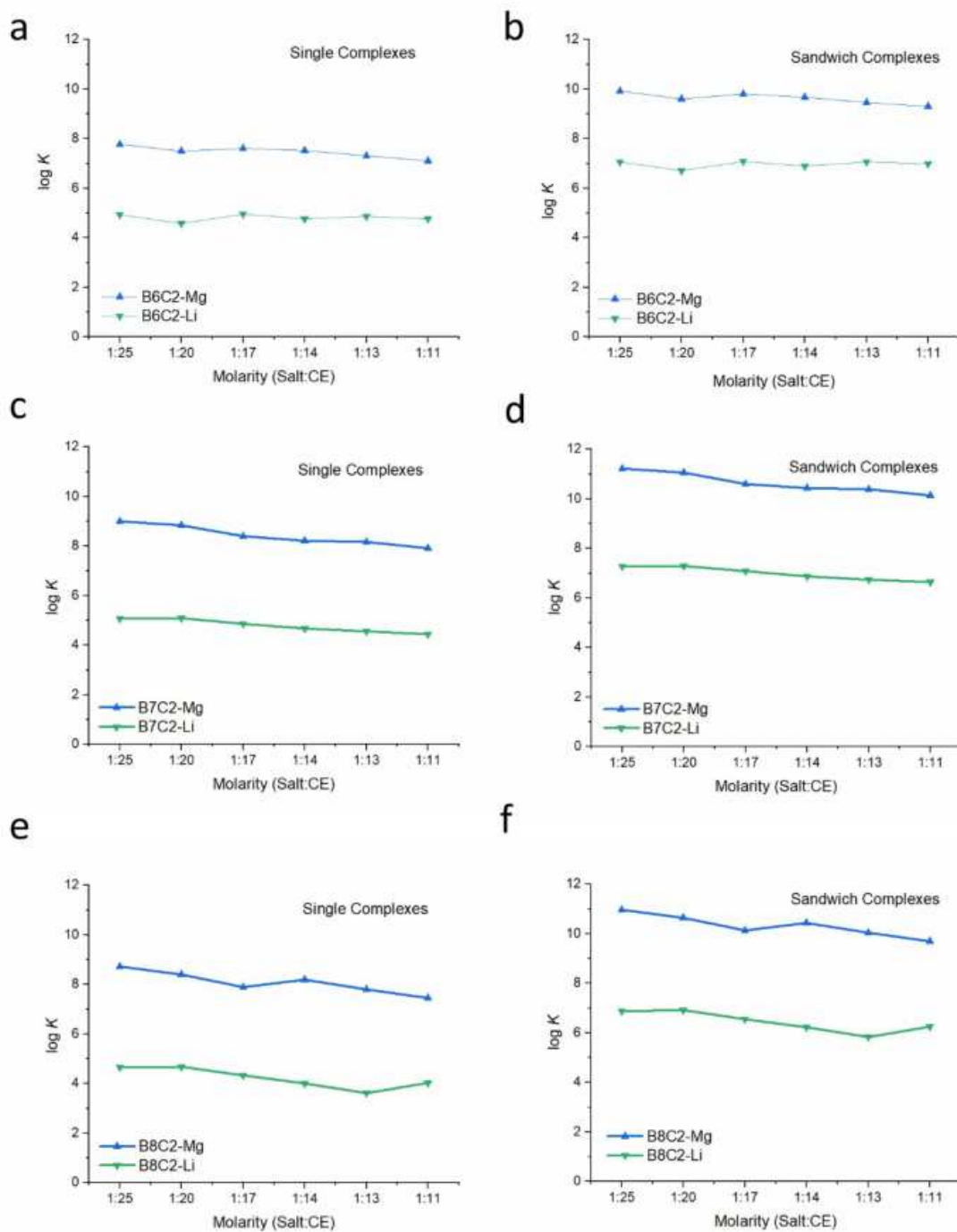


Fig. S14: logarithmic complexation stability K of a) B6C2 assuming single complexes, b) B6C2 assuming sandwich-type complexes, c) B7C2 assuming single complexes, d) B7C2 assuming sandwich-type complexes, e) B8C2 assuming single complexes, f) B8C2 assuming sandwich-type complexes. The green line shows the lithium, and the blue line the magnesium complexes with the CEs.

Van't Hoff Plot

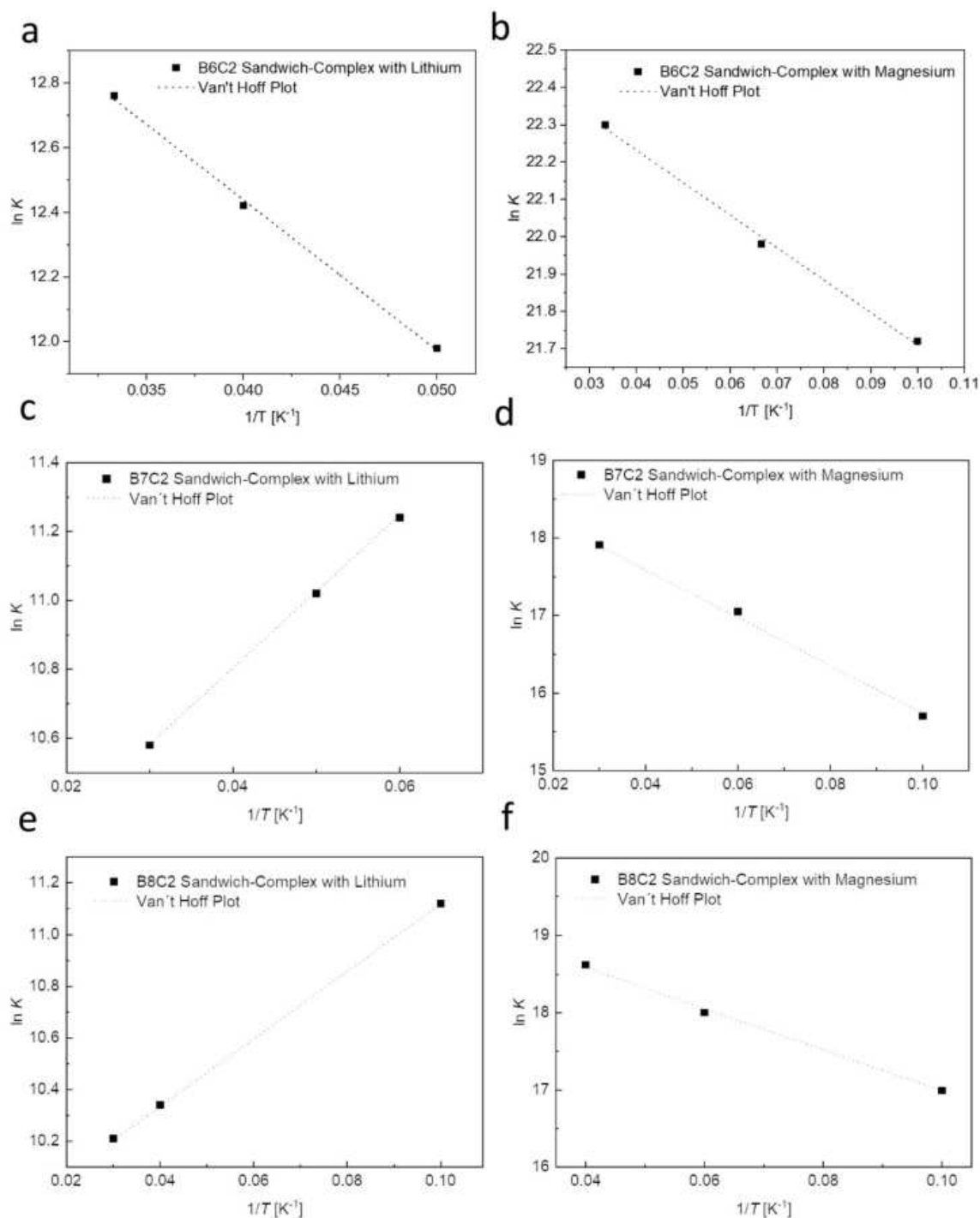


Fig. S15: Van't Hoff plot of the a) B6C2-Li complex b) B6C2-Mg complex, c) B7C2-Li complex, d) B7C2-Mg complex, e) B8C2-Li complex, and f) B8C2-Mg complex with a constant molar ratio of CE:salt = 14:1.

Tab. S1: Log K and Gibbs energy ΔG at 25 °C of the extraction of B6C2, B7C2 and B8C2 with Li^+ and Mg^{2+} .

B6C2-Li⁺			Sandwich	
CE:metal	log K	ΔG [kJmol ⁻¹]	log K	ΔG [kJmol ⁻¹]
1:25	4.9	-28	7.06	-40
1:20	4.6	-26	6.71	-38
1:17	5.0	-28	7.07	-40
1:14	4.8	-27	6.89	-40
1:13	4.9	-28	7.05	-40
1:11	4.8	-27	6.98	-40
B6C2-Mg²⁺			Sandwich	
CE:metal	log K	ΔG [kJmol ⁻¹]	log K	ΔG [kJmol ⁻¹]
1:25	7.8	-44	9.9	-57
1:20	7.5	-43	9.6	-55
1:17	7.6	-44	9.8	-56
1:14	7.5	-43	9.7	-55
1:13	7.3	-42	9.5	-54
1:11	7.1	-41	9.3	-53
B7C2-Li⁺			Sandwich	
CE:metal	log K	ΔG [kJmol ⁻¹]	log K	ΔG [kJmol ⁻¹]
1:25	5.1	-29	7.3	-42
1:20	5.1	-29	7.3	-42
1:17	4.9	-28	7.1	-40
1:14	4.7	-27	6.9	-39
1:13	4.6	-25	6.7	-39
1:11	4.5	-25	6.7	-38
B7C2-Mg²⁺			Sandwich	
CE:metal	log K	ΔG [kJmol ⁻¹]	log K	ΔG [kJmol ⁻¹]
1:25	9.0	-51	11	-64
1:20	8.8	-50	11	-63
1:17	8.4	-48	11	-61
1:14	8.2	-47	10	-60
1:13	7.9	-45	10	-59
1:11	7.6	-43	10	-58
B8C2-Li⁺			Sandwich	
CE:metal	log K	ΔG [kJmol ⁻¹]	log K	ΔG [kJmol ⁻¹]
1:25	4.7	-27	6.9	-39
1:20	4.7	-27	6.9	-39
1:17	4.3	-25	6.6	-37
1:14	4.0	-23	6.2	-36
1:13	3.6	-21	5.8	-33
1:11	4.0	-20	6.3	-36
B8C2-Mg²⁺			Sandwich	
CE:metal	log K	ΔG [kJmol ⁻¹]	log K	ΔG [kJmol ⁻¹]
1:25	8.7	-50	11	-63
1:20	8.4	-48	11	-61
1:17	7.9	-45	10	-58
1:14	8.2	-47	10	-60
1:13	7.8	-45	10	-57
1:11	7.5	-43	9.1	-55

Tab. S2: Slope and intercept values of the Van't Hoff plot and the determined data of ΔH , ΔS and ΔG (at 25 °C).

Li⁺	R²	Slope $\left(\frac{-\Delta H}{R}\right)$	Intercept $\left(\frac{\Delta S}{R}\right)$	ΔH [Jmol⁻¹]	ΔS [Jmol⁻¹K⁻¹]	ΔG VH [kJmol⁻¹]
B6C2	0.997	-46.6	14.3	387	119	-35
B7C2	0.998	20.1	15.0	-167	125	-37
B8C2	0.999	13.7	14.9	-114	124	-37
Mg²⁺	R²	Slope $\left(\frac{-\Delta H}{R}\right)$	Intercept $\left(\frac{\Delta S}{R}\right)$	ΔH [Jmol⁻¹]	ΔS [Jmol⁻¹K⁻¹]	ΔG VH [kJmol⁻¹]
B6C2	0.993	-8.70	22.6	72.3	188	-56
B7C2	0.997	-31.7	23.9	263	199	-59
B8C2	0.995	-28.0	25.0	233	208	-62

9.3 Supporting information of publication 2

The supporting information is reprinted with permission from I. Oral, S. Tamm, C. Herrmann and V. Abetz, *Separation and Purification Technology*, **2022**, *294*, 121142 – published by Elsevier.

Lithium Selectivity of Crown Ethers: The Effect of Heteroatoms and Cavity Size – Supporting Information

Iklima Oral, Sabrina Tamm, Carmen Herrmann, Volker Abetz

1. 15-membered Rings

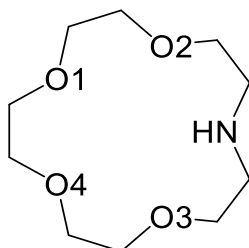


Figure S1: Lewis structure of aza-15C5.

1.1. Cavity Size d_{CE}

Table S1: The distances between the heteroatoms opposing each other as well as the cavity sizes d_{CE} of the empty CE (B15C5, aza-B15C5, thio-B15C5, and aza-15C5) and their complexes with Li^+ , Na^+ , K^+ , Mg^{2+} , and Ca^{2+} .

Complex	Distance / Å					cavity size d_{CE}
	O1-O4	O1-X	O2-O3	O2-X	O3-O4	
B15C5	4.4991	4.4497	4.4984	4.4492	4.6768	4.5146
B15C5- Li^+	4.1656	4.1738	4.1658	4.1739	4.1956	4.1749
B15C5- Na^+	4.3506	4.3830	4.3507	4.3831	4.3719	4.3678
B15C5- K^+	4.4246	4.1946	4.4249	4.1948	4.6769	4.3831
B15C5- Mg^{2+}	4.0344	4.0354	4.0344	4.0354	4.0160	4.0311
B15C5- Ca^{2+}	4.2927	4.2320	4.2929	4.2320	4.3787	4.2857
aza-B15C5	4.4958	4.2307	4.4958	4.2307	4.7499	4.4406
aza-B15C5- Li^+	4.1905	4.2831	4.1905	4.2831	4.2448	4.2384
aza-B15C5- Na^+	4.3557	4.4911	4.3556	4.4911	4.4074	4.4202
aza-B15C5- K^+	4.4514	4.2366	4.4515	4.2367	4.7337	4.4220
aza-B15C5- Mg^{2+}	3.6803	4.2199	3.7446	3.8615	3.9441	3.8901
aza-B15C5- Ca^{2+}	4.3086	4.3403	4.3086	4.3403	4.4230	4.3441
thio-B15C5	3.1569	4.9271	4.6851	4.9124	3.7239	4.2811
thio-B15C5- Li^+	3.4803	4.7346	3.8329	4.0794	3.7419	3.9738
thio-B15C5- Na^+	4.3465	4.8801	4.3465	4.8801	4.3404	4.5587
thio-B15C5- K^+	4.3371	5.2288	4.3371	5.2279	4.1099	4.6481
thio-B15C5- Mg^{2+}	3.5442	4.5671	3.8701	4.0614	3.8734	3.9832
thio-B15C5- Ca^{2+}	4.2858	4.9215	4.2858	4.9215	4.1733	4.5176
aza-15C5	4.7790	4.1060	4.7890	4.5980	4.1500	4.4844
aza-15C5- Li^+	3.9690	3.8700	4.5470	4.1550	4.6840	4.2450
aza-15C5- Na^+	4.2030	4.4450	4.5200	4.5610	4.4710	4.4400
aza-15C5- K^+	4.0290	4.4340	4.7760	4.8300	4.5560	4.5250
aza-15C5- Mg^{2+}	3.9760	3.7690	3.6080	4.0930	3.8240	3.8540
aza-15C5- Ca^{2+}	4.1940	4.4490	4.3760	4.5500	4.3170	4.3772

1.2. Metal Heteroatom Distance $d_{X-M^{n+}}$

Table S2: The distances and average distances between the heteroatoms of the CE (B15C5, aza-B15C5, thio-B15C5, and aza-15C5) and the complexed cations (Li^+ , Na^+ , K^+ , Mg^{2+} , and Ca^{2+}).

Complex	Distance / Å					Average distance
	O1-M	O2-M	O3-M	O4-M	X-M	
B15C5- Li^+	2.2154	2.2154	2.1946	2.1945	2.1652	2.1970
B15C5- Na^+	2.3034	2.3034	2.3046	2.3045	2.2980	2.3028
B15C5- K^+	2.7125	2.7125	2.7194	2.7193	2.6920	2.7111
B15C5- Mg^{2+}	2.1315	2.1315	2.1132	2.1132	2.1119	2.1202
B15C5- Ca^{2+}	2.3170	2.3170	2.3388	2.3388	2.3044	2.3232
aza-B15C5- Li^+	2.2455	2.2455	2.2102	2.2102	2.2554	2.2334
aza-B15C5- Na^+	2.3179	2.3179	2.3075	2.3075	2.4110	2.3324
aza-B15C5- K^+	2.7282	2.7281	2.7218	2.7219	2.7600	2.7320
aza-B15C5- Mg^{2+}	2.1667	2.0713	2.0558	2.0338	2.1848	2.1025
aza-B15C5- Ca^{2+}	2.3294	2.3294	2.3291	2.3291	2.4349	2.3504
thio-B15C5- Li^+	2.1902	2.0544	1.9778	2.0439	2.6207	2.1774
thio-B15C5- Na^+	2.3179	2.3179	2.3309	2.3309	2.7945	2.4184
thio-B15C5- K^+	2.7004	2.7003	2.7315	2.7315	3.1959	2.8119
thio-B15C5- Mg^{2+}	2.1209	2.0650	2.0519	2.0688	2.5375	2.1688
thio-B15C5- Ca^{2+}	2.3446	2.3446	2.3396	2.3396	2.8338	2.4404
aza-15C5- Li^+	2.0680	2.8060	2.1040	2.1930	2.0940	2.2530
aza-15C5- Na^+	2.3230	2.3590	2.3510	2.4390	2.3300	2.3604
aza-15C5- K^+	2.7000	2.6920	2.7240	2.8490	2.7030	2.7336
aza-15C5- Mg^{2+}	2.1080	2.0650	2.0340	2.1720	2.0660	2.0890
aza-15C5- Ca^{2+}	2.3300	2.3120	2.3520	2.4840	2.3060	2.3568

1.3. Hirshfeld Partial Charges

Table S3: Hirshfeld charge transfer between the oxygen, nitrogen, resp. sulfur atoms of B15C5, aza-B15C5, thio-B15C5, and aza-15C5 and the complexed cations (Li^+ , Na^+ , K^+ , Mg^{2+} , and Ca^{2+}), based on the difference in Hirshfeld partial charges between the empty CE and the coronates.

Complex	Charge transfer					Total
	O1-M	O2-M	O3-M	O4-M	X-M	
B15C5- Li^+	0.0198	0.0198	0.0309	0.0309	0.0299	0.1313
B15C5- Na^+	0.0095	0.0095	0.0214	0.0214	0.0203	0.0822
B15C5- K^+	0.0075	0.0075	0.0113	0.0113	0.0179	0.0554
B15C5- Mg^{2+}	0.0285	0.0285	0.0465	0.0465	0.0463	0.1962
B15C5- Ca^{2+}	0.0185	0.0185	0.0355	0.0355	0.0364	0.1443
aza-B15C5- Li^+	0.0113	0.0113	0.0182	0.0182	0.0609	0.1199
aza-B15C5- Na^+	0.0016	0.0016	0.0095	0.0095	0.0531	0.0752
aza-B15C5- K^+	-0.0015	-0.0015	-0.0004	-0.0004	0.0414	0.0377
aza-B15C5- Mg^{2+}	0.0174	0.0069	0.0344	0.0340	0.1088	0.2015
aza-B15C5- Ca^{2+}	0.0101	0.0102	0.0225	0.0225	0.0913	0.1566
thio-B15C5- Li^+	0.0007	0.0108	0.0085	0.0080	0.0831	0.1111
thio-B15C5- Na^+	-0.0082	0.0204	0.0040	0.0028	0.0662	0.0852
thio-B15C5- K^+	-0.0201	0.0085	-0.0003	-0.0014	0.0473	0.0340
thio-B15C5- Mg^{2+}	0.0101	0.0281	0.0283	0.0253	0.1511	0.2429
thio-B15C5- Ca^{2+}	-0.0034	0.0252	0.0176	0.0164	0.1273	0.1832
aza-15C5- Li^+	0.0203	0.0174	0.0136	0.0177	0.0593	0.1283
aza-15C5- Na^+	0.0114	0.0105	0.0106	0.0127	0.0528	0.0979
aza-15C5- K^+	0.0022	0.0056	0.0014	0.0077	0.0392	0.0561
aza-15C5- Mg^{2+}	0.0381	0.0348	0.0389	0.0353	0.1109	0.2580
aza-15C5- Ca^{2+}	0.0257	0.0235	0.0242	0.0275	0.0909	0.1918

1.4. NBO Analysis

Table S4: Stabilization energies $E^{(2)}$ (in kJ mol^{-1}) between the acceptor NBO of the complexed metal (Li^+ , Na^+ , K^+ , Mg^{2+} , and Ca^{2+}) and the donor NBOs of B15C5, aza-B15C5, thio-B15C5, and aza-15C5. LP1 and LP2 represent the donor NBOs corresponding to the free electron pairs of the heteroatoms.

Complex	Stabilization energy / kJ mol^{-1}										Sum
	O1		O2		O3		O4		X		
	LP1	LP2	LP1	LP2	LP1	LP2	LP1	LP2	LP1	LP2	
B15C5- Li^+	19.71	0.00	19.71	0.00	20.96	1.55	20.96	1.55	21.80	1.30	107.53
B15C5- Na^+	17.36	0.00	17.36	0.00	17.28	2.26	17.28	2.26	17.91	2.09	93.81
B15C5- K^+	5.82	0.00	5.82	0.00	8.45	0.00	8.45	0.00	6.15	0.25	34.94
B15C5- Mg^{2+}	40.58	1.88	40.58	1.88	33.64	19.83	33.64	19.83	35.52	16.95	244.35
B15C5- Ca^{2+}	17.57	1.00	17.57	1.00	20.00	3.81	20.00	3.81	14.39	5.77	104.93
aza-B15C5- Li^+	20.67	0.00	20.67	0.00	22.26	1.46	22.26	1.46	23.64	-	112.42
aza-B15C5- Na^+	18.28	0.00	18.28	0.00	18.54	2.05	18.54	2.05	2.05	-	79.79
aza-B15C5- K^+	6.02	0.00	6.02	0.00	8.79	0.00	8.79	0.00	7.15	-	36.78
aza-B15C5- Mg^{2+}	40.79	4.48	19.92	44.02	42.89	22.09	47.86	16.61	70.92	-	264.30
aza-B15C5- Ca^{2+}	19.50	1.26	19.50	1.26	20.42	3.10	20.42	3.10	25.36	-	113.89
thio-B15C5- Li^+	27.87	0.00	24.56	17.53	41.00	2.68	37.66	6.11	31.67	54.85	243.93
thio-B15C5- Na^+	18.54	0.00	18.54	0.00	18.49	2.51	18.49	2.51	20.71	36.57	136.36
thio-B15C5- K^+	7.82	0.54	7.82	0.54	6.86	0.59	6.86	0.59	14.90	12.43	58.95
thio-B15C5- Mg^{2+}	41.80	5.56	18.83	44.69	43.18	25.15	39.46	31.59	24.98	133.72	408.94
thio-B15C5- Ca^{2+}	21.55	0.00	21.55	0.00	14.43	3.51	14.43	3.51	20.38	64.60	163.97
aza-15C5- Li^+	28.91	0.75	9.62	2.22	24.77	0.96	25.02	1.00	26.02	-	119.29
aza-15C5- Na^+	18.16	2.09	18.07	2.55	17.49	1.97	19.20	1.38	20.96	-	101.88
aza-15C5- K^+	7.57	0.42	9.16	0.29	7.03	0.38	9.25	0.00	8.87	-	42.97
aza-15C5- Mg^{2+}	38.28	27.03	34.31	32.64	37.40	26.94	48.66	14.27	76.32	-	335.85
aza-15C5- Ca^{2+}	16.32	5.73	19.46	2.34	15.86	3.89	21.63	3.22	27.82	-	116.27

2. 12-membered Rings

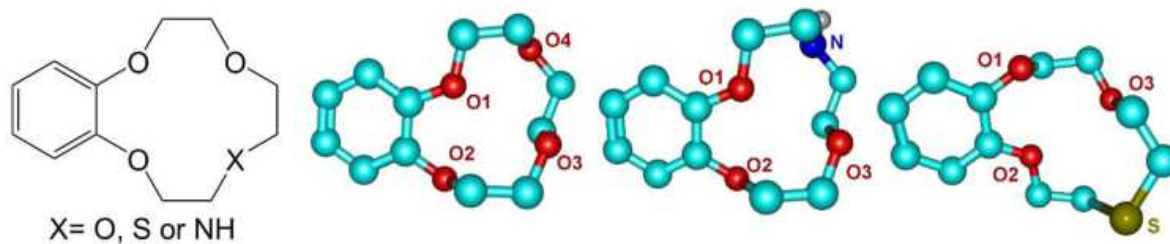


Figure S1: Lewis structure representation (left) and optimized structures of the empty crown ethers B12C4, aza-B12C4 and thio-B12C4 (from left to right).

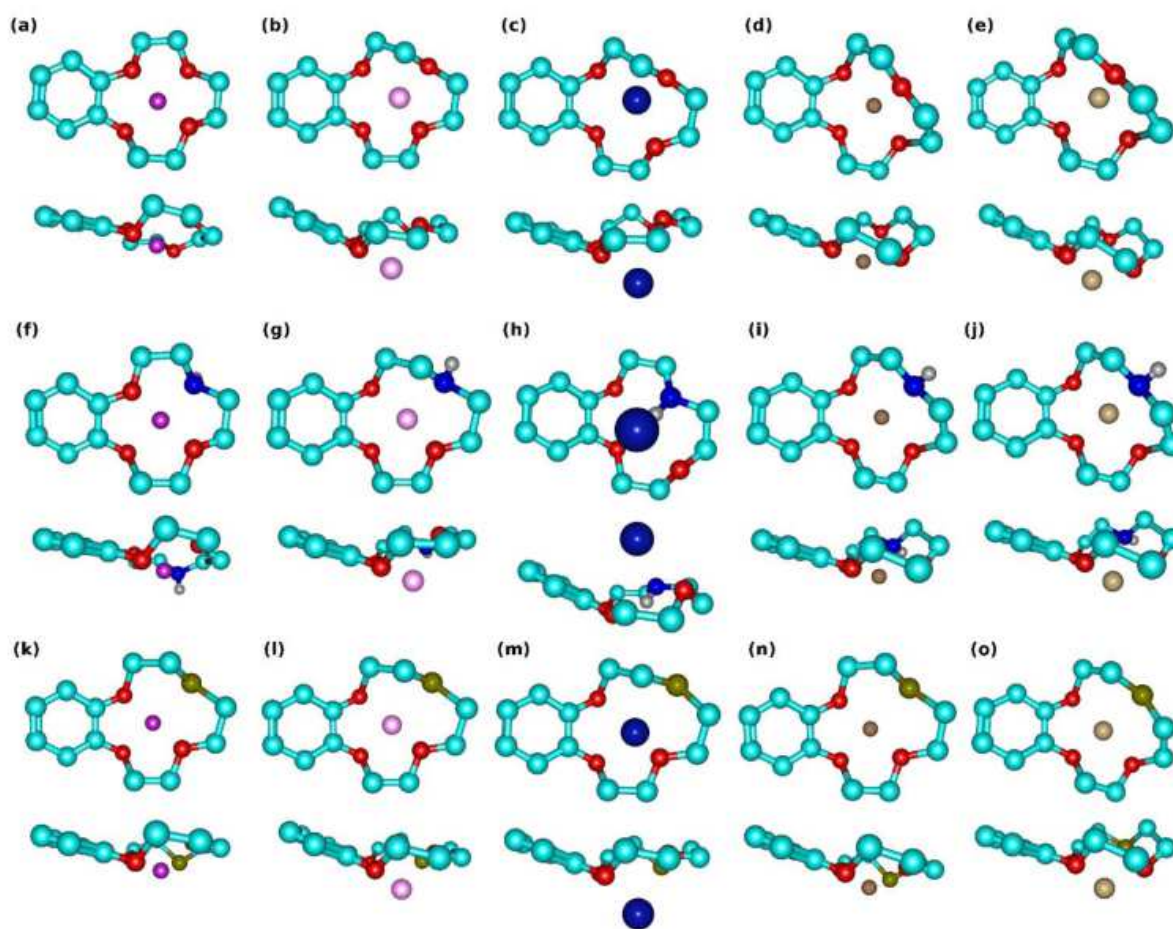


Figure S2: Optimized structures of the B12C4 (first row), aza-B12C4 (second row) and thio-B12C4 (third row) complexes with Li⁺ (violet; a, f, k), Na⁺ (pink; b, g, l), K⁺ (dark blue; c, h, m), Mg²⁺ (brown; d, i, n), and Ca²⁺ (beige; e, j, o), from two perspectives each.

2.1. Cavity Size d_{CE}

Table S5: The distances between the heteroatoms opposing each other as well as the cavity sizes d_{CE} of the empty CE (B12C4, aza-B12C4, and thio-B12C4) and their complexes with Li^+ , Na^+ , K^+ , Mg^{2+} , and Ca^{2+} .

Complex	Distance / Å		
	O1-X	O2-O3	cavity size d_{CE}
B12C4	3.0255	4.6405	3.8330
B12C4- Li^+	3.2267	3.8388	3.5327
B12C4- Na^+	3.7123	3.9695	3.8409
B12C4- K^+	4.0347	3.7944	3.9145
B12C4- Mg^{2+}	3.9100	3.3572	3.6336
B12C4- Ca^{2+}	4.1428	3.2566	3.6997
aza-B12C4	3.0279	4.6922	3.8601
aza-B12C4- Li^+	3.1846	3.9996	3.5921
aza-B12C4- Na^+	3.6782	4.1036	3.8909
aza-B12C4- K^+	4.4422	3.0966	3.7694
aza-B12C4- Mg^{2+}	3.9150	3.5730	3.7440
aza-B12C4- Ca^{2+}	4.1412	3.4748	3.8080
thio-B12C4	3.0639	5.0078	4.0358
thio-B12C4- Li^+	3.3844	4.4042	3.8943
thio-B12C4- Na^+	3.5718	4.5372	4.0545
thio-B12C4- K^+	3.6282	4.5808	4.1045
thio-B12C4- Mg^{2+}	3.5207	4.3551	3.9379
thio-B12C4- Ca^{2+}	4.0554	4.0654	4.0604

2.2. Metal-Heteroatom Distance $d_{X-M^{n+}}$

Table S6: The distances and average distances between the heteroatoms of the CE (B12C4, aza-B12C4, and thio-B12C4) and the complexed cations (Li^+ , Na^+ , K^+ , Mg^{2+} , and Ca^{2+}).

Complex	Distance / Å				
	O1-M	O2-M	O3-M	X-M	Average distance
B12C4- Li^+	1.88276	1.93689	1.90707	1.88562	1.9031
B12C4- Na^+	2.25056	2.32322	2.33354	2.48729	2.3487
B12C4- K^+	2.63358	2.75425	2.72497	3.3917	2.8761
B12C4- Mg^{2+}	2.01429	1.99333	1.99924	1.99691	2.0009
B12C4- Ca^{2+}	2.3165	2.3117	2.32801	2.30168	2.3145
aza-B12C4- Li^+	1.87088	1.97566	2.03397	1.88438	1.9412
aza-B12C4- Na^+	2.25933	2.32952	2.41851	2.44828	2.3639
aza-B12C4- K^+	3.93576	3.15176	2.73397	2.78264	3.1510
aza-B12C4- Mg^{2+}	2.015	1.998	1.999	2.105	2.0293
aza-B12C4- Ca^{2+}	2.31307	2.30893	2.47131	2.29894	2.3481
thio-B12C4- Li^+	1.89609	1.98914	1.93381	2.48055	2.0749
thio-B12C4- Na^+	2.27169	2.32707	2.39736	2.78747	2.4459
thio-B12C4- K^+	2.67233	2.71239	2.94127	3.196	2.8805
thio-B12C4- Mg^{2+}	1.96279	2.01405	1.9642	2.4574	2.0996
thio-B12C4- Ca^{2+}	2.33247	2.31118	2.31433	2.81501	2.4432

2.3. Hirshfeld Partial Charges

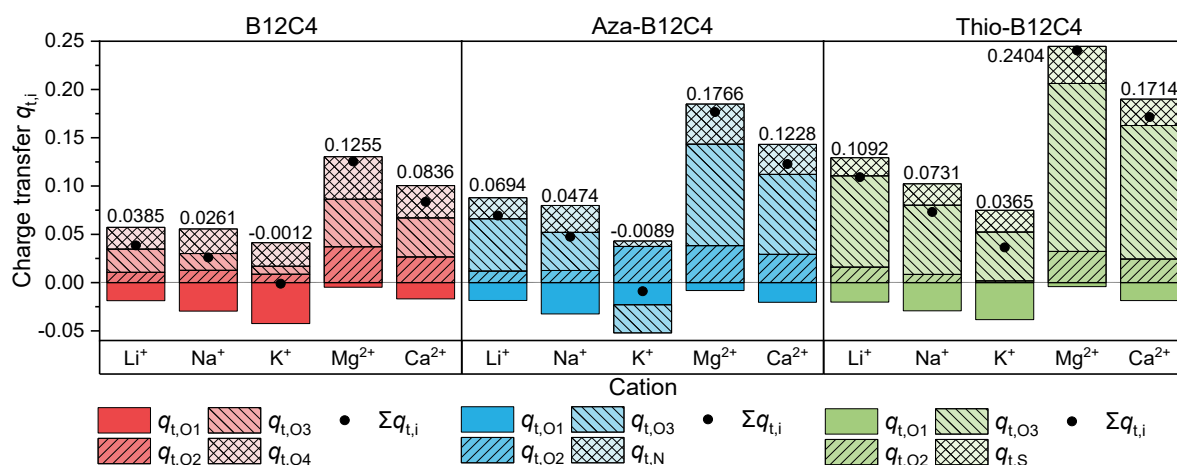


Figure S3: Hirshfeld charge transfer q_t between the donor atoms (O, S, and N) and Li^+ , Na^+ , K^+ , Mg^{2+} , resp. Ca^{2+} within the complexes with the B12C4, aza-B12C4 and thio-B12C4 CE. The sums of the charge transfers are given above the bars.

2.4. NBO Analysis

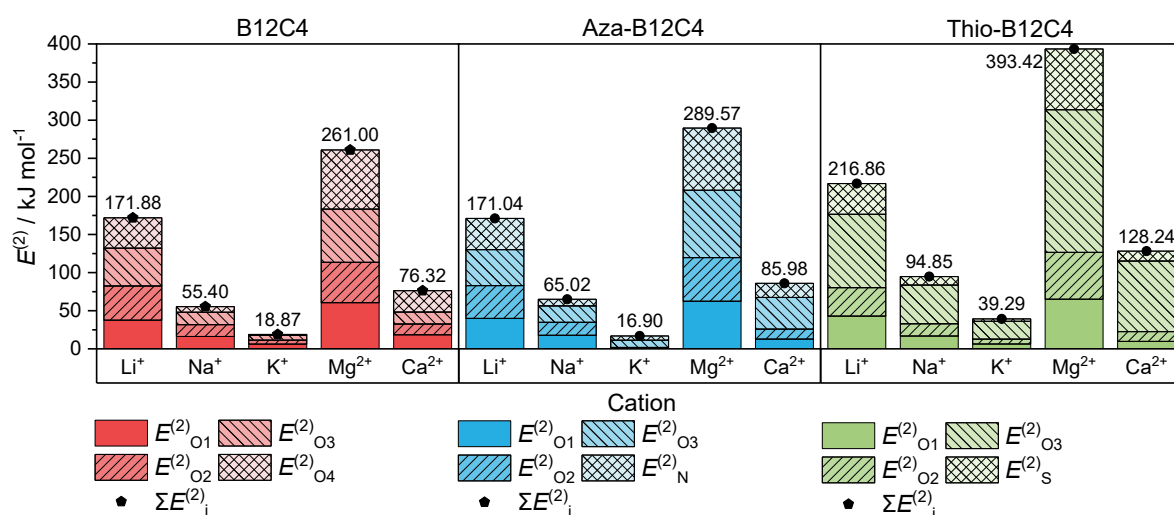


Figure S4: Stabilization energies $E^{(2)}$ within the complexes of the B12C4, aza-B12C4 and thio-B12C4 CE with Li^+ , Na^+ , K^+ , Mg^{2+} , and Ca^{2+} . The contributions of the lone pair donor NBOs (LP1 and LP2 combined) to the interaction with the acceptor NBOs and the sum of these, above the bars, are given.

3. 9-membered Rings

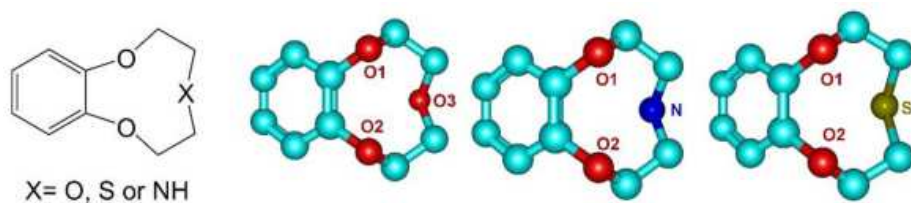


Figure S5: Lewis structure representation (left) and optimized structures of the empty crown ethers B9C3, aza-B9C3 and thio-B9C3 (from left to right).

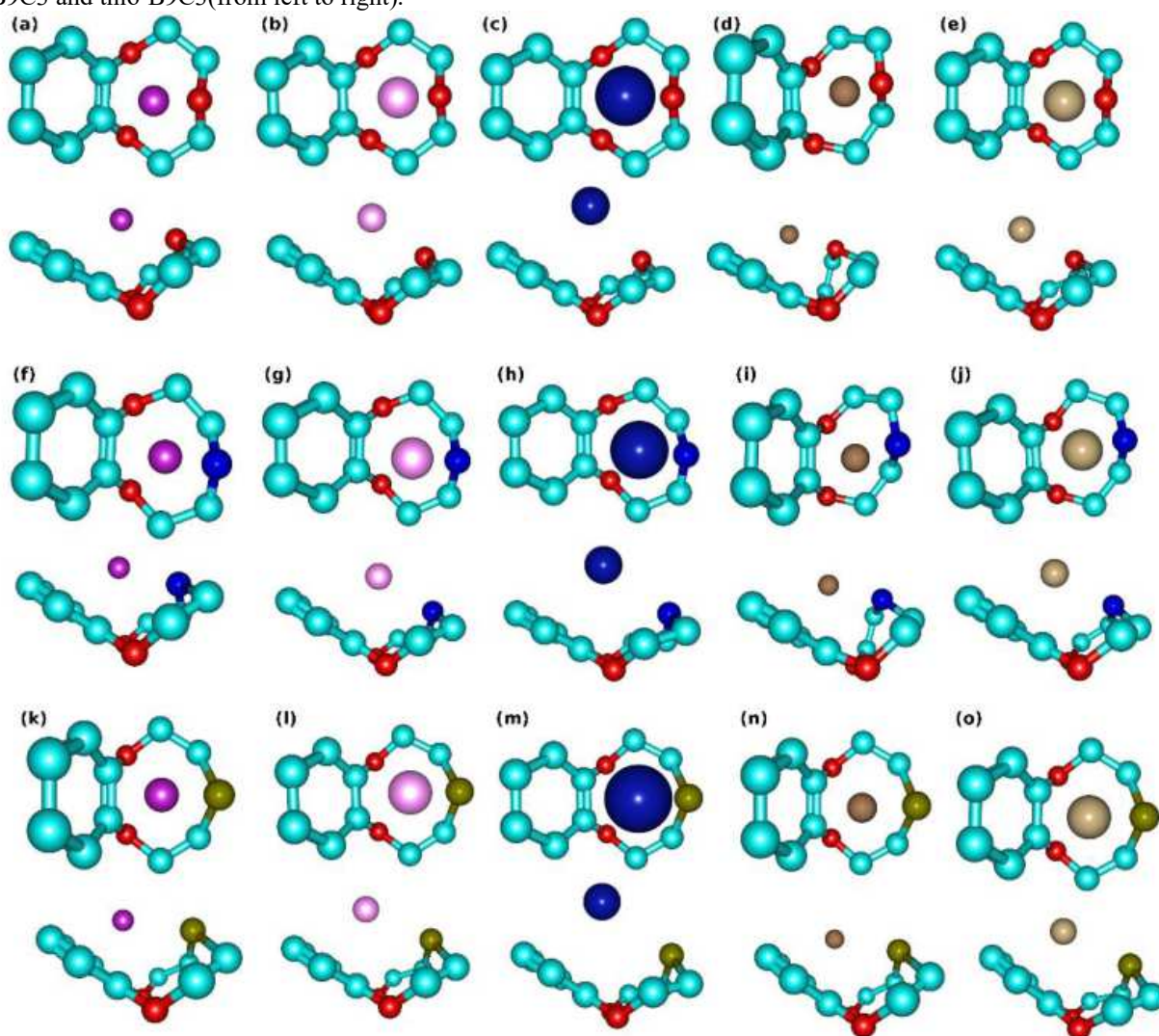


Figure S6: Optimized structures of the B9C3 (first row), aza-B9C3 (second row) and thio-B9C3 (third row) complexes with Li⁺ (violet; a, f, k), Na⁺ (pink; b, g, l), K⁺ (dark blue; c, h, m), Mg²⁺ (brown; d, i, n), and Ca²⁺ (beige; e, j, o), from two perspectives each.

3.1. Cavity Size d_{CE}

Table S7: The distances between the heteroatoms opposing each other as well as the cavity sizes d_{CE} of the empty CE (B9C3, aza-B9C3, and thio-B9C3) and their complexes with Li^+ , Na^+ , K^+ , Mg^{2+} , and Ca^{2+} .

Complex	Distance / Å			
	O1-O2	O1-X	O2-X	cavity size d_{CE}
B9C3	2.7619	2.9516	2.9518	2.9517
B9C3- Li^+	2.7599	2.8265	2.8265	2.8265
B9C3- Na^+	2.7554	2.8565	2.8564	2.8564
B9C3- K^+	2.7517	2.8793	2.8791	2.8792
B9C3- Mg^{2+}	2.6673	3.0147	2.6719	2.8433
B9C3- Ca^{2+}	2.7251	2.8200	2.8200	2.8200
aza-B9C3	2.7453	3.0029	3.0031	3.0030
aza-B9C3- Li^+	2.7362	2.8485	3.1312	2.9898
aza-B9C3- Na^+	2.7275	2.8903	3.1850	3.0376
aza-B9C3- K^+	2.7263	2.8632	3.2438	3.0535
aza-B9C3- Mg^{2+}	2.6455	3.2238	2.8452	3.0345
aza-B9C3- Ca^{2+}	2.7091	3.1877	2.8194	3.0036
thio-B9C3	2.7144	3.3362	3.3362	3.3362
thio-B9C3- Li^+	2.6959	3.2706	3.2704	3.2705
thio-B9C3- Na^+	2.6957	3.3104	3.3104	3.3104
thio-B9C3- K^+	2.6939	3.3169	3.3142	3.3156
thio-B9C3- Mg^{2+}	2.6580	3.2959	3.2959	3.2959
thio-B9C3- Ca^{2+}	2.6544	3.2475	3.2475	3.2475

3.2. Metal-Heteroatom Distance $d_{X-M^{n+}}$

Table S8: The distances and average distances between the heteroatoms of the CE (B9C3, aza-B9C3, and thio-B9C3) and the complexed cations (Li^+ , Na^+ , K^+ , Mg^{2+} , and Ca^{2+}).

Complex	Distance / Å			
	O1-M	O2-M	X-M	Average distance
B9C3- Li^+	3.03717	3.0372	1.90168	2.6587
B9C3- Na^+	3.48023	3.48044	2.29895	3.0865
B9C3- K^+	3.96879	3.96868	2.70061	3.5460
B9C3- Mg^{2+}	3.23355	3.24632	1.97804	2.8193
B9C3- Ca^{2+}	3.46233	3.46233	2.30701	3.0772
aza-B9C3- Li^+	2.98015	3.07539	2.04977	2.7018
aza-B9C3- Na^+	3.38056	3.44922	2.44694	3.0922
aza-B9C3- K^+	3.82026	3.90454	2.90715	3.5440
aza-B9C3- Mg^{2+}	3.22019	3.27441	2.09757	2.8641
aza-B9C3- Ca^{2+}	3.4907	3.45066	2.47986	3.1404
thio-B9C3- Li^+	3.23056	3.23053	2.48556	2.9822
thio-B9C3- Na^+	3.7947	3.79472	2.79966	3.4630
thio-B9C3- K^+	4.33251	4.33238	3.22413	3.9630
thio-B9C3- Mg^{2+}	3.32405	3.32405	2.47001	3.0394
thio-B9C3- Ca^{2+}	3.63854	3.63854	2.80637	3.3612

3.3. Hirshfeld Partial Charges

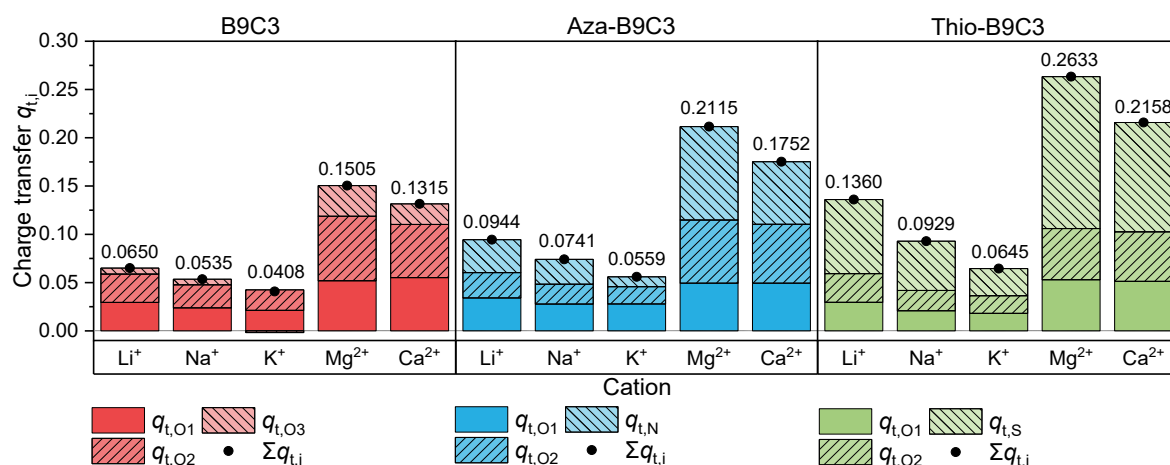


Figure S7: Hirshfeld charge transfer q_i between the donor atoms (O, S, and N) and Li^+ , Na^+ , K^+ , Mg^{2+} , resp. Ca^{2+} within the complexes with the B9C3, aza-B9C3 and thio-B9C3 CE. The sums of the charge transfers are given above the bars.

3.4. NBO Analysis

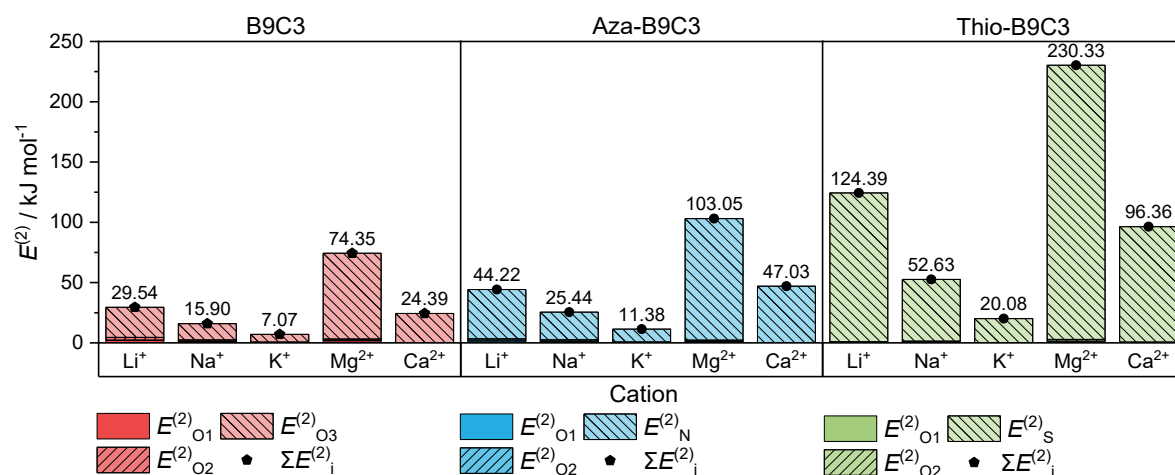


Figure S8: Stabilization energies $E^{(2)}$ within the complexes of the B9C3, aza-B9C3 and thio-B9C3 CEs with Li^+ , Na^+ , K^+ , Mg^{2+} , and Ca^{2+} . The contributions of the lone pair donor NBOs (LP1 and LP2 combined) to the interaction with the acceptor NBOs and the sum of these, above the bars, are given.

4. Aza-15-crown-5

Table S9: Cavity size, metal–donor atom distance, Hirshfeld charge transfer, and NBO stabilization energy $E^{(2)}$ calculated via DFT for complexes of aza-15C5 with Li^+ , Na^+ , K^+ , Mg^{2+} , and Ca^{2+} .

Complex	Cavity size		Hirshfeld partial	NBO
	$d_{\text{CE}} / \text{Å}$	$d_{\text{X-M}^{n+}} / \text{Å}$	charge	$E^{(2)} / \text{kJ mol}^{-1}$
$\text{M}^{n+} = \text{none}$	4.48	-	-	-
$\text{M}^{n+} = \text{Li}^+$	4.25	2.25	0.13	119.29
$\text{M}^{n+} = \text{Na}^+$	4.44	2.36	0.10	101.88
$\text{M}^{n+} = \text{K}^+$	4.53	2.73	0.06	42.97
$\text{M}^{n+} = \text{Mg}^{2+}$	3.85	2.09	0.26	335.85
$\text{M}^{n+} = \text{Ca}^{2+}$	4.38	2.36	0.19	116.27

5. Thermodynamic Calculations

5.1. Entropy and Enthalpy

Table S10: Changes in enthalpy H and entropy S for the complexation of Li^+ , Na^+ , K^+ , Mg^{2+} and Ca^{2+} with aza-15-crown-5, simulated in vacuum and solvent environment as modeled by a polarizable continuum model.

Complex	Vacuum		DCM	
	$\Delta S [\text{kJ mol}^{-1}\text{K}^{-1}]$	$\Delta H [\text{kJ mol}^{-1}]$	$\Delta S [\text{kJ mol}^{-1}\text{K}^{-1}]$	$\Delta H [\text{kJ mol}^{-1}]$
$\text{M}^{n+} = \text{Li}^+$	-0.13	-433.04	-0.14	-68.95
$\text{M}^{n+} = \text{Na}^+$	-0.14	-349.72	-0.13	-71.27
$\text{M}^{n+} = \text{K}^+$	-0.13	-244.29	-0.14	-57.42
$\text{M}^{n+} = \text{Mg}^{2+}$	-0.15	-1247.75	-0.16	-181.85
$\text{M}^{n+} = \text{Ca}^{2+}$	-0.15	-932.80	-0.17	-83.59

5.2. Equilibrium Constant and Gibbs Free Energy

Table S11: Equilibrium constants K for the complexation of Li^+ , Na^+ , K^+ , Mg^{2+} and Ca^{2+} with aza-15-crown-5, benzo-15-crown-5, aza-benzo-15-crown-5 and thio-benzo-15-crown-5, simulated in vacuum.

Complex	B15C5	aza-B15C5	thio-B15C5	aza-15C5
$\text{M}^{n+} = \text{Li}^+$	$1.9 \cdot 10^{64}$	$4.1 \cdot 10^{67}$	$1.4 \cdot 10^{69}$	$9.8 \cdot 10^{68}$
$\text{M}^{n+} = \text{Na}^+$	$1.8 \cdot 10^{48}$	$2.8 \cdot 10^{52}$	$9.5 \cdot 10^{53}$	$1.5 \cdot 10^{54}$
$\text{M}^{n+} = \text{K}^+$	$1.2 \cdot 10^{29}$	$2.3 \cdot 10^{33}$	$3.6 \cdot 10^{36}$	$7.0 \cdot 10^{35}$
$\text{M}^{n+} = \text{Mg}^{2+}$	$7.9 \cdot 10^{197}$	$1.6 \cdot 10^{208}$	$2.0 \cdot 10^{206}$	$4.0 \cdot 10^{210}$
$\text{M}^{n+} = \text{Ca}^{2+}$	$1.6 \cdot 10^{144}$	$6.3 \cdot 10^{152}$	$1.3 \cdot 10^{153}$	$4.3 \cdot 10^{155}$
Complex	B12C4	aza-B12C4	thio-B12C4	
$\text{M}^{n+} = \text{Li}^+$	$2.7 \cdot 10^{56}$	$2.7 \cdot 10^{60}$	$4.9 \cdot 10^{57}$	
$\text{M}^{n+} = \text{Na}^+$	$9.2 \cdot 10^{37}$	$3.0 \cdot 10^{41}$	$1.3 \cdot 10^{39}$	
$\text{M}^{n+} = \text{K}^+$	$5.0 \cdot 10^{25}$	$1.4 \cdot 10^{22}$	$1.3 \cdot 10^{26}$	
$\text{M}^{n+} = \text{Mg}^{2+}$	$1.1 \cdot 10^{178}$	$1.1 \cdot 10^{185}$	$1.7 \cdot 10^{178}$	
$\text{M}^{n+} = \text{Ca}^{2+}$	$1.0 \cdot 10^{128}$	$1.5 \cdot 10^{132}$	$1.5 \cdot 10^{126}$	
Complex	B9C3	aza-B9C3	thio-B9C3	
$\text{M}^{n+} = \text{Li}^+$	$1.82 \cdot 10^{34}$	$1.6 \cdot 10^{37}$	$9.5 \cdot 10^{34}$	
$\text{M}^{n+} = \text{Na}^+$	$2.18 \cdot 10^{23}$	$7.6 \cdot 10^{24}$	$2.4 \cdot 10^{24}$	
$\text{M}^{n+} = \text{K}^+$	$2.48 \cdot 10^{15}$	$2.8 \cdot 10^{15}$	$7.5 \cdot 10^{15}$	
$\text{M}^{n+} = \text{Mg}^{2+}$	$3.12 \cdot 10^{126}$	$1.0 \cdot 10^{134}$	$5.1 \cdot 10^{132}$	
$\text{M}^{n+} = \text{Ca}^{2+}$	$3.18 \cdot 10^{88}$	$1.1 \cdot 10^{92}$	$1.2 \cdot 10^{91}$	

Table S12: Equilibrium constants K for the complexation of Li^+ , Na^+ , K^+ , Mg^{2+} and Ca^{2+} (non-complexed simulated in H_2O) with aza-15-crown-5, benzo-15-crown-5, aza-benzo-15-crown-5 and thio-benzo-15-crown-5, simulated in DCM as modeled by a polarizable continuum model. No convergence of SCF runs could be achieved for B9C3- Ca^{2+} .

Complex	B15C5	aza-B15C5	thio-B15C5	aza-15C5
$\text{M}^{n+} = \text{Li}^+$	$2.87 \cdot 10^5$	$1.02 \cdot 10^4$	$2.51 \cdot 10^2$	$8.48 \cdot 10^4$
$\text{M}^{n+} = \text{Na}^+$	$5.61 \cdot 10^4$	$2.46 \cdot 10^3$	$3.98 \cdot 10^5$	$3.26 \cdot 10^5$
$\text{M}^{n+} = \text{K}^+$	$1.53 \cdot 10^3$	$2.87 \cdot 10^1$	$6.02 \cdot 10^2$	$7.87 \cdot 10^2$
$\text{M}^{n+} = \text{Mg}^{2+}$	$1.45 \cdot 10^{19}$	$5.93 \cdot 10^{18}$	$2.62 \cdot 10^{15}$	$2.52 \cdot 10^{23}$
$\text{M}^{n+} = \text{Ca}^{2+}$	$1.33 \cdot 10^1$	$4.98 \cdot 10^1$	2.00	$7.43 \cdot 10^5$
Complex	B12C4	aza-B12C4	thio-B12C4	
$\text{M}^{n+} = \text{Li}^+$	$5.26 \cdot 10^{-3}$	7.78	$1.25 \cdot 10^{-2}$	
$\text{M}^{n+} = \text{Na}^+$	$5.33 \cdot 10^{-3}$	$2.58 \cdot 10^{-1}$	$2.76 \cdot 10^{-3}$	
$\text{M}^{n+} = \text{K}^+$	$1.83 \cdot 10^{-1}$	1.62	$2.09 \cdot 10^{-2}$	
$\text{M}^{n+} = \text{Mg}^{2+}$	$1.76 \cdot 10^7$	$2.16 \cdot 10^{10}$	$1.76 \cdot 10^4$	
$\text{M}^{n+} = \text{Ca}^{2+}$	$2.26 \cdot 10^{-6}$	$6.12 \cdot 10^{-6}$	$2.26 \cdot 10^{-9}$	
Complex	B9C3	aza-B9C3	thio-B9C3	
$\text{M}^{n+} = \text{Li}^+$	$4.69 \cdot 10^{-11}$	$4.67 \cdot 10^{-11}$	$3.70 \cdot 10^{-9}$	
$\text{M}^{n+} = \text{Na}^+$	$1.59 \cdot 10^{-8}$	$2.15 \cdot 10^{-8}$	$2.45 \cdot 10^{-9}$	
$\text{M}^{n+} = \text{K}^+$	$4.09 \cdot 10^{-6}$	$2.15 \cdot 10^{-7}$	$3.64 \cdot 10^{-7}$	
$\text{M}^{n+} = \text{Mg}^{2+}$	$3.40 \cdot 10^{-30}$	$2.36 \cdot 10^{-26}$	$9.27 \cdot 10^{-27}$	
$\text{M}^{n+} = \text{Ca}^{2+}$		$4.96 \cdot 10^{-29}$	$4.06 \cdot 10^{-31}$	

Table S13: Change in Gibbs free energy [kJ mol^{-1}] for the complexation of Li^+ , Na^+ , K^+ , Mg^{2+} and Ca^{2+} with aza-15-crown-5, benzo-15-crown-5, aza-benzo-15-crown-5 and thio-benzo-15-crown-5, simulated in vacuum.

Complex	B15C5	aza-B15C5	thio-B15C5	aza-15C5
$\text{M}^{n+} = \text{Li}^+$	-366.967931	-385.918522	-394.651777	-393.807461
$\text{M}^{n+} = \text{Na}^+$	-275.411458	-299.385098	-308.118353	-3.09E+02
$\text{M}^{n+} = \text{K}^+$	-165.988916	-190.476277	-208.684827	-204.605988
$\text{M}^{n+} = \text{Mg}^{2+}$	-1129.61508	-1188.40758	-1177.56236	-1202.09562
$\text{M}^{n+} = \text{Ca}^{2+}$	-823.09497	-872.183852	-873.896255	-888.348062
Complex	B12C4	aza-B12C4	thio-B12C4	
$\text{M}^{n+} = \text{Li}^+$	-322.088187	-344.965297	-329.275511	
$\text{M}^{n+} = \text{Na}^+$	-216.682853	-236.711809	-223.284796	
$\text{M}^{n+} = \text{K}^+$	-146.689133	-126.423925	-149.012282	
$\text{M}^{n+} = \text{Mg}^{2+}$	-1016.28182	-1056.22949	-1017.37384	
$\text{M}^{n+} = \text{Ca}^{2+}$	-730.657888	-754.514133	-720.220781	
Complex	B9C3	aza-B9C3	thio-B9C3	
$\text{M}^{n+} = \text{Li}^+$	-195.561522	-212.322998	-199.650356	
$\text{M}^{n+} = \text{Na}^+$	-133.213664	-142.014262	-139.174031	
$\text{M}^{n+} = \text{K}^+$	-87.8715131	-88.1651408	-90.6184412	
$\text{M}^{n+} = \text{Mg}^{2+}$	-722.033206	-764.91108	-757.477086	
$\text{M}^{n+} = \text{Ca}^{2+}$	-505.171328	-525.398708	-519.91034	

Table S14: Change in Gibbs free energy [kJ mol⁻¹] for the complexation of Li⁺, Na⁺, K⁺, Mg²⁺ and Ca²⁺ (non-complexed simulated in H₂O) with aza-15-crown-5, benzo-15-crown-5, aza-benzo-15-crown-5 and thio-benzo-15-crown-5, simulated in DCM as modeled by a polarizable continuum model. No convergence of SCF runs could be achieved for B9C3-Ca²⁺.

Complex	B15C5	aza-B15C5	thio-B15C5	aza-15C5
Mⁿ⁺ = Li⁺	-31.1511765	-22.8745056	-13.6973962	-28.1322325
Mⁿ⁺ = Na⁺	-27.1060243	-19.3569447	-31.9623417	-31.4666175
Mⁿ⁺ = K⁺	-18.1809235	-8.32393318	-15.8656407	-16.530148
Mⁿ⁺ = Mg²⁺	-109.376992	-107.15886	-88.0119127	-133.572312
Mⁿ⁺ = Ca²⁺	-6.42082573	-9.68894657	-1.72199231	-33.511882
Complex	B12C4	aza-B12C4	thio-B12C4	
Mⁿ⁺ = Li⁺	13.00701249	-5.08469486	10.8623421	
Mⁿ⁺ = Na⁺	12.97550428	3.36264548	14.6109061	
Mⁿ⁺ = K⁺	4.205318921	-1.20227804	9.59185333	
Mⁿ⁺ = Mg²⁺	-41.3599515	-58.9843441	-24.2316419	
Mⁿ⁺ = Ca²⁺	32.22747873	29.7572805	49.3531055	
Complex	B9C3	aza-B9C3	thio-B9C3	
Mⁿ⁺ = Li⁺	58.95546155	58.9693891	48.129879	
Mⁿ⁺ = Na⁺	44.52047632	43.7621102	49.1483592	
Mⁿ⁺ = K⁺	30.75743796	38.0531303	36.753017	
Mⁿ⁺ = Mg²⁺	168.206478	146.283669	148.594899	
Mⁿ⁺ = Ca²⁺		161.560871	173.474914	

5.3. Solvent Simulation for 9-, 12- and 15-membered Crown Ethers

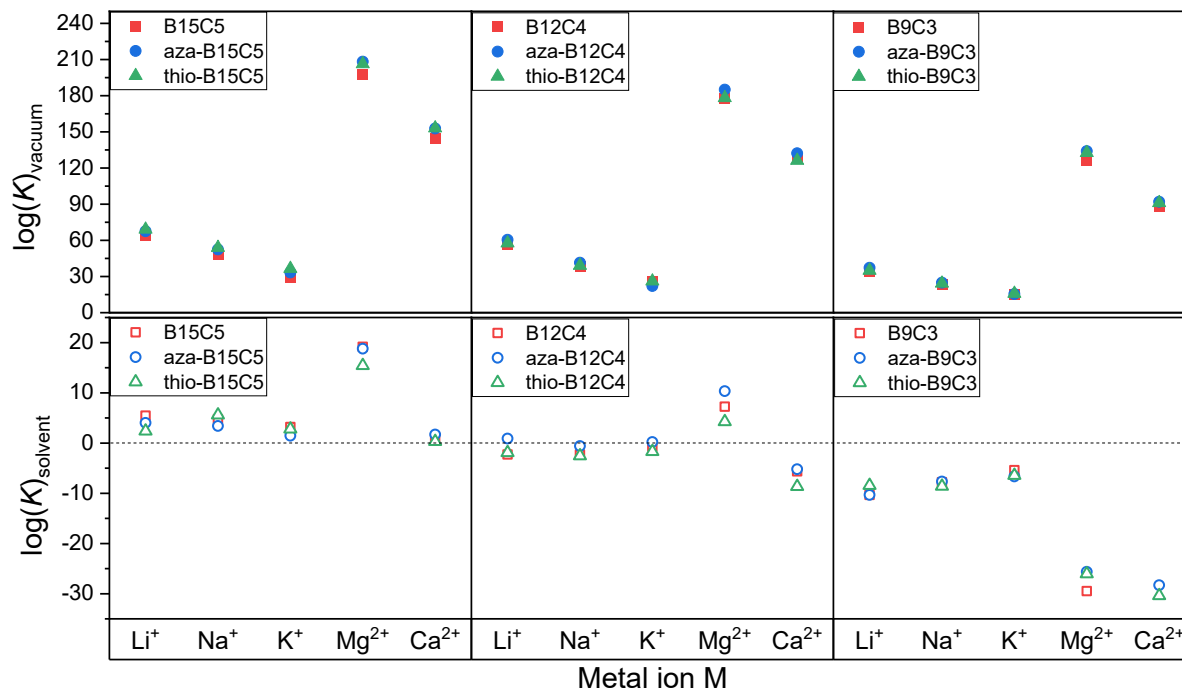


Figure S9: Logarithm of the equilibrium constant of complex formation of 15-, 12- and 9-membered CEs with different metal ions in vacuum (top) and with solvent simulation (bottom, Polarizable Continuum Model). No convergence of SCF runs could be achieved for B9C3-Ca²⁺. Values were determined via DFT according to Equations 6 and 7. The dotted line illustrates $\log(K)_{\text{solvent}}=0$.

Compared to the results obtained in vacuum, the solvent-based complexation constants are significantly lower, due to the charged species in vacuum lacking the stabilization by the solvent as present in the experiment. In analogy to the observations in vacuum, a loss of stability of the complexes with decreasing ring size is evident. Negative values for $\log(K)$ indicate unfavorable formation of 9-membered complexes, 12-membered complexes with larger cations (Na⁺, K⁺, and Ca²⁺) as well as (thio-)B12C4-Li⁺. This might be due to the unfavorable size-relation between CE cavity and cation radius, possibly resulting in a ML₂ (sandwich) type complex. Based on this behavior, the complexation of Na⁺, K⁺, and Ca²⁺ can be selectively avoided. Independent of the heteroatom, a preferential complexation of Mg²⁺ for 15- and 12-membered CEs is present. Only for the 9-membered CEs, both divalent cations are complexed less than Li⁺, Na⁺ and K⁺. In solvent environment, the trend for the alkali metal ions is less pronounced compared to vacuum. Similarly, however, the dimensions do not differ decisively. For B15C5, aza-B15C5 and B12C4, Li⁺ complexation is favored, whereas thio-B15C5 appears to complex Na⁺ preferentially. In fact, for nitrogen and sulfur analogs of B12C4, very small deviations are observed, and no clear trend can be identified. B12C4, along with the 9-membered CEs, exhibits the following trend: K⁺ > Na⁺ > Li⁺, noticeably with a narrow variation.

Dependent on the type of complex, heteroatom substitution can lead to an improvement in complex stability. The presence of a sulfur atom in the CE ring leads in all cases (except for thio-B15C5-Na⁺ and thio-B9C3-Li⁺) to a reduced stability of the complexes, compared to the oxygen and nitrogen containing CEs. Although no significant influence of the substitution of an oxygen atom in the 15-membered system (with the exception of a slight improvement for thio-B15C5-Na⁺) on the complex stability can be observed, the 12-membered CEs indicate a positive effect of the introduction of a nitrogen atom as a donor atom. Interestingly, the presence

of nitrogen in aza-B12C4 enables lithium to be complexed in the first place. The Mg/Li ratio, which is particularly interesting for selective lithium extraction from seawater, changes for the stable complexes as follows: aza-B12C4 < thio-B15C5 < aza-B15C5 < B15C5, with the most stable Li⁺ incorporation into B15C5.

5.4. Calculation of the complex constant K from the liquid-liquid extraction

The following equations present more detailed information on the calculation of the equilibrium constant K from the experimental data. Due to the electroneutrality condition, only the activity, representing the deviation between the ideal and the real response of a salt in solution, of the entire system can be determined. Therefore, the mean activity coefficient $\gamma_{(+,-)}$ is applied for γ_+ and γ_- . According to Eq. Fehler! Verweisquelle konnte nicht gefunden werden.), $\gamma_{(+,-)}$ is calculated from the ionic charges z_+ and v_- , a dimensionless factor A (literature values, here: 0.5019) and the ionic strength I_a (Eq. Fehler! Verweisquelle konnte nicht gefunden werden.)). The stoichiometric coefficient Q can be calculated by Eq. Fehler! Verweisquelle konnte nicht gefunden werden.) based on the stoichiometric factors of the cation and anion, m and x .

$$\log(\gamma_{+,-}) = |z_+v_-| \cdot A \cdot \sqrt{I_a} \quad (1)$$

$$I_a = \frac{1}{2} \sum_i c_i \cdot z_i^2 \quad (2)$$

$$Q = (m^m \cdot x^x)^{\frac{1}{m+x}} \quad (3)$$

The concentration of the salt $[M_m^{z+}X_x^{v-}]$ and the CE before complexation $[CE]_{bc}$ are known. The amount of the CE-metal complex can be determined by the salts of the aqueous phase. The indices bc and ac refer to the situation *before* and *after complexation*. The concentration of the complex $[(M_mCE_n)^{mz_+}(X_x)_{(org)}^{xv_-}]$ can be calculated from Eq. (4). The concentrations of cations and anions after the complexation are determined as shown in Eq. (5) and Eq. (6), with m and x being the stoichiometric factors of the metal ion and the corresponding anion. The concentration of the free CE after the complexation process is calculated from Eq. (7).

$$[(M_mCE_n)^{mz_+}(X_x)_{(org)}^{xv_-}] = [complex] = [M_m^{z+}X_x^{v-}]_{bc} - [M_m^{z+}X_x^{v-}]_{ac} \quad (4)$$

$$[M^{z+}]^m = [M_m^{z+}X_x^{v-}]_{bc} - (m \cdot [complex]^m) \quad (5)$$

$$[X^{v-}]^x = \frac{x}{m} [M_m^{z+}X_x^{v-}]_{bc} - (x \cdot [complex]^x) \quad (6)$$

$$[CE]^n = [CE]_{bc} - (n \cdot [complex]^n) \quad (7)$$

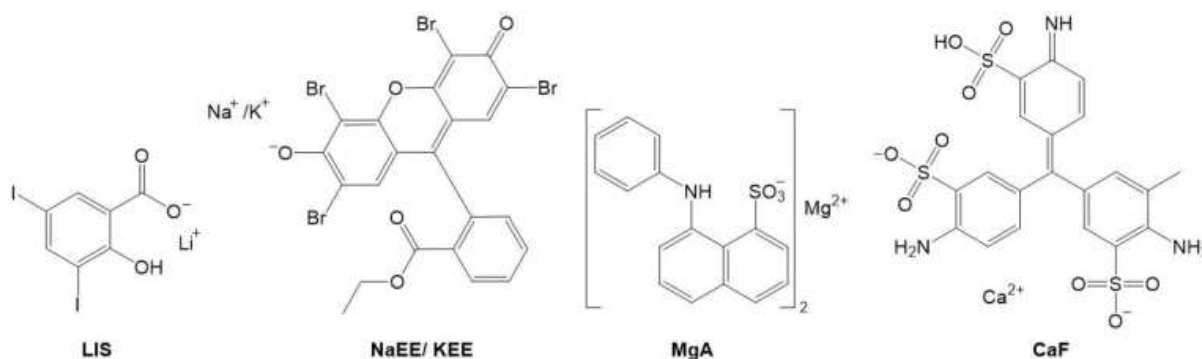


Figure S10: Salts used for LLE.

6. Input file for optimization of aza-15C5 in vacuum

```
%nprocshared = 32
%mem = 56GB
%Chk=aza-15c5_optfreqC.chk
#p opt=tight int=ultrafine freq b3lyp/def2tzvp geom=connectivity
empiricaldispersion=gd3bj
```

aza-15C5

0 1

C	1.50651492	-2.59255480	0.29029936
C	2.50326811	-1.46811358	0.33640907
O	0.20629625	-2.01868596	0.43898998
H	1.69523453	-3.31641665	1.08809791
H	1.57080198	-3.10180208	-0.67586402
O	2.14506904	-0.57898581	-0.71537429
H	3.51618205	-1.85531717	0.18821047
H	2.46435589	-0.96404534	1.30891925
C	2.95010820	0.59057235	-0.81644058
C	2.48770787	1.64217882	0.17076442
H	2.81383405	0.95534821	-1.83387050
H	4.00806831	0.35648045	-0.66749646
H	2.96433236	2.60127161	-0.05302052
H	2.72546045	1.37581821	1.20640756
C	0.44494361	2.81880549	0.67971992
C	-0.95491994	2.88691736	0.12523841
H	0.97455193	3.75542632	0.48552540
H	0.43612842	2.63508282	1.75932401
O	-1.49628330	1.57649699	0.24786410
H	-0.92801925	3.17863168	-0.93006478
H	-1.56030560	3.61104153	0.67837327
C	-2.71150190	1.36612425	-0.46422334
C	-3.14262941	-0.04043589	-0.14481834
H	-2.53739688	1.49513559	-1.53843626
H	-3.48056843	2.07649519	-0.14675870
O	-2.03151662	-0.89426852	-0.41340376
H	-4.00766069	-0.32979657	-0.74832146
H	-3.40882712	-0.11552377	0.91420091
C	-2.14052412	-2.17103524	0.21112221
C	-0.83669802	-2.88696875	-0.00459218
H	-2.96357538	-2.74779581	-0.22161096
H	-2.33079646	-2.03558562	1.28113511
H	-0.68889351	-3.11612721	-1.06507766
H	-0.82671654	-3.82293322	0.56179965
N	1.07620022	1.73338780	0.00578402
H	1.47032481	2.58888077	-0.76265393

1 2 1.0 3 1.0 4 1.0 5 1.0

2 6 1.0 7 1.0 8 1.0

3 30 1.0

4

5

6 9 1.0

7

8
9 10 1.0 11 1.0 12 1.0
10 13 1.0 14 1.0 35 1.0
11
12
13
14
15 16 1.0 17 1.0 18 1.0 35 1.0
16 19 1.0 20 1.0 21 1.0
17
18
19 22 1.0
20
21
22 23 1.0 24 1.0 25 1.0
23 26 1.0 27 1.0 28 1.0
24
25
26 29 1.0
27
28
29 30 1.0 31 1.0 32 1.0
30 33 1.0 34 1.0
31
32
33
34
35 36 1.0
36

Input file for optimization of aza-15C5 in DCM (based on optimization in vacuum):

```
%nprocshared = 32
%mem = 56GB
%Chk=aza-15c5_optfreqC.chk
#p opt freq b3lyp/def2tzvp geom=allcheck scrf=(solvent=dichloromethane)
empiricaldispersion=gd3bj formcheck
```

Input file for Hirshfeld analysis of aza-15C5 (based on optimization in vacuum):

```
%nprocshared = 32
%mem = 56GB
%Chk=aza-15c5_Hirshfeld.chk
#p SP b3lyp/def2tzvp geom=allcheck Pop=hirshfeld
```

Input file for NBO analysis of aza-15C5 (based on optimization in vacuum):

```
%nprocshared = 32
%mem = 56GB
%Chk= Li_azab15c5_NBO.chk
#p SP b3lyp/def2tzvp geom=allcheck Pop=(FULL,NBoread,savenbos) formcheck

$NBO PLOT FILE= NAME $END
```

9.4 Supporting information of publication 3

The supporting information is reprinted with permission from I. Oral, L. Grossmann, E. Fedorenko, J. Struck and V. Abetz, *Polymers*, **2021**, *13*, 3675 – published by MDPI.

Article

Synthesis of Poly(methacrylic acid)-*block*-Polystyrene Diblock Copolymers at High Solid Contents via RAFT Emulsion Polymerization

Iklima Oral ¹, Larissa Grossmann ¹, Elena Fedorenko ¹, Jana Struck ¹ and Volker Abetz ^{1,2,*}

¹ Institute of Physical Chemistry, Universität Hamburg, Grindelallee 117, 20146 Hamburg, Germany; iklima.oral@chemie.uni-hamburg.de (I.O.); larissa.grossmann@studium.uni-hamburg.de (L.G.); elena.fedorenko@chemie.uni-hamburg.de (E.F.); jana.struck@chemie.uni-hamburg.de (J.S.)

² Helmholtz-Zentrum Hereon, Institute of Membrane Research, Max-Planck-Straße 1, 21502 Geesthacht, Germany

* Correspondence: volker.abetz@hereon.de; Tel.: +49-40-42838-3460

Supplementary Materials

Citation: Oral, I.; Grossmann, L.; Fedorenko, E.; Struck, J.; Abetz, V. Synthesis of Poly(methacrylic acid)-*block*-Polystyrene Diblock Copolymers at High Solid Contents via RAFT Emulsion Polymerization. *Polymers* **2021**, *13*, 3675. <https://doi.org/10.3390/polym13213675>

Academic Editor: Leonard Ionut Atanase

Received: 3 October 2021

Accepted: 15 October 2021

Published: 25 October 2021

Publisher's Note: MDPI stays neutral with regard to jurisdictional claims in published maps and institutional affiliations.



Copyright: © 2021 by the authors. Submitted for possible open access publication under the terms and conditions of the Creative Commons Attribution (CC BY) license (<https://creativecommons.org/licenses/by/4.0/>).

Table S1. Kinetic Data of the Polymerization of PMAA at 70 °C and a molar ratio of [CTA]/[ACVA] = 10 and [MAA]/[CTA] = 120. $M_{n,theo}$ represents the theoretical number-average molecular weight of PMAA and $M_{n,exp}$ the experimental theoretical number-average molecular weight measured by SEC. The dispersity M_w/M_n was determined by aqueous SEC using PEO calibration. CTA1 represents the RAFT CTA with a propyl terminus as a Z-group and CTA2 the butyl terminus.

CTA	Solvent	Time [min]	Conversion [%]	$M_{n,theo}$ [kDa]	$M_{n,exp}$ [kDa]	M_w/M_n
CTA1	water	0	0	0	-	-
CTA1	water	60	33.9	3.59	32.1	1.10
CTA1	water	120	75.8	8.04	37.2	1.08
CTA1	water	180	89.8	9.52	39.7	1.07
CTA1	water	240	97.3	10.3	40.2	1.12
CTA1	water	300	98.5	10.4	41.2	1.06
CTA1	water	360	99.1	10.5	42.0	1.07
CTA1	ethanol	0	0	0	-	-
CTA1	ethanol	60	0	0	-	-
CTA1	ethanol	120	23.2	2.46	17.9	1.10
CTA1	ethanol	180	36.3	4.46	21.2	1.10
CTA1	ethanol	240	48.3	5.93	24.6	1.09
CTA1	ethanol	300	59.4	7.30	27.2	1.09
CTA1	ethanol	360	69.1	8.50	31.9	1.08
CTA1	1,4-dioxane	0	0	0	-	-
CTA1	1,4-dioxane	60	30.5	3.74	-	-
CTA1	1,4-dioxane	120	54.6	6.71	28.8	1.14
CTA1	1,4-dioxane	180	64.0	7.87	34.2	1.11
CTA1	1,4-dioxane	240	75.2	9.24	35.9	1.10
CTA1	1,4-dioxane	300	78.8	9.69	36.8	1.10
CTA2	water	0	0	0	-	-
CTA2	water	60	7.00	0.743	-	-
CTA2	water	120	51.5	5.47	51.3	1.18
CTA2	water	180	73.3	7.78	59.2	1.18
CTA2	water	240	90.1	9.56	63.4	1.19
CTA2	water	300	95.2	10.1	66.6	1.20
CTA2	water	360	97.8	10.4	66.9	1.20
CTA2	ethanol	0	0	0	-	-
CTA2	ethanol	60	40.0	4.24	20.7	1.17
CTA2	ethanol	120	50.6	5.37	30.0	1.19
CTA2	ethanol	180	54.7	5.81	36.8	1.19
CTA2	ethanol	240	65.4	6.95	43.9	1.17
CTA2	ethanol	300	65.9	7.00	46.9	1.18
CTA2	ethanol	360	66.7	7.08	51.4	1.18
CTA2	1,4-dioxane	0	0	0	-	-
CTA2	1,4-dioxane	60	22.8	2.42	39.4	1.13
CTA2	1,4-dioxane	120	36.9	3.92	50.8	1.06
CTA2	1,4-dioxane	180	55.1	5.85	53.2	1.12
CTA2	1,4-dioxane	240	58.9	6.26	54.9	1.12
CTA2	1,4-dioxane	300	68.5	7.27	55.8	1.13
CTA2	1,4-dioxane	360	72.6	7.71	58.5	1.13

Table S2. Kinetic Data of the Polymerization of PMAA with CTA3 with a molar ratio of [MAA]/[CTA3] = 120. $M_{n,theo}$ represents the theoretical number-average molecular weight of PMAA and $M_{n,exp}$ the experimental theoretical number-average molecular weight measured by SEC. The dispersity M_w/M_n was determined by aqueous SEC using PEO calibration. CTA3 represents the RAFT CTA with a dodecyl- terminus as a Z-group.

[CTA]/ [ACVA]	Solvent	Time [min]	Temperature [°C]	Conversion [%]	$M_{n,theo}$ [kDa]	$M_{n,exp}$ [kDa]	M_w/M_n
10	1,4-dioxane	0	70	0	0	-	-
10	1,4-dioxane	60	70	8.00	0.968	10.6	1.73
10	1,4-dioxane	120	70	12.5	1.35	11.0	1.72
10	1,4-dioxane	180	70	17.6	1.87	12.3	1.67
10	1,4-dioxane	240	70	23.2	2.49	13.2	1.66
10	1,4-dioxane	300	70	27.5	2.95	14.4	1.59
10	1,4-dioxane	1170	70	75.1	8.06	19.3	1.51
10	ethanol	0	70	0	0	-	-
10	ethanol	60	70	3.80	0.410	4.30	1.74
10	ethanol	120	70	2.70	0.295	4.70	1.78
10	ethanol	180	70	5.20	0.557	4.80	1.78
10	ethanol	240	70	3.70	0.393	5.10	1.78
10	ethanol	300	70	7.20	0.770	5.30	1.78
10	ethanol	1170	70	45.8	4.91	18.3	1.27
10	1-propanol	0	70	0	0	-	-
10	1-propanol	60	70	0	0	-	-
10	1-propanol	120	70	0	0	-	-
10	1-propanol	180	70	0	0	-	-
10	1-propanol	240	70	0	0	-	-
10	1-propanol	300	70	0	0	-	-
10	1,4-dioxane	0	80	0	0	-	-
10	1,4-dioxane	60	80	19.5	2.10	11.6	1.70
10	1,4-dioxane	120	80	29.6	3.17	14.9	1.59
10	1,4-dioxane	180	80	32.3	3.47	17.0	1.48
10	1,4-dioxane	240	80	40.7	4.37	19.5	1.40
10	1,4-dioxane	300	80	41.8	4.49	19.4	1.43
10	1,4-dioxane	360	80	43.5	4.66	19.6	1.43
10	ethanol	0	80	0	0	-	-
10	ethanol	60	80	9.20	0.990	5.50	1.73
10	ethanol	120	80	11.4	1.23	6.90	1.64
10	ethanol	180	80	11.4	1.23	7.10	1.65
10	ethanol	240	80	9.86	1.06	7.30	1.65
10	ethanol	300	80	13.9	1.49	7.60	1.64
10	ethanol	360	80	12.5	1.34	7.70	1.63
10	1-propanol	0	80	0	0	-	-
10	1-propanol	60	80	17.6	1.89	15.7	1.15
10	1-propanol	120	80	29.5	3.16	19.2	1.12
10	1-propanol	180	80	37.7	4.05	21.5	1.11
10	1-propanol	240	80	42.3	4.54	22.7	1.11
10	1-propanol	300	80	42.9	4.61	23.1	1.11
10	1-propanol	360	80	42.0	4.51	23.1	1.16
5	1,4-dioxane	0	80	0	0	-	-
5	1,4-dioxane	60	80	32.4	3.48	16.8	1.53
5	1,4-dioxane	120	80	49.1	5.27	21.3	1.41

[CTA1]/ [ACVA]	Solvent	Time [min]	Temperature [°C]	Conversion [%]	$M_{n,theo}$ [kDa]	$M_{n,exp}$ [kDa]	M_w/M_n
5	1,4-dioxane	180	80	65.1	6.99	26.4	1.34
5	1,4-dioxane	240	80	80.1	8.59	29.9	1.27
5	ethanol	0	80	0	0	-	-
5	ethanol	60	80	23.2	2.49	8.70	1.55
5	ethanol	120	80	40.3	4.32	14.3	1.38
5	ethanol	180	80	53.0	5.69	18.7	1.29
5	ethanol	240	80	60.5	6.49	22.1	1.24
5	ethanol	300	80	63.5	6.81	23.8	1.21
5	ethanol	360	80	64.4	6.91	24.9	1.21
5	1-propanol	0	80	0	0	-	-
5	1-propanol	60	80	24.6	2.64	17.9	1.13
5	1-propanol	120	80	56.0	6.01	26.1	1.13
5	1-propanol	180	80	69.7	7.48	28.7	1.09
5	1-propanol	240	80	75.6	8.11	30.4	1.09
5	1-propanol	300	80	77.7	8.34	30.4	1.09
5	1-propanol	360	80	79.0	8.47	30.6	1.09

Table S3. Kinetic Data of the Polymerization of PMAA₅-*b*-PS₉₅⁵⁴ with CTA1 at 80 °C in water and a targeted styrene DP of 502 with a [CTA1]/[ACVA] molar ratio of 5. r_{TEM} represents the number-average radius obtained by TEM. $M_{n,theo}$ represents the theoretical number-average molecular weight of PMAA-*b*-PS and $M_{n,theo}^*$ the theoretical number-average molecular weight of PMMA-*b*-PS. The dispersity M_w/M_n was determined by SEC THF using PS calibration.

Time [min]	Conversion [%]	r_{TEM} [nm]	$M_{n,theo}$ [kDa]	$M_{n,theo}^*$ [kDa]	$M_{n,exp}$ [kDa]	M_w/M_n
35	3.1	-	4.48	4.90	-	-
40	16	15 ± 2	11.1	11.5	12.5	1.13
45	20	18 ± 2	13.5	14.0	25.5	1.26
50	56	25 ± 2	31.9	32.3	43.2	1.30
55	74	24 ± 3	42.0	42.0	56.2	1.30
60	85	27 ± 3	47.4	47.8	64.2	1.27
120	99	29 ± 3	54.4	54.8	69.1	1.33

Table S4. Kinetic Data of the Polymerization of PMAA₁₀-*b*-PS₉₀⁴⁵ with CTA1 at 80 °C in water and a targeted MAA DP of 50 and a styrene DP of 400 with a [CTA1]/[ACVA] molar ratio of 5 at 20 wt%. r_{TEM} represents the number-average radius obtained by TEM and r_{DLS} by DLS. $M_{n,theo}$ represents the theoretical number-average molecular weight of PMAA-*b*-PS and $M_{n,theo}^*$ the theoretical number-average molecular weight of PMMA-*b*-PS. The dispersity M_w/M_n was determined by SEC THF using PS calibration after methylation.

Time [min]	Conversion [%]	r_{DLS} [nm]	<i>PDI</i>	r_{TEM} [nm]	$M_{n,theo}$ [kDa]	$M_{n,theo}^*$ [kDa]	$M_{n,exp}$ [kDa]	M_w/M_n
60	48	24 ± 1	0.3 ± 0.2	-	22.3	22.7	-	-
70	56	28.88 ± 0.06	0.09 ± 0.02	-	25.8	26.2	30.0	1.17
80	78	31.79 ± 0.06	0.08 ± 0.02	-	36.3	36.3	53.8	1.28
90	93	31.9 ± 0.2	0.07 ± 0.02	-	43.2	43.2	66.7	1.28
120	97	32.0 ± 0.5	0.04 ± 0.02	24 ± 3	45.0	44.9	69.5	1.26

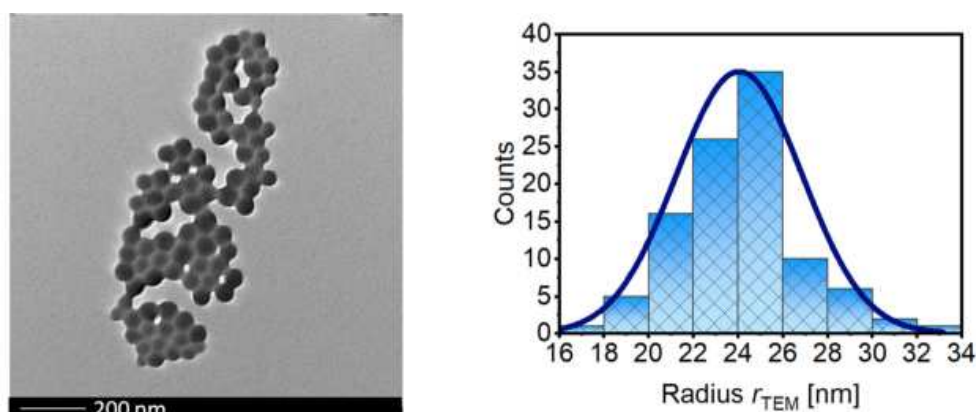


Figure S1. TEM image (left) and histogram (right) of the number-average radius of the PMAA₁₀-*b*-PS₉₀⁴⁵ with CTA1 copolymer and 20 wt% after 120 minutes reaction time.

Table S5. Kinetic Data of the Polymerization of PMAA₁₀-*b*-PS₉₀⁴⁵ with CTA1 at 80 °C in water and a targeted MAA DP of 50 and a styrene DP of 400 with a [CTA1]/[ACVA] molar ratio of 5 at 25 wt%. r_{TEM} represents the number-average radius obtained by TEM and r_{DLS} by DLS. $M_{n,theo}$ represents the theoretical number-average molecular weight of PMAA-*b*-PS and $M_{n,theo}^*$ the theoretical number-average molecular weight of PMMA-*b*-PS. The dispersity M_w/M_n was determined by SEC THF using PS calibration after methylation.

Time [min]	Conversion [%]	r_{DLS} [nm]	<i>PDI</i>	r_{TEM} [nm]	$M_{n,theo}$ [kDa]	$M_{n,theo}^*$ [kDa]	$M_{n,exp}$ [kDa]	M_w/M_n
50	1.8	-	-	-	1.09	1.10	-	-
60	7.5	26 ± 1	0.4 ± 0.2	-	3.84	3.89	-	-
70	34	28.88 ± 0.06	0.09 ± 0.02	-	15.9	16.2	27.3	1.35
80	67	30.6 ± 0.3	0.07 ± 0.02	24 ± 2	31.1	31.5	51.7	1.35
90	86	32.5 ± 0.6	0.08 ± 0.03	-	39.8	40.4	70.8	1.40
120	94	33.1 ± 0.3	0.04 ± 0.01	29 ± 3	43.6	44.2	71.0	1.50

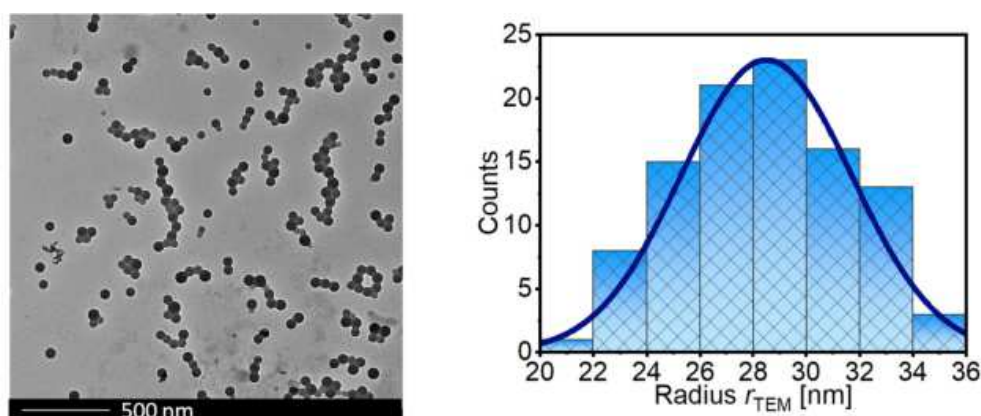


Figure S2. TEM image (left) and histogram (right) of the number-average radius of the PMAA₁₀-*b*-PS₉₀⁴⁵ with CTA1 copolymer and 25 wt% after 120 minutes reaction time.

Table S6. Kinetic Data of the Polymerization of PMAA₁₀-*b*-PS₉₀⁴⁵ with CTA1 at 80 °C in water and a targeted MAA DP of 50 and a styrene DP of 400 with a [CTA1]/[ACVA] molar ratio of 5 at 30 wt%. r_{TEM} represents the number-average radius obtained by TEM and r_{DLS} by DLS. $M_{n,theo}$ represents the theoretical number-average molecular weight of PMAA-*b*-PS and $M_{n,theo}^*$ the theoretical number-average molecular weight of PMMA-*b*-PS. The dispersity M_w/M_n was determined by SEC THF using PS calibration after methylation.

Time [min]	Conversion [%]	r_{DLS} [nm]	<i>PDI</i>	r_{TEM} [nm]	$M_{n,theo}$ [kDa]	$M_{n,theo}^*$ [kDa]	$M_{n,exp}$ [kDa]	M_w/M_n
180	6.9	-	-	-	3.44	3.49	-	-
240	18	-	-	-	8.38	8.50	-	-
300	28	42.1 ± 0.3	0.56 ± 0.04	26 ± 2	13.0	13.2	26.0	1.38

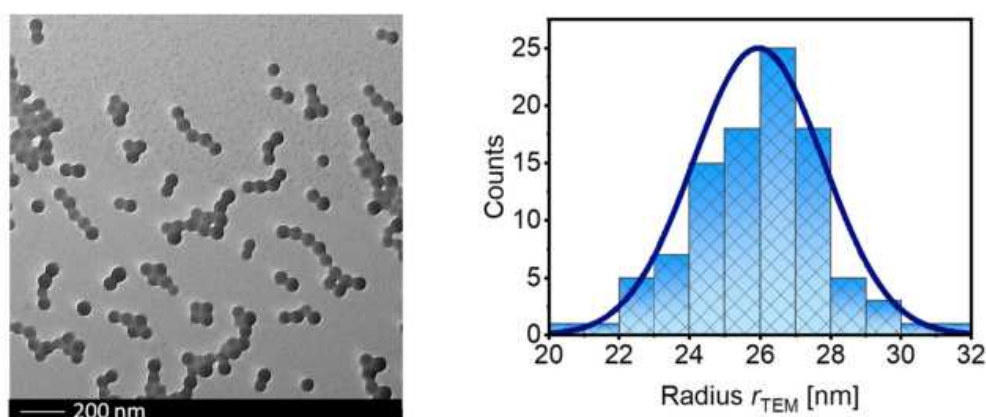


Figure S3. TEM image (left) and histogram (right) of the number-average radius of the PMAA₁₀-*b*-PS₉₀⁴⁵ with CTA1 copolymer and 30 wt% after 300 minutes reaction time.

Table S7. Polymerization of PMAA₂₀-*b*-PS₈₀¹⁸ with CTA3 at 80 °C in water and a targeted styrene DP of 200 with a [CTA3]/[ACVA] molar ratio of 5. r_{TEM} represents the number-average radius obtained by TEM and r_{DLS} by DLS. $M_{n,theo}$ represents the theoretical number-average molecular weight of PMAA-*b*-PS. The dispersity M_w/M_n was determined by SEC THF + 35 mmol TFA using universal PS calibration. The PMAA-CTA3 macro-CTA was synthesized in ethanol and determined with NMR and aqueous SEC using PEO calibration with $M_{n,theo} = 3.8$ kDa and a $M_w/M_n = 1.11$.

(<i>w/w</i>) solids [%]	Time [min]	Conversion [%]	r_{TEM} [nm]	r_{DLS} [nm]	<i>PDI</i>	$M_{n,theo}$ [kDa]	$M_{n,exp}$ [kDa]	M_w/M_n
40	10	0	-	-	-	3.8	-	-
40	20	0	-	-	-	3.8	-	-
40	30	6.5	-	36.0 ± 0.5	0.15 ± 0.06	4.8	-	-
40	40	24	-	40.2 ± 0.4	0.03 ± 0.02	7.4	-	-
40	50	45	-	44.6 ± 0.1	0.07 ± 0.01	10	35	1.17
40	60	65	-	48.2 ± 0.5	0.05 ± 0.05	13	46	1.20
40	70	78	-	49.6 ± 0.4	0.02 ± 0.02	15	53	1.20
40	80	91	45 ± 3	51.8 ± 0.6	0.05 ± 0.02	17	59	1.23
50	10	0	-	-	-	3.8	-	-
50	20	0	-	-	-	3.8	-	-
50	30	9.4	-	34.9 ± 0.5	0.14 ± 0.09	5.3	-	-
50	40	40	-	38.9 ± 2.5	0.21 ± 0.23	9.7	35	1.18
50	50	63	-	44.6 ± 0.3	0.06 ± 0.05	13	46	1.18
50	60	77	-	47.2 ± 0.6	0.03 ± 0.02	15	55	1.20
50	70	92	-	48.7 ± 0.6	0.04 ± 0.03	17	62	1.21
50	80	94	41 ± 2	50 ± 1	0.06 ± 0.05	18	63	1.23

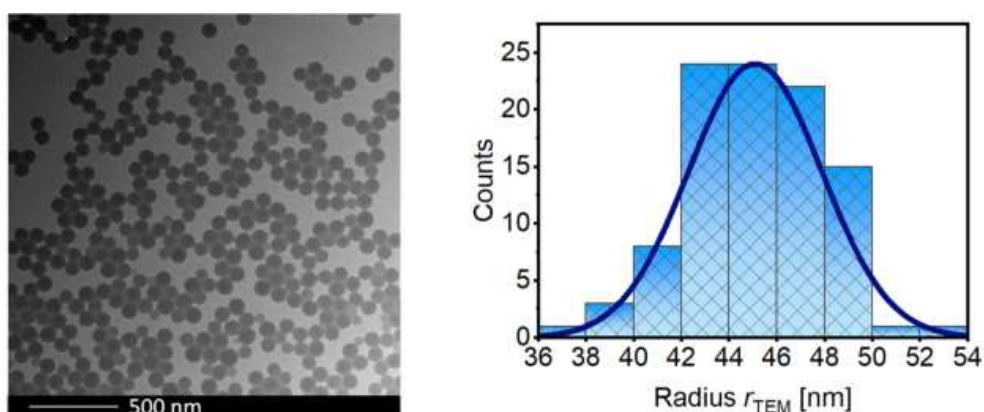


Figure S4. TEM image (left) and histogram (right) of the number-average radius of the PMAA₂₀-*b*-PS₈₀¹⁸ with CTA3 copolymer and 40 wt%.

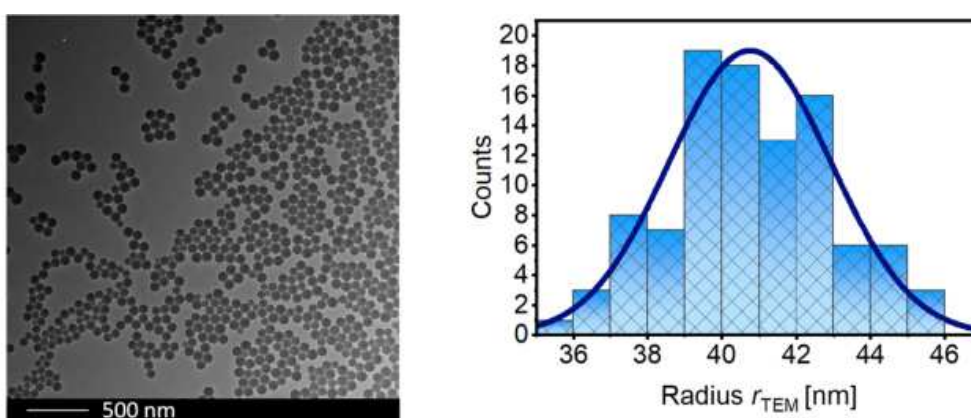


Figure S5. TEM image (left) and histogram (right) of the number-average radius of the PMAA₂₀-*b*-PS₈₀¹⁸ with CTA3 copolymer and 50 wt%.

Table S8. Kinetic Data of the Polymerization of PMAA₂₀-*b*-PS₈₀⁴² with CTA3 at 80 °C in water with a targeted styrene DP of 320 with a [CTA3]/[ACVA] molar ratio of 5 at 50 wt%. r_{TEM} represents the number-average radius obtained by TEM and r_{DLS} by DLS. $M_{n,theo}$ represents the theoretical number-average molecular weight of PMAA-*b*-PS and $M_{n,theo}^*$ the theoretical number-average molecular weight of PMMA-*b*-PS. The dispersity M_w/M_n was determined by SEC THF + 35 mmol TFA using universal PS calibration. The PMAA-CTA3 macro-CTA was synthesized in 1-propanol and determined with NMR and aqueous SEC using PEO calibration with $M_{n,theo} = 8.5$ kDa and a $M_w/M_n = 1.09$.

Time [min]	Conversion [%]	r_{DLS} [nm]	<i>PDI</i>	r_{TEM} [nm]	$M_{n,theo}$ [kDa]	$M_{n,exp}$ [kDa]	M_w/M_n
20	0	-	-	-	-	-	-
40	2.2	41.1 ± 0.7	0.55 ± 0.05	-	9.2	-	-
60	32	48 ± 1	0.06 ± 0.04	32 ± 3	19	27.6	1.16
80	74	53.2 ± 0.8	0.05 ± 0.03	42 ± 4	33	50.3	1.20
100	95	57 ± 1	0.05 ± 0.05	42 ± 4	40	58.9	1.21
120	98	58 ± 1	0.02 ± 0.02	-	41	59.2	1.22
140	98	56.2 ± 0.8	0.05 ± 0.02	-	41	59.6	1.22

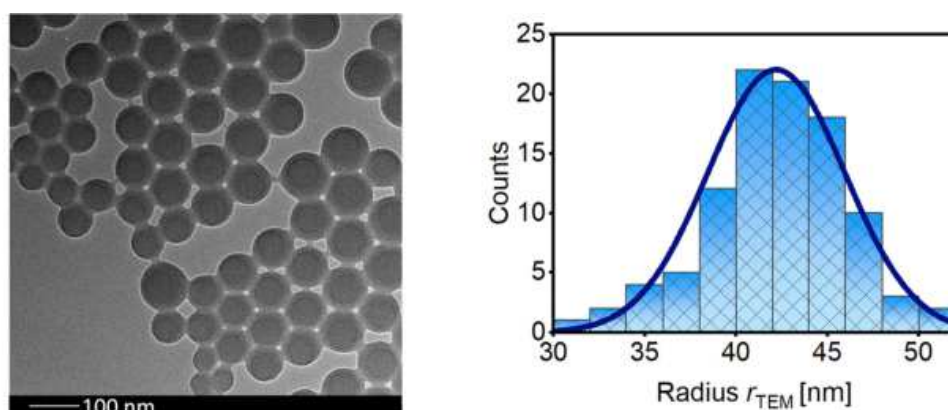


Figure S6. TEM image (left) and histogram (right) of the number-average radius of the of PMAA₂₀-*b*-PS₈₀⁴² after 100 minutes reaction time with CTA3 copolymer and 50 wt% and 80 % weight fraction of styrene.

Table S9. Kinetic Data of the Polymerization of PMAA₁₀-*b*-PS₉₀⁸⁶ with CTA3 at 80 °C in water with a targeted styrene DP of 740 with a [CTA3]/[ACVA] molar ratio of 5 at 50 wt%. r_{TEM} represents the number-average radius obtained by TEM and r_{DLS} by DLS. $M_{n,theo}$ represents the theoretical number-average molecular weight of PMAA-*b*-PS and $M_{n,theo}^*$ the theoretical number-average molecular weight of PMMA-*b*-PS. The dispersity M_w/M_n was determined by SEC THF + 35 mmol TFA using universal PS calibration. The PMAA-CTA3 macro-CTA was synthesized in 1-propanol and determined with NMR and aqueous SEC using PEO calibration with $M_{n,theo} = 8.5$ kDa and a $M_w/M_n = 1.09$.

Time [min]	Conversion [%]	r_{DLS} [nm]	<i>PDI</i>	r_{TEM} [nm]	$M_{n,theo}$ [kDa]	$M_{n,exp}$ [kDa]	M_w/M_n
20	0	-	-	-	-	-	-
40	0	-	-	-	-	-	-
60	2.0	-	-	-	10	-	-
80	5.1	50.1 ± 0.5	0.07 ± 0.02	-	12	10.2	2.63
120	22	59.2 ± 0.5	0.04 ± 0.02	39 ± 4	26	41.9	1.27
145	38	62.7 ± 0.5	0.03 ± 0.03	52 ± 6	38	57.7	1.32
160	45	65.3 ± 0.8	0.07 ± 0.02	55 ± 4	43	69.9	1.40
180	60	69.6 ± 0.2	0.1 ± 0.1	60 ± 5	55	91.4	1.43

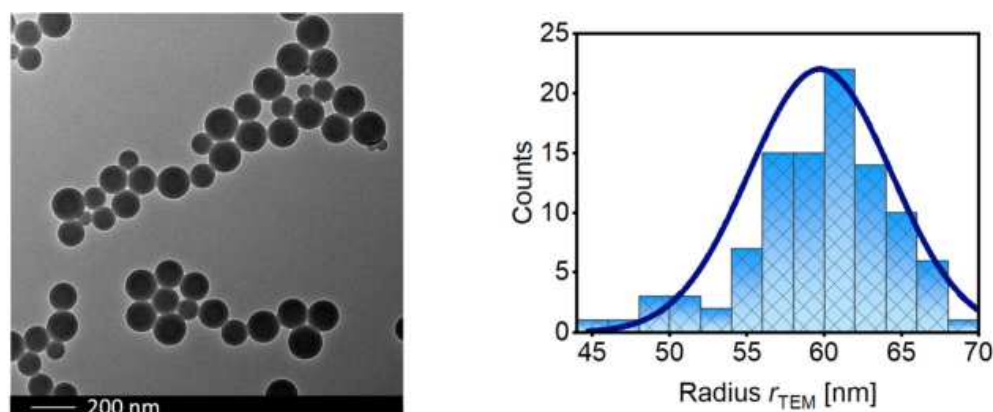


Figure S7. TEM image (left) and histogram (right) of the number-average radius of the of PMAA₁₀-*b*-PS₉₀⁸⁶ after 180 minutes reaction time with CTA3 copolymer and 50 wt% and 90 % weight fraction of styrene.

Table S10. Kinetic Data of the Polymerization of PMAA₅-*b*-PS₉₅¹⁶⁵ with CTA3 at 80 °C in water with a targeted styrene DP of 1500 with a [CTA3]/[ACVA] molar ratio of 5 at 50 wt%. r_{TEM} represents the number-average radius obtained by TEM and r_{DLS} by DLS. $M_{n,theo}$ represents the theoretical number-average molecular weight of PMAA-*b*-PS and $M_{n,theo}^*$ the theoretical number-average molecular weight of PMMA-*b*-PS. The dispersity M_w/M_n was determined by SEC THF + 35 mmol TFA using universal PS calibration. The PMAA-CTA3 macro-CTA was synthesized in 1-propanol and determined with NMR and aqueous SEC using PEO calibration with $M_{n,theo} = 8.5$ kDa and a $M_w/M_n = 1.09$.

Time [min]	Conversion [%]	r_{DLS} [nm]	<i>PDI</i>	r_{TEM} [nm]	$M_{n,theo}$ [kDa]	$M_{n,exp}$ [kDa]	M_w/M_n
20	0	-	-	-	-	-	-
40	0	-	-	-	-	-	-
60	0	-	-	-	-	-	-
80	1	-	-	-	10	-	-
100	3	58.4 ± 0.1	0.07 ± 0.02	-	14	34.1	1.15
120	6.9	61.1 ± 0.7	0.06 ± 0.02	-	19	37.1	1.24
140	8.9	64.6 ± 0.8	0.06 ± 0.05	-	22	43.5	1.28
160	11	66.7 ± 0.5	0.06 ± 0.02	-	26	45.1	1.30
180	13	69.5 ± 0.4	0.06 ± 0.02	55 ± 7	28	45.7	1.40

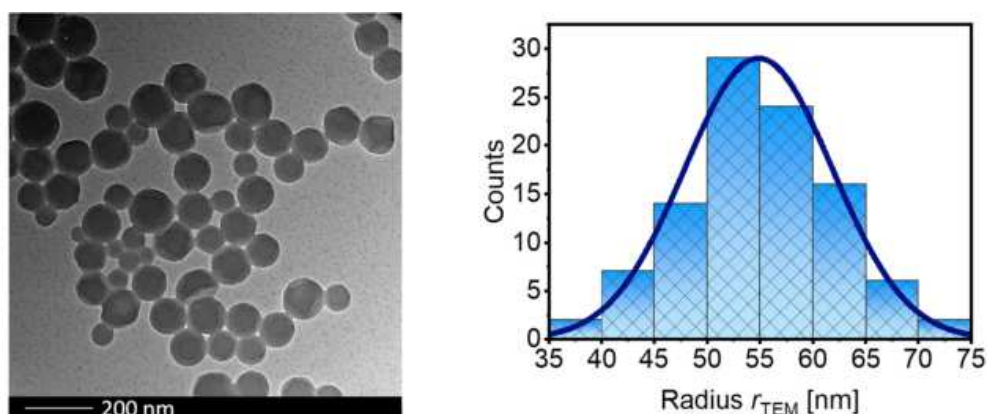


Figure S8. TEM image (left) and histogram (right) of the number-average radius of the of PMAA₅-*b*-PS₉₅¹⁶⁵ after 180 minutes reaction time with CTA3 copolymer and 50 wt% and 90 % weight fraction of styrene.

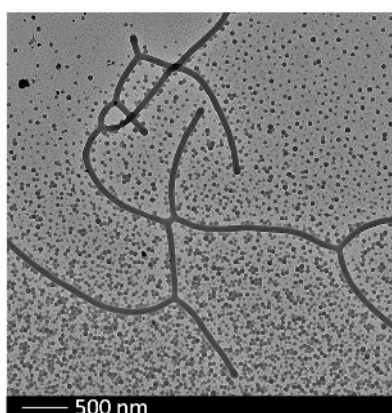


Figure S9. TEM image of PMAA₄₀-*b*-PS₆₀⁴⁶ after full conversion with CTA1 copolymer and 20 wt%.

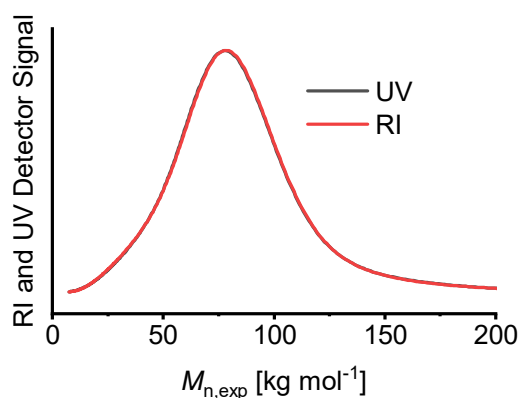


Figure S10. SEC results of PMAA₂₀-*b*-PS₈₀⁴² with CTA3 at 50 wt% after full conversion.

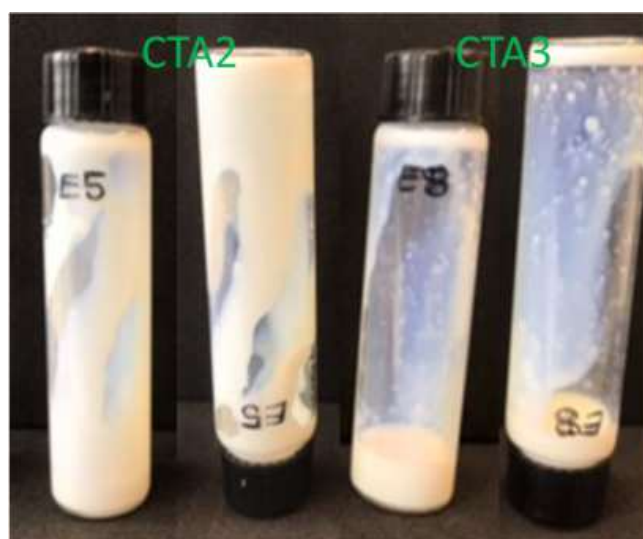


Figure S11. Pictures of the polymerization of PMAA-*b*-PS with CTA2 and CTA3 at 40 wt%. The polymerization with CTA2 shows clearly a more viscous medium.

Table S11. Overview of the PMAA-*b*-PS polymerizations with the corresponding macro-CTAs. SEC data for macro-CTA1 for polymer PMAA₁₀-*b*-PS₉₀⁴⁵ was determined with aqueous SEC using PAA calibration. All other macro-CTAs were measured against PEO calibration as it was mentioned in the previous tables. For more detailed information see Table S3-S10.

Targeted polymer	Time [min]	(<i>w/w</i>) solids [%]	Macro-CTA	DP PMAA	$M_{n,theo}$ PMAA [kDa]	M_n, M_w PMAA	Targeted DP PS	Targeted PS $M_{n,theo}$ [kDa]	PS Conversion	$M_{n,exp}$ PMAA- <i>b</i> -PS [kDa]	M_n, M_w PMAA- <i>b</i> -PS
PMAA ₀₅ - <i>b</i> -PS ₉₅ ⁵⁴	120	20	CTA1	30	2.9	1.06	502	52.3	99	69.1	1.33
PMAA ₁₀ - <i>b</i> -PS ₉₀ ⁴⁵	120	20	CTA1	50	4.5	1.25	400	41.7	97	69.5	1.26
PMAA ₁₀ - <i>b</i> -PS ₉₀ ⁴⁵	120	25	CTA1	50	4.5	1.25	400	41.7	94	71.0	1.50
PMAA ₁₀ - <i>b</i> -PS ₉₀ ⁴⁵	300	30	CTA1	50	4.5	1.25	400	41.7	28	26.0	1.38
PMAA ₂₀ - <i>b</i> -PS ₈₀ ⁴⁶	240	35	CTA2	101	8.7	1.17	360	37.4	99	166	1.57
PMAA ₂₀ - <i>b</i> -PS ₈₀ ⁴⁶	240	40	CTA2	101	8.7	1.17	360	37.4	99	158	1.61
PMAA ₂₀ - <i>b</i> -PS ₈₀ ¹⁸	80	40	CTA3	43	3.8	1.11	140	33.2	91	59.0	1.23
PMAA ₂₀ - <i>b</i> -PS ₈₀ ¹⁸	80	50	CTA3	43	3.8	1.11	140	33.2	94	63.0	1.23
PMAA ₂₀ - <i>b</i> -PS ₈₀ ⁴²	140	50	CTA3	95	8.5	1.09	320	33.2	99	59.6	1.22
PMAA ₁₀ - <i>b</i> -PS ₉₀ ⁸⁶	180	50	CTA3	95	8.5	1.09	740	77.0	60	91.4	1.43
PMAA ₀₅ - <i>b</i> -PS ₉₅ ¹⁶⁵	180	50	CTA3	95	8.5	1.09	1500	156	13	45.7	1.40

9.5 Supporting information of publication 4

The supporting information is reprinted with permission from I. Oral and V. Abetz, *Macromol. Rapid Commun.*, **2021**, *42*, 2000746 – published by Wiley-VCH GmbH.



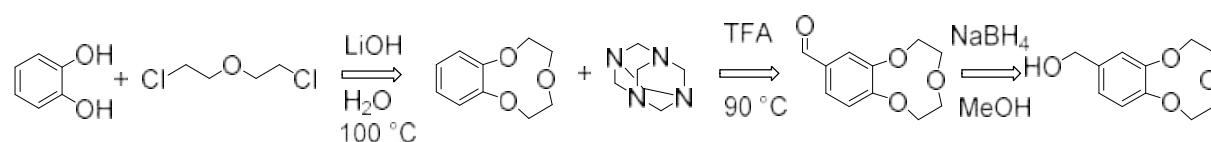
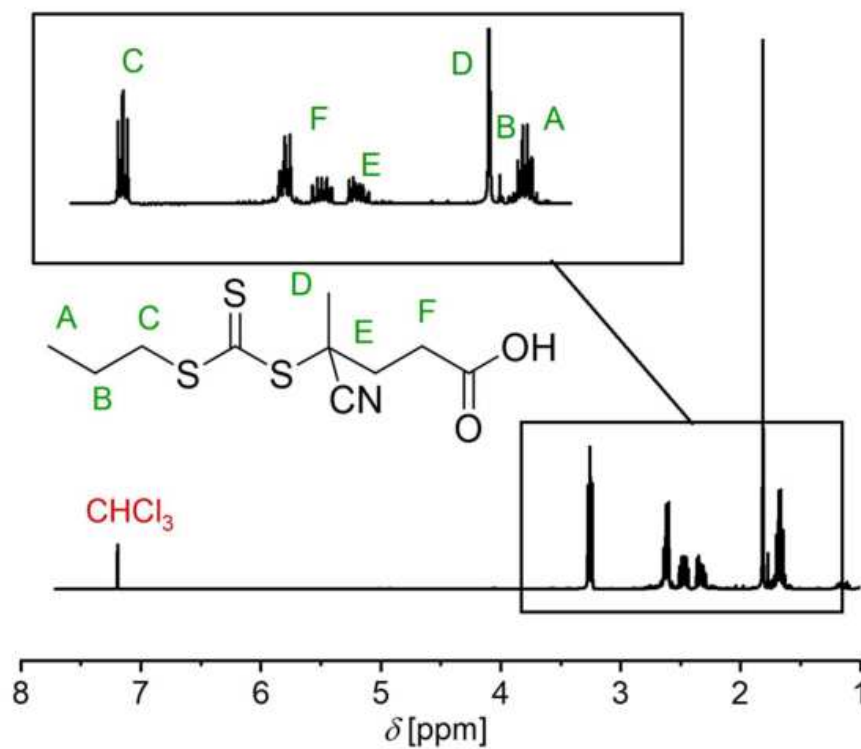
Supporting Information

for *Macromol. Rapid Commun.*, DOI: 10.1002/marc.202000746

A Highly Selective Polymer Material using Benzo-9-Crown-3 for the Extraction of Lithium in Presence of Other Interfering Alkali Metal Ions

Iklima Oral and Volker Abetz*

Supporting Information

A Highly Selective Polymer Material using Benzo-9-Crown-3 for the Extraction of Lithium in Presence of other Interfering Alkali Metal Ions*Iklima Oral, Volker Abetz****Synthetic Route B9C3-OH****Figure S1.** Schematic illustration of the synthesis of B9C3-OH.**NMR Data Analysis****Figure S2.** ¹H NMR spectroscopy of the CPP CTA.

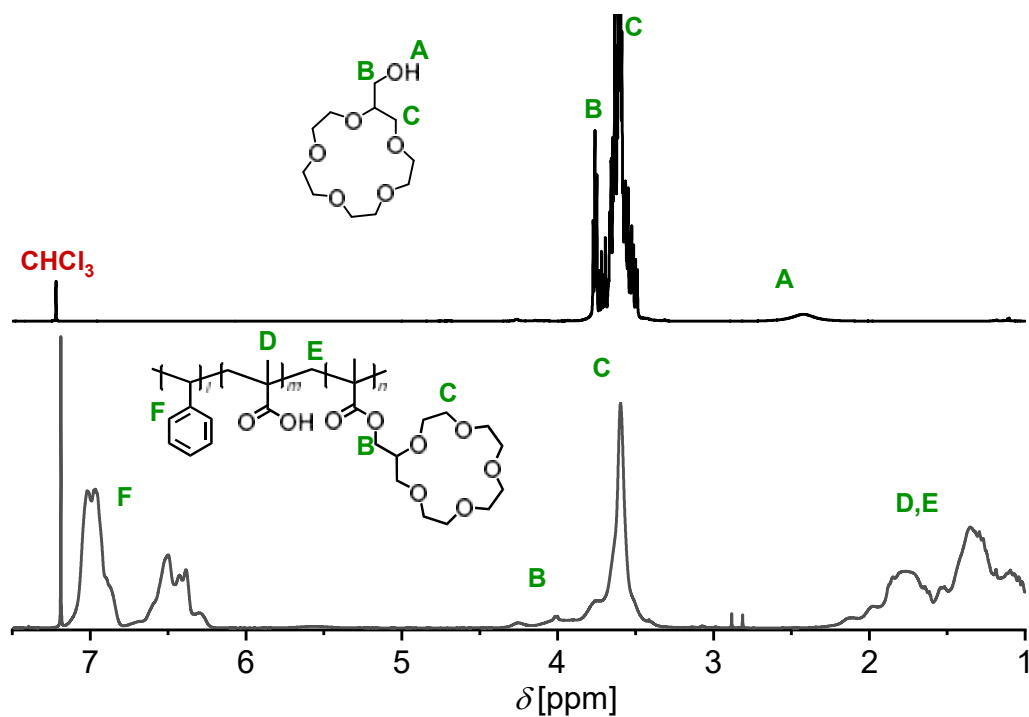


Figure S3. ¹H NMR spectrum of 15-crown-5 CE (top) and PS₅₁-*b*-P(MAA₂₅-*r*-CE5MA₂₄)⁵⁶ diblock copolymer containing randomly distributed CE units (bottom).

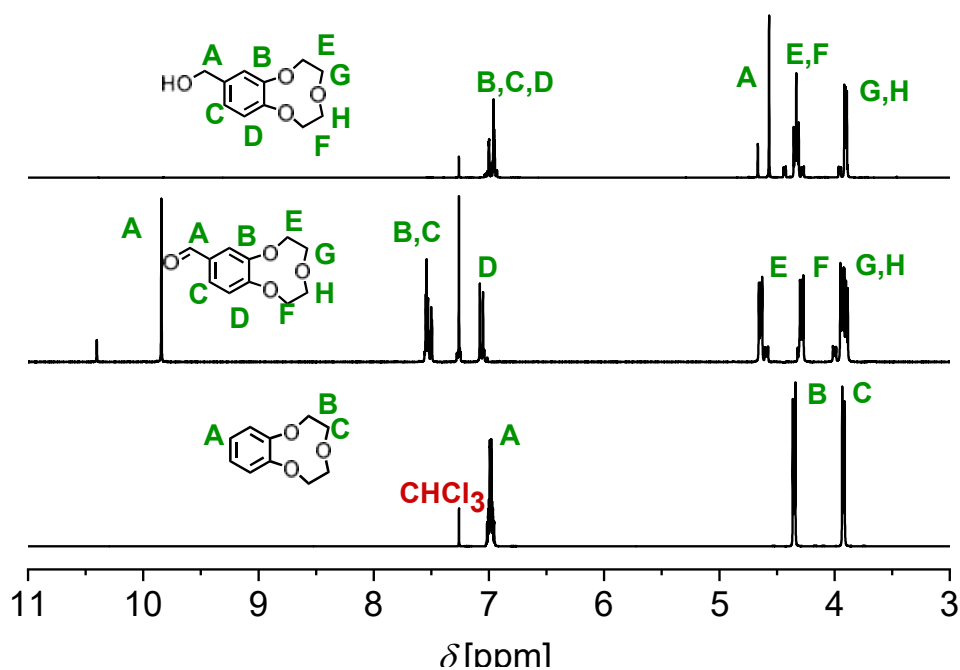


Figure S4. ¹H NMR spectroscopy of B9C3 CE (bottom), B9C3 CHO (middle), and B9C3-OH (top).

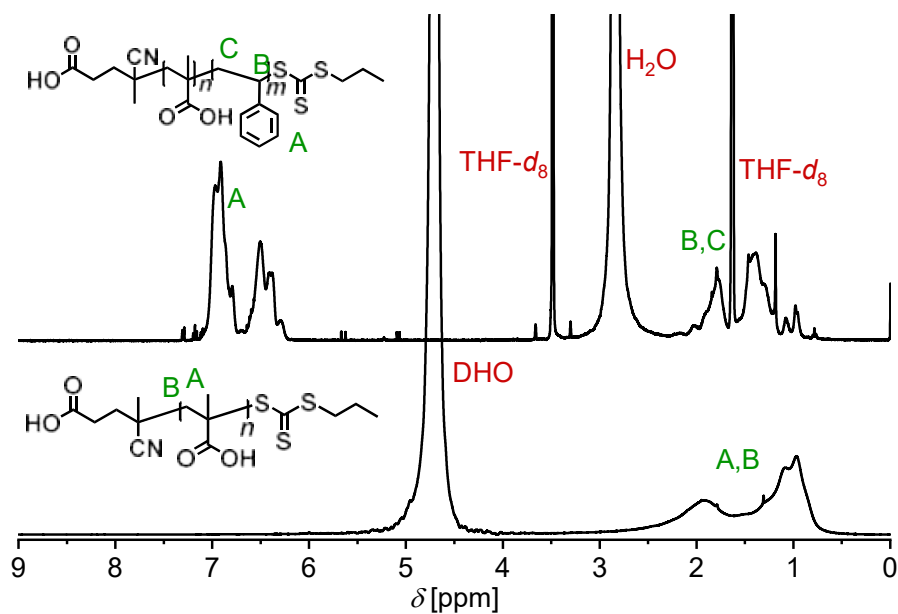


Figure S5. ¹H NMR spectrum of PMAA¹⁷ in D₂O (bottom) and PS₆₂-*b*-PMAA₃₈⁴⁶ in THF-*d*₈ (top) during the one-pot solution-emulsion polymerization.

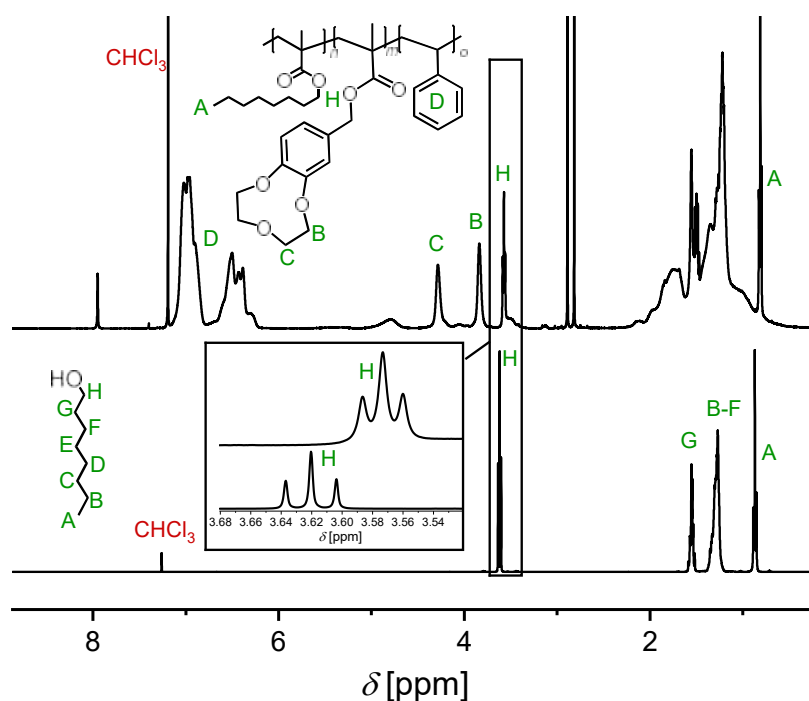


Figure S6. ¹H NMR spectrum of 1-octanol (bottom) and PS₄₅-*b*-P(octylmethacrylate(OMA)₂₄-*r*-CE3MA₃₁)⁸⁷ (bottom).

GC-MS Analysis

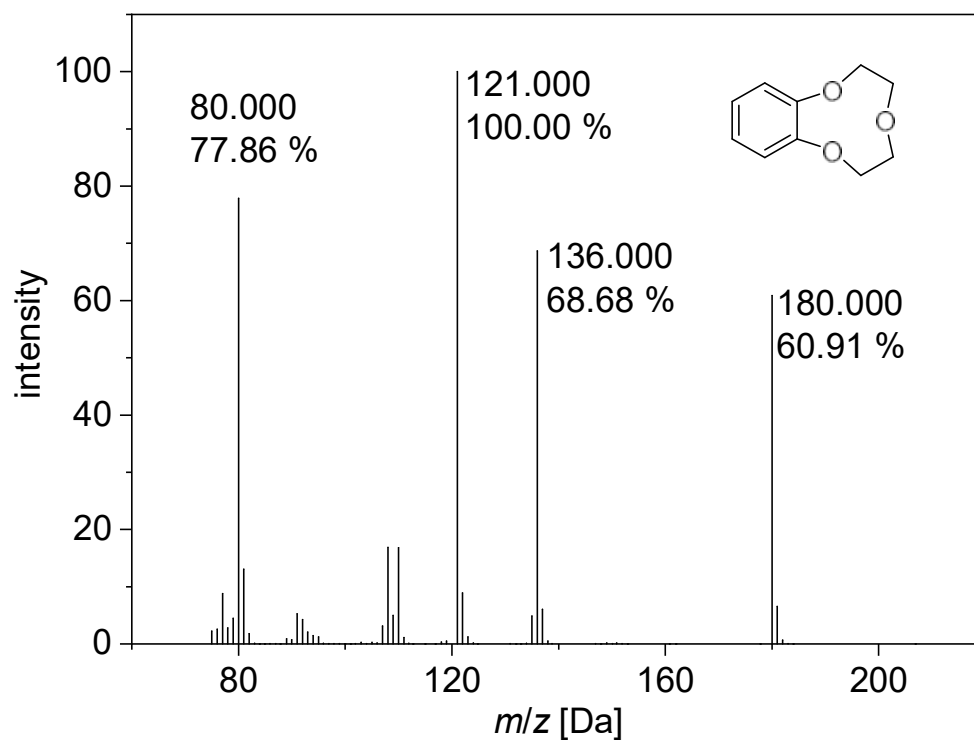


Figure S7. GC-MS of B9C3.

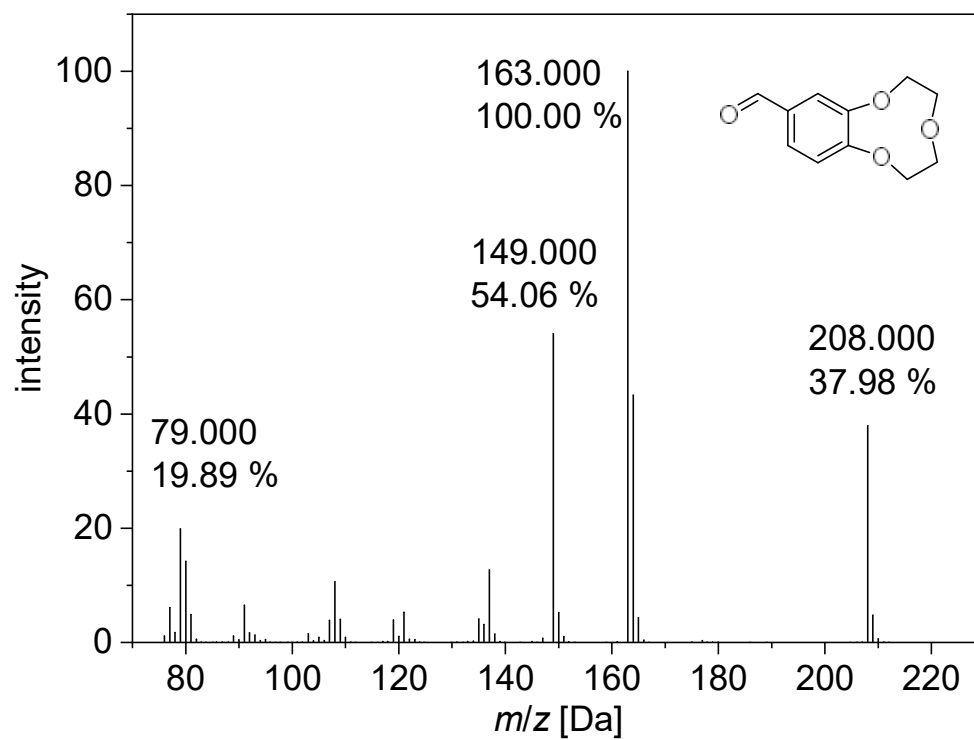


Figure S8. GC-MS of B9C3-CHO.

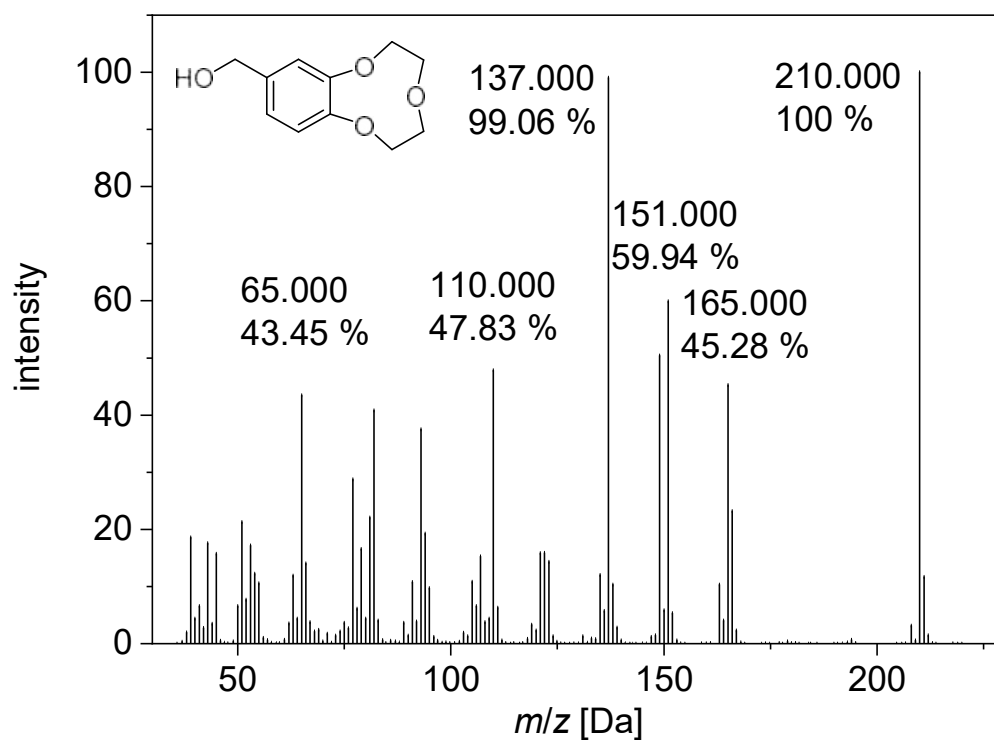


Figure S9. GC-MS of B9C3-OH.

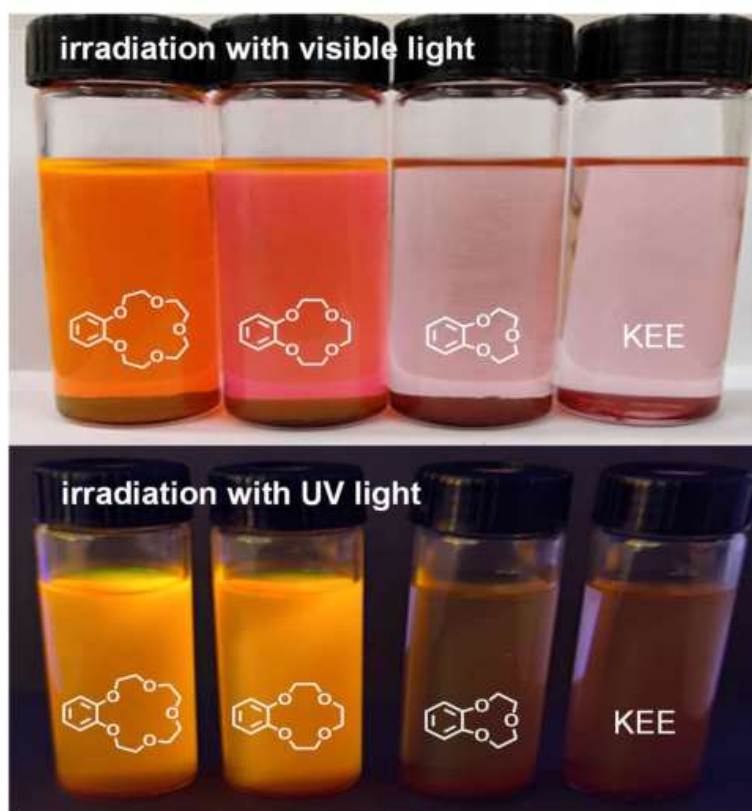


Figure S10. Optical experiment with KEE in DCM (right) and additionally added CEs.

Results of the Liquid-Liquid Extraction

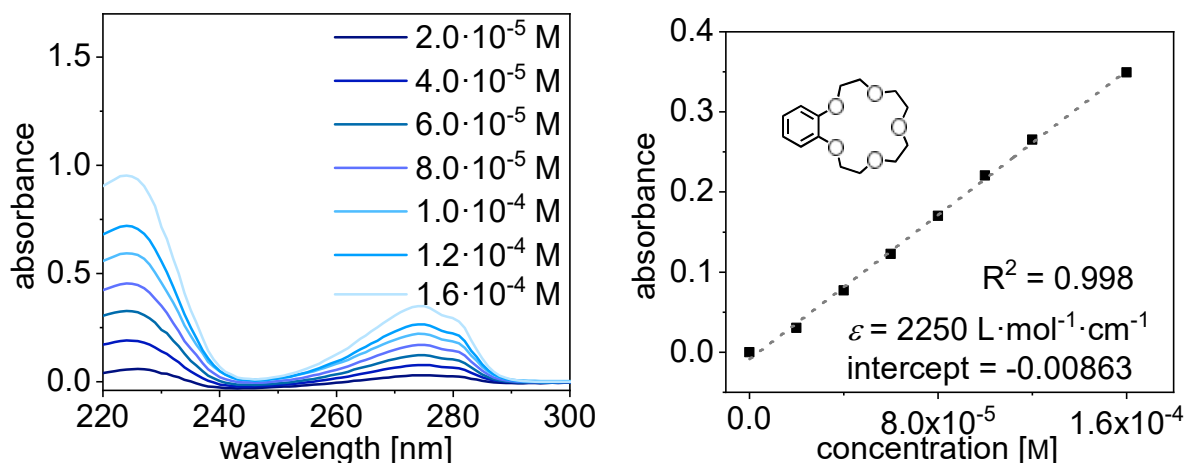


Figure S11. UV-vis spectra (left) and its calibration curve (right) of B15C5 CE in water.

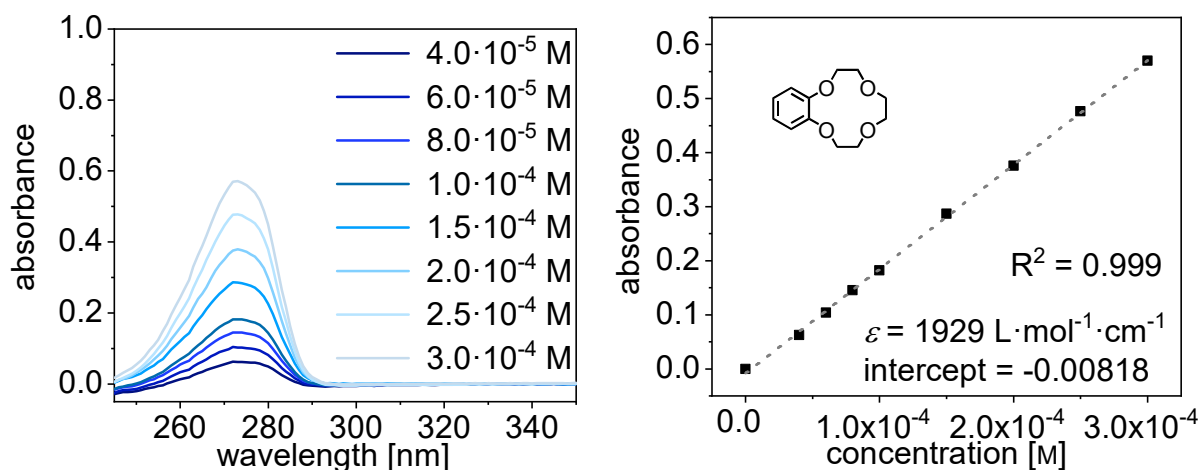


Figure S12. UV-vis spectra (left) and calibration curve (right) of B12C4 CE in water.

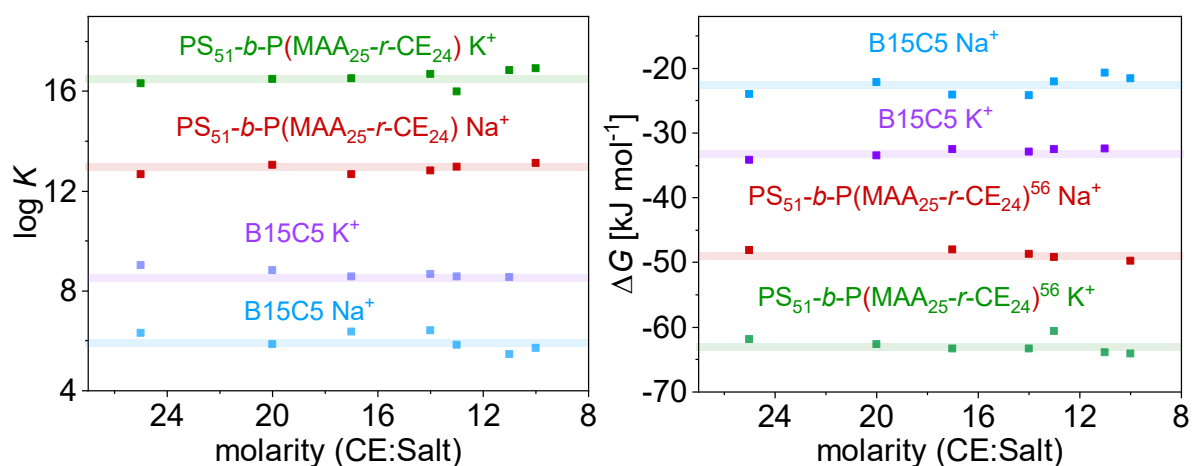


Figure S13. Comparison of the complex stability (left) and Gibbs energy (right) of free B15C5 CE and polymer-bound CE system $\text{PS}_{51}\text{-}b\text{-P}(\text{MAA}_{25}\text{-}r\text{-CE}_{5}\text{MA}_{24})^{56}$ with NaEE and KEE at different CE:salt molar ratios. The salt concentrations were kept constant.

UV-vis spectra

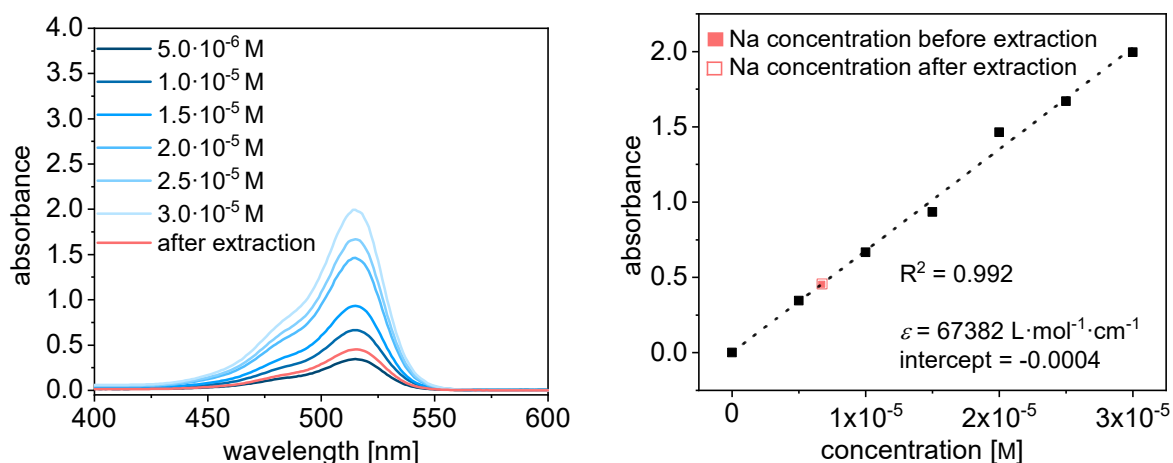


Figure S14. UV-vis spectra of the different Na-EE salts for calibration (blue curves) and the remained NaEE salt concentration in the aqueous phase after extraction of the $\text{PS}_{60}\text{-}b\text{-P}(\text{MAA}_{20}\text{-}r\text{-CE3MA}_{20})^{49}$ with NaEE (pink curve) (left). The calibration curve and the concentration before and after extraction are shown in the right figure. The pink square represents the sodium concentration in the water phase before extraction and the hollow square represents the concentration after the extraction. Both squares overlay (right).

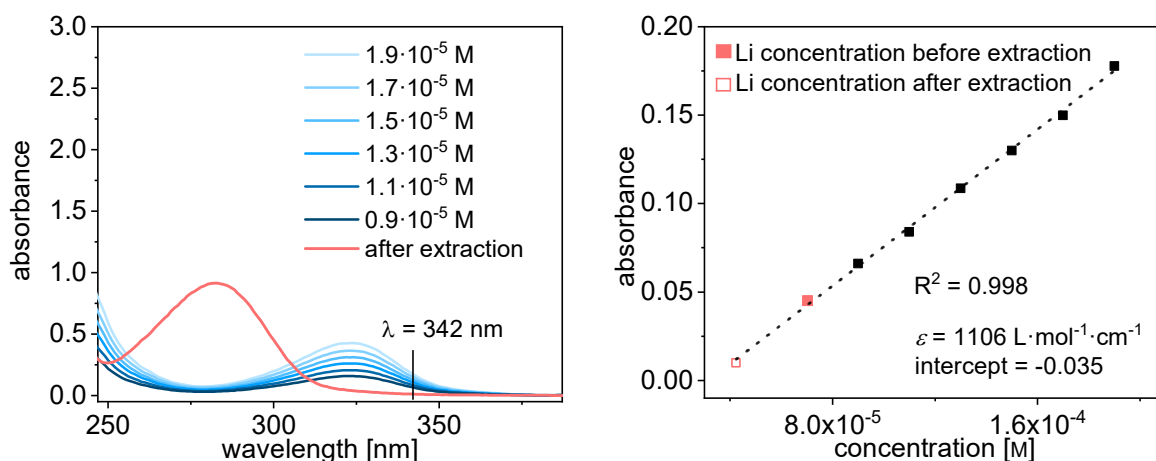


Figure S15. UV-vis spectra of the calibration points (blue gradient) and of $\text{PS}_{52}\text{-}b\text{-P}(\text{MAA}_{12}\text{-}r\text{-CE3MA}_{36})^{76}$ with LIS (pink) after the extraction. A new signal at 280 nm appears, which is referred to the PS signal of the polymer (left). Calibration curve and the concentration before and after extraction (right). The pink square represents the lithium concentration in the water phase before extraction and the hollow square the concentration after the extraction.

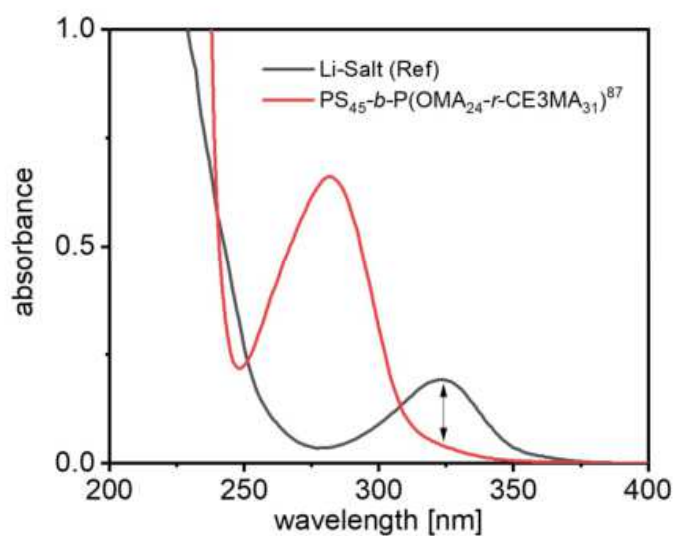


Figure S16.: UV-vis spectrum of the aqueous phase before extraction (black curve) and after extraction (red curve) of the LLE with the LIS salt and the $\text{PS}_{45}\text{-}b\text{-P}(\text{OMA}_{24}\text{-}r\text{-CE3MA}_{31})^{87}$ copolymer.

IR Data

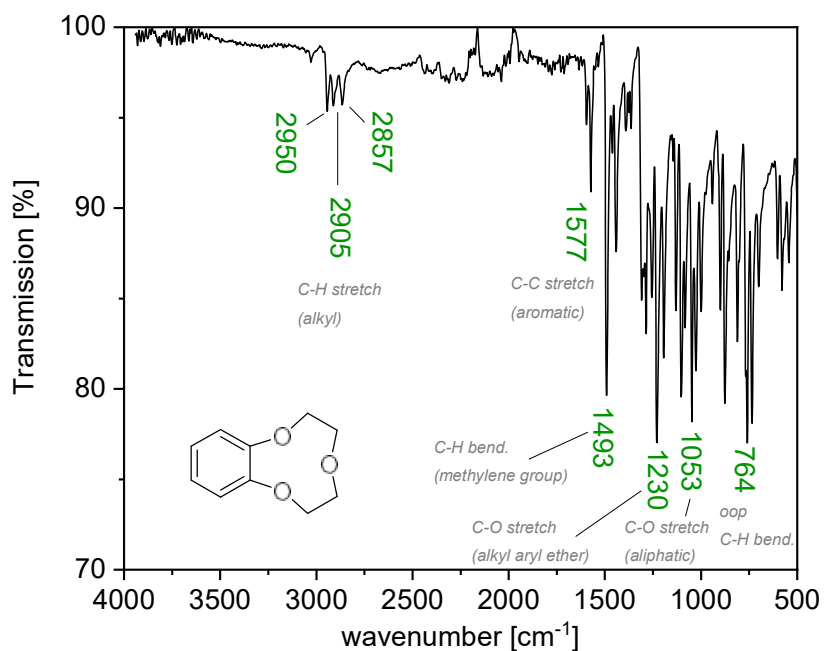


Figure S17: IR spectrum of B9C3 CE.

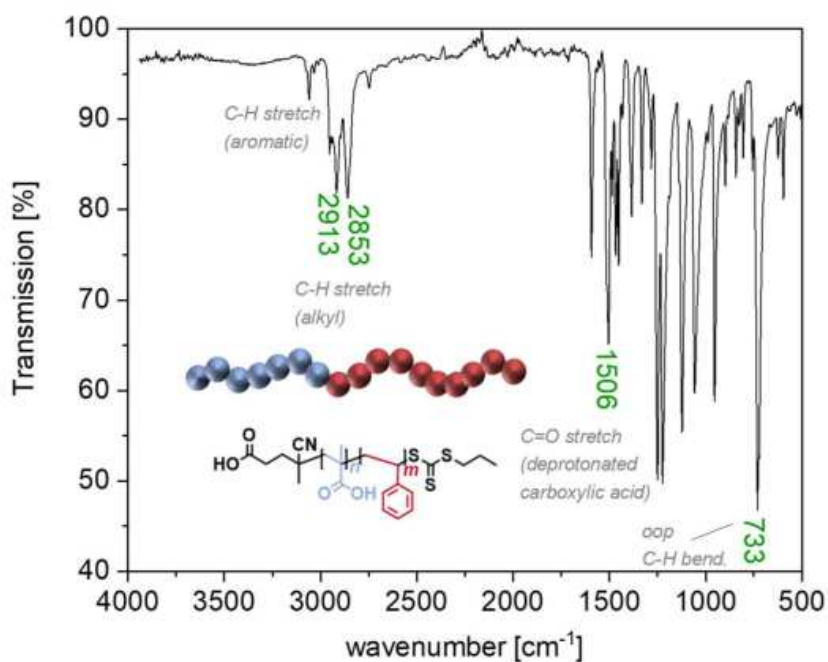


Figure S18: IR spectrum of the PS₇₀-*b*-PMAA₃₀⁴² diblock copolymer.

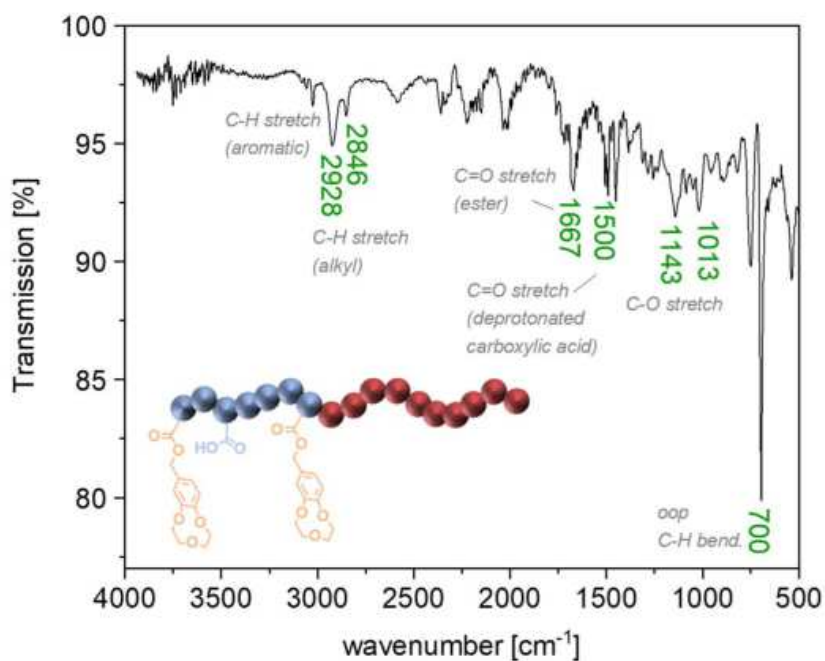


Figure S19: IR spectrum of the PS₇₀-*b*-P(MAA₇-*r*-CE3MA₂₃)¹²⁰ copolymer.

Eq.1 represents the calculation of the complex constant K in more detail with c_{start} being the starting salt concentration in the aqueous phase and $c_{\text{CE,start}}$ being the starting CE concentration in the organic phase. The value Q is referred to 1, since only monovalent metal ions were used.

$$K = \frac{[c_{\text{complex}}]}{(Q \cdot (\gamma_+ [c_{\text{salt,start}} - m \cdot c_{\text{complex}}]^m) \cdot (\gamma_- [c_{\text{salt,start}} - x \cdot c_{\text{complex}}]^x)) \cdot [c_{\text{CE,start}} - n \cdot c_{\text{complex}}]^n} \quad (1)$$

9.6 Supporting information of publication 5

The supporting information is reprinted with permission from I. Oral and V. Abetz, *Soft Matter* **2022**, *18*, 934 – published by the Royal Society of Chemistry.

Supporting Information

Improved Alkali Metal Ion Capturing utilizing Crown ether-based Diblock Copolymers in a Sandwich-type complexation

Iklima Oral^a and Volker Abetz^{a,b,*}

^a*Institute of Physical Chemistry, Universität Hamburg, Grindelallee 117, 20146 Hamburg, Germany.*

^b*Helmholtz-Zentrum Hereon, Institute of Membrane Research, Max-Planck-Straße 1, 21502 Geesthacht, Germany. E-mail: volker.abetz@hereon.de*

Experimental Section

Materials

2',4',5',7'-tetrabromoeosin ethyl ester sodium salt (>99%, NaEE, Waldeck, Münster, Germany), 2',4',5',7'-tetrabromoeosin ethyl ester potassium salt (>99%, KEE, Carl Roth, Karlsruhe, Germany), lithium 3,5-diidosalicylate (>99%, LIS, Sigma-Aldrich, Schnelldorf, Germany), catechol (99%, Sigma-Aldrich, Schnelldorf, Germany), Bis-2-chloroethylether (99%, TCI Chemicals, Eschborn, Germany), benzo-15-crown-5 (98%, B15C5, TCI Chemicals, Eschborn, Germany), benzo-12-crown-4 (98%, B12C4, TCI Chemicals, Eschborn, Germany), 12-crown-4-hydroxyl (12C4-OH, Sigma-Aldrich, Schnelldorf, Germany), 15-crown-5-hydroxyl (15C5-OH, Sigma-Aldrich, Schnelldorf, Germany), hexamethylenetetramine (98%, Sigma-Aldrich, Schnelldorf, Germany), sodium borohydride (98%, B15C5, Sigma-Aldrich, Schnelldorf, Germany), dicyclohexylcarbodiimid (98%, DCC, Sigma-Aldrich, Schnelldorf, Germany), 4-(dimethylamino)-pyridin (98%, DMAP, Sigma-Aldrich, Schnelldorf, Germany), 1-propanethiol (99%, Sigma-Aldrich, Schnelldorf, Germany), MAA (>99%, Merck, Darmstadt, Germany), potassium hydroxide (KOH) (85%, Merck, Darmstadt, Germany), carbon disulfide (CS₂) (99%, Merck, Darmstadt, Germany), *p*-tosyl chloride (98%, Merck, Darmstadt, Germany), 4,4-azobis(4-cyanovaleric acid) (ACVA) (>98%, Sigma-Aldrich, Schnelldorf, Germany), *N,N*-dimethylformamide (DMF) (99%, VWR Chemicals, Darmstadt, Germany), tetrahydrofuran (THF) (>99%, VWR Chemicals, Darmstadt, Germany), styrene (99%, Grüssing, Filsum, Germany), dichloromethane (DCM) (>99%, Acros, Schwerte, Germany), acetone (>99%, Merck, Darmstadt, Germany), *n*-hexane (95%, VWR Chemicals, Darmstadt, Germany), chloroform-*d*₁ (>99%, EurisoTop, Saarbrücken, Germany), THF-*d*₈ (>99%, Euriso-Top), dimethylsulfoxide-*d*₆ (>99%, Germany), deuterium oxide (D₂O) (>99%, Euriso-Top, Saarbrücken, Germany), trifluoroacetic acid (TFA) (99%, TCI Chemicals, Eschborn, Germany), NaHCO₃ (>99%, Grüssing, Filsum, Germany), Mg₂SO₄ (>99%, Grüssing, Filsum, Germany), and activated basic aluminum oxide (>99%, grain size between 0.063–0.200 mm, Merck, Darmstadt, Germany) were used as received without further purification unless noted otherwise. Styrene was purified by filtration through basic activated aluminum oxide to remove the inhibitor. Deionized water was purified with a Milli-Q® integral water purification system. The subscripts in the designation of the polymers represent the fraction of the respective block in wt% and the superscript represents the overall molecular weight in kDa.

General Methods

NMR spectroscopy

¹H NMR and ¹³C NMR spectra were recorded at ambient temperature using a 300 or 400 MHz Bruker AVANCE II spectrometer in either CDCl₃-*d*₁, D₂O or THF-*d*₈. The residual signals at $\delta = 7.26$ for CDCl₃-*d*₁, $\delta = 4.80$ ppm for D₂O and $\delta = 3.58$ ppm for THF-*d*₈ were used as an internal standard for the chemical shifts.

UV-vis spectroscopy

The UV-Vis spectra were recorded with a spectrophotometer UV5 from METTLER TOLEDO at room temperature. The sample was measured from 190 to 1100 nm. The scan time was 10 s.

The synthetic procedures, the two-phase extraction, as well as a more detailed calculation of the complex constant K were published elsewhere.¹

Reaction Overviews

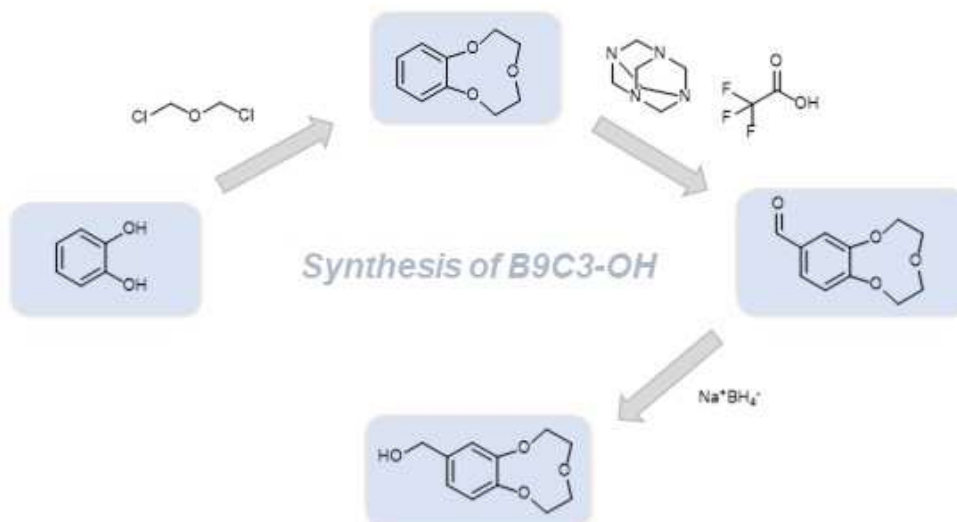


Fig. S1: Reaction overview of the B9C3-OH functionalization starting from catechol.

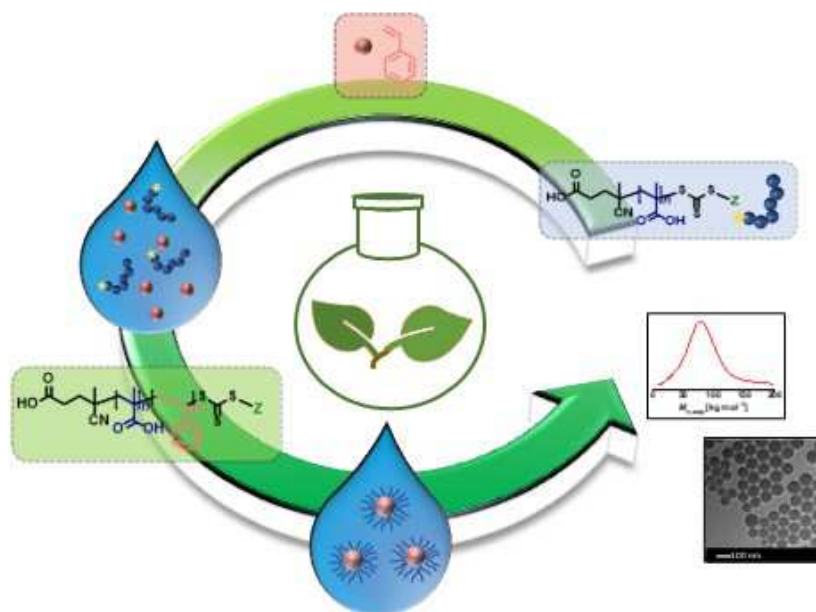


Fig. S2: Reaction overview of the one-pot PMAA-*b*-PS RAFT emulsion polymerization using water and achieving well-controlled reactions conditions.

Calibration Curves of the Salt Dyes

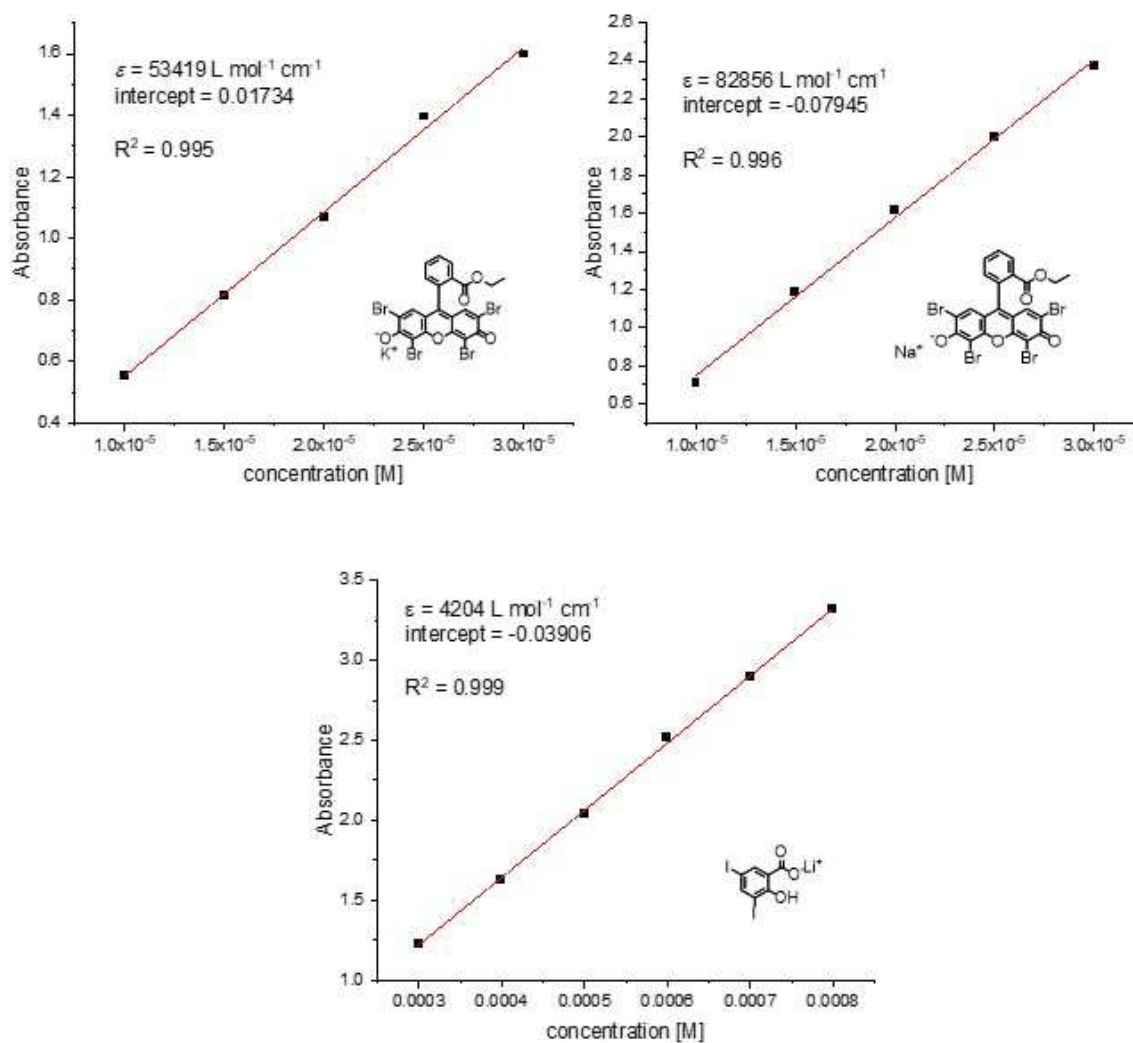


Fig. S3: Example calibration curves of the used salt dyes 2',4',5',7'-tetrabromoeosin ethyl ester potassium, 2',4',5',7'-tetrabromoeosin ethyl ester sodium and lithium 3,5-diiodosalicylate salt.

NMR spectra of the crown ethers and the polymer-based crown ethers

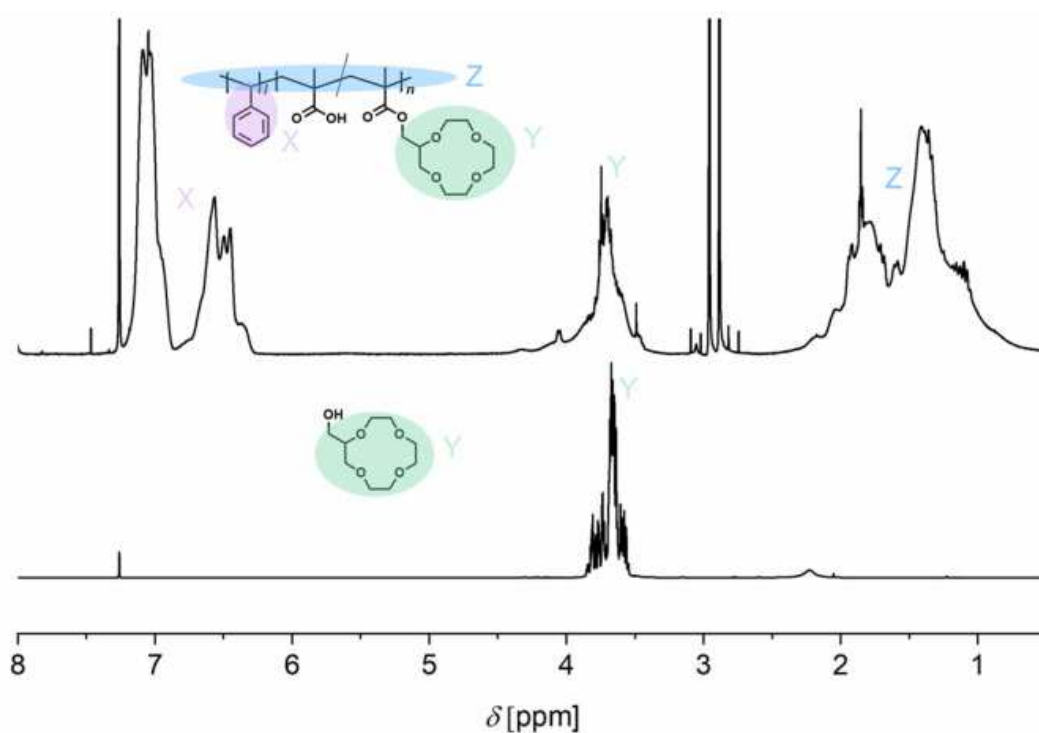


Fig. S4: ¹H NMR spectrum of 12C4-OH (bottom) and P(MAA₂₁-*r*-12C4MA₁₉)-*b*-PS₆₀^{48.6} diblock copolymer containing randomly distributed CE units (top) in CDCl₃.

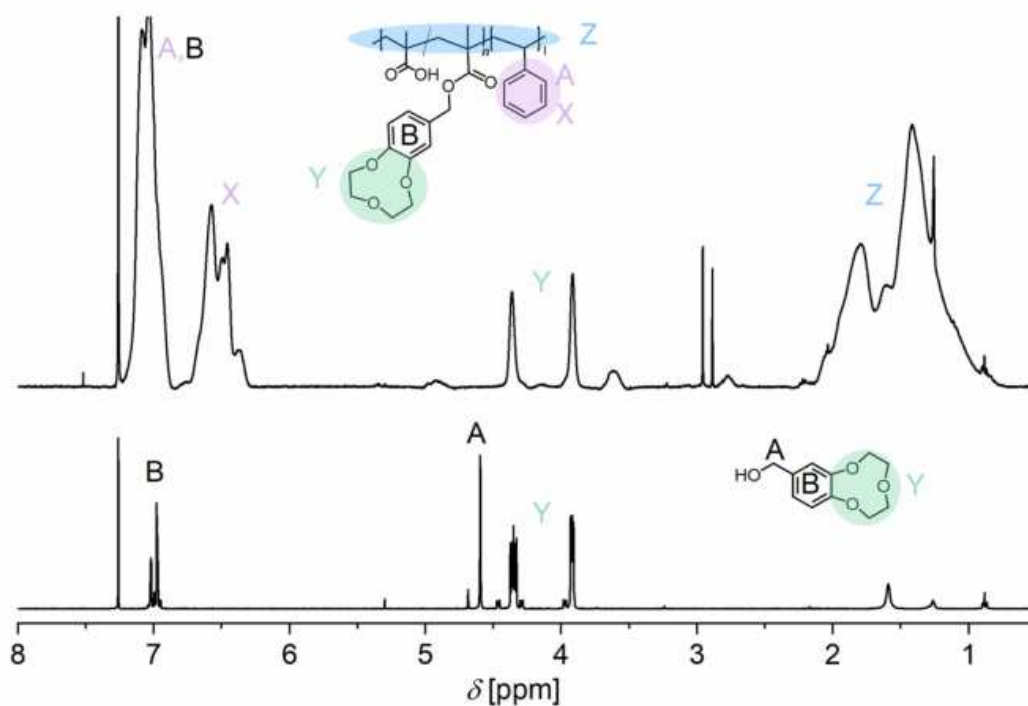


Fig. S5: ¹H NMR spectrum of B9C3 (bottom) and P(MAA₂₀-*r*-B9C3MA₂₀)-*b*-PS₆₀^{49.1} diblock copolymer containing randomly distributed CE units (top) in CDCl₃.

Determination of the Degree of Functionalization

The theoretical molecular weights of all polymers are calculated from the following Eq. 1:²

$$M_{n,th} = \frac{[M]_0 \cdot p \cdot M_M}{[CTA]_0} + M_{CTA} \quad (1)$$

where $[M]_0$ and $[CTA]_0$ are the initial concentrations of monomer and chain transfer agent, p the monomer conversion and M_M and M_{CTA} are the molar masses of monomer and chain transfer agent. For calculating the degree of polymerization (DP) for PMAA or PS the molecular weight of the polymer block is divided by the formula weight of the repeating unit.

The average number of CE-esterified repeating units per chain will be called n_{CE} – not “degree of polymerization” which would, by definition, be incorrect in a statistical copolymer block. n_{CE} is calculated from ¹H NMR spectroscopy and given by Eq. 2.

$$n_{CE} = \frac{\int Y / H_Y}{\int X / H_X} \cdot DP_{PS} \quad (2)$$

The integral X corresponds to the phenyl protons of PS, integral Y corresponds to characteristic protons of the CE (see Fig. S4) and H_X and H_Y to the corresponding protons of one respective repeating unit. DP_{PS} labels the DP of PS.

With the known DP of the PMAA (from Eq. 1, before esterification reaction) the degree of functionalization (DF) can be determined by Eq. 3.

$$\frac{n_{CE}}{DP_{PMAA}} = DF \quad (3)$$

References

- 1 I. Oral and V. Abetz, *Macromol. Rapid Commun.*, 2021, **42**, 2000746.
- 2 S. Perrier, *Macromolecules*, 2017, **50**, 7433–7447.

9.7 Solubility parameters

Table 9.1: Contributions for first-order functional groups for the dispersive partial solubility parameter δ_d , the polar partial solubility parameter δ_p , the partial solubility parameter for hydrogen bonding δ_h , and the solubility parameters for the case of low values below 3 MPa^{1/2} ($\delta_{p,low}$, $\delta_{h,low}$). All values are given in MPa^{1/2}.

Group	δ_d	δ_p	δ_h	$\delta_{p,low}$	$\delta_{h,low}$
-CH ₃	-0.9714	-1.6448	-0.7813	-0.7241	0.2990
-CH ₂ -	-0.0269	-0.3045	-0.4119	-0.1403	-0.1161
-CH<	-0.6450	0.6491	-0.2018	-0.5898	-0.1386
>C<	-1.2686	2.0838	0.0866	-	-
CH ₂ =CH-	-1.0585	-2.0838	-1.2985	-0.2977	-1.3552
-CH=CH-	0.0048	-0.2984	-0.04	-0.2286	-0.4819
CH ₂ =C<	-0.4829	-0.7794	-0.826	0.64816	0.11148
-CH=C<	0.5372	-0.9024	-1.8872	1.22566	-0.03066
>C=C<	0.3592	1.0526	-15.4659	*	-0.12117
CH ₂ =C=CH-	-1.6518	*	-0.998	-0.32258	*
CH≡C-	0.232	-1.3294	1.0736	-0.74895	0.43846
C≡C	-0.2028	-0.7598	-1.1083	*	-0.35107
ACH	0.1105	-0.5303	-0.4305	-0.19313	0.13532
AC	0.8446	0.6187	0.0084	0.16369	-0.17405
ACCH ₃	0.2174	-0.5705	-1.1473	-0.47724	-0.28733
ACCH ₂ -	0.6933	0.6517	-0.1375	-0.33086	-0.88084
ACCH<	-	-	-	0.86718	-1.44666
-CH ₃ CO	-0.3551	2.3192	-1.3078	-	-
-CH ₂ CO-	0.6527	3.7328	-0.5344	-	-
-CHO (aldehyde)	-0.403	3.4734	0.1687	-	-
COOH	-0.291	0.9042	3.7391	-	-
-CH ₃ COO	-0.5401	-0.397	1.5826	1.71923	*
-CH ₂ COO	0.2913	3.6462	1.2523	2.16274	*
HCOO	*	1.9308	2.1202	-	-
COO	0.2039	3.4637	1.1389	1.60913	0.37204
OH	-0.3462	1.1404	7.1908	1.84013	*
ACOH	0.5288	1.101	6.958	-	-
CH ₃ O	-0.5828	0.1764	0.146	-0.4032	*
CH ₂ O	0.031	0.8826	-0.1528	*	*
CHO (ether)	0.8833	1.6853	0.4470	*	-0.40667
-C ₂ H ₅ O ₂	-0.1249	3.6422	8.3579	-	-

Table 9.1: Contributions for first-order functional groups for the dispersive partial solubility parameter δ_d , the polar partial solubility parameter δ_p , the partial solubility parameter for hydrogen bonding δ_h , and the solubility parameters for the case of low values below $3 \text{ MPa}^{\frac{1}{2}}$ ($\delta_{p,\text{low}}, \delta_{h,\text{low}}$). All values are given in $\text{MPa}^{\frac{1}{2}}$.

Group	δ_d	δ_p	δ_h	$\delta_{p,\text{low}}$	$\delta_{h,\text{low}}$
CH ₂ O (cycl.)	0.2753	0.1994	-0.161	-0.33305	*
CH ₂ NH ₂	-0.5828	1.4084	2.592	*	*
CHNH ₂	0.0112	-1.1989	0.3818	-	-
CHNH	-	-	-	1.25999	*
CH ₃ NH	*	0.6777	5.6646	-	-
CH ₂ NH	0.8116	0.9412	1.34	0.83214	*
CH ₃ N	0.8769	1.2046	1.6062	*	-0.17004
CH ₂ N	1.4681	2.8345	1.2505	0.65229	-1.03686
ACNH ₂	1.6987	1.6761	4.5274	-	-
CONH ₂	-0.0689	6.0694	5.228	-	-
CON(CH ₃) ₂	0.4482	5.7899	3.002	-	-
CH ₂ SH	1.2797	-0.8223	4.4646	-	-
CH ₃ S	*	0.4944	-1.4861	-	-
CH ₂ S	1.0595	0.753	-0.2287	-	-
I	0.7797	0.6777	0.2646	-	-
Br	0.5717	0.6997	-1.0722	-	-
CH ₂ Cl	0.2623	0.597	-0.5364	*	0.48952
CHCl	0.4462	2.806	-1.4125	*	0.12996
CCl	2.7576	2.0406	0.1101	-	-
CHCl ₂	1.1797	1.8361	-3.2861	*	0.52541
CCl ₂	0.3653	0.1696	-1.4334	-	-
CCl ₃	*	1.2777	-2.6354	-	-
ACCl	0.8475	-0.0339	-0.784	-0.10778	0.44238
CCl ₂ F	-	-	-	*	*
ACF	0.117	0.1856	-0.7182	*	-0.37183
Cl-(C=C)	0.2289	2.3444	3.8893	*	0.66062
CF ₃	-0.2293	-1.9735	-1.4665	*	-0.08871
CH ₂ NO ₂	*	6.8944	-1.2861	-	-
CHNO ₂	*	8.0347	-2.3167	-	-
ACNO ₂	1.4195	4.4838	-0.7167	-	-
CH ₂ CN	-0.3392	6.5341	-0.8892	-	-
CF ₂	-0.9729	*	*	-	-
CF	0.1707	*	*	-	-

Table 9.1: Contributions for first-order functional groups for the dispersive partial solubility parameter δ_d , the polar partial solubility parameter δ_p , the partial solubility parameter for hydrogen bonding δ_h , and the solubility parameters for the case of low values below 3 MPa $^{\frac{1}{2}}$ ($\delta_{p,low}$, $\delta_{h,low}$). All values are given in MPa $^{\frac{1}{2}}$.

Group	δ_d	δ_p	δ_h	$\delta_{p,low}$	$\delta_{h,low}$
F**	-0.7069	*	*	-	-
CH ₂ =C=C<	-0.2804	*	-1.9167	1.20154	*
O**	0.0472	3.3432	0.0256	-0.48942	*
Cl**	0.2256	1.8711	-0.3295	*	1.12515
>C=N-	-0.3074	-0.0012	-5.3956	-	-
-CH=N-	0.9672	1.9728	0.7668	-	-
NH**	*	0.0103	2.2086	-	-
CN**	0.0861	6.5331	-0.6849	-	-
O=C=N	-0.1306	1.6102	4.0461	-	-
SH**	1.0427	1.9813	4.8181	-	-
CH ₂ S	-	-	-	*	0.14606
S**	1.4899	9.2072	-0.625	0.11058	*
SO ₂	1.5502	11.1758	0.1055	-	-
>C=S	0.7747	0.0683	3.408	-	-
>C=O	-0.4343	0.7905	1.8147	*	-0.05529
N**	1.5438	2.578	1.1189	-	-

Table 9.2: Contributions for second-order functional groups for the dispersive partial solubility parameter δ_d , the polar partial solubility parameter δ_p , the partial solubility parameter for hydrogen bonding δ_h , and the solubility parameters for the case of low values below 3 MPa $^{\frac{1}{2}}$ ($\delta_{p,low}$, $\delta_{h,low}$). All values are given in MPa $^{\frac{1}{2}}$.

Group	δ_d	δ_p	δ_h	$\delta_{p,low}$	$\delta_{h,low}$
(CH ₃) ₂ -CH-	0.046	0.0019	0.3149	0.200694	0.00000001
(CH ₃) ₃ -C-	-0.0738	1.188	-0.2966	-	-
C-5 ring	2.343	0.6491	-0.2018	-0.8979	0.19438
C-6 ring	-0.3874	-3.6432	*	-0.956852	0.00000002
-C=C-C=C-	-0.1355	-3.5085	-1.0795	0.648793	*
CH ₃ -C=	-0.0785	0.3316	0.3875	-0.008375	-0.06137
-CH ₂ -C=	-0.3236	-2.3179	-0.5836	0.011009	0.06599
>CH or C-C=	-0.2798	*	-1.1164	-0.3972	0.342229
chain in ring	-0.1945	*	*	*	-0.280859
CH ₃ (CO)CH ₂ -	-0.0451	-0.3383	-0.4083	-	-
C _{cyc} =O	-0.2981	0.4497	-0.4794	-	-

Table 9.2: Contributions for second-order functional groups for the dispersive partial solubility parameter δ_d , the polar partial solubility parameter δ_p , the partial solubility parameter for hydrogen bonding δ_h , and the solubility parameters for the case of low values below 3 MPa $^{\frac{1}{2}}$ ($\delta_{p,low}$, $\delta_{h,low}$). All values are given in MPa $^{\frac{1}{2}}$.

Group	δ_d	δ_p	δ_h	$\delta_{p,low}$	$\delta_{h,low}$
ACCOOH	-0.2293	-0.6349	-0.903	-	-
>CH or C-COOH	*	-0.2187	1.146	-	-
CH ₃ (CO)OCH or C<	-0.522	-0.0652	0.3085	-	-
(CO)CH ₂ COO	*	-2.3792	0.8412	-	-
(CO)C(CO)	-0.2707	-1.0562	1.6335	-	-
ACHO	0.3772	-1.811	-1.0096	-	-
>CHOH	0.1123	0.2564	-0.1928	-	-
>C<OH	-0.068	0.1075	1.2931	-	-
-C(OH)C(OH)-	*	0.6419	0.387	-	-
-C(OH)C(N)	-0.0809	0.5683	-0.6326	-	-
C _{cyc} -(OH)	-0.0876	-3.522	0.5914	-	-
C-O-C=C	0.2063	0.608	1.1344	-	-
AC-O-C	0.2568	0.8153	0.6092	-	-
>NH or C (cyc)	0.2218	-2.2018	-0.0452	-	-
-S- (cyc)	0.4892	0.304	0.2297	-	-
ACBr	0.1234	-0.4495	0.3397	-	-
(C=C)-Br	-0.4059	-0.0024	-1.1304	-	-
C-3 ring	0.02	1.8288	-0.8073	-	-
ACCOO	-0.1847	0.4059	-0.1921	-	-
AC(ACH _m) ₂ AC(ACH _n) ₂	-0.3751	-1.298	0.6844	0.013012	0.086424
O _{cyc} -C _{cyc} =O	0.2468	2.7501	0.122	-	-
AC-O-AC	-0.5646	-3.4329	2.083	-	-
C _{cyc} H _m =B _{cyc} H _n =C _{cyc} H _p	0.7002	0.0691	-2.7661	-	-
N _{cyc} H _m -C _{cyc} =O	0.2956	2.8958	1.3125	-	-
O-CH _m -O-CH _n -	0.0839	0.3451	0.3451	-	-
C(=O)-C-C(=O)	-0.4862	-0.4888	1.2482	-	-

Table 9.3: Contributions for functional groups according to the Hoy theory.

Group	$F_{t,i}$	$F_{p,i}$	V_i	$\Delta_{T,i}$	$\Delta_{T,i}^P$
-CH ₃	303.35	0.00	29.21	0.0363	0.0226
-CH ₂ -	268.98	0.00	17.51	0.0138	0.02
>CH-	175.89	0.00	6.46	-0.0079	0.0131

Table 9.3: Contributions for functional groups according to the Hoy theory.

Group	$F_{t,i}$	$F_{p,i}$	V_i	$\Delta_{T,i}$	$\Delta_{T,i}^P$
>C<	65.52	0.00	-4.18	-0.0291	0.004
CH ₂ =	258.84	66.89	27.77	0.018	0.0192
-CH=	248.59	59.52	15.15	0.0106	0.0184
>C=	172.87	63.00	0.22	0.0173	0.0129
CH _{arom}	239.94	62.18	14.54	0.0081	0.0178
C _{arom}	200.70	64.84	2.11	0.011	0.0149
C ₆ H ₄	1361.16	378.42	63.62	0.066	0.101
O _{ether}	235.19	216.00	5.00	0.0073	0.0175
O _{acetone}	204.55	204.55	6.77	0.021	0.0175
O _{epoxy}	360.42	360.42	20.60	0.014	0.0267
OH _{prim}	673.79	673.79	9.99	0.057	0.0493
OH _{sec}	591.56	591.56	10.42	0.082	0.044
OH _{ter}	798.56	798.56	10.74	0.082	0.0593
OH _{arom}	349.76	349.78	6.93	0.0285	0.006
-OH- (H-bonded)	485.81	485.81	10.70	0.082	0.0343
CO	537.88	525.69	14.16	0.0181	0.04
CHO	598.60	530.81	28.15	0.0227	0.0445
COO	668.02	524.06	18.87	0.0466	0.0497
-COOH	1382.96	661.92	28.00	0.085	0.062
(CO) ₂ O	1160.39	1159.80	28.79	0.086	0.0863
-NH ₂	463.43	463.51	17.67	0.031	0.0345
>NH	368.25	368.19	7.39	0.031	0.0274
>N	124.94	124.98	-4.59	-0.0002	0.0093
N _{arom}	235.23	122.73	4.98	0.007	0.007
-CN	725.25	724.52	23.27	0.0554	0.0539
-NO ₂	797.75	961.39	24.84	0	0
-N=C=O	733.64	608.95	31.75	0.054	0.0539
-CO-NH ₂	1206.64	989.20	23.01	0.071	0.0897
-CO-NH-	1134.64	893.88	12.73	0.071	0.0843
-CO-N-	812.68	1189.05	-0.49	0.054	0.0729
HCO-N	1017.02	724.11	18.62	0.0001	0.0546
O-CO-NH-	1261.87	892.25	23.26	0.078	0.0938
F	84.54	73.23	16.14	0.0289	0.006
Cl _{prim}	419.45	306.83	25.00	0.0224	0.031
Cl _{sec}	426.02	315.01	24.03	0.017	0.0317
Cl _{arom}	329.33	81.41	25.10	0.017	0.0245

Table 9.3: Contributions for functional groups according to the Hoy theory.

Group	$F_{t,i}$	$F_{p,i}$	V_i	$\Delta_{T,i}$	$\Delta_{T,i}^P$
Br	527.49	122.73	28.12	0.0193	0.0392
Br _{arom}	420.55	100.23	26.60	0.01	0.0313
-S-	428.37	428.33	13.00	0.015	0.0318
-SO-	869.34	1059.57	12.54	0.0088	0.035
-SO ₂ -	1206.85	1984.14	17.70	0	0
-OP	1740.72	1390.94	22.00	0.0675	0.0675
-P(=O)	1037.07	742.52	3.00	0.0046	0.0046

Table 9.4: Contributions for configuration of groups according to the Hoy theory.

Group	$F_{t,i}$	$F_{p,i}$	V_i	$\Delta_{T,i}$	$\Delta_{T,i}^P$
Hacdimer<	-103.99	-108.41	0.00	0	0
Isopropyl	0.00	0.00	1.56	0	0.0048
<i>t</i> -Butyl	0.00	0.00	0.51	0.0241	0
Cis	-14.58	-14.52	-0.18	0	-0.001
Trans	-27.61	-27.61	-3.14	-0.0064	-0.002
Conjug.	47.78	-19.84	-19.84	0	0.0035
<i>o</i> -subst.	19.82	-13.30	-1.18	0	0.0015
<i>m</i> -subst.	13.50	-24.34	0.00	0	0.001
<i>p</i> -subst.	82.50	-33.75	-1.58	0	0.006
4-Ring (not aromatic)	159.06	200.46	10.50	-0.028	0.0118
5-Ring (not aromatic)	42.94	84.89	6.77	0.0035	0.003
6-Ring (not aromatic)	-47.95	60.96	3.20	0.0025	-0.0035
Norbor	46.15	0.00	6.77	21.00	-0.028
Norbor-5 (not aromatic)	127.78	0.00	31.50	-0.035	-0.035

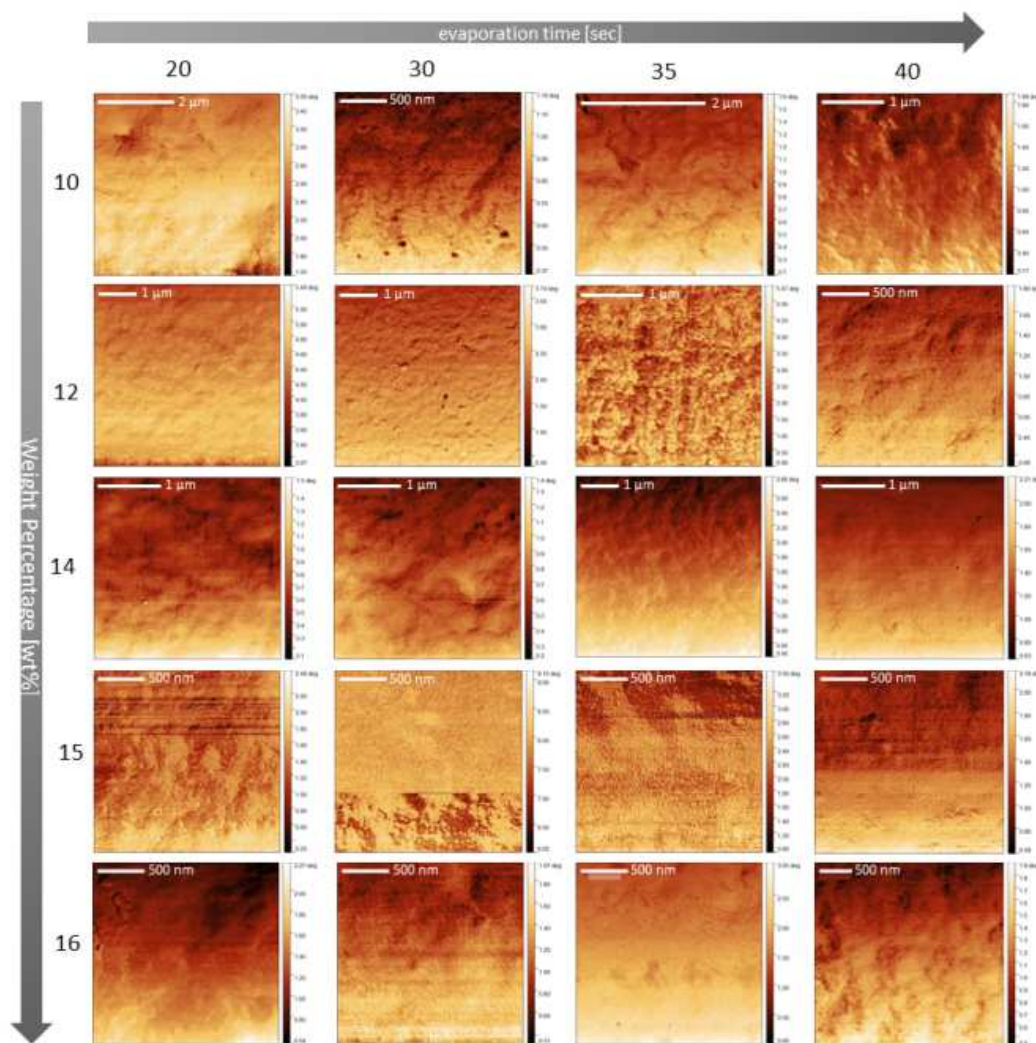


Figure 9.1: AFM images of the phase correction for the PMAA-b-PS polymer with a $M_n = 75$ kDa and PS:PMAA weight percent ratio of 90:10 at different total polymer concentrations between 10-16 and evaporation times between 20-40s.

9.8 Safety

Table 9.5: Hazardous substances according to GHS.


Substance	Symbols	Hazard Statement	Precautionary Statement
Acetic acid		226, 314	210, 280, 301+330+331, 303+361+353, 305+351+338

Table 9.5: Harzardous substances according to GHS.

Substance	Symbols	Hazard Statement	Precautionary Statement
Acetic anhydride		226, 314	210, 280, 301+330+331, 303+361+353, 305+351+338
Acetone		EUH066, 225, 319, 336	210, 233, 240, 241, 242, 243, 264, 280, 303+361+353, 305+351+338, 337+313, 370+378, 403+235, 501
Acetonitril		225, 302+312+332	210, 240, 302+352, 305+351+338, 403+233
Acid Red 52	n.h.	n.h.	n.h.
Acid Fuchsin calcium salt	n.h.	n.h.	n.h.
Activated basic aluminum oxide		222, 229, 319, 336	210, 251, 305+351+338, 405, 410+412, 501
8-Anilino-1-naphthalenesulfonic acid hemimagnesium salt	n.h.	n.h.	n.h.
Aza-15-crown-5		315, 319, 335	261, 305, 351, 338
4,4'-Azobis(4-cyanopentanoic acid)		228, 242, 412	210, 220, 231, 240, 241, 273, 280, 370+378, 403+235, 411, 420, 501
Benzo-15-crown-5	n.h.	n.h.	n.h.
Bis-2-chlorethylamine		302, 315, 319, 341	501, 201, 261, 280, 308+313, 337+313
Bromcresol green sodium salt	n.h.	n.h.	n.h.
1-Butanol		226, 302, 318, 315, 335, 336	210, 280, 302+352, 304+340, 305+351+338, 313
Catechol		301+311, 315, 317, 318, 332, 341	201, 280, 301+310+330, 302+352+312, 304+340+312, 305+351+338+310

Table 9.5: Harzardous substances according to GHS.













Substance	Symbols	Hazard Statement	Precautionary Statement
Chloroform		302, 331, 315, 319, 351, 361d, 336, 372	261, 281, 305+351+338, 311
4-cyano-4-[(dodecylsulfanylthiocarbonyl)sulfanyl]-pentanoic acid		302	-
deuterated chloroform		302, 315, 350, 373	201, 202, 260, 264, 280, 281, 301+312, 305+352, 308,313, 321, 330, 332, 313, 362, 405, 501
1,3-Dibromopropan		226, 301, 315, 319, 411	210, 301+312+330, 305+351+338, 370+378
1,4-Dibromopropan		301, 315, 318, 335	280,302+352, 305+351+338
1,5-Dibromopropan		315, 319	305+351+338
Deuterium oxide	n.h.	n.h.	n.h.
Dehydroacetic acid		302	-
Dichloromethane		315,319,336,351	210, 302,+352, 305+351+338, 308+313
<i>N,N'</i> -dicyclohexylcarbodiimide		302, 315, 350, 373	201, 202, 260, 264, 280, 281, 301+312, 305+352, 308,313, 321, 330, 332, 313, 362, 405, 501
<i>N,N'</i> -dimethylacrylamide		302, 312, 330	260, 304+340, 320, 330, 405, 501
Diethyl ether		224, 302, 336, EUH019, EUH066	210, 240, 403+235
1,3-dimethylbarbituric acid		302, 318	280, 301+312+330, 305+351+338, 308+313

Table 9.5: Harzardous substances according to GHS.









Substance	Symbols	Hazard Statement	Precautionary Statement
Dimethylformamide		312, 319, 332, 360d	201, 202, 261, 264, 380, 381, 302+352, 304+340, 305+351+338, 308+313, 312+ 322, 337+313, 363, 405, 501
Dimethyl sulfoxide- d_6	n.h.	n.h.	n.h.
1,4-Dioxane		EUH019, EUH066, 225, 319, 335, 351	201, 202, 210, 240, 241, 242, 243, 261, 264, 280, 281, 303+361+353, 304+340, 305+351+338, 308+313, 312, 337+313, 370+378, 403+233, 403+235, 405, 501
Ethanol		225	210, 233, 240, 241, 242, 243, 280, 303+361+353, 370+378, 403+235, 501
Ethanolamine		302+312+332, 314, 335, 412	273, 280, 301+312+330, 303+361+353, 304+340+312, 305+351+338+310
Ethyl eosin sodium/potassium salt	n.h.	n.h.	n.h.
<i>n</i> -Hexane		225, 304, 315, 336, 361f, 373, 411	201, 202, 210, 233, 240, 241, 242, 243, 260, 264, 273, 280, 281, 301+310, 302+352, 303+361+353, 303+313, 370+378, 391, 403+235, 405, 501
2-Hydroxymethyl-16-crown-5		315, 319, 335	261, 305+351+338
Lithiumhydroxide		302, 314	280, 305+351+338, 303+361+353, 301+330+331, 310
Lithium-3,5-diiodosalicylate		2315, 319, 335	261, 305+351+338

Table 9.5: Harzardous substances according to GHS.

Substance	Symbols	Hazard Statement	Precautionary Statement
Methacrylic acid		302+332, 311, 314, 335	261, 280, 305+351+338, 310
Methanol		225, 301+311+331, 370	210, 280, 302+352+312, 304+340+312, 370+378, 403+235
Methanol- d_4		225, 301+311+331, 370	210, 280, 301+310+330, 302+352+312, 304+340+311
Methyltrioctylammoniumbrom		315, 319, 335	302+352, 305+351+338
Potassium carbonate		315, 319, 335	305+351+338
Petrolether		225, 304, 315, 336, 361f, 373, 411	201, 210, 301+310, 311, 370+378, 501
1-Propanol		225, 318, 336	210, 240, 280, 305+351+338, 313, 403+233
Propan-2-ol		225, 319, 336	210, 223, 240, 305+335+338, 403+235
Tetrahydrofuran		EUH019, 225, 319, 335, 351	201, 202, 210, 233, 240, 241, 242, 243, 260, 264, 280, 281, 302+352, 303+361+353, 304+340, 305+351+338, 308+313, 337+313, 370+378, 403+235, 405, 501

Table 9.5: Harzardous substances according to GHS.








Substance	Symbols	Hazard Statement	Precautionary Statement
Tetrahydrofuran- d_8		EUH019, 225, 319, 335, 351	201, 202, 210, 240, 241, 242, 243, 261, 264, 280, 281, 303+361+353, 304+340, 305+351+338, 308+313, 321, 312, 337+313, 370+378, 403+233 403+235, 405, 501
5-Sulfoisophthalic acid sodium salt		319	264, 280, 305+351+338, 337+313
Sodium hydroxide		290, 314	280, 301+330+331, 303+361+353, 305+351+338+310
Styrene		226, 315, 319, 332, 361d, 372	201, 202, 210, 233, 240, 241, 242, 243, 260, 264, 280, 281, 305+352, 303+361+353, 304+340, 305+351+338, 308+313, 321, 330, 332+313, 337+313, 370+378, 403+233, 403+235, 405, 501
<i>p</i> -tosyl chloride		290, 312, 315, 318	280, 301+330+331, 302+352, 305+351+338, 310, 402+404, 501
Toluene		225, 304, 315, 336, 361d, 373	210, 240, 301+ 310+330, 302+352, 314, 403+233
Triethylamine		225, 302, 322+331+314, 335	210, 280, 303+361+353, 304+340, 310, 305+351+338, 403+233

Table 9.6: CMR Substances according to GHS.

Substance	CAS-Number	Category	Used Amounts
<i>N,N'</i> -Dimethylformamide	68-12-2	1B	20 L
Catechol	128-80-9	1B	100 g

Acknowledgments

In this Section, I would like to thank the people who gave me strength, courage, and motivation at this time.

First of all, I would like to thank Prof. Volker Abetz. Early in my studies, I found my way into your working group and immediately felt at home. You gave me the courage to go a semester abroad during my master's studies and supported me where possible. In the master's thesis, we went into a foreign field together and developed it to such an extent in the doctoral dissertation that many new projects can be built on it. Together we worked on a great topic that could positively impact society in the near future. We have learned a lot about the issue of lithium over the last three years, and therefore I also owe it to you that I have found a job through your support in which I can continue to deal with lithium extraction. I thank you for the great conversations, thematically as well as privately. You always had an understanding of different challenges in life. Thank you for guiding me through my studies and doctor.

I want to thank Prof. Horst Weller for taking over the second supervision of this thesis.

A big thanks goes to the working group of Prof. Abetz. I want to start with you, Tilman. Somehow we were both constantly in the AK Abetz but never met in the AK Abetz. Our spontaneous meeting in the foyer, where we prepared for the OC exam, was the beginning of a friendship, and I'm happy we could spend the Ph.D. time together. I have found a great friend in you, and I am sure we will share many more excellent moments. Keep your big heart and your sincerity.

Felix and Stephan (the early risers of AK Abetz), I have to thank you for a great time in the 360 office. In my first master's week, you showed me how things work in AK Abetz. I had a lot of fun with you guys; I got a lot of advice from, and listening when the research was frustrating helped me a lot. Playing darts always was a nice distraction, even though I still have to honor some betting debts. I want to thank Felix for the many discussions, you always had advice ready, and when I was not so motivated, you built up the necessary pressure to continue working diligently. Stephan, you always brightened our day with your great cat videos, your good mood, and your stresslessness was excellent compensation. You also brightened our evening with your apples. It was fun to play darts with you unless we both had to finish double 1. Thank you two for a great time; I will always keep this in mind and look forward to a beautiful Skype evening with a glass of wine in the future.

Philipp, I would like to thank you for the many evening discussions on my or your topic. The exchange with you was always precious. The incredible pictures you sent from your travels made me feel like I was there. Stay so motivated and cheerful and full of life energy even if you are too much in the sun, in my opinion. Next to you, I look like a ghost.

Sascha, you always had an open ear for me. Our nightly stays at the university will always remain in my memory. Thank you for all the delicious candies from the bakery. Thank you also for the countless corrections of manuscripts and this work. I wish you all the best. Keep your warm heart.

Sabrina, thank you for being a great master's student. The weekly meetings at Corona time were a nice change. It was enjoyable to work with you, to learn a new method that was foreign to us and *crowned* with a beautiful Publication. I certainly could not have done it alone. We are a great team. I am sure that you will make a successful PhD. With you, I have found a great successor. Keep your love and helpfulness; nothing will stand in your way.

Jingcong, or as Tilman names you, JC, I thank you for your always helpful, kind, and friendly conversations. I hope you will be happy in China and have a wonderful life. Thank you for the scientific discussions, and I will miss your great sweaters/t-shirts.

Maria, thank you for the nightly stays at the university and evening TV shows and dinners. I always enjoyed sitting in your office after lab, especially during my solo office times. Keep your sarcastic mind, it is awesome.

Siraphat we were office mates only for a short time, but it was adorable and pleasant. I wish you much success in Hamburg and for your future goals.

I would also like to thank Martin and Maggie for their tremendous support in the lab. With you, Martin, I could always talk for hours about martial arts. Thanks for the lovely time between the reactions. Maggie, in you, I found a precious friend, and I am sure we will share many more excellent moments. You are a great person who carries so much life energy that it is immediately transferred to one. I wish you all the best from my heart.

Sigi, thank you for your support over the past years. Your kindness has always motivated me and helped me out of some crises. I wish you a restful retirement, which you have earned.

Andreas and Birgit, thank you for your support regarding questions about the AFM or DLS.

A special thank you goes to my students with whom I have successfully worked on many projects. I thank you for your diligence, commitment, and curious questions, which often helped me. Thanks to Elena, Larissa, Jana, Fanny, Tuan, Cristina, Andres, and Sabrina.

Thank you to Elisabeth, Steffen, Siraphat, Philipp, Sascha, Sabrina, Maria, Theresa, Veronika, Irina, Maurice, Stephan, and Felix for correcting this work.

Irina and Cristina, we have experienced so many beautiful as well as exhausting times together. I found two new sisters at the university. We have already shared many beautiful moments. You are lovely, and I thank you for your great friendship and for always being there for me. I love you guys.

Theresa and Veronika, our monthly meeting, which we manage so far in a good way,

although we are so far away from each other, is dimmer and more beautiful, and I am happy to have found such great people at the university.

Away from the university, I would like to thank two people in particular. Nadine, I don't know what I would do without you. You are always there for me and got me through tough times. I thank you for your great understanding when I got into university work again. You are my soul mate. Thank you for just being there.

Maurice, I also thank you for your constant support, big heart, and weekly evenings after university. I will never forget our legendary bike rides. Thank you for always making time for me and being there for me.

Finally, I would like to thank my family. I thank my parents for their diligence and hard work that made it possible for me to get this far. I couldn't imagine better parents; your love and kindness are incredible. I thank my siblings Ewin and Cemil for everything. You are with me every second of my life and I thank you for the countless distracting conversations and non-sense discussions. I appreciate your support and love.

A big thanks goes to my cousin Nihal; you are a great role model for me. You go your way independently and courageously and have always been an inspiration for me since we were little. Sirma, even though you are no longer with us, I don't know how to put into words what you have always done for me. Your constant good humor and fighting spirit also motivated me and gave me the strength to make decisions I would not have dared to make without you. I miss you every second. But I am sure you are looking down on me with a glass of champagne and are celebrating.

Eidesstattliche Versicherung

Hiermit versichere ich an Eides statt, die vorliegende Dissertation selbst verfasst und keine anderen als die angegebenen Hilfsmittel benutzt zu haben. Die eingereichte schriftliche Fassung entspricht der auf dem elektronischen Speichermedium. Ich versichere, dass diese Dissertation nicht in einem früheren Promotionsverfahren eingereicht wurde.

Hamburg, 29.12.2022

Ort, Datum



Unterschrift